Kalisadhan Mukherjee
Rama Kanta Layek
Debasis De *Editors*

Tailored Functional Materials

Select Proceedings of MMETFP 2021

MOREMEDIA ▶

🦄 Springer

Springer Proceedings in Materials

Volume 15

Springer Proceedings in Materials publishes the latest research in Materials Science and Engineering presented at high standard academic conferences and scientific meetings. It provides a platform for researchers, professionals and students to present their scientific findings and stay up-to-date with the development in Materials Science and Engineering. The scope is multidisciplinary and ranges from fundamental to applied research, including, but not limited to:

- Structural Materials
- Metallic Materials
- Magnetic, Optical and Electronic Materials
- Ceramics, Glass, Composites, Natural Materials
- Biomaterials
- Nanotechnology
- Characterization and Evaluation of Materials
- Energy Materials
- Materials Processing

To submit a proposal or request further information, please contact one of our Springer Publishing Editors according to your affiliation:

European countries: **Mayra Castro** (mayra.castro@springer.com)
India, South Asia and Middle East: **Priya Vyas** (priya.vyas@springer.com)
South Korea: **Smith Chae** (smith.chae@springer.com)
Southeast Asia, Australia and New Zealand: **Ramesh Nath Premnath** (ramesh.premnath@springer.com)
The Americas: **Michael Luby** (michael.luby@springer.com)
China and all the other countries or regions: **Mengchu Huang** (mengchu.huang@springer.com)

This book series is indexed in **SCOPUS** database.

Kalisadhan Mukherjee · Rama Kanta Layek ·
Debasis De

Editors

Tailored Functional Materials

Select Proceedings of MMETFP 2021

Springer

Editors
Kalisadhan Mukherjee
Pandit Deendayal Energy University
Gandhinagar, India

Debasis De
RGIPT—Energy Institute Bengaluru
(Centre of Rajiv Gandhi Institute
of Petroleum Technology)
Bengaluru, India

Rama Kanta Layek
Department of Separation Science
School of Engineering Science
LUT University
Lahti, Finland

Symposium Organizers

Patron

Prof. S. Sundar Manoharan, Director General, PDEU

Vice Patron

Prof. Sunil Khanna, Director, School of Technology, PDEU

Chairmen

Prof. Rajib Bandyopadhyay, Head, Department of Chemistry, PDEU
Prof. A. R. Jani, Chairman, MRSI, Gujarat Chapter

Convener

Dr. Kalisadhan Mukherjee

Co-conveners

Dr. Satyam Mahendrarao Shinde
Dr. Balanagulu Busupalli
Dr. Prahlad K. Baruah

Theme Coordinator

Dr. Ankur Solanki
Dr. Mohendra Roy
Dr. Nandini Mukherjee
Dr. Rama Gaur

Treasurer

Dr. Tapan Pal
Dr. Vasudev Trivedi

Technical Committee

Dr. Ranjan Kumar Pati
Dr. Sheetal Rawat
Dr. Syed Sahabuddin
Dr. Anup V. Sanchela
Dr. Prakash Chandra
Dr. Nitin Chaudhari
Dr. Megha Balha
Dr. Anu Manhas
Mr. Abhishek Atulbhai Gor

Advisory Committee

Prof. Tarun Shah, Registrar, PDEU, India
Prof. Chaitanyamoy Ganguly, PDEU, India
Prof. Anurag Gupta, PDEU, India
Prof. S. B. Krupanidhi, President MRSI, IISc, Bengaluru, India
Prof. P. S. Anil Kumar, Chairman MRSI, IISc, Bengaluru, India
Prof. Suresh Das, Immediate Past President, MRSI, India
Prof. G. U. Kulkarni, JNCASR, Bengaluru, India
Prof. S. M. Shivaprasad, JNCASR, Bengaluru, India
Prof. Naga Hanumaiah, CMTI Bengaluru, India
Prof. Susanta Banerjee, IIT Kharagpur, India
Prof. Alika Khare, IIT Guwahati, India
Prof. Samit Kumar Ray, SNBNCBS, Kolkata, India

Prof. Tata Narasinga Rao, ARCI, Hyderabad, India
Prof. B. L. V. Prasad, NCL, Pune, India
Prof. Asim Bhaumik, IACS, Kolkata, India
Prof. Parameswar K. Iyer, IIT Guwahati, India
Prof. Ashish Garg, IIT Kanpur, India
Dr. Asit Kumar Das, Reliance Industries Limited, India

Preface

International Symposium on Materials of the Millennium: Emerging Trends and Future Prospects (MMETFP-2021) was organized by Pandit Deendayal Energy University (PDEU), Gandhinagar, India, in association with Materials Research Society of India, Gujarat Chapter, at PDEU campus during November 19–21, 2021. It was a hybrid mode (both online and on-campus) event involving more than 400 participants. MMETFP aimed to provide a platform to the researchers to unveil the complete potential of smart materials in disruptive technologies and help in tackling current and upcoming challenges of the millennium. The meticulous effort of each and every members of organizing team and whole-hearted contribution from participant have put forward toward making the event a successful one.

This book presents the select proceedings of MMETFP-2021. It discusses the synthesis, tailoring, and characterization of different materials for functional applications in various sectors which include, but not limited to, energy, environment, biomedical/health care, construction, transportation, etc. Topics covered in this book are synthesis and characterization of polymers, ceramics, composites, biomaterials, carbon-based nanostructures as well as materials for green environment, structural materials, modeling, and simulation of materials. We thank all the authors, reviewers, springer editorial board members for their careful efforts and valuable time toward arranging the articles for this proceeding.

Gandhinagar, India   Dr. Kalisadhan Mukherjee
Lahti, Finland   Dr. Rama Kanta Layek
Bengaluru, India   Dr. Debasis De

List of Reviewers

Dr. Prahlad Kumar Baruah, Pandit Deendayal Energy University, Gandhinagar, India
Dr. Subhasis Roy, University of Calcutta, Kolkata, India
Dr. Suvendu Manna, University of Petroleum and Energy Studies, Dehradun, India
Dr. Arpan Kumar Nayak, Vellore Institute of Technology, Vellore, India
Dr. K. Vipindas, IIITDM Kurnool, India
Dr. Sanjay Pratihar, CSIR-CSMCRI, Bhavnagar, India
Dr. Nandini Mukherjee, Pandit Deendayal Energy University, Gandhinagar, India
Dr. Anirban Das, Pandit Deendayal Energy University, Gandhinagar, India
Dr. Anu Manhas, Pandit Deendayal Energy University, Gandhinagar, India
Dr. Brijesh Tripathi, Pandit Deendayal Energy University, Gandhinagar, India
Dr. Tapan K. Pal, Pandit Deendayal Energy University, Gandhinagar, India
Dr. Dipanjan Sengupta, Institute of Nano Science and Technology, Mohali, India
Dr. Prosenjit Saha, JIS Institute of Advanced Studies and Research, Kolkata, India
Dr. Debasis De, Energy Institute Bengaluru (Centre of Rajiv Gandhi Institute of Petroleum Technology), Bengaluru, India
Dr. Rama Kanta Layek, LUT University, Finland
Dr. Chandi C. Malakar, NIT Manipur, India
Dr. Sumit Bhawal, Navrachana University, India
Dr. Mrityunjoy Mahato, North Eastern Hill University, India
Dr. Bipin Kumar Singh, Goel Institute of Technology and Management, India
Dr. Ashish Unnarkat, Pandit Deendayal Energy University, Gandhinagar, India
Dr. Rohit Srivastava, Pandit Deendayal Energy University, Gandhinagar, India
Dr. Rama Gaur, Pandit Deendayal Energy University, Gandhinagar, India
Dr. Adarsh Kumar Arya, University of Petroleum and Energy Studies, Dehradun, India
Dr. Ayan Mukherjee, CSIR-IMMT, India
Dr. Ankit Deshmukh, Pandit Deendayal Energy University, Gandhinagar, India
Dr. Ayyanna Habal, Pandit Deendayal Energy University, Gandhinagar, India
Dr. Shobhit Chaturvedi, Pandit Deendayal Energy University, Gandhinagar, India
Dr. Debashis Ghosh, CSIR-CMERI, Durgapur, India
Dr. A. A. Prasanna, Malnad College of Engineering, Hassan, Karnataka, India

Dr. Uma Chaduvula, Pandit Deendayal Energy University, Gandhinagar, India
Dr. Sheetal Rawat, Pandit Deendayal Energy University, Gandhinagar, India
Dr. Abhisek Maikap, IIT BHU, India
Dr. Kamalika Tiwari, Dr. B. C. Roy Engineering College, Durgapur, India
Dr. Rajat Saxena, Pandit Deendayal Energy University, Gandhinagar, India
Dr. Anu Manhas, Pandit Deendayal Energy University, Gandhinagar, India
Dr. Nakul Kumar, Sabarmati University, India
Dr. Satya Verma, GITM Lucknow, India
Dr. Ram Krishna Upadhyay, National Rail and Transportation Institute, India
Dr. Santosh S. Kolte, Alpha College of Engineering and Technology, Gujarat, India
Dr. Krunal Modi, Ganpat University, India

Contents

About the Editors

Dr. Kalisadhan Mukherjee is presently working as Assistant Professor at Pandit Deendayal Energy University, Gandhinagar, India. Dr. Mukherjee completed his M.Sc. in Chemistry from The University of Burdwan, India, in 2006 and Ph.D. from Indian Institute of Technology, Kharagpur, India, in 2012. After Ph.D., he was involved with the research and academic activities at CSIR-Central Mechanical Engineering Research Institute (CSIR-CMERI), Durgapur, India; Academy of Scientific and Innovative Research (AcSIR), New Delhi, India; and George Washington University, Washington DC, USA. His current research interests include nanomaterials, chemical sensor, photovoltaic, and adsorbents. He is Recipient of prestigious Fulbright-Nehru Postdoctoral fellowship from United States India Educational Foundation (USIEF); Inspire Faculty fellowship from Department of Science and Technology, Government of India; and Young Scientist in Materials Processing-2017 from Venus International Foundation. Dr. Mukherjee has published more than 50 articles in renowned peer-reviewed journals. He has supervised two Ph.D. theses. Two patents are in his credit. He is acting as Reviewer for various journals published by ACS, RSC, IOP, ECS, Elsevier, AIP, etc. Dr. Mukherjee is playing the role as Associate Editor, *Journal Frontiers in Materials* and *PlosOne.*

Dr. Rama Kanta Layek has been working as Assistant Professor in biopolymers and their utilizations at the Department of Separation Science, LUT University, Finland, since January 2021. Before that, he was working at Tampere University as Academy Postdoctoral Researcher. He has completed a Ph.D. from the Indian Association for the Cultivation of Science (Jadavpur University), Kolkata, in 2013. He has performed his postdoctoral research at Chonbuk National University, South Korea, and worked as Guest Scientist at Leibniz Institute for Polymer Research, Dresden, Germany. He has published two chapters and more than 40 research articles in internationally reputed scientific journals and presented his work in reputed scientific conferences. He is engaged in broad areas of polymer/biopolymer science and material chemistry. His main research interests are synthesis, processing and characterization of novel biopolymers and their composites, surface modification of biopolymers for biomedical applications, and surface functionalization of multifunctional fillers such as

graphene, boron nitride, MXene nanosheets and lignin, nanocellulose for fabrication of high-performance polymer/biopolymers composites, the structure–property relationship of polymer/biopolymer composites, valorization of lignocellulosic biomass-derived biopolymers, antibacterial biopolymers and textiles, gas barrier property of biopolymers and their composites for packaging application, and surface coating of nano-biocomposites for demanding applications.

Dr. Debasis De is currently working as Assistant Professor in Energy Institute, Bengaluru (Center of R.G.I.P.T, Jais, Amethi), India. After his undergraduate degree in Electronics and Telecommunication Engineering from Nagpur University and postgraduate degree in Nanoscience and Technology from Jadavpur University India, he earned Ph.D. degree in the area of Nanoscience and Technology from IIT Kharagpur in January 2012. Following a brief postdoctoral stint at University of Quebec at Chicoutimi, Quebec, Canada, in 2013, he served as Assistant Professor of Dr. B. C. Roy Engineering College, Durgapur, India. He was selected as one of the fourteen Indian student delegates to attend the JSPS-DST Asia Science Seminar held at Yokohama, Japan, in 2010. He has received Quebec Merit Scholarship for foreign student in 2012 from Ministère de l'Éducation, du Loisir et du Sport for a research visit at the Université du Québec à Chicoutimi (UQAC) in Chicoutimi, Québec, Canada. He is Active Member of the International Solar Energy Society and The Institute of Engineers (India). Dr. De has published more than 28 research publications in peer-reviewed journals and conference proceedings. He has attended and presented his research work in more than 15 international/national conferences/workshops. He has delivered invited talks in conferences/colleges. He has supervised four M.Tech. and ten B.Tech. theses. Currently, one Ph.D. and ten M.Tech. students are working under him. He is Editor of the preceding of Innovations in sustainable Energy and Technology, published in Springer book series—*Advances in Sustainability Science and Technology*. His current research interests include fabrication of dye sensitized, perovskite, and thin film solar cells, OER/HER by electrolysis or photocatalysis, fabrication of bio-inspired surfaces, nanostructures for electronics and advanced materials, and energy materials.

Sustainable Concrete Strength Prediction Using ARIMA Model

Pushpalatha Sarla, Sandela Hari Priya, Gobinath Ravindran, Manisha Shewale, and Archana Reddy

1 Introduction

Concrete is essential in the construction industry [1] because it is the only material that is regularly used in construction [2–5], and as a result, it plays a big role in the overall industry. The casting of concrete cubes with dimensions of 15 cm × 15 cm × 15 cm and three number blocks was the subject of this investigation. For the calibration of non-destructive testing equipment such as the rebound Hammer testing machine [6–10], the cubes were cast and allowed to cure for twenty-eight days before being utilized. It is a significant step up in sophistication to coring existing structures to determine the strength of the concrete. Several studies have demonstrated that the use of non-destructive techniques (NDM) is a viable choice [11–13] due to the advantages that it brings (e.g., lower cost, faster technique, etc.). For destructive testing (DT, for example, compressive test machine) and non-destructive testing (NDT, for example, rebound Hammer and ultrasonic pulse velocity (UPV), statistical analysis has been performed on specimens created under 7- and 28-day curing conditions for the purpose of relationship research. ARIMA, or autoregressive integrated moving average, is a mathematical formula that combines the notions of three different concepts: autoregression, moving average, and integration. It is also known as the ARIMA formula. ARIMA was developed in 1970 by Box and Jenkin and is still

P. Sarla
Department of Mathematics, Sumathi Reddy Institute of Technology for Women, Warangal, India

S. H. Priya · G. Ravindran
Department of Civil Engineering, SR University, Ananthasagar, Hasanparthy, Warangal, Telangana 506371, India

M. Shewale (✉)
Department of Civil Engineering, Dr. D. Y. Patil Institute of Technology, Pimpri, Pune, India
e-mail: manisha.surve1484@gmail.com

A. Reddy
Department of Mathematics, SR University, Warangal, India

in use today. Among the most accurate forecasting models available are short-term models such as ARIMA [14], and ARIMA is an active predictor that links past and present data with future projections [15]. The ARIMA model has been used to investigate a vast range of micro- and macro-dynamics that have been separated from one another. A smartphone application with a fever GPS to plan, control, and warn people away from high-risk regions was developed by SOMBONSAK, who combined the ARIMA model with innovation [16] to achieve his goal of combining the ARIMA model and innovation. He used the ARIMA model to forecast the predicted amount of people with particular forms of fever based on the distribution of people in different locations, and he used a smartphone application with a fever GPS to plan, control, and warn people away from potentially dangerous areas. Jiang and Zhang devised an ARIMA–ANN model, which is a hybrid model that combines ARIMA and an artificial neural network, in order to improve the stock price forecast of highly developed capital markets [17]. A statistical and computational technique created by Arifin and Habibie that blends ARIMA with a disruptive formula to enable more accurate cellular data traffic forecasting in a future dominated by disruptive technologies is described in detail in the paper [14]. Also, noteworthy is that the ARIMA model is a significant participant in the world of challenging financial instruments, such as cryptocurrencies [18].

2 Materials and Methods

2.1 Time Series Data Description

The compressive strength of concrete can be found by two methods; one is destructive method, and another is non-destructive method [19–21]. Rebound Hammer test is one of the non-destructive methods to find out the compressive strength of concrete. Non-destructisve techniques are easy to carry experiments compared to destructive methods because these will not disturb or dismantle the concrete structures. In this study, three concrete blocks have been prepared and immersed in fresh and clean water for curing for twenty-eight days. After the curing period is finished, the concrete blocks have been removed from water and cleaned so that it is free from the moisture content. Then, by using the rebound Hammer test, the compressive strength of each concrete block has been determined up to the seventy-fifth hours, and ninety hours is predicted by using the ARIMA model (Fig. 1).

Table 1 presents the descriptive statistics for Blocks-1, 2, and 3. As mentioned in Sect. 1, the data for each block consist of 75 h.

Fig. 1 Representing the curing of concrete blocks

2.2 Autoregressive Integrated Moving Average Process

In electrical engineering, the auto-regressive integrated moving average (ARIMA) is an adaption of discrete-time filtering algorithms established in the 1930s and 1940s (Norbert Wiener et al.). In the 1970s, statisticians George Box and Gwilym Jenkins devised systematic ways for applying them to business and economic data (hence the term "Box–Jenkins models"). Box and Jenkins models are still in use today.

Moving average processes are defined as those in which the dependent variable is regressed on current and lagged error terms and the dependent variable is then estimated through the use of a constant and a moving average of the error terms. If you run a regression on the dependent variable with one lagged error term, you will see that it follows a first-order moving average process, which is indicated by the letter MA (1). Furthermore, a model with q number of error components is subjected to a qth-order moving average process, which is denoted by the symbol MA (q). A MA(q) process can be defined as follows:

$$Y_t = \mu + \beta_0 \mu_t + \beta_1 \mu_{t-1} + \beta_2 \mu_{t-2} + \ldots + \beta_q \mu_{t-q} \tag{1}$$

This assumes white noise for the error terms and a constant for the constant (Gujarati and Porter 2008). A MA model's error term is typically scaled to make _0

Table 1 Descriptive statistics of Block-1, Block-2, and Block-3

Block-1			Block-2		Block-3	
Hours	Compressive strength	Density	Compressive strength	Density	Compressive strength	Density
1	28.66	2248.504	30.33	2296.951	16.2	2331.148
2	34.36	2343.934	22.8	2385.159	16.85	2388.104
3	32.56	2318.589	19.13	2327.262	17.4	2353.281
4	33.83	2355.713	24.13	2367.491	15.73	2408.716
5	39.96	2322.674	20.23	2340.116	23.96	2366.279
6	32.56	2319.093	37.63	2412.961	21.96	2380.122
7	34.9	2465.288	37.6	2489.972	20	2526.998
8	34.22	2221.912	30.23	2235.886	21.66	2221.912
9	33.82	2252.096	24	2254.987	16.25	2252.096
10	34.35	2515.024	25	2373.798	18.23	2515.024
11	33.13	2402.402	23	2432.432	32.14	2402.402
12	36.6	2385.727	30.23	2338.543	17.25	2388.676
13	34.63	2383.635	34.56	2371.776	22.14	2389.564
14	32.61	2345.029	32.25	2342.105	18.25	2397.661
…	…	…	…	…	…	…
…	…	…	…	…	…	…
74	26.83	2480.401	27.36	2480.401	19.54	2555.66
75	32.82	2463.145	30.23	2463.145	20.87	2509.214

equal to one in order to achieve this (Chatfield 2003). Because the dependent variable frequently exhibits characteristics of both the autoregressive and the moving average processes, it is conceivable to combine the two processes. An autoregressive and moving average procedure, often known as ARMA, is used to achieve this result. It is designated ARMA (1, 1) and defined as follows if both of the underlying AR and MA models are of the first order.

$$Y_t = \theta + \alpha_1 Y_{t-1} + \beta_0 \mu_t + \beta_1 \mu_{t-1} \tag{2}$$

where θ is the constant (Fig. 2).

Fig. 2 ARIMA model flow chart
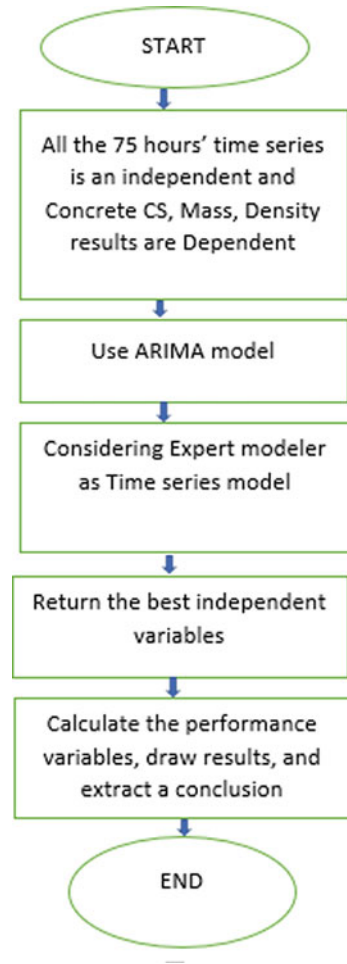
3   Results and Discussion

3.1   Stationarity Checking

After running a sequential plot for the real data of mass, compressive strength and density results of concrete separately on the *y*-axis and time on the *x*-axis for three number blocks, it was discovered that the data were non-seasonal and stationary, and that the ARIMA model could be used for further forecasting. Figures 3, 4, and 5 provide an example of this. There is no continuous trend line since, according to the time, there were ups and downs in different ways for blocks 1, 2, and 3. It has been found that their statistical properties are not constant with time.
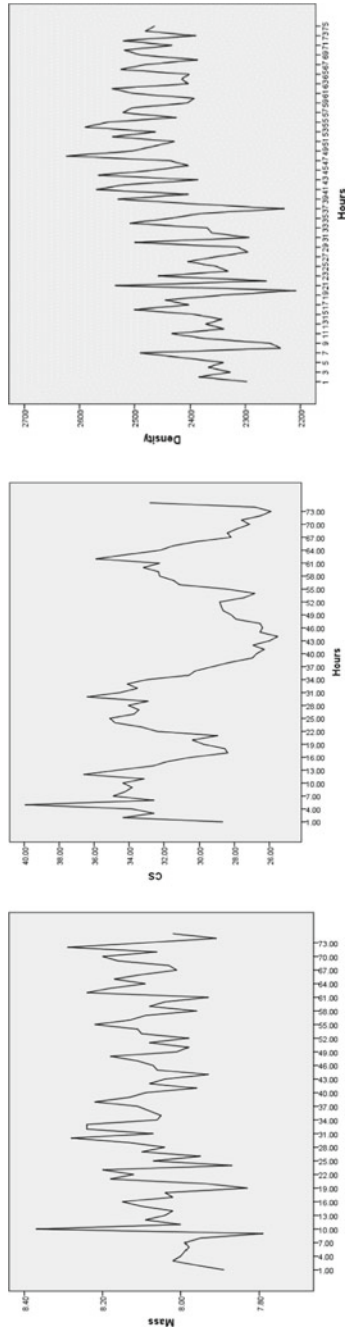
Fig. 3 Sequence plots of mass, compressive strength, density of Block-1 for 75 days
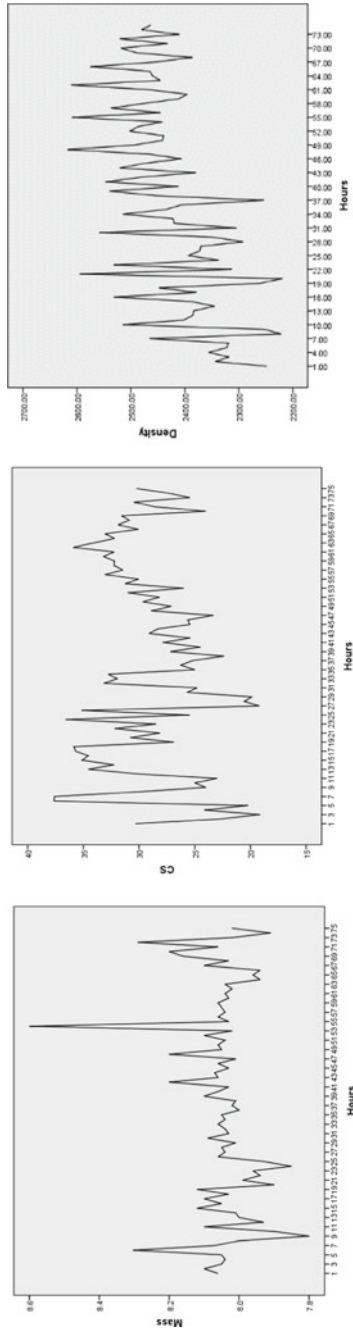
Fig. 4 Sequence plots of mass, compressive strength, density of Block-2 for 75 days
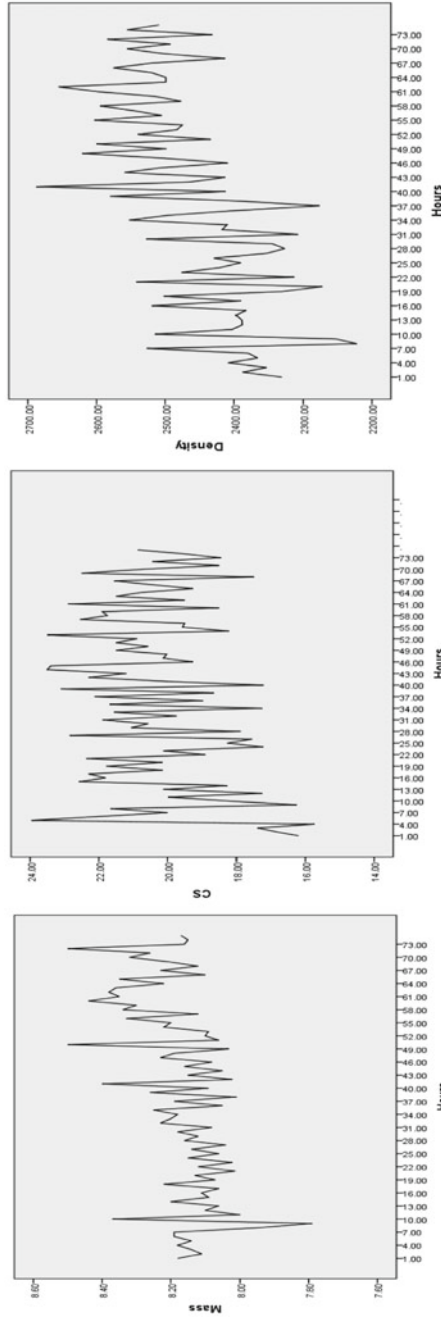
Fig. 5 Sequence plots of mass, compressive strength, density of Block-3 for 75 days

Table 2 Model description

			Model type
Model ID	Mass	Model_1	ARIMA(0,1,14)
	CS	Model_2	ARIMA(0,1,14)
	Density	Model_3	ARIMA(0,1,14)

3.2 Modelling Block-1 Time Series Data of Mass, CS, Density of Concrete

The best-fitted ARIMA model for the data, according to the expert modeler, is an ARIMA (0,1,14). The model includes zero autoregressive components, one moving average component, and is integrated of the fourteenth order. The purpose of the natural logarithmic transformation is to reduce the influence of outliers. Since the natural logarithmic transformation is applied to the data and the ARIMA model is integrated of the first order, the right side of the equation forecasts the rate of return between two periods. In order to forecast a period, the previous period has to be moved from the left side to the right side of the equation. The Ljung–Box–Jenkins methodology is followed to validate the chosen model. Table 2 shows the appropriate results that reveal the best ARIMA model can be formulized as ARIMA (0,1,14) using expert modeler in SPSS.

In Table 3, Stationary R^2 value specifies the high degree of correlation between the dependent variable is 0.859 (mass, CS, density) able to describe by the predictor variable (time). Also, it showed root mean square error, maximum absolute prediction error, maximum absolute error for mean and standard deviation and percentiles for each of the statistics.

Table 4 shows the model fit statistics with R^2 values (represents the percentage of variation between the dependent variables) are 0.859, 0.904, 0.953 for mass compressive strength and density using Ljung–Box test statistics clearly reveal that those are closure to 1 ($0 \leq R \leq 1$) it means that corresponding model best fits the data and indicates there is no significant difference of dependent variable values like mass, CS, density of Block-1 with 4 degrees of freedom, and the significant values 0.023, 0.036, 0.003 which are strictly less than the *p*-value, i.e., 0.05 level of significance.

We have the data for 75 h of mass, CS, density test results of concrete would like to predict up to 90 h. Table 5 shows the forecast results of each model; there are upper- and lower-control limits for each forecast results.

In Fig. 6, a visual demonstration of the fitted values in relation to the observed values for Block-1 is illustrated. Also, it displays the Block-1 forecasts.

When the data are in non-seasonality, the ARIMA comes into picture most effectively; more or less replicating the observed data, there are some ups and downs for Block-1 test results of concrete showed in Fig. 7. Also the patterns that has been exhibited for predicted and observed data almost unique using appropriate ARIMA model fitting using SPSS tool.

Table 3 Model fit for Block-1 concrete test results

Fit statistic	Mean	SE	Minimum	Maximum	Percentile							
					5	10	25	50	75	90	95
Stationary R-squared	0.859	0.197	0.774	0.953	0.774	0.774	0.774	0.859	0.6953	0.953	0.953
R-squared	0.428	0.270	0.188	0.721	0.188	0.188	0.188	0.374	0.721	0.721	0.721
RMSE	27.726	46.307	0.107	81.187	0.107	0.107	0.107	1.884	81.187	81.187	81.187
MAPE	2.418	1.508	0.909	3.925	0.909	0.909	0.909	2.419	3.925	3.925	3.925
MaxAPE	10.205	6.058	4.643	16.660	4.643	4.643	4.643	9.312	16.660	16.660	16.660
MAE	19.958	33.437	0.073	58.561	0.073	0.073	0.073	1.238	58.561	58.561	58.561
MaxAE	70.917	117.569	0.389	206.639	0.389	0.389	0.389	5.725	206.639	206.639	206.639
Normalized BIC	2.734	6.655	−3.604	9.666	−3.604	−3.604	−3.604	2.140	9.666	9.666	9.666

Table 4 Ljung–Box test statistics for mass, CS, density of Block 1 concrete

Model statistics				
Model	Model fit statistics	L Jung–Box Q (18)		
	Stationary R-squared	Statistics	DF	Sig.
Mass-Model _1	0.859	7.423	4	0.023
CS-Model _2	0.904	10.297	4	0.036
Density-Model _3	0.953	5.955	4	0.003

Table 6 shows the appropriate results that reveals the best ARIMA model can be formulized as ARIMA (0,1,14) using expert modeler in SPSS. In Table 7 Stationary R^2 value specifies the high degree of correlation between the dependent variables such as mass, CS, density. Also, showed root mean square error, maximum absolute percentage error, maximum absolute error for mean, and standard deviation and percentiles for each of the statistics. Here mean squared error i.e stationary R-squared is 0.492 is acceptable for fitted model. The adequacy model was confirmed by exploring the Normalized Bayesian Information Criterion. In class of significant ARIMA(p,d,q) models fitted statistically to the data, the ARIMA(0,1,14) model had the least BIC value of −3.520.

Table 8 showed the model fit statistics with R^2 values 0.492 is acceptable, 0.832 and 0.917 are indicates a good fit for the model using Ljung–Box test statistics its clearly reveal that there is no significant difference of dependent variable values like Mass, CS, Density of Block-1 with 4 degrees of freedom and the significant values 0.000, 0.012, 0.031 which is strictly less than the p-value i.e., 0.05 level of significance. The Ljung–Box test (named after Greta M. Ljung and George E. P. Box) is a statistical test that determines whether any of a collection of time series autocorrelations is different from zero. It is a portmanteau test since it examines "overall" randomness based on a lot of lags rather than assessing randomness at each individual lag. In this work, we had used Ljung–Box test to predict the mass, compressive strength, and also density of concrete which shows significant values in prediction.

Table 9 shows the forecast results of each model; there are upper and lower control limits for each forecast results. Figure 8, a visual demonstration of the fitted values in relation to the observed values for Block-1, is illustrated. Also, it displays the Block-1 forecasts. Block-2 test results of concrete are shown in Fig. 9. Also the patterns in green line is predicted values and blue is observed values from Fig. 9 the lines, that has been exhibits almost accurately unique using appropriate ARIMA model fitting using SPSS tool. Table 10 shows the model fit statistics for Block-3 interpreted R-squared values as 0.62 approximately indicates the good fit for ARIMA(0,1,14). The Normalized Bayesian Information criterion is −3.36 approximately for some percentile values shows data best fit for the fitted model.

Table 11 showed the model fit statistics with R^2 values using Ljung–Box test statistics are 0.98, 0.100 and 0.91 its clearly reveal that there is no significant difference of dependent variable values like Mass, CS, Density of Block-3, also the test

Table 5 Forecasted results along with upper and lower limits of concrete test results of Block-1

Model		76	77	78	79	80	81	82	83	84	85	86	87	88	89	90
Mass-Model_1	Forecast	8.08	8.13	8.16	8.12	8.04	7.96	8.02	8.13	8.11	8.17	8.1	8.1	8.1	8.12	8.12
	UCL	8.28	8.33	8.36	8.32	8.25	8.17	8.25	8.38	8.37	8.43	8.36	8.36	8.36	8.39	8.39
	LCL	7.89	7.93	7.96	7.92	7.84	7.76	7.8	7.88	7.86	7.91	7.84	7.84	7.84	7.86	7.86
CS-Model_2	Forecast	32.34	34.24	34.3	32.61	32.46	33.69	31.3	33.16	32.98	31.83	30.76	29.18	28.63	29.8	29.27
	UCL	35.64	38.49	39.31	38.6	38.82	40.25	38.62	40.57	40.66	39.8	38.83	37.31	36.81	37.94	37.91
	LCL	29.04	29.98	29.28	26.62	26.1	27.13	23.99	25.75	25.3	23.87	22.69	21.05	20.56	21.66	21.63
Density-Model_3	Forecast	2482.4	2491.8	2467.3	2467.3	2438.9	2500.2	2430	2516.3	2452.1	2508.6	2477.76	2496.2	2490.3	2493.2	2495.2
	UCL	2637.6	2650.6	2629.5	2629.5	2602.4	2669.2	2602	2692.7	2629.6	2693.4	2662.64	2686.6	2680.7	2685.2	2688.6
	LCL	2327.1	2332.9	2305.1	2305.1	2275.4	2331.1	2257.9	2339.8	2274.6	2323.8	2292.88	2305.9	2999.9	2301.1	2301.8
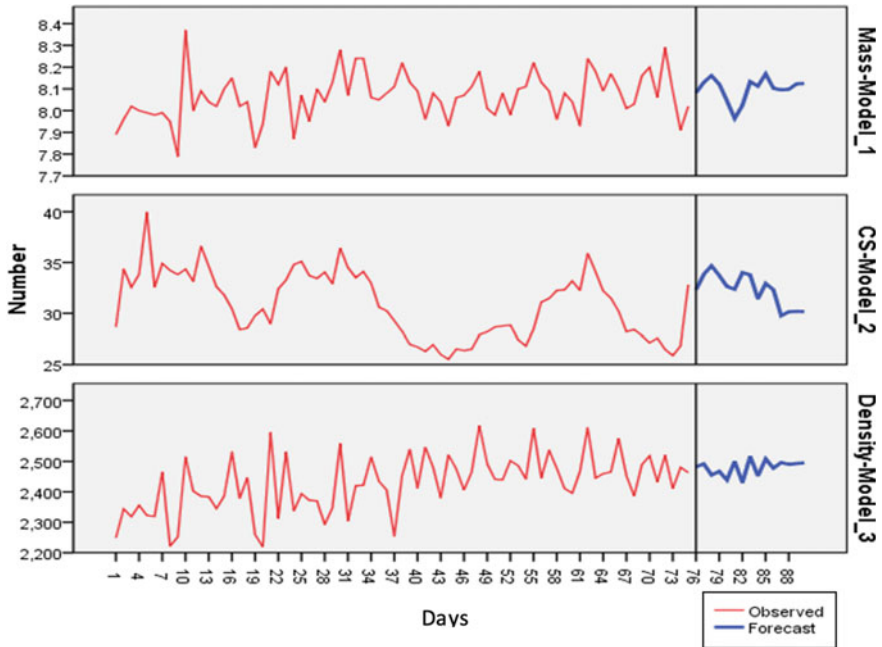
Fig. 6 Sequence chart of Block-1 results of observed and forecasted models

statistics using Ljung–Box Statistics indicates 19.274, 17.385 and 15.540 with 15 degrees of freedom and the significant values 0.002,0.001, 0.02 which is strictly less than the p-value is 0.05 level of significance. Therefore the hypothesis for the Block-3 data strictly acceptable for the fitted model. Table 12 shows the forecast results of each model; there are upper and lower control limits for each forecast results.

In Fig. 10, a visual demonstration of the fitted values in relation to the observed values for Block-3 is illustrated. Also, it displays the Block-3 forecasts. There are some ups and downs for Block-1 test results of concrete showned in Fig. 11. Also the patterns that has been exhibits the forcast almost accurately same for observed values (blue line) and predicted values (green line) using appropriate ARIMA model fitting using SPSS tool.

In the world of software engineering, a sequence diagram, also known as a system sequence diagram (SSD), depicts object interactions in temporal order. It represents the scenario's objects as well as the sequence of messages exchanged between them in order to carry out the scenario's functionality. In the logical view of the system under development, sequence diagrams are usually coupled with use case realizations. Event diagrams and event scenarios are other names for sequence diagrams. Figure 10 provides the sequence plot used in this study which shows the correlation between observed and forecast plots. Forecasted values show good correlation and matching from the observed values, and hence, this can be effectively used to predict the compressive strength of concrete.
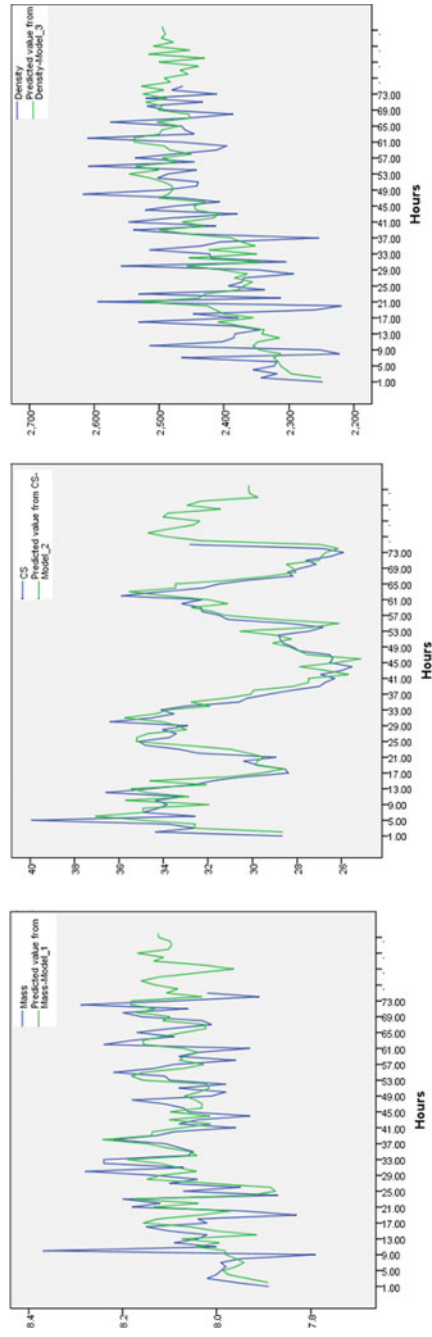
Fig. 7 Predicted and observed model of Block-1

Table 6 Model description for Block-2

Model ID	Mass	Model_1	Model type ARIMA(0,1,14)
	CS	Model_2	ARIMA(0,1,14)
	Density	Model_3	ARIMA(0,1,14)

Table 7 Model fit for Block-2 concrete test results

Fit statistic	Mean	SE	Minimum	Maximum
Stationary R-squared	0.492	0.063	0.432	0.557
R-squared	0.241	0.130	0.094	0.341
RMSE	29.492	47.427	0.111	84.206
MAPE	4.687	5.260	0.839	10.681
MaxAPE	17.785	18.206	5.522	38.705
MAE	21.480	34.640	0.068	61.445
MaxAE	71.475	112.806	0.475	201.550
Normalized BIC	3.314	6.639	−3.520	9.739

Fit statistic	Percentile						
	5	10	25	50	75	90	95
Stationary R-squared	0.432	0.432	0.432	0.487	0.557	0.557	0.557
R-squared	0.094	0.094	0.094	0.290	0.341	0.341	0.341
RMSE	0.111	0.111	0.111	4.159	84.206	84.206	84.206
MAPE	0.839	0.839	0.839	2.542	10.681	10.681	10.681
MaxAPE	5.522	5.522	5.522	9.128	38.705	38.705	38.705
MAE	0.068	0.068	0.068	2.927	61.445	61.445	61.445
MaxAE	0.475	0.475	0.475	12.402	202.550	202.550	202.550
Normalized BIC	−3.520	−3.520	−3.520	3.723	9.739	9.739	9.739

Table 8 Ljung–Box test statistics for mass, CS, density of Block-2 concrete

Model	Model fit statistics	Ljung–Box Q(18)		
	Stationary R-squared	Statistics	DF	Sig
Mass-Model_1	0.492	4.286	4	0.000
CS-Model_2	0.832	4.506	4	0.012
Density-Model_3	0.917	3.233	4	0.031

4   Conclusion

The research was centered on a statistical analysis of 75 h of data from concrete blocks in the areas of mass, compressive strength, and density, respectively. For the

Table 9 Forecasted results along with upper and lower limits of concrete test results of Block-2

Model		76	77	78	79	80	81	82	83
Mass-Model_1	Forecast	8.05	8.01	8.00	8.01	8.11	8.12	8.06	8.12
	UCL	8.26	8.23	8.22	8.23	8.33	8.34	8.28	8.235
	LCL	7.83	7.80	7.78	7.79	7.89	7.9	7.83	7.9
CS-Model_2	Forecast	27.59	29.13	31.16	28.87	28.26	29.28	30.98	30.33
	UCL	35.17	37.26	40.23	37.96	37.7	38.54	40.53	40.06
	LCL	20.01	21.00	22.1	19.79	19.53	20.02	21.42	20.6
Density-Model_3	Forecast	2501.3	2498.6	2512.11	2523.89	2496.2	2516.6	2504	2508.2
	UCL	2665.4	2663.2	2677.17	2689.11	2662.3	2684.9	2673.5	2679.1
	LCL	2337.2	2334	2347.05	2358.66	2330.2	2348.3	2334.5	2337.4

Model		84	85	86	87	88	89	90
Mass-Model _1	Forecast	8.11	8.06	8.04	8.06	8.08	8.08	8.08
	UCL	8.34	8.28	8.27	8.30	8.32	8.31	8.31
	LCL	7.89	7.83	7.81	7.83	7.84	7.84	7.84
CS-Model _2	Forecast	28.92	31.36	31.16	29.29	29.48	29.96	29.97
	UCL	39.06	41.56	41.39	39.52	39.97	40.49	40.51
	LCL	18.78	21.15	20.94	19.06	19	19.42	19.42
Density -Model _3	Forecast	2503.2	2516.5	2513.1	2518	2519.1	2525.9	2527.9
	UCL	2675.4	2695.1	2692.4	2697.4	2699.2	2706.8	2708.8
	LCL	2330.9	2337.9	2333.8	2338.6	2339.1	2344.9	2346.9
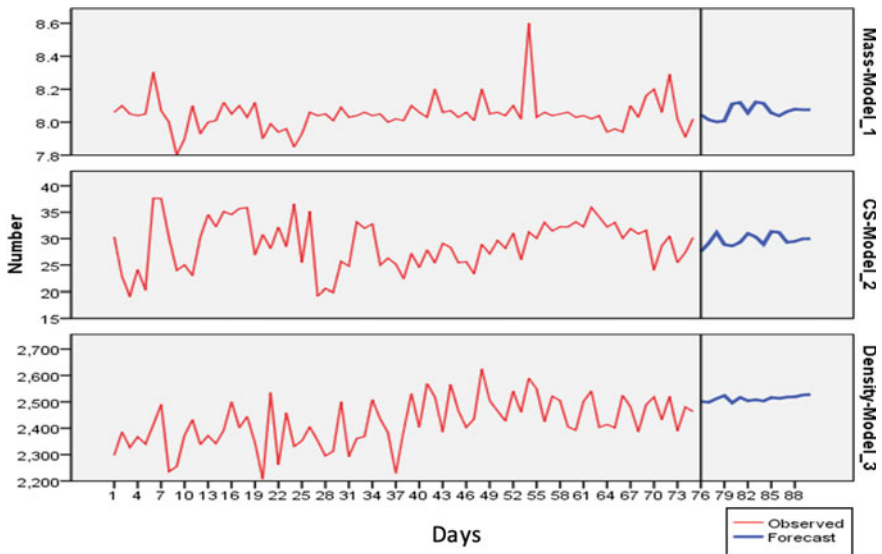
Fig. 8 Sequence chart of Block-2 results of observed and forecasted models
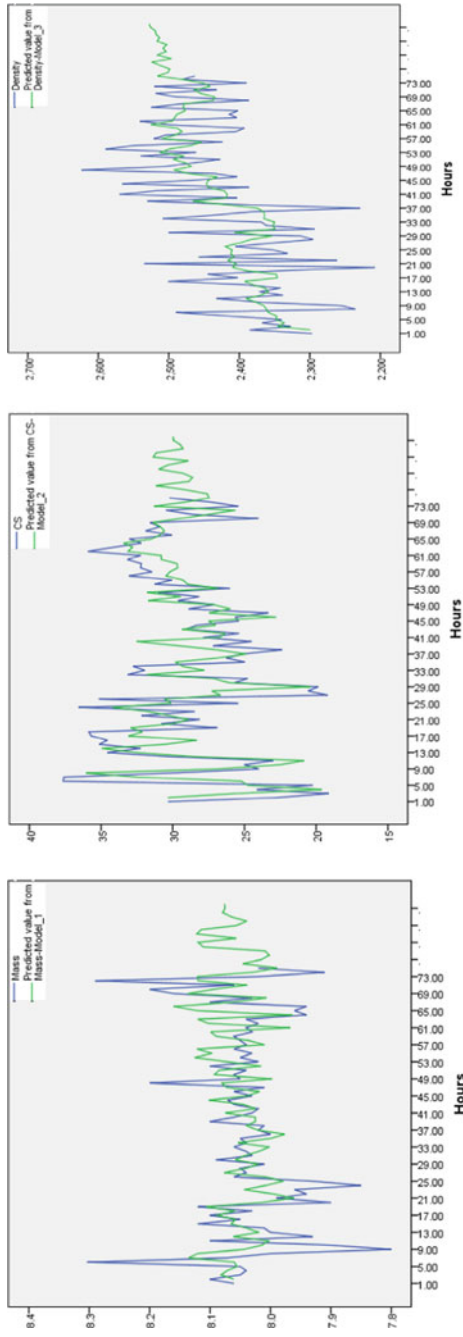
Fig. 9 Predicted and observed model of Block-2

Table 10   Model fit for Block-3 concrete test results

Model					
Fit statistics	Mean	SE	Minimum	Maximum	Percentile
					5
Stationary R Squared	0.628	0.012	0.616	0.64	0.616
R Squared	0.278	0.171	0.106	0.448	0.106
RMSE	28.001	46.226	0.12	81.36	0.12
MAPE	3.491	3.267	0.976	7.184	0.976
MaxAPE	15.152	15.478	4.794	32.944	4.794
MAE	19.423	32.265	0.08	56.67	0.08
MaxAE	66.314	105.49	0.373	187.979	0.373
Normalized BIC	3.009	6.523	−3.366	9.67	−3.366
Model					
Fit statistics					
	10	25	50	75	90	95
Stationary R Squared	0.616	0.616	0.63	0.64	0.64	0.64
R Squared	0.106	0.106	0.28	0.448	0.45	0.45
RMSE	0.12	0.12	2.52	81.36	81.4	81.4
MAPE	0.976	0.976	2.31	7.184	7.18	7.18
MaxAPE	4.794	4.794	7.72	32.94	32.9	32.9
MAE	0.08	0.08	1.52	56.67	56.7	56.7
MaxAE	0.373	0.373	10.6	188	188	188
Normalized BIC	−3.366	−3.37	2.72	9.67	9.67	9.67

Table 11   Model statistics (Ljung–Box test)

Model	Model fit statistics	Ljung–Box Q(18)		
	Stationary R-squared	Statistics	DF	Sig
Mass-Model_1	0.98	19.274	15	0.002
CS-Model_2	0.100	17.385	15	0.001
Density-Model_3	0.91	15.540	15	0.002

purposes of this work, the expert modeler in SPSS was used to estimate the most well-fitting ARIMA models for Block-1, Block-2, and Block-3. It has been determined that the ARIMA model ARIMA (0,1,14) is the most appropriate for simulating and forecasting and that the MPE and MAPE were computed using the out-of-sample forecasts and the actual outcomes, allowing for comparison with inferior fitted models and models used in previous studies. The Ljung–Box–Jenkins methodology was used to validate the models. When the expert modeler calculates a suitable ARIMA model

Table 12 Forecasted results along with upper and lower limits of concrete test results of Block-3

Model		76	77	78	79	80	81	82	83
Mass-Model _1	Forecast	8.23	8.23	8.2	8.25	8.28	8.34	8.3	8.25
	UCL	8.46	8.46	8.43	8.49	8.53	8.59	8.55	8.5
	LCL	8.00	8.00	7.96	8.02	8.04	8.09	8.06	8.0
CS-Model _2	Forecast	20.34	19.8	18.8	19.88	19.73	19.61	21.76	20.61
	UCL	24.85	24.26	23.19	24.39	24.22	24.37	27.87	26.13
	LCL	16.18	15.7	14.77	15.73	15.59	15.24	16.65	15.59
Density - Model _3	Forecast	2559.5	2585.76	2565.6	2591	2588.1	2642.7	2572.9	2619.1
	UCL	2719.5	2746.95	2728.9	2755	2752.4	2811.8	2740.6	2788.4
	LCL	2403.2	2428.25	2406	2430	2427.6	2477.5	2409.2	2453.9
Model		84	85	86	87	88	89	90	
Mass-Model _1	Forecast	8.26	8.23	8.27	8.31	8.3	8.29	8.3	
	UCL	8.52	8.49	8.53	8.58	8.57	8.56	8.56	
	LCL	8.02	7.97	8.01	8.05	8.04	8.03	8.03	
CS-Model _2	Forecast	20.74	20.05	20.44	20.42	20.67	20.94	20.95	
	UCL	26.45	25.72	26.19	26.16	26.65	27.04	27.06	
	LCL	15.57	14.92	15.25	15.23	15.28	15.44	15.45	
Density - Model _3	Forecast	2577.99	2610.4	2621.1	2585.7	2614	2605.99	2608.9	
	UCL	2749.9	2780.4	2793.1	2757.3	2788.2	2786.96	2790	
	LCL	2414.08	2444.4	2453.3	2418.4	2444.1	2429.61	2432.4	

for a time series, the process was followed. By using line charts as a graphical tool to analyse the data, the researchers discovered that the ARIMA models had the same p, d, and q values, which confirmed the suggested models. Furthermore, the Ljung–Box statistic was used to verify the residuals of the models to ensure that they were within acceptable limits. The validation of the suggested models using the Box–Jenkins approach demonstrates that the expert modeler was an appropriate tool for estimating ARIMA models for the time series in question, which supports this conclusion. Recently, it has been discovered that the observed and anticipated values are extremely similar to one another. Using the statistical parameters stationary R2, R2, root mean square error (RMSE), mean absolute percentage error (MAPE), and normalized Bayesian information criterion (BIC), we tested the validity and applicability of the developed ARIMA models. The results revealed that the models fit reasonably well with the observed data series, indicating that the models are valid and applicable. Further methods for confirming the applicability and correctness of the ARIMA models constructed using different single-noise metric combinations include the Ljung–Box analysis and the standardized residual error analysis.
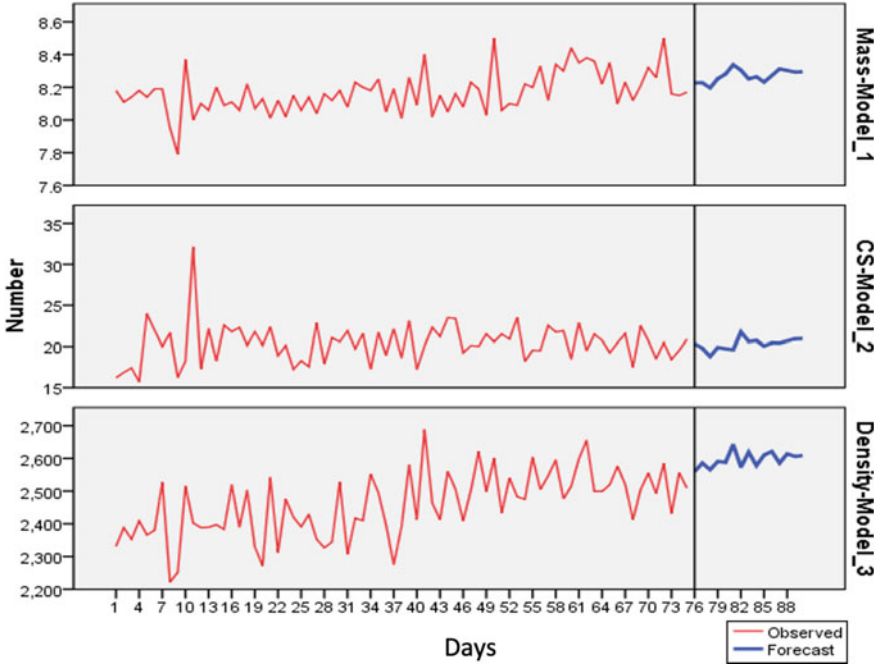
Fig. 10 Sequence chart results of observed and forecasts
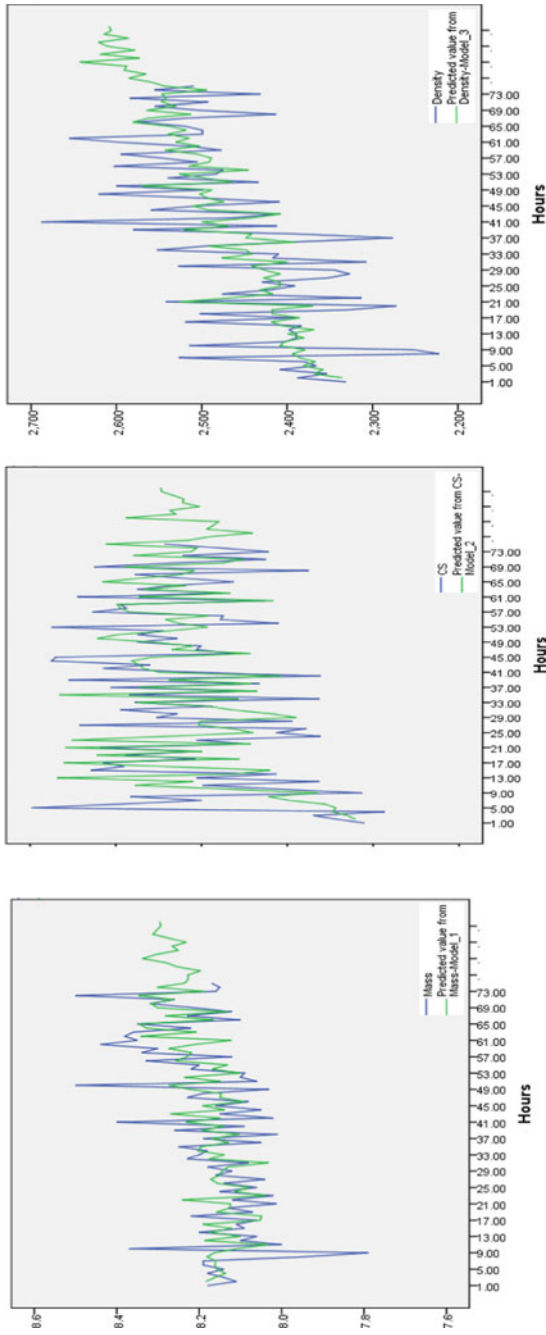
Fig. 11 Predicted and observed model of Block-3

References

1. Saleem M, Al-Kutti WA, Al-Akhras NM, Haider H (2016) Non-destructive testing procedure to evaluate the load-carrying capacity of concrete anchors. J Constr Eng Manag 142(5):04015104. https://doi.org/10.1061/(asce)co.1943-7862.0001105
2. Juimo Tchamdjou WH, Cherradi T, Abidi ML, Pereira-de-Oliveira LA (2018) Mechanical properties of lightweight aggregates concrete made with Cameroonian volcanic scoria: destructive and non-destructive characterization. J Build Eng 16:134–145. https://doi.org/10.1016/j.jobe.2018.01.003
3. Khan MDI, Abdy Sayyed MA, Yadav GS, Varma SH (2020) The impact of fly ash and structural fiber on the mechanical properties of concrete. Mater Today Proc :0–4. https://doi.org/10.1016/j.matpr.2020.08.242
4. Prasanna EL, Tipraj B, Haripriya S, Khan M, Gobinath R (2019) Mechanical properties of fly ash based concrete aided with recycled aggregates and manufactured sand. Int J Recent Technol Eng 8(4):9848–9851. https://doi.org/10.35940/ijrte.d9138.118419
5. Khan I, Challa B, Haripriya Varma S, Sayyed MAA (2019) Sorptivity and durability assessment of dolomite impregnated ternary concrete. Int J Recent Technol Eng 8(2). https://doi.org/10.35940/ijrte.B2896.078219
6. Ikramullahkhan Haripriya Varma S (2020) Strength characteristics of recycled aggregate concrete by Ann. Int J Innov Technol Explor Eng 9(3):1210–1214. https://doi.org/10.35940/ijitee.c8624.019320
7. Poorarbabi A, Ghasemi M, Azhdary Moghaddam M (2020) Concrete compressive strength prediction using neural networks based on non-destructive tests and a self-calibrated response surface methodology. J Nondestruct Eval 39(4. https://doi.org/10.1007/s10921-020-00718-w
8. Müller P, Novák J, Holan J (2019) Destructive and non-destructive experimental investigation of polypropylene fibre reinforced concrete subjected to high temperature. J Build Eng 26:100906. https://doi.org/10.1016/j.jobe.2019.100906
9. Hatır ME, Korkanç M, Başar ME (2019) Evaluating the deterioration effects of building stones using NDT: the Küçükköy Church, Cappadocia Region, Central Turkey. Bull Eng Geol Environ 78(5):3465–3478. https://doi.org/10.1007/s10064-018-1339-x
10. Qurashi MA et al (2019) Sustainable design and engineering: a relationship analysis between digital destructive and non-destructive testing process for lightweight concrete. Processes 7(11). https://doi.org/10.3390/pr7110791
11. Hover KC (2019) Case studies of non-destructive test results and core strengths at age of 3-days. Constr Build Mater 227:116672. https://doi.org/10.1016/j.conbuildmat.2019.116672
12. Craeye B, van de Laar H, van der Eijk J, Gijbels W, Lauriks L (2017) On-site strength assessment of limestone based concrete slabs by combining non-destructive techniques. J Build Eng 13:216–223. https://doi.org/10.1016/j.jobe.2017.08.006
13. Lasisi A, Sadiq MO, Balogun I, Tunde-Lawal A, Attoh-Okine N (2019) A boosted tree machine learning alternative to predictive evaluation of nondestructive concrete compressive strength. In: Proceedings—18th IEEE international conference machine learning application. ICMLA 2019, pp 321–324. https://doi.org/10.1109/ICMLA.2019.00060
14. Arifin AS, Habibie MI (2020) The prediction of mobile data traffic based on the ARIMA model and disruptive formula in industry 4.0: a case study in Jakarta, Indonesia. Telkomnika 18:907–918
15. Kim S, Heo J-M (2017) Time series regression-based pairs trading in the Korean equities market. J Exp Theor Artif Intell 29:755–768
16. Somboonsak P (2020) Development innovation to predict dengue affected area and alert people with smartphones. Int J Online Biomed Eng (IJOE) 16:62–79
17. Jiang X-Q, Zhang L-C (2019) Stock price fluctuation prediction method based on time series analysis. Discret Contin Dyn Syst-S 12:915–927
18. Abu Bakar SRN (2017) Autoregressive Integrated Moving Average (ARIMA) model for forecasting cryptocurrency exchange rate in high volatility environment: a new insight of bitcoin transaction. Int J Adv Eng Res Sci 4:130–137

19. Fattahi H (2017) Applying soft computing methods to predict the uniaxial compressive strength of rocks from schmidt hammer rebound values. Comput Geosci 21(4):665–681. https://doi.org/10.1007/s10596-017-9642-3

20. Tan Y, Yu H, Mi R, Zhang Y (2018) Compressive strength evaluation of coral aggregate seawater concrete (CAC) by non-destructive techniques. Eng Struct 176:293–302. https://doi.org/10.1016/j.engstruct.2018.08.104

21. Kocáb D, Misák P, Cikrle P (2019) Characteristic curve and its use in determining the compressive strength of concrete by the rebound hammer test. Materials (Basel) 12)(7). https://doi.org/10.3390/ma12172705

3D Thermal Spike Simulation: Swift Heavy Ion Irradiation of Embedded a-SiC Nano-Zone Inside 4H-SiC

Anusmita Chakravorty, Ch Dufour, and Debdulal Kabiraj

1 Introduction

Silicon carbide (SiC) has shown tremendous potential for high-temperature and high-radiation applications and is being investigated as a possible option for reactor core components and structural materials [1]. Its properties meet the primary criteria for long-term service as cladding materials in respect of resistance to corrosion, retention ability for the activated fission products, low neutron absorption cross-section, and excellent mechanical properties [1, 2]. Moreover, 4H-SiC has been favored for high-power device applications because of its strong breakdown electric field, high carrier mobility, and low anisotropy, as well as its availability as high-quality single-crystal wafers [3]. Today, the 4H-SiC-based super-junction is a cornerstone of the power industry. A super-junction is formed by creating p-type, high-aspect-ratio columns in n-doped vertical drift zones. Currently, the manufacturing of SiC super junctions deploys an advanced approach, whereby an extended implanted ion profile is achieved using monoenergetic MeV ions [4]. Thus, it is essential to model the effects of irradiation with swift heavy ions to predict the different possibilities of material modifications and allow preservation of the device integrity in various applications.

When an energetic ion beam collides with a target, the ions slow down in two ways: elastic/nuclear energy loss (S_n) and inelastic/electronic energy loss (S_e). For ion energies ranging from keVs to a few MeVs, atomic displacements in the crystalline lattice can be directly predicted by simulating the displacements caused by S_n. For high energy heavy ions (MeVs to GeVs), also known as "Swift heavy ion (SHI)," the inelastic energy loss (S_e) is often two orders of magnitude greater than

A. Chakravorty (✉) · D. Kabiraj
Inter-University Accelerator Centre, Aruna Asaf Ali Marg, New Delhi, India
e-mail: anusmitachakravorty@iuac.res.in

C. Dufour
CIMAP, CEA/CNRS/ENSICAEN/Université de Caen, 6 Boulevard du Maréchal Juin, 14050 Caen cedex 4, France

S_n. In this energy loss regime, no atomic movements are expected to be observed. However, experimental observations demonstrate structural changes such as deformations, amorphization, and recrystallization even when SHIs interact with materials. When SHIs collide with a material target, severe lattice distortions including amorphization are frequently detected within the material under specific circumstances. The observed ion trajectories in materials are often referred to as "Latent ion tracks" [5, 6]. It is worth mentioning that SHIs do not result in observable track formation but have been found to have annealing effects in pre-damaged crystalline SiC making it crucial to comprehend the mechanisms involved in ion beam-induced recrystallization.

This simulation work has been carried out to understand and interpret the experimentally observed results in the case of 100 meV Ag ion irradiation at room temperature and low temperature (~80 K) in pristine and pre-damaged 4H-SiC [7–9]. The beam parameters are selected based on experimental availability and TRIM simulations [10] to quantify the ratio of inelastic energy to elastic energy loss (S_e/S_n). The energy is chosen considering the Bragg peak, which approximately occurs at 1 meV/nucleon for the case 100 meV Ag. On the Bragg curve, which depicts the energy loss of ionizing radiation as it passes through matter, the Bragg peak is where the maximum occurs. Out of the available energies and beams from the 15-UD Pelletron at IUAC India, 100 meV Ag provides the maximum S_e with the ion energy of 1 meV/nucleon. High S_e is required to maximize thermal spike temperature.

The energy loss by ions in the low energy regime occurs via elastic energy dissipation in atomic collision cascades, which is easily described by molecular dynamics simulations. At considerably higher ion energies (MeVs to GeVs) where energy loss to electrons dominates, an inelastic thermal spike model (TSM), first presented by Vineyard [11] and more thoroughly developed [12] lately, can represent the connection between electronic energy loss (S_e) mechanisms and atomic processes. More recently, the 3D version [13] of the thermal spike model has been developed and applied to embedded nanoparticles inside a dielectric matrix. In the present work, we simulate the radial and temporal temperature profiles observed after the bombardment of pristine and embedded systems with SHI. We perform the 3D Thermal Spike Model simulation for a-SiC, 4H-SiC, and spherical amorphous nano-zone embedded in 4H-SiC, irradiated with 100 meV Ag at room temperature.

2 Methodology

In the TSM, the incoming ion causes significant electronic excitations and electron–electron scattering along its path. The electron–phonon coupling causes this energy to transfer from electrons to the lattice atoms, leading to a localized thermal spike [10–12]. A detailed description of the coupled electronic and atomic subsystems is given by a set of two heat diffusion equations as follows:

$$C_{e}\frac{\partial T_{e}}{\partial t} = \frac{1}{r}\frac{\partial}{\partial r}\left[rK_{e}\frac{\partial T_{e}}{\partial r}\right] - g(T_{e} - T_{a}) + A(r,t) \tag{1}$$

$$C_{a}\frac{\partial T_{a}}{\partial t} = \frac{1}{r}\frac{\partial}{\partial r}\left[rK_{a}\frac{\partial T_{a}}{\partial r}\right] + g(T_{e} - T_{a}) \tag{2}$$

where,

T_{e}: electronic temperature (K)
T_{a}: atomic temperatures (K)
C_{e}: heat capacity of the electronic system (J cm^{-3} K^{-1})
C_{a}: heat capacity of the atomic system (J cm^{-3} K^{-1})
K_{e}: electronic thermal conductivity (W cm^{-3} K^{-1})
K_{a}: lattice thermal conductivity (W cm^{-3} K^{-1})
$A(r,t)$: energy deposition from the incident high energy heavy ion to the electronic subsystem (W cm^{-3})
g: electron–phonon coupling parameter which controls the flux of heat or energy from the electrons the phonons per unit time and volume (W cm^{-3} K^{-1})

The work presented in this paper utilizes a computer code for performing the thermal spike simulation. The computations are done using the High-Performance Computing Facility at Inter-University Accelerator Centre, New Delhi, India. M. Toulemonde, Ch. Dufour, and colleagues [14] wrote the first versions of the computer code for thermal spike calculations in Fortran. Vladimir Khomenkov recently converted the source code into the C programming language under the supervision of Ch. Dufour and the 3D implementations were mathematically integrated into the code. So far, the 3D version of the algorithm has been applied to nanoparticles inside a dielectric matrix [13], and we are extending this model to simulate SHI irradiation effects in an amorphous zone inside a crystalline material. The simulated results are plotted using the OriginPro data analysis and graphing software.

The parameters for the crystalline 4H-SiC lattice used for performing the thermal spike simulations in this investigation, such as thermal conductivity and lattice specific heat, are reported in [15, 16]. The electron–phonon coupling strength is taken from [17]. As a low limiting scenario for the model, the electron–phonon coupling and specific heat for amorphous SiC are considered to be the same as for crystalline SiC due to a lack of available data. The lattice thermal conductivity values of amorphous SiC are one order of magnitude lower than those of its crystalline counterpart, according to the literature [18].

3　Results and Discussion

The TSM equations (1) and (2) are solved to yield local heating profiles from S_{e} deposited by 100 meV Ag in 4H-SiC and a-SiC. As shown in Fig. 1a, b, the lattice
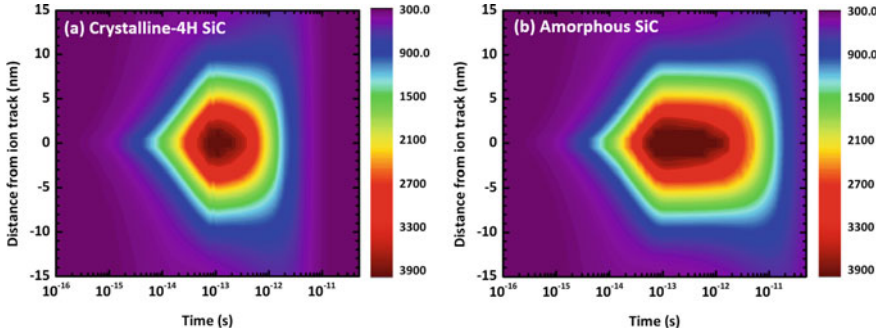
Fig. 1 Atomic temperature (in K) profiles for **a** Crystalline 4H-SiC and **b** Amorphous SiC bombarded with 100 meV Ag simulated using the 3D Thermal spike model

temperature exceeds the melting point for both a-SiC (2445 K) and crystalline 4H-SiC (3500 K) but the spike lasts for a longer duration in the case of a-SiC. A longer duration of spike quenching allows some more time for atomic movement in the molten phase. As a consequence, it increases the probability for the defects to anneal out during irradiation in the case of a pre-damaged material.

Finally, we look at how the TSM may be used to better understand the thermal behavior of a pre-damaged 4H-SiC with an amorphous inclusion. The lattice thermal spike profiles due to an ion impact can be evaluated by considering the above system as a case similar to embedded systems where we have an amorphous spherical nano-zone inside the 4H-SiC crystalline matrix. According to the simulated lattice temperature profiles presented in Fig. 2a, b, it can be suggested that the swift Ag can cause complete melting within the embedded amorphous nano-zone. Given the
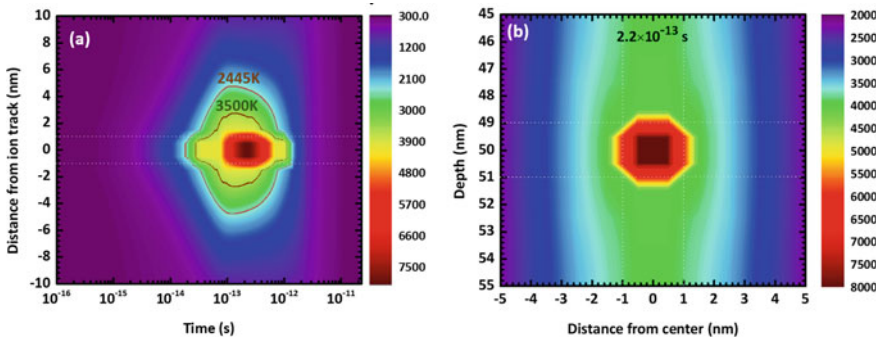
Fig. 2 The 3D Thermal spike model simulated atomic temperature (in K) profiles for 100 meV Ag ion-irradiated amorphous SiC nano-zone (radius: 1 nm) embedded inside crystalline 4H-SiC. **a** Atomic temperature profile with time and radial distance from the ion trajectory. The Contour lines mark the amorphous SiC (2445 K), and 4H-SiC (3500 K) melting temperatures. **b** Atomic temperature profile as a function of radial distance from the ion trajectory at time $= 2.2 \times 10^{-13}$ when the lattice reached its maximum temperature

higher melting temperature of the crystalline phase than the amorphous phase, melt-flow can also occur in the crystalline regions surrounding the amorphous pockets as SHI-induced melting occurs within a radius of roughly 3 nm from the center of the ion's path. This result implies that the temperature increase is high enough to allow recrystallization at the crystalline–amorphous interface via melting and rapid re-solidification within ~1 ps. This is to be expected, given that the surrounding crystalline areas supply the required seed for epitaxial recrystallization to occur.

4   Conclusions

We presented the 3D implementation of the thermal spike model to simulate the thermal behavior of a pre-damaged 4H-SiC crystal, having an embedded amorphous nano-zone, after swift heavy ion interaction. Using the amorphous (nano-zone) and crystalline thermal parameters, it is shown that the heating of the nano-zone starts from the center toward the outer layers. This provides enough energy to melt the whole nano-zone and the crystalline–amorphous interfacial area. The simulations proposed in this work provide a background for the understanding of swift heavy-induced recovery effects in pre-damaged 4H-SiC.

References

1. Zinkle SJ, Busby JT (2009) Structural materials for fission and fusion energy. Mater Today 12:12–19
2. Zinkle SJ, Was GS (2013) Materials challenges in nuclear energy. Acta Mater 61:735–758
3. Islam MdR, Galib RH, Sarkar M, Chowdhury S (2019) Wide-bandgap semiconductor device technologies for high-temperature and harsh environment applications. Wiley-VCH Verlag GmbH & Co, KGaA
4. Tian R, Ma C, Wu J, Guo Z, Yang X, Fan Z (2021) A review of manufacturing technologies for silicon carbide superjunction devices. J Semicond 42:061801
5. Young DA (1958) Etching of radiation damage in lithium fluoride. Nature 182(4632):375–377
6. Fleischer RL, Price PB, Walker RM (1975) Nuclear tracks in solids. University of California Press
7. Chakravorty A, Singh B, Jatav H, Ojha S, Singh J, Kanjilal D, Kabiraj D (2020) Intense ionizing irradiation-induced atomic movement towards recrystallization in 4H-SiC. J Appl Phys 128:165901
8. Chakravorty A, Singh B, Jatav H, Meena R, Kanjilal D, Kabiraj D (2021) Controlled generation of photoemissive defects in 4H-SiC using swift heavy ion irradiation. J Appl Phys 129:245905
9. Chakravorty A, Dufour Ch, Singh B, Jatav H, Umapathy GR, Kanjilal D, Kabiraj D (2021) Recovery of ion-damaged 4H-SiC under thermal and ion beam-induced ultrafast thermal spike-assisted annealing. J Appl Phys 130:165901
10. Ziegler JF, Ziegler MD, Biersack JP (2010) Nucl Instrum Methods Phys Res Sect B 268:1818

11. Vineyard GH (1976) Thermal spikes and activated processes. Rad Effects 29:245–248
12. Toulemonde M, Assmann W, Dufour C, Meftah A, Studer F, Trautmann C (2006) Thermal spike model in the electronic stopping power regime. Mat Fys Medd 52:263
13. Dufour Ch, Khomenkov V, Rizza G, Toulemonde M (2012) Ion-matter interaction: the three-dimensional version of the thermal spike model. Application to nanoparticle irradiation with swift heavy ions. J Phys D: Appl Phys 45:065302
14. Toulemonde M, Dufour C, Paumier E (1992) Transient thermal process after a high-energy heavy-ion irradiation of amorphous metals and semiconductors. Phys Rev B 46:14362–14369
15. Snead LL, Nozawa T, Katoh Y, Byun TS, Kondo S, Petti DA (2007) Handbook of SiC properties for fuel performance modeling. J Nucl Mater 371:329
16. Benyagoub A, Audren A (2009) Mechanism of the swift heavy ion induced epitaxial recrystallization in predamaged silicon carbide. J Appl Phys 106:083516
17. Zhang Y, Xue H, Zarkadoula E, Sachan R, Ostrouchov C, Liu P, Wang X-L, Zhang S, Wang TS, Weber WJ (2017) Coupled electronic and atomic effects on defect evolution in silicon carbide under ion irradiation. Curr Opin Solid State Mater Sci 21:285
18. Snead LL, Zinkle SJ (2002) Structural relaxation in amorphous silicon carbide. Nucl Instrum Methods Phys Res B 191:497

Enhancement of Heat Transfer in Solar Dehydrator for Agriculture Products

A. Ponshanmugakumar and R. Rajavel

1 Introduction

In recent years, other methods have been developed to obtain a greater understanding of research in drying the agriculture species and seeds. In this method, biological material is exposed either directly or indirectly to light to dehydrate it [1]. Dehydration reduces a product's moisture content to levels that allow it to be stored for longer periods of time without losing quality. This study looks into the species as well as the solar dehydrator. Infectious diseases, disruption linked with discomfort, poor digestion, and diarrhoea are all medical uses for the species. Among the principal components of species are unwanted acid compounds. Essential oils are odorous compounds extracted by water vapour or hydrodistillation from aromatic and species. The quality of dried plants is degraded by solar radiation, which causes oil loss and colour shifts [2]. Temperature and light (sunny hours) have a bigger influence on essential oils and azulene concentrations than soil type. If the ambient temperature is 37 °C or above, the flowers are fragile and dry in 5–7 days; however, if the ambient temperature is 37 °C or higher, it takes 3–5 days. A vacuum sealer is the best way to maintain M. essential oil and prochamazulene content. It is a good idea to dry Chamomile blossoms affectedly with a detonation of air at 40–45 °C.

Concentration and volume of aromatic plant oils are greatly influenced by the drying process [3]. It was designed to determine time drying and velocity testing of species drying in constant circumstances, which include air that does not change considerably from input to output over time. The amount of moisture lost per unit of time determines the drying velocity. The moisture per cent was computed by multiplying the difference between the before and after drying masses, as well as the before drying mass, difference between drying masses, as well as the before drying mass. The temperature and thickness of the species layer were modified in

A. Ponshanmugakumar (✉) · R. Rajavel
Academy of Maritime Education and Training, Chennai 603102, India
e-mail: shnmgkmr8@gmail.com

preliminary laboratory and pilot scale testing. Solar drying was also used to conduct pilot experiments with resistors and a temperature controller. The species required more than 28 h to reach 14.5% moisture in an oven test at 30 °C, but only 12% at 45 °C after the same amount of time [4]. After 45 °C and 27 h of solar drying, the species had a moisture content of 11.7%. Fuel expenditure, change in temperature, and moisture were all measured. The average temperature was 45 °C.

2 Objective of the Work

The purpose of this research is to design solar drier that can dry grains via the cabinet's glass walls and roof using both direct and indirect sunlight, as well as warm air from the solar collector.

3 Literature Review

Crop drying is the farm's most energy-intensive process. Agricultural food is dried to remove moisture and make it easier to handle and store for longer periods of time. Crops are also dried by blowing air through them before or during storage to prevent spontaneous combustion and fermentation. According to Hartman, poor handling of seeds and a lack of post-harvest, and seed separation equipment adoption cause will cause more wastages (1991). Grain and seed are commonly collected with moisture levels ranging from 18 to 40%. Moisture level of the agriculture products are 7-11%. A grain crop may need to be stored for a while after harvesting before being sold or used as feed. How long a crop may be adequately stored depends on the state in which it was collected as well as the sort of storage facility employed. Grains can be stored for lengthy periods of time at low temperatures and with low moisture content before losing their quality.

Solar energy technologies that convert solar radiation directly into heat are predicted to be widely used in the near future. Of course, the reliability of solar energy can be enhanced by storing a portion of it while it is not in use and using it when needed. Solar drying is a decentralised solar energy thermal use that could benefit developing countries [5]. As a result, employing a solar dryer allows you to take advantage of the sun's free energy while yet ensuring good product quality with precise radiative heat management. All around the world, solar energy has been used to dry objects. Due to the wide range of solar dryers available, grain, fruits, meat, vegetables, and fish are all commonly solar-dried products. In five key categories, a typical solar drier outperforms an open-air sun system [6].

3.1 Solar Dryers that Are Exposed to the Sun Directly

In direct solar dryers, the dehydrated product is exposed to direct sunshine. Traditional methods of drying food and clothing in the sun included hanging them on lines, laying them on rocks, and stacking them on top of tents. Mongolians continue to dry cheese and meat using the top of their gers (tents) as a solar dryer. By removing more saturated air from the products to be dried, air movement (wind) promotes sun drying in these systems. Complex drying racks and solar tents have recently been used to construct sun dryers.

3.2 Solar-Powered Clothes Dryers (Indirect)

Indirect sun dryers use a black surface to heat entering air instead of directly heating the material to be dried. After passing over the object to be dried, warm air is forced upwards, often through a chimney, carrying moisture with it. They might be as basic as a slanted cold frame covered in black fabric, or as complex as a completely insulated brick construction with active ventilation and backup heating. Using the indirect technique, food, or any other item, can be better protected from contamination by wind, insects, or animals. Furthermore, exposure to bright sunshine can alter the chemical composition of some foods, making them less appetising. The current study examines CSP technology as well as the advantages of solar tower collectors (STC).

This work proposes a mechanism for calculating on a mix of previous research findings and current meteorological data. Finally, it shows weather predictions for a number of STC locations. Describes how to use forecasts to create a simulation of the plant configuration required for the best STC.

3.3 Design of Solar Dryers

Plywood panels, Steel frames, wooden boards, galvanised iron sheets, clear glass, and a mini axial fan were used to build the dryer, all of which were inexpensively accessible locally. 4–5 mm was chosen as the thickness of slices. Since then, an indirect sort of sun drier has been investigated unlike a direct type, and it does not alter the colour or nutritional value of the vegetables. Furthermore, there is no localised heating; thus, the drying is consistent. Flat plate collectors are commonly utilised since they are simple to construct and cost less. Because GI sheet is a good conductor and cost-effective, the collector is made of 0.6 mm thick GI sheet. To maximise the heat absorption, it was painted black. Glass thickness of 5 mm [7] is recommended for collectors. In a tropical climate, a 5-cm air gap is recommended

[8]. Plywood was chosen as the insulating material since it is both effective and eco-friendly. Other common insulating materials, such as glass wool, have carcinogenic consequences. An air sand layer was placed among two pieces of plywood panel to prevent heat loss. Aluminium foil is wrapped around the inside of the chamber to further limit heat loss through radiation and avoid moisture absorption by wood. The trays were made of food-safe stainless steel mesh, and the bananas were placed on food-safe wooden skewers. An axial flow fan was chosen to produce a consistent flow rate of air during the experiment based on calculations of pressure loss in the system and the requisite flow rate limit of air at 3 m/s.

4　Thermal Storage

4.1　Phase-Changing Materials

PCMs have revolutionised thermal systems during the last four decades [8]. Several review studies, as well as evaluations of techniques to enhance poor thermal conductivity and appropriate characterisation approaches, have established that paraffin has a high latent heat. There is a lot of information on the use in low-temperature thermal energy storage and thermal management systems, of paraffin waxes, particularly in overlapping industries such as battery thermal management, photovoltaics, buildings, solar chimneys, and sun dryers. The authors should be applauded for their extensive research and data gathering efforts. A summary of peer-reviewed papers on a variety of themes is shown in Fig. 1.

Fig. 1 Phase change-dependent classification
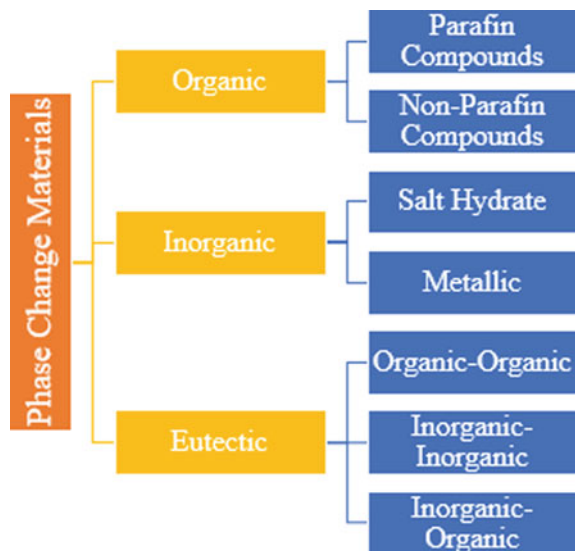
4.2 Paraffin Wax Functions and Classification

The phase change theory and a phase change diagram are given for paraffin waxes. Based on the overlapping fields, the roles of paraffin waxes are also summarised. Section 3 goes into the thermophysical properties of paraffin waxes, covering production procedures, thermal reinforcements, a systematic flowchart to help understand how to build exceptional thermal composites, and thermal composite performance evaluation characterisation methodology. Section 4 delves into the topic of complicated thermal systems. The study finishes with a critical analysis of thermal system design and fabrication issues using thermal composites, as well as possible conclusions and recommendation.

4.3 Paraffin Wax Functions and Classification

The state of matter has traditionally been used to classify phase transitions. In the solid state, however, another sort of phase shift can occur. As shown in Fig. 1, crystal structures shift, providing fractional latent heat to total phase transition processes.

Figures 1 and 2 show phase change-dependent classification and paraffin wax functions, respectively. It provides instances and essential topics. Fig. 2 depicts the suggested taxonomy, which links these two basic categories with PMs implicated. Figure 2 displays the ideal phase change diagram, which contains discrete regimes of thermal excitation as well as certain types of thermal energy, to summarise and characterise the full phase transition process of solid–liquid PCMs, notably paraffin waxes.

Fig. 2 Functions of paraffin waxes

5 Design Considerations

5.1 Temperature

This work is conducted in response to the need to enhance the drying product at pure and to remove the moisture. As a result, drying these agriculture products at 45 °C or above has become very common in all places.

5.2 Preparation

The dryer was designed with the goal of reaching the greatest temperature feasible. $T_0 = 60$ °C, $T_1 = 30$ °C; $T_0 = 60$ °C, $T_1 = 30$ °C; $T_0 = 60$ °C, $T_1 = 30$ °C; $T_0 = 60$ °C, $T_1 = 30$ °C; $T_0 = 60$ °C, $T_1 = 30$ °C; $T_0 = 60$ °C, $T_1 = 30$ °C; $T_0 = 60$ °C, $T_1 = 30$ °C; $T_0 = 60$ °C, $T_1 = 30$ °C; T (approximately outdoor temperature).

5.3 Air Gap

For passive solar dryers in hot climates, a 5 cm space between the air vent (inlet) and the air route is recommended.

5.4 A Glass Collector or a Flat Plate

The glass covering should be 4–5 m thick, according to the requirements. The thickness of the translucent glass utilised in this project was 4 mm. He also recommended a metal sheet thickness of 0.8–1.0 mm; in this case, galvanised steel with a thickness of 1.0 mm was used. Glass covered the collector's cover, which measured 103 × 100 cm^2.

5.5 Dimensions

Masnaji designed, constructed, and deployed the system. The system has a dry maximum capacity of 5 kg and a volumetric capacity of 0.55 m^3 in Fig. 3. The dehydrator's air intake is at the bottom, while the exhaust is at the top. Glass is transparent in practically all wavelengths relevant to thermal energy, as is widely known [9]. Using thermometers and hygrometers, the temperature and humidity of the input and output air were measured. The most successful dehydration necessitates the use

Fig. 3 shows how to set up a solar dehydrator

of instruments. The following are the properties of the sensor: A DS18B20 digital thermometer with a resolution of 9 bits to 12 bits in Celsius was used to take the temperature measurements. It is precise to 0.5 °C and has a temperature range of -55 to $+125$ °C. The DHT11 humidity sensor provides a 20–90% relative humidity detection range and a humidity accuracy of 5% relative humidity.

Cabinets are the most common; however, cardboard boxes and translucent nylon or polythene can be used to improve some of them. The theoretical foundation for the design in question is provided by the greenhouse effect and thermo syphon [10].

6 Result and Discussion

The measurement was taken by changing the unit's inclinations which ever possible [11]. And repeated trials are taken to obtain the comprehensive attributes of dehydrated solar in different days and seasons. Collector's temperature T output climbed to 14 °C after sampling the air with a one-minute interval, as shown in Fig. 4.

Figure 5 explains the mass flow rate vs the increase in thermal power output. Figure 6 shows the variation of thermal efficiency with the hot air mass flow rate. Figures 7 and 8 compare the time delay with temperature range for both without using PCM and using PCM storage performance. Figure 9 explains high temperatures affect the quantity and quality of essential oils in aromatic and species plants not

Fig. 4 Setup for experiments
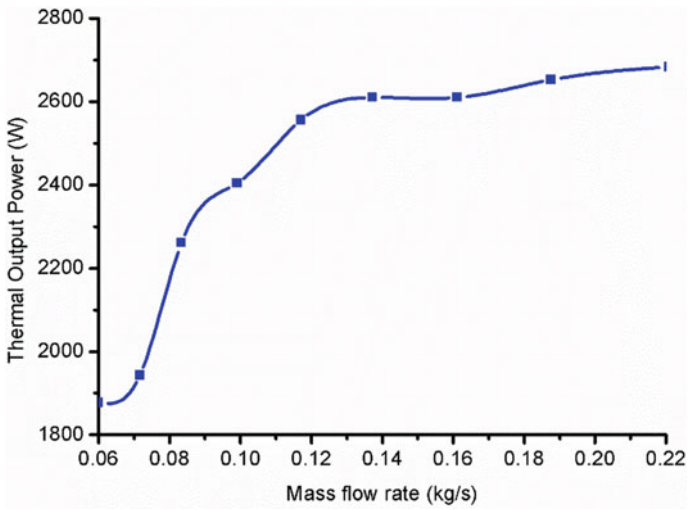
Fig. 5 The effect of changing the mass flow rate on the solar air heaters' thermal output power
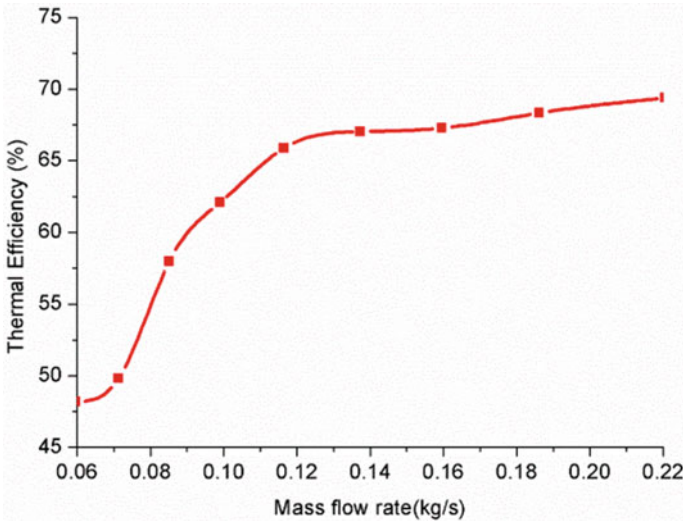
Fig. 6 Variation in mass flow rate has an impact on the solar air heater's thermal efficiency
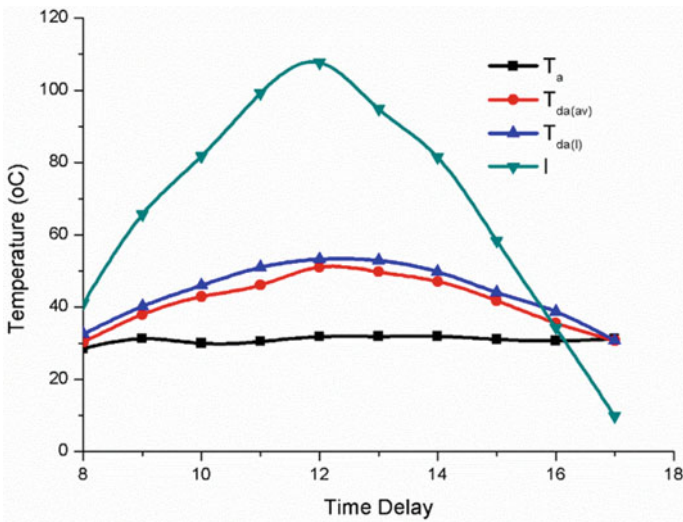
Fig. 7 Without employing the PCM, temperature variation of indirect solar dryer

only during drying but also throughout the storage. The impact of drying on the volume and value of essential oils has been extensively investigated. Relevance to Sari and Himsar [12], the temperature of air is increased during species drying from 30 to 50 °C reduced dehydrating time from 52 to 3.5 h without affecting essential oil concentration. It varies between 15 and 25% depending on how dry the air is.
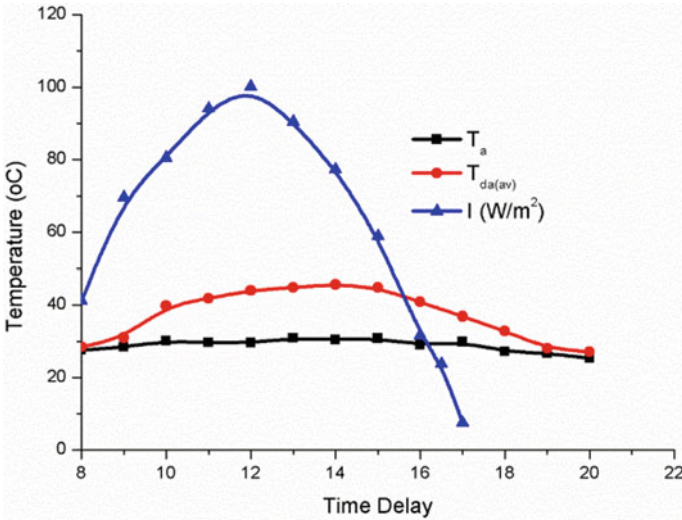
Fig. 8 While utilising the PCM, temperature variation of indirect solar dryer
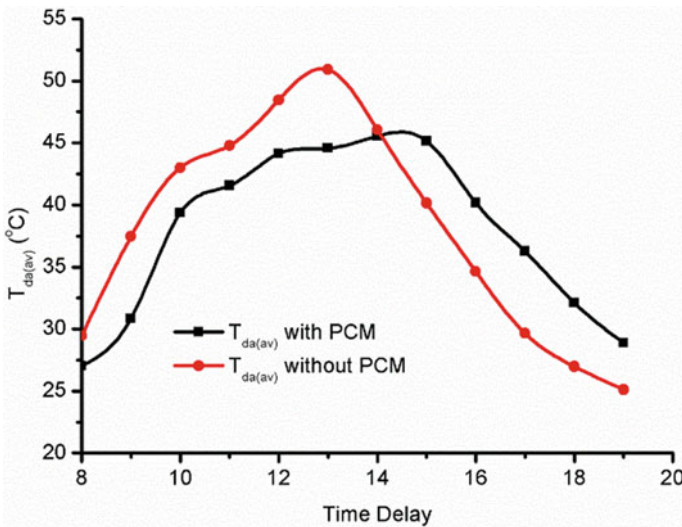
Fig. 9 Comparing the $T_{da\,(av)}$ in the ISD using and without using the PCM

Investigated the chemical composition and synthesis of species essential oil after drying in a fixed layer at 80 °C.

7 Conclusion

In this study, the sun dehydrator method was found to be effective in preserving the species' characteristics throughout dehydration.

- Drying species led in a decrease in essential oil concentration and chemical composition, according to the findings. Drying air temperatures of 50–60 °C, on the other hand, appear to be suitable for a wide variety of species.
- The new system generates more thermal energy without raising the cost of the system. The dehydrated samples meet the standard's standards to a satisfactory extent.
- The moisture content of aromatics and species determines their physical and chemical properties. When a plant is dried, its weight and bulk are reduced, making it easier to transport and store.
- It may also make plant marketing easier and help maintain a regular supply.

References

1. Cetina-Quiñones AJ, López López J, Ricalde-Cab L, Amina El Mekaoui, San-Pedro L, Bassam A (2021) Experimental evaluation of an indirect type solar dryer for agricultural use in rural communities: relative humidity comparative study under winter season in tropical climate with sensible heat storage material. Sol Energy 224:58–75
2. Udomkun P, Romuli S, Schock S, Mahayothee B, Sartas M, Wossen T, Njukwe E, Vanlauwe B, Müller J (2020) Review of solar dryers for agricultural products in Asia and Africa: an innovation landscape approach. J Environ Manage 268
3. Singh A, Sarkar J, Sahoo RR (2020) Experimental performance analysis of novel indirect-expansion solar-infrared assisted heat pump dryer for agricultural products. Sol Energy 206:907–917
4. Lakshmi DVN, Muthukumar P, Layek A, Nayak PK (2019) Performance analyses of mixed mode forced convection solar dryer for drying of stevia leaves. Sol Energy 188:507–518
5. El Khadraoui A, Hamdi I, Kooli S, Guizani A (2019) Drying of red pepper slices in a solar greenhouse dryer and under open sun: experimental and mathematical investigations. Innov Food Sci Emerging Technol 52:262–270
6. Goud M, Reddy MVV, Chandramohan VP, Suresh S (2019) A novel indirect solar dryer with inlet fans powered by solar PV panels: drying kinetics of *Capsicum annum* and *Abelmoschus esculentus* with dryer performance. Sol Energy 194:871–885
7. Ponshanmugakumar A, Aldrich Vincent A (2014) Simulation of solar intensity in performance of flat plate collector. Int J Res Eng Technol 03(06):36–41
8. Desa WNM, Mohammad M, Fudholi A (2019) Review of drying technology of fig. Trends Food Sci Technol 88:93–103
9. Bal LM, Satya S, Naik SN (2010) Solar dryer with thermal energy storage systems for drying agricultural food products: a review. Renew Sustain Energy Rev 14(8):2298–2314
10. Nukulwar MR, Tungikar VB (2021) A review on performance evaluation of solar dryer and its material for drying agricultural products. Mater Today: Proc 46(Part 1):345–349

11. Ponshanmugakumar A, Rajavel R (2019) Experimental analysis of vapour absorption generator integrated with thermal energy storage system. Mater Today: Proc 16(Part 2):1158–1167
12. Dina SF, Ambarita H, Napitupulu FH, Kawai H (2015) Study on effectiveness of continuous solar dryer integrated with desiccant thermal storage for drying cocoa beans. Case Stud Thermal Eng 5:32–40

A Review on Potential of Graphene Reinforced Geopolymer Composites

R. S. Krishna , **Jyotirmoy Mishra** , **Shaswat K. Das** ,
Bharadwaj Nanda , **Sanjaya K. Patro, and Syed M. Mustakim**

Abbreviations

GRGC	Graphene reinforced geopolymer composites
FA	Fly ash
BA	Bottom ash
GGBFS	Ground granulated blast furnace slag
RHA	Rice husk ash
AR	Agricultural residues
RM	Red mud
GO	Graphene oxide
rGO	Reduced graphene oxide
GC	Geopolymer composite
BFS	Blast furnace slag
FCS	Ferrochrome slag
FCA	Ferrochrome ash
OBA	Olive biomass ash
FS	Ferronickel slag
SBA	Sugarcane bagasse ash
PFA	Palm fuel ash
KOH	Potassium hydroxide
SF	Silica fume
EPS	Expanded polystyrene

R. S. Krishna (✉) · J. Mishra · B. Nanda · S. K. Patro
Veer Surendra Sai University of Technology, Burla, Sambalpur 768018, India
e-mail: rskrishna_mtechmda@vssut.ac.in

S. K. Das · S. M. Mustakim
CSIR-Institute of Minerals and Materials Technology, Bhubaneswar 751013, India

S. K. Das
Grøn Tek Concrete and Research, Bhubaneswar 751010, India

GN   Graphene nanosheets
GNPs   Graphene nanoplatelets
XRD   X-ray diffraction
FTIR   Fourier transform infrared spectroscopy
SEM   Scanning electron microscopy
TEM   Transmission electron microscope

1 Introduction

Geopolymers belong to a new class of aluminosilicate composites which serves to be an alternative to cement-based composites, was conceptualized by Joseph Davidovits, and has drawn increasing worldwide attention in a short span due to low cost, high compressive strength, outstanding thermal properties, environmentally friendly nature [1, 2]. The constituents for geopolymer composites include a precursor element abundant in aluminum and silica along with an alkaline solution, generally a mix of sodium hydroxide/or silicates. These precursor materials (i.e., binders) mostly include industrial wastes rich in aluminosilicate such as coal FA, GGBFS, RHA, AR, RM, etc. Additionally, geopolymerization technology is instrumental in promoting the circular economy, as it efficiently converts many inorganic wastes into useful products. The utilization of industrial wastes in the development of eco-friendly constructional materials is a huge leap in terms of sustainable development. The production of geopolymer composites significantly enhances waste immobilization and encapsulation by utilizing industrial waste materials in producing environmentally sustainable construction materials [3–5].

However, geopolymers are considered to have low flexural and tensile strength and are known to be brittle which limits their implementation for wide structural applications [6]. Therefore, there is a need for the valuable introduction of secondary reinforcement particles into the geopolymer matrix, and several progressive efforts have been undertaken in this regard to modulate geopolymers using carbon fibers [7], α-Al$_2$O$_3$ particle filler [8], cotton fibers [9] for enhancement of mechanical properties of geopolymers. The use of graphene, a unique two-dimensional carbonaceous nanomaterial, as a reinforcing agent into the geopolymer matrix could potentially improve microstructural and strength properties [10–12].

Graphene has sparked enormous interest across the world due to its remarkable characteristics including low density, large surface area, and unique thermal, electrical, and mechanical capabilities [13–15]. Therefore, mixing graphene and its subsidiaries; graphene oxide (GO), and reduced graphene oxide (rGO) to form superior geopolymer composites seems to be a progressive approach toward the development of advanced eco-friendly composites. In this paper, a review-based study that presents a brief review of the developments of graphene reinforced geopolymers has been undertaken to reach a better understanding of the subject.

2 Geopolymer Composites

Geopolymer composites (GCs) have emerged as an eco-friendly substitution of conventional cementitious and polymeric composites. The term "geopolymers" indicates a group of inorganic aluminosilicate polymers that are synthesized artificially in a way similar to the natural/artificial synthesis of zeolites or molecular sieves. The versatility of geopolymers has transformed itself into a material with several applications; it can be used as a binder for cement-less concrete, an adhesive for composites with high thermal applications, a coating for fireproof elements, etc. Moreover, monumental developments have been seen in this field with several breakthrough research findings; the use of 100% industrial waste as geopolymer precursor material at present is one of them, whereas initial geopolymeric materials were based on natural occurring aluminosilicates. The synergic efforts by several researchers to develop high-strength GC at ambient temperature curing is another major accomplishment that has widened its scope for in situ applications and lessens the embodied energy of GC. However, several research works have utilized different kinds of wastes such as coal ash, industrial slag, agricultural residue, etc. as shown in Fig. 1 to produce GC, in some cases the wastes have been used as the binder whereas, in certain cases as aggregates. The following subsection discusses the utilization of different wastes in geopolymers.

Fig. 1 Sustainable industrial waste utilization and management through geopolymers
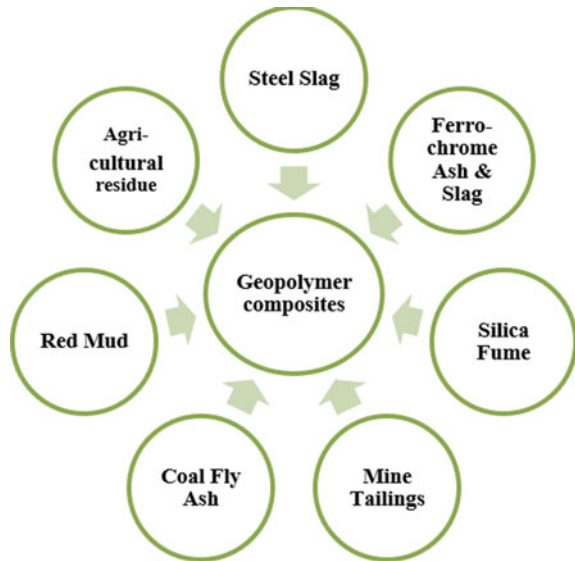
2.1   Coal Ash

The term coal ash specifies both fly ash (FA) and bottom ash (BA). FA has high fineness with pozzolanic properties, whereas BA shows very little reactivity due to large particle size and presence of unburnt carbon. Due to high reactivity and a good amount of alumina-silica content, FA is considered one of the best precursor materials for geopolymer synthesis. Numerous investigations have utilized FA as the major source material due to its higher degree of geopolymerization in an alkaline environment, and the ability to reduce hydration heat and thermal cracking [16–21]. However, there exists some research where FA has been used as a replacement to fine aggregates in GC [18]. Furthermore, as some researchers have indicated, BA can be utilized as an aluminosilicate precursor for geopolymer synthesis [16]. Xie et al. disclosed that BA performs very poorly as a source material (binder) in ambient curing conditions due to the lower degree of geopolymerization and remains mostly unreacted in the composite matrix while adversely affecting the strength of the resulting composites [17]. Therefore, Ghose et al. suggested BA could be used as a replacement to sand (fine aggregate) in GC, thus providing a sustainable alternative to river sand [19]. It could provide additional reinforcement to the composite matrix owing to its rougher and porous surface of coarser, irregular particles. Since both the FA and BA can be used extensively in the GC production process, as per the physiochemical properties of coal ash, they can be suitably used in GC as aggregates or binders for sustainable waste management.

2.2   Industrial Slag and Ash

The industrial slag is generally generated during the metal extraction or alloy manufacturing process in metallurgical industries. Different types of slag are generated depending upon the extraction process, type of material, and furnace. The blast furnace slag (BFS), LD slag, ferrochrome slag (FCS), ferrochrome ash (FCA), ferronickel slag (FS), etc. are the most common type of waste and generated in humongous quantity. Multiple studies have explored the possible utilization of BFS in GC [22–25], the results of those experiments are also very promising. The GC achieves a considerable amount of compressive strength and other key engineering properties like FA-GC when BFS was induced into the GC system [26]. The high calcium content of BFS helps the GC to set early at atmospheric conditions by generating some extra heat through hydration reaction during the origination of C–S–H. However, the percentage of CaO in the BFS also enriches the GC complex with C–A–S–H gel along with C–S–H which helps in achieving a considerable amount of early-age strength. Very few attempts have been made to utilize ferrochrome wastes in GC. Mishra et al. examined the possibility of utilizing FCA as the primary source material for GC production with BFS at room temperature conditions [27–29]. Some limited research work has also been conducted taking FCS (ground) as a precursor

material for GC with Na-based alkaline activators [30, 31]. The use of FCS has been investigated as coarse aggregate in GC by Jena and Panigrahi in their study; they have reported that FCS shows promising results in both mechanical and microstructural performances [32].

2.3 Agricultural Residues

Some of the agricultural industries also generate some inorganic residual wastes. RHA, SBH, PFA, etc. contain a high amount of aluminosilicate therefore could be used as source material for GC preparation. Several researchers have attempted to use RHA in GC alongside FA or BFS [33–36], and some researches have been conducted utilizing RHA as the sole precursor for GC [37, 38]. Das et al. evaluated the impact of RHA in FA-BFS-based GC at ambient temperature curing and suggested that up to 5% RHA can be utilized. In contradicting their statement, some authors suggested that RHA can be induced in GC up to 30% without hampering its mechanical and durability properties [36]. It is well established that the high silica content of the RHA induces more silica precursors for reaction during geopolymerization; thus, a higher amount of reaction product generates which enhances the properties of GC. Amin et al. suggested that the SBH can be taken as a precursor along with china clay for GC preparation; the performance of SBH in GC was comparable with that of FA or BFS [39]. Alonso et al. inspected the feasibility of utilizing OBA as an alternative activator in geopolymer development, due to the high silica and calcium content of OBA; they have successfully synthesized this novel binder [40]. Moreover, several authors have reported the utility of PFA in geopolymers [41–43], Olivia et al. investigated FA-PFA geopolymer mortars and concluded that PFA can partially replace FA, however with increasing content of PFA the durability properties of GC reduce [41]. The sustainable utilization of coconut shell has also been undertaken by another research group; they have suggested the possible utilization of this waste into GC [44].

3 Requirement of Property Enhancers for Geopolymer Applications

To increase the strength and durability properties of GC, several strength-enhancing materials, namely silica fume, nanosilica, rice husk ash, have been introduced to the geopolymer matrix [45, 46]. Mechanical strength characteristics of GC such as compressive strength, flexural strength, drying shrinkages, modulus of elasticity were [47] greatly enhanced after the inclusion of these materials into the system as reported in previous literature [34, 48, 49]. In the case of geopolymers, the strength advancement is majorly determined by the quality and amount of calcium aluminosilicate hydrate (C–A–S–H) and sodium aluminosilicate hydrate (N–A–S–H) gels.

Hence, these strength-enhancing materials help in reducing the overall porosity of the composite matrix and in the generation of extra gels or act as a catalyst for accelerating the geopolymerization process. Porosity in GC is governed by the ability of alkali ions to migrate inside the binder matrix which leads to adverse effect on the strength and durability of the composite [50]. However, because GC is inherently quasi-brittle, its ductility may be enhanced by employing suitable reinforcing elements such as fibers [47]. Moreover, with better tension properties, the requirement for external reinforcement gets minimized. Most fibers behave as reinforcement material without taking part in the reaction in the binder phase, whereas there exist few fibers that take part in reaction to produce additional reaction products, viz. basalt fibers [51–54]. As a result, the introduction of strength-enhancing materials has become necessary to improve the mechanical characteristics of GC. Mostly, these materials are supplements to the precursors or fibers [55] that induce better tensile properties by preventing fractures in a gel phase in the composite matrix. In addition to the prior discussion, graphene derivatives have proven to be beneficial by displaying remarkable performance improvements in geopolymer composite materials for various applications. Graphene derivatives could serve to enhance microstructural and strength characteristics at very low doses primarily due to their strong chemical bonding and mechanical interaction with the geopolymer matrix resulting from the wrinkling as well as the reduction in overall porosity [56, 57]. Figure 2 highlights different property enhancers utilized in geopolymer composites.

4 Graphene–Geopolymer Composites

4.1 Synthesis of Graphene

According to IUPAC, graphene is a single layer of carbon atoms attained from a graphite structure arranged in a 2D hexagonal lattice. It holds exceptional mechanical, thermal as well as electrical properties which allow it to be a promising reinforcing material for manufacturing composite materials. Various techniques have been highlighted by Dasari et al. to synthesize graphene which includes exfoliation, chemical vapor deposition (CVD), organic synthesis, and chemical derivation of graphene (production of GO and rGO). Each of these approaches has its own set of benefits, drawbacks, and cost-effectiveness [58]. The group of graphene derivatives has been quickly developing, particularly during the last decade. Despite the huge research in the field of graphene, only fluorinated and completely hydrogenated graphene, namely fluorographene and graphane, is recognized [59]. Another study by Inagaki et al. analyzed graphene derivatives by underlining various experimental results and elucidated that hydrogenated, fluorinated, and oxidized graphenes are relied upon to have fascinating properties, which are called graphane, fluorographene, and graphene oxide as illustrated in Fig. 3 [60]. GO is an oxidized form of graphene and holds outstanding properties, but it carries certain defects due to which it can be reduced
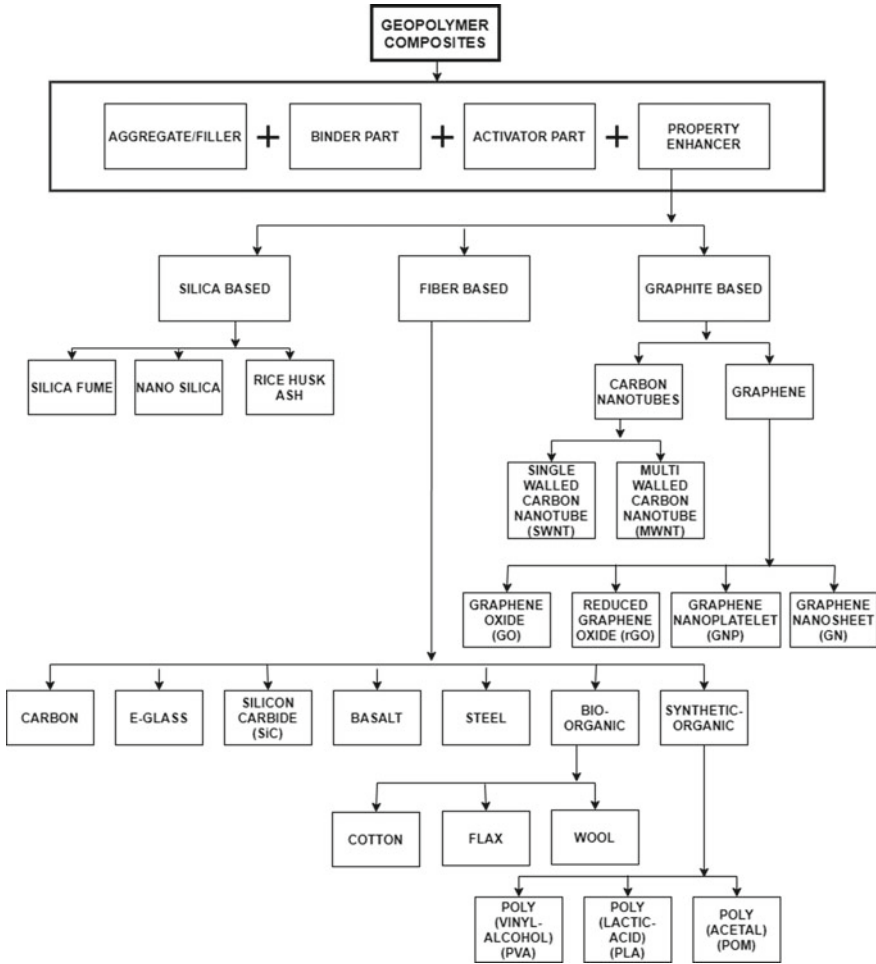
Fig. 2 Schematic representation of different property enhancers utilized in geopolymer composites

through various reduction processes and reducing agents to obtain graphene-related materials similar to that of pristine graphene [61]. Graphene and its derivatives (GO, rGO) seize expanding consideration because of their remarkable physicochemical properties, and when fused suitably, they can altogether enhance the physical properties of host polymers at very low loading [62]. Physiochemical properties of GO and rGO mostly depend on their different functional groups such as epoxy, hydroxyl, carbonyl, and carboxyl groups along with varying dispersion efficiencies. Graphene derivatives demonstrate distinct effectiveness in enhancing the hydration degree and mechanical behavior of geopolymer composite matrix [63]. A report by Saafi et al. demonstrated that the incorporation of graphene derivatives like GO and rGO in geopolymeric composites yields enhanced properties and reduces the overall porosity
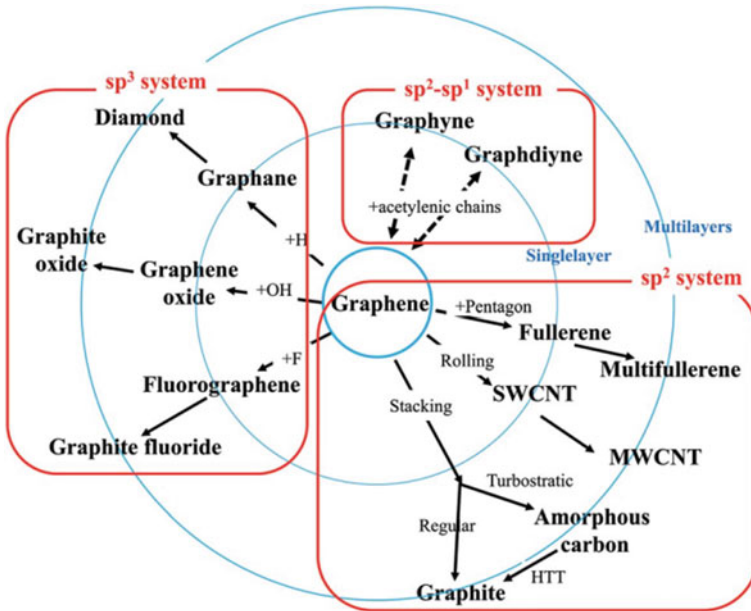
Fig. 3 Graphene and its derivatives [60]

of geopolymers [64]. Synthesis of GO and rGO plays a crucial role in determining the properties of the incorporated geopolymeric composites. Various approaches for synthesizing graphene and its derivatives along with polymer composite materials have been introduced in a study by Tang et al. [65]. The large-scale production and industrial application of GO and rGO have been a major obstacle so far. The primary challenges of industrial-scale GO and rGO production are basically correlated with the hazards involving strong corrosive acids, reducing agents, and explosive oxidants, but these hazards can be overcome with recent developing industrial chemical processes, and further research while paving way for various GRGC applications [66].

4.2 Preparation and Properties of GRGC

Preparation of GRGC includes certain steps and procedures, specifically the type of reinforcing material, introduction to the composite, binders, and the curing conditions which primarily decide its concluding properties. Figure 4 demonstrates the prevailing procedure for the development of graphene–geopolymer composites. As an alkaline solution in the fabrication of geopolymer composites, sodium silicate (Na_2SiO_3), sodium hydroxide (NaOH), and potassium hydroxide (KOH) have been widely utilized. An experimental study by Ranjbar et al. reported the aftermath of
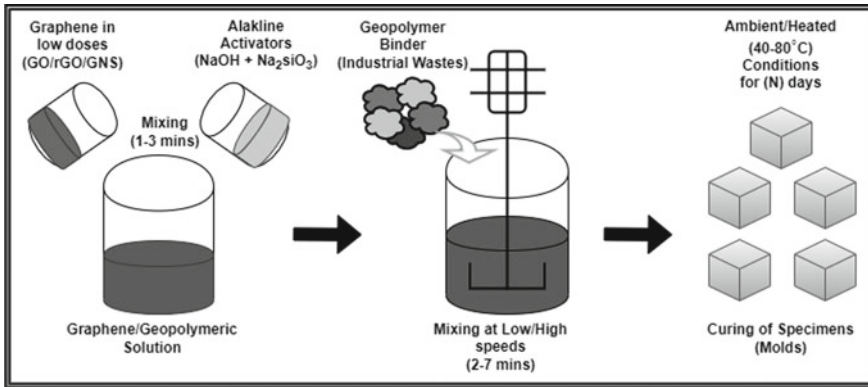
Fig. 4 Graphical representation for the preparation of geopolymer reinforced geopolymer composites

adding graphene nanoplatelets (GNPs, 1 wt%, 1–7 μm) in fly ash-based geopolymer composites without getting agglomerated. NaOH and Na_2SiO_3 were gradually added to the geopolymer mixture along with GNPs and were dried at 65 °C in the oven for 24 h to obtain increased compressive (144%), flexural strength (216%), and nominal flexural toughness (300%) [67]. Another author Saafi et al. introduced rGO sheets (0.35 wt%) into geopolymeric composite cement by curing it at 60 °C for 24 h which resulted in enhanced flexural strength (134%), Young's modulus (376%), and toughness (56%) of the composite. rGO sheets were obtained through chemical reduction of pristine GO sheets (1.1 nm, 0.5–5 μm) by NaOH soln. and mild sonication [64]. Further, Table 1 provides detailed mechanical improvement of GC with the inclusion of graphene nanofillers. It can be observed that irrespective of the

Table 1 Property improvements of geopolymers due to graphene nanofiller inclusion

Binder	Alkaline activator	Graphene		Compressive strength (improvement %)	Flexural strength (Improvement %)	Reference
		Type	wt%			
Fly ash (F)	Na_2SiO_3 + NaOH (16 M)	GNP	1	144	216	[67]
Metakaolin	KOH + Silica Soln	rGO	1	–	470	[72]
Metakaolin	Na_2SiO_3 + NaOH	–	3	287	–	[71]
GGBFS	NaOH	–	0.02	31.10	96.20	[73]
GGBFS + SF + EPS Beads	Na_2SiO_3 + NaOH	rGO	0.04	29.8	26.5	[74]
PFA	Na_2SiO_3 + KOH (10 M)	GN	0.7	74.19	–	[75]

binder type and alkali activators, considerable growth in the mechanical strength of GC can be witnessed with very low doses of graphene additives. Graphene can be homogeneously blended in the geopolymer composite owing to its lamellar structure and exceptional physical properties. Further, the inclusion of graphene helps in the formation of dense microstructures while reducing porosity and obstructing the origination of nanodimensional cracks. Moreover, the production of graphene-enhanced geopolymer composites is a complex, time-consuming, and expensive process [68]. According to Yan et al., alkaline geopolymeric solution prepared by a mixture of silica and KOH solution could be used partially for in situ reductions of GO to rGO within a short period of time at ambient conditions. Later, the metakaolin granules were introduced to the rGO/geopolymeric composite slurry and dried at 60 °C over 7 days, progressively increasing the composite's fracture toughness and flexural strength [69]. Furthermore, Yan et al. explored the influence of heat on the reduction reaction of GO underneath the impact of an alkaline medium during the production process of rGO/geopolymer composite materials. Homogeneously dispersed rGO sheets were found to be well bonded with the geopolymer matrix, while the matrix exhibited an amorphous structure. With increasing temperature, the reduction degree of rGO grew concurrently with the C/O ratio, from 2.48 (GO) to 3.36 (rGO, 80 °C) [70]. Most of the researchers focused on improving the mechanical properties of the composites. Furthermore, Zhang et al. focused on improving the compressive (46.9 MPa) and bending strength (6.7 MPa) of graphene–geopolymer composite which used metakaolin as raw material and NaOH and Na_2SiO_3 as alkali excitant. Graphene dispersant of 99% purity was implemented into the composite through injection mold curing at ambient temperature to ensure optimum results. It can be noted that the strength of the composites and the amount of graphene additives are directly proportional to each other but only to a certain extent [71]. Graphene derivatives (GO, rGO, GNPs), according to several studies, have been shown to improve many critical mechanical characteristics of geopolymer composites while assuring optimal industrial waste use through geopolymerization.

4.3   Characterization

Wide commercial acceptance of graphene-based geopolymer composites requires a simultaneous understanding of its microstructure through several characterization techniques such as XRD, FTIR, SEM, and TEM. Therefore, in this section of the present study, a comprehensive review of microstructure characterization of a few prior studies conducted in the field of graphene-based geopolymer composites has been discussed. Studies by Ranjbar et al. reported the XRD data models for FA, FA geopolymer, and FA geopolymer containing graphene nanoplatelets (GNPs) 1% by wt. [67] as shown in Fig. 5d. The data models indicate the presence of crystalline phases of quartz, mullite, and albite within the FA geopolymer matrix. The addition of GNPs into the geopolymer matrix did not aid in the formation of any other phases as confirmed by XRD analysis because of their low dosage as confirmed by
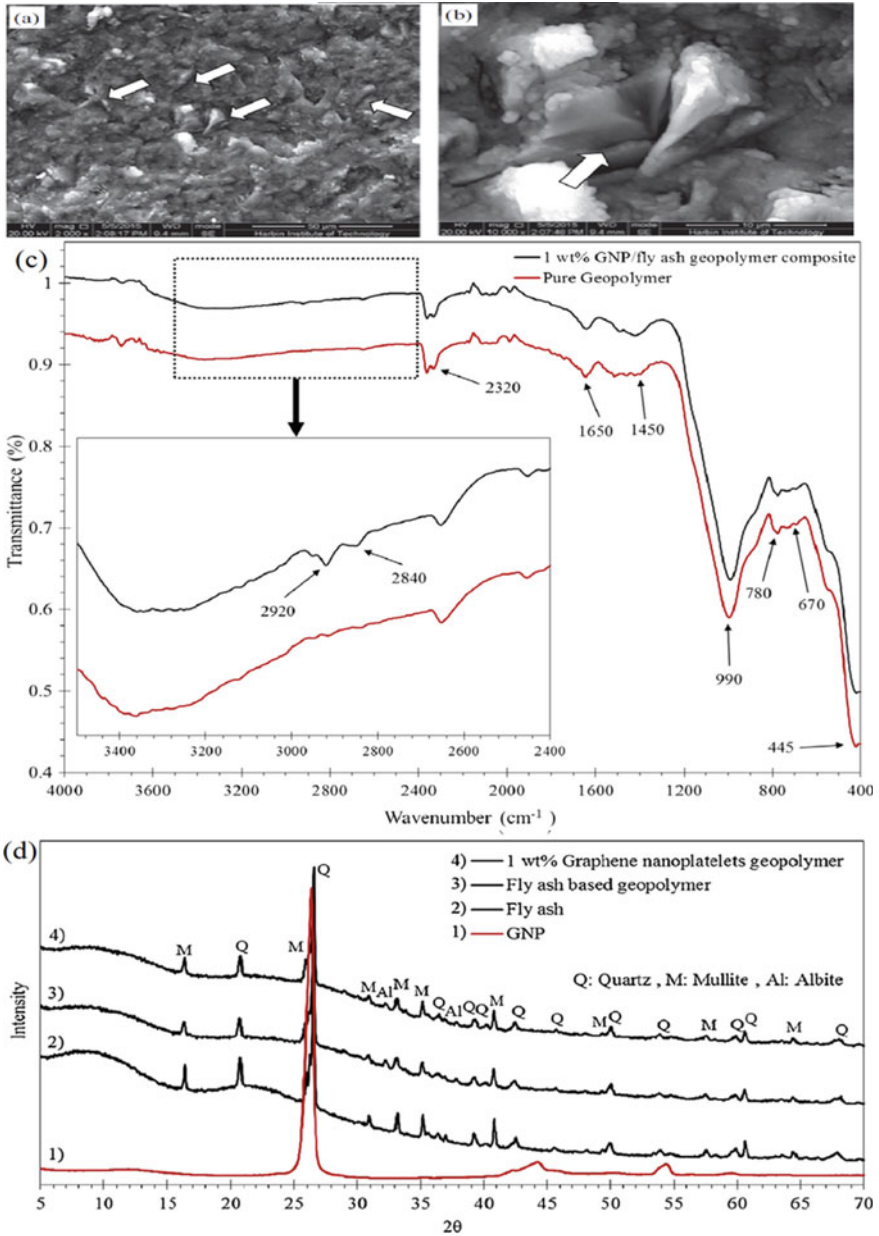
Fig. 5 **a**, **b** SEM images of rGO/geopolymer composites, **c** FTIR spectra of the pure geopolymer and GNP/fly ash geopolymer composite, **d** XRD patterns of the fly ash-based geopolymer composites [67, 70]

certain studies [69, 70, 72, 76]. The authors also analyzed the FTIR spectra of normal geopolymer and geopolymer composite reinforced with GNPs as shown in Fig. 5c and observed that the major bands of both the samples are quite similar. The intensity band at 445 cm^{-1} was assigned to Si–O–Si bending vibration, while the band at 990 cm^{-1} was identified due to Si–O–Al asymmetric stretching vibration. Similarly, the band near 780 cm^{-1} is coupled with crystalline quartz. Figure 5d shows that the band was allotted O–H bending at 1650 cm^{-1}. The bands positioned at 2920 cm^{-1} and 2840 cm^{-1} respectively indicate asymmetric and symmetric stretching of methylene groups (CH_2). Further, Yat et al. studied the XRD data models of rGO/geopolymer containing GO (1 wt%) which is decreased at 60 °C [70]. Similar data models were observed for pure geopolymer and rGO/geopolymer composites exhibiting broad elevated projections around 28° at 2θ indicating that the presence of rGO does not influence the resulting configuration of the GO/geopolymer composite. The presence of rGO could be detected through SEM observation as illustrated in Fig. 5a, b. The availability of rGO sheets that were uniformly distributed throughout the geopolymer matrix was discovered through the SEM images. XRD data models of rGO/geopolymer composite with varied rGO substitution levels were examined in another research by the same investigators [69], revealing a wide amorphous bump at 28° without any phase structural change of rGO/geopolymer samples. Several additional peaks, however, were detected and classified as quartz. XRD study did not reveal any identifiable rGO spikes, but Raman spectroscopy provided compelling evidence. TEM was used to analyze the specimens, and it was discovered that there is a strong bonding phase between the crystalline rGO and the geopolymer matrix, which contains fine microspheres. The XRD data models revealed typical geopolymer wide humps about 17–32° at 2θ as well as a minor α–quartz phase [76]. The FTIR spectra of reaction products of geopolymer with and without rGO were also analyzed which were formed at different reaction times. The FTIR spectrum of both specimens, with and without rGO, was found to be essentially unaltered. The spectra at 463, 593, and 717 cm^{-1} showed that the reaction products contained a high number of Si–O–Si, Si–O–Al, and AlO_4 structural units.

5   Concluding Remarks

Since geopolymers incorporate most of the industrial and agricultural wastes as binders or aggregates, it widens the scope of achieving sustainable development goals in construction sectors. Almost every type of industrial waste can suitably be induced into a geopolymer system depending upon its physicochemical properties. Several experimental studies have been discussed which shows the potential of GC in industrial waste management promoting a circular economy. Furthermore, researches have demonstrated the strength-enhancing properties of graphene nanomaterials in geopolymer matrix composites, but even after the tremendously promising outcomes acquired from numerous observations, to the best knowledge of the authors', a suitable number of studies are not being conducted to investigate the
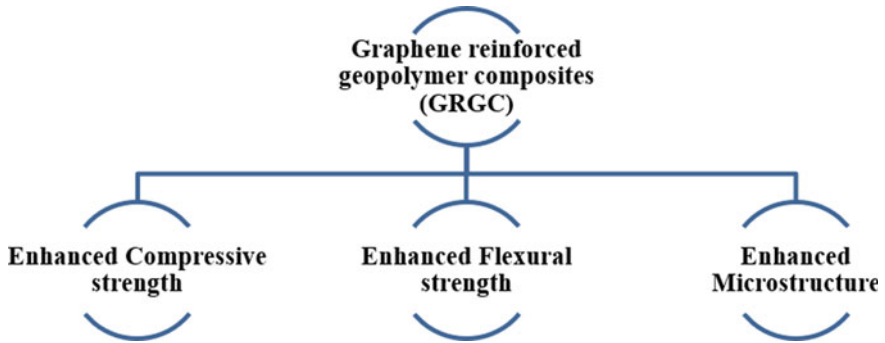
Fig. 6 Graphene as property enhancer of geopolymer composites

mechanisms involved and suitability of graphene derivatives in various geopolymer binder's hydration systems.

The reinforcement of the geopolymer matrix through graphene provides an opportunity to replace conventional fiber/silica/graphite reinforcements while reducing the utilization of scarce materials. Even if graphene variants have been demonstrated to have a broad range of applications, real-life applications of the composites are impeded by the following: negative effects on the workability, high cost, and understanding of interference factors in the matrix. Further, the involvement of industrial wastes/by-products in the production of geopolymers develops improved waste immobilization/utilization methods and facilitates the sustainable use of waste products. Recent studies have uncovered several industrial by-products as potential precursors for geopolymers which provide hope for further research.

This review paper highlights the role of graphene derivatives as a property enhancer to geopolymer composites, as depicted in Fig. 6. Graphene indubitably is a strength and property enhancer for a wide range of geopolymer composites regardless of the configuration or form of graphene used. Based on the current review, it could be stated that graphene reinforced geopolymer composites bear promising properties to be applied in different fields that will further increase the implementation and acceptability of geopolymer composites.

References

1. Davidovits J (2002) 30 years of successes and failures in geopolymer applications. Market trends and potential breakthroughs. In: Geopolymer 2002 conference

2. Davidovits J (1991) GEOPOLYMERS: inorganic polymerie new materials. J Therm Anal 37:1633–1656. https://doi.org/10.1007/bf01912193

3. Das SK, Krishna RS, Mishra S, Mustakim SM, Jena MK, Tripathy AK, Sahu T (2021) Future trends nanomaterials in alkali-activated composites. In: Colangelo F, Cioffi R, Farina I (eds) Handbook of sustainable concrete and industrial waste management, Matthew Deans. https://doi.org/10.1016/B978-0-12-821730-6.00012-7

4. Krishna RS, Shaikh F, Mishra J, Lazorenko G, Kasprzhitskii A (2021) Mine tailings-based geopolymers: properties, applications and industrial prospects. Ceram Int 47:17826–17843. https://doi.org/10.1016/j.ceramint.2021.03.180

5. Lazorenko G, Kasprzhitskii A, Shaikh F, Krishna RS, Mishra J (2021) Utilization potential of mine tailings in geopolymers: physicochemical and environmental aspects. Process Saf Environ Prot 147:559–577. https://doi.org/10.1016/j.psep.2020.12.028

6. He P, Jia D, Lin T, Wang M, Zhou Y (2010) Effects of high-temperature heat treatment on the mechanical properties of unidirectional carbon fiber reinforced geopolymer composites. Ceram Int 36:1447–1453. https://doi.org/10.1016/j.ceramint.2010.02.012

7. Bernal SA, Bejarano J, Garzón C, Mejía De Gutiérrez R, Delvasto S, Rodríguez ED (2012) Performance of refractory aluminosilicate particle/fiber-reinforced geopolymer composites. Compos B Eng 43:1919–1928. https://doi.org/10.1016/j.compositesb.2012.02.027

8. Lin TS, Jia DC, He PG, Wang MR (2009) Thermo-mechanical and microstructural characterization of geopolymers with α-Al_2O_3 particle filler. Int J Thermophys 30:1568–1577. https://doi.org/10.1007/s10765-009-0636-9

9. Yunsheng Z, Wei S, Zongjin L (2006) Impact behavior and microstructural characteristics of PVA fiber reinforced fly ash-geopolymer boards prepared by extrusion technique. J Mater Sci 41:2787–2794. https://doi.org/10.1007/s10853-006-6293-5

10. Candamano S, Sgambitterra E, Lamuta C, Pagnotta L, Chakraborty S, Crea F (2019) Graphene nanoplatelets in geopolymeric systems: a new dimension of nanocomposites. Mater Lett 236:550–553. https://doi.org/10.1016/j.matlet.2018.11.022

11. Saafi M, Piukovics G, Ye J (2016) Hybrid graphene/geopolymeric cement as a superionic conductor for structural health monitoring applications. Smart Mater Struct 25. https://doi.org/10.1088/0964-1726/25/10/105018

12. Zhong J, Zhou GX, He PG, Yang ZH, Jia DC (2017) 3D printing strong and conductive geopolymer nanocomposite structures modified by graphene oxide. Carbon 117:421–426. https://doi.org/10.1016/j.carbon.2017.02.102

13. Geim AK, Novoselov KS (2007) The rise of graphene. Nat Mater 6:183–191. https://doi.org/10.1038/nmat1849

14. Bai H, Li C, Shi G (2011) Functional composite materials based on chemically converted graphene. Adv Mater 23:1089–1115. https://doi.org/10.1002/adma.201003753

15. Park S, Ruoff RS (2009) Chemical methods for the production of graphenes. Nat Nanotechnol 4:217–224. https://doi.org/10.1038/nnano.2009.58

16. Ul Haq E, Padmanabhan SK, Licciulli A (2014) Synthesis and characteristics of fly ash and bottom ash based geopolymers—a comparative study. Ceram Int 40:2965–2971. https://doi.org/10.1016/j.ceramint.2013.10.012

17. Xie T, Ozbakkaloglu T (2015) Behavior of low-calcium fly and bottom ash-based geopolymer concrete cured at ambient temperature. Ceram Int 41:5945–5958. https://doi.org/10.1016/j.ceramint.2015.01.031

18. Parvathy S, Sharma AK, Anand KB (2019) Comparative study on synthesis and properties of geopolymer fine aggregate from fly ashes. Constr Build Mater 198:359–367. https://doi.org/10.1016/j.conbuildmat.2018.11.231

19. Ghosh R, Gupta SK, Kumar A, Kumar S (2019) Durability and mechanical behavior of fly ash-GGBFS geopolymer concrete utilizing bottom ash as fine aggregate. Trans Indian Ceram Soc 78:24–33. https://doi.org/10.1080/0371750X.2019.1581092

20. Nath SK, Kumar S (2020) Role of particle fineness on engineering properties and microstructure of fly ash derived geopolymer. Constr Build Mater 233. https://doi.org/10.1016/j.conbuildmat.2019.117294

21. Cai J, Tan J, Li X (2020) Thermoelectric behaviors of fly ash and metakaolin based geopolymer. Constr Build Mater 237. https://doi.org/10.1016/j.conbuildmat.2019.117757
22. Prusty JK, Pradhan B (2020) Effect of GGBS and chloride on compressive strength and corrosion performance of steel in fly ash-GGBS based geopolymer concrete. Mater Today Proc 850–855. Elsevier Ltd, https://doi.org/10.1016/j.matpr.2020.04.210
23. Nath P, Sarker PK (2014) Effect of GGBFS on setting, workability and early strength properties of fly ash geopolymer concrete cured in ambient condition. Constr Build Mater 66:163–171. https://doi.org/10.1016/j.conbuildmat.2014.05.080
24. Adesina A (2019) Properties of alkali activated slag concrete incorporating waste materials as aggregate: a review. In: Materials science forum. Trans Tech Publications Ltd, pp 214–220. https://doi.org/10.4028/www.scientific.net/MSF.967.214
25. Nath P, Sarker PK (2017) Fracture properties of GGBFS-blended fly ash geopolymer concrete cured in ambient temperature. Mater Struct/Materiaux et Constructions 50. https://doi.org/10.1617/s11527-016-0893-6
26. Krishna RS, Mishra J, Meher S, Das SK, Mustakim SM, Singh SK (2020) Industrial solid waste management through sustainable green technology: case study insights from steel and mining industry in Keonjhar, India. Mater Today Proc 5243–5249. Elsevier Ltd, https://doi.org/10.1016/j.matpr.2020.02.949
27. Mishra J, Das SK, Krishna RS, Nanda B, Patro SK, Mustakim SM (2020) Synthesis and characterization of a new class of geopolymer binder utilizing ferrochrome ash (FCA) for sustainable industrial waste management. Mater Today Proc 5001–5006. Elsevier Ltd, https://doi.org/10.1016/j.matpr.2020.02.832
28. Kumar BC, Yaragal SC, Das BB (2020) Ferrochrome ash—its usage potential in alkali activated slag mortars. J Clean Prod 257. https://doi.org/10.1016/j.jclepro.2020.120577
29. Mishra J, Das SK, Krishna RS, Nanda B (2020) Utilization of ferrochrome ash as a source material for production of geopolymer concrete for a cleaner sustainable environment. Indian Concr J 94:40–49
30. Nath SK (2018) Geopolymerization behavior of ferrochrome slag and fly ash blends. Constr Build Mater 181:487–494. https://doi.org/10.1016/j.conbuildmat.2018.06.070
31. Falayi T (2019) Sustainable solidification of ferrochrome slag through geopolymerisation: a look at the effect of curing time, type of activator and liquid solid ratio. Sustain Environ Res 1. https://doi.org/10.1186/s42834-019-0022-7
32. Jena S, Panigrahi R (2019) Performance assessment of geopolymer concrete with partial replacement of ferrochrome slag as coarse aggregate. Constr Build Mater 220:525–537. https://doi.org/10.1016/j.conbuildmat.2019.06.045
33. Jindal BB, Jangra P, Garg A (2020) Effects of ultra fine slag as mineral admixture on the compressive strength, water absorption and permeability of rice husk ash based geopolymer concrete. Mater Today Proc 871–877. Elsevier Ltd, https://doi.org/10.1016/j.matpr.2020.04.219
34. Hwang CL, Huynh TP (2015) Effect of alkali-activator and rice husk ash content on strength development of fly ash and residual rice husk ash-based geopolymers. Constr Build Mater 101:1–9. https://doi.org/10.1016/j.conbuildmat.2015.10.025
35. Kusbiantoro A, Nuruddin MF, Shafiq N, Qazi SA (2012) The effect of microwave incinerated rice husk ash on the compressive and bond strength of fly ash based geopolymer concrete. Constr Build Mater 36:695–703. https://doi.org/10.1016/j.conbuildmat.2012.06.064
36. Das SK, Mishra J, Singh SK, Mustakim SM, Patel A, Das SK, Behera U (2020) Characterization and utilization of rice husk ash (RHA) in fly ash—blast furnace slag based geopolymer concrete for sustainable future. Mater Today Proc 5162–5167. Elsevier Ltd, https://doi.org/10.1016/j.matpr.2020.02.870
37. Kaur K, Singh J, Kaur M (2018) Compressive strength of rice husk ash based geopolymer: The effect of alkaline activator. Constr Build Mater 169:188–192. https://doi.org/10.1016/j.conbuildmat.2018.02.200
38. Hajimohammadi A, van Deventer JSJ (2017) Solid reactant-based geopolymers from rice hull ash and sodium aluminate. Waste Biomass Valorization 8:2131–2140. https://doi.org/10.1007/s12649-016-9735-6

39. Noor-Ul-Amin M, Faisal K, Muhammad S (2016) Gul, synthesis and characterization of geopolymer from bagasse bottom ash, waste of sugar industries and naturally available China clay. J Clean Prod 129:491–495. https://doi.org/10.1016/j.jclepro.2016.04.024

40. Alonso MM, Gascó C, Morales MM, Suárez-Navarro JA, Zamorano M, Puertas F (2019) Olive biomass ash as an alternative activator in geopolymer formation: a study of strength, durability, radiology and leaching behavior. Cem Concr Compos 104. https://doi.org/10.1016/j.cemcon comp.2019.103384.

41. Olivia M, Wulandari C, Sitompul IR, Darmayanti L, Djauhari Z (2016) Study of fly ash (FA) and palm oil fuel ash (POFA) geopolymer mortar resistance in acidic peat environment. In: Materials science forum, Trans Tech Publications Ltd, pp 126–132. https://doi.org/10.4028/www.scientific.net/MSF.841.126

42. Ranjbar N, Mehrali M, Behnia A, Alengaram UJ, Jumaat MZ (2014) Compressive strength and microstructural analysis of fly ash/palm oil fuel ash based geopolymer mortar. Mater Des 59:532–539. https://doi.org/10.1016/j.matdes.2014.03.037

43. Sukmak P, Kunchariyakun K, Sukmak G, Horpibulsuk S, Kassawat S, Arulrajah A (2019) Strength and microstructure of palm oil fuel ash-fly ash–soft soil geopolymer masonry units. J Mater Civ Eng 31:04019164. https://doi.org/10.1061/(asce)mt.1943-5533.0002809

44. Ikponmwosa EE, Ehikhuenmen S, Emeshie J, Adesina A (2021) Performance of coconut shell alkali-activated concrete: experimental investigation and statistical modelling. SILICON 13:335–340. https://doi.org/10.1007/s12633-020-00435-z

45. Amran M, Fediuk R, Murali G, Vatin N, Karelina M, Ozbakkaloglu T, Krishna RS, Kumar AS, Kumar DS, Mishra J (2021) Rice husk ash-based concrete composites: a critical review of their properties and applications. Curr Comput-Aided Drug Des 11:1–33. https://doi.org/10.3390/cryst11020168

46. Krishna RS, Mishra J, Zribi M, Adeniyi F, Saha S, Baklouti S, Shaikh FUA, Gökçe HS (2021) A review on developments of environmentally friendly geopolymer technology. Materialia 20. https://doi.org/10.1016/j.mtla.2021.101212

47. Mishra J, Panigrahi R (2020) Mini-review on structural performance of fiber reinforced geopolymer concrete. Int J Innov Technol Interdisc Sci 3:435–442. www.ijitis.org, https://doi.org/10.15157/IJITIS.2020.3.2.435-442

48. Liu Y, Shi C, Zhang Z, Li N, Shi D (2020) Mechanical and fracture properties of ultra-high performance geopolymer concrete: Effects of steel fiber and silica fume. Cem Concr Compos 112:103665. https://doi.org/10.1016/j.cemconcomp.2020.103665

49. Assaedi H, Alomayri T, Shaikh F, Low IM (2019) Influence of nano silica particles on durability of flax fabric reinforced geopolymer composites. Materials 12. https://doi.org/10.3390/ma1209 1459

50. Zhuang XY, Chen L, Komarneni S, Zhou CH, Tong DS, Yang HM, Yu WH, Wang H (2016) Fly ash-based geopolymer: clean production, properties and applications. J Clean Prod 125:253–267. https://doi.org/10.1016/j.jclepro.2016.03.019

51. Dhand V, Mittal G, Rhee KY, Park SJ, Hui D (2015) A short review on basalt fiber reinforced polymer composites. Compos B Eng 73:166–180. https://doi.org/10.1016/j.compositesb.2014.12.011

52. Korniejenko K, Frączek E, Pytlak E, Adamski M (2016) Mechanical properties of geopolymer composites reinforced with natural fibers. Procedia Eng 388–393. https://doi.org/10.1016/j.proeng.2016.07.395

53. Niu D, Su L, Luo Y, Huang D, Luo D (2020) Experimental study on mechanical properties and durability of basalt fiber reinforced coral aggregate concrete. Constr Build Mater 237. https://doi.org/10.1016/j.conbuildmat.2019.117628

54. Shaikh F, Haque S (2018) Behaviour of carbon and basalt fibres reinforced fly ash geopolymer at elevated temperatures. Int J Concr Struct Mater 12. https://doi.org/10.1186/s40069-018-0267-2

55. Ranjbar N, Zhang M (2020) Fiber-reinforced geopolymer composites: a review. Cem Concr Compos 107. https://doi.org/10.1016/j.cemconcomp.2019.103498

56. Porwal H, Grasso S, Reece MJ (2013) Review of graphene-ceramic matrix composites. Adv Appl Ceram 112:443–454. https://doi.org/10.1179/174367613X13764308970581
57. Krishna RS, Mishra J, Das SK, Mustakim SM (2022) An overview of current research trends on graphene and it's applications. Worls Scientific News, vol 132, pp 206–219. http://www.worldscientificnews.com/wp-content/uploads/2019/06/WSN-132-2019-206-219.pdf. Accessed 18 January 2022
58. Dasari BL, Nouri JM, Brabazon D, Naher S (2017) Graphene and derivatives—synthesis techniques, properties and their energy applications. Energy 140:766–778. https://doi.org/10.1016/j.energy.2017.08.048
59. Sturala J, Luxa J, Pumera M, Sofer Z (2018) Chemistry of graphene derivatives: synthesis, applications, and perspectives. Chem Eur J 24:5992–6006. https://doi.org/10.1002/chem.201704192
60. Inagaki M, Kang F (2014) Graphene derivatives: graphane, fluorographene, graphene oxide, graphyne and graphdiyne. J Mater Chem A 2:13193–13206. https://doi.org/10.1039/c4ta01183j
61. Krishna RS, Mishra J, Adetayo A, Das SK, Mustakim SM (2020) Green synthesis of high-performance graphene reinforced geopolymer composites: a review on environment-friendly extraction of nanomaterials. Iran J Mater Sci Eng 17:10–24. https://doi.org/10.22068/IJMSE.17.4.10
62. Paszkiewicz S, Szymczyk A, Roslaniec Z (2016) Graphene derivatives in semicrystalline polymer composites. In: Tiwari A, Syväjärvi M (eds) Advanced 2D materials. Scrivener Publishing LLC, pp 147–192. https://doi.org/10.1002/9781119242635.ch5
63. Krishna RS, Mishra J, Nanda B, Patro SK, Adetayo A, Qureshi TS (2021) The role of graphene and its derivatives in modifying different phases of geopolymer composites: a review. Constr Build Mater 306. https://doi.org/10.1016/j.conbuildmat.2021.124774
64. Saafi M, Tang L, Fung J, Rahman M, Liggat J (2015) Enhanced properties of graphene/fly ash geopolymeric composite cement. Cem Concr Res 67:292–299. https://doi.org/10.1016/j.cemconres.2014.08.011
65. Tang L-C, Zhao L, Guan L-Z (2017) Graphene polymer composite materials: processing, properties and applications. In: Advanced composite materials: properties and applications. De Gruyter Open Poland, pp 349–419. https://doi.org/10.1515/9783110574432-007
66. Lowe SE, Zhong YL (2016) Challenges of industrial-scale graphene oxide production. Wiley. https://doi.org/10.1002/9781119069447.ch13
67. Ranjbar N, Mehrali M, Mehrali M, Alengaram UJ, Jumaat MZ (2015) Graphene nanoplatelet-fly ash based geopolymer composites. Cem Concr Res 76:222–231. https://doi.org/10.1016/j.cemconres.2015.06.003
68. Danial NS, Che Halin DS, Ramli MM, Abdullah MMA, Mohd Salleh MAA, Mat Isa SS, Talip LFA, Mazlan NS (2019) Graphene geopolymer hybrid: a review on mechanical properties and piezoelectric effect. IOP Conf Ser Mater Sci Eng. Institute of Physics Publishing. https://doi.org/10.1088/1757-899X/572/1/012038
69. Yan S, He P, Jia D, Yang Z, Duan X, Wang S, Zhou Y (2016) Effect of reduced graphene oxide content on the microstructure and mechanical properties of graphene–geopolymer nanocomposites. Ceram Int 42:752–758. https://doi.org/10.1016/j.ceramint.2015.08.176
70. Yan S, He P, Jia D, Yang Z, Duan X, Wang S, Zhou Y (2016) Effects of treatment temperature on the reduction of GO under alkaline solution during the preparation of graphene/geopolymer composites. Ceram Int 42:18181–18188. https://doi.org/10.1016/j.ceramint.2016.08.134
71. Zhang G, Lu J (2018) Experimental research on the mechanical properties of graphene geopolymer. AIP Adv 8. https://doi.org/10.1063/1.5020547
72. Yan S, He P, Jia D, Duan X, Yang Z, Wang S, Zhou Y (2016) Crystallization kinetics and microstructure evolution of reduced graphene oxide/geopolymer composites. J Eur Ceram Soc 36:2601–2609. https://doi.org/10.1016/j.jeurceramsoc.2016.03.026
73. Zhang YJ, Zhang YX, Yang MY (2018) Synthesis of environment-friendly graphene reinforced slag-based nanocomposite and performance of photocatalytic H_2 generation. Ferroelectrics 522:36–44. https://doi.org/10.1080/00150193.2017.1391609

74. Long WJ, Lin C, Tan XW, Tao JL, Ye TH, Luo QL (2020) Structural applications of thermal insulation alkali activated materials with reduced graphene oxide. Materials 13. https://doi.org/10.3390/ma13051052
75. Amri A, Hendri YB, Zultiniar, Malindo E, Rahman MM (2019) Graphene nanosheets (GNs) addition on the palm oil fuel ash (POFA) based geopolymer with KOH activator. J Phys Conf Ser 1351. https://doi.org/10.1088/1742-6596/1351/1/012101
76. Yan S, He P, Jia D, Duan X, Yang Z, Wang S, Zhou Y (2017) Effects of graphene oxide on the geopolymerization mechanism determined by quenching the reaction at intermediate states. RSC Adv 7:13498–13508. https://doi.org/10.1039/c6ra26340b

Overview on Medicinal Impacts of 1,2,4-Triazole Derivatives

Arup K. Kabi, Raghuram Gujjarappa, Aakriti Garg, Anupam Roy, Abhishek Sahoo, Sreya Gupta, and Chandi C. Malakar

Abbreviations

U.S. FDA	United State Food and Drug Administration
HIV	Human immunodeficiency virus
NAD	Nicotinamide adenine dinucleotide
DNA	Deoxyribonucleic acid
HER2	Human epidermal growth factor receptor 2
COX	Cyclooxygenase
XPO1	Exportin 1
OAT4	Organic anion carrier 4
URAT1	Uric acid carrier 1
DPP-4	Dipeptidyl peptidase-4
PARP	Poly(ADP-ribose)polymerase
RNA	Ribonucleic acid
SAR	Structure–activity relationship
GLP-1	Glucagon-like peptide 1
AIDS	Acquired immune deficiency syndrome
GIP	Gastric inhibitory polypeptide
TNFα	Tumour necrosis factor α
HSV	Herpes simplex viruses

A. K. Kabi · R. Gujjarappa · A. Roy · A. Sahoo · C. C. Malakar (✉)
Department of Chemistry, National Institute of Technology Manipur, Langol, Imphal, Manipur 795004, India
e-mail: cmalakar@nitmanipur.ac.in; chdeepm@gmail.com

A. K. Kabi
e-mail: kabiarup1992@gmail.com

A. Garg · S. Gupta
Department of Medicinal Chemistry, National Institute of Pharmaceutical Education and Research (NIPER), Chunilal Bhawan, 168, Maniktala Main Road, Kolkata 700054, India

JNK   Jun N-terminal kinase

1 Introduction

1,2,4-Triazole-embedded heterocycles have acquired immense attention as effective bioactive molecules because of their diverse range of pharmacological properties associated to anti-inflammatory activity [1], antimicrobial activity [2, 3], antihypertensive activity [4], anticancer activity [5–8], antiparasitic activity [9], CNS stimulants sedatives [10, 11], antitubercular activity [12, 13], antiviral activity [14], antioxidant activity [15], thymidine phosphorylase inhibitory activity [16], antimalarial activity [17–19], antimycotic activities [20] and diuretic activities [21]. The 1,2,4-triazole molecular architecture are ubiquitous in valuable pharmaceuticals, including triazolam, maraviroc, alprazolam, deferasirox and etizolam sitagliptin. Triazolam is referred for the treatment of insomnia under the brand name Halcion. Alprazolam (Xanax) is utilized towards the cure of panic disorders, anxiety disorders and anxiety which are associated with depression. Etizolam (Etizola) is indicated as hypnotic and anxiolytic agents (Fig. 1) [22–24].

2 1,2,4-Triazoles and Their Pharmaceutical Drugs

The thione- and mercapto-embedded compounds of 1,2,4-triazoles are also attributed to a variety of biological activities like antimicrobial, antibacterial, antidepressant and antifungal activities [25] (Figs. 2, 3 and 4).
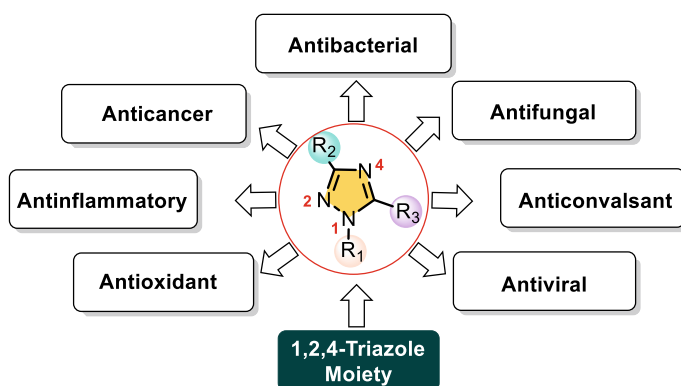
Fig. 1 Role of 1,2,4-triazole in the field of medicinal chemistry [1–4]
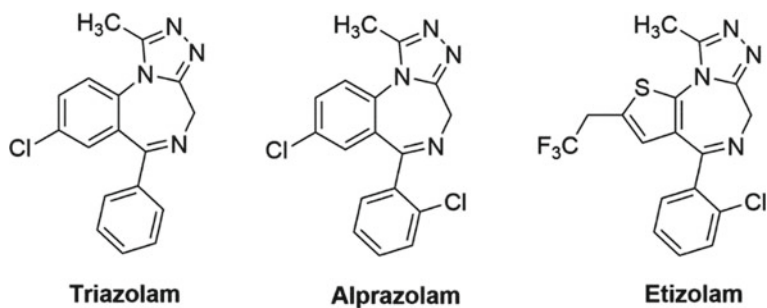
Fig. 2 Important pharmaceuticals possessing 1,2,4-triazole scaffold [5–10]
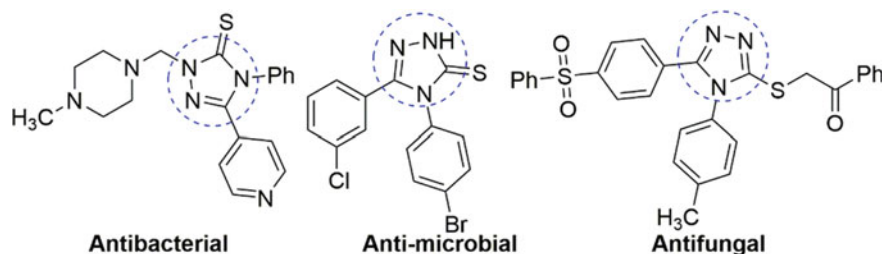
Fig. 3 Biologically important 1,2,4-triazole-3-thione derivatives [11–19]

3 Biological Importance of 1,2,4-Triazole Derivatives

1,2,4-Triazole compounds are known as the key heterocyclic ring ubiquitous in various biologically active agents. They reveal a spectrum of biological activities like antibacterial, antiviral, antifungal, antitubercular, analgesic, anti-inflammatory, anti-cancer, anticonvulsant, anxiolytic, antioxidant activities and other biological properties [26, 27]. The significance of the imidazole scaffolds as a pharmaceutically active molecular architecture, resulted to the induced attention on the triazole core structure as it performs as the bioisostere for the imidazole ring [28]. The targeting affinity of the azole containing antifungals to the lanosterol 14α-demethylase hinges upon both the fixation of the nitrogen atom of azole moiety to the haem iron in the active site (N-3 of imidazole or N-4 of triazole) and N-1 substituent for the apoprotein unit of the enzyme. The N-1 unit resides on the azole moiety enhances or diminishes the antifungal properties. The occurrences of benzimidazole or 1,2,4-triazole exhibits maximum attraction towards the enzymes [29]. The antifungal property of triazole scaffolds is related to the activity of fluconazole, and some of the molecules displayed greater activity [30].

The structure–activity relationship (SAR) of 1,2,4-triazoles having antituberculosis activity reveals that electronegative atom on phenyl of benzyl ring in benzoimidazole has significant effect on antimicrobial activity (Fig. 5). Many of the newly
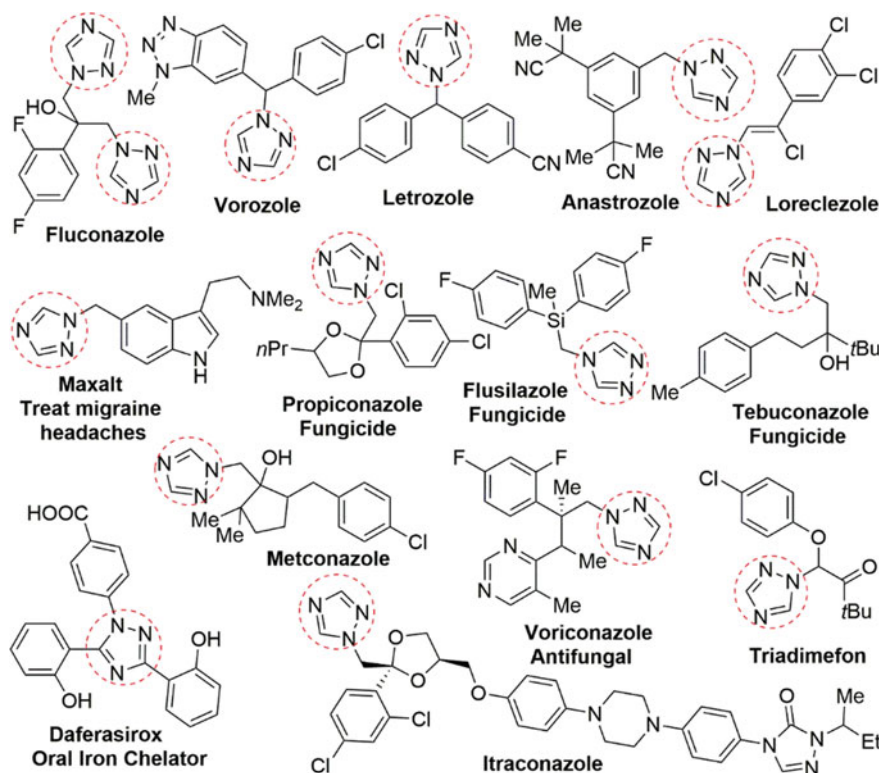
Fig. 4 Commercial drug molecules embedded with 1,2,4-triazole scaffold [4–19]

synthesized derivatives are compared with the rifampicin. It was found that these newly synthesized exhibits an enhanced or similar activity with the rifampicin. The MIC value of the drug molecule was realized to be within the range of 12.5–3.12 ug/ml. It has been also revealed that the functionalized triazole molecules illustrate the inhibition of M. tuberculosis H37Rv within the range of 94–98% at the concentration range of 6.25–3.125 µg/ml. Moreover, chloro- and fluoro-substitution on benzene ring have shown excellent antimicrobial activity (>96% inhibition on 6.25 µg mL^{-1}) on H37Rv strain of M. *tuberculosis*. The secondary antituberculosis screening (MABA assay) reveals that electron withdrawing substituents have much higher efficacy over electron donating motif in MIC value [31].

Several functionalized 1,2,4-triazoles displayed favourable anti-inflammatory properties when compared with the performance of phenylbutazone at a dose of 100 mg/kg body weight. These molecules have also witnessed with moderate analgene properties, when compared to aspirin. The compelling anti-inflammatory functions were exhibited in the presence of chloro-group in one of the phenyl rings at 4th position and in the presence of allyl or propyl group in the 5th position [28]. Triazoles embedded with perimidine derivatives were examined for the anti-inflammatory

GI(%)* = <90%
MIC** = --

GI(%) = 96%
MIC = 3.13 μg.mL^{-1}

GI(%) = 96%
MIC = 1.56 μg.mL^{-1}

GI(%) = 96%
MIC = 3.13 μg.mL^{-1}

GI(%) = 96%
MIC = 0.58 μg.mL^{-1}

GI(%) = 96%
MIC = 0.36 μg.mL^{-1}
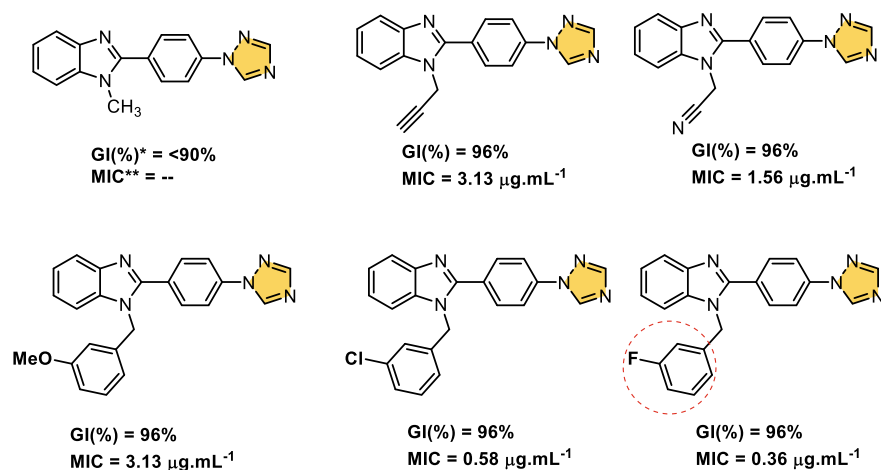
* GI(%) = Growth inhibition of virulent H37Rv strain of *M. tuberculosis* at concentration of 6.25 μg.mL^{-1}
** MIC = Actual inhibitory concentration (MABA assay).

Fig. 5 Structure–activity relationship (SAR) of 1,2,4-triazole compounds in antituberculosis activity

activities which resulted in more potent molecules than ibuprofen. The inhibition rate was noticed with 49.26% at a dose of 50 mg/kg, whereas the inhibition rate of ibuprofen was realized to be 28.13%, when studied in the xylene-induced ear inflammation model. These molecules are familiar to function as COX-II inhibitors [31].

Antineoplastic appearance of the triazole derivatives hinges upon the affinity to the biotargets, such as tumour necrosis factor TNFα, JNK-stimulatingphosphatase-1(JSP-1), integrin avb3 receptor, anti-apoptic biocomplex Bcl-XL-BH3, etc. The triazole core structures amalgamated with other heterocycles provide new pharmacological profiles, either by enhancing their ability of performance or reducing of toxicity. The imidazole molecules possess cytotoxic actions on the DNA structure of breast cancer cell. Few compounds encountered with cytotoxicity and the activity rely upon the functionalization pattern of the side chains at C-2 position and 4-triflouromethylanilino group at C-7 position [32].

Additionally, the triazole derivatives have found to be suitable for pursuing their antiviral activities. Ribavirin is proven as a remarkable antiviral drug. Substitution of amide group by alkynyl group within the structure of ribavirin led to the formation of nucleoside triazole, which is more efficient as antiviral compound. It has been observed that the alteration of substitution on the triazole moiety was very effective when compared with reference drug like azidothymidine. These molecules are found potent towards inhibition of the HIV-1 reverse transcriptase catalytic activity with higher cytotoxicity and greater selectivity index than zalcitabine and didanosine. Moreover, it was investigated that when the triazole ring was replaced with the other

heterocyclic ring, it led towards reduced protease inhibition which acknowledge the significance of triazole ring against the antiviral activities [4].

The importance of FDA-approved 1,2,4-triazole containing drug molecules is represented in this section (Table 1) [26–32].
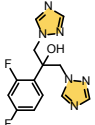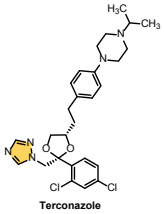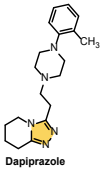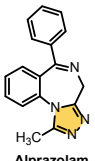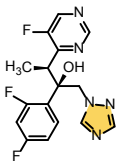
4 Mechanism of Action of 1,2,4-Triazole Drug Derivatives

4.1 Antifungal Agents

1,2,4-trazoles, commonly known as azoles, are well-known heteroaromatic compounds used as an antifungal agent. Among the numerous azole derivatives, fluconazole [33], terconazole [34], dapiprazole, voriconazole [34], posaconazole [34], eficonazole [34], itraconazole [34], isavuconazole [34], isavuconazolium [34], etc. are widely used in medical practices worldwide. Interestingly, the antifungal azole family congeners are working through the common action of mechanism, impairment of ergosterol synthesis in fungal cell membrane of the fungi. Ergosterol, a member of sterol family, is an important component of cell membrane of fungi which mainly resides on the surface of cell membrane to provide adequate fluidity to the membrane similar to the cholesterol for mammalian cells. Ergosterol biosynthesis from intermediate lanosterol is one of the utmost essential event for the fungal replication and survival. Without adequate production of ergosterol, fungal membrane becomes permeable and subsequently start leaking of intracellular components essential for survival. Lanosterol-14-α-demethylase, also known as fungal cytochrome P450, is the key enzyme responsible for biotransformation of lanosterol to ergosterol in fungus and thus becomes pivotal drug target against the fungal infection. Inhibition of P450 could disrupt the ergosterol biosynthesis in fungus and eventually destroy the membrane rigidity of the fungal colony. Azoles eventually found worthy small molecule inhibitor against fungal P450, which efficiently inhibits oxidative demethylation possesses of lanosterol and ultimately interrupt the membrane stability of fungus (Fig. 6).
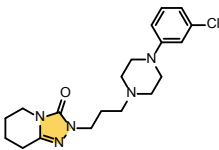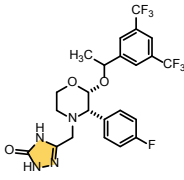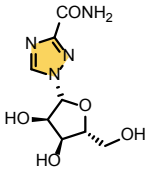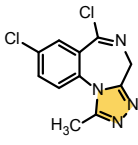
Azoles are known for the cure of candidiasis and to manage the oropharyngeal or esophageal candidiasis and vaginal candidiasis. It is also employed for the medication of cryptococcosis in AIDS and cryptococcal meningitis. There are multiple adverse actions associated with this medication hepatotoxicity, abdominal pain, flatulence, vomiting, nausea and diarrhoea. The metabolism of fluconazole is observed via glucuronide conjugation [25].

Table 1 1,2,4-Triazole containing drugs and their mode of action [26–32]

Structure of the drug name of the drug (Drug bank ID)	Category/indication	Mechanism of action
Fluconazole DB00196	Referred for the medication of the fungal infections	This acts as a selective inhibitor of enzyme *lanosterol 14-α-demethylase* which is fungal cytochrome P450 dependent
Terconazole DB00196	Terconazole is recommended for the cure of candidiasis (which is a yeast-like fungal infection) of the vulva and vagina	Terconazole is employed for the antifungal performances by agitating the permeability of membranes of normal fungal cell
Dapiprazole DB00298	Dapiprazole is normally utilized for the medication of iatrogenically inspired mydriasis generated by parasympatholytic (tropicamide) and adrenergic (phenylephrine) agents employed in specific eye examinations	Dapiprazole functions via the hindering the alpha1-adrenergic receptors in smooth muscle
Alprazolam DB00404	Alprazolam is employed for the control of anxiety associated with depression, anxiety disorder, panic disorder with agoraphobia and panic disorder. Alprazolam may also be indicated for premenstrual syndrome, insomnia and depression	Alprazolam functions on benzodiazepine receptors BNZ-1 and BNZ-2
Voriconazole DB00582	Voriconazole indicated for the medication of invasive pulmonary aspergillosis, esophageal candidiasis and serious fungal infections induced by *Fusarium spp* and *Scedosporium apiospermum*	Voriconazole associates and prohibits ergosterol synthesis by hindering CYP450-governed 14-alpha sterol demethylase. The blockage of 14-alpha sterol demethylase led to the damage of ergosterol in fungal cell membrane
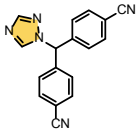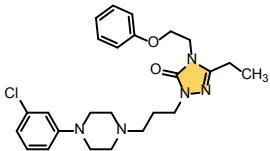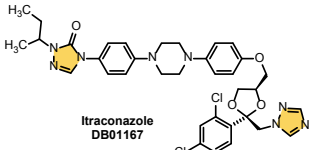
Table 1 (continued)

Structure of the drug name of the drug (Drug bank ID)	Category/indication	Mechanism of action
 Trazodone **DB00656**	Trazodone is used for the cure of major depressive disorder (MDD)0.21 It has been employed off-label to treat anxiety and insomnia, and off-label for adjunct therapy in alcohol dependence.21 This is also recommended for off-label for the recovery of symptoms of Alzheimer's disease, dementia, schizophrenia, fibromyalgia and eating disorders, which is because of its assistance on numerous neurotransmitter receptors	Trazodone is accepted to hinder the reuptake of serotonin and block both alpha-1-adrenergic and histamine receptors
 Aprepitant **DB00673**	Aprepitant is utilized for the obstruction of vomiting and nausea affiliated to highly emetogenic cancer chemotherapy, including high-dose cisplatin	Human PET and animal experiments with aprepitant have resulted that it crosses the blood brain barrier and occupies brain NK1 receptors
 Ribavirin **DB00811**	Ribavirin employed for the medication of chronic Hepatitis C virus (HCV) infection in association with other antiviral agents which desire to cure the endorsed virologic response	Ribavirin results in the obstruction of viral RNA and protein synthesis. Blockage of host inosine monophosphate dehydrogenase (IMPDH) and consequent damage of GTP pool is recommended to be another mode of action for ribavirin
 Triazolam **DB00897**	Triazolam is employed for the interim medication of insomnia	Benzodiazepines associate unselectively to benzodiazepine receptors BNZ1, which intervene sleep, and BNZ2 induces muscle relaxation, motor coordination, anticonvulsant activity and memory
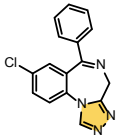
Table 1 (continued)

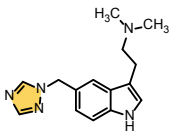| Structure of the drug name of the drug (Drug bank ID)	Category/indication	Mechanism of action
Rizatriptan DB00953	Rizatriptan recommended for cure of acute migraine attacks with or without aura	There are three noticeable biological conducts have been associated in the antimigraine response of the triptans: (1) expedition of presynaptic 5-HT1D receptors, which deals to hinder both inflammation and dural vasodilation; (2) direct prohibition of trigeminal nuclei cell excitability via 5-HT1B/1D receptor agonism in the brainstem and (3) vasoconstriction of dural, meningeal, cerebral, or pial vessels as an outcome of vascular 5-HT1B receptor agonism
Letrozole DB01006	Letrozole is recommended for the prolonged adjuvant medication of early breast cancer in postmenopausal women gone through 5 years of adjuvant tamoxifen therapy	Letrozole is familiar as a nonsteroidal competing preventer of the aromatase enzyme system; this hinders the transformation of androgens to oestrogens
Nefazodone DB01149	Nefazodone is utilized for the medication of depression	Within the serotonergic system, nefazodone performs as fluoxetine-type antidepressants, antagonist at type 2 serotonin (5-HT2) post-synaptic receptors and, prohibits presynaptic serotonin (5-HT) reuptake
Itraconazole DB01167	Itraconazole is employed for the medication of the fungal infections in non-immuno-compromised and immuno-compromised patients. The types of fungal infections are extrapulmonary, pulmonary, aspergillosis, histoplasmosis, blastomycosis and onychomycosis	Itraconazole cooperates with 14-α demethylase, a cytochrome P-450 enzyme requires transforming lanosterol to ergosterol
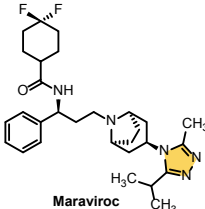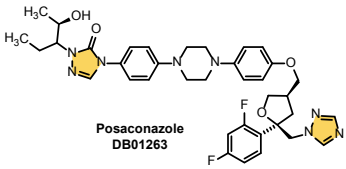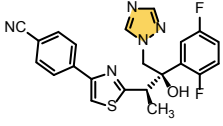
(continued)

Table 1 (continued)

Structure of the drug name of the drug (Drug bank ID)	Category/indication	Mechanism of action
Estazolam DB01215	Estazolam is utilized for the interim control of insomnia identified by severely frequent nocturnal awakenings, in falling asleep and/or early morning awakenings	Benzodiazepines affiliated non-selectively to benzodiazepine receptors. This induces anticonvulsant activity, muscle relaxation and motor coordination
Anastrozole DB01217	Anastrozole is employed for the medication of hormone receptor-positive early breast cancer in women with postmenopausal. This is also used as a first-line medication for hormone receptor-positive metastatic breast cancer and locally advanced for women with postmenopausal	Anastrozole exercises the anti-estrogenic activities via specific and competitive prohibition of the aromatase enzyme realized broadly in the liver, adrenal glands and fatty tissues
Sitagliptin DB01261	Sitagliptin is recommended for the control of glycemic regulation in type 2 diabetes mellitus along with exercise and diet	Suppression of DPP-4 by sitagliptin reduces DPP-4-assisted incretins inactivation like GLP-1 and GIP. Labe l,2 Incretins are liberated during the day and up-regulated in response to meals as part of glucose homeostasis
Deferasirox DB01609	Deferasirox is recommended for the management of excessive chronic iron, which is because of transfusions of blood (transfusional hemosiderosis) in the patients of 2 years of age and older	One atom of iron can be accommodated by two molecules of Deferasirox. Deferasirox also functions for treatment of iron toxicity by associating trivalent iron, which delivers a stable complex that discharged via the kidneys
Fosaprepitant DB06717	Fosaprepitant is used for the suppression of vomiting and nausea related with highly emetogenic cancer chemotherapy	In animal models to hinder emesis assisted by cytotoxic chemotherapeutic agents, such as cisplatin, via central actions
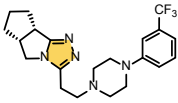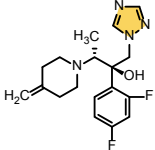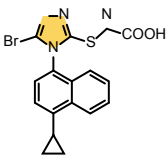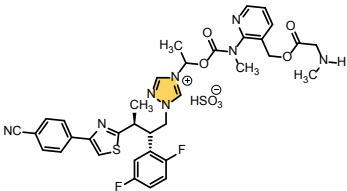
Table 1 (continued)

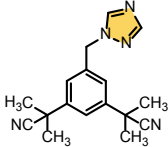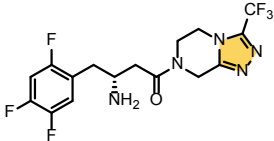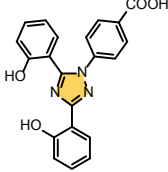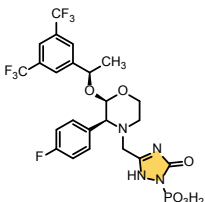| Structure of the drug name of the drug (Drug bank ID)	Category/indication	Mechanism of action
Doravirine DB12301	Doravirine is employed in addition with other antiretroviral agents for the cure of HIV-1 infection in adult patients associated with no prior antiretroviral treatment history	Doravirine is familiar as pyridinone non-nucleoside reverse transcriptase suppressor of HIV-1
Maraviroc DB04835	Maraviroc is well-known for the medication of adult patients infected with only CCR5-tropic HIV-1, with indication of viral replication and HIV-1 strains resistant to multiple antiretroviral agents	Maraviroc is an entry inhibitor and functions by hindering HIV from penetrating human cells. Specifically maraviroc is a slowly reversible and specific small molecule antagonist of the cooperation between HIV-1 gp120 and human CCR5
Posaconazole DB01263	Posaconazole is represented for prophylaxis of invasive Candida and Aspergillus infections in patients	Posaconazole operates the antifungal activity through hindering sterol 14α-demethylase and the cytochrome P-450-dependent enzyme in fungi by associating to the haem cofactor located on the enzyme. This leads to the obstruction of the synthesis of ergosterol, a key ingredient of the fungal cell membrane, and accession of methylated sterol precursors. This concludes in blockage of fungal cell growth and finally led to the cell death
Isavucon-azole DB11633	Isavuconazole is utilized for the patients of 18 years of age and older for the cure of invasive aspergillosis, invasive mucormycosis including patients gone through inappropriate medication of amphotericin B	Isavuconazole represents fungicidal performances by agitating the biosynthesis of ergosterol
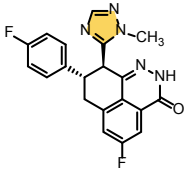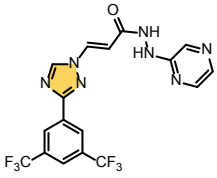
(continued)

Table 1 (continued)

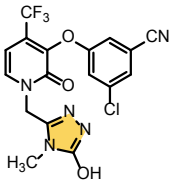| Structure of the drug name of the drug (Drug bank ID)	Category/indication	Mechanism of action
Lorpiprazole **DB09195**	Lorpiprazole is noticeable as an antipsychotic remedy which is employed to treat hallucination, a state of delusion, paranoia or disordered thoughts. On the other hand, an anxiolytic is a medication applied for the cure of severe, debilitating, or chronic anxiety	Lorpiprazole is recognized as a serotonin antagonist and reuptake suppressor. Hence, action is conducted by antagonizing the 5-HT2C and 5-HT2A serotoninergic receptors. These actions may also be performed by H1 histaminergic receptors, alpha1 and alpha2 adrenergic receptors, and at high doses, hindering the SERT serotonin transporter
Efinaconazole **DB09040**	Efinaconazole is familiar for the cure of fungal infection of the nail, known as onychomycosis	Efinaconazole is an azole-based antifungal drug. Efinaconazole hinders fungal lanosterol 14α-demethylase associated in the biosynthesis of ergosterol, which is a constituent of fungal cell membranes
Lesinurad **DB11560**	Lesinurad usually utilized in combination with a xanthine oxidase blocker, for the remedy of hyperuricemia related to in patients who have not realized target serum uric acid levels with a xanthine oxidase inhibitor alone	Lesinurad suppresses the performances of and organic anion carrier 4 (OAT4) and uric acid carrier 1 (URAT1). URAT1 is a major carrier enzyme accountable for reuptake of uric acid from the renal tubules. Inhibition of URAT1 operation thereby induces excretion of uric acid
Isavucon-Azonium **DB06636**	Isavuconazonium is employed for the medication of invasive mucormycosis and invasive aspergillosis	Isavuconazonium target and hinder the sterol 14-α-demethylase (Erg11p), which is an important player in the demethylation process of the biosynthetic pathways of ergosterol

Table 1 (continued)

Structure of the drug name of the drug (Drug bank ID)	Category/indication	Mechanism of action
Talazoparib DB11760	Talazoparib is employed for the cure of HER2 negative metastatic or locally advanced breast cancer in adults	Talazoparib associated with and hinders PARP1 and PARP2 at the NAD+ binding site which leads a Ki of 1.2 and 0.87 nM, respectively 1. The inhibitory actions on PAR synthesis refers to an EC50 of 2.51 nM
Selinexor DB11942	Selinexor is recognized for the medications of refractory or relapsed multiple myeloma in addition with dexamethasone	Selinexor targets to and suppresses exportin-1 (XPO1)
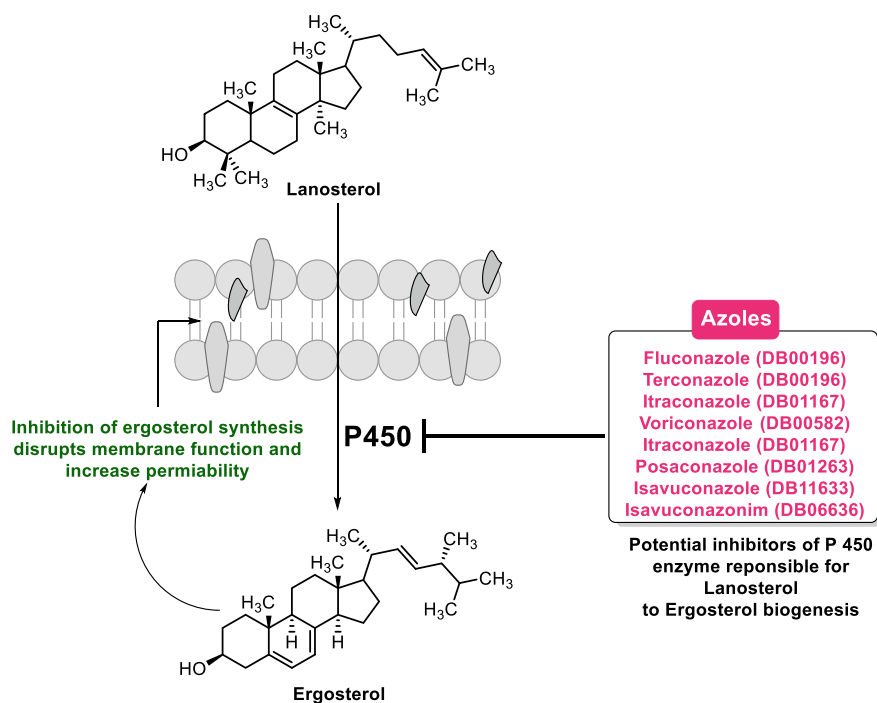
Fig. 6 Mechanism of action of azoles against fungal infection

4.2 Psychoactive Agents

Alprazolam (trade name Xanax) and triazolam (trade name Halcion) are familiar psychoactive drugs used as a tranquilizer [35]. Both of them are categorized as a member of classical benzodiazepine (BZD) congener family, where 1,2,4-traiazole and benzodiazepine ring are fused together. The antidepressant activity of alprazolam and triazolam is originated from their positive allosteric modulation on the γ-amino butyric acid (GABA)-A receptor (GABA-A receptor is a synaptic Cl-ion channel, modulated by various ligands) [36].

GABA-A receptor, a trans-membrane glycoprotein, composed of 5 subunits: two α-subunits, two β-subunits and one γ-subunit (Fig. 7). The benzodiazepine-specific binding site is located in the intersection of α- and γ-subunit. The histidine residues (H101, H126 and H105) of α-subunit is responsible to bind benzodiazepine (BZD) congeners such as alprazolam and triazolam. The binding of BZD to the specific receptor imparts conformational alteration in GABA binding site and results allosteric inhibition of GABA-mediated synaptic responses.
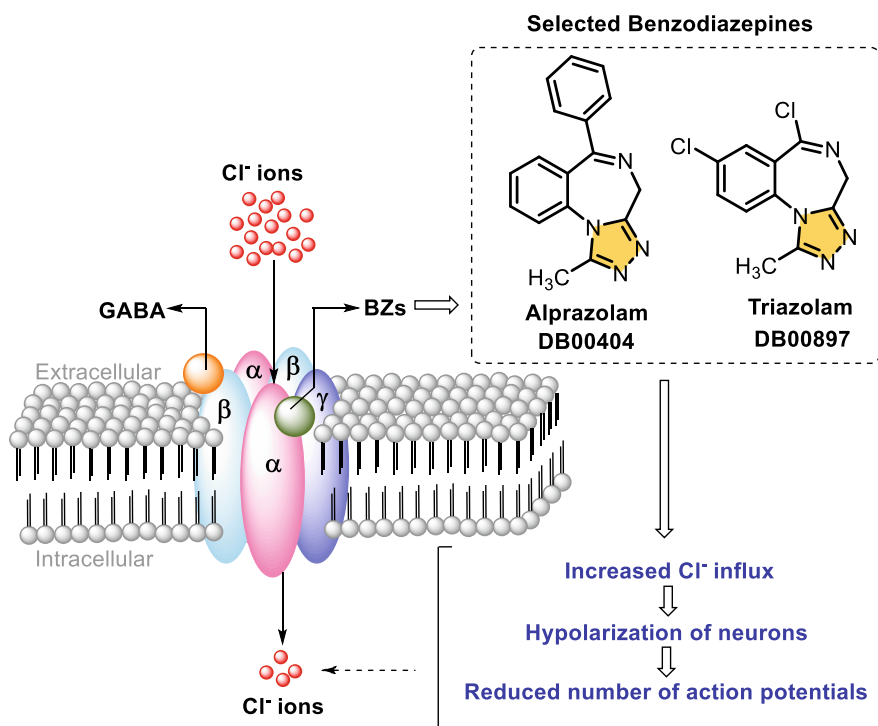
Fig. 7 Mechanism of action of alprazolam and triazolam against synaptic dysfunction

4.3 Antidiabetic Agent

Diabetes mellitus (DM), commonly known as diabetes, is a metabolic disorder which increases the level of sugar in the blood. Insulin is an anabolic hormone, a key peptide hormone which control the sugar level in the blood. Generally, pancreatic beta cells are activated and produce adequate amount of insulin after consumption of food. Insulin regulates the metabolism of carbohydrate by increasing absorption of glucose from the blood to the liver, fat and skeletal muscle cells. The glucose level in the blood is disrupted either when the lowered amount of insulin is secreted from beta cell or insulin becomes inactive and consequently sets up DM. Glucagon, another class of peptide hormone, secreted from pancreatic alpha cells, is the hormone responsible for the enhancing level of sugar in the bloodstream. Over-production of glucagon could increase the blood sugar level and sets up DM. Thus, the homeostasis of blood sugar is precisely balanced by insulin and glucagon activity.

Glucose-dependent insulinotropic polypeptide (GIP) and glucagon-like peptide (GLP-1) are two main incretin hormones, regulating the secretion of insulin and glucagon production from pancreas [37]. Thus, GIP and GLP-1 activity plays a crucial role on set of DM. Interestingly, the effect of GIP and GLP-1 on the production of glucagon and insulin is precisely regulated by a cell surface glycoprotein dipeptidyl peptidase-4 (DPP-4 or CD26). The proteolytic activity of DPP-4 readily inactivates GLP-1 and consequently reduce the production of insulin. Eventually, DPP-4 becomes an interesting drug target to control blood sugar level.

Sitagliptin, piperazine fused 1,2,4-triazole congener, produces adequate inhibition of DPP-4 and becomes very successful drug against DM (Fig. 8). For individual, a significant glycaemic control was observed either by monotherapy of sitagliptin or fixed dose combination with metformin. Although sitagliptin has shown excellent efficacy in control of blood sugar level, the main concern is off target effect of sitagliptin on prolong. Dipeptidyl peptidases include a large number of enzymes in which DPP-4, -8 and -9 are very similar in their structure. Thus, a severe side effects
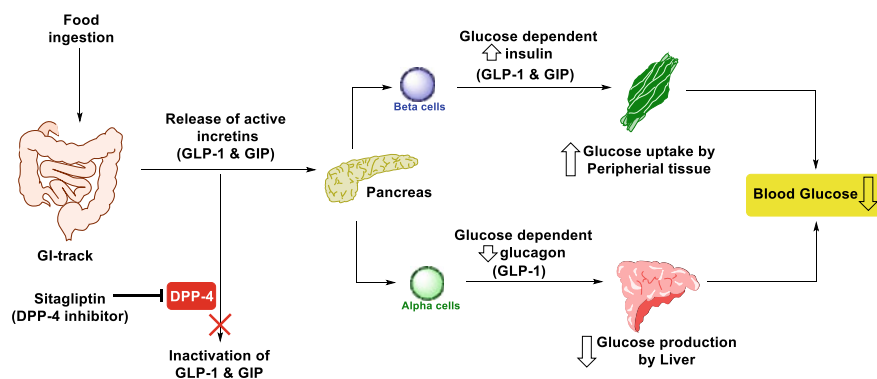
Fig. 8 Mechanism of action of sitagliptin in DPP-4 inhibition and glycemic control

could be originated by off target binding to DPP-8 and -9 by sitagliptin on prolong use.

4.4 Antiviral Agent

Maraviroc, 1,2,4-triazole attached spirodiketopiperazine compound, is a the first licenced CCR5 antagonist (a chemokine receptor) for HIV-1 patients [38]. CCR5, a G-protein couple receptor (seven membered GPCR), is responsible for cell trafficking in T-lymphocytes, macrophages and immature dendritic cells. CCR5 along with CD4 receptor is the main membrane protein which allow HIV-1 to fuse with host cell. During host cellular invasion of HIV-1, extracellular loop of CCR5 interacts with V3 protein on virous tip. Small molecule maraviroc selectively binds to the hydrophobic pocket of host CCR5 protein and inhibits the communication with virous envelope protein (Fig. 9).

The detail binding mode of maraviroc and engineered human CCR5 was elucidated through X-ray crystallography in the range of 2.7 Å resolution [39]. In deep analysis reveals that the binding site of maraviroc is distinct from either chemokine binding site or gp120 receptor of HIV-1. This observation concludes that maraviroc has shown anti-HIV activity through allosteric inhibition of CCR5. Through crystallographic analysis, it is also revealed that 1,2,4-triazole motif of maraviroc plays a pivotal role CCR5 binding; nitrogen atom at position 1 in 1,2,4-triazole make a H-bond with Tyr-37 and the same nitrogen also bond with Tyr-89 through H-bond via water molecule. Among the five crucial H-bond interaction among maraviroc with CCR5, two of them are attached with triazole ring (Fig. 10).

5   Summary/Conclusion

1,2,4-tiazole and its derivatives have an ample position in the modern chemical community and drug discovery. Among the family of *N*-heterocycles, 1,2,4-tiazole derivatives exhibit diverse biological properties such as anticancer, hypotensive, anti-histaminic, antimicrobial, anti-allergic, antiviral, cytostatic and are generally used in clinical practice. The pioneering of the 1,2,4-tiazole moiety into scaffolds of an organic substrate quite often accompany an improvement in the efficiency as well as an increased prolongation of drug action. However, last few years have witnessed a considerable expansion in the number of patents and publications on new drugs as well as 1,2,4-tiazole containing biologically and FDA approved pharmaceutically active scaffolds. The unique features of 1,2,4-tiazole such as different biological activity and applications are discussed in this chapter. Considering the rapid progress in the field and potential of these moieties towards novel drug candidates, it may be expected on appearance of 1,2,4-triazole scaffolds as potent drug molecules to cure a number of life-threatening diseases.
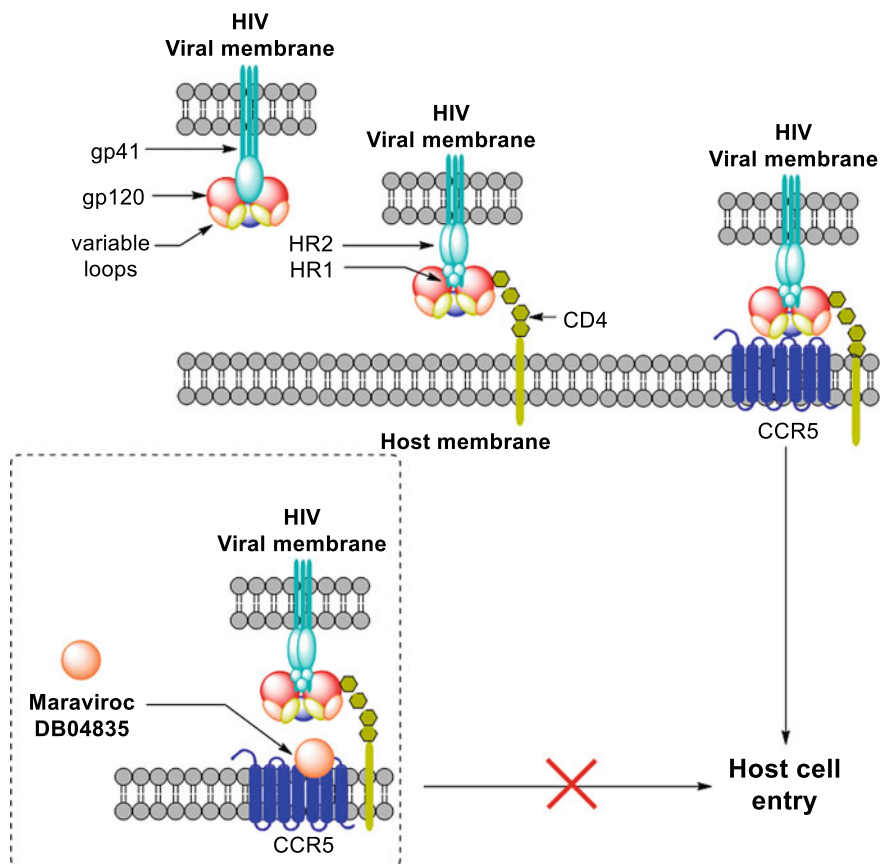
Fig. 9 Mechanism of action of maraviroc against HIV host cell entry
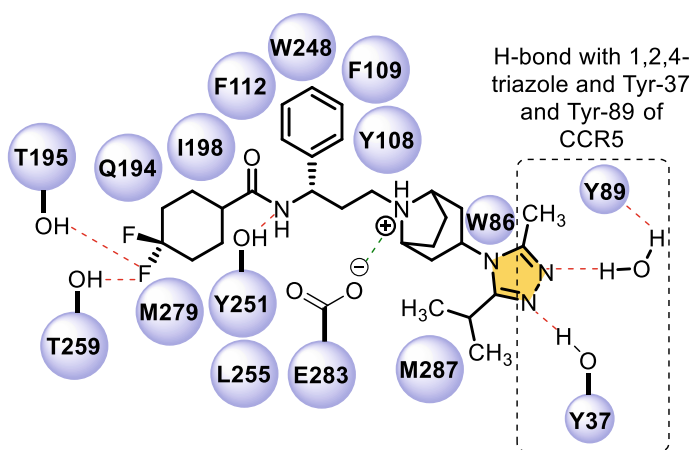
Fig. 10 Interaction of CCR5 aminoacid residues with maraviroc

References

1. Li Z, Cao Y, Zhan P, Pannecouque C, Balzarini J, Clercq ED, Liu X (2013) Synthesis and anti-HIV evaluation of novel 1,2,4-triazole derivatives as potential non-nucleoside HIV-1 reverse transcriptase inhibitors. Lett Drug Des Discov 10:27–34
2. Wade PC, Vogt BR, Kissick TP, Simpkins LM, Palmer DM, Millonig RC (1982) 1-Acyltriazoles as antiinflammatory agents. J Med Chem 25:331–333
3. Strzelecka M, Świątek P (2021) 1,2,4-triazoles as important antibacterial agents. Pharmaceuticals 14:224
4. Asif M (2015) Antiviral and antiparasitic activities of various substituted triazole derivatives: a mini review. Chem Int 1:71–80
5. El-Emary TI, El-Mohsen SAA (2012) Multi-component one-pot synthesis and antimicrobial activities of 3-methyl-1,4-diphenyl-7-thioxo-4,6,8,9 tetrahydropyrazolo[5,4-*b*]pyrimidino[5,4-*e*]pyridine-5-one and related derivatives. Molecules 17:14464–14483
6. Luo Y, Zhang S, Liu Z-J, Chen W, Fu J, Zeng Q-F, Zhu H-L (2013) Synthesis and antimicrobical evaluation of a novel class of 1,3,4-thiadiazole: derivatives bearing 1,2,4-triazolo[1,5-*a*]pyrimidine moiety. Eur J Med Chem 64:54–61
7. Abdelhamid AO, Fahmi AA, Ali AA (2013) Synthesis of some new fused azolopyrimidines, azolotriazines and pyridines containing coumarines moieties. Int J Adv Res 1:627–644
8. Nassar MY, Aly HM, Moustafa ME, Abdelrahman EA (2017) Synthesis, characterization and biological activity of new 3-substitued-4-amino-5-hydrazino-1,2,4-triazole Schiff bases and their Cu(II) complexes: a new approach to CuO nanoparticles for photocatalytic degradation of methylene blue dye. J Inorg Organomet Polym 27:1220–1233
9. Sayed HH, Morsy EMH, Felfel EM (2010) Synthesis and reactions of some novel nicotinonitrile, thiazolotriazole, and imidazolotriazole derivatives for antioxidant evaluation. Synth Commun 40:1360–1370
10. Valenti VE, Abreu LC, Sato MA, Ferreria C (2010) ATZ (3-amino-1,2,4-triazole) injected into the fourth cerebral ventricle influences the Bezold-Jarisch reflex in conscious rats. Clinics 65:1339–1343
11. Al-Salahi R, El-Tahir K-E, Alswaidan I, Lolak N, Hamidaddin M, Marzouk M (2014) Biological effects of a new set 1,2,4-triazolo[1,5-*a*]quinazolines on heart rate and blood pressure. Chem Cent J 8:3–10
12. Upadhyay K, Manvar A, Loddo R, La Colla P, Virsodiya V, Trivedi J, Chaniyara R, Shah A (2013) Syntheses and in vitro biological screening of 1-aryl-10*H*-[1,2,4]triazolo[3′,4′:3,4][1,2,4]triazino[5,6-*b*]indoles. Med Chem Res 22:3675–3686
13. Asif M (2017) Pharmacological activities of triazole analogues as antibacterial, antifungal, antiviral agents. Pharm Sci Asia 44:59–74
14. Boechat N, Pinheiro LCS, Silva TS, Aguiar ACC, Carvalho AS, Bastos MM, Costa CCP, Pinheiro S, Pinto AC, Mendonca JS, Dutra KDB, Valverde AL, Santos-Filho OA, Ceravolo IP, Krettli AU (2012) New trifluoromethyl triazolopyrimidines as anti-plasmodium falciparum agents. Molecules 17:8285–8302
15. Khrishna KM, Inturi B, Pujar GV, Purohit MN, Vijaykumar GS (2014) Design, synthesis and 3D-QSAR studies of new diphenylamine containing 1,2,4-triazoles as potential antitubercular agents. Eur J Med Chem 84:516–529
16. Shah MH, Mhasalkar MY, Patki VM, Deliwala CV, Sheth UK (1969) New 1,2,4(*H*)-triazole derivatives as diuretic agents. J Pharm Sci 58:1398–1401
17. Bera H, Dolzhenko AV, Sun L, Gupta SD, Chui WK (2013) Synthesis and in vitro evaluation of 1,2,4-triazolo[1,5-*a*][1,3,5]triazine derivatives as thymidine phosphorylase inhibitors. Chem Biol Drug Des 82:351–360
18. Bera H, Chui WK, Gupta SD (2013) Synthesis, in vitro evaluation of thymidine phosphorylase inhibitory activity, and in silico study of 1,3,5-triazin-2,4-dione and its fused analogues. Med Chem Res 22:6010–6021

19. Hassan GS, El-Sherbeny MA, El-Ashmawy MB, Bayoumi SM, Maarouf AR, Badria FA (2013) Synthesis and antitumor testing of certain new fused triazolopyrimidine and triazoloquinazoline derivatives. Arab J Chem 10:1345–1355
20. Wu W-N, Jiang Y-M, Fei Q, Du H-T, Yang M-F (2020) Synthesis and antifungal activity of novel 1,2,4-triazole derivatives containing an amide moiety. J Heterocycl Chem 57:1379–1386
21. Xu J, Cao Y, Zhang J, Yu S, Zou Y, Chai X, Wu Q, Zhang D, Jiang Y, Sun Q (2011) Design, synthesis and antifungal activities of novel 1,2,4-triazole derivatives. Eur J Med Chem 46:3142–3148
22. Mange YJ, Isloor AM, Malladi S, Isloor S, Fun HK (2013) Synthesis and antimicrobial activities of some novel 1,2,4-triazole derivatives. Arab J Chem 6:177–181
23. Huang H, Guo W, Wu W, Li CJ, Jiang H (2015) Copper-catalyzed oxidative C(sp^3)-H functionalization for facile synthesis of 1,2,4-triazoles and 1,3,5-triazines from amidines. Org Lett 17:2894–2897
24. Kuang J, Chena B, Ma S (2014) Copper-mediated efficient three-component synthesis of 1,2,4-triazoles from amines and nitriles. Org Chem Front 1:186–189
25. Blum RA, D'Andrea DT, Florentino BM, Hilligoss DM, Gardner MJ, Henry EB, Goldstein H, Schentag JJ (1991) Increased gastric pH and the bioavailability of fluconazole and ketoconazole. Ann Intern Med 114:755–757
26. Asif M (2016) Biological potentials of biological active triazole derivatives: a short review. Org Chem Curr Res 5:173
27. Kumudha D, Reddy RR, Kalavathi T (2012) 1,2,4-triazoles: as biologically important agents. Int J Pharm Sci Res 3:4562–4572
28. Asif M (2014) A brief review on antitubercular activity of pharmacological active some triazole analogues. Glob J Res Rev 1:51–58
29. Can NÖ, Çevik UA, Sağlık BN, Levent S, Korkut B, Özkay Y, Kaplancıklı ZA, Koparal AS (2017) Synthesis, molecular docking studies, and antifungal activity evaluation of new benzimidazole-triazoles as potential lanosterol 14α-demethylase inhibitors. J Chem 2017
30. Sinha J, Kadawla M (2017) Triazoles as antimicrobial: a review. Int J Chem Stud 5:1–7
31. Jadhav GR, Shaikh MU, Kale RP, Shiradkar MR, Gill CH (2009) SAR study of clubbed [1,2,4]-triazolyl with fluorobenzimidazoles as antimicrobial and antituberculosis agents. Eur J Med Chem 44:2930–2935
32. Zhang HJ, Wang XZ, Cao Q, Gong GH, Quan ZS (2017) Design, synthesis, anti-inflammatory activity, and molecular docking studies of perimidine derivatives containing triazole. Bioorg Med Chem Lett 27:4409–4414
33. Kharb R, Sharma PC, Yar MS (2011) Pharmacological significance of triazole scaffold. J Enzyme Inhib Med Chem 26:1–21
34. Bing J, Hu T, Zheng Q, Muñoz JF, Cuomo CA, Huang G (2020) Experimental evaluation identifies adaptive aneuploidy as a mechanism of fluconazole resistance in candida auris. Antimicrob Agents Chemother 65:1–14
35. Heeres J, Meerpoel L, Lewi P (2010) Conazoles. Molecules 15:4129–4188
36. Griffin CE, Kaye AM, Beuno FR, Kaye AD (2013) Benzodiazepine pharmacology and central nervous system-mediated effects. Ochsner J 13:214–223
37. Masiulis S, Desai R, Uchański T, Martin IS, Laverty D, Karia D, Malinauskas T, Zivanov J, Pardon E, Kotecha A, Steyaert J, Miller KW, Aricescu R (2019) GABA$_A$ receptor signalling mechanism revealed by structural pharmacology. Nature 565:454–459
38. Gallwitz B (2019) Clinical use of DPP-4 inhibitors. Front Endocrinol 10:1–10
39. Ryst EVD (2015) Maraviroc-a CCR5 antagonist for the treatment of HIV-1 infection. Front Immunol 6:1–4
40. Tan Q, Zhu Y, Li J, Chen Z, Han GW, Kufareva I, Li T, Ma L, Fenalti G, Li J, Zhang W, Xie X, Yang H, Jiang H, Cherezov V, Liu H, Stevens RC, Wu B (2013) Structure of the CCR5 chemokine receptor-HIV entry inhibitor maraviroc complex. Science 341:1387–1390

Overview on Diverse Biological Activities of Benzisoxazole Derivatives

Arup K. Kabi, Raghuram Gujjarappa, Aakriti Garg, Abhishek Sahoo, Anupam Roy, Sreya Gupta, and Chandi C. Malakar

Abbreviations

ABSSSI	Acute bacterial skin and skin structure infection
ADP	Adenosine di-phosphate
AIDS	Acquired immune deficiency syndrome
AMP	Adenosine monophosphate
ARB	Angiotensin II receptor blocker
COX	Cyclooxygenase
DNA	Deoxyribonucleic acid
DNMT	DNA methyltransferases
ER	Endoplasmic reticulum
GABA	Gamma-aminobutyric acid
HepG-2	Human liver cancer cell line
HIV	Human immunodeficiency virus
HMG-CoA	3-hydroxy-3-methyl-glutaryl-coenzyme A
HSV	Herpes simplex viruses
NS3	Nonstructural protein 3
PARP	Poly (ADP-ribose) polymerase
RNA	Ribonucleic acid
SAR	Structure–activity relationship
MRSA	Methicillin-resistant *Staphylococcus aureus*

A. K. Kabi · R. Gujjarappa · A. Sahoo · A. Roy · C. C. Malakar (✉)
Department of Chemistry, National Institute of Technology Manipur, Langol, Imphal, Manipur 795004, India
e-mail: cmalakar@nitmanipur.ac.in

A. Garg · S. Gupta (✉)
Department of Medicinal Chemistry, National Institute of Pharmaceutical Education and Research (NIPER), Kolkata, Chunilal Bhawan, 168, Maniktala Main Road, Kolkata 700054, India
e-mail: sreyog83@gmail.com

OGTT   Oral glucose tolerance test
U.S. FDA   United State Food and Drug Administration
WHO   World Health Organization

1 Introduction

The heterocyclic molecules are a remarkable class of scaffolds, and these molecules have been treated with customized attention for a broad spectrum of biological and pharmacological studies [1]. Among these molecules, benzisoxazole and their derivatives signify among the beneficial scaffold in medicinal chemistry, and in recent years, there have been enormous number of reports witnessed on benzisoxazole-embedded compounds. The exceptional properties of benzisoxazole molecule also reveal an outstanding efficacy as anticancer, antimicrobial, anti-glycation, anti-inflammatory, antipsychotic agents and anti-tubercular. Few scaffolds consist of benzisoxazole-accommodating drug molecules which are represented below (Fig. 1). The 1,2-benzisoxazole-embedded drug molecules such as risperidone and zonisamide are exhibited as anticonvulsant actions [2]. It has been described that the variants with fluorine functionalization lead to realize a severe effect on drug capacity, related to clearance of drug, distribution of drug and intensity of drug metabolism. These scaffolds and their analogues are extended for the utilization towards fabrication of a spectrum of functional materials in synthetic chemistry and also widely witnessed in diverse valuable drug molecules. In this context, researchers working in the fields of medicinal chemistry need to pay more attention in exploring the wide spectrum applications of these motifs. In addition, it is worthwhile examining the various synthetic approaches towards benzisoxazole analogues and their potential challenges.

The anthranilic acid derivatives are the precursors for the biosynthesis of benzisoxazole motifs which are in turn accessed from chorismic acid (Scheme 1).

These benzisoxazole derivatives are dismantled into their primary components during the process of drug action in presence of enzymes. For example, zonisamide on reaction with NADPH and proton in presence of cytochrome P450 gets reduced to 2-sulfamoylacetylphenol and ammonia (Scheme 2).

Properties of FDA-approved benzisoxazole-containing drug molecules are described below (Table 1).

1.1 Synthesis of Benzisoxazole-Containing Drug Molecules

The FDA-approved drug risperidone can be synthesized from the precursor **1** by following series of chemical transformations. The reaction **1** with con. HCl under reflux conditions gives acetyl deprotected product **2**, which on condensation with **3**
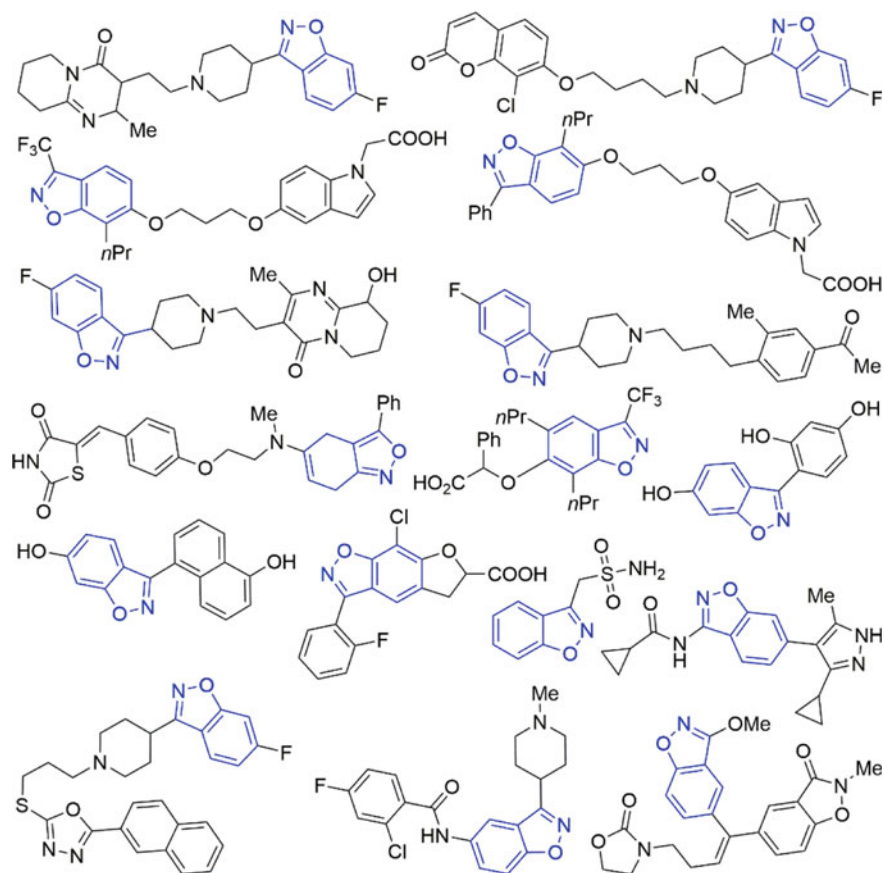
Fig. 1 Benzisoxazole analogues with biological potential [5–9]
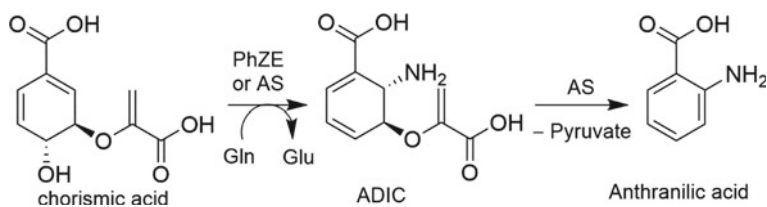
Scheme 1 Biosynthesis of anthranilic acid [3]

and subsequent reduction with sodium cyanoborohydride produces **4**. The condensation of hydroxyl amine **5** with **4** results in an imine **6** which on intramolecular cyclization in presence of base delivers the desired product risperidone (Scheme 3).
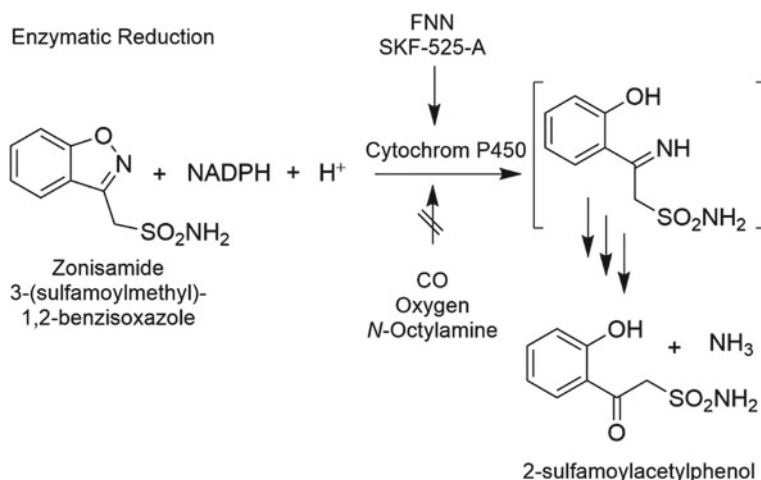
Scheme 2 Enzymatic reduction of zonisamide [4]

Similarly, iloperidone can be synthesized from isonipecotic acid (**7**) through a wide range of chemical transformations. The compound **7** on reaction acetic anhydride and DMF yields the compound **8**, which on reaction of 3,5-difluorobenzene (**9**) in AlCl$_3$ gives compound **10**. The reaction of **10** in presence of hydroxylamine **5** followed by deformylation reaction results in compound **11**. The successive nucleophilic substitution reactions of **11** with **12** and **14** delivers the desired product iloperidone (Scheme 4).

2 Antimicrobial Activity of Benzisoxazole Derivatives

Fungal, bacterial and microbial infections allege a noticeable health hazard to the human life and society. The investigation of novel and active drugs remains still an alert to expand the assets of accessible antimicrobial and antibacterial drugs. Here in this section, modern advancements in the development of benzisoxazoles-based pharmacologically active antimicrobial compounds are highlighted (Fig. 2). The compounds **A** and **K** are screened for their inhibitory performances on the progress of fungi and pathogenic bacteria, and they displayed enhanced auspicious activities. To examine the structure–activity relationship (SAR), the inclusion of S in place of O in the urea has resulted to boost the results. The existence of electron retreating functional groups, mainly F, is investigated to be crucial for strong performances associated to electron-donating substituent [12]. In addition, elastin/amino acid-embedded peptides consolidated to a benzisoxazole moieties have been examined for antimicrobial activities. The associated compound **B** divulged that conjugation indulges a prominent function in hindering the advancement of microorganisms and displaying

Table 1 FDA-approved benzisoxazole-containing drug molecules

Drug name (drug bank ID)	Structure of drug	Category/Indication	Mechanism of action
Risperidone (DB00734)		Referred for the medication of acute manic or mixed events affiliated with bipolar I disorder, schizophrenia and irritability correlated with autistic disorder	Prevents the receptors of 5-HT$_{2A}$ serotonergic and receptors of D$_2$ dopaminergic in the brain
Zonisamide (DB00909)		Recommended for the adjunctive therapy in adult patients suffering from partial-onset seizures and sulfonamide anticonvulsant	Suppress the uptake of the GABA an inhibitory neurotransmitter, whereas accelerating the uptake of glutamate an excitatory neurotransmitter
Paliperidone (DB01267)		Paliperidone is employed for the medication of schizophrenia	Assisted through a composition of type 2 serotonin (5-HT$_{2A}$) receptor antagonism and type 2 central dopamine (D$_2$)
Iloperidone (DB04946)		Iloperidone is employed of acute schizophrenia	Antagonist of type 2 dopamine (D$_2$) and 5-HT$_{2A}$ receptor, and performs as a neuroleptic agent
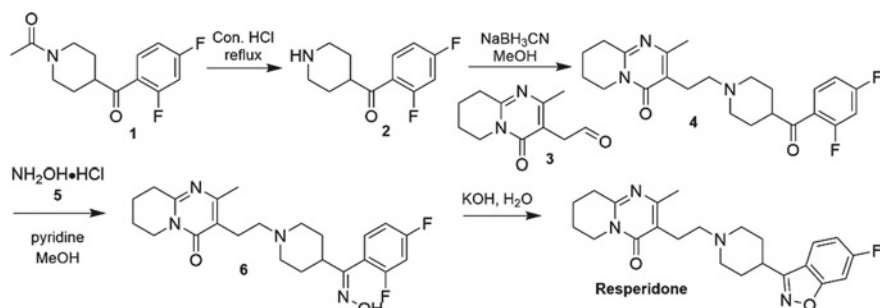
Scheme 3 Synthesis of risperidone [10]
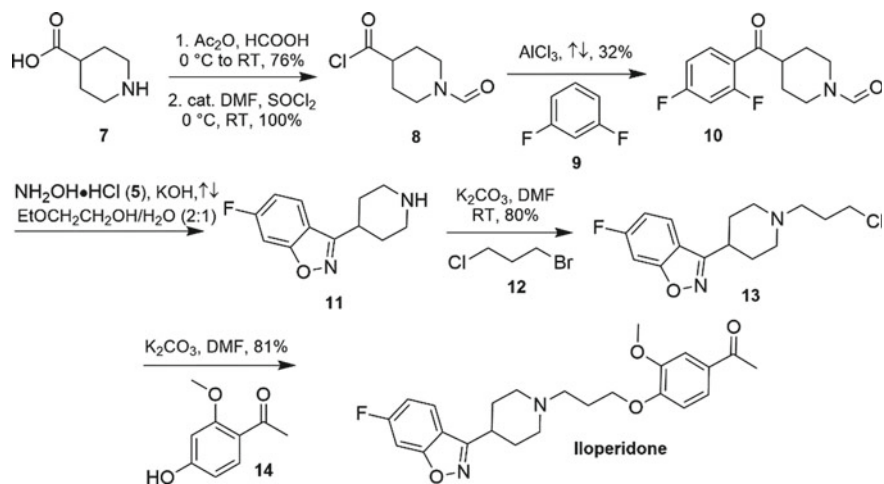
Scheme 4 Synthesis of iloperidone [11]
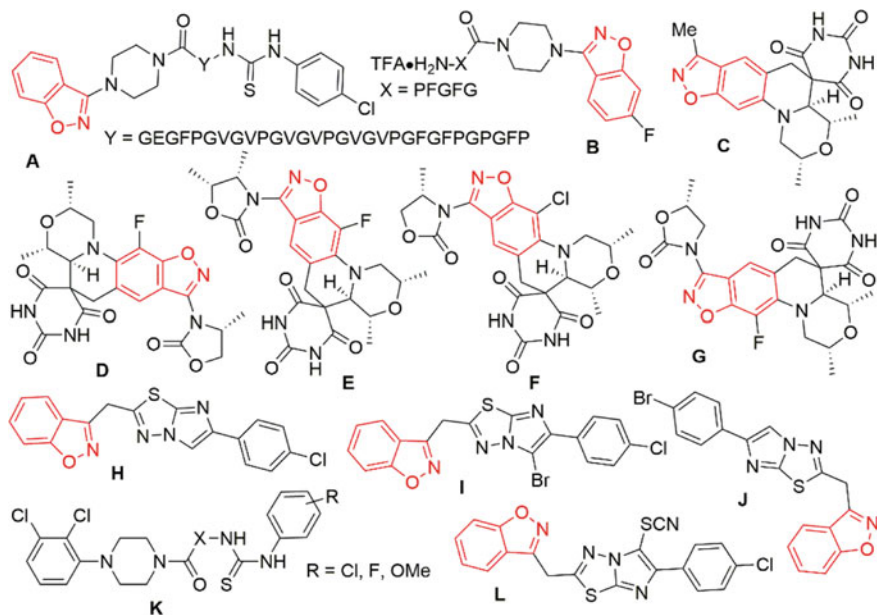
Fig. 2 Benzisoxazole-embedded molecules related to antimicrobial activities

remarkable antimicrobial performances compared to the standard antibiotics [13, 14]. In continuation, the compound **C** has not been capable of cross-resistant with other DNA gyrase preventers such as fluoroquinolone and aminocoumarin antibacterials as well as showed extensive potential for the action of infections resulted by bacteria of multi-drug resistant, along with *Staphylococcus aureus* [15]. Moreover, the derivatives **D**, **E**, **F** and **G** displayed exceptional activities in comparison with *Escherichia coli*, albeit the parameters were not satisfactorily low to visualize efficacies against the pathogen at legitimate doses and also compound **D** was recognized for improvement towards clinical trials in human for the medication of uncomplicated gonorrhoea [16]. Furthermore, the compounds **H**, **I**, **J** and **L** have revealed suitable activities against *E. coli-ATCC 35218* and *Bacillus subtilis-ATCC 6633*. Additionally, the compound **L** has displayed excellent performances against diverse bacterial strains. Nevertheless, the derivatives **H** and **I** were extremely effective against *E. coli-ATCC 35218*, in comparison with ampicillin which is referred as the standard drug. The structure–activity relationships (SAR) revealed that the occurrence of electron-withdrawing functionalities such as bromo and chloro exhibited admirable antimicrobial activities compared to the electron-donating substituents [17].

3 Anticonvulsant Activity of Benzisoxazole Derivatives

Epilepsy is examined towards the unusual and exaggerated release of neurons which is responsible for the interruptions or loss of consciousness with or without attributed physical activities. Seizures can be regulated only for less than 70% of patients using the commercially available anticonvulsant drugs. Incapability of drugs and their unexpected side effects such as headache, ataxia and anaemia urge the essence for search towards the novel antiepileptic agents having lower toxicity and more selectivity in medicinal chemistry perspective. In the research area of anticonvulsant agents, numerous derivatives are established with benzisoxazole molecules which are described here.

In past, the screening of anticonvulsant actions was realized using subcutaneous pentylenetetrazole (scPTZ) tests and maximal electroshock (MES) after intraperitoneal (IP) injection into mice. These are investigated as the maximum widely described and utilized models for early representation of anticonvulsant affiliated candidates. Their noteworthy neurological toxicity (NT) was persistent to employ in the rotarod test. The numerical assessment after oral administration in rats exhibited that the derivative **M** was most effective [18]. Additionally, the molecule **N** was found to be competent in the scPTZ test. However, the derivative **O** was recognized to be the most propitious anticonvulsant agent (Fig. 3) [19].
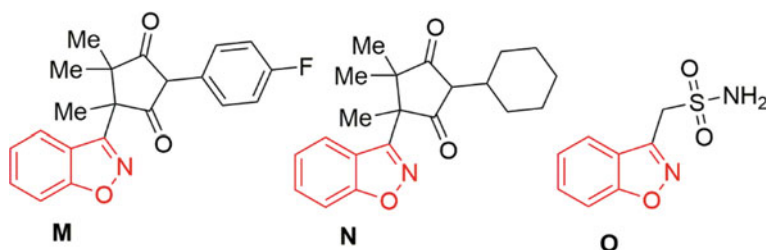
Fig. 3 Benzisoxazoles-related anticonvulsant agents

4 Anti-tubercular Activity of Benzisoxazole Derivatives

Currently, the prevalence of infections associated with *Mycobacterium tuberculosis* is flourishing rapidly because of the HIV/AIDS pandemic. Thus, the inefficacy of the anti-tubercular drug molecules and display of multi-drug-resistant to numerous strains of *M. tuberculosis* are the prime challenges. Among the anti-tubercular agents, some benzisoxazole-embedded derivatives exhibited excellent anti-tubercular activities. (Fig. 4) [15].

A broad range of benzisoxazole derivatives screened for their anti-tubercular performances against the *M. tuberculosis* H37Rv strain. Derivatives such as **P**, **Q** and **R** displayed excellent anti-tubercular actions [20]. Nevertheless, the derivatives such as **S**, **T** and **V** examined for their anti-tubercular performances against the *M. tuberculosis* (MTB) H37Rv strain. In addition, the molecules revealed minimum inhibitory concentrations (MIC) and appeared with extracurricular anti-tubercular
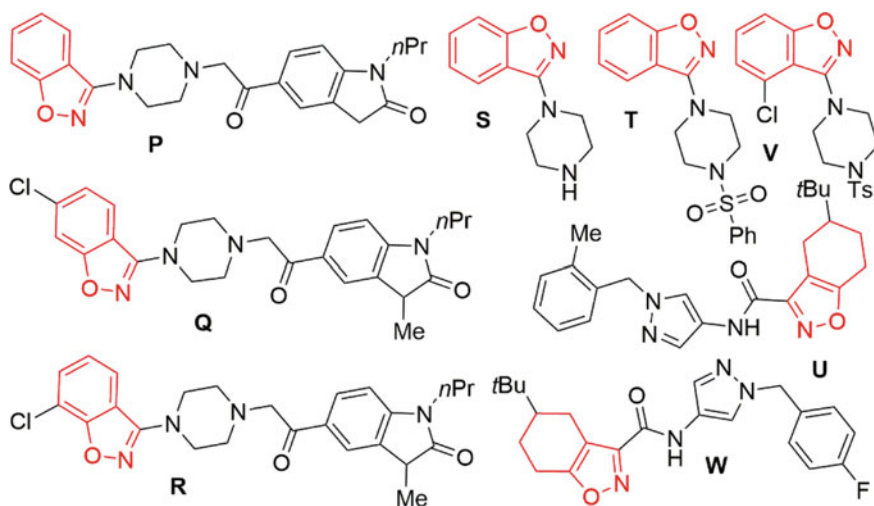
Fig. 4 Benzisoxazoles-related anti-tuberculosis agents

activities [21]. In continuation, a new series of benzisoxazole-containing molecules were studied for their competency as *M. tuberculosis* PS inhibitors. The derivatives **U** and **W** are evidenced with compelling anti-tuberculosis activities [22].

5 Anti-glycation Activity of Benzisoxazole Derivatives

Diabetes mellitus (DM) is witnessed as an essential metabolic infirmity, realized if the physical condition is inadequately competent to oxidize carbohydrates because of irregularities in the actions of insulin [23]. Diabetes mellitus lead a long-term suffering in numerous body actions which could result in the collapse of several organ functions [24]. According to the recent findings, approximately 150 million of population in the world are affected due to diabetes and it is presumed that the number could enhance up to 300 million by 2050 [25] and 90% of the community worldwide is afflicted by type II diabetes [26]. Initial investigations revealed that the derivatives embedded with methoxy group which is situated at the para-position and likewise the bromo-functionality embedded at the aryl moiety in the ortho-position including the thiourea component could essentially induce the anti-glycation actions. Additionally, anti-urease functions also induced by introducing these functional groups. The leading anti-urease action was realized for Phe-Pro (**X**) for urease embedded by a functional group like methoxy functionality at the para-position [27]. Moreover, a broad range of thiourea/urea molecules of Gly/Pro-amalgamated benzisoxazole compounds were examined for their anti-glycation performances. The derivatives **Y** and **Z** appeared with extraordinary activity in comparison with the standard drug rutin [28]. Indeed, the leading anti-glycation characteristic was noticed for the benzisoxazole integrated with Tyr-Pro dipeptide (**AA**) analogue containing a methoxy substituent embedded at the para-position of aromatic residue (Fig. 5) [27].
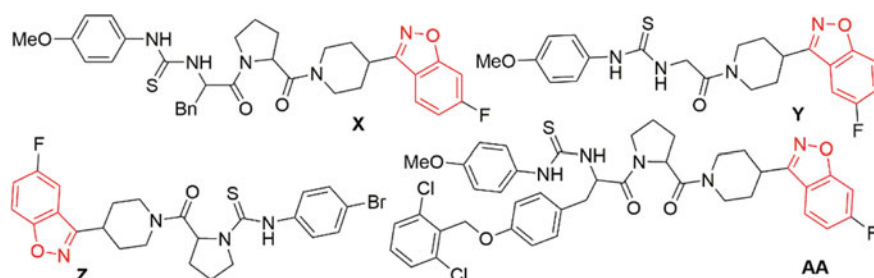
Fig. 5 Benzisoxazoles-related anti-glycation active compounds

6   Antipsychotic Activity of Benzisoxazole Derivatives

Antipsychotic medications composed of a series of heterocyclic molecules that are employed for the medication of particularly schizophrenia, psychotic problems and bipolar affective disorders. Heteroaromatic scaffolds such as benzisoxazole derivatives have found comprehensive application as antipsychotic drugs. The conventional antipsychotic drugs embedded with benzisoxazole include iloperidone, risperidone and paliperidone (Fig. 6).

The coumarins-embedded benzisoxazole molecules were described as potential multi-target antipsychotics. It is well known that the catalepsy investigation is a familiar and substantially employed as screening assessment during preclinical trials for the susceptibility of an antipsychotic drug to persuade EPS in humans [31]. The associated compound **AB** appeared with excellent proficiency for dopamine D3 and D2 and serotonin receptors such as 5-HT2A and 5-HT1A, having a reduce compatibility for the H1 receptor. The molecule AB had high efficacy for the medication of illnesses related to schizophrenia without producing catalepsy. The molecule AB also had an excellent edge for catalepsy affirmation associated with the market available active molecules like antipsychotics, risperidone and clozapine. However, this derivative is immense for appearing a characteristics class of drug molecules for the cure of schizophrenia. Moreover, the derivative **AC** (QF1018B) displayed moderate to high efficacies for 5-HT2A and D2 receptors, and its 5-HT2A/D2 ratio was significant towards an antipsychotic profile [32]. In continuation, the molecule **AD** occupies extraordinary pharmacological structures, as well as exceptional affinities for dopamine D3/D2 and serotonin 5-HT2A/5-HT1A receptors. Additionally, it holds low affections for H1 and 5-HT2C receptors (to limit the hazard of obesity caused by the chronic medication) and hERG channels (to weaken the frequency of torsade des points) [33]. Indeed, the derivative **AE** (QF1004B) was employed as a tool to elaborate the role of 5-HT2C receptors to intervene the antipsychotic

Fig. 6
Benzisoxazoles-related
marketed antipsychotic
drugs [29–34]
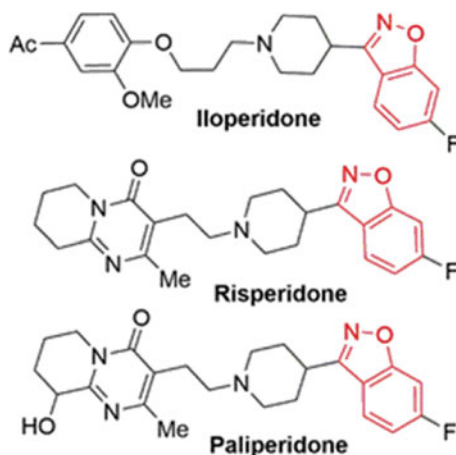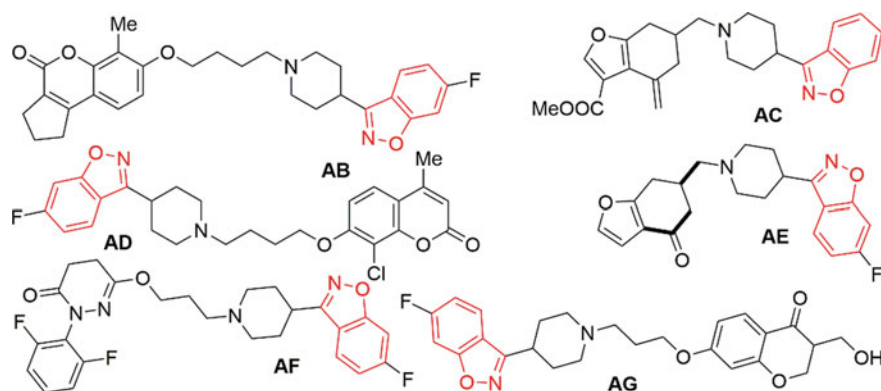
Fig. 7 Benzisoxazoles-related antipsychotic compounds

actions and metabolic adverse actions [32]. Furthermore, in contradiction to risperidone, the derivative **AF** appeared with an excellent psychotic edge and this may be favourable in the investigation of a potential class of drug molecules for the cure of schizophrenia. In continuation, the molecule **AG** featured an excellent binding efficacy for the D2 receptor and 5-HT2A receptor. Furthermore, the derivative **AG** (FI-8602, abaperidone) has been delegated for clinical progress (Fig. 7) [34].

7 Anticancer Activity of Benzisoxazole Derivatives

The advancement of novel anticancer derivatives is one of the prime desires in biological and medicinal chemistry. The disease such as cancer is raised all over the world. There is always a substantial appeal for novel anticancer drug molecules, and a broad range of new natural or synthetic molecules are described successively by scientists and researchers. Numerous anticancer derivatives are established with benzisoxazole scaffolds which are represented here.

The derivatives **AH** and **AI** appeared with solid prevention against acetylcholinesterase (AChE) from different sources: human serum, electric eel and rat brain homogenate [35]. In addition, a broad range of benzisoxazole-functionalized allyl compounds were established for anticancer and antioxidant activities. The derivatives **AK**, **AI**, **AL** and **AN** were witnessed as the outstanding potency against HT-29 cells of colon cancer in human [36]. In continuation, among the amide-embedded analogues, the hindering activity was acknowledged by **AM** against HepG-2 cells. Further, the molecule **AP** divulged anti-proliferation actions against HepG-2 cells. Consequently, the derivative **AO** disclosed a mitigated anti-proliferation performance against HepG-2 cells [37]. Moreover, 1,2,3-triazoles acquired from benzisoxazole analogues were elaborated for their anti-proliferative action on human acute myeloid leukaemia (AML) cells. The molecule **AQ** was established to be the most competent
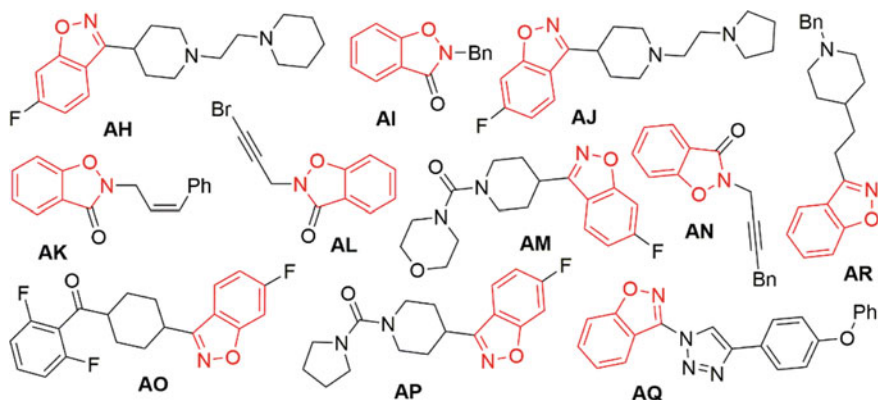
Fig. 8 Benzisoxazoles-related anticancer agents

anti-proliferative agent against MV4-11 cells. The molecule was affirmed as the most adequate cytotoxic agent against a series of AML cell lines (MOLM13, MOLM14 and MV4-11 cells) while featuring selectivity over bone marrow cells [38]. Additionally, *N*-benzylpiperidine contains benzisoxazoles **AR**, as practical and active blockers of the enzyme acetylcholinesterase (AChE). Moreover, it is favourable for therapeutic treatment of Alzheimer's disease (Fig. 8) [39].

8 Biological Importance of Benzisoxazole Derivatives [19–47]

The heterocyclic scaffolds appear to be a cutting-edge perception in recognizing diversity in bioactive molecules. These scaffolds can also be successfully employed for the development of novel structural entities that cooperate as valuable pharmacophores for a series of pharmacological properties [41]. The benzisoxazole acquired analogues, like molecule **AS** admitted with potent human PPARδ transactivation action [42] The heat shock protein 90 (Hsp90) is referred as a molecular chaperone that is accountable for exhilarating series of signalling proteins and is a favourable hit in tumour biology. The benzisoxazole-embedded molecule such as **AT** acts as an Hsp90 inhibitors [43]. Additionally, the derivative **AU** manifested prevention against extra-pancreatic tissue damage to the lungs and kidneys . In continuation, the molecules **AV**, **AW** and **AX** revealed threefold to fivefold greater effective cytotoxins than the controls, which are depleting in the phosphoramide mustard-related group (Fig. 9) [44].

   In addition, a broad range of novel metabolically potent benzisoxazole specific PPARc modulators (molecule **AY**)are witnessed and investigated in details toward a series of biological properties. The derivative **AY** referred to as a partial agonist, and it disclosed reduced adipogenesis in human adipocytes [45]. Moreover, the 5-HT4 partial agonist molecule **AZ** was appeared for more clinical enlargement [46].
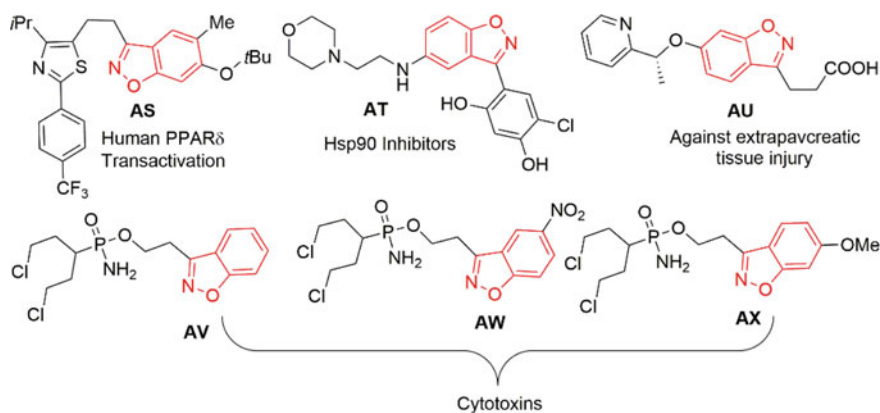
Fig. 9 Benzisoxazoles-related biological agents

Furthermore, the derivative **BA**, a benzisoxazole molecule in the absence of functional groups on the aromatic ring, enacted decent antibacterial action against *E. coli*, *Salmonella* typhi, *Klebsiella pneumoniae* and *B. subtilis*. The benzisoxazole derivatives **BB** and **BC** containing methyl and methoxy functional groups, respectively, rendered excellent antioxidant activities, whereas the derivatives embedded with deactivating groups evident to perform anti-inflammatory actions. In continuation, the molecules **BD** and **BE** containing the electron-withdrawing nitro group are witnessed with good anti-inflammatory performances (Fig. 10) [47].

9   Synthesis of Benzisoxazole Derivatives [48–54]

Realizing the biological and medicinal importance of benzisoxazole derivatives, several synthetic approaches have been devised by employing wide range of synthon [48–54]. The general way of synthesizing benzisoxazole core **18** is by reacting 2-hydroxy derivative of aldoximes/ketoxime **15** in presence of thionyl chloride **16** (Scheme 5).

In addition, the synthesis of benzisoxazoles has been largely realized by utilizing 2-hydroxy derivatives of nitriles, imines, oximes and many more. Few of selected transformations have been shown in Scheme 6.

10   Summary/Conclusion

The benzisoxazole moiety is a significant pharmacophore in modern synthesis and drug discovery. Attention has been progressively more specified to the synthesis of benzisoxazole derivatives as an origin of novel biological and medicinal agents.
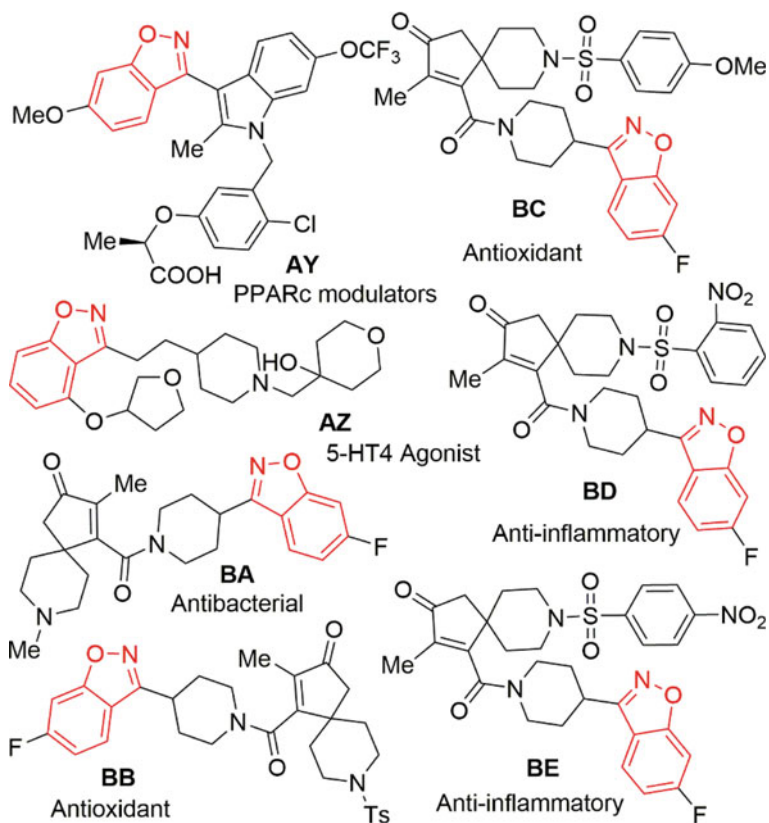
Fig. 10 Benzisoxazoles-based biologically active molecules
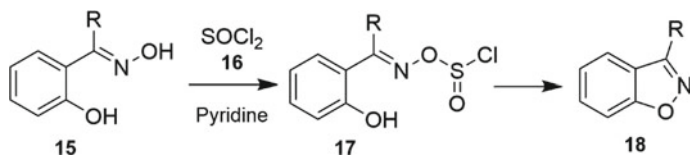
Scheme 5 Synthesis of benzisoxazoles **18** [48]

The recognition obtained by various researches has proposed that the substituted benzisoxazole and related *N*-heterocycles, which are the structural isosteres of nucleotides, acknowledge them to relate simply with the biopolymers and acquire pharmacological and biological activity with lower toxicities. Deviations in the benzisoxazole structures have afforded high biological activities that have proven effectiveness for the evolution of new medicinal agents having revised potency and lesser toxicity. This chapter highlights the several synthesized benzisoxazole derivatives possessing diverse activities such as anti-inflammatory, antifungal, antioxidant,
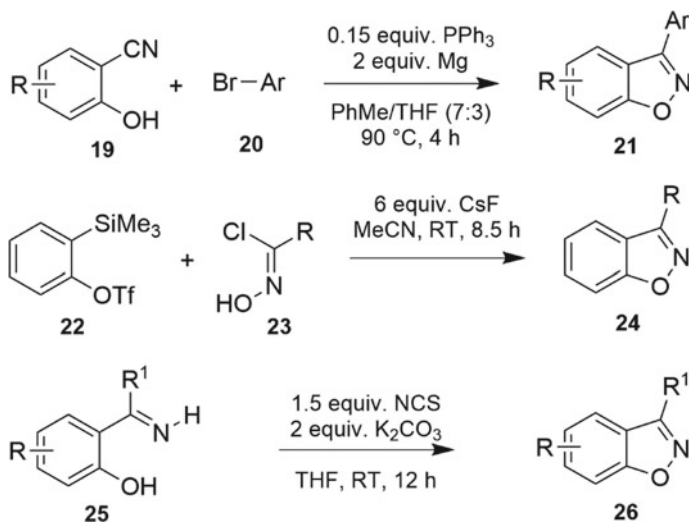
Scheme 6 Various approaches towards benzisoxazoles [49–51]

analgesic, anti-HIV, anticancer, anti-tubercular and antiviral activity. We aspire that the components of this book chapter would engross the interest of broad range of readers associated with biology and chemistry fields to extend the dominance of these motifs in drug discovery research.

References

1. Eguchi S (2007) Topics in heterocyclic chemistry. In: Bioactive heterocycles II, vol 8, XII, p 249
2. Park BK, Kitteringham NR (1994) Effects of fluorine substitution on drug metabolism: pharmacological and toxicological implications. Drug Metab Rev 26:605–643
3. Guttenberger N, Schlatzer T, Leypold M, Tassoti S, Breinbauer R (2018) Synthesis of novel ligands targeting phenazine biosynthesis proteins as a strategy for antibiotic intervention. Monatsh Chem Chem Monthly 149:847–856
4. Wilfong AA, Willmore LJ (2006) Zonisamide—a review of experience and use in partial seizures. Neuropsychiatric Dis Treat 2:269–280
5. Deng BL, Cullen MD, Zhou Z, Hartman TL, Buckheit RW, Pannecouque C, Clercq ED, Fanwick PE, Cushman M (2006) Synthesis and anti-HIV activity of new alkenyldiaryl-methane (ADAM) non-nucleoside reverse transcriptase inhibitors (NNRTIs) incorporating benzoxazolone and benzisoxazole rings. Bioorg Med Chem 14:2366–2374
6. Deng BL, Zhao Y, Hartman TL, Watson K, Buckheit RW Jr, Pannecouque C, Clercq ED, Cushman M (2009) Synthesis of alkenyldiarylmethanes (ADAMs) containing benzo[d]isoxazole and oxazolidin-2-one rings, a new series of potent non-nucleoside HIV-1 reverse transcriptase inhibitors. Eur J Med Chem 44:1210–1214
7. Hrib NJ, Jurcakm JG, Burgher KL, Conway PG, Hartman HB, Kerman LL, Roehr JE, Woods AT (2003) Benzisoxazole- and benzisothiazole-3-carboxamides as potential atypical antipsychotic agents. J Med Chem 37:2308–2314

8. Khedekar PB, Bahekar RH, Chopadec RS, Umathec SN, Rao ARR, Bhusaria KP (2003) Synthesis and anti-inflammatory activity of alkyl/arylidene-2-aminobenzothiazoles and 1-benzothiazol-2-yl-3-chloro-4-substituted-azetidin-2-ones. Drug Res 53:640–647

9. Aiello S, Wells G, Stone EL, Kadri H, Bazzi R, Bell DR, Stevens MF, Matthews CS, Bradshaw TD, Westwell AD (2008) Synthesis and biological properties of benzothiazole, benzoxazole, and chromen-4-one analogues of the potent antitumor agent 2-(3,4-dimethoxyphenyl)-5-fluorobenzothiazole (PMX 610, NSC 721648). J Med Chem 51:5135–5139

10. Kim D-M, Kang M-S, Kim JS, Jeong J-H (2005) An efficient synthesis of risperidone via stille reaction: antipsychotic, 5-HT$_2$, and dopamine-D$_2$-antagonist. Arch Pharm Res 28:1019–1022

11. Vardanyan R (2017) Piperidine-based nonfused biheterocycles with C–N and C–C coupling. In: Piperidine-based drug discovery. Heterocyclic drug discovery. Elsevier, Amsterdam, pp 241–267

12. Rakesh KP, Shantharam CS, Sridhara MB, Manukumar HM, Qin H-L (2017) Benzisoxazole: a privileged scaffold for medicinal chemistry. Med Chem Commun 8:2023–2093

13. Suhas R, Chandrashekar S, Gowda DC (2011) Synthesis of elastin based peptides conjugated to benzisoxazole as a new class of potent antimicrobials—a novel approach to enhance biocompatibility. Eur J Med Chem 46:704–711

14. Suhas R, Chandrashekar S, Gowda DC (2012) Synthesis of uriedo and thiouriedo derivatives of peptide conjugated heterocycles—a new class of promising antimicrobials. Eur J Med Chem 48:179–191

15. Basarab GS, Brassil P, Doig P, Galullo V, Haimes HB, Kern G, Kutschke A, McNulty J, Schuck VJA, Stone G, Gowravaram M (2014) Novel DNA gyrase inhibiting spiropyrimidinetriones with a benzisoxazole scaffold: SAR and in vivo characterization. J Med Chem 57:9078–9095

16. Basarab GS, Doig P, Galullo V, Kern G, Kimzey A, Kutschke A, Newman JP, Morningstar M, Mueller J, Otterson L, Vishwanathan K, Zhou F, Gowravaram M (2015) Discovery of novel DNA gyrase inhibiting spiropyrimidinetriones: benzisoxazole fusion with N-linked oxazolidinone substituents leading to a clinical candidate (ETX0914). J Med Chem 58:6264–6282

17. Lamani RS, Shetty NS, Kamble RR, Khazi IAM (2009) Synthesis and antimicrobial studies of novel methylene bridged benzisoxazolylimidazo[2,1-b][1,3,4]thiadiazole derivatives. Eur J Med Chem 44:2828–2833

18. Malik S, Ahuja P, Sahu K, Khan SA (2014) Design and synthesis of new of 3-(benzo[d]isoxazol-3-yl)-1-substituted pyrrolidine-2, 5-dione derivatives as anticonvulsants. Eur J Med Chem 84:42–50

19. Uno H, Kurokawa M, Masuda Y, Nishimura H (1979) Studies on 3-substituted 1,2-benzisoxazole derivatives. 6. Syntheses of 3-(sulfamoylmethyl)-1,2-benzisoxazole derivatives and their anticonvulsant activities. J Med Chem 22:80–183

20. Naidu KM, Gajanan RN, Chandra Sekhar KVG (2019) Design, synthesis and biological evaluation of 5-(2-(4-(substituted benzo[d]isoxazol-3-yl)piperazin-1-yl)acetyl)indolin-2-one and 5-(2-(4-substitutedpiperazin-1-yl)acetyl)indolin-2-one analogues as novel anti-tubercular agents. Arab J Chem 12:2418–2429

21. Naidu KM, Suresh A, Subbalakshmi J, Sriram D, Yogeeswari P, Raghavaiah P, Chandra Sekhar KVG (2014) Design, synthesis and antimycobacterial activity of various 3-(4-(substitutedsulfonyl)piperazin-1-yl)benzo[d]isoxazole derivatives. Eur J Med Chem 87:71–78

22. Subash V, Brunsteiner M, Uddin R, Wan B, Franzblau SG, Petukhov PA (2008) 5-tert-butyl-N-pyrazol-4-yl-4,5,6,7-tetrahydrobenzo[d]isoxazole-3-carboxamide derivatives as novel potent inhibitors of *Mycobacterium tuberculosis* pantothenate synthetase: initiating a quest for new antitubercular drugs. J Med Chem 51:1999–2002

23. Abesundara KJM, Matsui T, Matsumoto K (2004) α-Glucosidase inhibitory activity of some Sri Lanka plant extracts, one of which, *Cassia auriculata*, exerts a strong antihyperglycemic effect in rats comparable to the therapeutic drug acarbose. J Agric Food Chem 52:2541–2545

24. Funke I, Melzig MF (2006) Traditionally used plants in diabetes therapy phytotherapeutics as inhibitors of a-amylase activity. Braz J Pharmacognosy 16:1–5

25. Li Y, Wen S, Kota BP, Peng G, Li GQ, Yamahara J, Roufogalis BD (2005) *Punica granatum* flower extract, a potent alpha-glucosidase inhibitor, improves postprandial hyperglycemia in Zucker diabetic fatty rats. J Ethnopharmacol 99:239–244

26. Youn JY, Park HY, Cho KH (2004) Anti-hyperglycemic activity of *Commelina communis* L.: inhibition of α-glucosidase. Diabetes Res Clin Pract 66:149–155

27. Shantharam CS, SuyogaVardhan DM, Gowda DC (2013) Synthesis and evaluation of urea/thiourea derivatives of dipeptide linked benzisoxazole as a new class of antiglycation and urease inhibitory agents. Int J Chem Pharm Sci 4:102–112

28. Shantharam CS, SuyogaVardhan DM, Suhas R, Sridhara MB, Gowda DC (2013) Inhibition of protein glycation by urea and thiourea derivatives of glycine/proline conjugated benzisoxazole analogue—synthesis and structure-activity studies. Eur J Med Chem 60:325–332

29. Cao X, Chen Y, Zhang Y, Qiu Y, Yu M, Xu X, Liu X, Liu BF, Zhang G (2016) Synthesis and biological evaluation of new 6-hydroxypyridazinone benzisoxazoles: potential multi-receptor-targeting atypical antipsychotics. Eur J Med Chem 124:713–728

30. Chen Y, Lan Y, Wang S, Zhang H, Xu X, Liu X, Yu M, Liu BF, Zhang G (2014) Synthesis and evaluation of new coumarin derivatives as potential atypical antipsychotics. Eur J Med Chem 74:427–439

31. Xiberas X, Martinot JL, Mallet L, Artiges E, Loc'H C, Maziere B, Paillère-Martinot ML (2001) Extrastriatal and striatal D(2) dopamine receptor blockade with haloperidol or new antipsychotic drugs in patients with schizophrenia. Br J Psychiatry 179:503–508

32. Aranda R, Villalba K, Ravina E, Masaguer CF, Brea J, Areias F, Domínguez E, Selent J, López L, Sanz F, Pastor M, Loza MI (2008) Synthesis, binding affinity, and molecular docking analysis of new benzofuranone derivatives as potential antipsychotics. J Med Chem 51:6085–6094

33. Chen Y, Wang S, Xu X, Liu X, Yu M, Zhao S, Liu S, Qiu Y, Zhang T, Liu B-F, Zhang G (2013) Synthesis and biological investigation of coumarin piperazine (piperidine) derivatives as potential multi-receptor atypical antipsychotics. J Med Chem 56:4671–4690

34. Bolos J, Anglada L, Gubert S, Planas JM, Agut J, Princep M, Fuente ADL, Sacristan A, Ortiz J (1998) 7-[3-(1-piperidinyl)propoxy]chromenones as potential atypical antipsychotics. 2. Pharmacological profile of 7-[3-[4-(6-Fluoro-1,2-benzisoxazol-3-yl)-piperidin-1-yl]propoxy]-3-(hydroxymethyl)chromen-4-one (Abaperidone, FI-8602). J Med Chem 41:5402–5409

35. Rangappa KS, Basappa (2005) New cholinesterase inhibitors: synthesis and structure-activity relationship studies of 1,2-benzisoxazole series and novel imidazolyl-d2-isoxazolines. J Phys Org Chem 18:773–778

36. Anand M, Selvaraj V, Alagar M (2014) Synthesis, characterization and evaluation of antioxidant and anticancer activities of novel benzisoxazole-substituted-allyl derivatives. Korean J Chem Eng 31:659–663

37. Benaka Prasad SB, Vinaya CSK, Kumar A, Swarup S, Rangappa KS (2009) Synthesis of novel 6-fluoro-3-(4-piperidinyl)-1,2-benzisoxazole derivatives as antiproliferative agents: a structure–activity relationship study. Invest New Drugs 27:534–542

38. Ashwini N, Garg M, Mohan CD, Fuchs JE, Rangappa S, Anusha S, Swaroop TR, Rakesh KS, Kanojia D, Madan V, Bender A, Koeffler HP, Basappa, Rangappa KS (2015) Synthesis of 1,2-benzisoxazole tethered 1,2,3-triazoles that exhibit anticancer activity in acute myeloid leukemia cell lines by inhibiting histone deacetylases, and inducing p21 and tubulin acetylation. Bioorg Med Chem 23:6157–6165

39. Villalobos A, Blake JF, Biggers CK, Butler TW, Chapin DS, Chen YL, Ives JL, Jones SB, Liston DR, Nagel AA, Nason DM, Nielsen JA, Shalaby IA, White WF (1994) Novel benzisoxazole derivatives as potent and selective inhibitors of acetylcholinesterase. J Med Chem 37:721–2734

40. Walker AL, Ancellin N, Beaufils B, Bergeal M, Binnie M, Bouillot A, Clapham D, Denis A, Haslam CP, Holmes DS, Hutchinson JP, Liddle J, McBride A, Mirguet O, Mowat CG, Rowland P, Tiberghien N, Trottet L, Uings I, Webster SP, Zheng X, Mole DJ (2017) Development of a series of kynurenine 3-monooxygenase inhibitors leading to a clinical candidate for the treatment of acute pancreatitis. J Med Chem 60:3383–3404

41. Li Z, Zhan P, Liu X (2011) 1,3,4-oxadiazole: a privileged structure in antiviral agents. Mini-Rev Med Chem 11:1130–1142

42. Sakuma S, Endo T, Kanda T, Nakamura H, Yamasaki S, Yamakawa T (2011) Biological evaluation of novel benzisoxazole derivatives as PPARδ agonists. Bioorg Med Chem 19:3255–3264

43. Gopalsamy A, Shi M, Golas J, Vogan E, Jacob J, Johnson M, Lee F, Nilakantan R, Petersen R, Svenson K, Chopra R, Tam MS, Wen Y, Ellingboe J, Arndt K, Boschelli F (2008) Discovery of benzisoxazoles as potent inhibitors of chaperone heat shock protein 90. J Med Chem 51:373–375

44. Jain M, Kwon CH (2003) 1,2-benzisoxazole phosphorodiamidates as novel anticancer prodrugs requiring bioreductive activation. J Med Chem 46:5428–5436

45. Liu K, Black RM, Acton JJ 3rd, Mosley R, Debenham S, Abola R, Yang M, Tschirret-Guth R, Colwell L, Liu C, Wu M, Wang CF, MacNaul KL, McCann ME, Moller DE, Berger JP, Meinke PT, Jones AB, Wood HB (2005) Selective PPARγ modulators with improved pharmacological profiles. Bioorg Med Chem Lett 15:2437–2440

46. Brodney MA, Johnson DE, Sawant-Basak A, Coffman KJ, Drummond EM, Hudson EL, Fisher KE, Noguchi H, Waizumi N, McDowell LL, Papanikolaou A, Pettersen BA, Schmidt AW, Tseng E, Stutzman-Engwall K, Rubitski DM, Vanase-Frawley MA, Grimwood S (2012) Identification of multiple 5-HT4 partial agonist clinical candidates for the treatment of Alzheimer's disease. J Med Chem 55:9240–9254

47. Shivaprasad CM, Jagadish S, Swaroop TR, Mohan CD, Roopashree R, Sharath Kumar KS, Rangappa KS (2014) Synthesis of new benzisoxazole derivatives and their antimicrobial, antioxidant and anti-inflammatory activities. Eur J Chem 5:91–95

48. Kalkote UR, Goswmi DD (1977) New synthesis of 1,2-benzisoxazole derivatives. Aust J Chem 30:1847–1850

49. Chen G, Liu H, Li S, Tang Y, Lu P, Xu K, Zhang Y (2017) A novel PPh3 mediated one-pot method for synthesis of 3-aryl or alkyl 1,2-benzisoxazoles. Org Lett 19:1792–1795

50. Dubrovskiy AV, Larock RC (2010) Synthesis of benzisoxazoles by the [3 + 2] cycloaddition of in situ generated nitrile oxides and arynes. Org Lett 12:1180–1183

51. Chen C-Y, Andreani T, Li H (2011) A Divergent and selective synthesis of isomeric benzoxazoles from a single N-Cl imine. Org Lett 13:6300–6303

52. Shastri RA (2016) Review on synthesis of 3-substituted 1,2-benzisoxazole derivatives. Chem Sci Trans 5:8–20

53. Rodrigo E, Baunis H, Suna E, Waldvogel SR (2019) Simple and scalable electrochemical synthesis of 2,1-benzisoxazoles and quinoline N-oxides. Chem Commun 55:12255–12258

54. Majeed K, Zhou F, Zhang Q (2021) Metal-free tandem reactions of 2-iodoaryl ynones with sodium azide for the synthesis of benzoisoxazole containing 1,2,3-triazoles. Org Biomol Chem 19:3707–3716 (references cited there in)

Highlights on Biological Activities of 1,3,4-Thiadiazole and Indazole Derivatives

Arup K. Kabi, Raghuram Gujjarappa, Aakriti Garg, Anupam Roy, Abhishek Sahoo, Sreya Gupta, and Chandi C. Malakar

Abbreviations

AIDS	Acquired immune deficiency syndrome
DNA	Deoxyribonucleic acid
DPP-4	Dipeptidyl peptidase-4
GIP	Gastric inhibitory polypeptide
GLP-1	Glucagon-like peptide 1
HER2	Human epidermal growth factor receptor 2
HIV	Human immunodeficiency virus
OAT4	Organic anion carrier 4
OGTT	Oral glucose tolerance test
OLIG2	Oligodendrocyte lineage transcription factor 2
PARP	Poly (ADP-ribose) polymerase
RNA	Ribonucleic acid
SAR	Structure–activity relationship
TNFα	Tumor necrosis factor α
URAT1	Uric acid carrier 1
U.S. FDA	United State Food and Drug Administration
XPO1	Exportin 1

A. K. Kabi · R. Gujjarappa · A. Roy · A. Sahoo · C. C. Malakar (✉)
Department of Chemistry, National Institute of Technology Manipur, Langol, Imphal, Manipur 795004, India
e-mail: cmalakar@nitmanipur.ac.in

A. Garg · S. Gupta (✉)
Department of Medicinal Chemistry, National Institute of Pharmaceutical Education and Research (NIPER), Kolkata, Chunilal Bhawan, 168, Maniktala Main Road, Kolkata 700054, India
e-mail: sreyog83@gmail.com

1 Introduction

Thiadiazole is recognized as a five-membered heterocyclic ring embedded with sulfur and nitrogen atom, which exhibits as "two-electron donor system" and "hydrogen binding domain." They appear in four isomeric forms such as 1,2,5-thiadiazole, 1,2,4-thiadiazole, 1,2,3-thiadiazole, and 1,3,4-thiadiazole moieties. It has been witnessed that the molecules accommodated with five-membered heterocyclic ring reveal noteworthy chemical phenomenon and a series of talented biological activities [1–5]. Among these scaffolds, the 2,5-functionalized 1,3,4-thiadiazoles are identified with divergent biological actions apparently due to the occurrence of –N=C–S– moieties. On the other hand, the indazole scaffolds are evident with a broad spectrum of pharmacological properties [6–8]. In recent years, a series of indazole derivatives have been described with admirable bioactivities. Moreover, the indazole moieties constitute a class of pharmacologically influential molecules appearing with a broad range of biological actions, [9] including anti-inflammatory, HIV protease inhibition, antitumor, antiplatelet, antimicrobial, and anticancer activities. Here, we represent the current aspects in the improvement of indazole-embedded pharmacologically active molecules [10–14]. Here, in this section the versatility of thiadiazoles and indazoles in medicinal chemistry is discussed (Fig. 1.1 and Table 1.1).
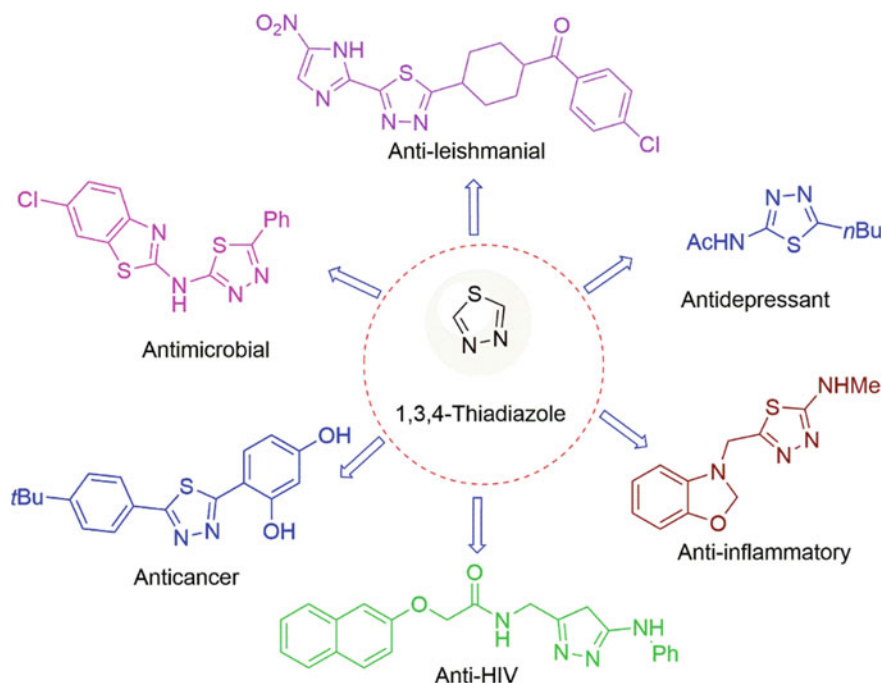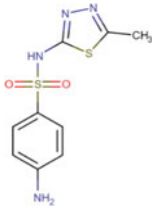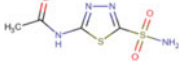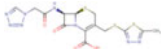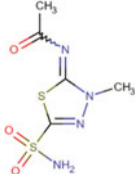
Fig. 1.1 Importance of 1,3,4-thiadiazole cores

Table 1.1 FDA-approved drugs containing 1,3,4-thiadiazole-based molecules

Drug name (drug bank ID)	Structure	Category/Indication	Mechanism of action
Sulfamethizole (DB00576)		Sulfamethizole is employed for the medication of urinary tract infection	This functions as a competitive blocker of bacterial enzyme dihydropteroate synthetase
Acetazolamide (DB00819)		Acetazolamide is referred for the ancillary treatment of (1) edema arises because of congestive heart failure; (2) centrencephalic epilepsies; (3) chronic simple (open-angle) glaucoma; and (4) drug-instigated edema	It acts toward the lead inhibition of carbonic anhydrase in the CNS
Cefazolin (DB01327)		Cefazolin is primarily employed for the cure of bacterial infections of the skin	It effects the prevention of synthesis of cell wall by targeting to selective penicillin-binding proteins (PBPs)
Methazolamide (DB00703)		Methazolamide is utilized as a diuretic and in the medication of glaucoma	It acts as blocker of carbonic anhydrase

2 1,3,4-Thiadiazoles and Their Pharmaceutical Drugs

The prudent liposolubility of the sulfur-atom in 1,3,4-thiadiazoles scaffold could also have an affirmative effect on the biological actions and pharmaceutical characteristics of thiadiazole-embedded molecules. Albeit the thiadiazole derivatives have preferences over other commonly identified therapeutic molecules, eventually their toxicity still persists a major concern. In recent years, a series of thiadiazole-embedded marketed drug molecules are recognized. Among these molecules, the methazolamide and acetazolamide are well known as diuretic and act as inhibitor of carbonic anhydrase. It is described that the derivatives of these drug molecules reveal other pharmacological performances such as anti-convulsant and intended inhibition of carbonic anhydrase [15]. A part of other thiadiazole-associated drugs

are occurred in the market which include cefazedone, cefazolin sodium, xanome-line, timolol, and megazol (Fig. 1.2) [16]. The cefazedone and cefazolin sodium are witnessed as first generation cephalosporins, whereas the timolol is a suppressor of the non-selective β-adrenergic receptor, which is employed for the cure of angina and hypertension. The xanomeline performs as a prudent agonist of muscarinic acetylcholine receptor subtypes M4 and M1, and megazol is recognized as an anti-parasitic drug, respectively. 1,3,4-thiadiazole is a crucial scaffold ubiquitous in a series of drug molecules and possesses a number of pharmacological actions such as anti-inflammatory, antiviral, antimicrobial, antiepileptic, analgesic, antitubercular agents, antineoplastic, cytotoxic activities, and anti-oxidant properties [17, 18]. Thia-diazolidiones (TZDs) display anti-diabetic activities by transactivation of PPAR-ϒ and reduce the glucose level in blood. These derivatives are not associated with any side effects like hepatotoxic, weight gain, and cardio-toxic effects. The acti-vation of PPAR-ϒ may also lead in its anticancer properties as the processes such as differentiation, cell proliferation, and apoptosis are involved [18]. A novel series of thiazolyl-2,4-thiazolidinediones/rhodanines were prepared, and these molecules were examined for the anticancer properties in two HCC cell lines such as PLC/PRF/5 (PLC) and Huh7 for preliminary screening, one breast cancer cell line such as MCF7 for secondary screening, and five hepatocellular carcinoma (HCC) cell lines [Huh7, Snu449, Hep3B, Plc, and HepG2]. In this strategy, three novel derivatives were identified which are associated with outstanding anticancer properties. The thiazole-embedded derivatives containing a lipophilic functional group such as TZD or rhodamine ring at N-3 position reveal potent anticancer properties [19].

A broad range of 5-((3-aryl-1-phenyl-1*H*-pyrazol-4-yl)methylene) thiazolidine-2,4-diones were described, and these derivatives were exposed toward the anti-bacterial studies against *Staphylococcus aureus*, *Bacillus subtilis*, *Escherichia coli*, and *Pseudomonas aeruginosa* and also correlated with the standard drug ciprofloxacin. The experiments resulted with the outcome of good activities against Gram +ve bacteria. Moreover, one of the molecules apprises toward more potent activity with the MIC of 32 µg/ml against *B. subtilis* and 16 µg/ml against *S. aureus* [20].
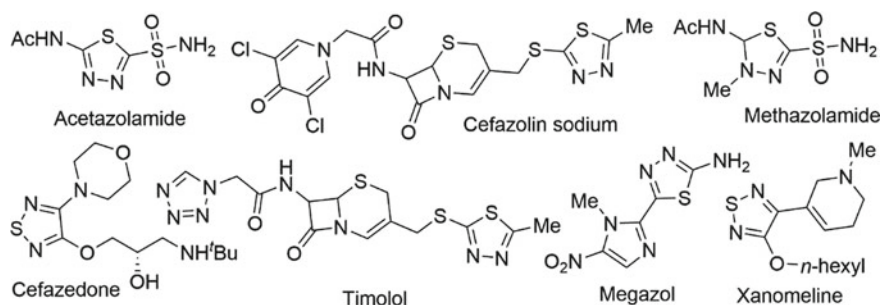
Fig. 1.2 Pharmaceutically important molecules embedded with 1,3,4-thiadiazole moiety

The 1,3,4-thiadiazole derivatives embedded with pyrazole and pyrrole containing the carboxamide group at 3rd position have exhibited compelling anti-inflammatory properties. It was also identified that three derivatives have conceded the adequate anti-inflammatory effect with inhibition in paw edema of 77, 76, and 76% at 3 h, whereas the indomethacin revealed 75% of inhibition. Furthermore, after 5 h, the inhibition of 81, 80, and 79% was identified; nevertheless, indomethacin affirmed 80% inhibition [21].

The 1,3,4-thiadiazole molecules embedded with amino group functionalization at 2nd position and sulfonyl group functionalization at 5th position were prepared and examined toward their anti-depressant and anxiolytic properties. These derivatives were compared with the standard drugs such as diazepam and imipramine, which discloses that one molecule has admitted with good anxiolytic and anti-depressant activities at a therapeutic dose range and liabilities of side effects such as amnesia and sedation were minimum [22].

The linezolid is witnessed as a bacteriostatic molecules, and its analogs embedded with a nitroaryl-1,3,4-thiadiazole moiety possess the antimicrobial properties by inhibiting the protein synthesis against the generation of 70S complex. Moreover, one of these derivatives exposed more potent activity against Gram −ve and Gram +ve bacteria, when correlated to the standard drug such as ciprofloxacin [23].

3   Indazole-Containing Pharmaceutical Drugs

Axitinib (in trade name it is known as Inlyta) is referred to as a tyrosine kinase small molecule inhibitor (A) that has been described to prevent the progress of breast cancer expressively. Also, it establishes a property against renal cell carcinoma in the clinical trials [24] (Fig. 1.3).

In addition, the granisetron (also known as Sancuso in the trade name) is recognized as a careful 5-HT3 receptor antagonist (B), which has been employed medicinally to prevent the emesis and nausea caused by the intake of cancer chemotherapeutic agents [25, 26]. Compound 1H-indazole-3-carboxylic acid (K) shows selective and potent anti-spermatogenic activity. Indazole derivatives L and M act as liver receptor agonist, and compound 1-(4-fluro-phenyl)-1*H*-indazole (N) is most effective against acute and chronic inflammatory conditions (Fig. 1.3 and Table 1.2).

In addition, 3-aminoindazole is a clinically immense N-heterocyclic scaffold that has been normally employed for pharmaceutical strategy. The derivatives with this distinct moiety have been established to have important biological performances, which include suppressing melanin-concentrating hormone (MCH) receptor-1 as exhibited by compounds Q and R [27].Indeed, the detailed inhibition capacities were studied for Janus kinase-2 (JAK-2), multi targeted receptor tyrosine kinase (RTK), and cyclin-dependent kinase with the exposure of ABT-869 (S) [28], compounds T [29] and P [30] respectively. [28][29] [30. In continuation, 1-phenyl-4,5,6,7-tetrahydro-1*H*-indazole-5-carboxylic acid (compound U) displayed anti-inflammatory characteristics, whereas the 2-methyl-3-methylamino-4,5,6,7-tetrahydroindazole (compound V) also showed the good anti-inflammatory
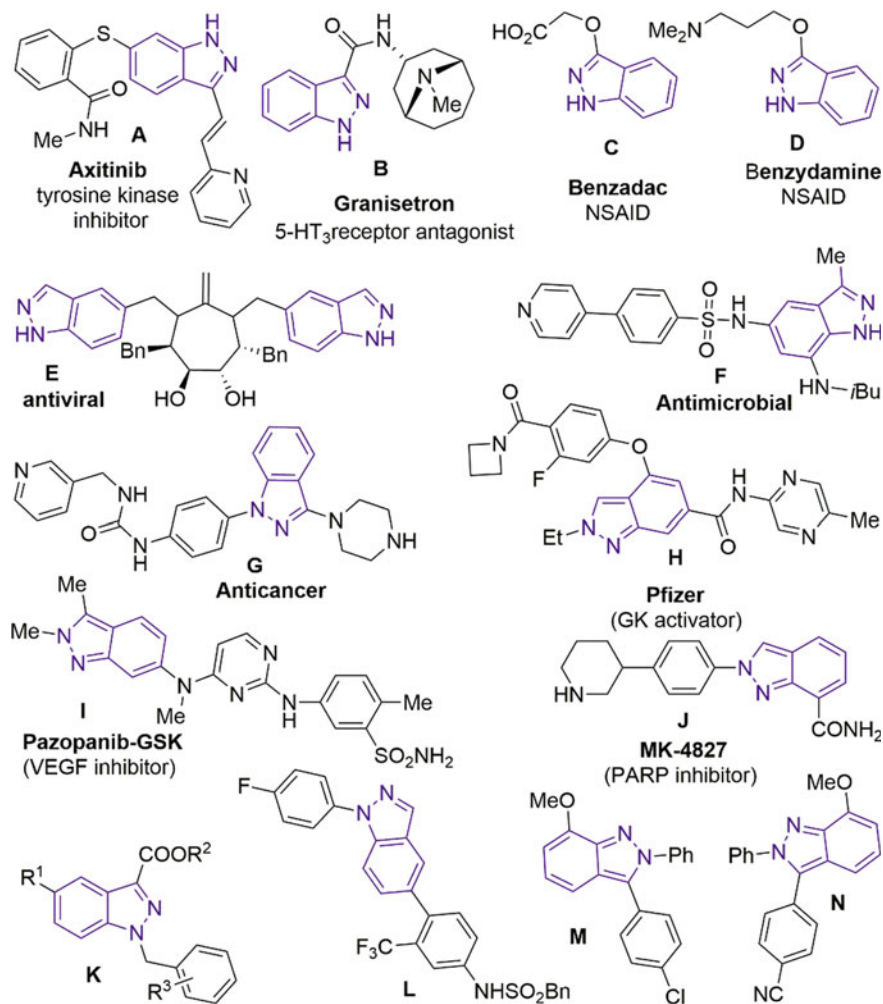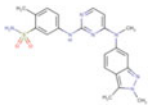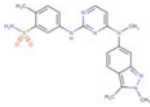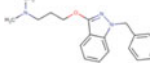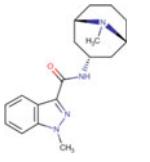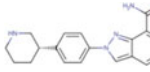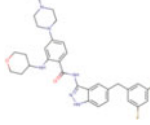
Fig. 1.3 Biologically active indazole derivatives
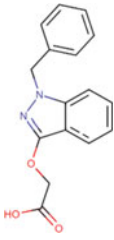
activity. Additionally, compound W exhibited anti-bacterial activity and compound X displayed both anti-inflammatory and antimicrobial activity (dual agent). Indeed, the compounds Y (A-674563) and Z (A-443654) were Akt inhibitors in cancer treatment. In addition, compound AA is used in the treatment of chronic obstructive pulmonary disease. In addition, the compound AB exhibited anti-tuberculosis activity, whereas compound AC and AD were ketohexokinase inhibitors and glucocorticoid receptors agonists and antagonists, respectively. In another, lonidamine (synonym diclondazolic acid) signifies an orally administrating hexokinase inactivator, as well as anti-spermatogenic and anticancer agents (AE) [31, 32] (Fig. 1.4).

Table 1.2 FDA-approved indazole-containing drugs

Drug name (drug bank ID)	Structure of drug	Category/Indication	Mechanism of action
Pazopanib (DB06589)		Pazopanib is well known for the medication of cancer in renal cell at advanced stage and also used for soft tissue sarcoma in advanced stage	Pazopanib induces the generation of blood vessel in tumor toward the endurance and advancement of tumor
Axitinib (DB06626)		Axitinib is recommended for cancer in the kidney cell and described toward the cure of thyroid and pancreatic cancer	Axitinib is familiar as specific blocker of the VEGFR-1, VEGFR-2, and VEGFR-3
Benzydamine (DB09084)		Benzydamine is recognized as analgesic acting locally. This is also employed for the medication of inflammatory disorders and releases from the painful conditions	Benzydamine performs by preventing the generation of cytokines (pro-inflammatory) like interleukin-1β (IL-1β) and TNF-α
Granisetron (DB00889)		Granisetron is recommended toward suppressing vomiting and nausea identified after emetogenic cancer therapy, radiation and post operation (during initial and repeat courses). This disorder may be associated with high dose *cis*-platin	Granisetron is been witnessed as a potent, selective antagonist of 5-HT$_3$ receptors
Niraparib (DB11793)		Niraparib has been realized to treat ovarian cancer	Niraparib is witnessed as an orally active PARP inhibitor
Entrectinib (DB11986)		Entrectinib is recommended for the medication of solid tumors (NTRK gene fusion positive) and non-small cell lung cancer which is ROS1-positive metastatic	Entrectinib is familiar as tropomyosin receptor tyrosine kinase (TRK) such as TRKA, TRKB, TRKC, anaplastic lymphoma kinase, and proto-oncogene tyrosine-protein kinase ROS1 inhibitor

(continued)

Table 1.2 (continued)

Drug name (drug bank ID)	Structure of drug	Category/Indication	Mechanism of action
Bendazac (DB13501)		Bendazac is known for an anticataract action, anti-inflammatory, anti-necrotic, choleretic, and anti-lipidemic characteristics, useful in managing and delaying the progression of ocular cataracts	Bendazac is inhibiting the denaturation of ocular lens proteins and inhibits prostaglandin synthesis by inhibiting cyclooxygenase activity in converting arachidonic acid to cyclic endoperoxides
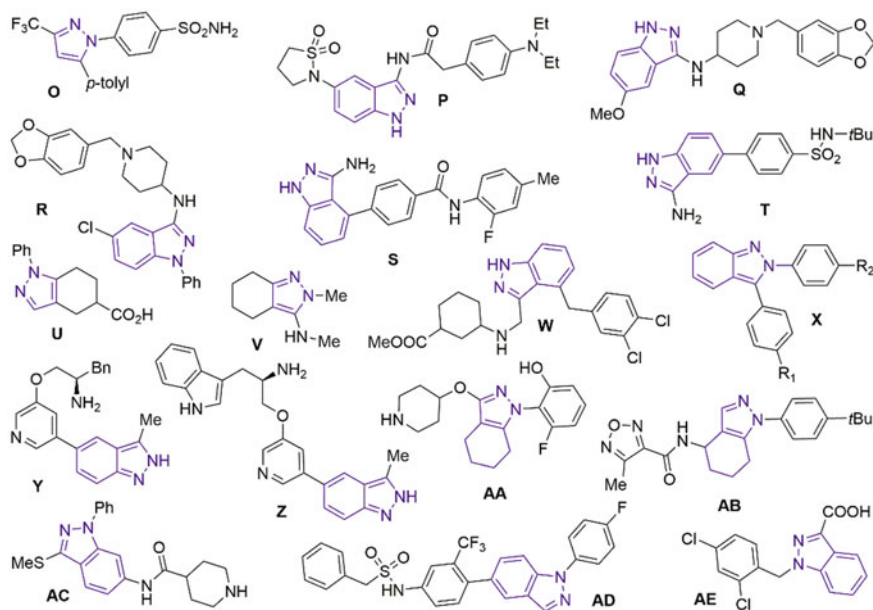
Fig. 1.4 Pharmacologically important indazole derivatives

Indazole is a heterocyclic skeleton which exhibits potent pharmacological activities like antitumor, antiviral, anti-inflammatory, antiplatelet, antimicrobial, HIV protease inhibition, antitubercular, anti-spermatogenic, antifungal, anti-bacterial activity, protein kinase C-B/Akt inhibition, anti-pyretic, NSAID, and analgesic [33, 34]. Indazoles also play a role in angiogenesis and metastasis in solid cell line tumor.

Indazole substitution at different positions exhibits different pharmacological activities. Indazole with a sulphonamide moiety exhibits good anti-proliferative activity. Some of the indazole-containing compounds induced block of cell division in G2/M phase. N-[6-indazolyl] aryl sulfonamides were synthesized, and they

are evaluated for the anti-proliferative activity. Two compounds have shown a good anti-proliferative activity in the cell lines, namely A2780 and A549 with the IC_{50} value of 4.21 µM and 18.6 µM and 5.47 µM and 7.73 µM, respectively [33].

3-substituted indazoles were synthesized, i.e., 3-arylindazoles and N-methyl-3-aryl indazoles, and they were evaluated for the antimicrobial activity and the anti-cancer activity. The anticancer activity of the synthesized compounds was evaluated in cell lines such as HT-29 (human colorectal adenocarcinoma cell line) and MDA-MB-231 (human breast cancer cell line). These compounds exhibited the IC50 value in the range of 0.8-6.8 and 1.2-7.6 µM respectively in cell lines Ht-29 and MDA-MB-231. ₀ Four compounds have exhibited excellent activity with 29, 25.8, 27, and 20 mm values at the concentration of 100 µg/ml against bacterial strain *S. aureus,* and two compounds are active against *Klebsiella pneumoniae* with 22.2 and 19 mm, respectively. Docking of the above compounds was performed, and the role of indazoles in establishing hydrogen bond interaction with the receptor was known. It indicates that the indazoles exhibit good anticancer and good anti-bacterial property [35].

4 Summary/Conclusion

The significance of thiadiazole and indazole motifs can be contemplated by their unambiguous presence in several pharmaceuticals and related molecules. The indazole derivatives mark their presence by their substantial activities like antimicrobials, antitumors, antivirals, NSAIDs, antifungals, and anticancer agents. In parallel, thiadiazole derivatives pursue a wide range of pharmaceutical properties to cure some of the life-threatening diseases. Owing to the importance affiliated toward thiadiazole and indazole derivatives, researchers around the globe have been constantly probing toward the isolation of more potent molecules embedded with thiadiazole and indazoles. This chapter has been written in light of providing adequate information on medicinal and pharmacological aspects of thiadiazole and indazole derivatives. This chapter also shed lime light on the biological importance and mode of action of thiadiazole- and indazole-containing drugs. We anticipate that the elements of this book chapter would captivate the interest of wide range of readers associated with chemical biology and biochemistry fields in enhancing the supremacy of these cores in drug discovery research.

References

1. Mohammad A, Harish K, Sadique AJ (2007) Synthesis and pharmacological evaluation of condensed heterocyclic 6-substituted-1,2,4-triazolo[3,4-b]-1,3,4-thiadiazole derivatives of naproxen. Bioorg Med Chem Lett 17:4504–4508
2. Mathew V, Keshavayya J, Vaidya VP (2006) Heterocyclic system containing bridgehead nitrogen atom synthesis and pharmacological activities of some substituted 1,2,4-triazolo[3,4-b]-1,3,4-thiadiazoles. Eur J Med Chem 41:1048–1058

3. Khalil NSAM (2007) N- and S-α-L-arabinopyranosyl-[1,2,4]triazolo[3,4b][1,3,4]thiadiazoles. First synthesis and biological evaluation. Eur J Med Chem 42:1193–1199

4. Karegoudar P, Prasad DJ, Ashok M, Mahalinga M, Poojary B, Holla BS (2008) Synthesis, antimicrobial and anti-inflammatory activities of some 1,2,4-triazolo[3,4-b][1,3,4]thiadiazoles and 1,2,4-triazolo[3,4-b][1,3,4]thiadiazines bearing trichlorophenyl moiety. Eur J Med Chem 43:808–815

5. El-Barbary AA, Abou-El-Ezz AZ, Abdel-Kader AA, El-Daly M, Nielsenc C (2004) Synthesis of some new 4-amino-1,2,4-triazole derivatives as potential anti-HIV and anti-HBV. Phosphorus Sulfur Silicon Relat Elem 179:1497–1508

6. Cerecetto H, Gerpe A, González M, Arán VJ, de Ocáriz CO (2005) Pharmacological properties of indazole derivatives: recent developments. Mini-Rev Med Chem 5:869–878

7. Jennings A, Tennant MJ (2007) Selection of molecules based on shape and electrostatic similarity: proof of concept of "electroforms." J Chem Inf Model 47:1829–1838

8. Magano J, Waldo M, Greene D, Nord E (2008) The synthesis of (S)-5-fluoro-1-(2-fluorophenyl)-3-(piperidin-3-ylmethoxy)-1H-indazole, a norepinephrine/serotonin reuptake inhibitor for the treatment of fibromyalgia. Org Process Res Dev 12:877–883

9. Li X, He L, Chen H, Wu W, Jiang H (2013) Copper-catalyzed aerobic C(sp2)-H functionalization for C-N bond formation: synthesis of pyrazoles and indazoles. J Org Chem 78:3636–3646

10. Chen G, Hu M, Peng Y (2018) Switchable synthesis of 3-substituted 1H-Indazoles and 3,3-Disubstituted 3H-Indazole-3-phosphonates tuned by phosphoryl groups. J Org Chem 83:1591–1597

11. Reddy GT, Venkatesh MV, Mohan RB, Reddy NCG (2017) Citric acid mediated one-pot regioselective synthesis of N-alkylated indazoles: an efficient green strategy. Trends Green Chem 4:1–1

12. Elsayed NMY, El Ella DAA, Serya RAT, Tolba MF, Shalabya R, Abouzid KAM (2016) Design, synthesis and biological evaluation of indazole–pyrimidine based derivatives as anticancer agents with anti-angiogenic and antiproliferative activities. Med Chem Commun 7:881–899

13. Genung NE, Wei L, Aspnes GE (2014) Regioselective synthesis of 2H-indazoles using a mild, one-pot condensation-cadogan reductive cyclization. Org Lett 16:3114–3117

14. Wang Q, Li X (2016) Synthesis of 1H-indazoles from imidates and nitrosobenzenes via synergistic rhodium/copper catalysis. Org Lett 18:2102–2105

15. Masereel B, Rolin S, Abbate F, Scozzafava A, Supuran CT (2002) Carbonic anhydrase inhibitors: anticonvulsant sulfonamides incorporating valproyl and other lipophilic moieties. J Med Chem 45:312–320

16. Haider S, Alam MS, Hamid H (2014) 1,3,4-thiadiazoles: a potent multi targeted pharmacological scaffold. Eur J Med Chem 92:156–177

17. Napoleon AA (2016) Review on recent developments and biological activities of 2, 4-thiazolidinediones. Int J PharmTech Res 9:429–443

18. Day C (1999) Thiazolidinediones: a new class of antidiabetic drugs. Diabet Med 16:179–192

19. Borde RM, Jadhav SB, Dhavse RR, Munde AS (2018) Design, synthesis, and pharmacological evaluation of some novel bis-thiazole derivatives. Asian J Pharm Clin Res 11:164–168

20. Borelli C, Schaller M, Niewerth M, Nocker K, Baasner B, Berg D, Tiemann R, Tietjen K, Fugmann B, Lang-Fugmann S, Korting HC (2008) Modes of action of the new arylguanidine abafungin beyond interference with ergosterol biosynthesis and in vitro activity against medically important fungi. Chemotherapy 54:245–259

21. Łączkowski KZ, Konklewska N, Biernasiuk A, Malm A, Sałat K, Furgała A, Dzitko K, Bekier A, Łączkowska AB, Paneth A (2018) Thiazoles with cyclopropyl fragment as antifungal, anticonvulsant, and anti-Toxoplasma gondii agents: synthesis, toxicity evaluation, and molecular docking study. Med Chem Res 27:2125–2140

22. Gong GH, Wang D, Zhang JF, Wei CX, Quan ZS (2014) Anticonvulsant activity of 2-(substituted-imino)thiazolidin-4-ones. Drug Res 64:5–9

23. De Rosa M, Bonomo MG, Vassallo A, Palma G, Calabrone L, Bimonte S, Silvestris N, Amruthraj NJ, Sinicropi MS, Salzano G, Arra C, Saturnino C (2018) Linezolid and its derivatives: the promising therapeutic challenge to multidrug-resistant pathogens. Pharmacologyonline 2:134–148
24. Rugo HS, Herbst RS, Liu G, Park JW, Kies MS, Steinfeldt HM, Pithavala YK, Reich SD, Freddo JL, Wilding G (2005) Phase I trial of the oral antiangiogenesis agent AG-013736 in patients with advanced solid tumors: pharmacokinetic and clinical results. J Clin Oncol 23:5474–5483
25. Hesketh PJ, Gandara DR (1991) Serotonin antagonists: a new class of antiemetic agents. J Natl Cancer Inst 83:613–620
26. Aapro M (2004) Granisetron: an update on its clinical use in the management of nausea and vomiting. Oncologist 9:673–686
27. Vasudevan A, Souers AJ, Freeman JC, Verzal MK, Gao J, Mulhern MM, Wodka D, Lynch JK, Engstrom KM, Wagaw SH, Brodjian S, Dayton B, Falls DH, Bush E, Brune M, Shapiro RD, Marsh KC, Hernandez LE, Collins CA, Kym PR (2005) Aminopiperidine indazoles as orally efficacious melanin concentrating hormone receptor-1 antagonists. Bioorg Med Chem Lett 15:5293–5297
28. Dai Y, Hartandi K, Ji Z, Ahmed AA, Albert DH, Bauch JL, Bouska JJ, Bousquet PF, Cunha GA, Glaser KB, Harris CM, Hickman D, Guo J, Li J, Marcotte PA, Marsh KC, Moskey MD, Martin RL, Olson AM, Osterling DJ, Pease LJ, Soni NB, Stewart KD, Stoll VS, Tapang P, Reuter DR, Davidsen SK, Michaelides MR (2007) Discovery of N-(4-(3-amino-1*H*-indazol-4-yl)phenyl)-N′-(2-fluoro-5-methylphenyl)urea (ABT-869), a 3-aminoindazole-based orally active multitargeted receptor tyrosine kinase inhibitor. J Med Chem 50:1584–1597
29. Antonysamy S, Hirst G, Park F, Sprengeler P, Stappenbeck F, Steensma R, Wilson M, Wang M (2009) Fragment-based discovery of JAK-2 inhibitors. Bioorg Med Chem Lett 19:279–282
30. Lee J, Choi H, Kim K-H, Jeong S, Park J-W, Baek C-S, Lee S-H (2008) Synthesis and biological evaluation of 3,5-diaminoindazoles as cyclin-dependent kinase inhibitors. Bioorg Med Chem Lett 18:2292–2295
31. Calviño E, Estañ MC, Simón GP, Sancho P, del Carmen Boyano-Adánez M, de Blas E, Bréard J, Aller P (2011) Increased apoptotic efficacy of lonidamine plus arsenic trioxide combination in human leukemia cells. Reactive oxygen species generation and defensive protein kinase (MEK/ERK, Akt/mTOR) modulation. Biochem Pharmacol 82:1619–1629
32. Sánchez Y, Simon GP, Calviño E, de Blas E, Aller P (2010) Curcumin stimulates reactive oxygen species production and potentiates apoptosis induction by the antitumor drugs arsenic trioxide and lonidamine in human myeloid leukemia cell lines. J Pharmacol Exp Ther 335:114–123
33. Abbassi N, Rakib EM, Chicha H, Bouissane L, Hannioui A, Aiello C, Gangemi R, Castagnola P, Rosano C, Viale M (2014) Synthesis and antitumor activity of some substituted indazole derivatives. Arch Pharm Chem Life Sci 347:1–9
34. Ivaturi KV, Allaka TR (2019) Design, synthesis and docking studies of new indazole derivatives as potent cytotoxic and antibacterial agents. Indian J Heterocycl Chem 28:467–475
35. Reddy GS, Viswanath IVK, Raom AT (2018) Design, synthesis and docking studies of new indazole derivatives as potent cytotoxic and antibacterial agents. Indian J Heterocycl Chem 28:467–475

Exploring the Scope of Developing Ionic Liquid-Based Drugs

Sumit Bhawal

1 Introduction

1.1 The Pharmaceutical Landscape is Dominated by Solid Active Forms

One unique feature that defines a solid is the ability of its constituents to arrange themselves in different ways. It is common for the component ions, atoms, or molecules to adopt more than one arrangement in three dimensions. Thus, it is possible to construct crystalline solids displaying different physical properties from a single-component organic crystal given the name polymorphism arising mainly due to differences in free energy of their respective crystalline and solvated state [1, 2]. One such property that gets affected due to different crystalline arrangement is the aqueous solubility, thus directly affecting the bioavailability and hence absorption of the solid drugs [2]. However, crystals containing more than one type of atom, ionic compound, or molecule will have different properties than do crystals made from singular constituent and are called cocrystals [1].

Cocrystals wherein active pharmaceutical ingredient (API) may be embedded in a pharmaceutically acceptable guest molecules have gained prominence as it offers a possibility to improve the physical characteristics of the API. However, cocrystals also suffer from the same old problem of polymorphism as do API [3].

Pharmaceutical industry hinges heavily on solid active forms like powders and tablets owing to ease of taking a pill orally and handling convenience. Liquid forms, on the other hand, not only offers different modes of delivery options but can also enhance the bioavailability translating to enhanced absorption [4]. The insolubility of the solid forms results in 40–70% failure of the total compounds entering the

S. Bhawal (✉)
School of Science, Navrachana University, Vasna-Bhayli, Vadodara 391410, India
e-mail: sumitb@nuv.ac.in

development stage because of the inability to convert them into more soluble forms for release into the bloodstream [4]. A pressing example is the temporary removal of antiretroviral medication Norvir in 1998 due to the appearance of an unknown polymorph Form II with substantially less water solubility, resulting in precipitation and late-stage failure even after product launch [5].

2 Discussion

2.1 Why Ionic Liquids (IL's) Are Emerging as a Rich Toolbox for Developing New Generation Liquid Drugs

While ionic liquids have not received enough attention largely due some toxicity and regulatory concerns [4]. It is important to realize though that they offer exciting prospect due to their tuneability and multitude of interaction between the drug and counter ions in contrast ionic interaction which is the mainstay for more than half of the solid drugs. In addition, their low symmetry and diffused charge can lead to poor packing of the constituent ions leading to the appearance of liquid state and may be an effective means to bypass the delivery problems encountered by solid dosage forms (Fig. 1).

Liquid salts at body temperature have the potential to enhance their solubility and absorptions. Also, ionic liquids can be customized to deliver more than one ingredient simultaneously. Judicious combination of drugs with "functional counterions" can expand the scope of treatment and/or reduce the side effects of the primary drug providing better therapeutic options. Effective use of "functional counterion" to produce liquid salts, rendering the "combined entity" to address more than one aspect of a disease is a promising area where quick strides can be made. A classic example involves combining pain-relieving properties of procaine with anti-inflammatory property of salicylic acid to generate procainium salicylate in a liquid state, opening up new, viable treatment regimen, and delivery options [6]. This is important as the current drug discovery processes are circuitous and clogged and

Fig. 1 The tuneability and liquid state of ionic liquid emerge from asymmetry, charge delocalization, and multiple interaction types

CATION   ANION
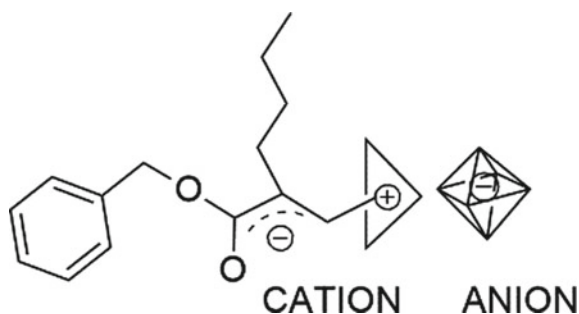
in part responsible for their high price and accessibility. In addition, pharmaceutical research should look beyond ionic interactions and engineer functional designer ions with wider spectrum of non-covalent interactions for better control of physical and biological properties. Regulation should also be revamped to focus more on clinical properties rather than physical forms [4, 7].

The scientific understanding behind the emerging paradigm is still evolving. For example, is there a way to predict a priori how an ion can be made liquid? purification of non-crystallizing active ingredients is a challenge. Is there a way to design nontoxic ions that may retain its multiple interactions with the active agent simultaneously interacting with the solvent system like water? central to this is aiming for ions capable multiple non-covalent interaction, and ionic liquids fills up the role to a great extent provided toxicity issues are addressed. Recently, Banerjee et al. [8] reported a highly effective and scalable oral insulin formulation stabilized by ionic liquid choline geranate (CAGE) that may be delivered in enterically coated capsules. The biocompatible formulation demonstrated profound efficacy at very low insulin doses in adult nondiabetic male Wister rats and had good stability. Promising results may be awaited following pre-clinical and clinical studies. Additionally, studies involving Insulin—CAGE—intestinal fluid interactions may uncover greater insights into the process of insulin absorption. Recently, novel electrospinning methods to disrupt bacterial film formation have been reported [9]. The choline geranate-based ionic liquids displayed enhanced skin penetration and were used to treat difficult skin lesions. They have demonstrated that protein scaffolds doped with different amount of choline geranate had multiple clinical application in the area of wound healing. Ranitidine docusate ([Ran][Doc]), the first liquid room temperature API-ILs introduced by Rogers et al. in 2007 [10], displayed improved API absorption, thus opening the door for new liquid form APIs with specific physicochemical and biological properties and/or more than one pharmacological action. In an interesting report, Hough et al. [11] demonstrated modified solubility, higher thermal stability, and significant enhancement (relative to lidocaine hydrochloride) of topical analgesia for Lidocaine docusate, a hydrophobic IL obtained by combination of topical pain reliever (lidocaine, Lid) and an emollient (docusate, doc) in two different models of mouse antinociception. The data is also suggestive of different mechanisms of action for [Lid][Cl] and [Lid][doc]. A case where counter ion modification confers novel bioactivity and delivery options due to the slow release of the API. In a relatively recent review [12], Rahman et al. discussed the need for discovering low-toxicity ILs and how the intrinsic properties of the ILs can be modified to get access to the structural diversity tailored to meet the current biopharmaceutical challenges. The review also sheds light on how biocompatible Ionic Liquids (ILs) are emerging as a major player in the oral and transdermal application of small molecules as well as macromolecules like peptides and proteins. New generation API-ILs can also discovered by a prodrug strategy wherein one of the ions undergoes enzymatic transformation to its active form in vivo. Generation of oligomeric ions by simple manipulation of the stoichiometry or introducing free acid/base of the conjugate base/acid with in the interaction domain is also being pursued [10].

Also, API designed to produce low melting liquid salt can be used to modify the solution properties of the API by enhancing the pairing interactions leading to superior transport through the cell membrane or skin barrier. Zakrewsky et al. [13] demonstrated a CAGE based deep eutectic solvent to treat biofilm penetration of recalcitrant *Pseudomonas aeruginosa* and *Salmonella enterica* and broad-spectrum antimicrobial activity against a number of drug-resistant bacteria, fungi, and viruses [13]. These include clinical isolates of *Staphylococcus* and C*andida albicans* as well as laboratory strains of Herpes Simplex Virus. Owing to the low toxicity of choline geranate ionic liquids, the molecular aggregation behavior was tracked using Small-angle X-ray scattering (SAXS) and [1]NMR studies [14]. The SAXS pattern revealed structural transition from nanoscale aggregation (until 17 vol% water) to lamellar phase (in the 25–50 vol% water) to micellar phase with more than 67% water. ^{1}H NMR studies indicated that water was located in close proximity to choline and the CO_2H group in geranic acid to facilitate proton exchange up to 17 vol% of water. While the ^{13}C NMR suggested that addition of water affected the hydrogen bonding between choline and geranic acid. Additionally, ^{13}C cross polarization magic angle spinning NMR suggested that the rigid component of the lamellar phase was primarily geranic acid. The aggregation behavior of CAGE is an important study as it has received considerable attention as a biocompatible, relatively nontoxic IL for drug delivery systems [15]. Several studies reported CAGE as an excellent penetration enhancer in the transdermal administration of low molecular wt% flavonoid, peptides, and proteins like ovalbumin and bovine serum albumin [16].

2.2   Synthetic Routes

Most of the API-ILs syntheses reported in literature employ metathesis reaction for combining the cation and anion with the precipitation of stable salts like NaCl. The cations and anions are generally pre-dissolved separately in solvents and mixed together and stirred at room temperature or heated, if necessary. The simplicity of the method is encouraging, however, the purity of the final API-ILs can be challenging requiring the removal of inorganic salts like NaCl, especially if the API-ILs have considerable water solubility. The salt can be eliminated through adequate selection of solvent or by employing additional purification methods [17]. Dean et al. proposed an alternative anticrystal engineering strategy to synthesize API-ILs by deliberately choosing asymmetric ions that do not pack well [18]. Thus, in the temperature range of interest, emphasis must be on the preparation of amorphous phase as the thermodynamically most stable form, wherein the salt is in a liquid or a glassy state but not as supercooled liquid. Their study revealed that complementary functional groups leading to strong supramolecular attractive intermolecular or interionic hydrogen bonding between donor and acceptor must be avoided in the preparation of liquid API—ILs. However, more studies and larger sample pool size are required for better understanding.

3 Conclusion

3.1 Future Prospect and Challenges

Overall, the dual nature (discrete ions) of ILs can be conveniently modulated to generate liquid APIs with additional biological function or modify the properties of the existing drugs in a beneficial way. Some of the properties that have been looked at include controlling solubility, bioavailability, stability, elimination of polymorphism, and opening novel delivery options like transdermal penetration as API-IL complex and conferring slow release of the active form and development of pharmaceutical cocktails for peptide-based therapeutic agents [19, 20]. While there are possibilities in waiting for development for IL mediated vaccine stabilization/storage and enabling API with targeting ligands as counterions. Nevertheless, there are several challenges like limited in vivo studies, lack of pharmacokinetic, and pharmacodynamic data [21]. Study of metabolic pathway in their uptake and alteration of toxicity relative to the precursor API and identification of a larger pool of biocompatible ions from renewable sources and their toxicological profiles is also important. The slow progress might be partly attributed to the lack of guidelines from the pharmaceutical entities for API-ILs which renders testing of the formulations difficult. Nevertheless, ILs offer huge scope for finding new roles for old drugs and improving their delivery and efficacy.

References

1. Stahly GP (207) Diversity in single- and multiple-component crystals. The search for and prevalence of polymorphs and cocrystals. Cryst Growth Des 7:1007–1026
2. Cruz-Cabeza AJ, Feeder N, Davey RJ (2020) Open questions in organic crystal polymorphism. Commun Chem Nat Res 3:1–4
3. Guo M, Sun X, Chen J, Cai T (2021) Pharmaceutical cocrystals: a review of preparations, physicochemical properties and applications. Acta Pharmaceutica Sinica B. Chinese Acad Med Sci 11:2537–2564
4. Shamshina J, Kelley S, Gurau G (2015) Develop ionic liquid drugs. Nature 528:188–189
5. Chemburkar SR, Bauer J, Deming K, Spiwek H, Patel K, Morris J et al (2000) Dealing with the impact of ritonavir polymorphs on the late stages of bulk drug process development. Org Process Res Dev 4(5):413–417
6. Endres F (2010) Physical chemistry of ionic liquids. Phys Chem Chem Phys 12(8):1648–1648
7. Callréus T, Schneider CK (2013) The emergence of regulatory science in pharmaceutical medicine. Pharmaceut Med. 27(6):345–351
8. Banerjee A, Ibsen K, Brown T, Chen R, Agatemor C, Mitragotri S (2018) Ionic liquids for oral insulin delivery. Proc Natl Acad Sci USA 115(28):7296–7301
9. Akhmetova A, Heinz A (2020) pharmaceutics electrospinning proteins for wound healing purposes: opportunities and challenges. 2020; Available from: https://doi.org/10.3390/pharma
10. Marrucho IM, Branco LC, Rebelo LPN (2014) Ionic liquids in pharmaceutical applications. Ann Rev Chem Biomol Eng Ann Rev Inc 5:527–546
11. Hough WL, Smiglak M, Rodríguez H, Swatloski RP, Spear SK, Daly DT et al (2007) The third evolution of ionic liquids: active pharmaceutical ingredients. New J Chem 31(8):1429–1436

12. Md Moshikur R, Chowdhury MR, Moniruzzaman M, Goto M (2020) Biocompatible ionic liquids and their applications in pharmaceutics. Green Chem Roy Soc Chem 22:8116–8139
13. Zakrewsky M, Lovejoy KS, Kern TL, Miller TE, Le V, Nagy A et al (2014) Ionic liquids as a class of materials for transdermal delivery and pathogen neutralization. Proc Natl Acad Sci USA 111(37):13313–13318
14. Takeda J, Iwao Y, Karashima M, Yamamoto K, Ikeda Y (2021) Structural evaluation of the choline and geranic acid/water complex by SAXS and NMR analyses. ACS Biomater Sci Eng 7(2):595–604
15. Zakrewsky M, Banerjee A, Apte S, Kern TL, Jones MR, Sesto RED et al (2016) Choline and geranate deep eutectic solvent as a broad-spectrum antiseptic agent for preventive and therapeutic applications. Adv Healthc Mater 5(11):1282–1289
16. Banerjee A, Ibsen K, Iwao Y, Zakrewsky M, Mitragotri S (2017) Transdermal protein delivery using choline and geranate (CAGE) deep eutectic solvent. Adv Healthc Mater 6(15)
17. Gutowski KE, Broker GA, Willauer HD, Huddleston JG, Swatloski RP, Holbrey JD et al (2003) Controlling the aqueous miscibility of ionic liquids: aqueous biphasic systems of water-miscible ionic liquids and water-structuring salts for recycle, metathesis, and separations. J Am Chem Soc 125(22):6632–6633
18. Dean PM, Turanjanin J, Yoshizawa-Fujita M, MacFarlane DR, Scott JL (2009) Exploring an anti-crystal engineering approach to the preparation of pharmaceutically active ionic liquids. Cryst Growth Des 9(2):1137–1145
19. Gomes A, Bessa LJ, Correia P, Fernandes I, Ferraz R, Gameiro P et al (2020) "Clicking" an Ionic liquid to a potent antimicrobial peptide: on the route towards improved stability. Int J Mol Sci 21(17):1–11
20. Saraswat J, Wani FA, Dar KI, Rizvi MMA, Patel R (2020) Noncovalent conjugates of ionic liquid with antibacterial peptide melittin: an efficient combination against bacterial cells. ACS Omega 5(12):6376–6388
21. Pedro SN, Freire CSR, Silvestre AJD, Freire MG (2020) The role of ionic liquids in the pharmaceutical field: an overview of relevant applications. Int J Molecular Sci MDPI AG; 21:1–50

A Review: A Novel Approach of Sulfur-Bearing Macro-Cyclic Compound and Its Sensing Application

Nihal Patel [ORCID] **, Keyur Bhatt** [ORCID] **, and Krunal Modi** [ORCID]

1 Introduction

This type of chemistry has surpassed simple molecules and established its control over non-covalent interactions [1]. It has developed a new measurement with the goal of detecting predominance over the intermolecular bond. In chemistry, the complexity (intricacy) has grown beyond atoms to super-molecules, and poly-molecular organization has been sorted out [2]. Supramolecular chemistry is a highly multidisciplinary subject of research that deals with the physical, chemical, and biological aspects of complex mixtures that are kept together and formed through intermolecular (non-covalent) communication techniques. This relatively new study area has been defined, conceived, and structured into a logical framework. Supramolecular chemistry, which involves both physical and biological phenomena, is rapidly increasing at the frontier of chemical study. Supramolecular science has advanced to the point that it has attracted the attention of many researchers. Supramolecular research has advanced to the point that it has attracted the attention of several scholars from other domains, such as chemical and biological science [3]. Supramolecules are the chemical building blocks of the future. They are additive but also the outcome of co-operative interactions, with hydrogen bonding, hydrophobic interaction, and coordination. Supramolecular structures are frequently better than some properties of each individual block. Supramolecular chemistry is as yet a young field, making it hard to characterize precisely what it envelops. It has grown quickly because of commitments from an assortment of related fields. The size of the desired sub-atomic framework is intimately linked to this order. Sub-atomic recognition (Molecular recognition)

N. Patel · K. Bhatt (✉) · K. Modi (✉)
Department of Chemistry, Faculty of Science, Mehsana Urban Institute of Sciences, Ganpat University, Kherva, Mehsana, Gujarat 384012, India
e-mail: kdb01@ganpatuniversity.ac.in

K. Modi
e-mail: kmodi5033@gmail.com

science [4, 5] deals with the smallest supramolecular frameworks (structures) and also involves partnerships between only a few particles. The chemistry of atomic groupings, on the other hand, might include sub-atomic frameworks made up of countless molecules [6].
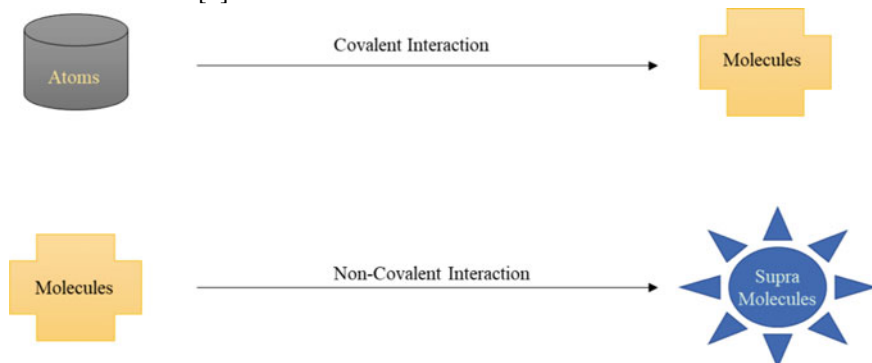
The binding or complexation process that occurs between a host and a guest is depicted by a supramolecular assembly, which has incredible structural flexibility. Crown ethers, cryptands, spherands, porphyrins, and calixarenes are examples of molecular receptors used in supramolecular chemistry. Supramolecules are divided into three groups based on their time scale generation (Fig. 1): (a) first generation (cyclodextrins), (b) second generation (crown ethers), and (c) third generation (supramolecules) (calix[n]arenes). Calixarenes have sparked attention in both practical and fundamental chemistry because of various types of supramolecular sensors they have generated [7].
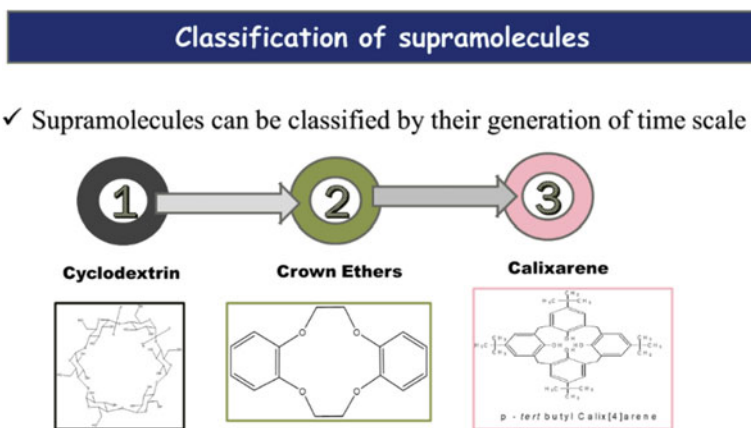
Fig. 1 Classification of Thiacalixarenes based on time scale

Fig. 2 Calixarenes chemistry

p - *tert* butyl Calix[4]arene
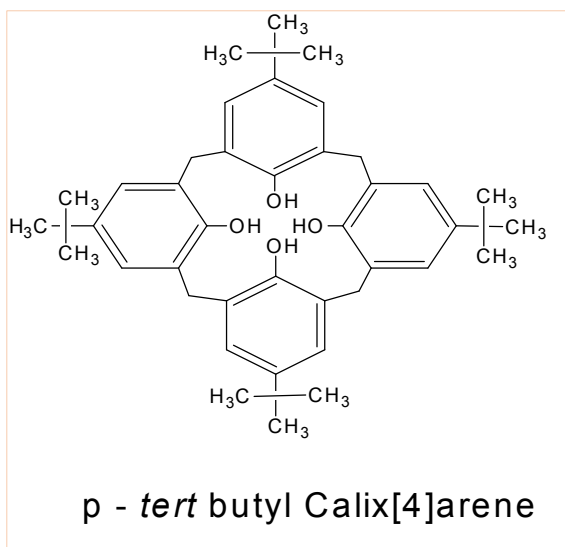
2 Calixarenes Chemistry

Calixarenes are the third generation of these supramolecular host molecules. They were grown later than crown ethers, and cyclodextrins yet have still been extensively investigated. Different hole (cavity) sizes have been planned, every one of which has conformational isomers. Calixarenes (Fig. 2) are cyclic oligomers in structure composed of phenolic (Ph–OH) units related to the methylene group. They are synthesized by the base-catalyzed condensation reaction of p-alkylphenols, and it can be modified by some functionalization of its upper and lower rime [8–10]. Calixarenes are known as macro cycles since they have limitless possibilities that are not considered by other normal hosts [11]. Various calixarene-based receptors have been integrated, and their capacities have been employed in various ways, such as in chromatography, sensory, and partition chemical applications, using these types of produced components [7]. Further, calixarenes are divided into two classes: Heteracolixarenes and Heterocalixarenes. In (i) Heterocalixarenes, hetero atoms such as N, S, and O, replace the scaffold methylene group; and (ii) Heterocalixarenes, heterocyclic moiety such as Furan and Pyrroles, replace the phenolic group.

3 Thiacalixarenes (TCA) Chemistry

The carbon bonds between aromatic units are replaced by heteroatoms in Heterocalixarenes, which are less discussed in substance writing [12]. Because they contain

Fig. 3 Thiacalixarenes
(TCA) chemistry
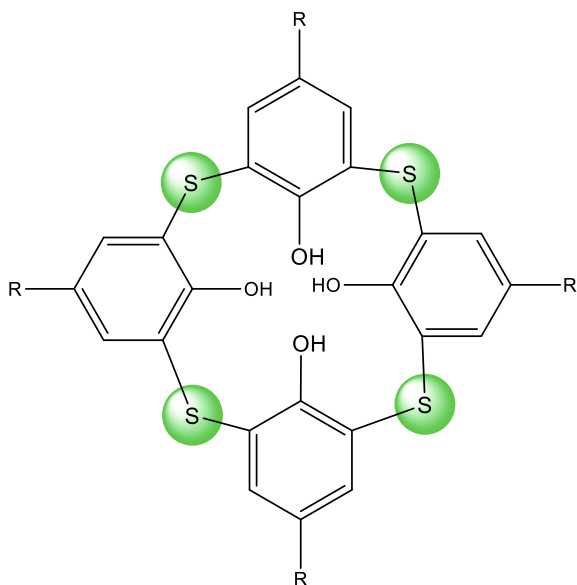
sulfur atoms instead of the normal methylene bunches, thiacalixarenes are orga-
nized as heterocalixarene elements [13]. Thiacalix[4]arene (TCA) was discovered in
1997 as a member of the heterocalixarene family and has since received a lot of atten-
tion from the supramolecular network [14]. Thiacalixarene have been investigated as
atomic stages for fascinating likely applications, for example, the consideration of an
assortment of guest molecules, the acknowledgment (recognition) of metal particles,
chiral and novel anion receptors, and novel dendritic-shelled sub-atomic receptors
[15–19]. Thiacalixarene is a radical modification of the traditional calix benzene
moiety. It has a larger carbon-sulfide bridge and more drawn-out bond length than
that of carbon–carbon bond. The ring linkages affiliating sulfur (S) with the phenolic
oxygens may act agreeably after restricting metal particles (Fig. 3).

3.1 Synthesis of TCA

Simplicity in the synthetic procedures of thiacalixarene has facilitated accessibility
to gram-scale quantities of these compounds. The popularity of thiacalix[4]arenes
comes from their altered cavity diameters and additional binding sites provided by
the proximity of sulfur molecules. For the derivatization of thiacalixarenes, appro-
priate procedures are being developed, in which the conformational effects become
essential.

- **General method**
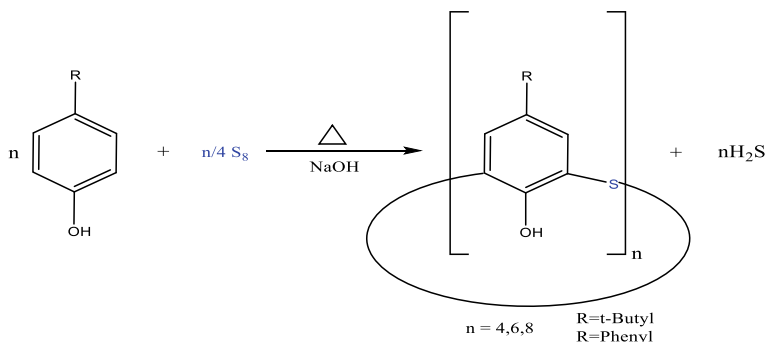
Scheme 1 General synthesis of Thiacalixarenes

Thiacalixarenes 1 ($n = 4, 6, 8$) are cyclic oligomers gotten under basic conditions from p-tert-butylphenol and natural sulfur (S_8), i.e., for the substitution of the methylene scaffold in traditional calixarene by sulfur (S) atoms (Scheme 1).

- **Single-Step Method**:- Kumagai et al. [14] gave this method. The yield is about 54%.
- **Two-Step Method:**- Sotaro et al. [20] proposed a convenient two-step procedure. The yield is about 75%.
- **Three-Step Method:**- Sone et al. [21] announced the principal combination of this class of heterocycles in 1993 by means of a stepwise procedure. The yield is very poor.

4 Conformers of TCA

The thiacalix[4]arene platform as customary calix[4]arene has two edges. The phenolic groups (Ph–OH) containing restricted edge is also known as the "lower rim," while para-substituents of platform are more extensive segment is known as the "upper rim." The four potential adaptations are displayed (Fig. 4) by thiacalix[4]arenes "cone," "partial cone," "1,2-alternate," and "1,3-alternate" as appeared into Fig. 4 and are conceivable from the direction of the phenolic units concerning one another. Graf et al. [18] reported the first X-beam structure of tetra-thiacalix[4]arene, confirming that TCA adopted a cone shape with true C_4 symmetry, which was achieved by a cyclic pattern of hydrogen bonding involving four phenolic units. This X-ray research reveals that the bond length between the bridging group and aromatic residues is 15% longer than the comparable calix[4]arene, showing that thiacalix[4]arene has a wider cavity than standard calix[4]arene [13].
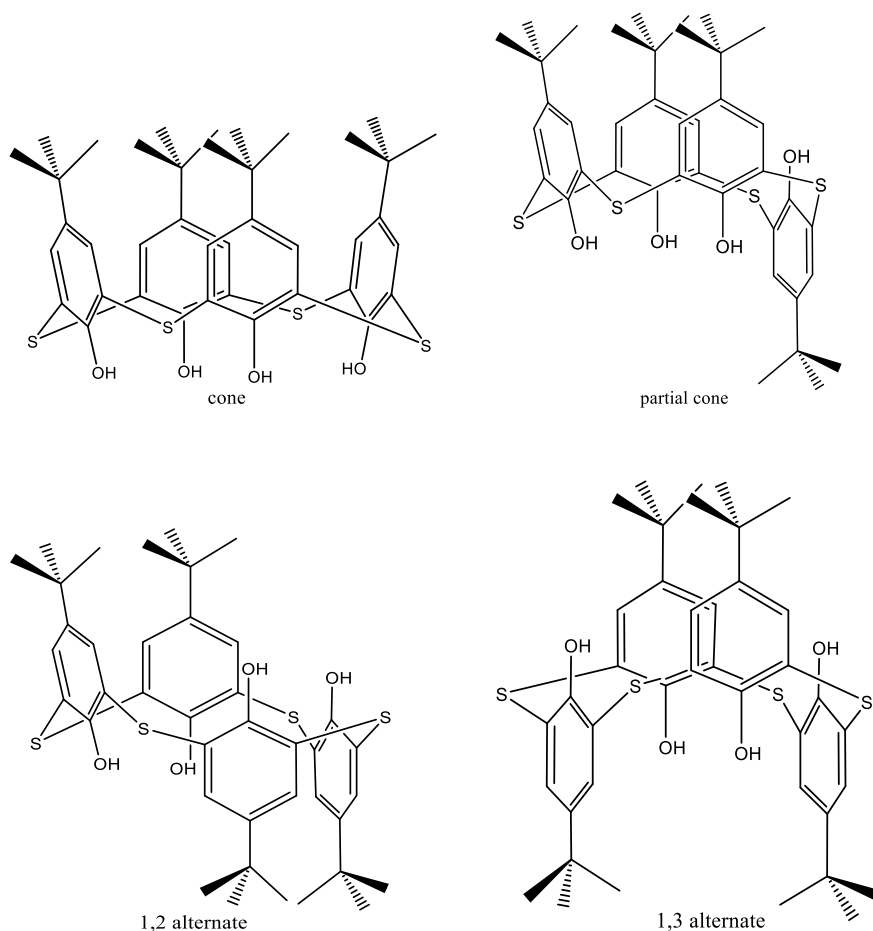
Fig. 4 Conformers of TCA

5 Functionalization of TCA

The chemical modification of TCA (Fig. 5) has led to a great variety of derivatives with modified solubilities, conformational mobilities, and complexation abilities for the synthesis of more elaborate supramolecular systems.

- Functionalization occurs at these three positions of TCA is given below:

    1. Oxidation of sulfide bridges [22–28]
    2. Upper-rim functionalization [16, 18, 29–34]
    3. Lower-rim functionalization [35–39].

Fig. 5 Functionalization of TCA
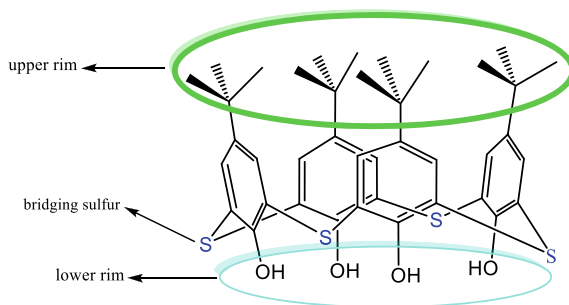
6 Applications of TCA

TCA has several benefits for lower rim, upper rim, and sulfide bridge functionalization (Fig. 6). Because of the sulfide group present at the bridging position, thiacalix[4]arene has a better bidding capacity with metal ions than typical calixarene. With the addition of oxygen, thiacalix[4]arene has been functionalized for good binding affinity with soft and hard metal ions. TCA has been modified to detect a variety of anions, cations, and neutral analytes. Self-assembled coordination networks, molecular switches, magnetic materials, logic gates, and luminous materials are some of the additional uses of thiacalix[4]arenes that have been documented.
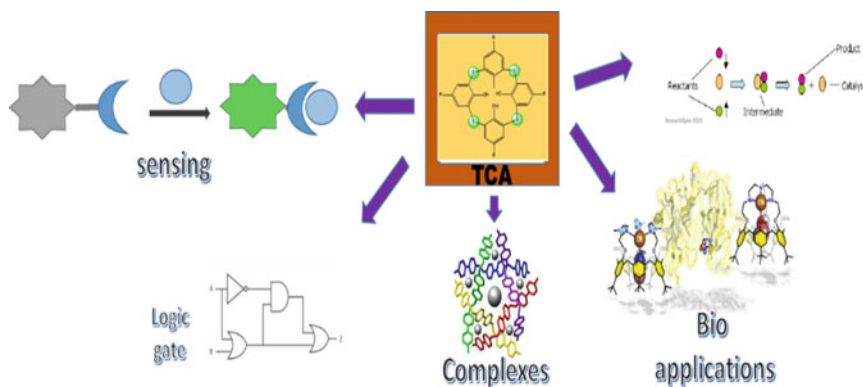
Fig. 6 Graphical illustration of application

6.1   Cationic Recognition Through UV/Fluorescence

Redshaw et al. [40, 41] reported a fluorescent sensor that is functionalized from the lower edge of thiacalix[4]arene (TCA) and has a triazole ring **(a)** as cationic binding sites with a 1,3-alternate conformation that specifically binds Ag^+ particles, resulting in a significant increase in pyrene monomer emissions and ratiometric fluorescence conduct. The presence of a nitrogen atom on the triazole moiety, as well as coordination between the ionophoric cavity and the sulfur atom of TCA, is thought to be responsible for the high affinity with Ag^+ ions. In the cone conformation of thiacalix [4] arene, Kumar et al. [42] discovered a tetra pyrene-appended **(b)** chemosensor. It has compliant behavior with metal ions in an aqueous media. Because of reverse photoinduced charge transfer [43] from pyrene units to carbonyl oxygen, the chemosensor showed great selectivity to Fe^{3+} particles by fluorescence extinguishing of excimer emission of pyrene units. The selectivity is unaffected by any variation cations, anions, amino acids, blood serum, or bovine serum albumin (BSA). That is why it is utilized as a selective sensor for Fe^{+3} ions in live cells (PC3 cells). Luo et al. [44] used UV–Vis and fluorescence spectroscopy as well as ^1H NMR titration to show that p-tert-butyl thiacalix[4]arene (with diagonal 8-hydroxyquinoline moieties) **(c)** is a very stable complex formation of ligand with Co^{2+}, Zn^{2+}, and Ni^{2+} ions. Co^{2+}, Zn^{2+}, and Ni^{2+} have stoichiometries of 1:2, 1:2, and 1:1, respectively, resulting in exceptionally stable complexes with these three metal ions, as seen by the results. We acknowledge the possibility of using the p-tert-butyl thiacalix[4]arene (diagonal 8-hydroxyquinoline moieties) derivative as a change metals' fluorescence test and natural light-emitting diodes. Asif Ali Bhatti et al. [45] reported a water-soluble fluorescent sensor that is functionalized from the lower rim of thiacalix[4]arene with rhodamine (TR) **(d).** It shows the selectivity toward the Hg^{+2} with changing in fluorescence Properties. TR-Hg^{2+} gives specific color change with increase in fluorescence intensity at 573 nm when excited at 335 nm. Photophysical properties of TR show that the presence of Hg^{2+} induce CHEF OFF → ON process, which is similar to photoelectron microscopy or X-ray diffraction. Zhu et al. [46] reported a water-soluble thiacalix[4]arene tetrasulfonate **(e)** was found to have preferential chromogenic recognition for copper (II) ion over other transition metal ions. The addition of copper (II) ions to thiacalix[4]arene tetrasulfonate (TCAS) induced a distinct chromogenic response, in which the aqueous solution changed from blue to salmon pink. Verma et al. [47] developed and synthesized a new thiacalix[4]arene N-(4-(tert-butyl) phenyl)-2-chloroacetamide **(f)** for the selective identification of Hg (II) ions. This probe has the potential to be an effective mercury ion sensor [48]. Its extraordinary selectivity toward Hg (II) ion over a series of common metal ions is indicated by a redshift in absorption maxima followed by a considerable increase in emission intensity. This probe's binding constant was measured to be $1.834 \times 10^6 \, M^{-1}$. The cationic recognition (sensing) absorbance and emission has been depicted in Table 1.

Table 1 Absorbance and emission data of functionalized TCA with analytes

Compound + Analyte	Absorbance	Emission		References
	λ max (nm)	Excitation (nm)	λ max (nm)	
(a) +Ag$^+$	–	360	378	[40, 41]
(b) +Fe^{+3}	342	350	478	[42]
(c) +Co^{+2}, Zn^{+2}, Ni^{+2}	340	394	440	[44]
(d) +Hg^{+2}	–	335	573	[45]
(e) Cu^{+2}	312	–	–	[46]
(f) +Hg^{+2}	334	325	399	[47]
(g) +F$^-$	470	420	561	[49]
(h) +F$^-$	360	320	385	[50]
(i) +F$^-$	440	344	413	[51]
(i) +CN$^-$	440	344	500	[51]

6.2   Anionic Recognition Through UV/Fluorescence

The fluorescent chemosensor was created by Bhatt et al. [49] using two quinoline moieties based on thiacalix[4]arene **(g)** and armed for fluoride ions. In tetrabutylammonium salt (TBA) using acetonitrile as the solvent, they found emission spectra of several anions such as Cl$^-$, F$^-$, Br$^-$, H$_2$PO$_4$$^-$, I$^-$, and CH$_3COO^-$. When fluoride ions (F$^-$) are added to the compound, the emission spectra shift to 470 nm (Fig. 7), indicating a red shift, whereas other anions have no effect on the adsorption spectra (Fig. 8). Due to hydrogen bonding, this shift in spectra provides information on the interaction of electronegative fluoride (F$^-$) ions with a particular moiety.

Fig. 7 Absorption Spectra of quinoline moieties of TCA on addition of various anions in ACN. Reproduced from the Ref. [49]. With permission from Elsevier, License no: 5225830200075

Fig. 8 Emission Spectra of quinoline moieties of TCA on addition of various anions in ACN. Reproduced from the Ref. [49]. With permission from Elsevier, License no: 5225830200075

With two naphthyl moiety of thiacalix[4]arene **(h)**, Kumar et al. [50] produced a fluorescent chemosensor for fluoride ions. UV–Vis, fluorescence spectroscopy was used to evaluate compound's anion binding characteristics. The UV–Vis titrations were done in DMSO (Fig. 9)**,** while the fluorescence titrations (Fig. 10) were done in tetrahydrofuran (THF) using aliquots of different anions' solutions. With a given receptor, a given moiety does not produce emission spectra; however, adding the

Fig. 9 Absorption Spectra of naphthyl moiety of TCA on addition of fluoride in DMSO. Reproduced from the Ref. [50]. With permission from Elsevier, License no: 5225800767732

Fig. 10 Fluorescent emission Spectra of naphthyl moiety of TCA on addition of fluoride in THF. Reproduced from the Ref. [50]. With permission from Elsevier, License no: 5225800767732

F^- (fluoride) ion to the moiety produces an emission spectra band. The increased selectivity of fluoride ions with a specific receptor is revealed by the spectrum data. The fluoride ions (F^-) are responsible for the rise in emission spectra, which is explained by the intramolecular pi–pi interaction excimer production between two naphthyl moieties. The intermolecular binding interaction of fluoride ions with the -NH group of thiourea moieties maintains this intramolecular connection. In diverse approaches, Kumar et al. [51] produced fluorogenic chemo-sensors for fluoride and cyanide ions of thiacalix[4]arene. The proximity of fluoride particles causes the fluorescence discharge to go into an "on state," whereas the proximity of cyanide particles causes "ratiometric conduct." The intramolecular charge transfer mechanism (ICT) [52] and high selectivity to fluoride (F^-) with increased Monomer emissions and cyanide (CN^-) ions with ratiometric character are provided by this pyrene-based fluoride sensor **(i)**. The anionic recognition (sensing) absorbance and emission has been depicted in Table 1.

7 Outline of Work

We have shown that several important intermediates for the upper-rim functionalization of thiacalixarenes are now available. They have shown nice cubic nonlinear optical properties, which make them interesting candidates for optical applications. Significant advances in the knowledge of the chemistry of those macro cycles have been reported.

References

 1. Steed JW, Atwood JL (2013) Supramolecular chemistry. Wiley
 2. Lehn J-M (1988) Supramolecular chemistry—scope and perspectives molecules, super-molecules, and molecular devices (Nobel Lecture). Angew Chem, Int Ed Engl 27(1):89–112
 3. Kumar R, Ok Lee Y, Bhalla V, Kumar M, Seung Kim J (2014) Recent developments of thiacalixarene based molecular motifs. Chem Soc Rev 43(13):4824–4870
 4. Bhatt KD, Gupte HS, Makwana BA, Vyas DJ, Maity D, Jain VK (2012) Calix receptor edifice; scrupulous turn off fluorescent sensor for Fe (III), Co (II) and Cu (II). J Fluoresc 22(6):1493–1500
 5. Darjee SM, Bhatt KD, Panchal US, Jain VK (2017) Scrupulous recognition of biologically important acids by fluorescent "turn off-on" mechanism of thaicalix reduced silver nanoparticles. Chinese Chem Lett 28(2):312–318
 6. Ariga K, Kunitake T (2006) Supramolecular chemistry-fundamentals and applications: advanced textbook. Springer Science & Business Media
 7. Mandolini L, Ungaro R (2000) Calixarenes in action World Scientific
 8. Shokova EA, Kovalev VV (2003) Thiacalixarenes-A new class of synthetic receptors. Russian J Organic Chem 39(1)
 9. Makha M, Raston CL (2001) Direct synthesis of calixarenes with extended arms: p-phenylcalix [4, 5, 6, 8] arenes and their water-soluble sulfonated derivatives. Tetrahedron Lett 42(35):6215–6217
10. Vicens J, Böhmer V (2012) Calixarenes: a versatile class of macrocyclic compounds. Springer Science & Business Media
11. Iki N, Kabuto C, Fukushima T, Kumagai H, Takeya H, Miyanari S, Miyashi T, Miyano S (2000) Synthesis of p-tert-butylthiacalix [4] arene and its inclusion property. Tetrahedron 56(11):1437–1443
12. König B, Hechavarria Fonseca M (2000) Heteroatom-Bridged Calixarenes. Eur J Inorganic Chem 11:2303–2310
13. Iki N, Miyano S (2001) Can thiacalixarene surpass calixarene? J Incl Phenom Macrocycl Chem 41(1):99–105
14. Kumagai H, Hasegawa M, Miyanari S, Sugawa Y, Sato Y, Hori T, Ueda S, Kamiyama H, Miyano S (1997) Facile synthesis of p-tert-butylthiacalix [4] arene by the reaction of p-tert-butylphenol with elemental sulfur in the presence of a base. Tetrahedron Lett 38(22):3971–3972
15. Suwattanamala A, Magalhães AL, Gomes JANF (2007) Theoretical study on the structure and conformational features of distally dibromo-dipropoxythiacalix [4] arene derivatives and their Zn 2+ complexes. Theoret Chem Acc 117(3):431–440
16. Parola S, Desroches C (2004) Recent advances in the functionalizations of the upper rims of thiacalix [4] arenes. a review. Collect Czech Chem Commun 69(5):966–983
17. Agrawal YK, Pancholi JP (2007) Analytical applications of thiacalixarenes: a review
18. Akdas H, Bringel L, Graf E, Hosseini MW, Mislin G, Pansanel J, De Cian A, Fischer J (1998) Thiacalixarenes: synthesis and structural analysis of thiacalix [4] arene and of p-tert-butylthiacalix [4] arene. Tetrahedron Lett 39(16):2311–2314
19. Morohashi N, Narumi F, Iki N, Hattori T, Miyano S (2006) Thiacalixarenes. Chem Rev 106(12):5291–5316
20. Kon N, Iki N, Miyano S (2002) Synthesis of p-tert-butylthiacalix [n] arenes (n= 4, 6, and 8) from a sulfur-bridged acyclic dimer of p-tert-butylphenol. Tetrahedron Lett 43(12):2231–2234
21. Sone T, Ohba Y, Moriya K, Kumada H (1993) Presented at the Abstr. No. B-36 (unpublished).
22. Iki N, Horiuchi T, Oka H, Koyama K, Morohashi N, Kabuto C, Miyano S (2001) Energy transfer luminescence of Tb 3+ ion complexed with calix [4] arenetetrasulfonate and the thia and sulfonyl analogue. The effect of bridging groups. J Chem Soc Perkin Trans 2(11):2219–2225
23. Iki N, Kumagai H, Morohashi N, Ejima K, Hasegawa M, Miyanari S, Miyano S (1998) Selective oxidation of thiacalix [4] arenes to the sulfinyl-and sulfonylcalix [4] arenes and their coordination ability to metal ions. Tetrahedron Lett 39(41):7559–7562

24. Lhoták P (2001) Regioselective and stereoselective oxidation of thiacalix [4] arene tetraacetate: synthesis of all possible sulfinylcalix [4] arenes. Tetrahedron 57(22):4775–4779
25. Lhoták P (2003) Jiří Morávek, Tomáš Šmejkal, Ivan Stibor, and Jan Sýkora, "Stereoselective oxidation of thiacalix [4] arenes with the NaNO3/CF3COOH system,." Tetrahedron Lett 44(39):7333–7336
26. Mislin G, Graf E, Wais Hosseini M, De Cian A, Fischer J (1998) Sulfone-calixarenes: a new class of molecular building block. Chem Commun 13:1345–1346
27. Morohashi N, Iki N, Sugawara A, Miyano S (2001) Selective oxidation of thiacalix [4] arenes to the sulfinyl and sulfonyl counterparts and their complexation abilities toward metal ions as studied by solvent extraction. Tetrahedron 57(26):5557–5563
28. Rao P, Hosseini MW, De Cian A, Fischer J (1999) Synthesis and structural analysis of mercaptothiacalix [4] arene. Chem Commun 21:2169–2170
29. Higuchi Y, Narita M, Niimi T, Ogawa N, Hamada F, Kumagai H, Iki N, Miyano S, Kabuto C (2000) Fluorescent chemo-sensor for metal cations based on thiacalix [4] arenes modified with dansyl moieties at the lower rim. Tetrahedron 56(27):4659–4666
30. Kabuto C, Higuchi Y, Niimi T, Hamada F, Iki N, Morohashi N, Miyano S (2002) Crystal Structures of Mono-, Di-, and Tri (p-tert-butyl)-thiacalix [4] arenes: Dimeric Self-inclusion Behavior. J Incl Phenom Macrocycl Chem 42(1):89–98
31. Lhoták P, Kaplánek L, Stibor I, Lang J, Dvořáková H, Hrabal R, Sýkora J (2000) NMR and X-ray analysis of 25, 27-dimethoxythiacalix [4] arene: unique infinite channels in the solid state. Tetrahedron Lett 41(48):9339–9344
32. Desroches C, Parola S, Vocanson F, Perrin M, Lamartine R, Létoffé J-M, Bouix J (2002) Nitration of thiacalix [4] arene using nitrosium nitrate complexes: synthesis and characterization of tetranitro-, tetraamino-, and tetra (4-pyridylimino) tetrahydroxythiacalix [4] arene. New J Chem 26(5):651–655
33. Kasyan O, Swierczynski D, Drapailo A, Suwinska K, Lipkowski J, Kalchenko V (2003) Upper rim substituted thiacalix [4] arenes. Tetrahedron Lett 44(38):7167–7170
34. Lhoták P, Himl M, Stibor I, Sykora J, Cisarová I (2001) Upper rim substitution of thiacalix [4] arene. Tetrahedron Lett 42(40):7107–7110
35. Akabori S, Sannohe H, Habata Y, Mukoyama Y, Ishii T (1996) Unusual thermodynamic stabilities of the four conformers of tetraacetoxy-p-tert-butylcalix [4] arene. Chem Commun 12:1467–1468
36. Himl M, Pojarová M, Stibor I, Sýkora J, Lhoták P (2005) Stereoselective alkylation of thiacalix [4] arenes. Tetrahedron Lett 46(3):461–464
37. Xiaojun H, Shi H, Shi X, Zhu Z, Sun Q, Li Y, Yang H (2005) Selective nitration of thiacalix [4] arene and an investigation of its acid–base properties with a chemometric method. Bull Chem Soc Jpn 78(1):138–141
38. Lhoták P, Himl M, Stibor I, Petříčková H (2002) Alkylation of thiacalix [4] arenes. Tetrahedron Lett 43(52):9621–9624
39. Šimánová M, Dvořáková H, Stibor I, Pojarová M, Lhoták P (2008) Synthesis and conformational behaviour of lower-rim tetraacetylated thiacalix [4] arenes. Tetrahedron Lett 49(6):1026–1029
40. Ni X-L, Zeng X, Hughes DL, Redshaw C, Yamato T (2011) Synthesis, crystal structure and complexation behaviour of a thiacalix [4] arene bearing 1, 2, 3-triazole groups. Supramolecular Chem 23(10):689–695
41. Ni X-L, Zeng X, Redshaw C, Yamato T (2011) Synthesis and evaluation of a novel pyrenyl-appended triazole-based thiacalix [4] arene as a fluorescent sensor for Ag+ ion. Tetrahedron 67(18):3248–3253
42. Kumar M, Kumar R, Bhalla V, Raj Sharma P, Kaur T, Qurishi T (2012) Thiacalix [4] arene based fluorescent probe for sensing and imaging of Fe^{3+} ions. Dalton Trans 41(2):408–412
43. Mishra DR, Darjee SM, Bhatt KD, Modi KM, Jain VK (2015) Calix protected gold nanobeacon as turn-off fluorescent sensor for phenylalanine. J Inclus Phenomena Macrocycl Chem 82(3):425–436

44. Zhang C-L, Gong S-L, Luo Z-Y, Xiao-Jun W, Chen Y-Y (2006) Synthesis, characterization and coordination properties of a novel thiacalix [4] arene with diagonal quinolin-8-yloxy pendants. Supramol Chem 18(6):483–489
45. Bhatti AA, Oguz M, Yilmaz M (2020) New water soluble p-sulphonatocalix [4] arene chemosensor appended with rhodamine for selective detection of Hg^{2+} ion. J Molecular Struct 1203:127436
46. Zhu S, Lilin L (2020) Selective chromogenic recognition of copper (II) ion by thiacalix [4] arene tetrasulfonate and mechanism. Molecules 25(3):612
47. Verma A, Modi K, Dey S, Kongor A, Panchal M, Vora M, Panjwani F, Jain VK (2022) Development of tBu-phenyl acetamide appended Thiacalix [4] arene as "Turn-ON" fluorescent probe for selective recognition of Hg (II) Ions. J Fluoresc 1–9
48. Pomal NC, Bhatt KD, Modi KM, Desai AL, Patel NP, Kongor A, Kolivoška V (2021) Functionalized silver nanoparticles as colorimetric and fluorimetric sensor for environmentally toxic mercury ions: an overview. J Fluoresc 1–15
49. Darjee SM, Mishra DR, Bhatt KD, Vyas DJ, Modi KM, Jain VK (2014) A new colorimetric and fluorescent chemosensor based on thiacalix [4] arene for fluoride ions. Tetrahedron Lett 55(51):7094–7098
50. Kumar M, Kumar R, Bhalla V (2009) F−-Induced 'turn-on' fluorescent chemosensor based on 1, 3-alt thiacalix [4] arene. Tetrahedron 65(22):4340–4344
51. Kumar M, Kumar R, Bhalla V (2013) Differential fluorogenic sensing of F− versus CN− based on thiacalix [4] arene derivatives. Tetrahedron Lett 54(12):1524–1527
52. Bhatt KD, Makwana BA, Vyas DJ, Mishra DR, Jain VK (2014) Selective recognition by novel calix system: ICT based chemosensor for metal ions. J Luminesc 146:450–457

Effect of Molar Ratio of Feed on the Facile Synthesis of Silicon Nanosheets from Laboratory Waste Glass

Moulie Ghosh, Snigdha Khuntia, and Sridhar Dalai

1 Introduction

Silicon (Si) has attracted immense importance as compared to other materials due its easy availability as silica, silicates silane, environmental friendliness and other novel properties [1, 2]. Si can be derived from various sources like rice husks [3–5], kaolinite [6], natural clay [7], sand [8–10], waste windshields [11], LCD [12], glass fibres [13], glass bottles [14, 15], etc. However, bulk Si shows inadequate properties as an active material; therefore, to overcome this, nanostructures of Si can be designed. Si with nanostructures exhibits outstanding functional properties in enormous fields [16] such as sensors [17, 18], drug delivery [19], bio imaging [20], catalysts [21], energy storage devices, solar cells [22], photovoltaics and flat-panel displays [10]. For the synthesis of Si nanostructures, various physical and chemical methods have been followed since decades such as ball milling, hydrothermal [23], chemical vapour deposition[24], laser ablation [25], reverse micelle process [26] and various metallothermic reduction approaches such as carbothermal, calciothermic, aluminothermic and magnesiothermic methods [8]. Most of these methods are limited owing to the involvement of toxic and expensive reactants, time-consuming complicated procedures and intensive energy usage. Therefore, in order to address a cost effective facile synthetic route to prepare Si nanosheets, magnesiothermic reduction method has turned out to be an excellent and efficient approach. This is due to the involvement of low operating temperature for reduction process and easy removal of the by-products [27, 28].

Herein, waste broken borosilicate glasswares collected from the laboratory has been utilized as a source for the production of silicon nanosheet (Si-NS). High silica

M. Ghosh · S. Khuntia · S. Dalai (✉)
School of Engineering and Applied Science, Ahmedabad University, Ahmedabad, Gujarat 380009, India
e-mail: sridhar.dalai@ahduni.edu.in

content, absence of preheat treatment and preacid leaching treatment making it appropriate for the direct use, and moreover contribution in recycling waste glass makes it worthwhile as a source of SiO_2 as compared to other source materials. The production of Si-NS has been performed via magnesiothermic reduction method. However, this reduction method gets significantly affected by various reaction parameters. And so, in this work, the noteworthy effect of molar ratios of the feed glass and magnesium reductant on the morphology and structure of Si-NS has been investigated.

2 Experimental

2.1 Materials

Waste borosilicate glasswares (WG) were collected from laboratory which were further crushed, then ground and sieved to get fine glass powder of required size. All the chemicals used for synthesis were of analytical grade and were used without involving any further purification. Magnesium powder (Mg) of 99.8% purity was purchased from Sigma-Aldrich. hydrochloric acid (HCl) and hydrofluoric acid (HF) were obtained from Merck India Pvt. Ltd and used as obtained.

2.2 Synthesis of Silicon Nanosheet (Si-NS)

About 3 g of waste borosilicate glass powder was well mixed with magnesium powder in three sets of different combination of molar ratios (WG: Mg) 1:0.5, 1:1 and 1:2 using mortar pestle. The mixtures were transferred to respective crucibles and kept for calcination in muffle furnace for 5 h at 650 °C. The after heat treated products were leached with 5 M HCl acid to etch out the Mg by-products such as MgO and Mg_2Si and followed by thorough washing with deionized water (DI H_2O). To remove the unreacted SiO_2, it was further etched in 0.2 wt% HF acid for 1 h with subsequent washing with DI H_2O. The final samples thus collected were dried in hot air oven at 120 °C for 4 h, labelled and stored in desiccator. The samples were labelled as M_XG_Y where 'M' stands for magnesium, 'G' stands for waste glass and 'X' and 'Y' in the subscript denote molar ratio of magnesium and waste glass, respectively [4, 6, 9, 11–13, 30].

2.3 Characterization

All the product samples were subjected to phase analysis using X-ray diffractometer (XRD). The morphology of the samples was analysed using scanning electron microscope (SEM) and transmission electron microscope (TEM).

Electron microscopy

The surface morphology of feed glass powder, magnesium and each of the product samples were initially analysed using SEM equipped with energy dispersive X-ray spectroscopy (EDS), JSM-6010 LA from Jeol Asia Ltd. Ultra-trace quantity of the sample powder was spread on a double-sided carbon tape stuck on to the SEM sample holder; sputter coated with a thin layer of gold–palladium and was used for SEM analysis. Transmission electron microscopy (TEM) on selected samples was done using TEM (JEM 1400 Plus from Jeol Asia Ltd.). The powder sample was dispersed in acetone and was spread on the TEM grid; evaporated the acetone under IR lamp and was used for TEM analysis.

X-ray Diffraction analysis

The feed and product samples were characterized using X-ray Diffraction technique. The XRD studies were done on the XRD system and Rigaku Smartlab 2. A known quantity of the sample powder was loaded in the XRD sample holder and was scanned using Cu Kα X-Ray radiations having wavelength of 1.54 Å, in the 2θ range of 10°–80°.

3 Results and Discussions

3.1 Synthesis of Silicon Nanosheet

The synthetic procedure of Si-NS involves the mixing of feed glass (G) powder and magnesium (M) in different combinations of molar ratios (G:M) of 1:0.5, 1:1 and 1:2 as depicted in Table 1. These mixtures are kept in muffle furnace at 650 °C for calcination, where SiO_2 contained in feed glass powder gets reduced by Mg to produce Si along with some other Mg by-products (Eq. 1). The heat treated sample

Table 1 Molar ratios of the feed glass and magnesium for the synthesis of silicon nanosheet

S. No.	Sample code	Molar ratio Glass (G): Magnesium (M)	Reaction condition
1	$M_{0.5}G_1$	1:0.5	650 °C; 5 M HCl; 0.2 wt% HF
2	M_1G_1	1:1	650 °C; 5 M HCl; 0.2 wt% HF
3	M_2G_1	1:2	650 °C; 5 M HCl; 0.2 wt% HF

is then etched in 5 M HCl followed by 0.2 wt% HF to leach out Mg by-products and unreacted SiO_2, respectively.

Generally, when Mg is present in excess, there can be a side reaction because excess Mg starts reacting with Si instead of SiO_2 to form magnesium silicide Mg_2Si (Eq. 2) [10, 13, 29]

$$SiO_2(s) + 2Mg (g) \rightarrow Si (s) + 2MgO (s) \tag{1}$$

$$Si (s) + 2 Mg (g) \rightarrow Mg_2Si (s) \tag{2}$$

In case of insufficient Mg in the mixture leads to the formation of magnesium silicate ($MgSiO_4$) at the interface of SiO_2 and MgO (Eq. 3) [29, 30].

$$SiO_2(s) + 2MgO (s) \rightarrow Mg_2SiO_4(s) \tag{3}$$
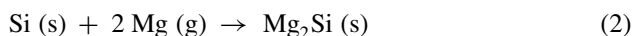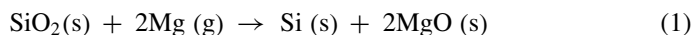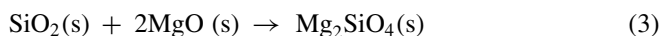
3.2 Experimental Observation

The physical appearance of the feed mixture and product samples is shown in Fig. 1. From Fig. 1, it has been observed that there is a change in the colour of the samples with different combinations of molar ratios before heat (BH) and after heat (AH) treatment which confirms the completion of magnesiothermic reduction. It is also
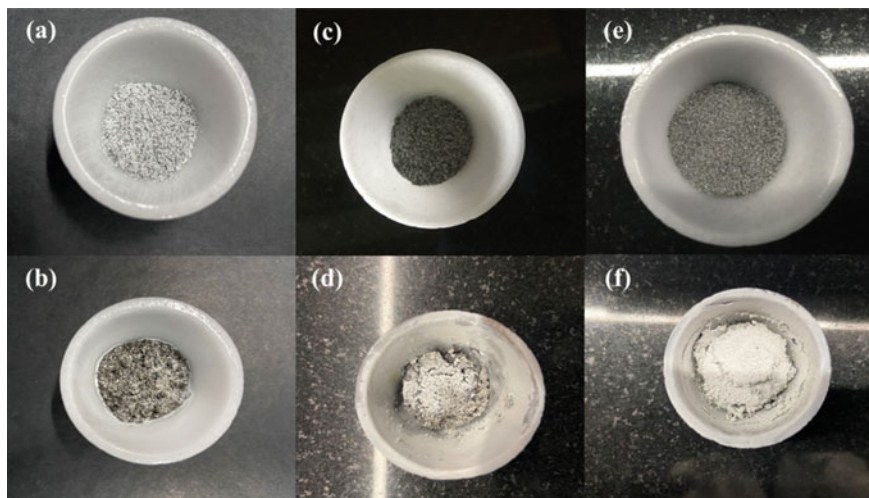
Fig. 1 Appearance of the samples before heat (BH) and after heat (AH) treatment with different ratios **a** $M_{0.5}G_1$_BH **b** $M_{0.5}G_1$_AH **c** M_1G_1 _BH **d** M_1G_1 _AH **e** M_2G_1_BH **f** M_2G_1_AH

observed that the colour and texture of after heat treated samples have changed with increase in the magnesium content in the feed mixture. The colour intensity of the after heat treated samples (Fig. 1b, d, f) is seen to be reduced from dark to light with increase in the Mg ratio. This confirms that there is an effect of molar ratio of reactants on the product morphology.

3.3   Effect of Molar Ratio on the Morphology of Silicon Nanosheets

In order to study the morphology, the SEM images with different magnification and corresponding EDX spectrum have been taken for all product samples which are shown in Fig. 2. It is clear from Fig. 2 that there is an effect of different molar ratio of feed mixture on the morphology and structure of Si-NS.

As it is shown in Fig. 2a, b, very few sheet like structures are found but mostly arranged in conglomerated form with no pores. The EDS in the inset of Fig. 2b shows the presence of Mg and O along with Si peak. This is due to the insufficient magnesium at the SiO_2/Mg reaction interface which further favouring the formation of Mg_2SiO_4 via Eq. 3. The reaction between SiO_2 and MgO devour SiO_2 completely and thereby reduces the yield of Si. The silicate of magnesium formed is not easily removed with the use of HCl, thereby it affects the properties of the Si product [29, 30].

It is observed from Fig. 2c and d, that sheets are arranged in a well-defined honeycomb like morphology with porous structure which is attributed to the complete reduction of SiO_2 to pure Si. The EDS in the inset of Fig. 2d also confirms the formation Si. This is also further confirmed by XRD analysis.

From Fig. 2e and f, it is observed that higher magnesium content shows agglomerated structure which is due to the uncontrollable reaction between Mg and Si and leads to the formation of Mg_2Si via Eq. 2 that consequently restricts the complete conversion of SiO_2. EDS in the inset of Fig. 2f also indicates the presence of O along with Si [10, 13]. Therefore, a huge amount of unreacted SiO_2 is found to be present in the final product that can be attributed to the insufficient concentration of HF or inadequate time for the etching purpose.

3.4   Comparative Study of Surface Morphology of Feed Glass, Magnesium and Product with 1:1 Ratio

The morphology and structure of feed glass, magnesium and product sample (M_1G_1) are shown in Fig. 3. The SEM images in Fig. 3 depict the significant difference in the morphology of the precursor materials feed glass, magnesium and the final product Si-NS (M_1G_1). The feed glass and magnesium are showing an irregular
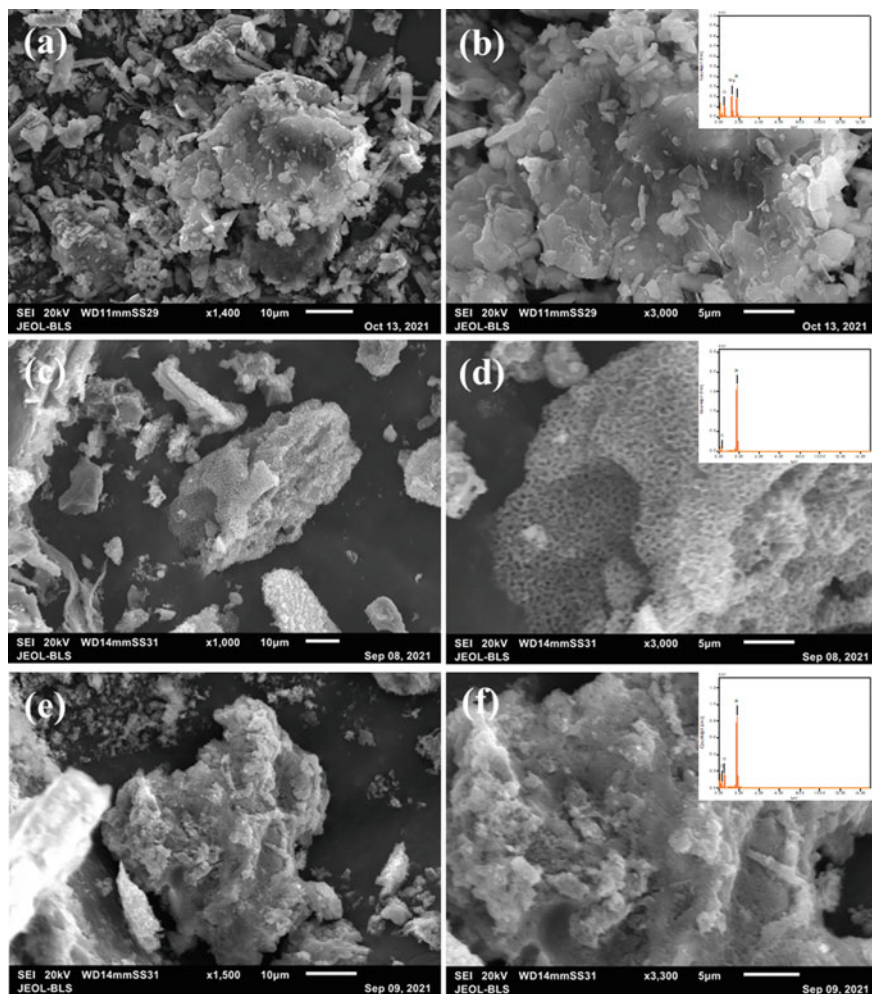
Fig. 2 SEM images of **a** $M_{0.5}G_1$ low magnification; **b** $M_{0.5}G_1$ high magnification with inset EDS; **c** M_1G_1 low magnification; **d** M_1G_1 high magnification with inset EDS; **e** M_2G_1 low magnification; **f** M_2G_1 high magnification with inset EDS

shape with micron-sized particles as shown in Fig. 3a, b. Figure 3c, d further confirm that after etching process, there is the formation of Si-NS arranged in honeycomb pattern along with porous structure.
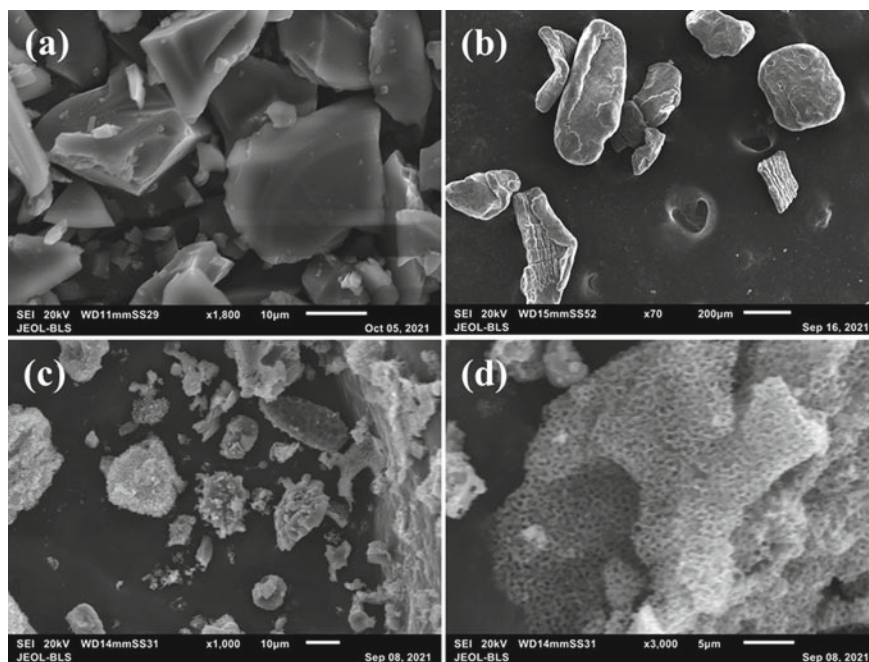
Fig. 3 SEM images of **a** feed glass; **b** magnesium; **c** M_1G_1 low magnification; **d** M_1G_1 high magnification

3.5 SEM and TEM Analysis of Silicon Nanosheet with (M:G) 1:1 Ratio

The SEM image of M_1G_1 (Fig. 4a) shows the formation of Si-NS that are arranged in honeycomb structure containing pores. This is further confirmed by TEM study
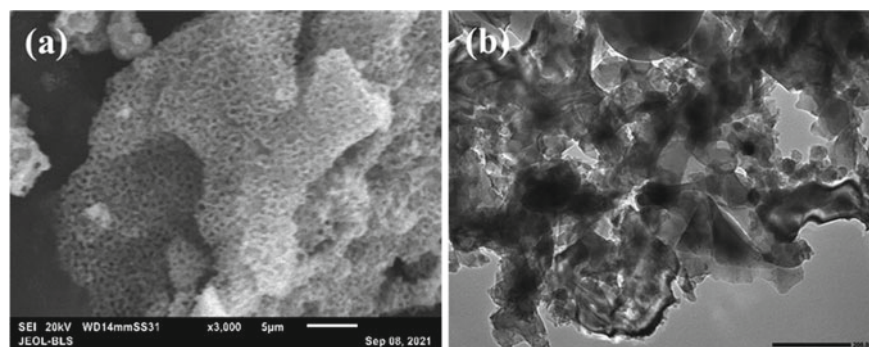
Fig. 4 **a** SEM image of M_1G_1; **b** TEM image of M_1G_1
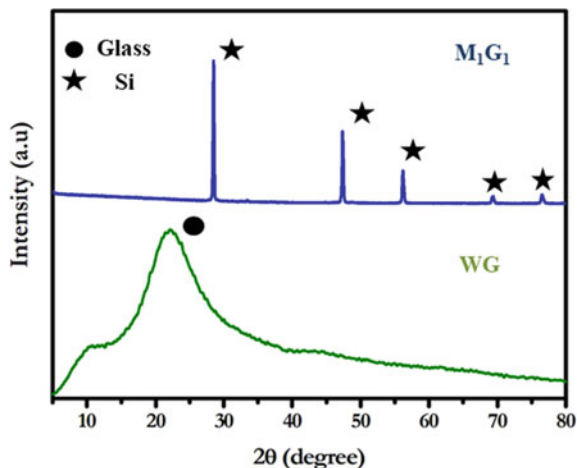
which also confirms the formation of Si-NS with porous structures (Fig. 4b). The generation of highly porous structure is attributed to the selective etching of Mg by-products, and the sheet formation is regarded as the complete reduction of SiO_2 to Si.

3.6 Phase Analysis by XRD

The study for purity and phase determination of Si-NS (M_1G_1) along with feed glass (WG) is investigated by wide angle powder XRD. Transformation of amorphous phase of SiO_2 to crystalline phase of Si has been observed from the XRD patterns. The XRD pattern of WG (Fig. 5; bottom) shows a hump centred at 2θ equal to $22°$ indicating the amorphous nature. The diffraction pattern of M_1G_1 (Fig. 5; top) showing narrow and sharp peaks without amorphous scattering, assures the well crystalline nature of Si. The pattern displaying obvious peaks at 2θ of $28.8°$, $47.8°$, $56.7°$, $69.7°$ and $77.1°$ of Si that corresponds to (111), (220), (311), (400) and (331) planes, respectively, are well indexed with typical cubic phase of Si (JCPDS 27–1402) [12, 15].

4 Conclusions

In a nutshell, Si-NS has been successfully synthesized by utilizing waste borosilicate glasses as a silica source via scalable, low cost and facile magnesiothermic reduction method. In this research, the effect of molar ratio of feed mixture for a cost-effective production of Si-NS has been studied by keeping all other parameters constant. SEM

and TEM analysis revealed that 1:1 ratio exhibit excellent formation of nanosheets arranged in well-defined porous honey comb structure. This unique porous nanostructure has originated from Mg diffusion and reaction with SiO_2 precursor followed by acid leaching process. The ratio of nearly one would lead to complete reduction of SiO_2 to Si. However, lower and higher molar ratios lead to the formation of reaction by-products like Mg_2SiO_4, Mg_2Si and unreacted SiO_2, respectively, hence, causes low yield of Si. It is strongly believed that following this low cost, sustainable synthetic approach and application of Si-NS using waste glass can be a promising solution for waste glass management.

References

1. Fukata N, Subramani T, Jevasuwan W, Dutta M, Bando Y (2017) Functionalization of silicon nanostructures for energy-related applications. Small 13(45):1701713. https://doi.org/10.1002/smll.201701713
2. Teo BK, Sun XH (2007) Silicon-based low-dimensional nanomaterials and nanodevices. Chem Rev 107(5):1454–1532. https://doi.org/10.1021/cr030187n
3. Liu N, Huo K, McDowell MT, Zhao J, Cui Y (2013) Rice husks as a sustainable source of nanostructured silicon for high performance Li-ion battery anodes. Sci Rep 3(1):1919. https://doi.org/10.1038/srep01919
4. Sekar S, Lee S (2021) Derivation of luminescent mesoporous silicon nanocrystals from biomass rice husks by facile magnesiothermic reduction. Nanomaterials 11(3), Art. no. 3. https://doi.org/10.3390/nano11030613
5. Larbi K, Barati M, Mclean A (2011) Reduction behaviour of rice husk ash for preparation of high purity silicon. https://doi.org/10.1179/000844311X13117643274677
6. Wang H et al (2020) Synthesis of silicon nanosheets from kaolinite as a high-performance anode material for lithium-ion batteries. J Phys Chem Solids 137:109227. https://doi.org/10.1016/j.jpcs.2019.109227
7. Ryu J, Hong D, Choi S, Park S (2016) Synthesis of ultrathin si nanosheets from natural clays for lithium-ion battery anodes. ACS Nano. https://doi.org/10.1021/acsnano.5b07977
8. Favors Z et al (2014) Scalable Synthesis of Nano-Silicon from Beach Sand for Long Cycle Life Li-ion Batteries. Sci Rep 4(1):5623. https://doi.org/10.1038/srep05623
9. Furquan M, Kathribail AR, Vijayalakshmi S, Mitra S (2018) Efficient conversion of sand to nano-silicon and its energetic Si-C composite anode design for high volumetric capacity lithium-ion battery. J Power Sources 382:56–68. https://doi.org/10.1016/j.jpowsour.2018.02.011
10. Yoo J-K et al (2014) Extremely high yield conversion from low-cost sand to high-capacity si electrodes for li-ion batteries. Adv Energy Mater 4(16):1400622. https://doi.org/10.1002/aenm.201400622

11. Choi M, Kim J-C, Kim D-W (2018) Waste windshield-derived silicon/carbon nanocomposites as high-performance lithium-ion battery anodes. Sci Rep 8(1):960. https://doi.org/10.1038/s41598-018-19529-1

12. Kang W, Kim J-C, Noh JH, Kim D-W (2019) Waste liquid-crystal display glass-directed fabrication of silicon particles for lithium-ion battery anodes. ACS Sustainable Chem Eng 7(18):15329–15338. https://doi.org/10.1021/acssuschemeng.9b02654

13. Kang W, Kim J-C, Kim D-W (2020) Waste glass microfiber filter-derived fabrication of fibrous yolk-shell structured silicon/carbon composite freestanding electrodes for lithium-ion battery anodes. J Power Sources 468:228407. https://doi.org/10.1016/j.jpowsour.2020.228407

14. Li C et al (2017) Silicon derived from glass bottles as anode materials for lithium ion full cell batteries. Sci Rep 7(1):917. https://doi.org/10.1038/s41598-017-01086-8

15. Mu T et al (2019) Scalable mesoporous silicon microparticles composed of interconnected nanoplates for superior lithium storage. Chem Eng J. https://doi.org/10.1016/J.CEJ.2019.121923

16. Lu Z et al (2011) Synthesis of ultrathin silicon nanosheets by using graphene oxide as template. Chem Mater 24(23):5293–5295. https://doi.org/10.1021/cm202891p

17. Zhu L, Peng X, Li H, Zhang Y, Yao S (2017) On–off–on fluorescent silicon nanoparticles for recognition of chromium(VI) and hydrogen sulfide based on the inner filter effect. Sens Actuators, B Chem 238:196–203. https://doi.org/10.1016/j.snb.2016.07.029

18. Hwang J et al (2016) Sensitive detection of copper ions via ion-responsive fluorescence quenching of engineered porous silicon nanoparticles. Sci Rep 6(1):35565. https://doi.org/10.1038/srep35565

19. Abramova E et al (2018) Porous silicon nanoparticles for drug delivery. IOP Conf Ser Mater Sci Eng 347:012048. https://doi.org/10.1088/1757-899X/347/1/012048

20. Ji X, Wang H, Song B, Chu B, He Y (2018) Silicon nanomaterials for biosensing and bioimaging analysis. Front Chem 6:38. https://doi.org/10.3389/fchem.2018.00038

21. Curtis IS, Wills RJ, Dasog M (2021) Photocatalytic hydrogen generation using mesoporous silicon nanoparticles: influence of magnesiothermic reduction conditions and nanoparticle aging on the catalytic activity. Nanoscale 13(4):2685–2692. https://doi.org/10.1039/D0NR07463B

22. Ahmadi N (2021) Efficiency enhancement in thin-film silicon solar cells by plasmonic nanodiscs array. JNP 15(3):036010. https://doi.org/10.1117/1.JNP.15.036010

23. Zhang J, Yu S-H (2014) Highly photoluminescent silicon nanocrystals for rapid, label-free and recyclable detection of mercuric ions. Nanoscale 6(8):4096–4101. https://doi.org/10.1039/C3NR05896D

24. Soni et al (2018) Facile graphitization of silicon nano-particles with ethanol based chemical vapor deposition. Nano-Struct Nano-Objects 16. https://doi.org/10.1016/j.nanoso.2018.04.001

25. Al-Kattan A et al (2018) Recent advances in laser-ablative synthesis of bare au and si nanoparticles and assessment of their prospects for tissue engineering applications. Int J Mol Sci 19:1563. https://doi.org/10.3390/ijms19061563

26. Nayfeh MH, Mitas L (2008) Silicon nanoparticles. new photonic and electronic material at the transition between solid and molecule. In: Nanosilicon, Elsevier Ltd., pp 1–78. https://doi.org/10.1016/B978-008044528-1.50002-6

27. Kim W-S, Hwa Y, Shin J-H, Yang M, Sohn H-J, Hong S-H (2014) Scalable synthesis of silicon nanosheets from sand as an anode for Li-ion batteries. Nanoscale 6(8):4297–4302. https://doi.org/10.1039/C3NR05354G

28. Tan Y, Jiang T, Chen GZ (2021) Mechanisms and product options of magnesiothermic reduction of silica to silicon for lithium-ion battery applications. Front Energy Res 9:98. https://doi.org/10.3389/fenrg.2021.651386

29. Entwistle J, Rennie A, Patwardhan S (2018) A review of magnesiothermic reduction of silica to porous silicon for lithium-ion battery applications and beyond. J. Mater. Chem. A 6(38):18344–18356. https://doi.org/10.1039/C8TA06370B

30. Bao Z et al (2007) Chemical reduction of three-dimensional silica micro-assemblies into microporous silicon replicas. Nature 446(7132):172–175. https://doi.org/10.1038/nature05570

Metal–Organic Frameworks (MOFs) for Heterogeneous Catalysis

Tapan K. Pal

1   Introduction

By definition, a catalyst is a substance that enhances the rate of a reaction without being consume or partly exhausted in the reaction. With the help of suitable catalyst, the desired reaction can be achieved with high conversion and selectivity under milder conditions. The term catalyst is already in human backbone since ancient age. Catalytic methodologies were utilized by several civilization to produce alcohol for beverages and preservation purpose, agricultural uprising via ammonia synthesis and bulk scale synthesis of chemicals [1]. Currently, the utilization of catalyst in every aspect is significantly increase in the production of over 10,000 products with worth $10 trillion annually corresponds to the world 15% gross domestic product (GDP). These figures itself carrying the significance for the importance of catalyst in various scientific research fields like chemistry, chemical engineering and materials science. Conventionally, all the catalysts are generally dividing into two major classes: homogeneous and heterogeneous catalyst. Both the systems are associated with the some pros and cons. However, the heterogeneous catalyst is prefer over homogeneous catalyst in terms of separation and purification of product, catalyst separation, recycling, etc. [2]. Thus, for real-time catalytic process and industrial application on a pilot scale, the heterogeneous catalyst is always desirable [3]. Recently, the metal–organic frameworks (MOFs) are the new emerging field of crystalline porous materials which behave as a promising heterogeneous catalyst [4]. The characteristic structural features of MOFs bestow them as a heterogeneous catalyst: (a) hybrid inorganic–organic architect, (b) potential for rational construction,

T. K. Pal (✉)

Department of Chemistry, School of Technology, Pandit Deendayal Energy University, Gandhinagar, Gujarat 382426, India

e-mail: tapan.pal@sot.pdpu.ac.in
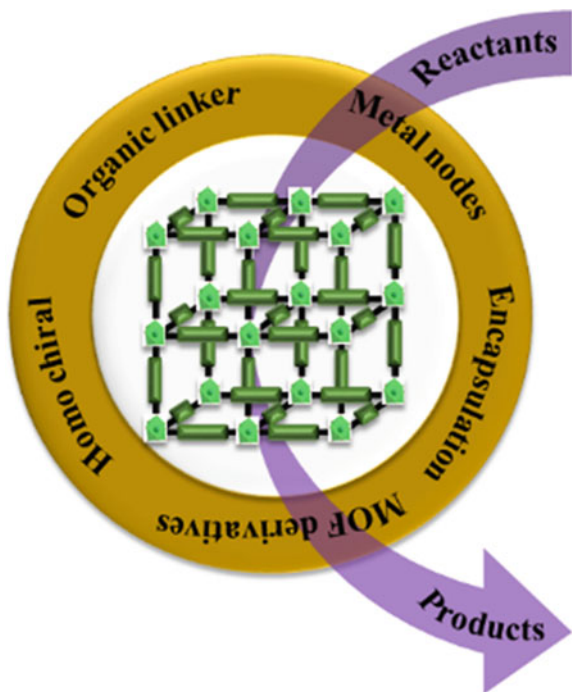
(c) dynamic structural flexibility, (d) controllable pore size and surface, (e) well-defined porosity, (f) post-synthetic ability and (g) last but not least the crystallographic recognition of atomistically location of catalytic active centre throughout the network allow us to establish the mechanism of the reaction. Indeed, these are the special features always reside on researchers mind as a wish list for catalytic engineering. The catalytic activity of MOF can be exhibited due to the presence of active metal centres/open metal sites (knows as Lewis acidic site), Lewis basic site and sometimes the bifunctional cooperative activity from both of them [5]. Moreover, the post-synthetic modification (PSM) allows for the inclusion of nanoparticles, [6] reactive metal complexes and the organocatalytic moiety [7] to accomplish the catalytic activities (Scheme 1). In this mini book chapter, we have presented the thermal catalytic activities of MOF for C–C bond formation.

2 Acid-Promoted Catalytic Reaction in MOF

Quite well known the open metal site behaved as a Lewis acidic in nature. During MOF synthesis, it is not always possible to have open metal site. Sometimes by removing weakly coordinated solvent molecules from the metal nodes or secondary building unit (SBU), the Lewis acidic site can be created for catalytic reaction.
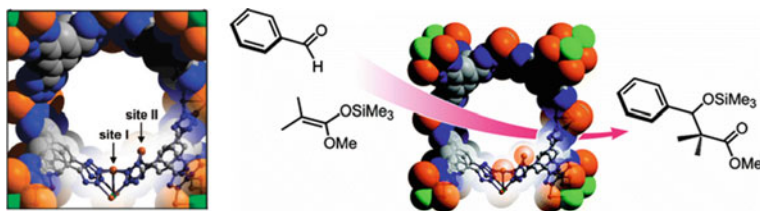
Fig. 1 Existence of various Mn(II) active sites exposed to the pore of the microporous MOF and its performance in the catalytic reaction

First catalytic reaction was reported by using cadmium based 2D MOF, where the as-synthesized MOF contains open metal site that performed facile cyanosilylation reaction between trimethylsilylnitrile and different aromatic aldehydes [8]. With the concept on open metal site, an amino acid derivative linker was used to construct a copper-based MOF, Cu(II)-MOF which contains distorted square-planar metal geometry with vacant site at axial position that efficiently accomplished cross-coupling reaction between imidazole and variety of arylboronic acids with very good yield in the range 55–97% [9]. In an another report by exposing of two different open Mn(II) centres in a microporous MOF (Fig. 1), the size selective cyanosilylation and Mukaiyama–aldol reactions were performed [10].

By removing weakly bound solvent molecules from the metal centres to generate catalytic active site for the execution of catalytic reaction is also possible. A copper-based MOF was solvothermally synthesized that consist paddle wheel SBU with water molecule at the axial position [11]. By thermal activation, the removal of these axial water molecules to produce Lewis acidic open metal site that displayed a series of three component one pot Biginelli reaction between different derivatives of aromatic aldehyde with ethyl acetoacetate in presence of urea with moderate to good yields. The incorporation of cuprous metal centres in Ti-based MOF, MIL-125-NH$_2$ is achieved by two steps: First, the abstraction of proton from μ_2-OH and then the ion exchanged with cuprous ion. The resulting MOF showed the hydrogenation of CO_2 to ethylene [12]. The presence of free acidic functional moiety is responsible for such high catalytic activity. When a linker having a number of carboxylic acid groups, it is quite conceivable to have MOFs where one or more carboxylic acid groups are remain free. These free Brönsted acid groups can execute the CO_2 fixation reaction with epoxide to cyclic carbonate. The free acidic site can activate the epoxide ring and CO_2 for the synthesis of desired product. For instance, a 3D framework, [Ni(btzip)(H$_2$btzip)]·2DMF·2H$_2$O contains free acidic carboxylic groups (Fig. 2) as an acidic heterogeneous catalyst for CO_2 fixation reaction [13].

The inclusion of new metallic centre or catalytically active site through PSM process, the catalytic reaction can be accomplish. With this process, the attaching of organocatalysis on the vacant metal sites in SBU is very attractive to bring the catalytic activity in MOF. An efficient organocatalytic compound 3/4-ppc is covalently link to the vacant chromium sites in MIL-101(Cr) (Fig. 3) [14]. The daughter MOFs performed aldol condensation reaction between variety of ketones and aldehyde with
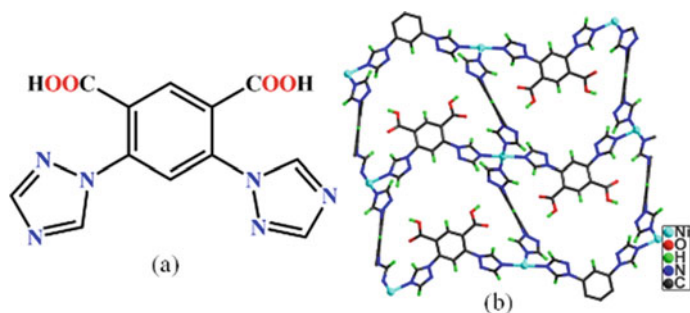
Fig. 2 **a** Ligand H$_2$btzip, **b** view of the porous network where the free carboxylates groups are directed towards the pore
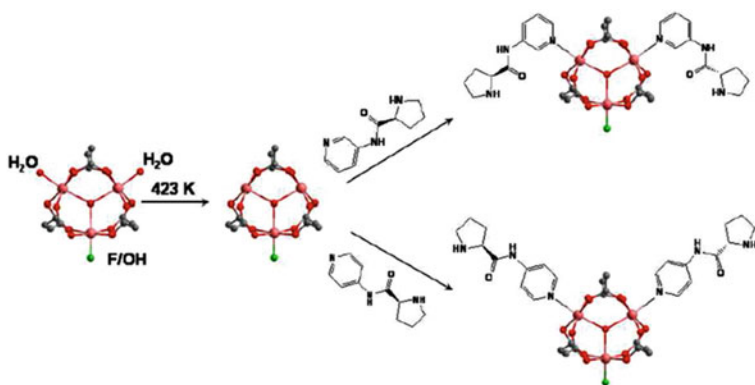
Fig. 3 PSM process to bring active organocatalytic site in MIL-101(Cr) to form C- MIL-101(Cr) to execute the aldol condensation reaction. 4-ppc=(S)-N-(pyridin-4-yl)-pyrrolidine-2-carboxamide and 3-ppc=(S)-N-(pyridin-3-yl)-pyrrolidine-2-carboxamide

yield in the range from 60 to 90% and the framework showed enantio-selectivity in case of R-isomers with enantiomeric excess 55–80%.

3   Linker-Promoted Catalytic Reaction

Another important component of MOF is linker. Several important properties including catalytic abilities can be tuned by choosing proper ligand [15]. The linker containing preconceived catalytically active site, then the MOF derived from it, would perform the catalytic reaction very efficiently. One of the interested examples is by incorporation of catalytically active proline moiety on the linker backbone to derive a catalytically active porous MOF, L$_{Cu}$PRO [16]. This MOF showed

Fig. 4 Synthesis of
L_{Cu}PRO and its application
in Baylis−Hillman reaction
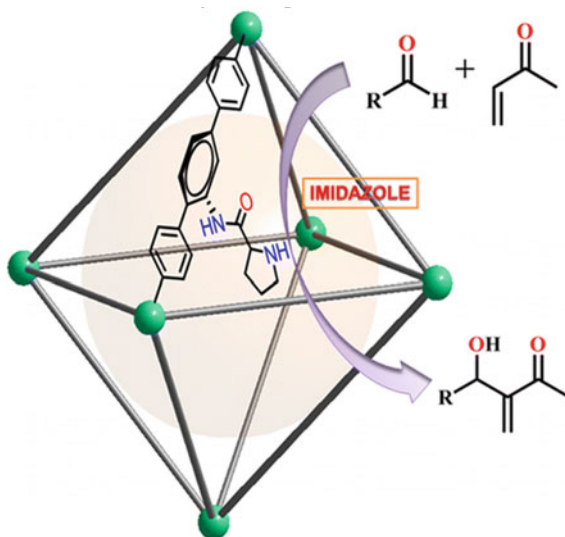
Baylis−Hillman reaction between α, β-unsaturated carbonyl compounds with variety of aromatic aldehydes in presence of imidazole as a cocatalyst (Fig. 4).

Recently, a chromophoric ligand, triphenylene-2,6,10-tricarboxylate, has been installed in the MOF network to efficiently performed the CO_2 valorization [17]. In another approach, the judicial selection of linker is leverage us to perform the PSM process to induce the catalytically active site. A well-known MOF, IRMOF-3 where the amino functionality on linker BDC-NH$_2$, is nicely oriented throughout the pore of the channel (Fig. 7).The stepwise PSM process of –NH$_2$ with salicylaldehyde followed by reaction with NaAuCl$_4$ to generate IRMOF-3[Au] (Fig. 5) [18]. Quite interestingly, the IRMOF-3[Au] performed the three-component coupling reaction between piperidine, paraformaldehyde and acetylene moiety with very good yield (Fig. 5).

Sometimes the linker containing metal ion, i.e. the metalloligand, can deliver the MOF for various catalytic reactions. A three different zirconium-based MOFs (mPT-MOF-Ir, BPV-MOF-Ir and mBPV-MOF-Ir) were synthesized from a various
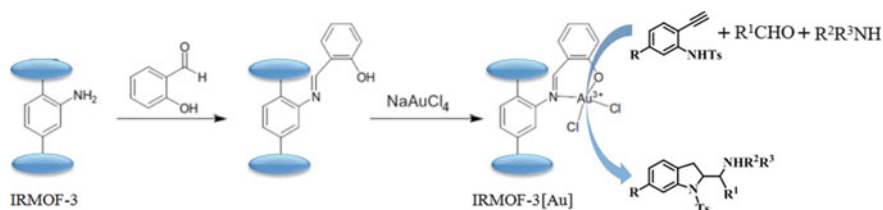
Fig. 5 Post-functionalization of **IRMOF-3** with salicylaldehyde followed by NaAuCl$_4$ to produce IRMOF-3[Au] and its catalytic application
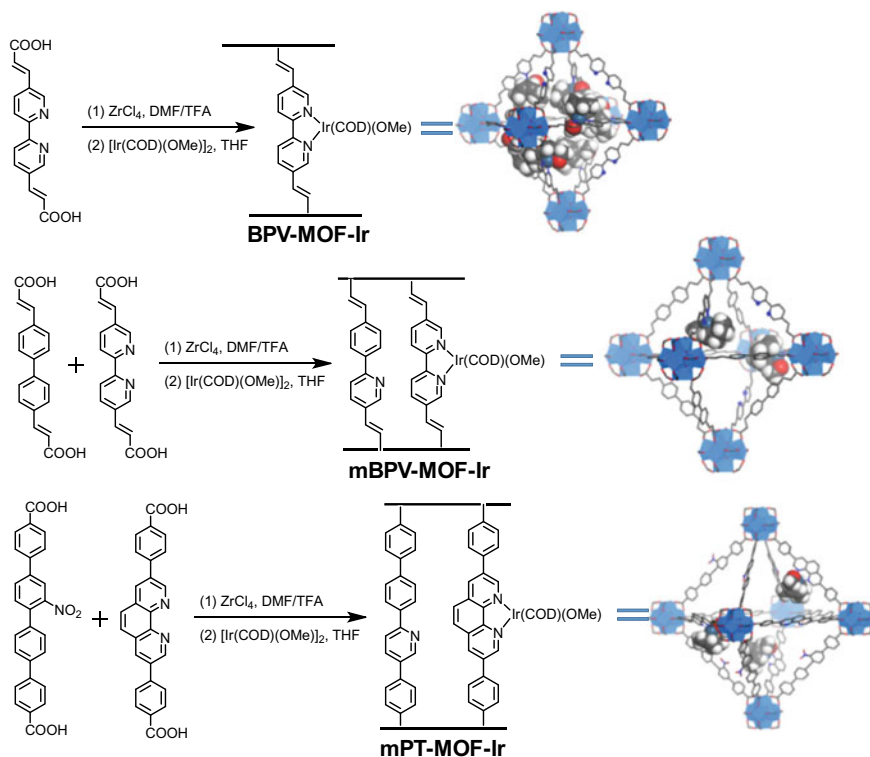
Fig. 6 Schematic presentation for the synthesis of three different zirconium-based MOF from metalloligands containing iridium metal ion as a catalytically active centre and the various catalytic activities displayed by them

metalloligands, and all the ligands are containing iridium metal ion (Fig. 6) [19]. These MOFs were able to perform the tandem catalytic reaction such as *ortho* silylation, hydrosilylation of *N*-methylbenzyl amines and aryl ketones/aldehydes, respectively. In addition, the aromatic C–H bond underwent the borylations reaction. All the catalytic reactions were executed at the iridium metal centre that is present in the metalloligand of the corresponding MOFs. Here, the chelating capability of the ligand can easily form chelate with the iridium metal ion to make the facile synthesis of metalloligand. Likewise, iridium ion chelate, the similar concept was used for the formation of rhodium-based metalloligand towards the synthesis of MOF catalyst. Well-known MOF, UiO-67 underwent PSM process with metalloligand, Cp*Rh(5,5′-dcbpy)Cl (Cp*=pentamethyl cyclopentadiene) to furnished Cp*Rh@UiO-67 that demonstrated photocatalytic reduction of CO_2 to formate [20]. Recently, by using same chelating fashion the silver ion post-synthetically incorporated inside the nitro-functionalized MOF, to delivered excellent catalytic host. This material demonstrated the conversion of CO_2 with propargylic alcohols to propargyl carbonate at room temperature in presence of base and acetonitrile as solvent [21]. The porphyrin ligand

Fig. 7 A view showing Zr_6 clusters connected by cyclam linkers
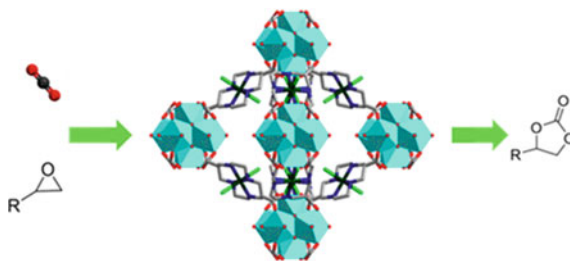
is behaved as well-known metalloligand because of its ability to take up metal ion in the core of the porphyrin ring. With this concept, several porphyrin-based MOFs were synthesized for the formation of C–C bond in several organic transformation reactions such as olefin epoxidation, cyclic carbonate synthesis, acyl group transfer, etc. [22, 23]. Similar to porphyrin, salen ligand can also accommodate the metal ion in its pocket and the MOF decorated with salen ligand can perform catalytic reaction [24, 25]. Recently, by taking cyclam moiety as a linker backbone, a suitable MOF catalyst would be constructed. For instance, macrocycle 1,4,8,11-tetraazacyclotetradecane (cyclam) was synthesized with two carboxylic groups at the two diagonally opposite C-atoms to delivered $[Cu(cyclam')]^{2+}$ or $[Ni(cyclam')]^{2+}$ where each metal ion is securely occupied the cavity [26]. This acted as a linker to Zr_6 clusters (Fig. 7) to form framework structures, VPI-100 (Cu) and VPI-100 (Ni). While the metal ion in the cavity was easily accessible by epoxides, the Zr^{4+} ion with empty coordination sites showed good CO_2 uptake capacity. This helped in the reaction of CO_2 with epoxides, including sterically encumbered ones with tetrabutylammonium bromide (TBAB) being the cocatalyst.

Alternatively, one can induce the catalytic power within the MOF by impregnation or encapsulation of nanoparticles (NPs) [27]. MOFs by virtue of its high surface area and functionalization ability can assist to cultivate the NPs inside the MOF cavity without disturbing the MOF network. To derive an efficient catalytic materials the shape, size and dispersion of the NPs are very crucial and MOFs are the promising candidates in this regards [28]. A gold NP impregnated within MOF-199 through microwave irradiation to form Au@MOF-199 for the execution of three-component coupling reaction between phenylacetylene, piperidine and paraformaldehyde [29]. The reactivity of gold loaded nanoparticle MOFs is much superior compare to the pristine MOF-199. Literature survey revealed that the tandem catalytic reaction by NP@MOFs are also realized. A well-known compound methyl isobutyl ketone (MIBK) was synthesized from ketone with the help of Pd@MIL-101 composite [30] under very low hydrogen pressure (7.5 bar). In general, for the synthesis of MIBK, the high pressure of hydrogen was required (50 bar). However, the presence of strong acidic moiety and the presence of palladium NPs the essential steps such as condensation followed by dehydration and then hydrogenation were executed very smoothly to delivered high conversion of acetone to MIBK under low pressure of hydrogen. Apart from the single NPs, the inclusion of bimetallic NPs within MOFs are also important for the tandem reaction. For example, PdAg@MIL-101 was synthesized

Fig. 8 Tandem reaction for the conversion of aldehydes to secondary amine from nitrobenzene through hydrogenation and concomitantly occurrence of reductive amination of benzaldehydes
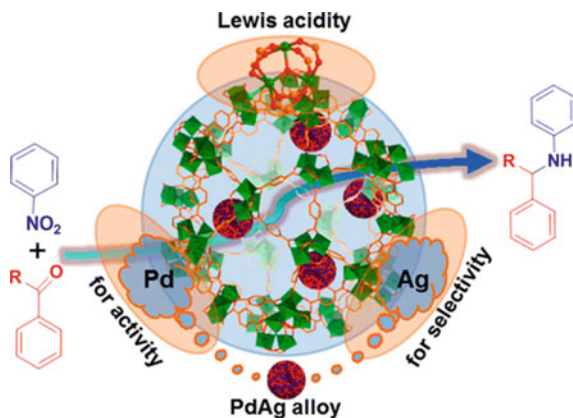
by double solvent method for catalysing the tandem reaction (Fig. 8) [31]. The beauty of this catalytic system is the presence of acidic moiety in the MOF and the palladium NPs control the hydrogenation steps, whereas the silver NPs regulate the selectivity of the reaction. Thus, this composite demonstrated the higher conversion and better selectivity for this tandem reaction compared to the mixture of Ag@MIL-101 and Pd@MIL-101. The role of NPs@MOF also exerted for the C–C bond formation in the synthesis of cyclic carbonate. The MOF, UiO-66-NH$_2$ was loaded with Ni nanoparticles to have Ni@ZrOF [32]. The catalytic activity by Ni@ZrOF in presence of TBAB was significant due to the synergistic effect of Zr^{4+} and Ni$^\circ$.

4 Homochiral MOFs for Catalytic Reaction

Homochiral MOFs are the smart catalytic materials as it has the ability to carry out asymmetric catalysis reaction under mild reaction condition. Apart from heterogeneous catalytic behaviour, the high surface area, easy installation of catalytically active site and creation of homochiral environment throughout the network, the MOF materials are highly attractive to scientific community [33]. Two carboxylate organic likers having spiro-type backbone were used to construct two highly porous Zr-based homochiral MOFs, spiro-1 and spiro-2 with the same topology, sjt (Fig. 9) [34]. Importantly, both the ligands consist phosphoric acid group which is hanging on the linker as a catalytic site to carry out catalytic reaction. Quite interestingly, the free acid group and Lewis acidic Zr(IV) part in MOF assist nicely to perform the cascade enantioselective asymmetric diacetalization-acetalization and Friedel–Crafts reaction with excellent yields. When bulky substrates were used then the yield of the desired product were less in both the catalytic reaction. This indicates that the catalytic reactions are occurring inside the pore of the MOF cavity rather than the surface of MOFs.
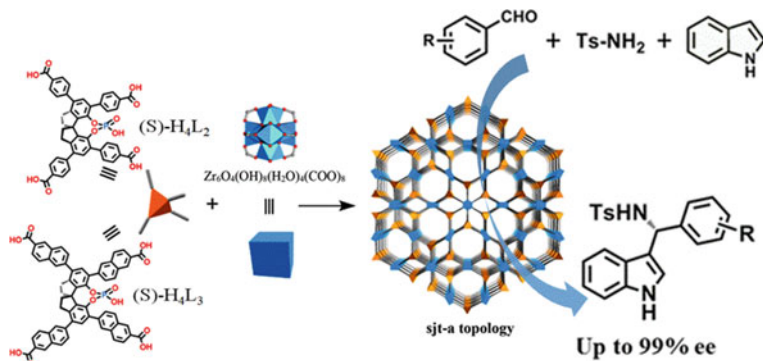
Fig. 9 *sjt* topology with Zr$_6$clusture developed from two different carboxylates organic linkers having spiro-type backbone

A highly stable and porous zinc-based homochiral MOF, [Zn$_4$O(L$_1$)$_{3/2}$]·16H$_2$O·4THF was synthesized that underwent PSM process with the exchange of H atom of the –OH group by the lithium ion from n-BuLi (Fig. 10) [35]. However, by control tuning of the mole ratio of n-BuLi and MOF, two daughter frameworks MOF-Li1 and MOF-Li2 were derived which are efficiently executed the enantioselective asymmetric cyanohydrin reaction between benzaldehyde with Me$_3$SiCN. The superior reaction rate and excellent yield of the desired product (ee > 99%) were noticed with the aldehydes containing electron-withdrawing substituents.

Various homochiral MOFs are reported based on the BINAP or BINOL backbone in the organic linker to accomplished the enantioselective asymmetric catalytic reaction [36, 37]. By using homochiral MOF, the synthesis of chiral cyclic carbonate is also achieved. To accomplished this, a chiral polyoxometalated MOF was synthesized from Zn(NO$_3$)$_2$·6H$_2$O, L-BCIP, TBA$_4$W$_{10}$O$_{32}$ and 4,4′-bipyridyl (Fig. 11) [38]. The chiral framework is capable to showed CO$_2$ fixation reaction with chiral epoxide (R/S) for enantioselective synthesis of chiral cyclic carbonate (ee > 90% and yield > 99%) with TBAB as a cocatalyst. Importantly, the framework can also display
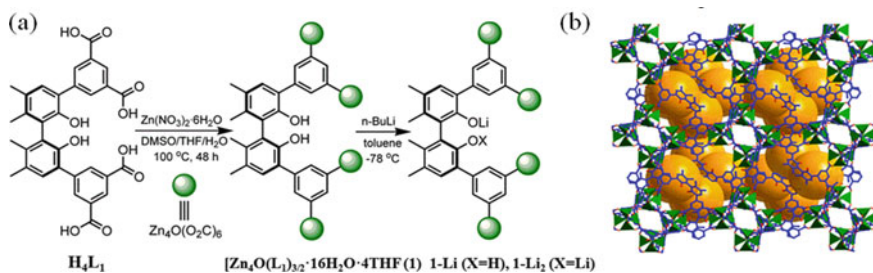
Fig. 10 a Schematic representation for MOF formation followed by lithiation, **b** 3D network along crystallographic *a* axis
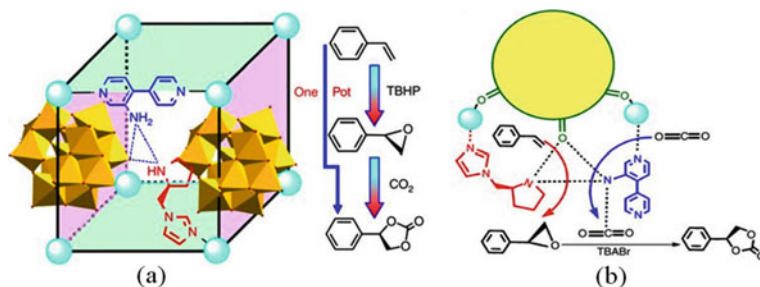
Fig. 11 a Homochiral framework is showing all the catalytically active components and **b** schematic presentation for the tandem conversion of alkene to cyclic carbonate

the enantioselective tandem catalytic reaction in the conversion of styrene to chiral phenyl carbonate in presence of butylhydroperoxide and CO_2 under milder reaction condition. The presence of Lewis base–NH_2 is assisting to enhance the CO_2 concentration, and $ZnW_{12}O_{40}{}^{6-}$ strongly activated the catalytic reagent to exert excellent yield and enantiomeric excess in this one pot cascade reaction.

5   Conclusion

MOF as a catalytic system possesses a potential activity of homogeneous and heterogeneous component into the single solid matrix. Mainly, by virtue of its numerous design possibilities, MOFs are recently appeared as a suitable podium in various catalytic applications. In this chapter, we have covered the installation of various active catalytic sites and their role in the catalytic reaction. However, several progresses have been achieved still researchers are trying to find the method to conduct the catalytic reaction under very benign condition such room temperature, normal atmospheric pressure, etc. All these parameters would be manipulated by the excellent features of MOFs, but still ample room is available for development and exciting chemistries to be discovered. By considering outstanding features of MOFs, the scientific community strongly trust that MOFs will garner favourable attention as a brilliant catalytic stalwarts in near future. The wide spectrum of catalytic method by MOFs paves the way towards its versatile applicability. For instance, the photocatalytic and electro chemical catalytic application of MOFs towards the formation of C–C bond. Some factors needs to consider in electrocatalytic application by MOFs: challenges in stability, conductivity and overall the efficiency. Similarly, for photocatalytic catalytic reaction apart from stability, the other important issue is the light absorption ability of the MOFs and/or it's composite. Literature survey revealed those issues have been continuously taking care very nicely by scientific community. However, for large-scale application MOFs are still in infancy stage as MOF-based catalytic system barely encounters the industrial requirements. Thus,

judicial design and manipulation of experimental conditions are very imperative for real-time application.

References

1. Adams C (2009) Applied catalysis: a predictive socioeconomic history. Top Catal 52:924–934
2. Pascanu V, Miera GG, Inge AK, Martín-Matute B (2019) Metal-organic frameworks as catalysts for organic synthesis: a critical perspective. J Am Chem Soc 141:7223–7234
3. Wang A, Li J, Zhang T (2018) Heterogeneous single-atom catalysis. Nat Rev Chem 2:65–81
4. De D, Pal TK, Neogi S, Senthilkumar S, Das D, Gupta SS, Bharadwaj PK (2016) A versatile CuII metal–organic framework exhibiting high gas storage capacity with selectivity for CO_2: conversion of CO_2 to cyclic carbonate and other catalytic abilities 22:3387–3396
5. De D, Pal TK, Bharadwaj PK (2020) Coord Chem Rev 408:213173
6. Leus K, Dendooven J, Tahir N, Ramachandran RK, Meledina M, Turner S, van Tendeloo G, Goeman JL, van der Eycken J, Detavernier C, Van Der Voort P (2016) Atomic layer deposition of Pt nanoparticles within the cages of MIL-101: amild and recyclable hydrogenation catalyst. Nanomaterials 6:45
7. Juan-Alcaniz J, Ferrando-Soria J, Luz I, Serra-Crespo P, Skupien E, Santos VP, Pardo E, Xamena FXLI, Kapteijn F, Gascon J (2013) The oxamate route, a versatile post-functionalization for metal incorporation in MIL-101(Cr): catalytic applications of Cu, Pd, and Au. J Catal 307:295–304
8. Fujita M, Kwon YJ, Washizu S, Ogura K (1994) Preparation, clathrationability, and catalysis of a two-dimensional square network material composed of cadmium(II) and 4,4′-bipyridine. J Am Chem Soc 116:1151–1152
9. Wu C-D, Li L, Shi L-X (2009) Heterogeneous catalyzed aryl–nitrogen bond formations using a valine derivative bridged metal–organic coordination polymer. Dalton Trans 6790–6794
10. Horike S, Dincă M, Tamaki K, Long JR (2008) Size-selective Lewis acid catalysis in a micro-porous metal-organic framework with exposed Mn^{2+} coordination sites. J Am Chem Soc 130:5854–5855
11. Pal TK, De D, Senthilkumar S, Neogi S, Bharadwaj PK (2016) A partially fluorinated, water stable Cu(II)–MOF derived via transmetalation: significant gas adsorption with high CO_2 selectivity and catalysis of Biginelli reactions. Inorg Chem 55:7835–7842
12. Zeng L, Cao Y, Li Z, Dai Y, Wang Y, An B, Zhang J, Li H, Zhou Y, Lin W, Wang C (2021) Multiple cuprous centers supported on a titanium-based metal—organic framework catalyze CO_2 hydrogenation to ethylene. ACS Catal 11:11696–11705
13. Li Y-Z, Wang H-H, Yang H-Y, Hou L, Wang Y-Y, Zhu Z (2018) An uncommon carboxyl-decorated metal-organic framework with selective gas adsorption and catalytic conversion of CO_2. Chem Eur J 24:865–871
14. Banerjee M, Das S, Yoon M, Choi HJ, Hyun MH, Park SM, Geo G, Kim K (2009) Postsynthetic modification switches an achiral framework to catalytically active homochiral metal—organic porous materials. J Am Chem Soc 131:7524–7525
15. Yang L, Cai P, Zhang L, Xu X, Yakovenko AA, Wang Q, Pang J, Yuan S, Zou X, Huang N, Huang Z, Zhou H-C (2021) Ligand-directed conformational control over porphyrinic zirconium metal—organic frameworks for size-selective catalysis. J Am Chem Soc 143:12129–12137
16. De D, Pal TK, Bharadwaj PK (2016) A porous Cu (II)-MOF with proline embellished cavity: cooperative catalysis for the Baylis-Hillman reaction. Inorg Chem 55:6842–6844
17. Gong Y-N, Liu J-W, Mei J-H, Lin X-L, Deng J-H, Li X, Zhong D-C, Lu T-B (2021) Incorporation of chromophores into metal—organic frameworks for boosting CO_2 conversion. Inorg Chem 60:14924–14931
18. Zhang X, Llabrési-Xamena FX, Corma A (2009) Gold(III)–metal organic framework bridges the gap between homogeneous and heterogeneous gold catalysts. J Catal 265:155–160

19. Manna K, Zhang T, Greene FX, Lin W (2015) Bipyridine- and phenanthroline-based metal-organic frameworks for highly efficient and tandem catalytic organic transformations via directed C-H activation. J Am Chem Soc 137:2665–2673

20. Chambers MB, Wang X, Elgrishi N, Hendon CH, Waksh A, Bonnefoy J, Canivet J, Quadrelli EA, Farrusseng D, Mellot-Draznieks C, Fontecave M (2015) Photocatalytic carbon dioxide reduction with rhodium-based catalysts in solution and heterogenized within metal–organic frameworks. Chemsuschem 8:603–608

21. Zhao J, Jiao Z-H, Hou S-L, Ma Y, Zhao B (2021) Anchoring Ag(I) into nitro-functionalized metal−organic frameworks: effectively catalyzing cycloaddition of CO_2 with propargylic alcohols under mild conditions. ACS Appl Mater Interfaces 13:45558–45565

22. Shultz AM, Farha OK, Hupp JT, Nguyen ST (2009) A catalytically active, permanently microporous MOF with metalloporphyrin struts. J Am Chem Soc 131:4204–4205

23. Farha OK, Shultz AM, Sarjeant AA, Nguyen ST, Hupp JT (2011) Active-site-accessible porphyrinic metal−organic framework materials. J Am Chem Soc 133:5652–5655

24. Cho S-H, Ma B, Nguyen ST, Hupp JT, Albrecht-Schmitt TE (2006) A metal–organic framework material that functions as an enantioselective catalyst for olefin epoxidation. Chem Commun 2563–2565

25. Shultz AM, Farha OK, Adhikari D, Sarjeant AA, Hupp JT, Nguyen ST (2011) Selective surface and near-surface modification of a noncatenated, catalytically active metal-organic framework material based on Mn(salen) struts. Inorg Chem 50:3174–3176

26. Zhu J, Usov PM, Xu W, Celis-Salazar PJ, Lin S, Kessinger MC, Alvarado CL, Cai M, May AM, Slebodnick C, Zhu D, Senanayake SD, Morris AJ (2018) A new class of metal-cyclam-based zirconium metal−organic frameworks for CO_2 adsorption and chemical fixation. J Am Chem Soc 140:993–1003

27. Li G, Zhao S, Zhang Y, Tang Z (2018) Metal–organic frameworks encapsulating active nanoparticles as emerging composites for catalysis: recent progress and perspectives. Adv Mater 30:1800702

28. Dhakshinamoorthy A, Garcia H (2012) Catalysis by metal nanoparticles embedded on metal–organic frameworks. Chem Soc Rev 41:5262–5284

29. Jiang Y, Zhang X, Dai X, Zhang W, Sheng Q, Zhuo H, Xiao Y, Wang H (2017) Microwave-assisted synthesis of ultrafine Aunanoparticles immobilized on MOF-199 in high loading as efficient catalysts for a three-component coupling reaction. Nano Res 10:876–889

30. Pan YY, Yuan BZ, Li YW, He DH (2010) Multifunctional catalysis by Pd@MIL-101: one-step synthesis of methyl isobutyl ketone over palladium nanoparticles deposited on a metal–organic framework. Chem Commun 46:2280–2282

31. Chen Y-Z, Zhou Y-X, Wang H, Lu J, Uchida T, Xu Q, Yu S-H, Jiang H-L (2015) Multifunctional PdAg@MIL-101 for one-pot cascade reactions: combination of host−guest cooperation and bimetallic synergy in catalysis. ACS Catal 5:2062–2069

32. Singh M, Solanki P, Patel P, Mondal A, Neogi S (2019) Highly active ultrasmall Ni nanoparticle embedded inside a robust metal-organic framework: remarkably improved adsorption, selectivity, and solvent-free efficient fixation of CO_2. Inorg Chem 58:8100–8110

33. Han Q, He C, Zhao M, Qi B, Niu J, Duan C (2013) Engineering chiral polyoxometalate hybrid metal-organic frameworks for asymmetric dihydroxylation of olefins. J Am Chem Soc 135:10186–10189

34. Gong W, Chen X, Jiang H, Chu D, Cui Y, Liu Y (2019) Highly stable Zr(IV)-based metal-organic frameworks with chiral phosphoric acids for catalytic asymmetric tandem reactions. J Am Chem Soc 141:7498–7508

35. Mo K, Yang Y, Cui Y (2014) A homochiral metal-organic framework as an effective asymmetric catalyst for cyanohydrin synthesis. J Am Chem Soc 136:1746–1749

36. Wu C-D, Hu A, Zhang L, Lin W (2005) A homochiral porous metal−organic framework for highly enantioselective heterogeneous asymmetric catalysis. J Am Chem Soc 127:8940–8941

37. Sawano T, Thacker NC, Lin Z, McIsaac AR, Lin W (2015) Robust, chiral, and porous BINAP-based metal−organic frameworks for highly enantioselective cyclization reactions. J Am Chem Soc 137:12241–12248

38. Han Q, Qi B, Ren W, He C, Niu J, Duan C (2015) Polyoxometalate-based homochiralmetal-organic frameworks for tandem asymmetric transformation of cyclic carbonates from olefins. Nature Comm 6:10007–10008

3D Hierarchical V and N-codoped MoS₂/rGO Composite as a Potential Electrode Material Towards Hydrogen Evolution Reaction in Acidic and Alkaline pH

Saikat Bolar, Subhasis Shit, Naresh Chandra Murmu, and Tapas Kuila

1 Introduction

Hydrogen energy is becoming a contemporary sustainable and renewable resource that can overcome the global energy crisis. High energy density (120 kJ mol^{-1}) and zero carbon emissions are the main driving factors for creating the interest on hydrogen production globally [1, 2]. Currently, hydrogen is mostly produced coal gasification technique which is not an environment friendly approach [3]. Therefore, hydrogen production by water electrolysis is attracting more attention globally. However, ~5% of the total hydrogen is produced by electrolysis. The use of potential electrocatalysts has a significant impact on water electrolysis [4]. The volcano plot suggests Pt as a promising electrode material for hydrogen evolution reaction (HER) through water electrolysis [1–5]. The low efficiency, slow kinetics, high overpotential, good durability, and high cost of electrocatalysts limit sustainable hydrogen production. In order to mitigate these issues, it is necessary to design low-cost, high-efficiency, durable, and selective electrocatalysts [6–12]. Recently, 2D molybdenum

S. Bolar · S. Shit · N. C. Murmu · T. Kuila (✉)
Surface Engineering and Tribology Division, Council of Scientific and Industrial Research—Central Mechanical Engineering Research Institute, Durgapur 713209, India
e-mail: tkuila@gmail.com

S. Bolar
e-mail: saikat.bolar@gmail.com

S. Shit
e-mail: subhasis09021994@gmail.com

N. C. Murmu
e-mail: ncmurmu@gmail.com

Academy of Scientific and Innovative Research (AcSIR), Ghaziabad 201002, India

disulphide (MoS_2) has gained attention in electrochemistry owing to the layered structure. The D-band electronic structure of MoS_2 is analogous with Pt. Therefore, MoS_2 has received extensive attention as the HER electrocatalyst [2]. However, high resistivity, poor surface active sites, unused crystal faces, and limited operational stability limit the wide applications of MoS_2 as a HER catalyst [2–5]. In this regard, it is necessary to overcome the limitation related to MoS_2. Doping is an emerging technique that improves the electrocatalytic activity by changing the crystal structure. Therefore, doping engineering is an emerging technology that can trigger the inert basal plane of 2D MoS_2 through the creation of strain and vacancies engineering [2, 5, 13–17]. However, in some cases, doping may form defects inside the crystal structure and improve the catalytic performance [2, 7, 9]. On contrary, in harsh electrolyte media, aerial oxidation, and low operating stability reduce the wide applicability of MoS_2 or MoS_2-supported electrocatalysts. Recently, carbon-containing materials have received considerable attention in catalyst synthesis due to the improvement in catalytic stability and electronic modification during composite formation [18]. Retention in harsh electrolytic media, high natural abundance, and huge structural robustness are considered as the significant advantages of carbonaceous materials as electrode material. Previous studies have shown that CVD-grown graphene and reduced graphene oxide have poor electrolytic performance in HER [7–15]. Most importantly, the high geometric surface area, outstanding electrical conductivity, excellent thermal stability, and tremendous mechanical strength of graphene encourage the researchers to investigate its effect on the catalytic performance of HER [7, 10, 18]. The synergistic effect within the composite structure has gained tremendous attention due to the improvement of catalytic performance. In this context, there is an urgent need to develop nanostructured composite materials to promote HER and receive great attention under different pH environment. Herein, a defect-rich V and N co-doped MoS_2 embedded in reduced graphene oxide (rGO) to prepare VNMSG composite by in situ hydrothermal technique. V and N doping appreciably modified the electronic structure of MoS_2 as reflected in the electrochemical analysis. The conductive rGO nanosheets improve the catalytic performance of VNMSG by decreasing the resistivity, catalytic stability, and activating the inert basal plane. The synergistic effect between MoS_2 and rGO nanosheets enhances the electrocatalytic performance in VNMSG.

2 Experimental Section

2.1 Material

All chemicals including, graphite powder (≥99.5%, Sigma Aldrich), sulphuric acid (H_2SO_4, ≥95–98%, Merck, India), nitric acid (Merck, India), potassium permanganate ($KMnO_4$, (Merck, India), hydrogen peroxide (H_2O_2, Merck, India), sodium meta vanadate ($NaVO_3$, Sigma Aldrich), thioacetamide ($CS(NH_2)_2$, Sigma Aldrich),

ammonia (33%, Merck), sodium dodecyl sulphate (SDS, SRL, India), sodium molybdate dihydrate (Na$_2$MoO$_4$·2H$_2$O, SRL, India), ethanol (98%, Himedia), and hydrochloric acid (HCl, 30%, Merck, India) were applied without further purification.

2.2 Synthesis of V and N Co-Doped MoS$_2$ (VNMS)

Vanadium and nitrogen were synthetically doped in MoS$_2$ by one-pot solvothermal method. Typically, requisite amount of precursors were taken in a beaker and stirred vigorously in 1:1 ethanol–water mixture for ~30 min. SDS was added (greater than CMC value) as a surfactant in the solution. The mixture of solution is kept inside the hydrothermal reactor for 18 h at 180 °C. A black-coloured product was obtained after filtration which again dried at 60 °C under vacuum oven. The resultant product was dispersed in 40 ml of water-ethanol (1:1) mixture-Solution A.

2.3 Synthesis of V and N Co-Doped MoS$_2$/rGO (VNMSG)

Graphene oxide (GO) was synthesized as illustrated in our previous report [19]. The two solutions (solution A and B) were mixed in a 1 L flask by drop-wise addition of continuous stirring for 2 h. The resultant solutions were transferred into Teflon lined hydrothermal reactor and kept for 8 h at 120 °C. A black-coloured product was obtained by filtration and successive drying method.

2.4 Physicochemical Analysis

X-ray diffraction (XRD) patterns of the electrocatalyst were recorded with D2 PHASER, Bruker, Germany using Cu Kα radiation (λ = 0.15418 nm). Raman spectra of the electrocatalysts were performed in a 100 nm sample spot size at a constant laser wavelength of 532 nm using Witec alpha 300 R. Field emission scanning electron microscopy (FE-SEM) image was collected from ∑igma HD, Carl Zeiss, Germany. High-resolution transmission electron microscopy (HR-TEM) images were recorded with JEM 2100 h-TEM (Make JEOL, Japan). X-ray photoelectron spectroscopy (XPS) was carried out with Thermo Shimadzu ESCA 3400 by monochromatic X-ray source.

2.5 Electrode Fabrication

Catalytic ink was composed of ~5 mg of electrode material and 5 mL of stock solution (contain ~100% ethanol and 0.4 volume percentage of Nafion®, 10 wt percentage of carbon black, and DI water) in an ultrasonic bath sonicator for 45 min. Thereafter, the catalytic ink was deposited over the graphite rod electrode with a catalytic loading of 0.5 mg cm^{-2} having diameter 6 mm which again dried under room temperature at around 298 K. The electrochemical analysis was performed at 298 K using potentiostat/galvanometer (PARSTATE 4000) at 1 M KOH (pH ~ 13) and 0.5 M H$_2$SO$_4$ (pH ~ 1) electrolyte, respectively. The carbon rod electrode and Ag/AgCl electrode (saturated KCl solution) were used as the counter electrode and reference electrode, respectively.

All the electrochemical data were converted into the reversible hydrogen electrode (RHE) scale by using the following electrochemical equation: [2, 5]

$$E_{\text{RHE}} = E_{\text{Ag/Agcl/Sat.KCl}} + 0.059\text{pH} + 0.197 \tag{1}$$

A number of voltammetric cycles were collected at 100 mVs^{-1} scan rate prior to record the LSV plot. The current densities values were obtained by dividing the current response value with the geometric area of the working electrode. The linear scan voltammetry (LSV) was performed at low scan rate of 5 m Vs^{-1} to avoid electric double-layer charging current. The series/uncompensated resistance is eliminated by iR correction method. The Tafel slope value is acquired from the Tafel equation (2). [2, 5]

$$\eta = a + b \log j \tag{2}$$

The electrochemical parameters like η, j, and b represent the overpotential, current density, and Tafel slope, respectively. For HER, the overpotential (η) was obtained by subtracting potential from zero ($\eta = 0 - E_{\text{RHE}}$) [2, 5, 20].

The electrochemical active surface area (ECSA) and the roughness factor (RF) were calculated from the non-faradic capacitive current related to electrochemical double-layer capacitance (C_{dl}) values collected from the following equations [2, 5, 20]:

$$\text{ECSA} = \frac{C_{\text{dl}}}{C_{\text{s}}} \tag{3}$$

$$\text{RF} = \frac{\text{ECSA}}{\text{Geometric Area of Electrode}} \tag{4}$$

C_{s} is the specific capacitance of an automatically smooth planer surface of the working electrode. The area normalized specific capacitance was found to be 40 and 35 μFcm^{-2} in 1 M KOH and 0.5 M H$_2$SO$_4$, respectively [2, 5, 20, 21]. The C_{s} value of the electrocatalyst was measured from the multiple CV curves within a

specific potential window at different scan rates (ν). The specific capacitance values of the electrocatalyst were ascribed from Δj versus ν plot where Δj values were obtained from half of the difference between the anodic and cathodic current density (j_a and j_b).

$$\Delta j = (j_a - j_b)/2 \tag{5}$$

The chronoamperometric study was carried out at a fixed working potential to understand the long-term permanence of the electrocatalyst at different electrolyte (acidic and alkaline) medium. Electrochemical impedance spectroscopy (EIS) was performed within 10^5 to 0.1 Hz frequency range to investigate the dynamics related with the electrochemical changes that occur during the HER process at the electrode and electrolyte interface. Nyquist plot was performed after EIS analysis, and the Randles equivalent circuit model was fitted by using Z view® software (Scribner Associates Inc. USA).

3 Result and Discussion

3.1 Physicochemical Analysis

The crystal structure of the electrocatalyst was investigated by XRD analysis (Fig. 1). The XRD pattern of GO consisted of (001) and (100) crystal planes (Fig. 1a). The appearance of (100) diffraction peak indicated that the surface of GO was not fully interconnected with the oxygen functionalities [22]. The chemical reduction of GO in VNMSG was confirmed by the appearance of a broad (002) peak at $2\theta \approx 24°$ (Fig. 1b, f). The wide (002) diffraction peak suggest that the reduced GO (rGO) was amorphous in nature as confirmed by the HR-TEM and FE-SEM image analysis (Fig. 1f). The diffraction patterns of VNMSG at $2\theta \approx 14.05, 33.50, 39.82$, and $58.52°$ were ascribed as the (002), (100), (103), and (110) lattice planes of hexagonal MoS$_2$ crystal structure as demonstrated in Fig. 1b, c [2, 5]. Therefore, the XRD pattern of VNMSG matched well with the JCPDS card no #77–1716. A small shift in (002) peak position of VNMSG can be ascribed by the negligible change in lattice parameters on V and N co-doping in MoS$_2$ (Fig. 1d, e) [2, 5, 18]. Thiourea acting as the sulphide source of MoS$_2$ and reducing agent for GO to rGO conversion by H$_2$S formation during the solvothermal method. The broad diffraction peak of rGO in composite structure is attributed to the formation of stacked rGO sheets [23]. These observations suggested that the rGO nanosheets controlled nucleation and subsequent growth of MoS$_2$ over the conducting scaffold.

The existence of rGO in the VNMSG was investigated with Raman spectroscopy as depicted in Fig. 2a–c. Two characteristic peaks of hexagonal MoS$_2$ appeared at ~410 and 380 cm^{-1} in both MoS$_2$ and VNMSG composite belong to A$_{1g}$ (out of plane vibration of S atom) and E$^1_{2g}$ (in-plane Mo–S phonon mode) Raman modes
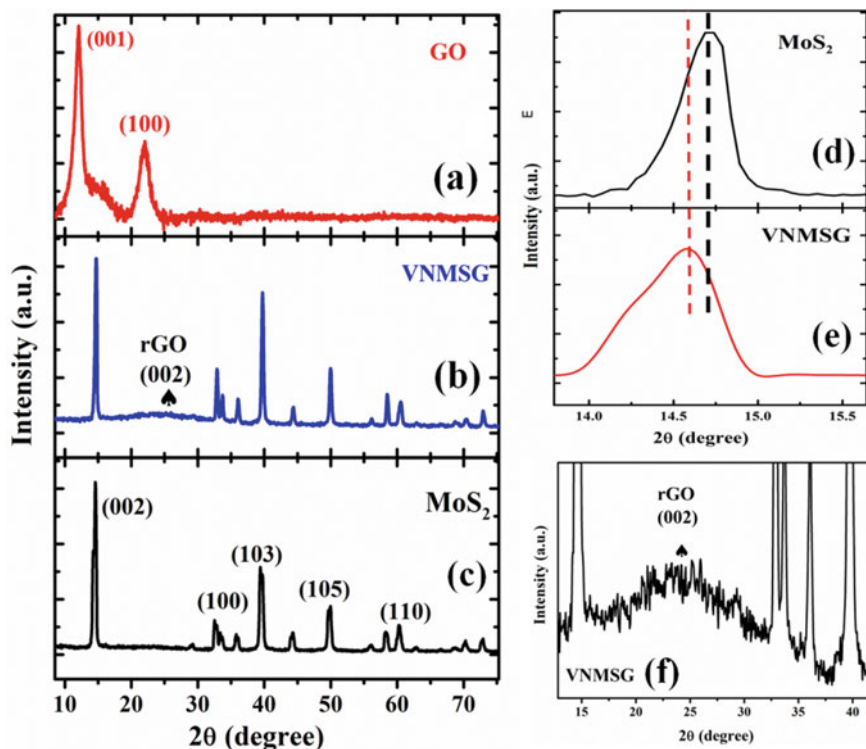
Fig. 1 **a–c** XRD pattern of graphene oxide, VNSMG, MoS_2; **d, e** (002) peak position of MoS_2, and VNMSG; **f** (002) crystal plane of VNMSG

(Fig. 2a, f) [2, 5, 18]. V and N co-doping in MoS_2 hardly reveal any additional peak in the Raman spectra conforming the successful formation of doped MoS_2. The shift in Raman modes (A_{1g} and E^1_{2g}) in VNMSG compared to pure MoS_2 confirmed the formation of lattice distortion due to the V and N dual doping in MoS_2 [2]. The lattice mismatch in VNMSG is observed due to the formation of V–S and Mo–N bonds in the MoS_2 crystal structure leading to the formation of stress in the VNMSG composite. In addition, the peak at ~1350 cm^{-1} (random agreement of graphite crystallites) is called the D-band and at ~1580 cm^{-1} (stretching vibration of sp^2 hybridized C atoms) called the G-band appeared in VNMSG and GO as shown in Fig. 2d, e [22, 23]. A gradual increase in intensity of the D to G-band ratio (I_D/I_G) in GO (value: 0.72) and VNMSG (value: 0.92) as shown in Fig. 2g. The higher I_D/I_G ratio confirmed that more sp^2 domains were formed indicating the defect structure of rGO in VNMSG (Fig. 2g). It is speculated that the catalytic performance of VNMSG was significantly improved with increasing the defect.

XPS was used to examine the surface structure, chemical state, and electronic interaction in the VNMSG composite. XPS survey spectra analysis confirmed that V and N atoms were successfully doped in the MoS_2 crystal lattice (Fig. S1). The atomic
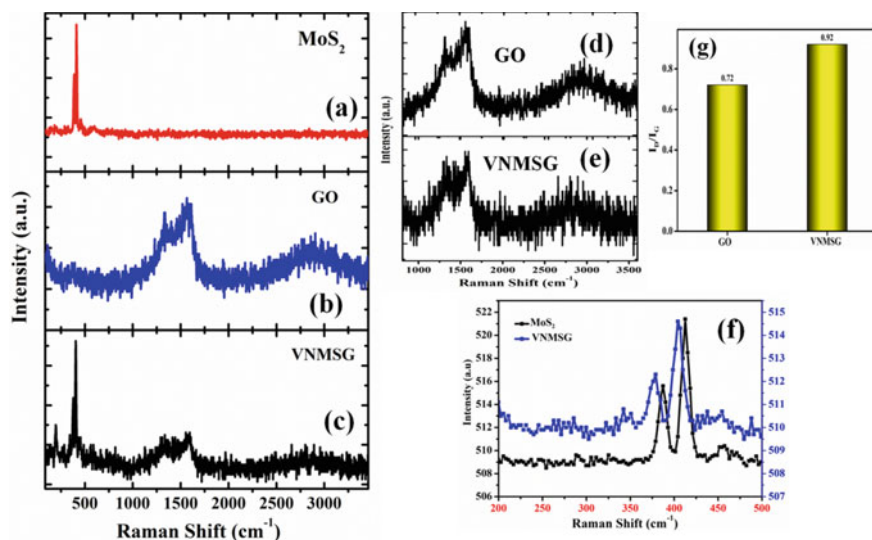
Fig. 2 **a**–**c** Raman spectra of MoS$_2$, GO, and VNSMG; **d**, **e** Raman spectra at selected region of GO and VNSMG; **f** Raman spectra at selected region of MoS$_2$ and VNSMG; **g** calculated I_D/I_G ratio of GO and VNSMG

percentage ratio of Mo and S implied that MoS$_2$ was formed in the VNMSG during the solvothermal synthetic process. The V doping percentage in MoS$_2$ was higher compared to the N, which can be attributed to the size of the dopant, the particular reaction conditions, and the source of the dopant. XRD and Raman spectra suggested that GO controlled the growth of MoS$_2$ which is reflected in Mo3d XPS spectra (Fig. 3b). The deconvoluted XPS spectrum of Mo3d of VNMSG was composed of four characteristic peaks. Two intense peaks of Mo 3d5/2 (229.5 eV) and Mo 3d3/2 (232.7 eV) suggested the presence of MoS$_2$ in VNMSG while peak of Mo 3d (235.9 eV) at high binding energy corresponds to MoO$_3$ or MoO$_4^{2-}$ formation during the solvothermal synthesis method (Fig. 3b) [2, 13, 15]. Due to the successful formation of composite structure, the small shift of the Mo3d peak position indicated the electron transfer phenomenon. Mo^{6+} oxidation state appeared due to the partial oxidation of Mo atoms at MoS$_2$ edges and defects formation in the MoS$_2$ crystal lattice during the composite structure formation. This occurrence implied the formation of a synergistic effect in VNMSG indicating the better catalytic efficiency. The deconvoluted S2p1/2 and S2p3/2 peaks at 162.70 and 163.92 eV for VNMSG appeared at relatively higher binding energy region than pure MoS$_2$ indicting the successful formation of the nanocomposite with rGO (Fig. 3c) [2, 24]. A small peak located at ~168.1 eV belongs to the oxidized sulphur which may be due to the composite structure formation. The low intensity of two doublet peaks at ~524.44 and 517.01 eV of V2p spectra in VNMSG suggested that V was successfully doped in VNMSG as shown in Fig. 3d [5]. The S/Mo total area ratio was calculated from the fitted S 2p and Mo 3d core-level spectra of MoS$_2$ and VNMSG (Fig. 3f). The
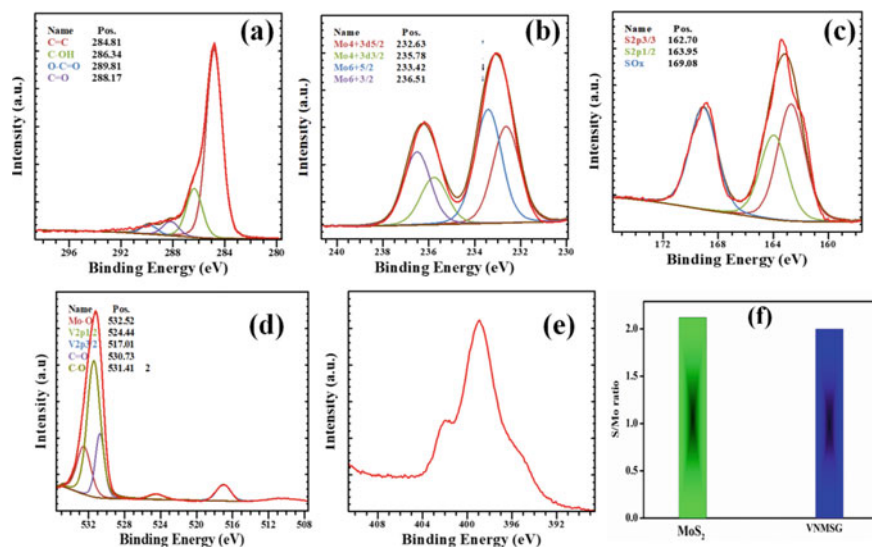
Fig. 3 Deconvoluted XPS data of C1s (**a**), Mo3d (**b**), S2p (**c**), V2p (**d**), and N1s (**e**), respectively

S/Mo ratio of VNMSG was lower than pure MoS_2 which suggested a creation of S vacancies in the VNMSG on doping. It is well evident that S vacancies improved the HER performance by activation of active basal plane and defect formation at edge sites of MoS_2. The shifts in deconvoluted V2p XPS spectra towards higher binding energy in composite can be attributed to the presence of electronic interaction between V-doped MoS_2 and rGO conducting scaffold [5, 25]. The intensity of V2p peak was lower than the O1s XPS spectra. Interestingly, the deconvoluted O1s spectra composed of characteristic peak of M–O, C=O, and C–O bond as present in VNMSG composite structure (Fig. 3d, S2). Figure 3e shows the presence of N 1 s in VNMSG and the absence of C–N bond in the deconvoluted XPS spectra of C1s implied that MoS_2 was doped with N. Therefore, nitrogen-doped rGO was not formed in the solvothermal method. The deconvoluted C1s spectra of VNMSG represented the presence of non-oxygenated C–C double bond along with other functional groups like C–C/C–H, C=O/O–C–O in rGO nanosheets in VNMSG (Fig. 3a) [23–26].

Morphological study showed that MoS_2 nanoflower was grafted over the rGO nanosheets. The rGO nanosheets present as a conducting template and controlled the growth of MoS_2 (Fig. 4a, b). The MoS_2 nanosheets were embedded on the rGO sheets through interfacial van der Walls interaction. TEM image of VNMSG showed a homogenous growth of MoS_2 over the conducting rGO scaffold that enhanced the overall active surface area of the electrocatalyst and reduced the agglomeration possibilities of MoS_2 (Fig. 4d). It is also assumed that the interfacial interaction between the doped MoS_2 and rGO sheets definitely modified the electronic structure and band alignment of the composite structure; thereby, electrochemical performance of the VNMSG composite was modified significantly. The IFFT pattern in R1 region
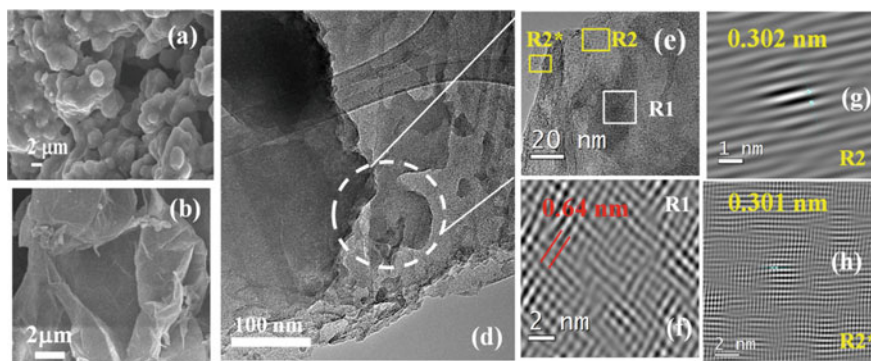
Fig. 4 FESEM image of **a** VNMSG, **b** GO; **d** TEM image of VNMSG, **e** HR-TEM image of VNMSG, **f** IFFT pattern of R1 represent (002) crystal plane of MoS$_2$; **g**, **h** IFFT pattern of R2 and R2* represent (002) plane of rGO nanosheets

indicates the presence of (002) crystal plane of MoS$_2$ in VNMSG composite (Fig. 4e, f) [2, 5, 13, 15]. The (002) crystal plane of rGO appeared in R2 and R2* regions implying the successful formation of the composite structure (Fig. 4g, h) [25, 26]. HR-TEM image analysis recommended a strong interfacial interaction present within the rGO nanosheets and MoS$_2$ which confirmed the existence of synergistic interaction in VNMSG nanocomposite. The HR-TEM image failed to confirm the formation of defect region within the composite structure. However, Raman and XPS analysis suggest the formation of defect-rich composite structure.

3.2 Electrochemical Analysis

The HER activity of the developed electrocatalyst was analysed in acidic and alkaline electrolyte. The polarization curves demonstrated that the catalytic performance of pure MoS$_2$ was improved upon doping and heterostructure formation. Figure 5a &6a suggested that VNMSG had lowest overpotential value than the other electrode materials. VNMSG required ~ 88 and 132 mV overpotential to attain 10 mAcm^{-2} current density [27, 28]. It is well established that the HER activity of an electrocatalyst was more facile in acidic electrolyte than in alkaline electrolyte as confirmed by the polarization curve (Table 1–2). The order of electrochemical performance depends on the electronic and structural modification of MoS$_2$ during synthesis. The enhanced electrochemical performance of VNMSG can be attributed to the synergistic interaction within the rGO nanosheets and MoS$_2$. However, the doping inside the MoS$_2$ has a potential impact on the electronic modification and improved catalytic activity. The adsorption–desorption performance of the electrocatalyst was augmented significantly upon doping inside the MoS$_2$ and composite structure formation with the rGO sheets. The enhanced adsorption–desorption ability of VNMSG can be attributed to
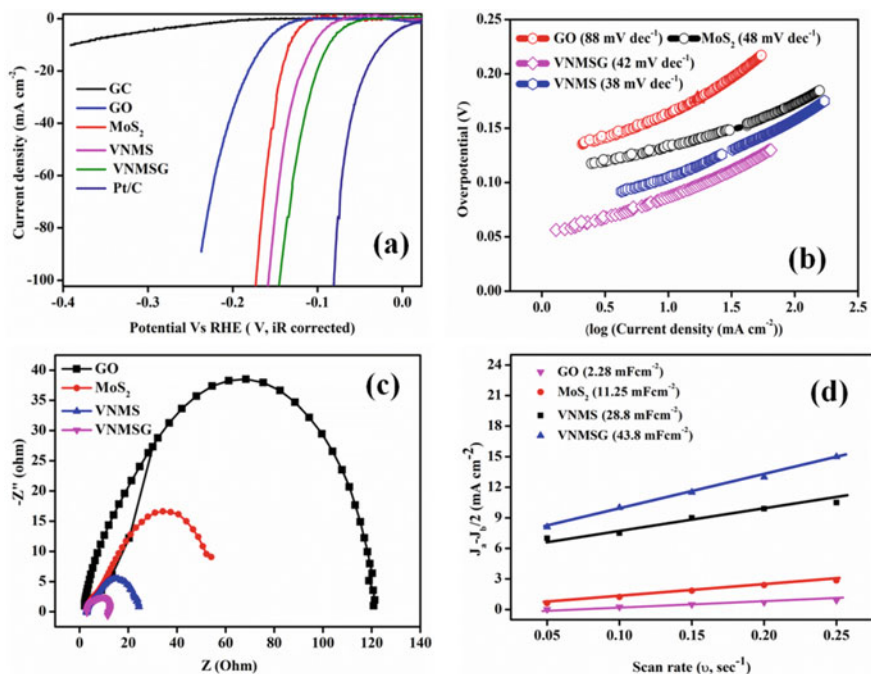
Fig. 5 **a** LSV plot; **b** Tafel slop; **c** EIS plot **d** ECSA of the electro catalysts (electrochemical tests were carried out in 0.5 M H_2SO_4 medium)

Table 1 Electrochemical performance for HER in acidic medium

Material	Electrolyte medium	Overpotential @ 10 mA cm^{-2} current density	Tafel slope (mV dec^{-1})	Exchange current density (mAcm^{-2})
GO	Acidic	163	88	3.02×10^{-2}
MoS$_2$	Acidic	134	48	6.5×10^{-2}
VNMS	Acidic	106	42	6.3×10^{-2}
VNMSG	Acidic	89	38	9.5×10^{-2}

Table 2 Electrochemical performance for HER in alkaline medium

Material	Electrolyte medium	Overpotential @ 10 mA cm^{-2} current density	Tafel slope (mV dec^{-1})
GO	Alkaline	191	208
MoS$_2$	Alkaline	146	145
VNMS	Alkaline	139	142
VNMSG	Alkaline	133	92
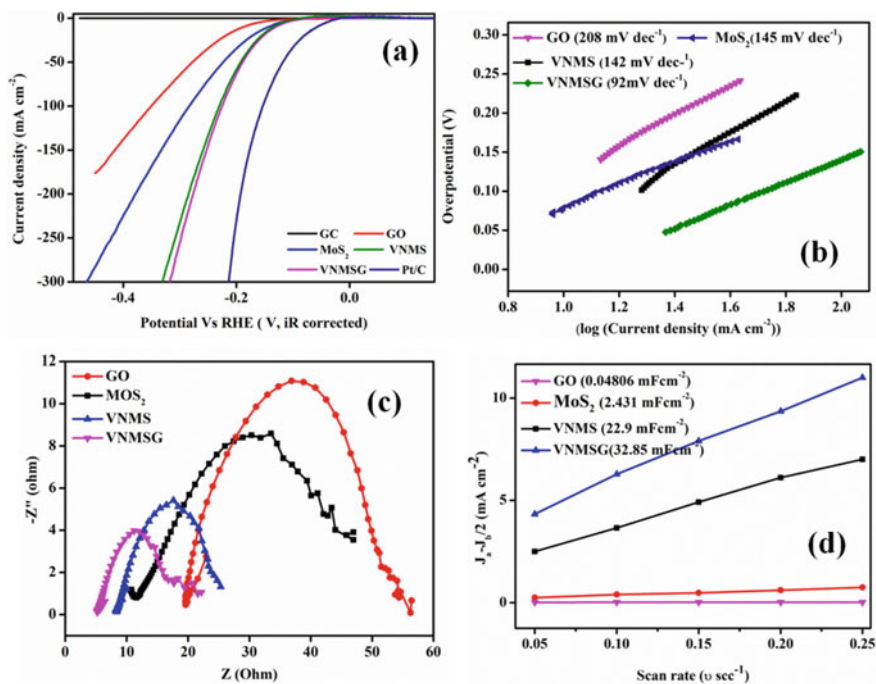
Fig. 6 **a** LSV plot; **b** Tafel slop; **c** EIS plot, **d** ECSA of the electrocatalysts (electrochemical tests were carried out in 1 M KOH medium)

the exposed surface active sites. The rGO nanosheets assisted to graft the MoS$_2$ nanopetals on its surface; thereby, the effective active surface are of the VNMSG was increased. The ECSA (Figs. 5d and 6d) values calculated from the CV plots (Figs. S3 and S4) confirmed the improvement in surface adsorption performance upon composite formation. In addition, V and N co-doping in MoS$_2$ lattice structure developed defects, thereby more exposed active sites were formed (Tables S4 and S5).

Tafel slope is considered as leading parameters in HER which signify the potential require enhancing the current response by an order of 10 times than the initial. Therefore, a low Tafel slope suggests a faster HER kinetics implies a better catalytic ability. Tafel plots were acquired from the linear region of the LSV plot as depicted in Figs. 5b and 6b. Interestingly, the Tafel slope values of the developed electrocatalyst were calculated from the linear region from Tafel equation ($\eta = b \log j + a$, where b = Tafel slope, j = current density). The Tafel slope value for VNMSG composite was smallest among other electrocatalyst in acidic and alkaline pH (Tables S1 and S2). The lowest Tafel slope value of VNMSG suggested a better catalytic performance. Above all the small Tafel slope of VNMSG nanohybrid was beneficial for catalytic application as it leads to a rapid increase in HER rate with the change in overpotential. The HER process includes Volmer step, Heyrovsky step, and Tafel steps, respectively.

The Volmer step allied with proton absorption is suggesting the rate-limiting step with a slope of $\sim$120 mVdec^{-1} while Heyrovsky and Tafel steps should recommend $\sim$40 and $\sim$30 mVdec^{-1} slope value to be a rate-limiting one [2, 5, 20, 29, 30]. Therefore, Tafel slope values of the synthesized electrocatalyst suggested a Volmer–Heyrovsky reaction mechanism. However, the electrochemical adsorption and desorption was considered as the rate-limiting step in both alkaline and acidic pH, respectively. The low Tafel slope values of VNMSG were recognized by the strong electronic coupling appeared due to interfacial interaction with the rGo nanosheets and V, N-codoped MoS$_2$. The charge transfer resistance (R_{ct}) values of the electrocatalyst supported the catalytic order in both acidic and alkaline medium (Figs. 5c and 6c) [31]. The improved Rct values can be ascribed as the combination effect of doping in MoS$_2$ and composite structure formation (Figs. S5 and S6). The synergistic effect developed in VNMSG increased the charge carrier density of VNMSG thereby the H adsorption–desorption process is getting augmented as reflected in the polarization plot [29]. The improved charge carried density of VNMSG was found as the highly conducting rGO nanosheets attached with the MoS$_2$ nanoflower, thereby the overall R$_{ct}$ resistance is decreased (Tables S5 and S6).

The electrocatalytic durability of the synthesized conducting scaffold supported doped MoS$_2$ composite was checked by polarization plot before and after the 1000 CV in the acidic and alkaline medium at a fixed scan rate of 10 mVs^{-1}. The polarization curves matched closely with the initial one with a negligible change in current response at fixed overpotential (depicted in Fig. 7a, b). The chronoamperometry study was prolonged at the current density of 55 mAcm^{-2} and 15 mAcm^{-2} for $\sim$7 h in acidic and $\sim$8 h for alkaline pH, respectively. A negligible change in potential demonstrated a negligible change in electrochemical performance (depicted in Fig. 7c, d).

4 Conclusions

In summary, V and N co-doped MoS$_2$ nanopetals embedded on rGO a nanosheet was developed by a facile solvothermal synthetic method. The defect-rich VNMSG nanocomposite exhibited enhanced catalytic activity and remarkable structural stability in acidic and alkaline electrolyte. Physicochemical analysis suggested the successful formation of doped composites. In addition, V and N doping in MoS$_2$ modified the electronic structure, thereby raising the valence band structure of the doped nanocomposite to the Fermi level. HR-TEM and XPS analysis confirmed the strong interfacial interaction between rGo nanosheets and MoS$_2$ nanopetals. Therefore, the participation of rGO nanosheets improved the overall conductivity of the composite, thereby promoting the HER process. The excellent HER performance was attributed to the large number of active surface sites, which can be ascribed by the high active site density and relatively large exposed surface area. The participation of rGO nanosheets significantly improved the catalytic durability in acidic and alkaline media. Most importantly, the synergistic action between rGO nanosheets and MoS$_2$ nanopetals facilitated to enhance the HER performance of VNMSG composites.
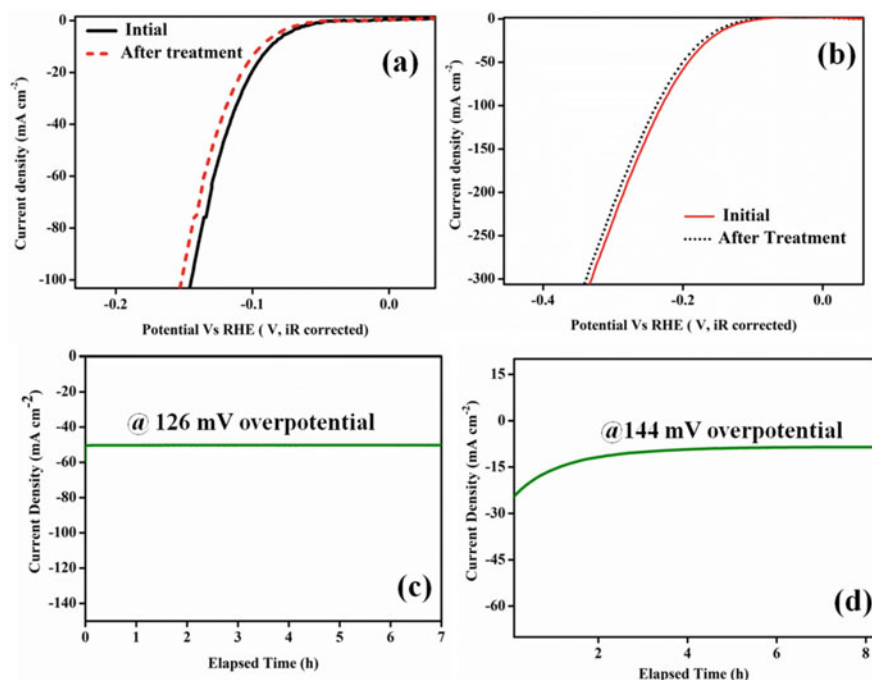
Fig. 7 **a**, **b** LSV plot of VNMSG before and after 1000 cycle at a scan rate of 10 mVs^{-1} in 0.5 M H$_2$SO$_4$ and 1 M KOH, respectively. **b** Chronoamperometric study in 0.5 M H$_2$SO$_4$ of VNMSG at 126 mV overpotential for ~7 h, **d** chronoamperometric study in 1 M KOH of VNMSG at 144 mV overpotential for ~8 h

References

1. Chu S, Majumdar A (2012) Opportunities and challenges for a sustainable energy future. Nature 488:294–303
2. Bolar S, Shit S, Murmu NC, Samanta P, Kuil T (2021) Activation strategy of MoS$_2$ as HER electrocatalyst through doping-induced lattice strain, band gap engineering, and active crystal plane design. ACS Appl Mater Interfaces 13:765–780
3. El-Emam RS, Ozcan H (2019) Comprehensive review on the techno-economics of sustainable large-scale clean hydrogen production. J Clean Prod 220:593–609
4. Zhao G, Rui K, Dou SX, Sun W (2018) Heterostructures for electrochemical hydrogen evolution reaction: a review. Adv Funct Mater 28:1803291
5. Bolar S, Shit S, Kumar S, Murmu NC, Ganesh S, Inokawa H, Kuila T (2019) Optimization of active surface area of flower like MoS$_2$ using V-doping towards enhanced hydrogen evolution reaction in acidic and basic medium. Appl Cat B 25:432–442

6. Guo Y, Park T, Yi JW, Henzie J, Kim J, Wang Z, Jiang B, Bando Y, Sugahara Y, Tang J, Yamauchi Y (2019) Nano architectonics for transition metal sulfide-based electrocatalysts for water splitting. Adv Mater 31:1807134

7. Wu Z, Song M, Zhang Z, Wang J, Wang H, Liu X (2019) Porous two dimensional layerd molybdenum compounds coupled with N-doped carbon based electrocatalysts for hydrogen evolution reaction. Appl Surf Sci 465:724–729

8. Sun H, Yan Z, Liu F, Xu W, Cheng F, Chen J (2020) Self-supported transition-metal-based electrocatalysts for hydrogen and oxygen evolution. Adv Mater 32:1806326

9. Chandrasekaran S, Yao L, Deng L, Bowen C, Zhang Y, Chen S, Lin Z, Peng F, Zhang P (2019) Recent advances in metal sulfides: from controlled fabrication to electrocatalytic, photocatalytic and photoelectrochemical water splitting and beyond. Chem Soc Rev 48:4178–4280

10. Noor S, Sajjad S, Leghari SAK, Flox C, Kallio T (2020) Efficient electrochemical hydrogen evolution reaction and solar activity via bi-functional GO/Co_3O_4-TiO_2 nano hybrid structure. Int J Hydrogen Energy 45:17410–17421

11. Eftekhari A (2017) Electrocatalysts for hydrogen evolution reaction. Int J Hydrogen Energy 42:11053–11077

12. Zhang X, Du Z, Luo X, Sun A, Wu Z, Wang D (2018) Template-free fabrication of hierarchical MoS_2/MoO_2 nanostructures as efficient catalysts for hydrogen production. Appl Surf Sci 433:723–729

13. Luo Z, Ge J, Liu C, Xing W (2020) Engineering the HER catalytic behavior of heteroatom-doped molybdenum disulfide via versatile partial cation exchange. J Energy Chem 41:15–19

14. Wei C, Wu W, Li H, Lin X, Wu T, Zhang Y, Xu Q, Zhang L, Zhu Y, Yang X, Liu Z, Xu Q (2019) Atomic plane-vacancy engineering of transition-metal dichalcogenides with enhanced hydrogen evolution capability. ACS Appl Mater Interfaces 11:25264–25270

15. Wang D, Zhang X, Bao S, Zhang Z, Fei H, Wu Z (2017) Phase engineering of a multiphasic 1T/2H MoS_2 catalyst for highly efficient hydrogen evolution. J Mater Chem A 5:2681–2688

16. Linghu Y, Wu C (2020) Strain engineering the behaviors of small molecules over defective MoS_2 monolayers in the 2H and 1T0 phases. J Mater Sci 55:10643–10655

17. Zhao M, Ma X, Yan S, Xiao H, Li Y, Hu T, Zheng Z, Jia J, Wu H (2020) Solvothermal synthesis of oxygen-incorporated MoS_2-x nanosheets with abundant under coordinated Mo for efficient hydrogen evolution. Int J Hydrog Energy 45:19133–19143

18. Dong W, Liu H, Liu X, Wang H, Li X, Tian L (2021) Defective-MoS_2/rGO heterostructures with conductive 1T phase MoS_2 for efficient hydrogen evolution reaction. Int J Hydrog Energy 46:9360–9370

19. Ghosh S, Samanta P, Samanta P, Murmu NC, Kuila T (2020) Investigation of electrochemical charge storage efficiency of $NiCo_2Se_4$/RGO composites derived at varied duration and its asymmetric supercapacitor device. Energy Fuels 34:13056–13066

20. Bolar S, Shit S, Murmu NC, Kuila T (2020) Doping-assisted phase changing effect on MoS_2 towards hydrogen evolution reaction in acidic and alkaline pH. ChemElectroChem 7:336–346

21. McCrory CCL, Jung S, Peters JC, Jaramillo TF (2015) Benchmarking hydrogen evolving reaction and oxygen evolving reaction electrocatalysts for solar water splitting devices. J Am Chem Soc 137(13):4347–4357

22. Kuila T, Bhadra S, Yao D, Kim NH, Bose S, Lee JH (2010) Recent advances in graphene based polymer composites. Prog Polym Sci 35:1350–1375

23. Smith AT, LA Chance AM, Zeng S, Liu B, Sun L (2019) Synthesis, properties, and applications of graphene oxide/reduced graphene oxide and their nanocomposites. Nano Mater Sci 1:31–47

24. Lu X, Lin Y, Dong H, Dai W, Chen X, Qu X, Zhang X (2017) One-step hydrothermal fabrication of three-dimensional MoS_2 nanoflower using polypyrrole as template for efficient hydrogen evolution reaction. Sci Rep 7:42309

25. Kuila T, Mishra AK, Khanra P, Kim NH, Lee JH (2013) Recent advances in the efficient reduction of graphene oxide and its application as energy storage electrode materials. Nanoscale 5:52–71

26. Dreyer DR, Park S, Bielawski CW, Ruoff RS (2010) The chemistry of graphene oxide. Chem Soc Rev 39:228–240

27. Li C, Baek JB (2020) Recent advances in noble metal (Pt, Ru, and Ir)-based electrocatalysts for efficient hydrogen evolution reaction. ACS Omega 5(1):31–40
28. Li Z, Ge R, Su J, Chen L (2020) Recent progress in low Pt content electrocatalysts for hydrogen evolution reaction. Adv Mater Interface 7(14):2000396
29. Shinagawa T, Esparza ATG, Takanabe K (2015) Insight on Tafel slopes from a microkinetic analysis of aqueous electrocatalysis for energy conversion. Sci Rep 5:13801
30. Bolar S, Shit S, Murmu NC, Kuila T (2020) FeNiSx@MoS$_2$ heterostructure: a bioinspired nonprecious electrocatalyst for the hydrogen evolution reaction in acidic and basic media. Chemelectrchem 7:3324–3335
31. Wei ZW, Wang HJ, Zhang C, Xu K, Lu XL, Lu TB (2021) Reversed charge transfer and enhanced hydrogen spillover in platinum nanoclusters anchored on titanium oxide with rich oxygen vacancies boost hydrogen evolution reaction. Angew Chem Int Ed 60:16622–16627

Modelling of an Improved Biomass Cook Stove for Rural Application

Himanku Bordoloi, Partha Pratim Dutta, and Raktim Jyoti Barpatra Gohain

1 Introduction

Varieties of fossil fuels have been widely employed for heat and power generation in various industrial and home purposes. However, it has a substantial impact on our ecosystem due to its toxic emissions. Biomass is a suitable sustainable energy source for overcoming the issue. It has been seen that biomass is sometimes burnt in an inefficient cook stove in the rural area. However, it is regarded as a limited thermal energy source. Cengel et al. [1] suggested a simple wood burning stove consisting of an enclosed metal box made of material like cast iron, with opening doors in the front for loading the fuel an enclosed metal box made of material like cast iron. It has a little smokestack called a flue to exhaust CO_2, steam, smoke, and other pollutants [1]. A wood burning stove may be used to supply heat in a single room, like a traditional coal fireplace in the developed countries. Therefore, an improved biomass furnace is a more advanced alternative for heating the developed countries. Biomass furnace may be a more advanced alternative for heating the entire building for cold region. Fichet et al. [2] proposed a furnace's ability to run on a specific type of biomass which is decided by its size, density, energy content, moisture content, and other factors. Because any fuel used in the system must be able to flow into the combustion system, the size of the chip is also a crucial consideration for biomass fuel.

2 Research Background

There have been many research works done on biomass cook stoves. This research part has been categorized into four parts. The first part is about various improved

H. Bordoloi (✉) · P. P. Dutta · R. J. B. Gohain
Department of Mechanical Engineering, School of Engineering, Tezpur University, Tezpur, India
e-mail: himankubordoloi666@gmail.com

designs of biomass cook stove, the second section discusses performance analysis of biomass cook stove based acquired from water boiling test (WBT), the third section discusses cook stove performance analysis based on numerical analysis, and the fourth part is related to pollution control.

Fichet et al. [2] had certain limitations in their efforts to develop a valid baseline CFD model. Since they only anticipated, CO and CO_2 emissions and they also had problems in predicting NO_X emissions. Quist et al. [3] studied different enhanced biomass cook stove designs according to measurements, input data uncertainties, etc. They calculated the propagation uncertainty for a simple brick channel cook stove. They discovered that the LHV of wood and char, moisture content, and water temperature changes all contributed to a significant portion of the variability in efficiency. Kshirsager et al. [4] investigated the use of multi-response robust parameter design for a hybrid draft biomass cook stove performance optimization. They predicted a maximum overall efficiency enhancement of up to 30%, as well as reductions in CO and PM2. 5 predicted a reduction of up to 1.8 and 20 mg/MJ. Djurovi et al. [5] used suitable furnace dimensioning for reducing high investment costs and they were able to reach an improved CO emission. Kumar et al. [6] examined biomass cook stove design, development, and technological advancement. The effects of traditional biomass burning methods on emissions and health susceptibility were studied and environmental influence. Tryner et al. [7] studied five natural-draft, top-lit-up-draft (TLUD) semi-gasifier cook stove configurations. They tested two biomass fuels to see how the design of the stove and the fuel source affected efficiency and pollutants. They discovered that pollutants and efficiency differed significantly depending on stove design and fuel type, and that the transient increases in co-emissions were common. It was moreover linked to refuelling.

Lombardi et al. [8] tried for eliminating harmful emissions from biomass combustion. Traditional cooking methods, as we all know, emit CO and particulate matter (PM). This can cause major respiratory difficulties, especially in children and women. To reduce harmful emissions from the catalytic oxidation process, they used a low-cost potassium-based catalyst in a chimneyless biomass burner. Rupakheti et al. [9] investigate inside the two types of kitchens. Fine particulate matter (FPM) and black carbon (BC) concentrations were continually changing. Under actual cooking particles, they were divided and attached to the main house. A field survey was conducted on the types of kitchens, fuel used, and cook stove before monitoring of pollutants. Sidhu et al. [10] examined several types of fuel stove combinations used for cooking in Punjab, India, the emission variables and non-CO_2 green gas (GHG) emissions were calculated. When compared to other fuels, they discovered that cow dung cake performed the worst.

Based on the WBT test, Bhuyan et al. [11] reviewed an industrial furnace. They compared the thermochemical characteristics of biomass with coal. They discovered that co-firing biomass and coal reduced SO_x and NO_x pollutants significantly. The proper biomass injection with complete information on ignition properties was also necessary to manage heating system efficiency, fabrication, and burnouts. Kare et al. [12] reviewed the WBT for evaluation of seven biomass fuels for six stoves. The results achieved that for some cookware types, certain biomass fuels would be more

efficient. Jain et al. [13] investigated the development of an energy utilization test for a biomass cook stove. They used the water boiling test to assess performance. For WBT, they used a fan as a primary airflow supply and multiple holes in the top of the stove as a secondary airflow source. They discovered that thermal efficiency and other parameters exhibited time-dependent behaviour at various airflow rates. They discovered a best airflow recipe depending on the results of the tests. Silva et al. [14] in their work conducted a study using CFD modelling to better understand combustion characteristics and flue gas emissions. The findings suggested that the furnace's mixing of gases and combustion air could be enhanced.

Barpatra Gohain et al. [15, 16] tested a better quality biomass cook stove. They saw thermal efficacy 33–35% WBT of the improved cook stoves. Bardalai et al. [17] studied bamboo and coal co-gasification. They saw combustion zone flame propagation rate better with (10–20) % of coal. Dutta et al. [18, 19] characterized samples of biomass. *Psidium guajava* had the heating value maximum (18.403 MJ kg^{-1}), (18.400 MJ kg^{-1}) was with bamboo chip, and *Ficus lepidosa* had (15.952 MJ kg^{-1}) the least. Dutta et al. [20, 21] experimented biomass gasifier for drying black tea with a producer gas burner. They found 6.274 MJ kg^{-1} as energy consumption (specific) with biomass for the tea dryer. The uprooted tea shrubs (*Camellia sinensis (L.) O. Kuntze*) derived producer gas had calorific values 18.50 and 4.2 MJ m^{-3}. The gasification efficiency (cold) was 65% with the tea shrubs. *Shisham* gave heating value (average) 4.83 MJ Nm^{-3} of producer gas [22].

3 Objective

The objective of the paper is thermal performance modelling of an improved biomass cook stove at different firepower. The design model is intended to compare with the contemporary improved biomass cook stoves.

4 Methodology and Approach

4.1 The Model

The model was designed in order to create a user-friendly mathematical tool for predicting the performance of an improved biomass cook stove. Figure 1 shows combustion chamber with grate, where the biomass was being burned and pot is showed at the upper part of combustion chamber. The entry for the primary air essential for the combustion process is same as the fuel entry gate.

Figures 1, 2 and 3 describe the designed cook stove's front and top views. Figure 1 shows the 3D view (front) of the cook stove with a pot at the upper part. Figure 2 shows the 3D view (top) of the cook stove with a pot. Figure 3 shows the front view
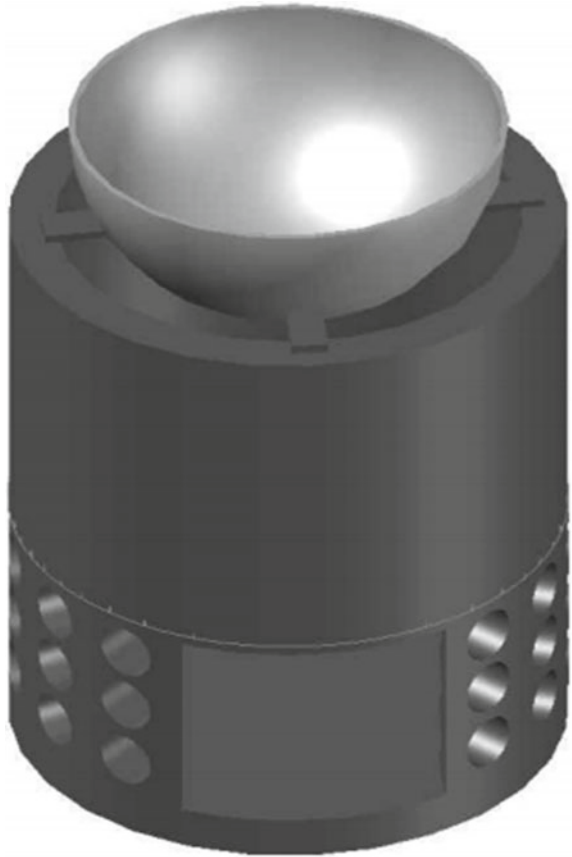
of the design cook stove with a chimney and hood. Figure 3 shows five zones. Zone 1 is the combustion zone whose height is 280 mm; the outer diameter is 240 mm, and the inner diameter is 200 mm. This combustion zone consists of fuel bed, fuel door, air supply ports, and grate. Zone 2 consists of 39 primary air supply ports whose diameter is 12 mm, and the fuel door and the upper part of this zone consists of fuel grate. Zone 3 is primarily made up of the pot vessel, which is situated in the combustion chamber's top part. Zone 4 is the chimney part, and zone 5 is the hood which is attached to the chimney part. The hood is used to detect emissions within the chamber.

Fig. 2 3D view (Top) of design cook stove with Pot
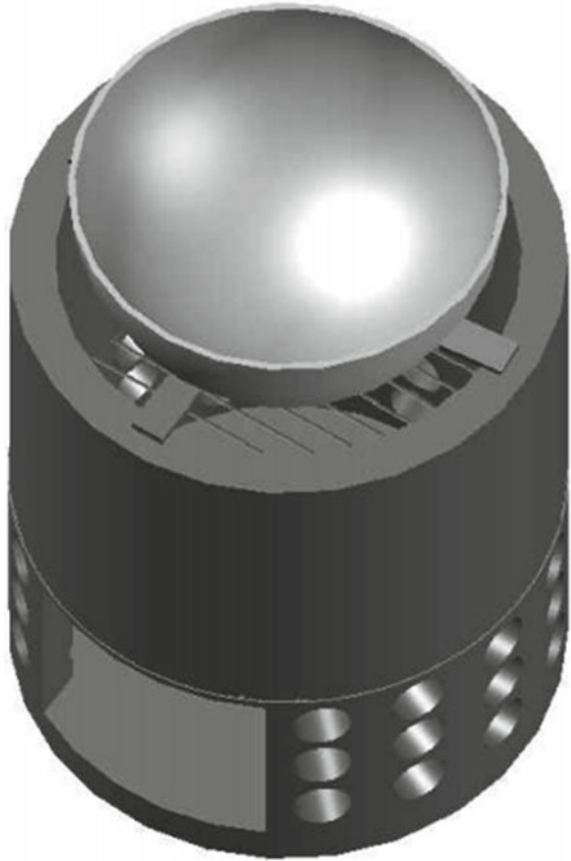
5 Mathematical Modelling Equations of Biomass Cook Stove

The mathematical equations are divided into different zones. Combustion zone, pot bottom zone, pot gap zone, and pot side zone are the zones. Kshirsagar and Kalamkar [4].

- Combustion Zone

$$\dot{Q}_{\text{char radiation}} = \frac{\sigma \times A \times \left(T_{\text{char}}^4 - T_p^4\right)}{\left(\frac{1-\varepsilon_c}{\varepsilon_c}\right) + \frac{2}{(1-F_{\text{char-pot}})}} \tag{1}$$

$$\dot{Q}_{\text{flame radiation}} = \sigma \times A \times \left(\varepsilon_g T_g^4 - \alpha_g T_p^4\right) \tag{2}$$

- Pot Bottom Zone

Fig. 3 Front view of design
cook stove
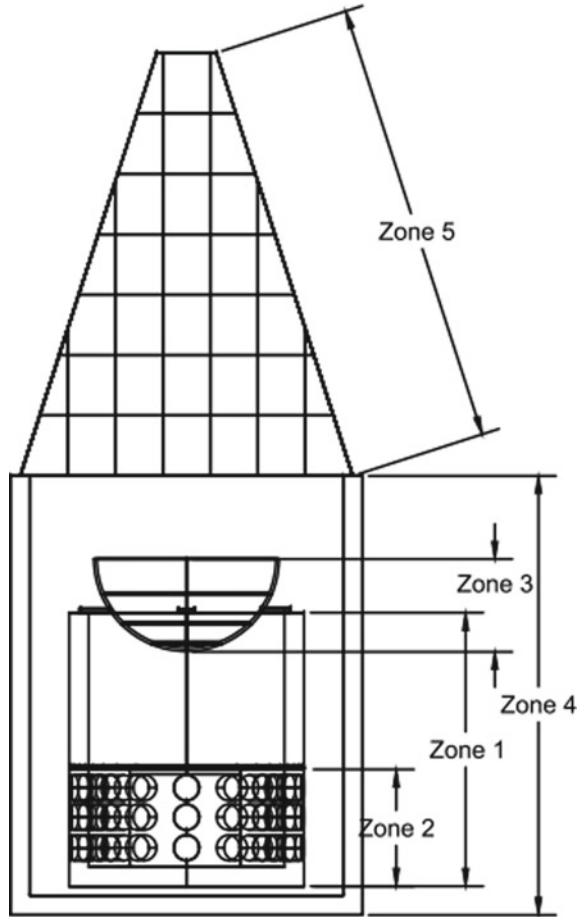
$$\dot{Q}_{\mathrm{con2}} = h_{\mathrm{bottom}} \times A \times \left\{ \left(\frac{T_g + T_e}{2} \right) - T_p \right\} \tag{3}$$

- Pot Gap Zone

$$\dot{Q}_{\mathrm{rad3}} = \sigma \times A_{\mathrm{pg}} \times \left\{ \varepsilon_3 \left(\frac{T_c + T_e}{2} \right)^4 - \alpha_3 \times T_p^4 \right\} \tag{4}$$

$$\dot{Q}_{\mathrm{con3}} = h_{\mathrm{pot\ gap}} \times A_{\mathrm{pg}} \times \left\{ \left(\frac{T_c + T_e}{2} \right) - T_p \right\} \tag{5}$$

- Pot Side Zone

$$\dot{Q}_{\text{rad4}} = \sigma \times A_{\text{side}} \times \left\{ \varepsilon_4 \left(\frac{T_c + T_o}{2} \right)^4 - \alpha_4 \times T_p^4 \right\} \tag{6}$$

$$\dot{Q}_{\text{con4}} = h_{\text{side}} \times A_{\text{side}} \times \left\{ \left(\frac{T_c + T_o}{2} \right) - T_p \right\} \tag{7}$$

Equation (1) gives the overall efficiency of the improved biomass cook stove, where different thermal losses are presented in the numerator of the mathematical expression and P is the firepower of the cook.

$$\eta_o = \frac{\dot{Q}_{\text{char radiation}} + \dot{Q}_{\text{flame radiation}} + \dot{Q}_{\text{conv2}} + \dot{Q}_{\text{rad3}} + \dot{Q}_{\text{conv 3}} + \dot{Q}_{\text{rad 4}} + \dot{Q}_{\text{conv4}}}{P}$$
$$\times 100 \tag{8}$$

where $\dot{Q}_{\text{char radiation}}$ from char bed to the pot bottom radiative heat transfer (kJ/kg of dry fuel), $\dot{Q}_{\text{char radiation}}$ from char bed to the pot bottom radiative heat transfer rate (W), $\dot{Q}_{\text{conv2}}$ convective heat transfer from pot bottom zone to the pot (kJ/kg of dry fuel), $\dot{Q}_{\text{conv 3}}$ convective heat transfer from pot gap zone to the pot (kJ/kg of dry fuel), $\dot{Q}_{\text{conv4}}$ convective heat transfer from pot side zone to the pot (kJ/kg of dry fuel), $\dot{Q}_{\text{door loss}}$ of heat radiation from the feed door opening (kJ/kg of dry fuel), $\dot{Q}_{\text{heat loss}}$ through insulation heat loss from the stove (kJ/kg of dry fuel), σ is the Steffen–Boltzmann constant (W/m^2 K^4), a combustion chamber cross-sectional area (m^2), T_{char} temperature of the char (K), T_p surface temperature of the pot (K), $F_{\text{char-pot}}$ char bed to pot bottom view factor, ε_c emissivity of the char, ε_g in combustion zone emissivity of the flue gas, T_g flame temperature/flue temperature inside the chimney (K), α_g in combustion zone absorptivity of flue gas, h_{bottom} pot bottom zone impinging jet heat transfer coefficient (W/m^2 K), T_e flue temperature at the entrance to the pot gap (K), T_c pot corner flue temperature (K), T_o at the exit temperature of the flue (K), A_{pg} pot gap area above the pot (m^2), A_{side} area of pot side (m^2), h_{side} pot side convective heat transfer coefficient (W/m^2 K), $h_{\text{pot gap}}$ pot gap zone impinging jet heat transfer coefficient (W/m^2 K), α_3 in pot gap zone absorptivity of flue gas, α_4 in pot side zone absorptivity of flue gas, ε_3 in pot gap zone emissivity of the flue gas, and ε_4 in pot side zone emissivity of the flue gas.

6 Results and Discussion

This section is divided into two sections. The first section is intended to the model's numerical analysis, which examines heat transfer within the combustion chamber. The generated model was evaluated using the commercial software ANSYS. The second section compares this model to another improved available model.

6.1 Numerical Analysis of the Model

The model was solved using the standard $(k-\varepsilon)$ turbulence model. The inlet and exit boundaries are both set to a constant mass flow rate and a constant static pressure. The primary air enters inside the combustion chamber with the help of holes at 0.6 m/s naturally at room temperature 300 K. In the fuel bed, 3 kg of fuel (wood) was used as an input parameter and the mass flow rate in the fuel bed was 0.0026 kg/s. At the time of combustion, the temperature in the fuel bed was 1150 K. SIMPLE's pressure correction scheme was used to solve the pressure–velocity coupling, and a second-order accurate discretization scheme was used to solve all governing equations. A convergence criterion of 10^{-6} was met for residuals of all flow variables across the flow domain.

Inside the combustion chamber, the air velocity contour and temperature fluctuation with height are shown in Figs. 4 and 5. Figure 4 helps us to understand the profile or path taken by the primary air inside the combustion chamber from the holes. The inlet velocity was calculated analytically. As can be seen from the figure, how the pattern of combustion air moves from inlet to outlet. The average velocity inside the combustion chamber was found 1.2 m/s. Figure 5 gives the temperature contour in outlet. As we can see from the figure, the primary air enters through the hole at the room temperature 300 K. The input temperature was 1150 K from the fuel bed and after the simulation. The temperature that touched the outlet phase is shown in Fig. 5. The light blue colour indicates a temperature of around 640 K, the sky blue colour
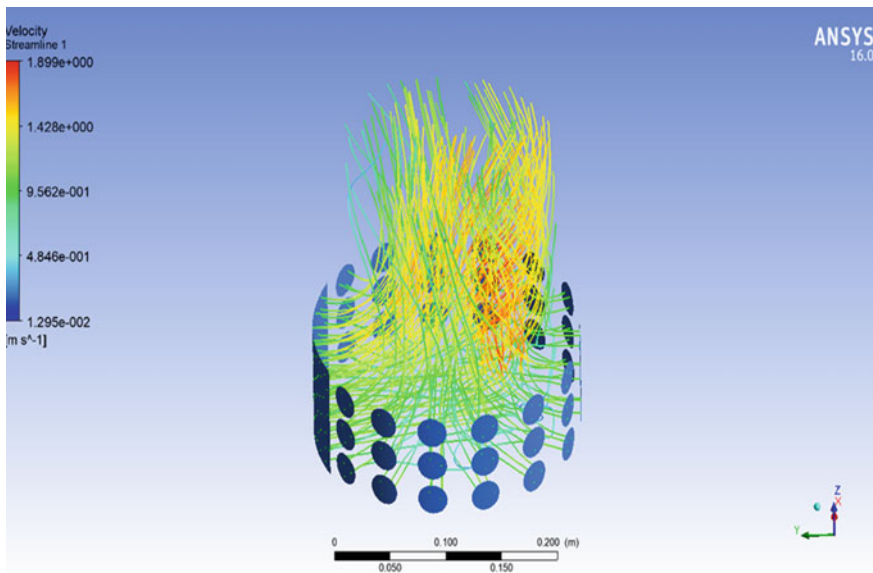
Fig. 4 Velocity contour(streamline) inside the combustion chamber
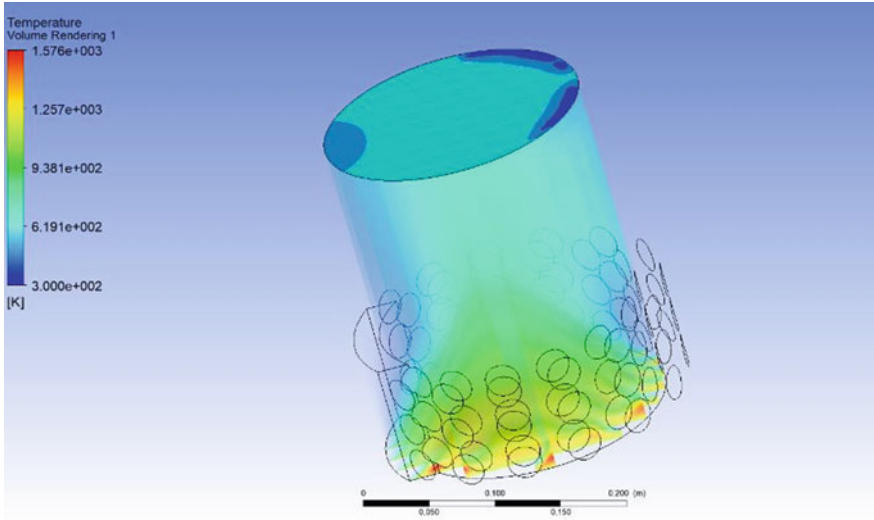
Fig. 5 Temperature contour in outlet

indicates a temperature of around 470 K, and the dark blue colour indicates a temperature of around 360 K. The average temperature in the outlet phase was around 630 K, which was the highest compared to the previously available models (Fig. 6). CFD analysis is a very efficient and effective way of evaluating a biomass cook stove's performance. The summery CFD analysis inside the combustion chamber was done with the help of ANSYS commercial software (Table 1).
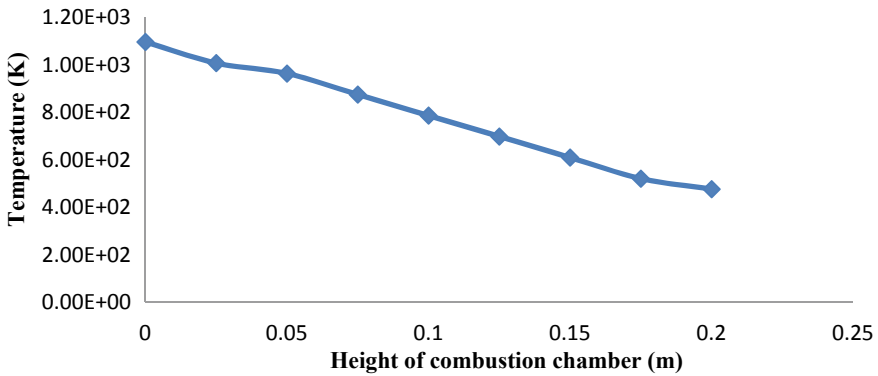
Fig. 6 Characteristics curve of temperature (K) versus height of combustion chamber (m)

Table 1 Geometrical input parameters

Sl. No	Parameter	Value	Unit
1	Inner diameter of the stove	200	mm
2	Outer diameter of the stove	240	mm
3	Height of the stove	280	mm
4	Chimney diameter	340	mm
5	Height of chimney	450	mm
6	Height of hood	450	mm
7	Ambient temperature	300	K
8	Char emissivity	0.86	
9	Char temperature	1150	K

6.2 Comparison Test

This model was created, and the theoretical results were compared to the predicted model of Kshirsagar and Kalamkar [4]. The table shows the predicted information set of the model, which includes data on overall efficiency for firepower variations (Table 2). The input parameters are listed in Table 3.

Figure 7 shows a fair comparison with bar representations for changes in overall efficiency with the firepower. The figure clearly shows that the overall efficiency of both the models and the overall efficiency beyond fire power 2.81 kW declines as the firepower increases due to a high temperature of combustion and loss also increases. However, for the present model, the highest overall thermal efficiency is 44.8% in

Table 2 Model predicted results comparison of two different models (Kshirsagar and Karmakar [4]and present model)

SN	Coefficient of discharge C_d	Firepower (kW)	Combustion efficiency η_c (%)	Overall efficiency η_o (%)	
				Kshirsagar	Present model
				Mpr	Mpr
1	0.308	1.43	0.971	28.7	33.2
2	0.285	1.85	0.976	26	35.4
3	0.307	2.15	0.987	24.6	37.5
4	0.295	2.43	0.99	24	40.2
5	0.277	2.81	0.995	23.6	44.8
6	0.38	2.96	0.995	21.9	41.3
7	0.326	3.57	0.994	22.1	36.4
8	0.195	3.69	0.928	22	29.7
9	0.303	3.73	0.995	22.4	25.4
10	0.214	4.08	0.908	20.2	23.2

Table 3 Simulation parameters for the improved biomass cook stove

SN	Parameter	Numerical value	Unit	Reference
1	Firepower	1.43–4.08	kW	Kshirsagar
2	Combustion efficiency	90.8–99.5	%	and Kalamkar [4]
3	Lower or net calorific value	18,280	kJ/kg	
4	Moisture content of fuel	7.0	%	
5	Pot surface temperature	373	K	
6	Ambient temperature	300	K	
7	Emissivity of the char	0.86		
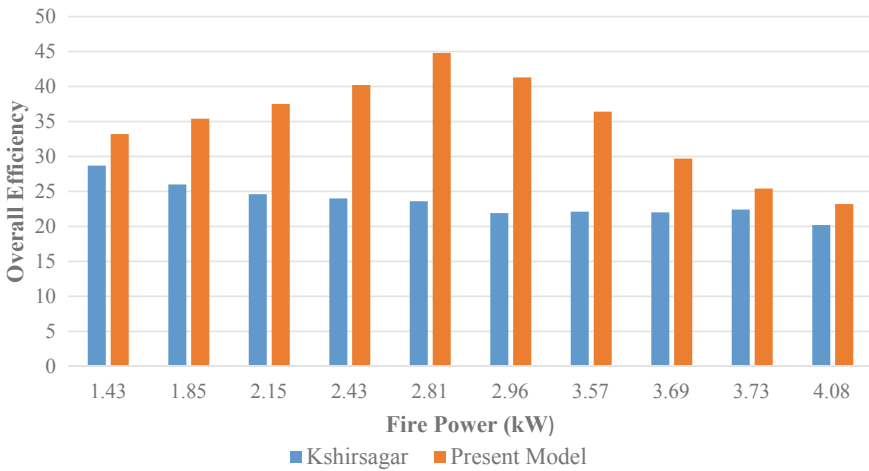
Fig. 7 Variation of thermal efficiency with firepower for Kshirsagar and Kalamkar [4] and present design (PD)

firepower 2.81 kW probably because of the optimum amount of air fuel ratio inside the chamber and the size of the biomass cook stove is more than the Kshirsagar and Kalamkar [4] predicted model.

7 Conclusions

- An improved biomass cook stove was modelled and designed. The design was done in AutoCAD software and initial step in the modelling process was to use the ANSYS commercial package.
- The proposed design was made to keep the optimum air fuel ratio inside the combustion chamber for better thermal efficiency.

- The ANSYS analysis aids in deciding the air inlet velocity and temperature fluctuations along with height inside the combustion chamber.
- A reliable mathematical method was designed for estimating the overall efficiency of the present model with a firepower range of 1.43–4.08 kW. The expected outcomes of the above-mentioned parameter were compared to the Kshirsagar and Kalamkar [4] model. Certain fixed input physical and geometrical parameters were considered. However, for the present model, the highest overall thermal efficiency is 44.8% in firepower 2.81 kW probably because of optimum amount of air fuel ratio inside the chamber and the size of the biomass cook stove is more than the Kshirsagar and Kalamkar [4] predicted model.

References

1. Cengel Y, Boles MA (2006) Thermodynamics: an engineering approach. 6th edn. Boston, McGraw-Hill
2. Fichet V, Plion P, Tabet F (2016) A comprehensive CFD based model for domestic biomass heating systems. J Energy Inst 89(2):199–214
3. Quist CM, Jones RB, Jones MR, Lewis RS (2016) Uncertainty analysis and design guidelines of biomass cookstove thermal efficiency studies. Energy Sustain Develop 34(2):54–61
4. Kshirsagar PM, Kalamkar RV (2015) A mathematical tool for predicting thermal performance of a natural draft biomass cooks stoves and identification of a new operational parameter. Energy 93(1):188–201
5. Djurovic D, Nemoda S, Repic B, Dakic D, Adzic M (2015) Influence of biomass furnace volume change on flue gases burn out process. Renew Energy 76(3):1–6
6. Kumar M, Kumar S, Tyagi S (2013) Design, development and technological advancement in the biomass cook stove: a review. Renew Sustain Energy Rev 26(3):265–285
7. Tryner J, Willson DB, Marchese JA (2016) The effects of fuel type and stove design on emissions and efficiency of natural-draft semi-gasifier biomass cookstoves. Energy Sustain Develop 23(1):99–109
8. Lombardi F, Riva F, Sacchi M, Colombo E (2019) Enabling combined access to electricity and clean cooking with PV micro grids: new evidences from a high-resolution model of cooking loads. Energy Sustain Dev 49(4):78–88
9. Rupakheti D, Kimoanh NT, Rupakheti M, Sharma RK, Panday AK, Puppala SP, Lawrence MG (2019) Indoor levels of black carbon and particulate matters in relation to cooking activities using different cook stove-fuels in rural Nepal. Energy Sustain Develop 48(2):25–33
10. Sidhu MK, Ravindra K, Mor S, John Y (2019) Emission factors and global warming potential of various solid biomass fuel-cook stove combustion. Atmos Pollut Res 142(2):230–483
11. Bhuiyan AA, Blicblau AS, Naser J, Islam S (2018) A review on thermochemical characteristics of coal/biomass co-firing in industrial furnace. J Energy Inst 91(1):1–18
12. Bhuiyan AA, Karim MR, Naser J (2018b) Effect of recycled flue gas ratios for pellet type biomass combustion in a packed bed furnace. Int J Heat Mass Transfer 120(4):1031–1043
13. Jain T, Sheth PN (2019) Design of energy utilization test for a biomass cook stove: formulation of an optimum air flow recipe. Energy 166(1):1097–1105
14. Silva J, Teixeira J, Teixeira S, Preziati S, Cassiano J (2017) CFD modeling of combustion in biomass furnace. In: INFU-11th European conference on industrial furnaces and boilers 120(8):665–672
15. Borpatra Gohain R, Dutta PP (2021) Modelling and performance analysis of improved biomass cook stove. In: Kakati B, Phukan BR, Rajbongshi T, Bora D Proceedings of international conference vol II. Tata McGraw Hill, New Delhi, pp 184–188

16. Barpatragohain R, Bharali N, Dutta PP (2021) Thermal performance evaluation of an improved biomass cook stove for domestic applications. In: Revankar S, Sen S, Sahu D Proceedings of international conference on thermofluids vol I. Springer, Singapore, pp 579–590
17. Bardalai M, Das B, Dutta PP, Mahapatra S (2021) Thermal performance study of bamboo and coal Co-gasification in a downdraft gasifier. In: Das B, Patgiri R, Bandyopadhaya S, Balas VM Modeling, simulation and optimization. Proceedings of CoMSO 2020 vol I. Springer, Singapore, pp 15–28
18. Dutta PP, Das A, Pandey V, Devi M (2014) Fuel characteristics of some locally available biomass as a potential gasification feed stock for thermal application. Ind Eng Chem Res J 53(51):19806–19813
19. Dutta PP, Pandey V, Das AR, Sen S, Baruah DC (2014) Downdraft gasification modelling and experimentation of indigenous biomass for thermal application. Energy Procedia 54(1):21–36
20. Dutta PP, Baruah DC (2014) Modeling and experimental studies of black tea using producer gas as fuel. Appl Therm Eng 63(2):495–502
21. Dutta PP, Baruah DC (2014) Gasification of up rooted tea shrubs for process heat generation in tea manufacturing. Biomass Bioenergy 66(1):27–38
22. Dutta PP, Baruah DC (2014) Possibility of Biomass gasification in tea manufacturing industries. Int J Renew Energy Technol 5(4):310–322
23. Bhuiyan AA, Karim MR, Naser J (2017) Co firing of biomass and slagging in industrial furnace: a review on modelling approach. J Energy Inst 90(6):838–854
24. Brandeleta B, Rosec C, Rogaumea C, Rogaumea Y (2018) Impact of ignition technique on total emissions of firewood stove. Biomass Bioenergy 108(1):15–24
25. Bryden KM, Maccarty NA (2015) Modelling of household biomass cook stoves: a review. Energy Sustain Develop 26(1):1–13
26. Pundle A, Sullivan B, Means P, Posner JD, Kramlich JC (2019) Predicting and analyzing the performance of biomass-burning natural draft rocket cook stoves using computational fluid dynamics. Biomass Bioenergy 131(1):105–402
27. Pratiti R, Vadala D, Kalynych Z, Sud P (2020) Health effects of household air pollution related to biomass cook stoves in resource limited countries and its mitigation by improved cook stoves. Environ Res 186(2):109–574

Parameters Involved in CVD Growth of CNT: A Review

Aunggat Shah, Gautam Saha, and Mrityunjoy Mahato

1   Introduction

Carbon is a light atom capable of forming single, double, and triple chemical bonds. CNTs were discovered by Ijima in 1991 [1] which have cylindrical structures, made by graphene sheets with sp^2 bonds open or closed ends [2, 3]. CNTs can be single-walled (diameter ~2–3 nm) and multi-walled (diameter ~20–30 nm). The length of CNT can be micrometer to centimeter range [4]. Based on the chiralities, CNTs can be of zig-zag, armchair, and chiral type. Zig-zag CNTs are hexagonal lattice and chiral CNTs have another pattern that may be semiconducting or semi-metallic. The lattice of armchair CNTs is rotated 90° with respect to the zig-zag pattern and possesses a metallic band structure [4]. The bandgap of CNTs may vary 0.18–1.8 eV and, hence, can have tunable electrical properties [5]. CNTs are lightweight materials with high mechanical strength such as Young's moduli ~1 TPa (5 times than steel) and the tensile strength of 63 GPa (50 times than steel) [6]. CNTs are chemically inert and have good thermal conductivity (~2000–6000 W/mK) [7, 8]**.** Due to the range of properties, CNTs have been applied in AFM or STM tips [9], microelectronics [10], electron field emission [11], energy storage [12], biosensors [13], composite materials [14], pharmaceutical [15], and solar cell [16]. However, CNT growth is a slow process and has a number of challenges for large-scale production. In this direction, quantification of the CNT growth process is important, and documenting the CNT growth parameters would be a valuable contribution.

A. Shah · M. Mahato (✉)
Physics Division, Department of Basic Sciences and Social Sciences, School of Technology, North-Eastern Hill University, Shillong, Meghalaya 793022, India
e-mail: mrityunjoyphy@gmail.com; mmahato@nehu.ac.in

G. Saha
Department of Information Technology, School of Technology, North-Eastern Hill University, Shillong, Meghalaya 793022, India

There are different methods to grow CNTs, such as arc discharge [17], laser ablation [18], electrolysis [19], polymer derived [20], and chemical vapor deposition (CVD) [21, 22]. Arc discharge method uses a high voltage through the graphite electrodes at high temperatures of 1700 °C and sub-atmospheric pressure. Some floating catalyst may be used, and the evaporated carbon from anode deposits on the cathode as CNTs [23]; however, the use of high temperature limits its scalability. Laser ablation uses a high-power laser with varying laser power, where a pure graphite is vaporized by laser with temperature of 1200 °C in an inert atmosphere [24]. The laser power is inversely proportional to the diameter of the SWCNTs [25]. Laser ablation suffers from scalability for industrial purpose. In CVD, a carbon source is passed through heated catalyst at temperatures 600–1100 °C under inert condition [21]. The nature of the hydrocarbons decides the types of CNTs, multi-walled or single-walled. CVD methods have been reported for large-scale productions of CNTs due to their economic viability and simplest reactor environment.

Recently, low temperature synthesis of CNTs has been tried where the carbon feedstocks are pretreated either at high temperature or by plasma. Mora et al [26] produced SWCNTs on Fe:Mo catalyst supported on Al_2O_3 powder at 300 °C by using plasma pretreated CH_4 gas. Nessim et al. [27] made preheating of incoming carbon source gasses at 770 °C to grow vertically aligned CNTs at 500 °C using Fe catalysts on Ta (Tantalum). Xiao et al. [28] demonstrated the growth of CNTs by PECVD using CH_4 gas at 450 °C over Ni–Al–Ni–layered catalysts (prepared by atomic layer deposition) over silicon wafer.

Despite plenty of literature on CNT growth, many components of the growth mechanisms in the CVD process are yet unknown [29–31]. Also, structural control of CNTs in terms of chirality, semiconducting/metallic ratio, and density of defects are still lacking in the CVD CNT growth process [32]. Allaedini et al. [4] reviewed the effect of various parameters and conditions of catalysts on the CNT production, such as catalyst size, shape, composition, concentration, and type of catalyst. However, some other parameters are also involved in the CNT production. In this review, we explore the effects of type of catalyst, temperature, nature of hydrocarbon feedstock, inert gas flow, and growth time on the yield and structural characteristics of CNTs. The experimentation on the variation of such parameters is still a challenge and such kinds of reproducible experimental data are poorly available in the literature. Thus, there is a great need in understanding the growth process and the parameters influencing the growth of CNTs by CVD route. In this review, effort is given to understand the effect of such parameters on CNT growth with the help of available literature.

2 Parameters in CVD Growth of CNTs

2.1 Effect of Catalyst

Catalysts play a critical role as the nucleation sites in CNT growth, and hence, a low cost, sustainable, and optimized catalyst is required for its optimum yield.

Metal, Metal oxide, and LDH Catalysts for CNT growth: Hussein et al. [33] reported the growth of MWCNTs using hexane gas over LDH catalysts (FeCoNiAl, CoNiAl, and FeNiAl), where CoNiAl catalyst gives a maximum yield of 183.5% with diameter of 20.60 nm. Nagaraju et al. [34] compared three catalysts, namely Co, Fe, and Co/Fe supported on alumina or silica, where alumina support giving better yield of MWCNTs at 700 °C. Seo et al. [35] compared Fe, Co, or Ni as the catalyst using acetylene carbon source at 720 °C with best yield found in Fe catalyst. Lee et al. [36] used thin film of Fe, Ni, and Co on silicon oxide substrate, where Ni resulted in best yield and Fe resulted in the best quality. In our earlier report, it was observed that NiO catalyst favors the growth of MWCNT [37, 38], whereas Fe_2O_3 and PbO favors the growth of amorphous carbon [39, 40].

Growth of CNTs on Porous Substrate/Catalyst: SWCNTs are often synthesized utilizing nanometer-sized particles as catalysts. However, Schneider et al. [41] prepared MWCNTs using other types of catalyst such as porous aluminum oxide at 900 °C using propylene as the carbon precursor.

Floating Catalysts for CNT Growth: Hussain et al. [42] used ferrocene as floating catalysts and ethylene as carbon source and produced SWCNTs of diameters 1.3–1.5 nm. Zhu et al. [43] pyrolyzed n-hexane (carbon source) in the presence of thiophene (sulfur source) where it was observed that the addition of sulfur favors SWCNTs. It has been reported that the addition of such compounds acts as a promoter for SWCNTs or DWCNTs [44] (Table 1).

2.2 Effect of Temperature

Growth temperature of CNTs is important for its crystallinity and the selectivity of catalysts. Mohammed et al. [46] observed carbon spheres in CVD reactions at temperatures below 650 °C. Thus, choosing the right temperature is critical for improving MWCNT selectivity and limiting the production of amorphous carbon and other types of carbon that may form as a result of side reactions. They used bimetallic Fe-Co catalysts supported on $CaCO_3$ to grow MWCNTs at 700 °C using acetylene as the carbon source with a yield of 170% in the temperature range of 700 °C to 750 °C. Bone and Coward [52] showed that acetylene undergoes polymerization at around 780 °C instead of forming CNTs. Liu et al. [47] prepared MWCNTs using PP plastic and HZSM-5 zeolite mixture over nickel catalyst and observed better graphitization at 800 °C than 750 °C with a lower yield. Venkatesan et al. [49] observed

Table 1 Summary of different parameters for CNT growth experimented in literature

Sl. No	Parameters	Optimized yield	Remarks	References
1	Effect of catalyst	183.5% (Catalyst + CNT)	Yields of different catalysts (FeCoNiAl, CoNiAl, FeNiAl), were 124.8, 183.5, and 110.5, respectively	[33]
		Fe was better than Co, Ni catalyst	CNT yields on metal catalysts with silica support were in the order Fe > Co > Ni	[35]
		Yield order: Ni > Co > Fe	CNT yields were better with Fe out of Ni, Fe, Co	[36]
		Floating Ferrocene catalyst	Ferrocene was used as the floating catalyst with ethylene as the carbon source to produce SWCNTs	[42]
		Floating Sulfur catalyst	It was observed that addition of sulfur in floating catalytic environment of ferrocene promoted the growth of SWCNTs	[43]
		On porous Al_2O_3 (POAX) substrate	CNTs were grown on POAX substrate without the use of any catalysts	[41]
		Yield with catalyst thickness	Density of CNTs increased with larger catalyst thickness of 3 nm, 5 nm, and 7 nm	[45]
2	Effect of temperature	170% (Catalyst + CNT)	Yields of CNTs were 170% and 50% at 700 °C and 750 °C, respectively	[46]
		Yield of CNT growth from PP was optimized at 750 °C	Yields of CNTs were maximum at 750 °C in the temperature range (500 °C to 800 °C)	[47]
3	Effect of carbon source	Yield increased with smaller chain hydrocarbons	Yield of CNTs was better with methane out of various gasses (hexane, methane, naphthalene, benzene, anthracene, etc.) on Fe catalyst	[48]
4	Effect of growth time	170% (Catalyst + CNT)	Yields of CNTs were 170% and 156% at 60 min and 45 min, respectively	[46]

Table 1 (continued)

Sl. No	Parameters	Optimized yield	Remarks	References
		Yield at 25 min	Yield with change in growth time (15, 25, and 35 min) showed CNT growth was best at 25 min	[49]
5	Effect of flow rate (carbon source)	170% (Catalyst + CNT) (acetylene)	Yields of CNTs achieved (at 700 °C and Ar flow of 230 ml/min) were 112% and 170% at acetylene flow of 150 ml/min and 190 ml/min, respectively	[47]
		185% (Catalyst + CNT) (methane)	Yield with flow rate of carbon (50 sccm) showed low defects CNT at 800 °C with a flow rate of 50 sccm	[50]
		Max yield at 100 sccm (ethylene)	Optimum yield at 100 sccm out of the experimented flow rate of 50, 75, 100, 125, and 150 sccm	[51]
		Max yield at 180 ml/min (acetylene)	Max yields at 180 ml/min among flow rates of 100, 140, 180 ml/min	[49]
	Effect of flow rate (inert gas)	170% (Catalyst + CNT)	Yields of CNTs were 170% and 134% at 230 ml/min and 290 ml/min of argon flow, respectively	[46]

the formation of amorphous carbon below 700 °C and above 1000 °C using NiO catalyst.

Li et al. [53] prepared CNTs at temperatures 500 °C, 600 °C, and 750 °C using Ni/NiO/Al$_2$O$_4$/Cu catalyst and methane carbon source. They observed CNTs above 720 °C and carbon fibers below 720 °C. Gulino et al. [54] produced MWCNTs at a large scale using Fe/Al$_2$O$_3$ catalyst and ethane as carbon precursor at 660 °C, while above 750 °C resulted in amorphous carbon. Zhou et al. [55] showed that sulfur is a growth promoter of CNTs at 1000 °C and yields of SWCNTs increases with increasing temperatures.

2.3   Effect of Carbon Source

The carbon precursor plays an important role in the growth of CNTs. The larger hydrocarbons are less stable, thus producing poor CNTs. However, smaller hydrocarbons are more stable and give higher quality CNTs.

Aliphatic Hydrocarbons as Carbon Source: Li et al. [48] used different hydrocarbons (methane, hexane, cyclohexane, benzene, anthracene, etc.) using Fe catalyst on MgO substrate for the growth of CNTs. The methane yielded to SWCNTs and cyclohexane/hexane produce MWCNTs. There must be a correlation between the molecular weight of carbon source and CNT growth; however, still it is not yet quantified. Shah et al. [50] reported yield of MWCNTs of 185% at 800 °C on Pt-W catalysts using methane as the carbon source.
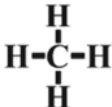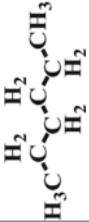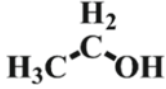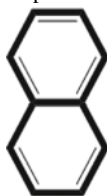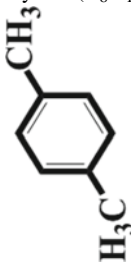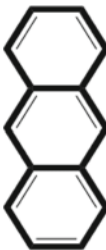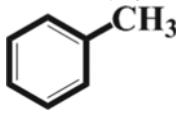
Aromatic Hydrocarbons as Carbon Source: Li et al. [56] experimented on different aromatic hydrocarbons like benzene, naphthalene, and anthracene and observed that smaller aromatic compounds (benzene) favor the growth of SWCNTs. Das et al. [57] used aromatic hydrocarbons: benzene, toluene, xylene, and trimethyl benzene using ferrocene as the catalyst, where toluene resulted in CNT yield 30.5% with 96% purity. Therefore, it can be concluded that aromatic hydrocarbons and methane favor SWCNTs, cyclic hydrocarbons (cyclohexane) favor MWCNTs, and linear chained hydrocarbons (hexane) favor carbon fibers.

Pyrolyzed Hydrocarbons from Plastics as Carbon Source: Plastics can also be used for the preparation of CNTs by the process of pyrolysis and subsequent deposition of the pyrolyzed hydrocarbons on the catalytic bed. This process is usually conducted in a two or three stage pyrolysis reactor. Demirba [58] showed that there is a decrease in chain length from C2–C8 to C2–C6 with an increase in pyrolysis temperature (650–875 °C) for PS (polystyrene). Encinar and Gonzalez [59] pyrolyzed plastic wastes at 800 °C which breaks down to smaller hydrocarbons of chain length C1–C3. Wu et al. [60] analyzed the pyrolyzed products of waste plastics at 500 °C and found the hydrocarbon chain length to be C1–C4. Thus, it is concluded that with an increase in pyrolysis temperature of plastics there is a decrease in the length of the hydrocarbons produced which consequently leads to a better formation of CNTs (Table 2).

2.4   Effect of Growth Time

Growth time plays an important role in the morphology of the CNTs produced during the CVD process. CNT formation takes place within just a few minutes of the growth process. The shorter reaction time favors the growth of CNTs with smaller diameters and longer growth times favor the growth of CNTs with longer diameters. However, Mohammed et al. 2017 [46] reported an increase in CNT yield with the increase in growth time from 45 to 60 min at 700 °C and also observed a decrease in CNT yield at 750 °C. Venkatesan et al. [49] showed that the optimum growth time is between 20

Table 2 Molecular structure of hydrocarbons used in CNT growth as carbon source (drawn using ChemDraw software)

Aliphatic hydrocarbon source

Methane (CH$_4$)	Acetylene (C$_2$H$_2$)	Ethane (C$_2$H$_4$)	Butylene (C$_4$H$_8$)
H–C–H (with H above and below)	HC≡CH	H$_3$C–CH$_3$	H$_2$C∕∖CH$_2$
Hexane (C$_6$H$_{14}$)	Ethanol (C$_2$H$_5$OH)	Ethylene (C$_2$H$_4$)	Carbon Monoxide (CO)
(structure)	H$_3$C–C(H$_2$)–OH	H$_2$C═CH$_2$	$^+$O≡C$^-$

Aromatic hydrocarbon source

Benzene (C$_6$H$_6$)	Naphthalene (C$_{10}$H$_8$)	Xylene (C$_8$H$_{10}$)	Anthracene (C$_{14}$H$_{10}$)
(structure)	(structure)	(structure)	(structure)
Cyclohexane (C$_6$H$_{12}$)	Toluene (C$_7$H$_8$)	–	–
(structure)	(structure)		

and 27 min while below 15 min and above 35 min lead to the formation of amorphous carbon and defective structures.

2.5 Effect of Flow Rate of Inert Gas and Carbon Source

Mohammed et al. [46] studied the effects of argon gas flow rate (230–290 ml/min) and hydrocarbon gas flow rate (150–190 ml/min). They observed that the yield of CNTs increased with an increase in acetylene flow but no change due to argon flow rate. Shukrullah et al. [51] experimented on ethylene flow rates from 50 to 100 sccm, where the optimum flow rate of 100 sccm led to the formation of well-structured

CNTs and above which the product showed structural defects. Venkatesan et al. [49] experimented on precursor gas flow rate (100–180 ml/min), where tubular structures formed above 180 ml/min and no graphitization below 100 ml/min.

2.6 Reactor Type and Size

Mullite versus Alumina Reactor Tube: Rodiles et al. [61] experimented on mullite ($Al_{4+2x}Si_{2-2x}O_{10-x}$ ($x \approx 0{:}4$)) and alumina (Al_2O_3) reactor type and observed the higher catalytic activity of mullite over alumina.

Hot Wall versus Cold Wall Reactor: CVD reactors can also be categorized by the temperature of the reactor wall, namely hot-wall CVD and cold-wall CVD. In hot-wall CVD, the entire reactor tube is maintained at the same temperature and is preferred for exothermic reactions. In contrast, cold-wall CVD employs heating of only the substrate within the reactor chamber by using RF induction or radiation lamps, while the walls of the reactor remain cold. The advantage of hot-wall CVD is the temperature uniformity across the entire reactor and possesses higher reaction volume; hence, it is more likely to be scaled up for better yield. Cold wall CVD is most useful for in situ analysis and experimentation [62].

2.7 Modeling and Optimizing of Different Parameters

There is very rare literature available which is dealing with the optimization and modeling of CNT growth using all possible parameters involved. However, some literature attempted to optimize a few parameters within a limited scope. Masouleh et al. [64] attempted to model the CNT growth using ferrocene as the floating catalyst and xylene as carbon source. They used a reactor reported by Maghrebi et al. [63] and assumed the decomposition of ferrocene to be a single-step process as shown in Eq. 1 (Fig. 1):
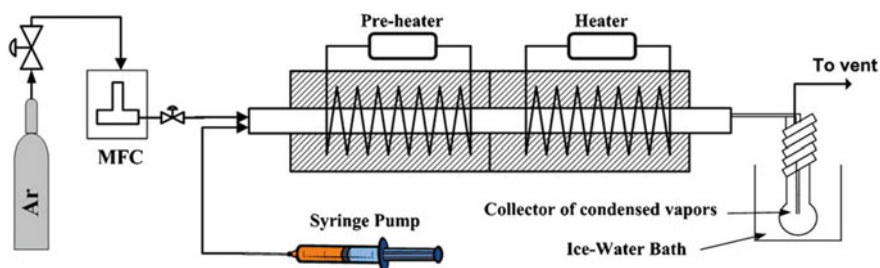
Fig. 1 The schematic diagram of CNT growth apparatus (Reproduced with prior permission from Maghrebi et al. [63])

$$Fe(C_5H_5)_2 \rightarrow Fe + 2(C_5H_5) \tag{1}$$
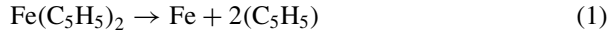
The rate of decomposition of ferrocene is given by [64]:

$$-rA = 1.0 \times 10^{14} [s^{-1}] \exp\left(\frac{-209\left[\frac{kJ}{mol}\right]}{RT}\right) C_{fer} \tag{2}$$

Hence, the mass balance equation for ferrocene decomposed in the reactor is given by [64]:

$$-kC_{fer} = U_r \nabla_z C_{fer} \tag{3}$$

The mass balance equation of iron production ferrocene is given by [64]:

$$kC_{fe} - \frac{4K_c D_{in} C_{fe}}{D_{out}^2 - D_{in}^2} = U_r \nabla_z C_{fer} \tag{4}$$

Xylene undergoes thermal decomposition into toluene, benzene, methane, and C2 hydrocarbons. However, Masouleh et al. assumed the conversion of xylene to CNTs as a one-step reaction as follows [64]:

$$-\left(k_A' + k_{CNT}'\right) C_X = U_r \nabla_z C_x \tag{5}$$

The amount of iron particles formed in the reactor directly affects the formation of CNTs as these iron particles act as nucleation sites for the growth of CNTs. The amount of iron nanoparticles formed is given by [64]:

$$\Theta = M_{fe} K_C C_{fe} \frac{D_{out}^2 - D_{in}^2}{4(D_{out} + D_{in})L} t \tag{6}$$

They observed that an increase in ferrocene concentration leads to an increase in the amount of iron produced which in turns increases CNT production following Eq. 7 [64]:

$$k_{CNT}' = k_{0CNT} \frac{4(D_{out} + D_{in})}{D_{out}^2 - D_{in}^2} \Theta \exp\left(\frac{-E_{CNT}}{RT}\right) \tag{7}$$

It was found that higher concentration of xylene and ferrocene leads to larger CNTs. Though, there is a 20% difference in the model prediction and the experimental value. They also observed that the maximum CNT heights were attained in the temperature range of 825–875 °C [64].

Where C_i = component (i) molar concentration (mol/m³); D_{in} = substrate diameter (m); D_{out} = quartz reactor diameter (m); k_{0A} = pre-exponential factor for the
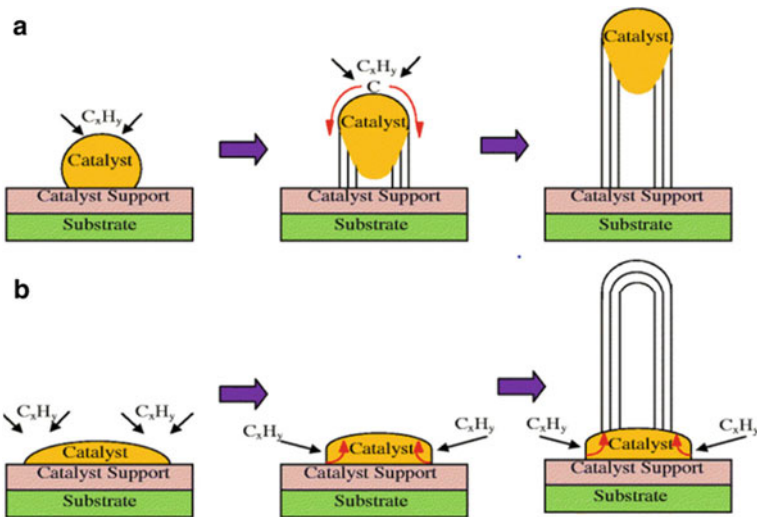
Fig. 2 Tip growth (**a**) and base growth (**b**) mechanisms of CNT (Reproduced with prior permission from Venkataraman et al. [65])

formation of amorphous carbon (m/s); k_{0CNT} = pre-exponential factor for the formation of graphitic carbon (m³/g of Fe); k'_{CNT} = rate constant of CNT formation (1/s); t = time (s); U_r = feedstock velocity (m/s); θ = weight by surface area of Fe (g/m²); r_A = ferrocene decomposition rate; and M_{Fe} = molecular weight Fe (56 kg/kmol).

Tip growth and base growth mechanism: The hydrocarbon vapor decomposes into carbon and hydrogen when it touches metal or catalyst and subsequently hydrogen gas evaporates. Tip growth or base growth model for CNT growth depends upon the type of catalyst–substrate interaction. Tip growth of CNT occurs by the poor interaction of the hydrocarbon with metal catalyst due to the low concentration of metal. The base growth of CNT is facilitated by the strong interaction of hydrocarbon vapor with the catalyst, due to the higher concentration of metal available in the reaction [65]. Gohier et al. [66] reported a base growth model of CNT with smaller structures like SWCNTs or FWCNTs. However, they observed that the growth model switches from tip growth to base growth with decreasing particle size of the catalyst (Fig. 2).

3 Conclusion

In this work, we have reviewed the effects of various reaction parameters for the growth of CNTs. The optimum and best conditions of the reaction parameters have been described. The transition metal-based catalysts were found to be the better catalysts for CNT growth alongside porous substrates. The optimum growth temperature

range is found to be 700–750 °C; however, the growth temperature for SWCNTs is around 1000 °C. It is found in many experiments that ferrocene plays an important role as floating catalysts alone or along with other catalysts. It is also to be noted that many experiments use sulfur-based compounds, which act as promoters for SWCNT growth. It is found from the literature that the long-chain aliphatic hydrocarbons favor the growth of MWCNTs and a stable carbon compound like aromatic hydrocarbons favor the growth of SWCNT. A moderate growth time (maybe 25–35 min) can be an optimized growth time for better graphitization of CNTs. Optimization of growth parameters with different reactor types is still a less studied topic and needs attention in future work. Future work may involve theoretical and modeling work to understand the underlying mechanism of CNT growth, along with extensive experimentation with the growth parameters to complement the modeling work.

References

1. Iijima S (1991) Helical microstructures of graphitic carbon. Nature 354:56–58
2. De Volder MFL, Tawfick SH, Baughman RH, Hart AJ (2013) Carbon nanotubes: present and future commercial applications. Science 339:535–539
3. Eatemadi A, Daraee H, Karimkhanloo H, Kouhi M, Zarghami N, Akbarzadeh A, Abasi M, Hanifehpour Y, Joo SW (2014) Carbon nanotubes: properties, synthesis, purification, and medical applications. Nanoscale Res Lett 9:393–406
4. Allaedini G, Tasirin SM, Aminayi P, Yaakob Z, MeorTalib MZ (2016) Carbon nanotubes via different catalysts and the important factors that affect their production: a review on catalyst preferences. Int J Nano Dimens 7:186–200
5. Elliott JA, Sandler JKW, Windle AH, Young RJ, Shaffer MSP (2004) Collapse of single-walled carbon nanotubes is diameter dependent. Phys Rev Lett 92(9):1–4
6. Saifuddin N, Raziah AZ, Junizah AR (2013) Carbon nanotubes: a review on structure and their interaction with proteins. J Chem 2013:1–18
7. Yu MF, Files BS, Arepalli S, Ruoff RS (2000) Tensile loading of ropes of single wall carbon nanotubes and their mechanical properties. Phys Rev Lett 84:5552–5555
8. Hana Z, Fina A (2011) Thermal conductivity of carbon nanotubes and their polymer nanocomposites: a review. Prog Polym Sci 36:914–944
9. Baughman RH, Zakhidov AA, Heer WA (2002) Carbon nanotubes: the route toward applications. Science 297:787–792
10. Ionescu AM, Riel H (2011) Tunnel field-effect transistors as energy-efficient electronic switches. Nature 479:329–337
11. Riggs JE, Guo Z, Carroll DL, Sun Y-P (2000) Strong luminescence of solubilized carbon nanotubes. J Am Chem Soc 122:5879–5880
12. Dai L, Chang DW, Baek JB, Lu W (2012) Carbon nanomaterials for advanced energy conversion and storage. Small 8:1130–1166
13. Köhler AR, Som C, Helland A, Gottschalk F (2008) Studying the potential release of carbon nanotubes throughout the application life cycle. J Cleaner Prod 16:927–937
14. Gojny F, Wichmann M, Köpke U, Fiedler B, Schulte K (2004) Carbon nanotube-reinforced epoxy-composites: enhanced stiffness and fracture toughness at low nanotube content. Compos Sci Technol 64:2363–2371

15. He H, Pham-Huy LA, Dramou P, Xiao D, Zuo P, Pham-Huy C (2013) Carbon nanotubes: applications in pharmacy and medicine. BioMed Res Int 4:145–156
16. Mahmood SS, Atiya AJ, Abdulrazzak FH, Alkaim AF, Hussein FH (2021) A review on applications of Carbon Nanotubes (CNTs) in solar cells. J Med Chem Sci 4:225–229
17. Mroz P, Tegos GP, Gali H, Wharton T, Sarna T, Hamblin MR (2008) Fullerenes as photosensitizers in photodynamic therapy. Med Chem Pharmacol Potential Fullerenes Carbon Nanotubes :79–106
18. Hu J, Odom TW, Lieber CM (1999) Chemistry and physics in one dimension: synthesis and properties of nanowires and nanotubes. Acc Chem Res 32:435–445
19. Iyer VS, Vollhardt KPC, Wilhelm R (2003) Near-quantitative solid-state synthesis of carbon nanotubes from homogeneous diphenylethynecobalt and–Nickel complexes. Angew Chem 115:4515–4519
20. Cho WS, Hamada E, Kondo Y, Takayanagi K (1996) Synthesis of carbon nanotubes from bulk polymers. Appl Phys Lett 69:278–279
21. Couteau E, Hernadi K, Seo JW, Thien-Nga L, Mikó C, Gaal R, Forro L (2003) CVD synthesis of high-purity multiwalled carbon nanotubes using $CaCO_3$ catalyst support for large-scale production. Chem Phys Lett 378:9–17
22. Wang Y, Gupta S, Nemanich R, Liu Z, Qin L (2005) Hollow to bamboolike internal structure transition observed in carbon nanotube films. J Appl Phys 98:014312 (1–6)
23. Grobert N (2007) Carbon nanotubes-becoming clean. Mater Today 10:28–35
24. Abbasi E, Aval SF, Akbarzadeh A, Milani M, Nasrabadi HT, Joo SW, Hanifehpour Y, Koshki KN, Asl RP (2014) Dendrimers: synthesis, applications, and properties. Nanoscale Res Lett 9:247–255
25. Yacaman MJ, Yoshida MM, Rendon L, Santiesteban JG (1993) Catalytic growth of carbon microtubules with fullerene structure. Appl Phys Lett 62:202–204
26. Mora E, Pigos JM, Ding F, Yakobson BI, Harutyunyan AR (2008) Low-temperature single-wall carbon nanotubes synthesis: feedstock decomposition limited growth. J Am Chem Soc 130:11840–11841
27. Nessim GD, Seita M, O'Brien KP, Hart AJ, Bonaparte RK, Mitchell RR, Thompson CV (2009) Low temperature synthesis of vertically aligned carbon nanotubes with electrical contact to metallic substrates enabled by thermal decomposition of the carbon feedstock. Nano Lett 9:3398–3405
28. Xiao Y, Ahmed Z, Ma Z, Zhou C, Zhang L, Chan M (2019) Low temperature synthesis of high-density carbon nanotubes on insulating substrate. Nanomaterials 9:473–482
29. Nessim GD (2010) Properties, synthesis, and growth mechanisms of carbon nanotubes with special focus on thermal chemical vapor deposition. Nanoscale 2:1306–1323
30. Tessonnier J, Su DS (2011) Recent progress on the growth mechanism of carbon nanotubes: a review. Chemsuschem 4:824–847
31. Dupuis A (2005) The catalyst in the CCVD of carbon nanotubes—a review. Prog Mater Sci 50:929–961
32. Jourdain V, Bichara C (2013) Current understanding of the growth of carbon nanotubes in catalytic chemical vapor deposition. Carbon 58:2–39
33. Hussein MZ, Jaafar AM, Yahaya AH, Masarudin MJ, Zainal Z (2014) Formation and yield of multi-walled carbon nanotubes synthesized via chemical vapour deposition routes using different metal-based catalysts of FeCoNiAl, CoNiAl and FeNiAl-LDH. Int J Mol Sci 15:20254–20265
34. Nagaraju N, Fonseca A, Konya Z, Nagy JB (2002) Alumina and silica supported metal catalysts for the production of carbon nanotubes. J Mol Catal A: Chem 181:57–62
35. Seo JW, Hernadi K, Miko C, Forro L (2004) Behavior of transition metals catalysts over laser-treated vanadium support surfaces in the decomposition of acetylene. Appl Catal A 260:87–91
36. Lee CJ, Park J, Yu JA (2002) Catalyst effect on carbon nanotubes synthesized by thermal chemical vapor deposition. Chem Phys Lett 360:250–255
37. Nath A, Shah A, Singh LR, Mahato M (2021) Waste plastic-derived NiO-MWCNT composite as visible light photocatalyst for degradation of methylene blue dye. Nanotechnol Environ Eng 6 (3):1–14

38. Senapati S, Shah A, Patra PK, Mahato M (2021) Measurement of elastic modulus of CNT composites: a nondestructive study. In: Fullerenes, nanotubes and carbon nanostructures 30:290–296
39. Samuel J, Shah A, Kumar D, Singh LR, Mahato M (2021) Preparation, characterization and some electrochemical study of waste derived iron Oxide-Carbon nanocomposite. Mater Today: Proc 47:1048–1053
40. Das HJ, Shah A, Singh LR, Mahato M (2021) Waste derived low cost PbO-Carbon nanocomposite and its energy storage application. Mater Today: Proc 47:1072–1077
41. Schneider JJ, Maksimova NI, Engstler J, Joshi R, Schierholz R, Feile R (2008) Catalyst free growth of a carbon nanotube–alumina composite structure. Inorg Chim Acta 361:1770–1778
42. Hussain A, Liao Y, Zhang Q, Ding E, Laiho P, Ahmad S, Wei N, Tian Y, Jianga H, Kauppinen E (2018) Floating catalyst CVD synthesis of single walled carbon nanotubes from ethylene for high performance transparent electrodes. Nanoscale 10:9752–9759
43. Zhu HW, Xu CL, Wu DH, Wie BQ, Vajtai R, Ajayan PM (2002) Direct synthesis of long single-walled carbon nanotube strands. Science 6:884–886
44. Cheng HM, Li F, Su G, Pan HY, He LL, Sun X (1998) Large-scale and low-cost synthesis of single-walled carbon nanotubes by the catalytic pyrolysis of hydrocarbons. Appl Phys Lett 72:3282–3284
45. Radhakrishnan JK, Pandian PS, Padaki VC, Bhusan H, Rao KUB, Xie J, Abraham JK, Varadan VK (2009) Growth of multiwalled carbon nanotube arrays by chemical vapor deposition over iron catalyst and the effect of growth parameters. Appl Surf Sci 255:6325–6334
46. Mohammed IA, Bankole MT, Abdulkareem AS, Ochigbo SS, Afolabi AS, Abubakre OK (2017) Full factorial design approach to carbon nanotubes synthesis by CVD method in argon environment. S Afr J Chem Eng 24:17–42
47. Liu J, Jiang Z, Yu H, Tang T (2011) Catalytic pyrolysis of polypropylene to synthesize carbon nanotubes and hydrogen through a two-stage process. Polym Degrad Stab 96:1711–1719
48. Li Y, Zhang X, Tao X (2004) Growth mechanism of multiwalled carbon nanotubes with or without bundles by catalytic deposition of methane on Mo/MgO. Chem Phys Lett 386:105–110
49. Venkatesan S, Visvalingam B, Mannathusamy G, Viswanathan V, Rao AG (2018) Effect of chemical vapor deposition parameters on the diameter of multi-walled carbon nanotubes. Int Nano Lett 8:297–308
50. Shah KA, Najar FA, Sharda T, Sreenivas K (2018) Synthesis of multi-walled carbon nanotubes by thermal CVD technique on Pt–W–MgO catalyst. J Taibah Univ Sci 12:230–234
51. Shukrullah S, Mohamed NM, Khan Y, Naz MY, Ghaffar A, Ahmad I (2017) Effect of gas flow rate on nucleation mechanism of MWCNTs for a compound catalyst. J Nanomater 2017:1–9
52. Bone WA, Coward HF (1908) The thermal decomposition of hydrocarbons. J Chem Soc Trans 93:1197–1225
53. Li Z, Chen J, Zhang X, Li Y, Fung KK (2002) Catalytic synthesized carbon nanostructures from methane using nanocrystalline Ni. Carbon 40:409–415
54. Gulino G, Vieira R, Amadou J, Nguyen P, Ledoux MJ, Galvagno S, Centi G, Huu C (2005) C_2H_6 as an active carbon source for a large-scale synthesis of carbon nanotubes by chemical vapor deposition. Appl Catal A 279:89–97
55. Zhou Z, Ci L, Chen X, Tang D, Yan X, Liu D (2003) Producing cleaner double-walled carbon nanotubes in a floating catalyst system. Carbon 41:2607–2611
56. Li Q, Yan H, Zhang J, Liu Z (2004) Effect of hydrocarbons precursors on the formation of carbon nanotubes in chemical vapor deposition. Carbon 42:829–835
57. Das N, Dalai A, Mohammadzadeh JSS, Adjaye J (2006) The effect of feedstock and process conditions on the synthesis of high purity CNTs from aromatic hydrocarbons. Carbon 44:2236–2245
58. Demirbas A (2004) Pyrolysis of municipal plastic wastes for recovery of gasoline-range hydrocarbons. J Anal Appl Pyrolysis 72:97–102
59. Encinar JM, González JF (2008) Pyrolysis of synthetic polymers and plastic wastes. Kinetic study. Fuel Process Technol 89:678–686

60. Wu C, Nahil MA, Miskolczi N, Huang J, Williams PT (2014) Processing real-world waste plastics by pyrolysis-reforming for hydrogen and high-value carbon nanotubes. Environ Sci Technol 48:819–826
61. Rodiles X, Reguero V, Vila M, Alemán B, Arévalo L, Fresno F, Shea VA, Vilatela JJ (2019) Carbon nanotube synthesis and spinning as macroscopic fibers assisted by the ceramic reactor tube. Sci Rep 9:9239–9249
62. Sengupta J (2018) Handbook of nanomaterials for industrial applications. In: Micro and nano technologies. Elsevier, Netherlands
63. Maghrebi M, Khodadadi AA, Mortazavi Y, Mhaisalkar S (2009) Detailed profiling of CNTs arrays along the growth window in a floating catalyst reactor. Appl Surf Sci 255:7243–7250
64. Masouleh LS, Mostoufi N, Khodadadi A, Mortazavi Y, Maghrebi M (2012) Modeling the growth of carbon nanotubes in a floating catalyst reactor. Ind Eng Chem Res 51:1143–1149
65. Venkataraman A, Amadi EV, Chen Y, Papadopoulos C (2019) Carbon nanotube assembly and integration for applications. Nanoscale Res Lett 14:220–267
66. Gohier A, Ewels CP, Minea TM, Djouadi MA (2008) Carbon nanotube growth mechanism switches from tip-to base-growth with decreasing catalyst particle size. Carbon 46:1331–1338

A Mini-Review on Emerging Trend of Co(II)/Ln(III) Complexes as Single-Molecule Magnets

Pooja Shukla, Manu Ezhava, Soumalya Roy, Asadulla Mallick, and Sourav Das

1 Introduction

The field of SMM which was first pioneered by the discovery of a dodecanuclear $[Mn_{12}O_{12}(CH_3CO_2)_{12}(H_2O)_4] \cdot 4H_2O \cdot 2CH_3COOH$ [1] (**1**) complex has sparked a worldwide research interest based on their multifarious application in the field of storage device [2], quantum computing [3], spintronic devices [4] and magnetic refrigeration [5], and others. The success (or not) of an SMM depends on two main parameters which are effective energy barrier U_{eff} and blocking temperature T_B [6]. The value of T_B is governed by the height of the anisotropy barrier which is regulated by ground-state spin S and negative anisotropy D. Later on theoretical studies have shown that large S and strong D cannot be simultaneously observed within one molecule [7]. This led to the blossoming of Ln-based SMM with the pioneering work of double-decker phthalocyanine (Pc) complexes $[LnPc_2]^-$ (Ln^{III} = Tb, Dy) [8], where Ln ions provide large magnetic anisotropy to the system. Using Ln ions remarkable energy barrier as high as 1837 K [9] and blocking temperature of 80 K [10] are reported. However, one major drawback of these Ln^{III}-based complexes is a decrease in blocking temperature because of quantum tunneling of magnetization (QTM) [11]. The main challenge for the researcher is to overcome QTM which can be reduced by the introduction of exchange interaction in complex, thereby increasing the exchange coupling interaction (J) which enhances the degree of covalency of the metal–ligand bond [12]. For that reason, 3d-4f heterometallic

P. Shukla · M. Ezhava · S. Roy · S. Das (✉)
Department of Basic Sciences, Chemistry Discipline, Institute of Infrastructure Technology Research and Management, Near Khokhra Circle, Maninagar East, Ahmedabad, Gujarat 380026, India
e-mail: souravdas@iitram.ac.in

A. Mallick
Department of Chemistry, Ramakrishna Mission Vidyamandira, Belur Math, Howrah, West Bengal 711202, India

architecture induces strong interaction between metal ions where magnetic exchange between the metal center occurs via super exchange mechanism through diamagnetic ligand which reduces the QTM and enhances U_{eff} and T_B. In that respect ligand designing plays an important role. An axial ligand field is required for the ions that possess largest angular momentum belongs from oblate states like Tb^{III}, Dy^{III}, and on the other hand, equatorial field is required for prolate states like Er^{III} and Yb^{III} [13]. So, to overcome the QTM several methods are applied; one of them includes synthesizes of heterometallic complexes. The first heterometallic metal complex SMM synthesized was a Cu_2Tb_2 complex whose structure is shown in Fig. 1 [14]. Later on, a variety of 3d metal ions were used owing to their individual characteristics. For example, Murray and group have reported a heterometallic $Cr_2^{III}Ln_2^{III}$ complex where strong magnetic interaction between Cr^{III} and Ln^{III} metal ions, QTM was significantly quenched, thereby enhancing the blocking temperature T_B [15]. Another aspect of heterometallic complexes is that by using several 3d metal ions one can elevate the crystal field present in lanthanide ions and thus can increase the energy barrier [16]. One of the main categories is cobalt lanthanide-based SMM. For Co^{II} ion, the magnetic anisotropy does not depend on first-order orbital angular momentum, however, based on second-order orbital angular momentum [17, 18]. This mixing of ground state to excited state is regulated by the geometry of the system. Further, the D value of the cobalt ion can also be tuned by utilizing certain multidentate ligands to link Co^{II} ions with other Ln^{III} ions. This becomes the main focus of this chapter where recent examples of Co(II)/Ln(III) are used to depict the importance of ligand design and coordination geometry on the magnetic properties. The later sections will deal with very recent examples based on their nuclearity.
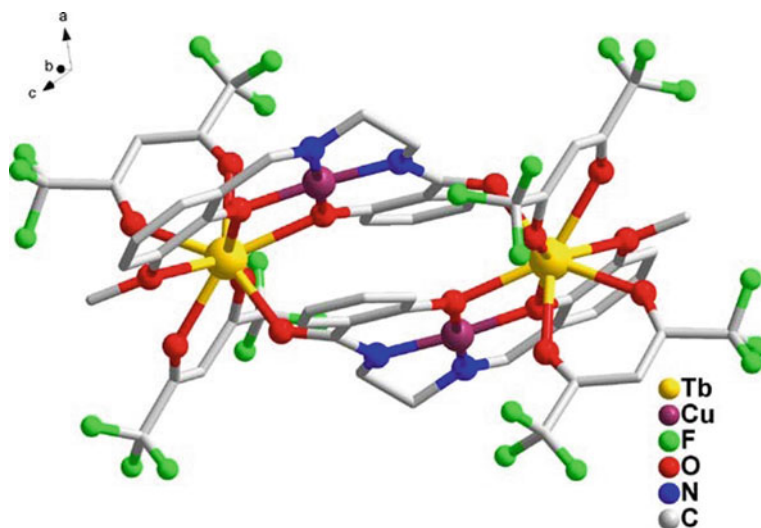
Fig. 1 Ball and stick diagram of Cu_2Tb_2 complex

2   Co/Ln Coordination Clusters with Various Nuclearity

2.1   Dinuclear Complexes

Ray and group have utilized a simple ligand LH = 3-methoxy-N-(2(methylsulfanyl) phenyl)salicylaldimine) to synthesize a new dinuclear Co^{II}/Ln^{III} complexes $[Ln^{III}Co^{II}L_2(NO_3)_3]\cdot H_2O$ {Ln^{III} = La(**2**), Gd(**3**), Tb(**4**), Dy(**5**), Ho(**6**)} whose detailed experimental and theoretical properties are studied [19]. The ligand used is chosen due to its coordination pockets which consists of coordination pockets favoring the binding of both Co^{II} and Ln^{III} ions simultaneously. Also, the binding of lanthanide metal ion provides a distortion to the geometry of Co^{II} ion which is further favored due to the presence of–SM e group at axial positon which due to its large size creates a large deviation in bond parameters. Thus, this feature makes this $Co^{II}–Ln^{III}$ family the first example of a dinuclear heterometallic complex having a distorted octahedral Co^{II} metal that exists in between *fac* and *mer* geometric isomers. These complexes are formed by the action of the ligand with LiOH in acetonitrile; to which $CoCl_2\cdot 6H_2O$ was added and stirred for three hours which was filtered to give red colored crystals. The neutral complex comprises of two ligand L^- bridging metal centers with two phenoxido bridges. Magnetic analysis reveals ferromagnetic interaction in compounds **3–6** between the Co–Ln ions. Theoretical calculations show **2** and **3** as weak SIM (single ion magnet) and SMM, respectively, solely based on anisotropy of Co^{II} ion. Kou and group [20] have synthesized a Co^{II}/Ln^{III} $[Co(H_{0.5}L)Dy(DBM)_2(H_2O)](ClO_4)_{0.5}\cdot 3H_2O$ (**7**) chiral complex where the enantiomer of **7** is obtained in the same pot. The complex **7** consists of a cationic structure $[Co(H_{0.5}L)Dy(DBM)_2(H_2O)]^{0.5+}$ with one ligand, Co^{II} ion, Dy^{III} ion along with two DBM^- molecules. The experimental $\chi_M T$ value of **7** is similar to that of the theoretical value for one Dy^{III} ion. Ac magnetic susceptibility measurement under 2000 Oe shows an energy barrier of 53.1 K and $\tau_0 = 2.0 \times 10^{-8}$ s. Further, the experimental energy barrier matches well with the theoretical value and depicts that QTM between two ground states was suppressed in fitting temperature range and the relaxation mechanism in **7** is governed by Orbach and Raman process (Fig. 2). Chandrasekhar and group [21] have used a ferrocene-based ligand to synthesize four complexes $[Co(\mu\text{-}L)(\mu\text{-}CCl_3COO)Y(NO_3)_2]\cdot 2CHCl_3\cdot CH_3CN\cdot 2H_2O$ (**8**), $[Co(\mu\text{-}L)(\mu CH_3COO)Y(NO_3)_2]\cdot CH_3CN$ (**9**), $[Co(\mu\text{-}L)(\mu\text{-}PhCOO)Y(NO_3)_2]\cdot 3CH_3CN\cdot 2H_2O$ (**10**), and $[Co(\mu\text{-}L)\text{-}(\mu\text{-}tBuCOO)Y(NO_3)_2]\cdot CHCl_3\cdot 2H_2O$ (**11**); all have them having $Co^{II}Y^{III}$ core. The complex was synthesized by the addition of ligand LH_2 in $CHCl_3/MeOH$ to $Co(ClO_4)_2$ and $Y(NO_3)_3$ along with base triethylamine. For complex **9**, $Co(OAc)_2$ is used instead of $Co(ClO_4)_2$ and the solution is refluxed for three hours. The experimental $\chi_M T$ value of all complexes is comparable with that of theoretical ones. Ac magnetic susceptibility measurement for all complexes was studied at 1200 Oe. The data from Arrhenius plot reveals energy barrier and τ_0 of 8.4(6) K and $3.2(4) \times 10^{-6}$ s for **8**; U_{eff} of 11.0(4) K and $\tau_0 = 2.5(2) \times 10^{-6}$ s for **9**; U_{eff} of
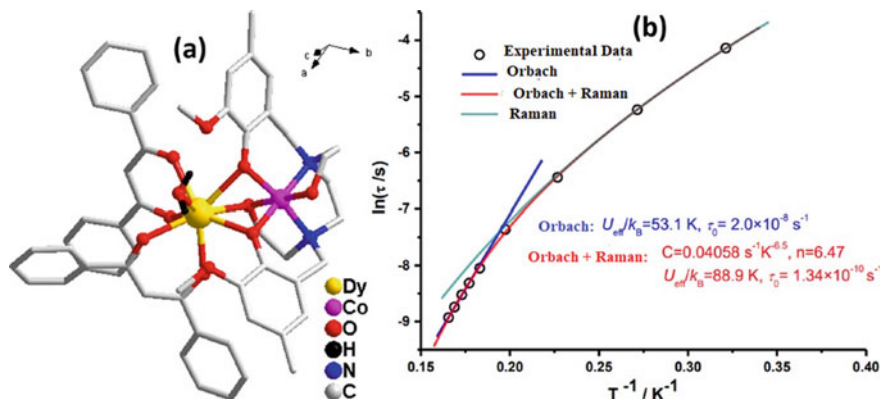
Fig. 2 **a** Ball and stick diagram of **7**. **b** Temperature dependence of relaxation time for **7**

13.7(8) K and $\tau_0 = 2.6(4) \times 10^{-6}$ s for **10** and U_{eff} of 18.7(6) K and $\tau_0 = 7.4(9) \times 10^{-7}$ s for **11**. The Debye model reveals a single relaxation process for **8–10**.

2.2 Trinuclear Complexes

The first Co^{II}/Ln^{III} SMM $[L_2Co_2Gd][NO_3]\cdot2CHCl_3$ (**12**) was synthesized by Chandrasekhar and group using a phosphorus-based tris hydrazone ligand where all metal ions Co–Gd–Co are arranged in a linear manner [22]. The structure involves two ligands holding together three metal ions along with one mole of nitrate ion. Ac magnetic susceptibility measurement shows an energy barrier of 27.2 K and $\tau_0 = 1.7 \times 10^{-7}$ s confirming the SMM behavior of the complex (Fig. 3).

Nguyen and group have synthesized a stable trinuclear complex $[LnCo_2(L)_2(\mu_{1,3}OOCCH_3)_2X]$ where Ln^{III} = La (**13**), Ce(**14**), Nd(**15**), Sm(**16**),
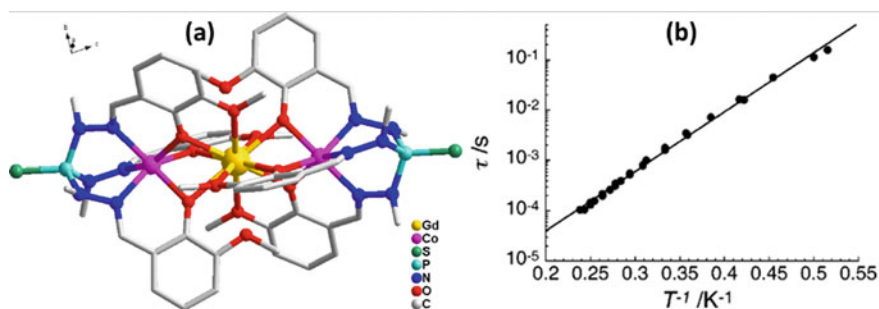
Fig. 3 **a** Ball and stick diagram of **12**. **b** τ versus T^{-1} plot at $H_{dc} = 0$

Gd(17), Dy(18), Er(19), and Yb(20) and X = κ_2-CH_3COO^- or Cl^- using one-pot reaction of 2,6-dipicolinoylbis(N, Ndiethylthiourea) with cobalt acetate and lanthanide chloride in methanol along with base trimethylamine [23]. The structure consists of two ligands with two moles of cobalt ion and one lanthanide ion along with two acetate ions acting as bridging mode between Co^{II} and Ln^{III} ion. Further, coordination around Ln^{III} ion is provided by acetate ion for **13**, **17,** while rest of complex is coordinated by chloride ion. Magnetic studies reveal weak antiferromagnetic interaction with $J_{Co-Co} = -0.49$ cm^{-1}. Further, CoDyCo analogue shows antiferromagnetic interaction while rest of the CoLnCo analogues shows ferromagnetic interaction. Papatriantafyllopoulou and group have employed di-2-pyridyl ketone, $(py)_2CO$ to prepare four Co^{II}/Ln^{III} clusters $[Co_2Ln\{(py)_2C(OEt)(O)\}_4(NO_3)(H_2O)]_2[M(NO_3)_5](ClO_4)_2$ (Ln^{III} = Gd (**21**), Dy (**22**), Tb (**23**), Y (**24**)) [24]. The cationic part of the complex consists of two Co^{II} ion, one Gd^{III} ion along with four ligands $(py)_2C(OEt)(O)^-$. Weak ferromagnetic interaction of $J_{Co-Co} = +1.3$ and $+0.40$ cm^{-1} is observed for **21** and **24,** respectively. Ac magnetic susceptibility measurement reveals a weak out-of-phase signal which might depict complex **22** being a weak SMM.

2.3 Tetranuclear Complexes

Ray and group have reported two families of $Co^{II/III}$–Ln^{III} $[Ln^{III}_2Co^{III}_2L_2(N-BuDEA)_2(O_2CCMe_3)_4(H_2O)_2]$ (Ln = Gd (**25**), Tb (**26**), Dy (**27**)) and pentanuclear $Ln^{III}_2Co^{II}Co^{III}_2 L_2(N-BuDEA)_2(O_2CCMe_3)_6(MeOH)_2$ (Ln = Dy (**28**), Ho (**29**)) using ligands H_2L (o-vanillin oxime) and N-BuDEAH$_2$ (N-butyldiethanolamine) (Fig. 4a) [25]. The tetranuclear series is formed by the reaction of $Co_2(\mu-OH_2)(O_2CCMe_3)_4(HO_2CCMe_3)_4$ and $Ln(NO_3)_3$ with N-BuDEAH$_2$ followed by addition of ligand and base in ratio 0.5:1:1:1:4 in MeOH/DCM. The tetranuclear complex consists of $\{Ln^{III}_2Co^{III}_2\}$ core with two ligands and two N-BuDEA^{2-}
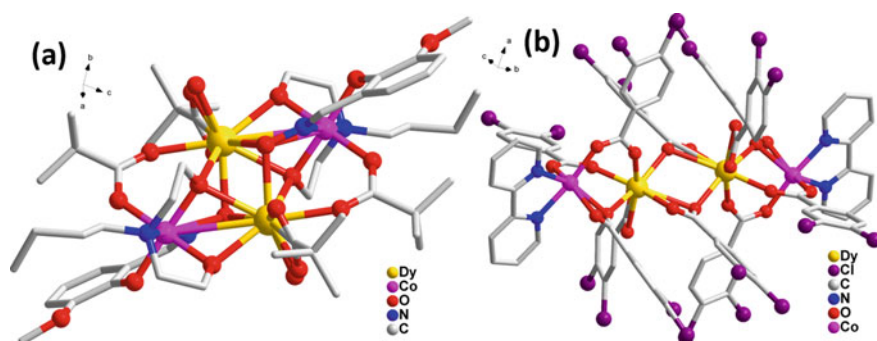
Fig. 4 Ball and stick diagram of **a 27** and **b 35** where H atoms apart from in water molecules are omitted

anions. With the J value of -0.09 cm^{-1}, the presence of weak antiferromagnetic exchange interaction between Gd^{III} centers is reported. No maxima peaks are reported for **27** in Ac magnetic susceptibility measurement. Dong and group have synthesized a linear [Ln$_2$Co$_2$(3,4-DCB)$_{10}$(2,2′bpy)$_2$] (Ln^{III} = Nd (**30**), Sm (**31**), Eu (**32**), Gd (**33**), Tb (**34**), Dy (**35**), and Er (**36**)) complex using 3,4-dichlorobenzoic acid (3,4-HDCB), 2,2-bipyridine (2,2′-bpy) as ligands (Fig. 4b) [26]. The structural analysis reveals complexes having linear arrangement Co^{II}–Ln^{III}–Ln^{III}–Co^{II} formed with two Co^{II} and Dy^{III}ions each, two 2,2′-bpy co-ligands and ten 3,4-DCB anions. Ac magnetic susceptibility measurements at zero dc field of **35** reveal frequency-dependent out-of-phase signal; however, no maxima peak is observed. Li and group have reported tetranuclear complexes [Ln$_2$Co$_2$(hfac)$_{10}$(NITPhPybis)$_2$] [Ln^{III} = Gd (**37**), Tb (**38**), Dy (**39**), and Ho (**40**); formed using nitronyl nitroxide biradical ligands having pyridine groups which grasps Co^{II} and Ln^{III} ions together [27]. A centrosymmetric cyclic structure is formed using Co^{II} and Ln^{III} depicting a rare octaspin motif. Ac magnetic susceptibility measurement reveals **38** and **39** displaying slow relaxation of the magnetization behavior.

2.4 Higher Nuclearity Complexes

In this section, complexes having nuclearity higher than four are described. Only recent representative examples are discussed.

The pentanuclear complexes **28** and **29** described in the previous section consist of {Ln^{III}$_2$ Co^{III}$_2$ Co^{II}} core with two L^{2-} and two N-BuDEA^{2-} anions [25]. The Co–Ln exchange interaction is ferromagnetic for **28** while it is antiferromagnetic for **29**. Magnetic analysis depicts out-of-phase susceptibility in **28**. Zhao and group have synthesized a hexanuclear Co^{III}$_4$Ln^{III}$_2$ clusters [Co$_4$Ln$_2$(μ_3-O)$_2$(μ-N$_3$)$_2$(OH)$_2$(H$_2$O)$_2$(HL)$_4$]·(CH$_3$CO$_2$)$_2$·20H$_2$O [Ln^{III} = Dy (**41**), Gd (**42**), Tb (**43**), Eu (**44**) and Ho (**45**)] using 2-[Bis(pyridin-2-ylmethyl)amino]-2-(hydroxymethyl)propane-1,3-diol ligand [28]. The structural arrangement consists of four Co^{III} ions, two Dy^{III} ions, four HL^{2-}, two N^{3-} ligands, two $_{\mu3}$-O^{2-}, two water molecules and two acetate ions forming a lucanidae like arrangement. Ac magnetic susceptibility measurements reveal an energy barrier of 73.51 K and $_{\tau0}$ = 1.68 × 10^{-8} s. Liang and group have recently explored the effect of solvent by synthesizing two decanuclear clusters [Dy$_2$Co$_8$(μ_3OCH$_3$)$_2$(L)$_4$(HL)$_2$(OAc)$_2$(NO$_3$)$_2$(CH$_3$CN)$_2$]·CH$_3$CN·H$_2$O (**46**) and [Dy$_4$Co$_6$(L)$_4$(HL)$_2$(OAc)$_6$(OCH$_2$CH$_2$OH)$_2$(HOCH$_2$CH$_2$OH)(H$_2$O)]·9CH$_3$CN (**47**) [29]. The only difference in the reaction process was the change of reaction solvent from methanol and acetonitrile in **46** to acetonitrile and ethylene glycol in **47**. The structure of **46** is formed by two Dy^{III}, eight Co^{II} ions, four L^{3-}, two HL^{2-}, two acetate ions, two (CH$_3$O)$^-$ and CH$_3$CN ligand. While for **47**, it contains four Dy^{III}, six Co^{II} ions, three L^{3-}, three HL^{2-}, six acetate ions, three coordinated (HOCH$_2$CH$_2$O)$^-$ ion along with one coordinated water molecule. Ac magnetic susceptibility measurements reveal an energy barrier of 14.89 K and $_{\tau0}$ = 1.68 ×
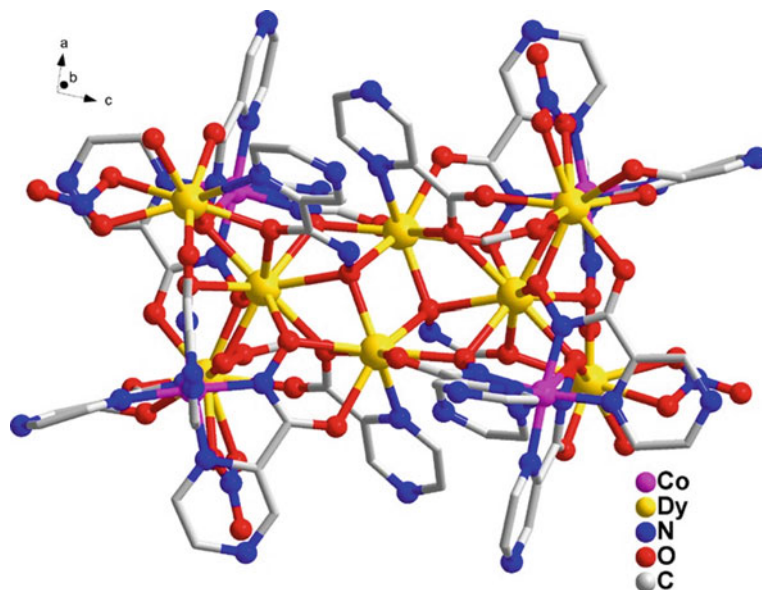
Fig. 5 Ball and stick diagram of **48**

10^{-7} s for **46** and energy barrier of 5.49 K and $\tau_0 = 2.88 \times 10^{-5}$ s for **47** at zero dc field. Dou and group have synthesized a series of butterfly shaped metallacrowns (MCs) $[Dy(pyzic)\{Dy_3Co_2(pyzha)_6(*pyzha)(NO_3)_2(H_2O)(MeOH)_2\}]_2$ ($Ln^{III} = Dy$ (**48**), Ho (**49**) and Tm (**50**)) using pyrazinehydroxamic acid and pyrazinic acid ligands (Fig. 5) [30]. At zero dc field, U_{eff} is 1.46 K and $\tau_0 = 2.4 \times 10^{-5}$ s for **48** (Table 1).

3 Summary

The heterometallic complexes of Co/Ln represent an interesting class of molecular magnets with fascinating structures and magnetic properties. Co^{II} provides a large spin–orbit coupling which when combined with highly anisotropic Ln^{III} ion can lead to the formation of SMMs with better properties. The role of ligand and the coordination geometry surrounding the metal ions plays a vital part in modulating the magnetic properties. While considerable progress is made in this field, proper designing of complexes can certainly lead to the development of SMM with superior properties. Apart from this, a chemist also requires a strong theoretical understanding of the complexes which seems to be lacking. Backed by this knowledge, synthetic chemists can strategically plan designs to enhance the SMM behavior of Co/Ln complexes.

Table 1 Magnetic parameter of Co^{II}/Ln^{III} complexes

Molecular formula	U_{eff}	τ_0	References
$[Co_2Dy_2(L)_2(CH_3COO)_4(OH)_2(H_2O)_2]\cdot(ClO_4)_2$ $H_2L =$ N1,N3-bis(3-methoxysalicylidene)diethylenetriamine	33.8 K	3.73×10^{-6} s	[31]
$[Co_2Dy(HL)_4]NO_3\cdot2CH_3CN$ $H_3L = 3$-[(2-Hydroxy-3-methoxy-benzylidene)-amino]-propane-1,2-diol	40 K	1.8×10^{-6} s	[32]
$[CoDy(mepao)_3(NO_3)_3]$ mepaoH = methyl 2-pyridyl ketone oxime	16 K	2.5×10^{-8} s	[33]
$[CoDy(HL)(OAc)_3(H_2O)_3]\cdot(OAc)(H_2O)_3$ 2-hydroxy-1,3-diaminopropane + o-vanillin	113 K	7.0×10^{-9} s	[34]
$[Ln_4Co_2(\mu_3\text{-}OH)_2(NO_3)_4(CH_3COO)_4L_4(DMF)_2]\cdot$ $2C_2H_5OH$ $H_2L = 2$-((2-(hydroxymethyl)phenylimino)methyl) phenol (H_2L)	41.9 K	1.21×10^{-7} s	[35]
$[Co_4Dy_3\text{-}L_4(\mu_4\text{-}O)_2(\mu\text{-}OMe)_2(\mu_{1,3}\text{-}OAc)_4(H_2O_2(NO_3)_2]\cdot NO_3\cdot3CH_3OH\cdot1.5H_2O$ $H_2L =$ 3-methoxysalicylaldehyde and 2-amino-2methyl1-1-propanol	73.954 K, 34.963 K	9.40×10^{-7} s, 6.91×10^{-7} s	[36]
$[Co_4Ln(L)_4(OAc)_2(S)_4](NO_3)(H_2O)$ $HL_2 = 6$-formyl-2-(hydroxymethyl)-4methylphenol	Slow magnetic relaxation	–	[37]
$[Co_2Dy_2(L)_4(NO_3)_2(THF)_2]$-4THF $L =$ o-vanillin and 2-aminophenol	15.827 K, 118.12 K	7.7×10^{-4} s, 6.2×10^{-7} s	[38]

References

1. Sessoli R, Gatteschi D, Caneschi A, Novak MA (1993) Magnetic bistability in a metal-ion cluster. Nature 365:141–143
2. Zhang P, Guo Y-N, Tang J (2013) Recent advances in dysprosium-based single molecule magnets: structural overview and synthetic strategies. Coord Chem Rev 257:1728–1763
3. Bogani L, Wernsdorfer W (2010) Molecular spintronics using single-molecule magnets. Nat Mater 7:194–201
4. Lehmann J, Gaita-Arino A, Coronado E, Loss DJ (2009) Quantum computing with molecular spin systems. J Mater Chem 19:1672–1677
5. Zheng Y-Z, Evangelisti M, Winpenny REP (2011) Co–Gd phosphonate complexes as magnetic refrigerants. Chem Sci 2:99–102
6. Harriman KL, Brosmer JL, Ungur L, Diaconescu PL, Murugesu M (2017) Pursuit of record-breaking energy barriers: a study of magnetic axiality in diamide ligated Dy^{III} single molecule magnets. J Am Chem Soc 139:1420–1423
7. Ruiz E, Cirera J, Cano J, Alvarez S, Loose C, Kortus J (2008) Can large magnetic anisotropy and high spin really coexist? Chem Comm 1:52–54
8. Ishikawa N, Sugita M, Ishikawa T, Koshihara S-Y, Kaizu Y (2003) Lanthanide doubledecker complexes functioning as magnets at the single-molecular level. J Am Chem Soc 125:8694–8695
9. Guo FS, Day BM, Chen YC, Tong ML, Mansikkamäki A, Layfield R (2017) A dysprosium metallocene single-molecule magnet functioning at the axial limit. Angew Chem Int Ed 129:11603–11607
10. Guo F-S, Day BM, Chen Y-C, Tong M-L, Mansikkamäki A, Layfield R (2018) Magnetic hysteresis up to 80 kelvin in a dysprosium metallocene single-molecule magnet. Science 362:1400–1403
11. Liu J-L, Chen Y-C, Tong M-L (2018) Symmetry strategies for high performance lanthanide-based single-molecule magnets. Chem Soc Rev 47:2431–2453
12. Ding YS, Yu KX, Reta D, Ortu F, Winpenny REP, Zheng YZ, Chilton NF (2018) Field- and temperature-dependent quantum tunneling of the magnetization in a large barrier single-molecule magnet. Nat Commun 9:3134
13. Lin PH, Yang BY, Tsai MH, Chen PC, Huang KF, Lin HH, Lai CH (2019) Manipulating exchange bias by spin-orbit torque. Nat Mater 18:335–341
14. Osa S, Kido T, Matsumoto N, Re N, Pochaba A, Mrozinski J (2004) A tetranuclear 3d–4f single-molecule magnet:$[Cu^{II}LTb^{III}(hfac)_2]_2$. J Am Chem Soc 126:420–421
15. Langley SK, Wielechowski DP, Vieru V, Chilton NF, Moubaraki B, Abrahams BF, Chibotaru LF, Murray KS (2013) A $Cr^{III}_2Dy^{III}_2$ single-molecule magnet: enhancing the blocking temperature through 3d magnetic exchange. Angew Chem Int Ed 52:12014–12019
16. Shao D, Wang XY (2020) Development of single-molecule magnets. Chin J Chem 38:1005–1018
17. Tripathi S, Dey A, Shanmugam M, Narayanan RS, Chandrasekhar V (2018) Cobalt (II) complexes as single-ion magnets. In: Organometallic magnets. Springer, pp 35–75
18. Dey A, Tripathi S, Shanmugam M, Narayanan RS, Chandrasekhar V (2018) Cobalt (II)/(III)–Lanthanide (III) complexes as molecular magnets. In: Organometallic magnets. Springer, pp 77–100
19. Basak D, Leusen JV, Gupta T, Kögerler P, Bertolasi V, Ray D (2020) Unusually distorted pseudo-octahedral coordination environment around Co^{II} from thioether Schiff base ligands in dinuclear [CoLn] (Ln = La, Gd, Tb, Dy, Ho) complexes: synthesis, structure, and understanding of magnetic behavior. Inorg Chem 59:2387–2405
20. Liu M-J, Yuan J, Wang B-L, Wu S-T, Zhang Y-Q, Liu C-M, Kou H-Z (2018) Spontaneous resolution of chiral Co(III)Dy(III) single-molecule magnet based on an achiral flexible ligand. Cryst Growth Des 18:7611–7617

21. Acharya J, Swain A, Chakraborty A, Kumar V, Kumar P, Gonzalez JF, Cador O, Pointillart F, Rajaraman G, Chandrasekhar V (2019) Slow magnetic relaxation in dinuclear $Co^{II}Y^{III}$ complexes. InorgChem 58:10725–10735

22. Chandrasekhar V, Pandian BM, Azhakar R, Vittal JJ, Clérac R (2007) Linear trinuclear mixed-metal $Co^{II}-Gd^{III}-Co^{II}$ single-molecule magnet: $[L_2Co_2Gd][NO_3] \cdot 2CHCl_3$ ($LH_3 =$ (S)P[N(Me)NCH$-C_6H_3$-2-OH-3-OMe]$_3$). Inorg Chem 46:5140–5142

23. Jesudas JJ, Pham CT, Hagenbach A, Abram U, Nguyen H (2019) Trinuclear $Co^{II}Ln^{III}Co^{II}$ complexes (Ln = La, Ce, Nd, Sm, Gd, Dy, Er, and Yb) with 2,6-dipicolinoylbis (N,N-diethylthiourea): synthesis, structures, and magnetism. Inorg Chem 59:386–395

24. Efthymiou CG, Ní Fhuaráin Á, Mayans J, Tasiopoulos A, Perlepes SP, Papatriantafyllopoulou C (2019) A novel family of triangular $Co^{II}_2Ln^{III}$ and $Co^{II}_2Y^{III}$ clusters by the employment of di-2-pyridyl ketone. Magnetochemistry 5:35

25. Basak D, Smythe L, Herchel R, Murrie M, Nemec I, Ray D (2021) From tetranuclear to pentanuclear [Co–Ln] (Ln = Gd, Tb, Dy, Ho) complexes across the lanthanide series: effect of varying sequence of ligand addition. Dalton Trans 50:11861–11877

26. Zhang J-W, Liu W-H, Wang C-R, Liu B-Q, Dong Y-P (2020) A series of linear $Co^{II}_2Ln^{III}_2$ clusters derived from 3,4-dichlorobenzoate and 2,2′-bipyridine: syntheses, structures, and properties. Inorganica Chim Acta 502:119343

27. Li H, Sun J, Yang M, Sun Z, Tang J, Ma Y, Li L (2018) Functionalized nitronyl nitroxide biradicals for the construction of 3d–4f heterometallic compounds. Inorg Chem 57:9757–9765

28. Li Q, Peng Y, Qian J, Yan T, Du L, Zhao Q (2019) A family of planar hexanuclear $Co^{III}_4Ln^{III}_2$ clusters with lucanidae-like arrangement and single-molecule magnet behavior. Dalton Trans 48:12880–12887

29. Yu S, Wang H-L, Chen Z, Zou H-H, Hu H, Zhu Z-H, Liu D, Liang Y, Liang F-P (2021) Two decanuclear $Dy^{III}_xCo^{II}_{10-x}$ (x = 2, 4) nanoclusters: structure assembly mechanism, and magnetic properties. Inorg Chem 60:4904–4914

30. Zhang H-G, Du Y-C, Yang H, Zhuang M-Y, Li D-C, Dou J-M (2019) A new family of Co_4Ln_8 metallacrowns with a butterfly-shaped structure. Inorg Chem Frontiers 6(7):1904–1908

31. Zhao L, Wu J, Xue S, Tang J (2012) A linear 3d–4f tetranuclear $Co^{III}_2Dy^{III}_2$ single-molecule magnet: synthesis, structure, and magnetic properties. Chem Asian J 7:2419–2423

32. Modak R, Sikdar Y, Gómez-García CJ, Benmansour S, Chatterjee S, Goswami S (2021) Slow magnetic relaxation in a Co_2Dy trimer and a Co_2Dy_2 tetramer. Chem Asian J 16:666–677

33. Polyzou C, Koumousi ES, Lada ZG, Raptopoulou C, Psycharis V, Rouzières M, Tsipis AC, Mathoniere C, Clerac R, Perlepes SP (2017) "Switching on" the single-molecule magnet properties within a series of dinuclear cobalt (III)–dysprosium (III) 2-pyridyloxime complexes. Dalton Trans 46:14812–14125

34. Dolai M, Ali M, Titiš J, Boča R (2015) Cu (II)–Dy (III) and Co (III)–Dy (III) based single-molecule magnets with multiple slow magnetic relaxation processes in the Cu (II)–Dy (III) complex. Dalton Trans 44:13242–13249

35. Zhang H, Liu R, Zhang J, Li Y, Liu W (2016) Chair-like $[Ln^{III}_4Co^{III}_2]$ (Ln = Dy, Eu, Gd, Tb) clusters including a $[Dy^{III}_4Co^{III}_2]$ single-molecule magnet. CrystEngComm 18:8246–8252

36. Roy S, Hari N, Mohanta S (2019) Synthesis, crystal structures, magnetic properties, and fluorescence of two heptanuclear $Co^{III}_4Ln^{III}_3$ compounds (Ln = Gd^{III}, Dy^{III}): multiple relaxation dynamics in the Dy^{III} analogue. Eur J Inorg Chem 2019:3411–3423

37. Chandrasekhar V, Das S, Dey A, Hossain S, Lloret F, Pardo E (2013) Synthesis, structure, and magnetic properties of a family of heterometallic pentanuclear $[Co_4Ln]$ (Ln = Gd^{III}, Dy^{III}, Tb^{III}, and Ho^{III}) assemblies. Eur J Inorg Chem 2013:4506–4514

38. Mondal KC, Sundt A, Lan Y, Kostakis GE, Waldmann O, Ungur L, Chibotaru LF, Anson CE, Powell AK (2012) Coexistence of distinct single-ion and exchange-based mechanisms for blocking of magnetization in a $Co^{II}_2Dy^{III}_2$ single-molecule magnet. Angew Chem Int Ed 51:7550–7554

Fluorescent Probes for Cellular Organelle-Specific Detection of Cysteine

Aayushi Joshi, Nikunjkumar Vagadiya, Mohil Odedara, Manoj Pandey, Anu Manhas, and Nandini Mukherjee

1 Introduction

Biothiols such as cysteine (Cys), homocysteine (Hcy), and glucathione (GSH) plays a crucial role in the living systems [1]. In particular, Cys performs various roles in biological processes like metabolism and protein synthesis [2]. Alterations in cellular Cys levels cause various diseases, like Alzheimer's [3], cancer [4], cardiovascular [5], diabetes mellitus [6], and skin disease [7]. As a result, monitoring Cys levels in the organelles is considered critical for the understanding of its biological roles, which could lead to early detection of the related disorders. Progress in this field still needs further optimization due to the difficulty in differentiating Cys from GSH and Hcy in sub-cellular level. Development of various analytical approaches for detecting Cys levels in vivo has recently piqued people's attention. Instrumental analytical techniques for Cys detection such as HPLC, capillary electrophoresis, mass spectrometry, and electrochemical methods are not convenient for high-throughput clinical analysis or research because of their inherent limitations of high costs and time-intensive process [1]. In recent times, chemosensor-based optical probes (fluorescent) have been extensively developed due to their high sensitivity, specificity, ease of implementation, and short reaction time [1, 2]. These fluorescent probes can detect Cys in cells without damaging them, because of their non-invasive characteristics. Recently Cys-triggered specific reaction probes depending on various mechanism like cyclization with aldehydes, Michael addition, cyclization with acrylates, nucleophilic substitution, and S_NAr reaction have been developed to understand the physiological function of Cys [8, 9]. The *in cellulo* and in vitro identification of biological Cys molecule in

A. Joshi · N. Vagadiya · M. Odedara · M. Pandey · A. Manhas (✉) · N. Mukherjee (✉)
Department of Chemistry, School of Technology, Pandit Deendayal Energy University,
Gandhinagar, Gujarat 382421, India
e-mail: Anu.Manhas@sot.pdpu.ac.in

N. Mukherjee
e-mail: Nandini.Mukherjee@sot.pdpu.ac.in

living organism has been examined in detail using fluorescence imaging and other approaches. For instance, Tao et al. have developed a BODIPY dye-based fluorescent probe [10], and Zhang's group designed a mitochondrial-targeted fluorescent probe for Cys detection [11]. Further, Fan's group has developed mitochondrial-based fluorescent probe for the detection of Cys/Hcy and H_2S simultaneous [12]. This review intended to give brief overview on fluorescent chemosensors based on their molecular scaffolds which were categorized by their mechanistic pathway for Cys detection. Moreover, discussion pertaining to the use of nanomaterials in Cys detection is also made. Finally, the obstruction and future scopes of fluorescent-based chemosensor for Cys detection in the field of bio-imaging have been discussed.

Owing to the importance of the specific role of each cellular organelle, like endoplasmic reticulum (ER), lysosome, and mitochondria in the functioning of the cells, and in the current work, focus is given on the studies regarding the in situ detection of Cys inside these organelles. For instance, Cys was identified to assist in the degradation of cysteine-containing protein in lysosome, which plays a key role in sub-cellular stress response involving the ER, Golgi apparatus, and regulating oxidative stress in mitochondria. Therefore, various fluorescent probes were developed to detect the Cys in lysosome, ER, and mitochondria. The design strategies for organelle-specific Cys probes are shown in the Table 1. It is obvious from the table that a number of fluorescent probes specific for Cys detection have been developed based on the thio group's high nucleophilicity and redox characteristics. Fluorescent probes are designed by certain cysteine-triggered mechanistic approach such as Cys-triggered reaction with acrylate, metal, α, β unsaturated ketone, and thioester. Following section presents a brief systematic account of these sensors.

2 Molecular Probes for Cys Detection

2.1 Cysteine Triggered Reaction with Acrylate

Cys-triggered reaction with acrylates is most promising addition cyclization reaction for the detection of Cys only. These kinds of probes followed the mechanism of protection of hydroxyl group with acrylate allowing nucleophilic addition reaction of cysteine in the C = C bond of acrylate. The addition reaction is further followed by cyclization to form a seven-membered ring by cleaving the hydroxy bond. GSH and Hcy can also react with acrylates, but due to eight and ten-membered ring formation, the cleavage reaction is extremely slow. Acrylates-based sensors provide most effective pathway for the specific detection of Cys. Songtao Cai et al. have developed a thioxanthene-indolium dye-based probe (probe 1) for Cys detection, which is used as a lysosome-targetable fluorescent probe [13] (Fig. 1). Probe 2 is developed based on the fluorophore merocyanine scaffold, which exhibits two photon excited fluorescence for specific detection of Cys in mitochondria [14]. Unlike 2, probe 3 having the acrylate unit as a fluorescence quencher was linked to hydroxyl group

Table 1 Cysteine-specific fluorescent molecular probes for specific organelle detection

Reaction pathway	Probe	$\lambda_{ex}/\lambda_{em}$ (nm)	LOD	Dynamic range	Organelle-specific Cys detection	Condition	Mechanism	Change	References
Cys-triggered reaction with acrylate	1	700/770	16 nM	0–2 μM	Lysosome	10 mM Ethanol:PBS (1:4v/v) pH:7.4	ICT	Fluorescence enhancement (11.9-fold)	[13]
	2	750/430–470 (Two-photon fluorescent probe)	150 μM	0.5–40 μM	Mitochondria (negative inner membrane potential of mitochondria assists in localization of the positively-charged fluorophore)	DMSO:PBS(1/1 v/v) pH:7.4	ICT	Fluorescence enhancement (tenfold)	[14]
	3	630/735	14.5 nM	5–15 μM	Mitochondria (cationic moiety as mitochondria targeting unit)	Ethanol/HEPES buffer (1:1 v/v, pH:7.4,37 °C	PET	Fluorescence enhancement	[15]
	4	303/non-fluorescent	0.80 μM	0–100 μM	Intracellular and exogenous Cys detection	10 mM HEPES buffer (10% DMSO,v/v) pH:7.2,25 °C	ESIPT	Fluorescence enhancement	[16]
	5	395/665	86.9 nM	0–30 μM	*In vivo* exogenous and endogenous Cys detection in mice	10 mM, PBS/DMSO mixtures (4:1,v/v) pH:7.4	ICT	Fluorescence enhancement (214-fold)	[18]
	6	400/504	80 nM	0–80 μM	Endogenous Cys detection in HeLa cells	10 mM DMSO:PBSbuffer, pH:7.4,37 °C	ICT	Large Stokes shift (104 nm)	[19]

(continued)

Table 1 (continued)

Reaction pathway	Probe	$\lambda_{ex}/\lambda_{em}$ (nm)	LOD	Dynamic range	Organelle-specific Cys detection	Condition	Mechanism	Change	References
	7	769/794	0.09 μM	0–20 μM	Iminium cationic unit as mitochondria targeting group	10 mM HEPES buffer,pH:7.4,37 °C	ICT	Color change green to red	[20]
	8	365/477	0.15 μM	0–200 μM	Endogenous and exogenous Cys detection in A549 cells	50 mM PBS buffer (40% DMSO) pH:7.4	ICT	Fluorescence enhancement (142-fold)	[21]
	9	309/472	0.12 μM	0–8 μM	Pyridinium unit as mitochondria targeting group	10 mM TRIS HCl buffered (1% DMSO) pH:7.0	ESIPT	Large Stokes shift (210 nm)	[17]
Cys-triggered cyclization reaction	**10**	450/660	79 nM	0–5 μM	Endogenous and exogenous Cys detection in HepG2 cells and mice	10 mM PBS (30%DMSO) pH:7.4	ICT	Large Stokes shift (210 nm)	[8]
	11	~363/515	105 nM	0–10 μM	Quinoline group for targeting Golgi apparatus	10 mM PBS/ethanol (8:2) pH:7.4	ICT	Fluorescence enhancement	[22]
	12	565/635	228 nM	0–250 μM	Quaternary ammonium indole group for Mitochondria targeting	10 mM DMSO/PBS (3:7) pH: 8.0	ICT	Fluorescent enhancement (35-fold)	[23]
	13	405/420–480	0.2 μM	0–35 μM	Mitochondria targeting by quaternary ammonium group	DMSO/saline = 1:9, v/v	–	Fluorescent enhancement (45 fold)	[24]

Table 1 (continued)

Reaction pathway	Probe	$\lambda_{ex}/\lambda_{em}$ (nm)	LOD	Dynamic range	Organelle-specific Cys detection	Condition	Mechanism	Change	References
Cys-triggered reaction with metal	14	430/489	0.72 μM	0–60 μM	Endoplasmic reticulum targeting by lipophilic CL ligand	20 mM HEPES aqueous buffer (DMSO: H_2O = 5:5) pH:7.4	Complexation/decomplexation interaction modulated	Fluorescent enhancement (43.4 fold)	[1]
Cys-triggered reaction with α, β unsaturated ketone	15	370/462	0.27 μM	0–120 μM	Exogenous and endogenous Cys detection in HeLa cells	DMSO/PBS(v/v, 1/1)		Fluorescence enhancement	[25]
Cys-triggered reaction with thioester	16	750/510–610	0.29 μM	2–10 μM (linear proportionality with F_{583nm}/F_{485nm})	Mitochondria targeting by positively-charged fluorophore	DMSO/PBS (1/1, v/v, pH:7.4	ICT	Fluorescence enhancement (34-fold)	[26]
	17	360/470	4.8 nM	0.1–5 μM	Intracellular Cys detection in HeLa cells	20 mM aqueous solution of phosphate buffer: 0.1% of ethanol pH:7.4	PET	Fluorescence enhancement (24.7-fold)	[27]
Cys-triggered reaction followed by rearrangement	18	430/non-fluorescent	27 nM	10–100 μM	Lysosome targeting by morpholine group	10 mM PBS buffer 20% DMSO pH:7.4	PET	Fluorescence enhancement (19.5-fold)	[28]
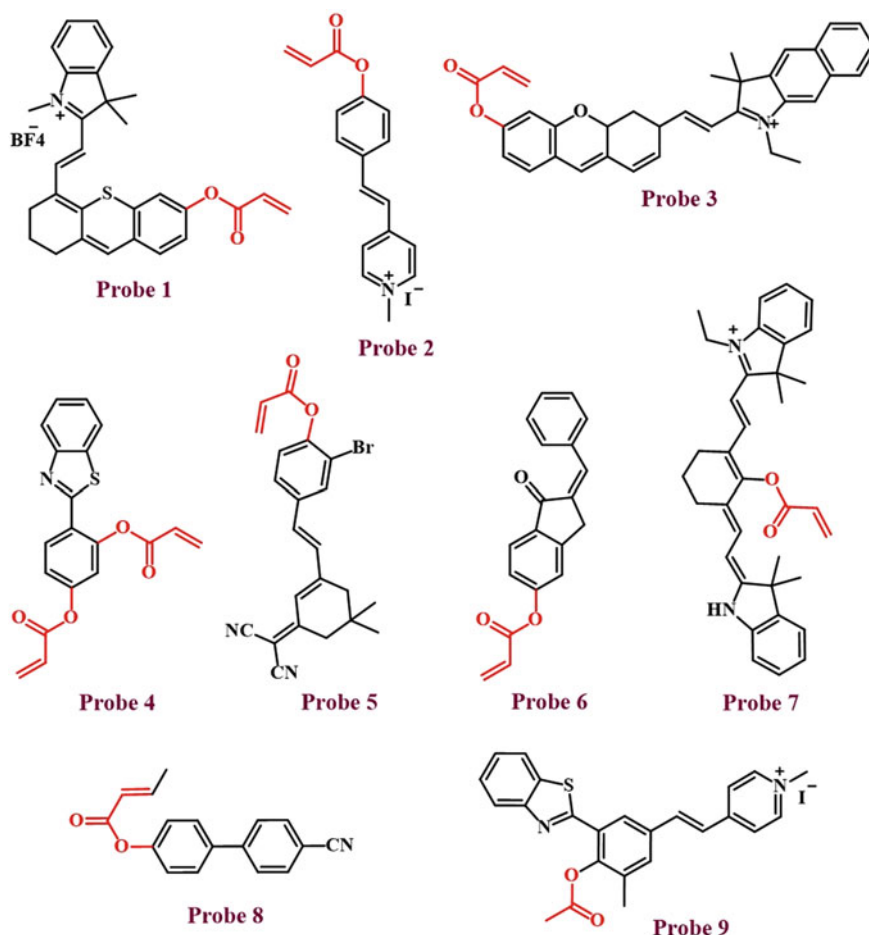
Fig. 1 Acrylate-based probes for organelle cysteine detection

of fluorescein derivative [15] and a lipophilic cation unit. It acts as the mitochondria biomarker which shows fluorescence enhancement with Cys in ethanol/HEPES buffer solution, which was specific for the mitochondrial Cys detection (Fig. 1). Probe **4** developed by using two acrylate moieties followed the excited state intramolecular charge transfer to achieve the specificity for Cys among other thiols [16]. Probe **9** followed the same mechanism as **4** and favors large Stokes shift of 210 nm when treated with Cys [17] (Fig. 1). Probe **5** showed an "ON–OFF" fluorescence response to Cys in 10 mM PBS/DMSO (4:1) at pH = 7.4 due to the presence of intramolecular charge transfer (ICT) [18] (Fig. 1). The absorption of probe **6** shows 214 fold times increase in the presence of Cys by rearranging the conjugated π-electron system of Cys fluorophore [19] (Fig. 1). Probe **7** when reacted with Cys caused large Stokes shift due to the arrangement of conjugated π-electron system of the fluorophore

[20] (Fig. 1). Guomin Zhao et al. has developed probe **eight**-based on the Michael addition/cyclization reaction mechanism to detect the presence of Cys [21] (Fig. 1).

2.2 Cysteine Triggered Cyclization Reaction

Cysteine detection involving nucleophilic attack at the probe followed by its cyclization is a well-known strategy. The $C = S$ bond of probe **10** is attacked by Cys through nucleophilic addition reaction with subsequent formation of a five-membered ring. This caused a 210 nm Stokes shift at 450 nm in 10 mM PBS (30% DMSO) solution [8] (Fig. 2). Probe **11** having $C = S$ group undergoes a similar nucleophilic attack by Cys followed by cyclization. Addition of Cys thus inhibits the PET process causing enhanced fluorescence [22] (Fig. 2). Probe **12** shows Cys-specific fluorescence enhancement due to cascade reaction (Fig. 2). A nucleophilic attack by Cys sulfydryl group on the active site of aromatic moiety was followed by keto-enol tautomerization to form a seven-membered stable ring as a byproduct [23]. Probe **13** shows 45-fold fluorescence enhancement when reacted with Cys owing to increase of conjugation in form of keto-enol tautomerism [24] (Fig. 2).
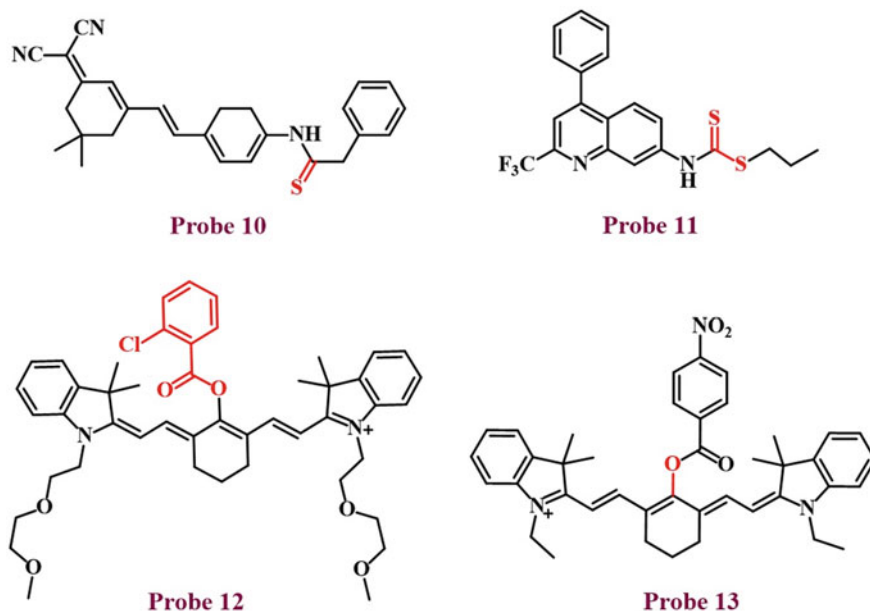
Fig. 2 Molecular probes for detection of Cys by nucleophilic attack and cyclization process
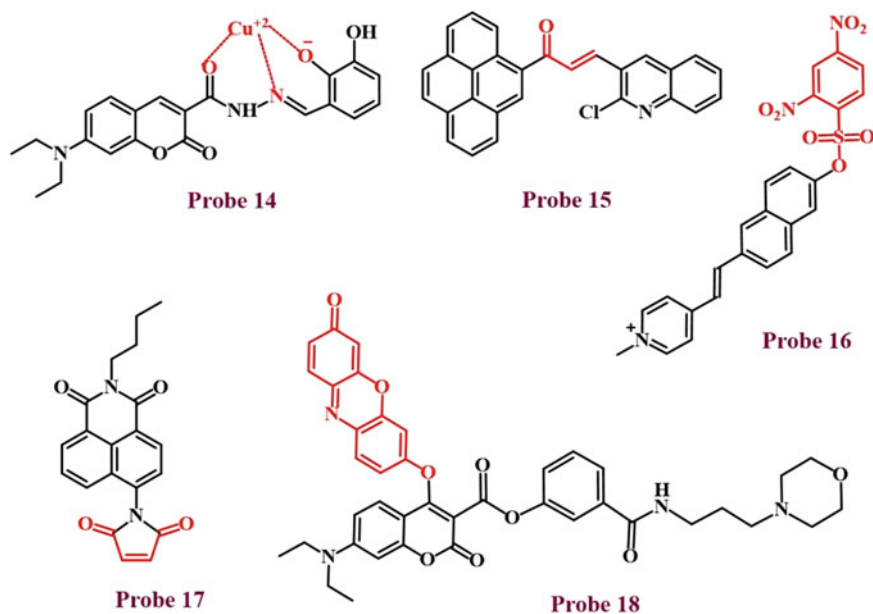
Fig. 3 Molecular probes for Cys detection mediated by metal ion, $S_N Ar$, and reaction with α, β unsaturated ketone and thioester

2.3 Cysteine Triggered Reaction with Metal

The fluorophore bearing hetero atoms like N, O, and S binds with metal site and form a fluorophore-metal coordination compounds. Probe **14** was designed based on the complexation-decomplexation mechanism (Fig. 3) for the detection of Cys. On the coordination of the ligand CL to Cu^{2+}, the probe **14** (CL-Cu) was formed and it detect Cys selectively in 20 mM DMSO-HEPES solution (1:1, v/v, pH 7.4) with increased fluorescence at 489 nm. Probe **14** was able to detect Cys selectively in ER [1].

2.4 Cysteine Triggered Reaction with ∝, β Unsaturated Ketone

Cysteine can react with α, β-unsaturated carbonyl compounds via the conjugate addition pathway, which can lead to the fluorescence changes while monitoring Cys in organelles. Jianb in Chao et al. developed probe **15**, in which when Cys is added, C = C double bond of the α, β-unsaturated ketone is attacked through the addition reaction, thereby breaking the conjugation (Fig. 3). Therefore, change in the fluorescence intensity can be observed with shorter response time [25].

2.5 Cysteine Triggered Reaction with Thioester

Li Fan et al. developed a two-photon ratiometric probe **16** for Cys detection in mitochondria which follows ICT mechanism (Fig. 3). The sulfonate ester bond of probe **16** upon reaction with Cys undergoes cleavage leading to the elimination of the byproduct, and thereby exhibiting red-shift in both absorption as well as emission spectra [26]. A new two-photon fluorescent (TPF) probe **17** based on maleimide-coupled naphthalimide molecular scaffold was reported for mitochondrial Cys detection, which shows d-PET process with 24.5-fold enhancement in fluorescence (Fig. 3) [27].

2.6 Cysteine Triggered Reaction Followed by Rearrangement

Rearrangement in molecular scaffold could results in the formation of different physical properties. Considering the same, Hui Zhang et al. developed the probe **18**. In PBS (pH 7.4, 20% DMSO), probe **18** reacted with Cys through an addition followed by S_NAr reaction to form an amino coumarin derivative with five-membered cyclic transition state, accompanied by the fluorescence enhancement by 19.5-folds [28].

3 Concluding Remarks

This review summarizes the fluorescent molecular probes for organelle-specific Cys detection. The probes have been categorized on the basis of their interaction/reaction mechanism with Cys. Incorporation of the organelle targeting groups for molecular engineering of the fluorescent probes have been indicated wherever applicable. Many of the probes reviewed showed the detection of Cys in the sub-micromolar to nanomolar range. Two-photo fluorescent probes as well as NIR probes with better cell penetration ability have been reported. Following observations were made during this literature review: (1) The emergence of new reaction-based Cys probes is in great supply because most of the response mechanisms can be triggered by biothiols. However, non-reaction-based Cys-specific probes that can show reversible detection of Cys is rarely reported. (2) Most of the probes that detect Cys also show similar positive response toward other biothiols, therefore, reducing Cys-specificity of such probes. (3) Mitochondria and lysosome specific Cys probes are not scarce, but there is a scope and necessity of development of efficient Cys probes for Golgi and ER. The mechanism of targeting the latter organelle is yet to be fully understood. (4) There is need to expand the research in the area of the photostability of fluorescent probe. However, the novel fluorescent molecular probes have enabled researchers to study the role of Cys in common metabolic process and as a biomarker for body's stress response and probable disorder. This review is expected to help the reader

in their quest for developing new efficient fluorescent probes for Cys detection in sub-cellular environment.

References

1. Meng Q, Jia H, Succar P, Zhao L, Zhang R, Duan C, et al (2015) A highly selective and sensitive ON–OFF–ON fluorescence chemosensor for cysteine detection in endoplasmic reticulum. Biosens Bioelectron [Internet]. Elsevier 74:461–468. Available from http://dx.doi.org/https://doi.org/10.1016/j.bios.2015.06.077

2. Yang X, Guo Y, Strongin RM (2011) Conjugate addition/cyclization sequence enables selective and simultaneous fluorescence detection of cysteine and homocysteine. Angew Chemie [Internet] 123:10878–10881. Available from https://onlinelibrary.wiley.com/doi/https://doi.org/10.1002/ange.201103759

3. Heafield MT, Fearn S, Steventon GB, Waring RH, Williams AC, Sturman SG (1990) Plasma cysteine and sulphate levels in patients with motor neurone, Parkinson's and Alzheimer's disease. Neurosci Lett [Internet] 110:216–220. Available from https://linkinghub.elsevier.com/retrieve/pii/030439409090814P

4. Toyokuni S, Ito F, Yamashita K, Okazaki Y, Akatsuka S (2017) Iron and thiol redox signaling in cancer: an exquisite balance to escape ferroptosis. Free Radic Biol Med [Internet] 108:610–626. Available from http://dx.doi.org/https://doi.org/10.1016/j.freeradbiomed.2017.04.024

5. Clemente Plaza N, Reig García-Galbis M, Martínez-Espinosa R (2018) Effects of the Usage of l-Cysteine (l-Cys) on Human Health. Molecules [Internet] 23:575. Available from http://www.mdpi.com/1420-3049/23/3/575

6. Bellia F, Pietropaolo A, Grasso G (2013) Formation of insulin fragments by insulin-degrading enzyme: the role of zinc(II) and cystine bridges. J Mass Spectrom [Internet] 48:135–140. Available from https://onlinelibrary.wiley.com/doi/https://doi.org/10.1002/jms.3060

7. Yang Y, Wang Y, Feng Y, Cao C, Song X, Zhang G, et al (2019) Light-driven visualization of endogenous cysteine, homocysteine, and glutathione using a near-infrared fluorescent probe. J Mater Chem B [Internet] Royal Society of Chemistry 7:7723–7728. Available from http://xlink.rsc.org/?DOI=C9TB01645G

8. Ge C, Shen F, Yin Y, Chang K, Zhang X, Zhou P, et al (2021) A novel NIR fluorescence probe with cysteine-activated structure for specific detection of cysteine and its application in vitro and in vivo. Talanta [Internet] 223:121758. Available from https://doi.org/10.1016/j.talanta.2020.121758

9. Zhang R, Yong J, Yuan J, Ping Xu Z (2020) Recent advances in the development of responsive probes for selective detection of cysteine. Coord Chem Rev [Internet] 408:213182. Available from https://doi.org/10.1016/j.ccr.2020.213182

10. Tao Y, Ji X, Zhang J, Jin Y, Wang N, Si Y, et al (2020) Detecting cysteine in bioimaging with a near-infrared probe based on a novel fluorescence quenching mechanism. ChemBioChem [Internet] 21:3131–3136. Available from https://onlinelibrary.wiley.com/doi/https://doi.org/10.1002/cbic.202000313

11. Zhang X-P, Wang T-T, Yuan Z-H, Zhou Y, Yang Y-S, Zhu H-L (2019) A quinoxalinone-derivated fluorescence sensor with optimized solubility for cysteine detection and biological imaging. Dye Pigment [Internet] 171:107716. Available from https://doi.org/10.1016/j.dyepig.2019.107716

12. Yang M, Fan J, Sun W, Du J, Peng X (2019) Mitochondria-anchored colorimetric and ratiometric fluorescent chemosensor for visualizing cysteine/homocysteine in living cells and daphnia magna model. Anal Chem [Internet] 91:12531–12537. Available from https://pubs.acs.org/doi/https://doi.org/10.1021/acs.analchem.9b03386

13. Cai S, Liu C, Jiao X, Zhao L, Zeng X (2020) A lysosome-targeted near-infrared fluorescent probe for imaging endogenous cysteine (Cys) in living cells. J Mater Chem B [Internet] 8:2269–2274. Available from http://xlink.rsc.org/?DOI=C9TB02609F

14. Niu W, Guo L, Li Y, Shuang S, Dong C, Wong MS (2016) Highly selective two-photon fluorescent probe for ratiometric sensing and imaging cysteine in mitochondria. Anal Chem [Internet] 88:1908–1914. Available from https://pubs.acs.org/doi/https://doi.org/10.1021/acs.analchem.5b04329

15. Han C, Yang H, Chen M, Su Q, Feng W, Li F (2015) Mitochondria-targeted near-infrared fluorescent off–on probe for selective detection of cysteine in living cells and in vivo. ACS Appl Mater Interfaces [Internet] 7:27968–27975. Available from https://pubs.acs.org/doi/https://doi.org/10.1021/acsami.5b10607

16. Zhang H, Feng W, Feng G (2017) A simple and readily available fluorescent turn-on probe for cysteine detection and bioimaging in living cells. Dye Pigment [Internet] 139:73–78. Available from http://dx.doi.org/https://doi.org/10.1016/j.dyepig.2016.12.011

17. Tang L, Xu D, Tian M, Yan X (2019) A mitochondria-targetable far-red emissive fluorescence probe for highly selective detection of cysteine with a large Stokes shift. J Lumin [Internet] 208:502–508. Available from https://doi.org/10.1016/j.jlumin.2019.01.022

18. Qian M, Xia J, Zhang L, Chen Q, Guo J, Cui H, et al (2020) Rationally modifying the dicyanoisophorone fluorophore for sensing cysteine in living cells and mice. Sensors Actuators B Chem [Internet] 321:128441. Available from https://doi.org/10.1016/j.snb.2020.128441

19. Zhao G, Yang W, Li F, Deng Z, Hu Y (2020) A turn-on fluorescent probe for real-time detection of endogenous cysteine in living cells. J Lumin [Internet] 226:117506. Available from https://doi.org/10.1016/j.jlumin.2020.117506

20. Zhang X, He N, Huang Y, Yu F, Li B, Lv C, et al (2019) Mitochondria-targeting near-infrared ratiometric fluorescent probe for selective imaging of cysteine in orthotopic lung cancer mice. Sensors Actuators B Chem [Internet] 282:69–77. Available from https://linkinghub.elsevier.com/retrieve/pii/S0925400518320100

21. Chen S, Hou P, Wang J, Fu S, Liu L (2018) A simple but effective fluorescent probe with large stokes shift for specific detection of cysteine in living cells. J Photochem Photobiol A Chem [Internet] 363:7–12. Available from https://doi.org/10.1016/j.jphotochem.2018.05.025

22. Zhang X, Liu C, Chen Y, Cai X, Sheng W, Zhu H, et al (2020) Visualization of the cysteine level during Golgi stress using a novel Golgi-targeting highly specific fluorescent probe. Chem Commun [Internet] 56:1807–1810. Available from http://xlink.rsc.org/?DOI=C9CC08796F

23. Niu L, Luo Y, Gan Y, Cao Q, Zhu C, Wang M, et al (2020) Novel cascade reaction-based fluorescent cyanine chemosensor for cysteine detection and bioimaging in living system. Talanta [Internet] 219:121291. Available from https://doi.org/10.1016/j.talanta.2020.121291

24. Yin K, Yu F, Zhang W, Chen L (2015) A near-infrared ratiometric fluorescent probe for cysteine detection over glutathione indicating mitochondrial oxidative stress in vivo. Biosens Bioelectron [Internet] 74:156–64. Available from http://dx.doi.org/https://doi.org/10.1016/j.bios.2015.06.039

25. Chao J, Wang Z, Zhang Y, Huo F, Yin C, Li M, et al (2021) A pyrene-based fluorescent probe for specific detection of cysteine and its application in living cell. J Fluoresc [Internet]. Journal of Fluorescence 31:727–732. Available from http://link.springer.com/https://doi.org/10.1007/s10895-021-02703-6

26. Fan L, Zhang W, Wang X, Dong W, Tong Y, Dong C, et al (2019) A two-photon ratiometric fluorescent probe for highly selective sensing of mitochondrial cysteine in live cells. Analyst [Internet]. Royal Society of Chemistry 144:439–447. Available from http://xlink.rsc.org/?DOI=C8AN01908H

27. Liu Y, Liu Y, Liu W, Liang S (2015) Two-photon fluorescent probe derived from naphthalimide for cysteine detection and imaging in living cells. Spectrochim Acta Part A Mol Biomol

Spectrosc [Internet] 137:509–515. Available from http://dx.doi.org/https://doi.org/10.1016/j.saa.2014.08.072

28. Zhang H, Xu L, Chen W, Huang J, Huang C, Sheng J, et al (2018) A lysosome-targetable fluorescent probe for simultaneously sensing Cys/Hcy, GSH, and H2S from different signal patterns. ACS Sensors [Internet] 3:2513–2517. Available from https://pubs.acs.org/doi/https://doi.org/10.1021/acssensors.8b01101

Recent Advances in Fluorescent Chemosensors for Aromatic Amino Acids Detection

Nikunjkumar Vagadiya, Mohil Odedara, Aayushi Joshi, Anu Manhas, and Nandini Mukherjee

1 Introduction

The biomolecules, like DNA, proteins, phospholipids, carbohydrates, etc., found in human beings are made up of different monomers or precursor molecules. Proteins are made up of 21 amino acids via peptide linkage, and these amino acids play multiple roles in the biological processes [1, 2]. To be synthesized in the human body, all biomolecules require a live cell environment and metabolism process. The biomolecule concentrations in living organisms varies, and in case of abnormal concentration, they cause various disorders and diseases. However, amino acids are one of the most significant biomolecules that play crucial roles in protein synthesis, neurotransmitters and many more. The deficiency of amino acids causes a variety of problems, such as nausea, sluggish development, dry mouth, lethargy, impaired vision, hair depigmentation, oedema, liver damage and muscle and fat loss [3, 4]. Aromatic amino acids, such as tyrosine, phenylalanine, tryptophan and histidine played a significant role in physiological and psychological processes. For instance, histidine is required for tissue expansion and regeneration, tryptophan is required for protein production [5–7] and tyrosine is essential for the production of neurotransmitters, such as norepinephrine, epinephrine and dopamine. Also, the deficiency of tyrosine may lead to neurological problems such as mood swings, poor memory and lower IQs as reported in phenylketonuria patients and people with hypertryptophanemia. As per the literature, tyrosine should be administered in the body only if phenylalanine is deficient or if phenylalanine to tyrosine conversion is hindered [5, 8]. Likewise, abnormal concentration of other amino acids is related to the generation of different

N. Vagadiya · M. Odedara · A. Joshi · A. Manhas (✉) · N. Mukherjee (✉)
Department of Chemistry, School of Technology, Pandit Deendayal Energy University, Gandhinagar, Gujarat 382426, India
e-mail: Anu.Manhas@sot.pdpu.ac.in

N. Mukherjee
e-mail: Nandini.Mukherjee@sot.pdpu.ac.in

diseases. Until now, high-performance liquid chromatography, gel permission chromatography, gas chromatography, high-performance liquid chromatography-mass spectrometry (HPLC–MS), gas chromatography-mass spectrometry (GC–MS) and NMR titration methods have been used to analyse amino acids quantitatively and/or qualitatively. However, these techniques are time-consuming, expensive and often require expert handling. Furthermore, one of the most significant limitations of these techniques is their incapability to detect and measure biomolecules in living cells and study their dynamic changes in a non-destructive manner. In contrast, rationally designed synthetic molecules, like, dye-based molecular probes [9–11], nanomaterials-based sensors [12, 13], fluorescent protein based molecules [14–16], and hybrid systems [17] were known to be selective and sensitive in displaying binding to a particular biomolecular species, which is visible in the fluorescence spectra. Fluorescent chemosensors are highly specific, selective and sensitive in nature with respect to the amino acids detection. Due to their ease of implementation and short reaction time, it can be implemented for cell bioimaging, thus making it a cost-effective approach. There are various organic fluorescent-based chemosensors developed such as, disulphide-based imine-linked receptor [18], pyrenedione [19], bis-camphor-derived probe [20], calixarene based probe [21], diarylacetylene-containing 1,1′-bi-2-naphthol derivative [22], chiral carbazole with urea-carboxylic acid moiety (CCS) [23] and 1,1′-binaphthyl-based imidazolium probe [24] for aromatic amino acids sensing. Dye-encapsulated supramolecular approach has been discussed to detect aromatic amino acid sensing via host guest interaction [25]. Many research groups have performed computational investigations via density functional theory or time-dependent density functional theory (DFT/TD-DFT), to unravel the sensing mechanisms, and optimum states of fluorescent probes and transitional states of probe-amino acid moiety [26, 27]. This review provides a summary of current developments in fluorescent chemosensors, their binding site, sensing mechanism and various types of interactions for the sensitive, selective and specific detection of aromatic amino acids. Finally, authors discuss the constraints and various opportunities in the sensing area and offered solutions for further knowledge enhancement.

2 Advanced Fluorescent Chemosensors for Aromatic Amino Acids Detection

2.1 Tryptophan/Histidine and Cations Sensing via Chiral Carbazole-Based Fluorescent Chemosensor

In 2020, Chi-Jung Chang et al. have synthesized a carbazole-based asymmetric chemosensor (CCS) (S)-Methyl-2-(3-(9-ethyl-9H-carbazol-3-yl)ureido)-3-phenyl propanoate probe (1) that bears a chiral "urea-carboxylic acid" coordination site for the detection of cation (Fe^{3+}), along with tryptophan/histidine in the aqueous environment (Fig. 1). [23] CCS fluorescent probe (1) can sense Fe^{3+} in the nanomolar

Fig. 1 Structure of probe **1**, i.e. (S)-Methyl-2-(3-(9-ethyl-9H-carbazol-3-yl) ureido)-3-phenylpropanoate or CCS
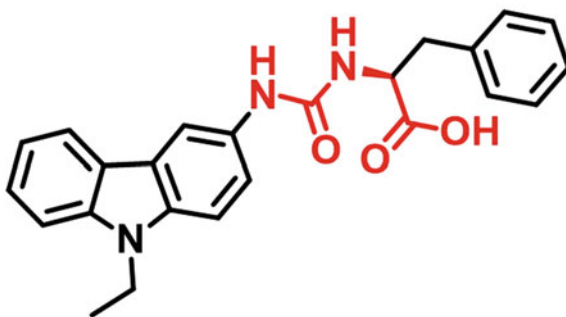
range with the limit of detection of 84 nM in 99% water. For the selective sensing of Fe^{3+}, colour change was observed (colourless to yellow) with the CCS in the solution of 99% water + 1% acetonitrile media. In a high-water content environment, probe **1** can detect tryptophan and histidine with low limit of detection, i.e. 0.31 μM and 7.64 μM, respectively. Probe **1** displays intramolecular charge transfer (ICT) process on forming complex with metal ions (Scheme 1). The reversibility of CCS/Fe^{3+} species was further confirmed by adding increasing quantities of sodium EDTA to the CCS-Fe^{3+} complex, which leads to turn-on fluorescence. The feasibility and validation of the CCS/Fe^{3+} fluorophore probe was confirmed by sensing
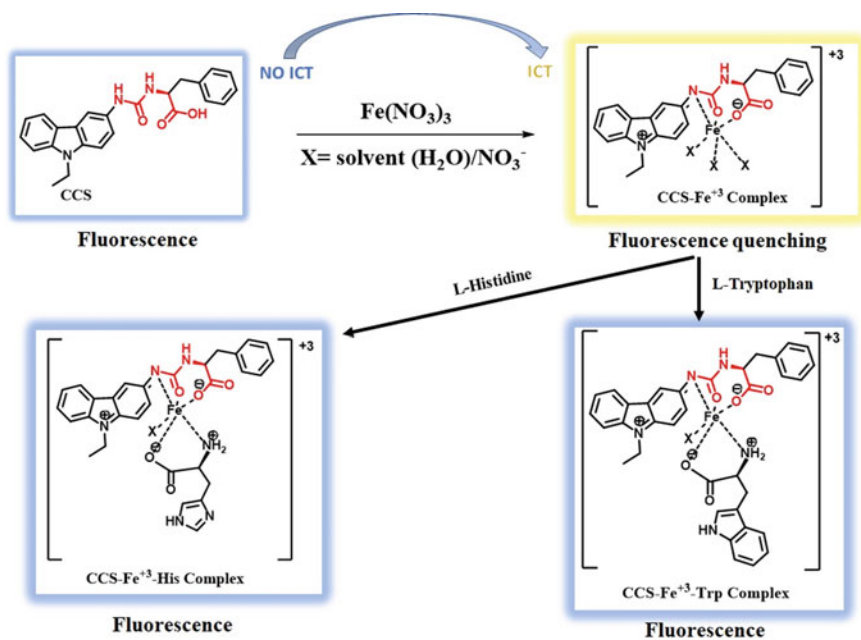
Scheme 1 Pictorial representation of the binding mechanism for Fe^{3+} sensing by CCS and CCS-Fe^{3+} complex for L-Histidine and L-Tryptophan

of the tryptophan in commercial sleep improving capsules. Further, they confirmed that other ingredients, like ziziphi spinosae semen, passion, melissa officinalis L, lavender, rosemary, gelatin, titanium dioxide, glycine, theanine, maltitol, vitamin B_2, vitamin C, acesulfame potassium and silicon dioxide, did not interfere the sensing mechanism of the tryptophan.

2.2 An Amide-Based Fluorophore Probe for the Detection of Al^{3+}, Fe^{3+} and Their Complex for D/L-Tryptophan Sensing

Suman Mukhopadhyay et al. have developed an organic amide-based fluorophore probe (2) for the sensing of Al^{3+} and Fe^{3+} in HeLa and A549 cells (Fig. 2). In addition, they were able to identify tryptophan instantly using the Pictate–Spengler reaction [28]. In the biological system, tryptophan was detected in aqueous media by an amide-based fluorophore probe with the 2.43×10^{-7} M limit of detection. The enhancement of fluorescence over the complexation represents the photo-induced electron transfer (PET)-based mechanism. The pyridyl ring acts as an electron pair acceptor since its resonance with the $C = O$ and N–H groups and reduces the availability of electro-density in the pyridyl ring. As a result, upon excitation, the electron-rich region the N-atom of isoquinoline undergoes the PET process by donating a lone pair to the pyridyl ring. Further, the capability of isoquinoline to donate electrons is reduced when Al^{+3} and Fe^{+3} ions or Trp is added. PET is inhibited because of the nitrogen atom's attraction to the pyridyl ring (Scheme 2), which was further confirmed by the computational studies like DFT and TD-DFT. The calculated energy gap of HOMO–LUMO orbitals in probe-metal complex decreases, which indicates the inhibition of PET and enhancement of fluorescence. Also, electrostatic potential surface of the fluorophore probe was generated that represents the most probable binding position of metal ions and amino acids. Their interaction was further confirmed by the UV–Vis spectra which shows intra-ligand π-π^* and n-π^* transitions. For the validation of the results sensing of the bovine serum albumin (BSA) protein that contains tryptophan amino acid was confirmed by the amide-based fluorophore.

Fig. 2 Structure of probe **2**, an amide-based chemosensor
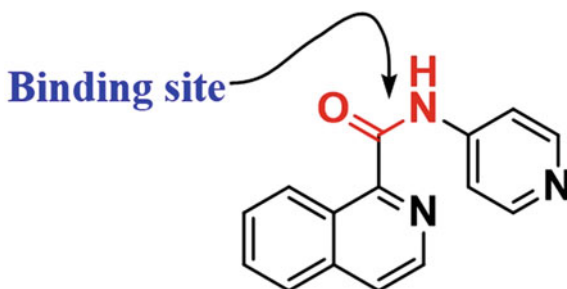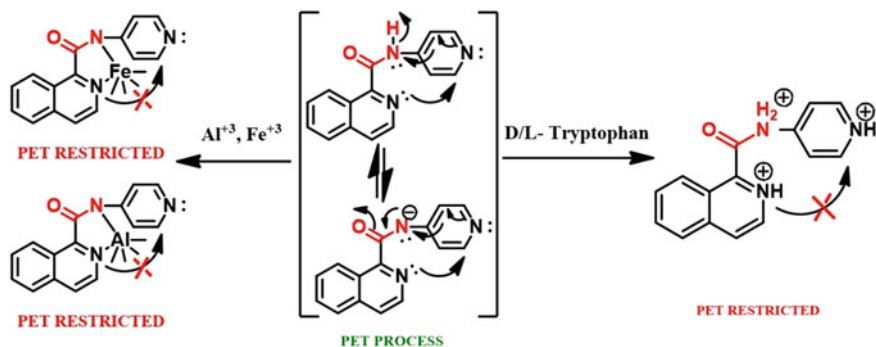
Scheme 2 Pictorial representation of the photo-induced transfer (PET) process-mediated sensing of Al^{+3} and Fe^{+3} and D/L-Tryptophan by probe **2**
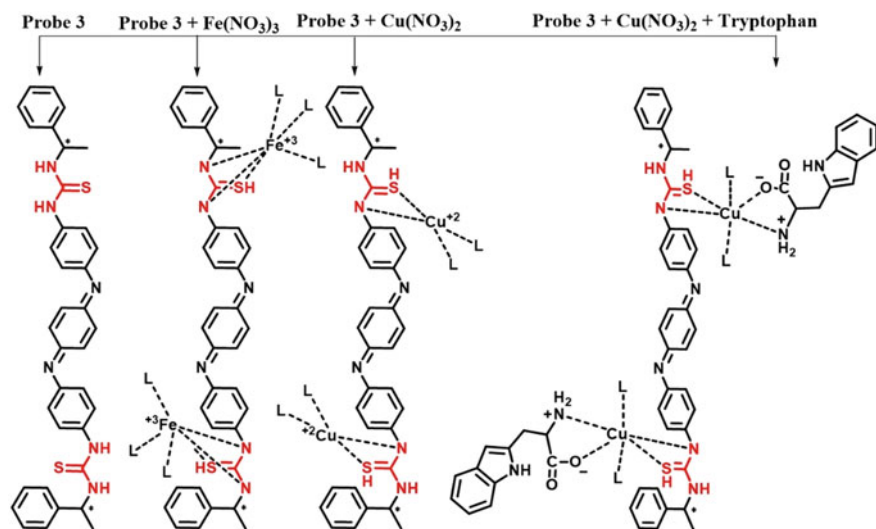
Fig. 3 Structure of probe **3**, an aniline oligomer-based receptor and its sensing mechanism by forming ternary complex after addition of tryptophan

2.3 An Aniline Trimer-Based Multifunctional Sensor for the Sensing of Fe^{3+}, Cu^{2+} and Ag^+ and Its Complex for the Detection of L-Tryptophan

In 2020, aniline oligomer-based receptor probe **(3)** that bears chiral thiourea binding site (CAS) was developed by the Chang research group for the sensing of Fe^{3+}, Cu^{2+} and Ag^+ and aniline oligomer-based complex for the detection of L-tryptophan by fluorescent sensing mechanism [29] (Fig. 3). The limit of detection for the Fe^{3+}, Cu^{2+}
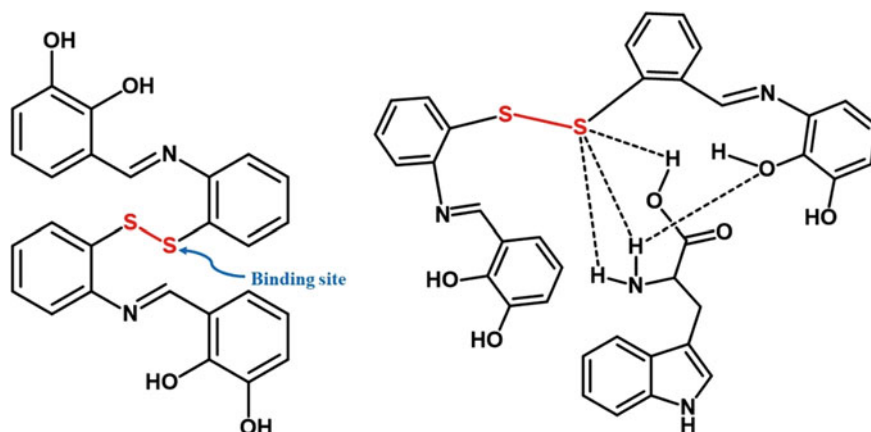
Fig. 4 Structure of probe **4,** i.e. 3,3'-((1E,1'E)-((disulfanediylbis(2,1-phenylene))bis (azanylylidene))bis(methanylylidene))bis(benzene1,2-diol)

and Ag$^+$ is reported to be 0.214, 0.099 and 0.147 µM, respectively. Detection of L-tryptophan was carried out by CAS/Cu^{2+}-based complex via turn-on fluorescence in DMSO/water. In L-tryptophan sensing, fluorescence is turned on by the ternary complexes, which causes the displacement of L-tryptophan from copper's weakest binding site. The chiral thiourea binding site is a multifunctional probe that responds to a variety of stimuli (amino acids, cations and pH).

2.4 Identification of Tryptophan Amino Acid in Aqueous Solutions by Disulphide-Based Imine-Linked Fluorescent Receptor

In 2017, Narinder Singh and his group published a red-coloured disulphide-based imine-linked fluorescent receptor, i.e. 3,3'-((1E,1'E)-((disulfanediylbis(2,1-phenylene))bis (azanylylidene))bis(methanylylidene))bis(benzene1,2-diol) probe **(4),** that forms intermolecular hydrogen bonding and electrostatic interactions with the tryptophan (Fig. 4) [18]. The probe was observed to be highly selective for tryptophan among all amino acids when investigated in aqueous solutions [10] with a detection limit of 47.6 nM. The involvement of π-π stacking and multiple hydrogen bonding in tryptophan receptor binding was discovered by theoretical calculations also. The computed interaction energy (372.84 kcal mol^{-1}) of the optimized structures shows the development of a stable complex between probe **4** and tryptophan. The complex was observed to form a hydrogen bond between the amine hydrogen of tryptophan and carboxylic hydrogen of the receptor and sulphur of the receptor. Moreover, the aromatic ring of the tryptophan form π-π stacking with the phenolic ring of the receptor. These interactions are responsible for providing the stability

to host–guest complex. Also, due to a putative charge transfer mechanism between probe **4** and tryptophan, and the band gap between HOMO and LUMO of probe **4** becomes narrower for the tryptophan complex.

2.5 Selective Recognition of Tryptophan in Aqueous Solutions by Using 1,1′-Binaphthyl-Based Imidazolium Chemosensors

Water-soluble 1,1′-Binaphthyl-based imidazolium-based fluorophore probes **(5, a-e)** were reported for highly selective detection of tryptophan in the aqueous solution by Jingsong and his co-worker in 2010 [24]. In addition, this group reported remarkable chiral recognition for the two enantiomers of tryptophan (L & D) via macrocyclic derivative of 1,1′-Binaphthyl-based imidazolium fluorophore probe. Sensing of tryptophan by 1,1′-Binaphthyl-based imidazolium chemosensors in aqueous media takes place by the formation of multiple hydrogen bonds and electrostatic interactions between the sensor and analyte. The addition of L-tryptophan resulted in a significant increase in fluorescence but L-tyrosine resulted in a fluorescent quenching effect. Through computational studies, it was observed that a 1: 1 stoichiometry for the multiple hydrogen-bonded complex between (R)-1 and L-tryptophan was formed. In that complex, the carboxyl group of L-tryptophan interacts with the three hydrogen bonds with the chiral ligand, which included two C_2-hydrogen atoms of two imidazolium rings and one aryl hydroxyl group. Additionally, the formation of extra hydrogen bonds also takes place between L-tryptophan and the receptor which favours its coordination over other amino acids. As a result, the receptor (R)-1 would have weak enantioselectivity for recognizing the enantiomers of tryptophan, which matched the actual findings (Fig. 5).

2.6 Aromatic Amino Acids and Dipeptides Sensing by a Crown-Ether-Functionalized Perylene Bisimide Fluorophore

In 2018, the Crown-Ether-functionalized Perylene Bisimide (PBI) fluorophore probe **(6)** was reported for the sensing of aromatic amino acids and dipeptides by Frank et al. (Fig. 6) [27]. They reported two-point interaction between the ammonium group and ammonium ion recognizing site. In addition, they reported π-π stacking and charge transfer between the electron-sufficient aromatic groups and an electron-deficient PBI moiety. The size and electrical nature of aromatic units, as well as the distance between the ammonium group and aromatic unit was considered as the important considerations for the binding strength. Photo-induced electron transfer mechanism was reported for L-tryptophan and L-tyrosine sensing by PBI fluorophore.
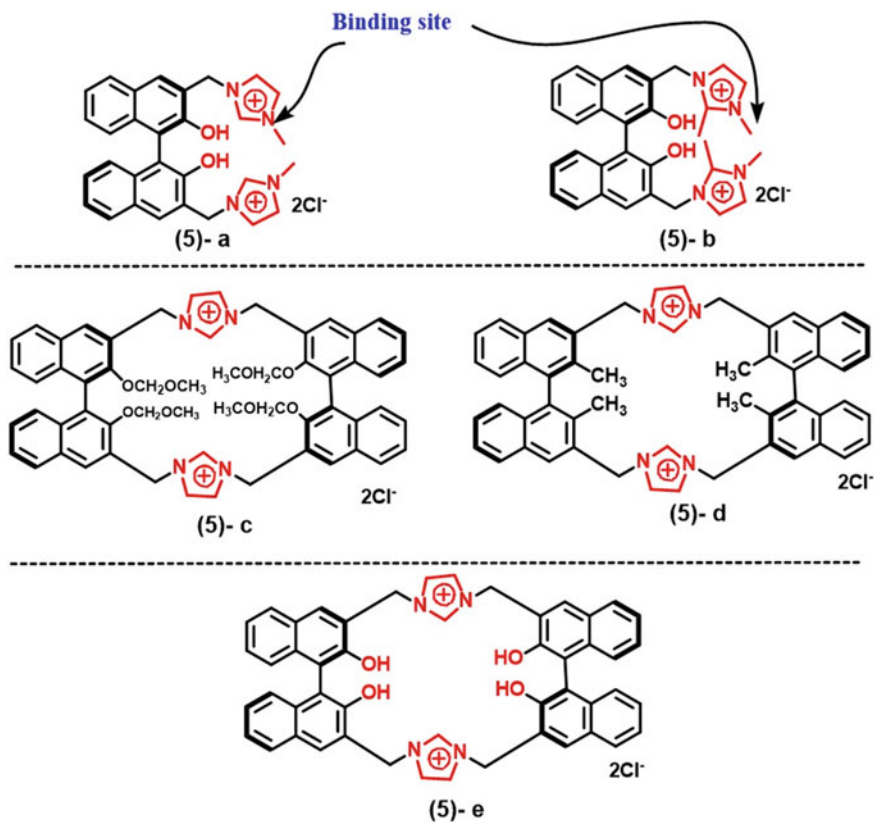
Fig. 5 Structure of probes **5 (a-e)**, i.e. 1,1′-Binaphthyl-based imidazolium-based fluorophore probes

2.7 Host–Guest Interaction-Mediated Sensing of Aromatic Amino Acid by Supramolecular Complex of Cucurbit[8]uril and Acridine Dye

In recent years, many approaches have been explored to enhance the selectivity of fluorescent dye for aromatic amino acid. In 2020, Weitao Xu et al. developed a complex which comprised of the supramolecule cucurbit[8]uri[CB] with encapsulated fluorescent dye acridine hydrochloride[AC] in its cavity to achieve better selectivity for the detection of aromatic amino acid [25]. Mechanistic pathway for the sensing follows indicator displacement principle. Cucurbit[8]uril forms 1:2 host guest complex [CB-AC] where acridine hydrochloride dye serves as a fluorescent "ON–OFF" probe for the detection of aromatic amino acid. The π-π interaction has been observed between two guest molecules of AC. In CB-AC host, cucurbit[8]uril shows different affinities towards guest dye molecule[AC] and analyte aromatic
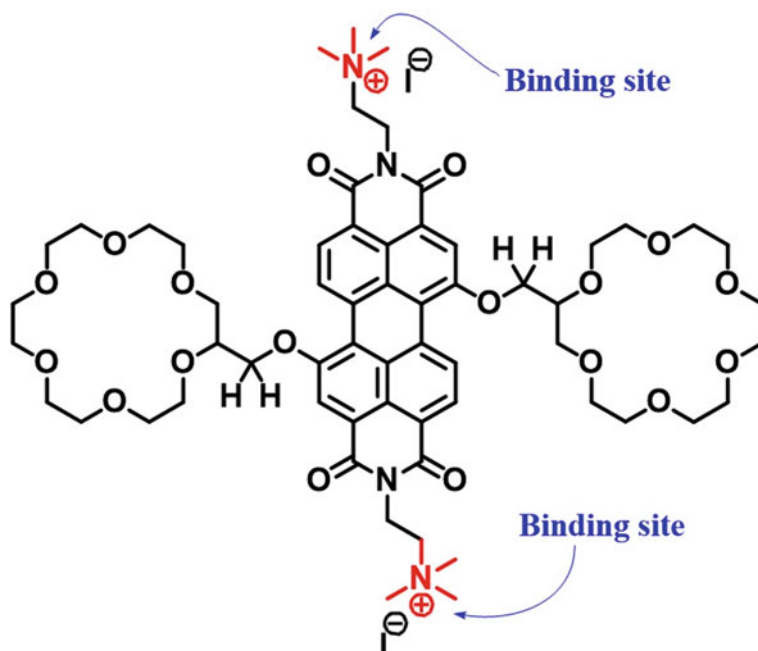
Fig. 6 Structure of probe **6,** i.e. Crown-Ether-functionalized Perylene Bisimide fluorophore probe
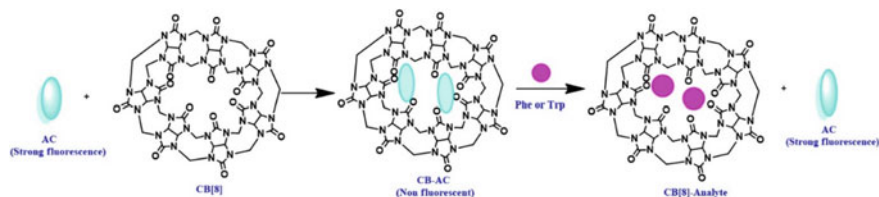
Fig. 7 Sensing of aromatic amino acid by Cucurbit[8]uril-acridine hydrochloride[CB-AC] complex via fluorescence indicator displacement method

amino acid. Cucurbit[8]uril in the [CB-AC] complex shows higher binding affinity towards aromatic amino in aqueous solution at pH 4 and thus the encapsulated AC dye gets displaced from its cavity and fluorescence enhancement is observed in the solution. Limit of detection for L-Phe and L-Trp were found to be 2.100×10^{-6} and 3.2×10^{-5} molL^{-1}, respectively (Fig. 7).

3   Conclusions

This review focuses on the various derivatized fluorophore probes which have their application in the sensing of the aromatic amino acids. Most of the research groups synthesized polyaromatic or heterocyclic compounds for the aromatic amino acid detection However, after sensing, recyclability of the probe becomes a challenging issue, and is reported in less studies. Most of the fluorophore chemosensors were water-insoluble, thus, lead to difficulty in the sensing of aromatic amino acids in aqueous media. Overall, among all the amino acids, aromatic amino acids, viz. tyrosine, phenylalanine, tryptophan and histidine are less reported for sensing via specific binding site holder-fluorophore probes. Researchers are trying to detect enantiomers of aromatic amino acids by using chiral fluorophore probes. However, within the aromatic amino acids, tryptophan sensing was highly reported by chiral/achiral fluorophore probes.

On observing the synthesis protocol followed by the above-mentioned literature, it was observed that the fluorophore probes were synthesized by using many harsh and costly organic precursor molecules/reagents. An alternate approach could be explored by employing green synthesis or extracting the precursor molecules from plants or living species using green chemistry methods for conducting the sensing of the aromatic amino acids. Moreover, it can be stated that fluorescence technique is more appropriate and specific in comparison with the colorimetric detection technique.

Conflict of Interest   The authors state that they have no known conflicting financial or personal interests that might have influenced the review work presented in this publication.

References

1. Weijzen ME, van Gassel RJ, Kouw IW, Trommelen J, Gorissen SH, van Kranenburg J, van Loon LJ et al (2022) Ingestion of free amino acids compared with an equivalent amount of intact protein results in more rapid amino acid absorption and greater postprandial plasma amino acid availability without affecting muscle protein synthesis rates in young adults in a double-blind randomized trial. J Nutr 152(1):59–67
2. Aguayo E, Martínez-Sánchez A, Fernández-Lobato B, Alacid F (2021) L-Citrulline: a non-essential amino acid with important roles in human health. Appl Sci 11(7):3293
3. Jin L, Bai X, Luan N, Yao H, Zhang Z, Liu W, Lu Q et al (2016) A designed tryptophan-and lysine/arginine-rich antimicrobial peptide with therapeutic potential for clinical antibiotic-resistant Candida albicans vaginitis. J Med Chem 59(5):1791–1799
4. Gietzen DW (2022) Brain signaling of indispensable amino acid deficiency. J Clin Med 11(1):191
5. Hof F (2016) Host–guest chemistry that directly targets lysine methylation: synthetic host molecules as alternatives to bio-reagents. Chem Commun 52(66):10093–10108

6. Carullo P, Cetrangolo GP, Mandrich L, Manco G, Febbraio F (2015) Fluorescence spectroscopy approaches for the development of a real-time organophosphate detection system using an enzymatic sensor. Sensors 15(2):3932–3951

7. Lim SK, Chen P, Lee FL, Moochhala S, Liedberg B (2015) Peptide-assembled graphene oxide as a fluorescent turn-on sensor for lipopolysaccharide (endotoxin) detection. Anal Chem 87(18):9408–9412

8. Snedden W, Mellor CS, Martin JR (1983) Familial hypertryptophanemia, tryptophanuria and indoleketonuria. Clin Chim Acta 131(3):247–256

9. Koshti B, Kshtriya V, Gour N (2021) A new azo dye for the selective detection of glycine

10. Ji X, Wang N, Zhang J, Xu S, Si Y, Zhao W (2021) Meso-pyridinium substituted BODIPY dyes as mitochondria-targeted probes for the detection of cysteine in living cells and in vivo. Dyes Pigm 187:109089

11. Kolińska J, Grzelakowska A (2021) Characterization of a novel styrylbenzimidazolium-based dye and its application in the detection of biothiols. Luminescence 36(2):409–417

12. Ahmed B, Elgorban AM, Bahkali AH, Lee J, Syed A (2022) SPR based gold nano-probe as optical sensor for cysteine detection via plasmonic enhancement in the presence of Cr3+. Spectrochim Acta Part A Mol Biomol Spectrosc 265:120356

13. Mehmandoust M, Erk N, Alizadeh M, Salmanpour S (2021) Voltammetric carbon nanotubes based sensor for determination of tryptophan in the milk sample. J Food Measur Characterization 15(6):5288–5295

14. Lu W, Jiao Y, Gao Y, Qiao J, Mozneb M, Shuang S, Li CZ et al (2018) Bright yellow fluorescent carbon dots as a multifunctional sensing platform for the label-free detection of fluoroquinolones and histidine. ACS Appl Mater Interfaces 10(49):42915–42924

15. Wang B, Han J, Bojanowski NM, Bender M, Ma C, Seehafer K, Bunz UH et al (2018) An optimized sensor array identifies all natural amino acids. ACS Sens 3(8):1562–1568

16. Marvin JS, Shimoda Y, Magloire V, Leite M, Kawashima T, Jensen TP, Looger LL et al (2019) A genetically encoded fluorescent sensor for in vivo imaging of GABA. Nat Methods 16(8):763–770

17. Coates C, Kerruth S, Helassa N, Török K (2020) Kinetic mechanisms of fast glutamate sensing by fluorescent protein probes. Biophys J 118(1):117–127

18. Tayade K, Sonawane M, Torawane P, Singh A, Singh N, Kuwar A (2017) A chemosensor selection for the fluorescence identification of tryptophan (Trp) amino acids in aqueous solutions with nanomolar detection. Sens Actuators, B Chem 246:563–569

19. Zhang Y, Yao W, Liang D, Sun M, Wang S, Huang D (2018) Selective detection and quantification of tryptophan and cysteine with pyrenedione as a turn-on fluorescent probe. Sens Actuators, B Chem 259:768–774

20. Wang Z, Zhang Y, Liang Y, Li M, Meng Z, Yang Y, Wang S et al (2022) Novel bis-camphor-derived colorimetric and fluorescent probe for rapid and visual detection of cysteine and its versatile applications in food analysis and biological imaging. J Agric Food Chem

21. Parikh J, Bhatt K, Modi K, Patel N, Desai A, Kumar S, Mohan B (2022) A versatile enrichment of functionalized calixarene as a facile sensor for amino acids. Luminescence

22. Mao Y, Abed MA, Lee NB, Wu X, Du G, Pu L (2021) Determining the concentration and enantiomeric composition of histidine using one fluorescent probe. Chem Commun 57(5):587–590

23. Pundi A, Chang CJ, Chen J, Hsieh SR, Lee MC (2021) A chiral carbazole based sensor for sequential "on-off-on" fluorescence detection of Fe3+ and tryptophan/histidine. Sens Actuators, B Chem 328:129084

24. Yang L, Qin S, Su X, Yang F, You J, Hu C, Lan J et al (2010) 1, 1′-Binaphthyl-based imidazolium chemosensors for highly selective recognition of tryptophan in aqueous solutions. Org Biomol Chem 8(2):339–348

25. Xu W, Feng H, Zhao W, Huang C, Redshaw C, Tao Z, Xiao X (2020) Amino acid recognition by a fluorescent chemosensor based on cucurbit [8] uril and acridine hydrochloride. Anal Chim Acta 1135:142–149

26. Lohar S, Safin DA, Sengupta A, Chattopadhyay A, Matalobos JS, Babashkina MG, Das D et al (2015) Ratiometric sensing of lysine through the formation of the pyrene excimer: experimental and computational studies. Chem Commun 51(40):8536–8539
27. Weißenstein A, Saha-Möller CR, Würthner F (2018) Optical sensing of aromatic amino acids and dipeptides by a crown-ether-functionalized perylene bisimide fluorophore. Chem Euro J 24(31):8009–8016
28. Kundu BK, Singh R, Tiwari R, Nayak D, Mukhopadhyay S (2019) An amide probe as a selective Al 3+ and Fe 3+ sensor inside the HeLa and a549 cell lines: pictet-spengler reaction for the rapid detection of tryptophan amino acid. New J Chem 43(12):4867–4877
29. Pundi A, Chang CJ, Chen YS, Chen JK, Yeh JM, Zhuang CS, Lee MC (2021) An aniline trimer-based multifunctional sensor for colorimetric Fe3+, Cu2+ and Ag+ detection, and its complex for fluorescent sensing of L-tryptophan. Spectrochim Acta Part A Mol Biomol Spectrosc 247:119075

Textured and Solid Lubricant-Based Tool Coatings: A Brief Review

Uttakantha Dixit and Ramesh K. Guduru

1 Introduction

Machining/cutting is a process of material removal from a workpiece in order to create a product with certain design. The machining/cutting quality is usually measured in terms of end product as well as tool life. The materials used to make cutting tools include cemented tungsten carbide (WC), high-speed steels, diamond, boron nitride, etc. Although each material has its own mechanical and tribological characteristics, cemented WC is the most widely employed one in the industry, particularly for steel cutting applications due to the fact that cemented WC is inexpensive and has a high hardness along with high boiling point [1]. Despite of such superior characteristics, WC-based tools undergo continuous failure due to poor shock and thermal resistance characteristics. As a result numerous hard coatings has been developed for WC-based cutting tools, with single to multilayer structures. Many of these hard coatings have been demonstrated to increase the batch size of work pieces that can be machined per tool by up to 10 times by slowing down the wear phenomenon of the cutting tools [2]. The most often utilised coating deposition processes are physical vapour deposition (PVD) and chemical vapour deposition (CVD) [3]. PVD and CVD coated tools were investigated by various researchers for coating and tool mechanical properties, brittleness, coating-tool adhesion, cutting edge preparation and their influence on cutting performance. Techniques like gas flame spray, arc discharge plasma and vacuum deposition were also employed to develop ceramic coatings on the steel substrates [4]. Plasma electrolytic oxidation (PEO)-based coatings were proven to be resistant in the corrosive and abrasive environments [5]. However, addition of tool coating always adds up to increased costs of the tools. In contrast, recent advances in smart surface engineering and coating technologies

---

U. Dixit · R. K. Guduru (✉)
Department of Mechanical Engineering, School of Technology, PD Energy University, Gandhinagar, Gujarat, India
e-mail: Ramesh.Guduru@sot.pdpu.ac.in

have opened up new avenues for minimising the friction and wear in the tools used for cutting, rolling, sliding and rotating. Such coatings, in particular, can also fulfil the increasingly multi-functional characteristics required for various tool applications [6]. Various studies have been conducted to develop nano-composite-based super-hard coatings for enhanced tool life [7]. In recent years, the surface manufacturing technologies like laser texturing, laser-glazing and shot-peening also showed promising potentials with enhanced machining performance and increased tool life. Surface texturing of tools has attracted a lot of attention through surface modification while reducing the friction and improving the lubrication. In recent years, the surface manufacturing technologies like laser texturing, laser-glazing and shot-peening have shown promising potentials with enhanced machining performance and increased tool life.

Surface texturing of tools has attracted a lot of attention through surface modification while reducing the friction and improving the lubrication. Combining the surface texturing with coatings is also one possible technique for improving tribological performance under severe conditions. Combining of tool texture with solid lubricant coatings can be adopted in two ways. First, the coatings themselves can be textured, where the smaller contact area of the textured coatings may result in less wear through removal of wear debris and extend the service life of the tools. This method is commonly used to create hard and wear resistant coatings. Secondly, the coatings can also be applied on prior textured substrates/tools while enabling the surface textures to store and re-supply the solid lubricant material to the contact or extend the life of the textured features of the tool surface [6].

Recently, Liu et al. [7] provided a review on warm shot-peening, warm laser shock peening, ultrasonic surface rolling processing, ultrasonic nanocrystal surface modification and some examples of thermally aided surface hardening procedures. Following the concept of minimum quantity lubrication (MQL) conditions, Pradhan et al. [8] have introduced micro and nano-textures on the rake face of the cutting tool inserts with or without solid lubricant; these tools are also known as self-lubricating tools. Rajsekara et al. [9] have reviewed nano-structured coatings as well as textured surfaces with feature size 10 nm or less. Machado et al. [10] highlighted the effect of texturing on machining, considering the parameters like formation of chips, cutting forces, cutting temperature, lubrication, surface integrity and tool life, where coating thickness and substrate roughness were showed to play an important role in enhancing the tribological properties of the tools. Along with development of various tool coatings, researchers have also worked on composite ceramic inserts doped with materials like MgO and CuO, etc., in order to provide self-lubricating properties for tool applications [11, 12], and these were reported to show better performance during the machining of high temperature alloys when compared with conventional tool inserts [13].

In 2021, Singh et al. [11] developed zirconia toughened alumina (ZTA)-based ceramic insert of square shape and infused with CuO as solid lubricant, and tested for turning operation on a conventional lathe machine. These studies showed an improvement of 20% in flank wear when compared with ZTA cutting inserts without CuO.

In another study, MgO-doped ZTA inserts showed a better performance in medium to high-speed machining of steels [12] with improvement in surface roughness.

Recently, Agarwal et al. [14] employed TiAlN coatings with boric acid as a solid lubricant and compared with wet machining (conventional cutting fluid to water in the ratio of 1:15) where the solid lubricant showed a better performance with a reduction in flank wear of almost 60%. At the same time, the surface roughness of the work piece was observed to go down up to 39%. These studies presented an improved performance of the tools with better chip formation and material removal rate (MRR) while cutting down the net specific energy required for machining.

Dry machining is also very much desirable to avoid the extra costs and environmental problems associated to cutting fluids. Hardened steel high-speed machining can yield a machined surface of high enough quality to avoid the requirement for finishing operations like as grinding and polishing. [15]. Thus to provide smooth machining, friction is the parameter to be eliminated. In order to overcome harmful outcomes of liquid cutting fluids, use of solid lubricants are proven to be a sustainable step. Solid lubricants are fine powders that can be divided into chemically and physically active substances based on their structure. Solid lubricant coatings are primarily used to control the friction and wear in rough application conditions (such as high vacuum, aerospace, high-speeds, high loads and very low or high temperatures), where the conventional materials and lubricants are unable to deliver the desired levels of performance or durability [16]. Table 1 lists some of the most prevalent and commonly used solid lubricants.

2 Layered, Textured and Solid Lubricated Coatings

2.1 Single Layer Coatings

In 1969, a thin coating of TiN was deposited via CVD on the surface of a cemented WC cutting tool to extend the life time, and later it was patented and commercialised [20]. Since the early 1970s, many successful thin coatings of TiC, TIN, Al_2O_3 and their combinations with thickness in the range of 5 microns were deposited on the cutting tools to improve wear life and/or cutting speed capabilities. CVD was used to create above coatings on the cemented WC for most of the part. Similarly, PVD coatings of TiN were also developed on HSS tools, and a review was provided in the reference [21]. Prengel et al. [22] have deposited monolayer TiN, TiAlN and TiB_2 on WC-6 tool using PVD. The PVD coatings provided performance benefits in applications that required peck cutting as well as finishing. In the early 1990's, graphite and MoS_2 were also used as solid lubricants because of their layered structure with weak interlayer bonding. These materials exhibited better lubrication properties when compared to the other types of solid lubricants. In another example, Fullerene (C_{60}) [23] was also used as a solid lubricant due to its various characteristics such as low surface energy, high chemical stability, spherical shape and weak

Table 1 Commonly used solid lubricants [6, 10, 18–19]

Solid Lubricants ↓	Structure-effective with layer lattice structure	Chemically effective with layer lattice structure	Chemically effective without layer lattice structure	Physically effective with layer lattice structure	Physically effective without layer lattice structure
MoS$_2$	////////////	/////////////////			
Graphite	////////////				
Zincpyrophosphate			/////////////		
Calcium hydroxide			/////////////		
Aluminium				//////////////	
Zinc sulphide				//////////////	
Zinc oxide				//////////////	
Calcium fluoride				//////////////	
Polytetrafluoroethylene (PTFE)					//////////////////
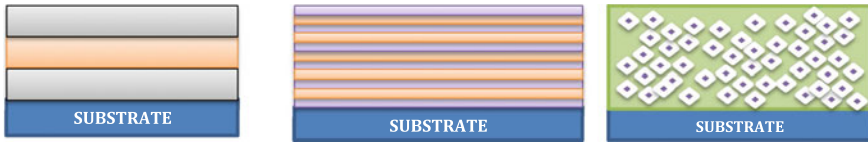
Fig. 1 Coatings used on tools. **a** Multilayer. **b** Superlattices. **c** Nano-composites [6]

intermolecular bonding, along with high load bearing capacity. These C_{60} fullerene films were deposited on a polished Silicon wafer at a high vacuum by sublimation. In late 1990's, the ultra-tough coatings, such as, diamond-like-coatings (DLC) was introduced. Salvadori et al. [24] have deposited DLC on Si surface along with hybrid-surface pre-treatment to increase the diamond film nucleation, as well as adhesion to the WC–Co tool inserts.

2.2 Multilayer/Multicomponent Coatings

To further obtain increased hardness and enhanced tool life in comparison with the single layer coatings, multi-layered coatings were developed on the tools. These multilayer coatings can be broken down into three functional layers in general. The bottom layer establishes coating/substrate adhesion; the middle layer transitions from the bottom to the top layer, forming a link between the layers and the hard top layer [25]. Figure 1 presents various types of textured coatings adapted so far in the tool coatings [26].

2.2.1 Multilayer Coatings

Coatings for cutting tools in the latest generation with multi-layered architecture ensure a dual nature of the coating, in that, coatings should improve not only the mechanical and physical characteristics of the cutting tool material, but also reduce the thermo-mechanical effect on the cutting tool, which determines wear intensity [27]. For example, Prengel et al. [22] worked on different variants of TiAlN-multilayer coatings deposited on WC-6 wt.% Co hard metal inserts, which showed performance advantages over the monolayer TiAlN coatings. TiN/TiCN/TiAlN-multilayer coating was particularly determined to provide enhanced performance at high speeds. Figure 2 shows the toughness enhancement mechanism in a multilayer coating. Palatnik [28] with multilayers of metal coatings showed a significant improvement in the strength when compared to the coating/layer thickness below 500 nm. Holleck et al. [29] introduced toughening approaches based on multilayer architectures in their publications. The relevance of dispersing fracture energy and deflecting cracks at interfaces in multilayer structures comprised of hard ceramic materials, such as TiC/TiB$_2$ or TiN/(Ti(C,N) materials was highlighted in
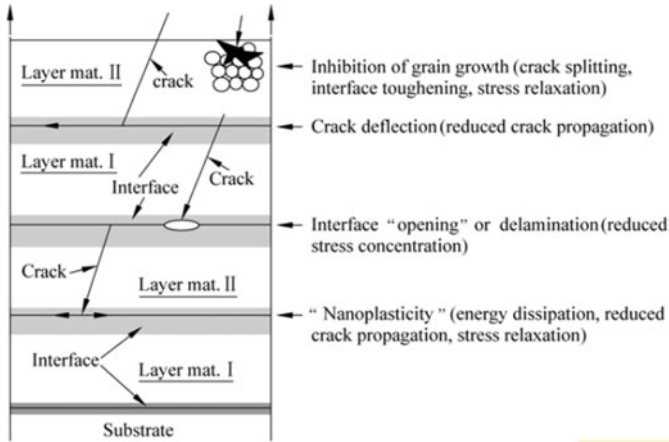
Fig. 2 Toughness enhancement in multilayer hard coatings [28]

their research. Wang and Du [30] have worked on developing composite coatings of MT-Ti(C,N) + Al_2O_3 using CVD and showed better wear resistance during dry milling. Lin and co-authors [31, 32] studied the improvement in tool life of cemented carbide inserts with a PVD-applied aluminium chromium nitride (AlCrN) coating (named Alcrona). They have conducted a thorough investigation on the effect of microstructures on wear progressions, such as, abrasive wear processes of AlCrN-coated cemented carbide tool inserts during dry and wet machining at very high cutting speeds. Figure 3 graphically shows the tool life under high-speed machining for dry and wet machining. Surface texturing at different face of the tool, such as flank face or rake face affects the tool wear, friction coefficient and cutting forces [33]. In an investigation performed by Zhao et al. [34] during down end milling of Ti6Al4V alloy, the efficiency of surface textured on the rake face, parallel to the

Fig. 3 Tool life under high machining for dry and wet cutting. Reproduced by permission [32], Copyright Elsevier, 2007)
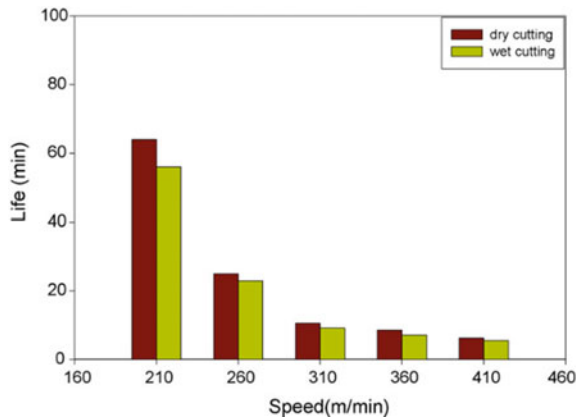
main cutting edge of uncoated (K10) cemented carbide tools of 10 mm diameter was studied. The textures were created with an Nd: YAG laser with a width of 100 μm, a spacing of 100 μm and a depth of 50 μm. The machining tests were carried out using both established conventional and nanofluids containing Fe_3O_4 nanoparticles with a diameter of 80 μm, which were applied under MQL conditions.

2.2.2 Gradients, Nano-structured and Superlattices Coatings

Superlattices, nanoscale multi-layered coatings have been developed to improve the hardness and strength of tools. With different layer composition and architectural design superlattice, coatings showed effective tool life enhancement when compared to monolayer coatings [35]. The downside of superlattices is that the influence of the nanolevels in the superlattices can be lost if the resultant layers do not follow the correct order [1]. Diamond and its coatings are the hardest known materials continue to draw a lot of attention for demanding applications involving high tribological conditions. Similarly, DLC coatings have sparked attention for a variety of industrial applications requiring high efficiency, performance and dependability. Erdemir et al. [19] offered a comprehensive overview of recent advances in the tribology of super-hard diamond and DLC films, with a focus on their friction and wear mechanisms, which are important to their exceptional tribological performance under challenging tribological conditions. DLC films may have mechanical and tribological properties that are comparable to crystalline diamond films, despite their amorphous nature. Mechanically, they can be made quite hard and stiff. In an investigation by Yang et al. [35] polycrystalline TiN/CrN superlattices with bilayer periods of 5.6–39 nm were deposited on a Ni-base alloy substrate by reactive unbalanced magnetron sputtering. The superlattices were annealed at various elevated temperatures for a certain period of time, in order to study the thermal stability of the coatings. In 2017, Zhang et al. [36] investigated the effect of WS_2 solid lubricant film on a femtosecond laser-textured rake face of PVD coated TiAlN on cemented carbide tools. First, a nanotextured coating was induced on the WC/Co substrate tool with various processing parameters using femtosecond laser scanning, the as-developed nanotextured substrate surface was then deposited with TiAlN film using the cathode arc-evaporation technique without using any interlayer. The nanotextured TiAlN-coated surface's surface micro-topography and mechanical properties were investigated. Selective laser melting (SLM) technique was applied to produce stainless steel, on which machining tests without cutting fluid were done using the proposed tool, as well as a cutting tool without laser pre-treatment for comparison. The results obtained shows that the femtosecond laser-induced periodic structure on the WC/Co substrate considerably improved the TiAlN coatings adhesiveness, and the critical load bearing capacity of the TiAlN coatings was increased from 57 to 73 N. Performance of nanotextured tools in drying cutting SLM 316 L stainless steel was accomplished, resulting in a 10–20% reduction in cutting forces, a 10–15% reduction in cutting temperature and a high-surface quality of the machined workpieces at high-cutting speeds [36].

In a similar study, Siddique et al. [37] used MoS_2 as a solid lubricant on laser-assisted textured tools for machining of Al6061-T6 alloys and reported a reduced flank wear of 24–35%; whereas; a reduction of 21–40% in the cutting temperatures during the machining process.

2.2.3 Composite Coatings

Malshe et al. [38] at the University of Arkansas have worked on developing a composite coating of cBN-TiN on WC–Co tool using two-step process of deposition, i.e. electrostatic spray coatings (ESC) of cBN particles followed by developing of TiN coating by chemical vapour infiltration (CVI). A scanning electron microscopy (SEM) image of the same is shown in Fig. 4. The reliability of the coatings has been examined using Taguchi. The plots between various parameters were obtained using MINITAB software. Their results showed excellent cBN-to-TiN substrate adhesion. This composite coating was later patented by Malshe et al. [39] stating that one phase material can be withhold another phase particle resulting in textured composite coatings.

Malshe and his group [40] have worked on MoS_2 and ZnO as solid lubricant to deposit it on a sample flat geometry with sub-microns and nano-sized particles. According to their studies, particle size has a significant impact on coating uniformity and powder transfer efficiency. Since nano-sized particles are prone to cluster formation, nano-sized ZnO deposition showed cluster deposition; whereas, micro-sized MoS_2 and ZnO showed discrete type of deposition. The investigation concluded that nano-sized particulate coating provides less friction when compared to micro-sized coating. In another study, Wang et al. [41] used nano-sized CaF_2 as a solid lubricant on tungsten-titanium carbide (WTC) composite cutting tools for machining of hardened carbon steels, which showed an imperative reduction in cutting force,

Fig. 4 SEM of ESC deposited cBN particulates on WC–Co tool. Reproduced by permission [38], Copyright Elsevier, 2003
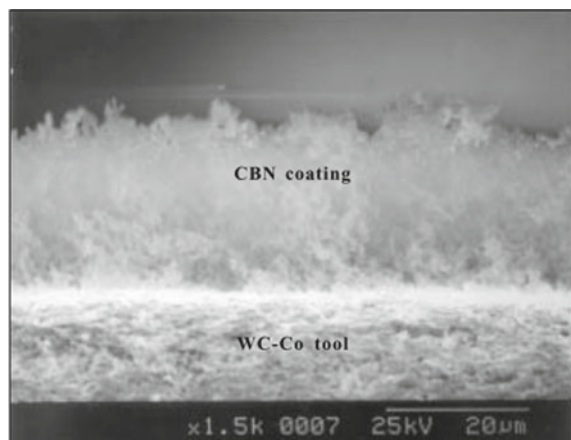
temperature and surface roughness of the work piece while the fracture toughness of the WTC composite tools were observed to increase by 13% with CaF_2.

3 Conclusions

During this review, various coatings and their effect on tool life have been considered. Following to the textured coatings, the article also review the advantage of using solid lubricants in enhancing tool life and eliminating the conventional coolants. Solid lubricants are considered for the proper and efficient operation of a variety of tribological systems. Solid lubricants include large structural materials, soft metals, diamond and DLC films. Their use is projected to increase in the coming years, owing to the fact that future tribosystem working conditions are getting more demanding, and liquid and grease-type lubricants are inappropriate due to the environmental issues. The majority of solid lubricants used in modern applications are manufactured as thin solid coatings on sliding surfaces. For the deposition of adherent solid lubricant films on a variety of substrates, including metallic, ceramic and polymeric types, various PVD and CVD processes are adopted. These methods help in producing solid lubricant films in gradient, duplex, multiplex, nano-structured and composite forms leading to improved performance and durability in the hostile environments. The tool coating and tool surface texturing presented significant improvement to increase the tool life and enhance machining process outputs during dry cutting. Dry cutting is better than wet cutting for TiAlN coating inserts under high cutting speed (around 200–400 m/min) [11]. TiAlN alternating multilayer-coated tools outperform TiAlN monolayer or TiN/TiCN/TiAlN-multilayer-coated inserts in dry milling of ductile cast irons and wet turning of Inconel 718 [25].

References

1. Atiqah Badaluddin N, Fathul Hakim Zamri WW, Faiz Md Din M, Fadhlina Mohamed I, Ghani JA (2018) Coatings of cutting tools and their contribution to improve mechanical properties: a brief review. Int J Appl Eng Res 13(14):11653–11664. http://www.ripublication.com
2. Narasimha M, Sridhar K, Reji Kumar R, Aemro Kassie A (2013) Improving cutting tool life a review. Int J Eng Res Dev 7(1):2278–2267
3. Zhao J, Liu Z, Wang B, Hu J, Wan Y (2021) Tool coating effects on cutting temperature during metal cutting processes: comprehensive review and future research directions. Mech Syst Signal Process 150:107302. https://doi.org/10.1016/j.ymssp.2020.107302
4. Zhao Z, Wang J, Liu Y (2010) The investigation of hot-dip aluminum and micro-arc oxidation multilayer coating on 080A15 steel. Adv Mater Res 139–141:406–409. https://doi.org/10.4028/www.scientific.net/AMR

5. Attarzadeh N, Molaei M, Babaei K, Fattah-alhosseini A (2021) New promising ceramic coatings for corrosion and wear protection of steels: a review. Surf Interfaces 23(September):100997. https://doi.org/10.1016/j.surfin.2021.100997

6. Rosenkranz A, Costa HL, Baykara MZ, Martini A (2021) Synergetic effects of surface texturing and solid lubricants to tailor friction and wear—a review. Tribol Int 155(10):106792. https://doi.org/10.1016/j.triboint.2020.106792

7. Liu J, Ye C, Dong Y (2021) Recent development of thermally assisted surface hardening techniques: a review. Adv Ind Manuf Eng 2(11):100006. https://doi.org/10.1016/j.aime.2020.100006

8. Soppa I, Pradhan S (2021) A brief review: study of machinability aspects of hard metals using micro textured inserts 143–149. https://doi.org/10.1007/978-981-15-6267-9_17

9. Moganapriya C, Vigneshwaran M, Abbas G, Ragavendran A, Ragavendra VCH, Rajasekar R (2021) Technical performance of nano-layered CNC cutting tool inserts—an extensive review. Mater Today Proc 45(000):663–669. https://doi.org/10.1016/j.matpr.2020.02.731

10. Machado AR et al (2021) State of the art of tool texturing in machining. J Mater Process Technol 293(June):117096. https://doi.org/10.1016/j.jmatprotec.2021.117096

11. Singh BK, Goswami S, Ghosh K, Roy H, Mandal N (2021) Performance evaluation of self lubricating CuO added ZTA ceramic inserts in dry turning application. Int J Refract Met Hard Mater 98(April):105551. https://doi.org/10.1016/j.ijrmhm.2021.105551

12. Singh BK, Roy H, Mondal B, Roy SS, Mandal N (2018) Development and machinability evaluation of MgO doped Y-ZTA ceramic inserts for high-speed machining of steel. Mach Sci Technol 22(6):899–913. https://doi.org/10.1080/10910344.2017.1415937

13. Sarıkaya M, Şirin Ş, Yıldırım ÇV, Kıvak T, Gupta MK (2021) Performance evaluation of whisker-reinforced ceramic tools under nano-sized solid lubricants assisted MQL turning of Co-based Haynes 25 superalloy. Ceram Int 47(11):15542–15560. https://doi.org/10.1016/j.ceramint.2021.02.122

14. Agarwal V, Agarwal S (2021) Performance profiling of solid lubricant for eco-friendly sustainable manufacturing. J Manuf Process 64(February):294–305. https://doi.org/10.1016/j.jmapro.2020.12.070

15. Narasimha M, Ramesh S (2014) Coating performance on carbide inserts. Int J Eng Tech Res 2(8):175–179

16. Donnet C, Erdemir A (2004) Solid lubricant coatings: recent developments and future trends. Tribol Lett 17(3):389–397. https://doi.org/10.1023/B:TRIL.0000044487.32514.1d

17. Erdemir A (2005) Review of engineered tribological interfaces for improved boundary lubrication. Tribol Int 38(3):249–256. https://doi.org/10.1016/j.triboint.2004.08.008

18. Krzanowski JE (2009) Fabrication and tribological properties of composite coatings produced by lithographic and microbeading methods. Surf Coatings Technol 204(6–7):955–961. https://doi.org/10.1016/j.surfcoat.2009.05.031

19. Erdemir A, Martin JM (2018) Superior wear resistance of diamond and DLC coatings. Curr Opin Solid State Mater Sci 22(6):243–254. https://doi.org/10.1016/j.cossms.2018.11.003

20. Rebenne HE, Bhat DG (1994) Review of CVD TiN coatings for wear-resistant applications: deposition processes, properties and performance. Surf Coatings Technol 63(1–2):1–13. https://doi.org/10.1016/S0257-8972(05)80002-7

21. Kustas FM, Fehrehnbacher LL, Komanduri R (1997) Nanocoatings on cutting tools for dry machining. CIRP Ann—Manuf Technol 46(1):39–42. https://doi.org/10.1016/s0007-8506(07)60771-9

22. Prengel HG, Jindal PC, Wendt KH, Santhanam AT, Hegde PL, Penich RM (2001) A new class of high performance PVD coatings for carbide cutting tools. Surf Coatings Technol 139(1):25–34. https://doi.org/10.1016/S0257-8972(00)01080-X

23. Bhushan B, Gupta BK, Van Cleef GW, Capp C, Coe JV (1993) Fullerene (C60) films for solid lubrication. Tribol Trans 36(4):573–580. https://doi.org/10.1080/10402009308983197

24. Silva S, Mammana VP, Salvadori MC, Monteiro OR, Brown IG (1999) WC-Co cutting tool inserts with diamond coatings. Diam Relat Mater 8(10):1913–1918. https://doi.org/10.1016/S0925-9635(99)00156-9

25. Carbide NWC, Musa MŠ, Sakoman M, Alar Ž, Cori D (2021) Analysis of different complex multilayer PACVD coatings on nanostructured WC-Co cemented carbide
26. Srikant Revuru R, Krishna Pasam V, Rao Posinasetti N (2020) Performance of coated cutting tools in machining: a review 792–802. https://doi.org/10.47412/jsid9445
27. Tabakov VP, Vereschaka AS, Vereschaka AA (2017) Multilayer composition coatings for cutting tools: formation and performance properties. Mech Ind 18(7). https://doi.org/10.1051/meca/2017063
28. Voevodin AA, Zabinski JS, Muratore C (2005) Recent advances in hard, tough, and low friction nanocomposite coatings. Tsinghua Sci Technol 10(6):665–679. https://doi.org/10.1016/S1007-0214(05)70135-8
29. Holleck H, Schulz H (1987) Advanced layer material constitution* @I Elsevier Sequoia/Printed in The Netherlands. Thin Solid Films 153:11–17
30. Qiu L et al (2019) Microstructure, mechanical properties and cutting performances of TiSiCN super-hard nanocomposite coatings deposited using CVD method under the guidance of thermodynamic calculations. Surf Coatings Technol 378(September):124956. https://doi.org/10.1016/j.surfcoat.2019.124956
31. Lin YJ, Agrawal A, Fang Y (2008) Wear progressions and tool life enhancement with AlCrN coated inserts in high-speed dry and wet steel lathing. Wear 264(3–4):226–234. https://doi.org/10.1016/j.wear.2007.03.007
32. Khrais SK, Lin YJ (2007) Wear mechanisms and tool performance of TiAlN PVD coated inserts during machining of AISI 4140 steel. Wear 262(1–2):64–69. https://doi.org/10.1016/j.wear.2006.03.052
33. Ranjan P, Hiremath SS (2019) Role of textured tool in improving machining performance: a review. J Manuf Process 43(November):47–73. https://doi.org/10.1016/j.jmapro.2019.04.011
34. Zhou C, Guo X, Zhang K, Cheng L, Wu Y (2019) The coupling effect of micro-groove textures and nanofluids on cutting performance of uncoated cemented carbide tools in milling Ti-6Al-4V. J Mater Process Technol 271(March):36–45. https://doi.org/10.1016/j.jmatprotec.2019.03.021
35. Yang Q, Zhao LR (2003) Thermal stability of polycrystalline TiN/CrN superlattice coatings. J Vac Sci Technol A Vacuum Surfaces Film 21(3):558–562. https://doi.org/10.1116/1.1559922
36. Zhang K, Guo X, Sun L, Meng X, Xing Y (2019) Fabrication of coated tool with femtosecond laser pretreatment and its cutting performance in dry machining SLM-produced stainless steel. J Manuf Process 42(1):28–40. https://doi.org/10.1016/j.jmapro.2019.04.009
37. Uddin Siddiqui T, Kumar Singh S (2020) Design, fabrication and characterization of a self-lubricated textured tool in dry machining. Mater. Today Proc 41(xxx):863–869. https://doi.org/10.1016/j.matpr.2020.09.259
38. Yedave SN, Malshe AP, Brown WD (2003) Novel composite CBN-TiN coating 30:154–162
39. Brown WD, Russell WC, Bhat DG, Rock L, Gilbreth MA (2003) (12) United States Patent 1(12)
40. Jiang W, Malshe AP, Brown WD (2004) Physical powder deposition of solid lubricant nanoparticles by electrostatic spray coating (ESC). Surf Coatings Technol 177–178:671–675. https://doi.org/10.1016/j.surfcoat.2003.08.005
41. Wang J, et al (2021) Mechanical property and cutting performance of (W,Ti)C based ceramic composites with the addition of nano-sized CaF_2. Int J Refract Met Hard Mater 99(June):105607. https://doi.org/10.1016/j.ijrmhm.2021.105607

Waste to Best: Chemical Recycling of Polyethylene Terephthalate (PET) for Generation of Useful Molecules

Rushik Radadiya, Syed Shahabuddin, and Rama Gaur

1 Introduction

A growing interest toward the consumption of plastic products is a major concern to the environment. Generally, commercial plastic is made up of thermoplastic polymers. Thermoplastic polymers such as polyethylene, polystyrene, and polyethylene terephthalate (PET) have significant corrosion resistance properties which have made them the most demanding consumable materials. The resistance of these polymers has enhanced the curiosity of researchers to find a facile way of disposal or recycling which is appropriate to maintain a safer environment as well as low cost [1]. Focusing on one such type, polyethylene terephthalate (PET or PETE) is a member of the polyester family of polymers, and it consists of polymerized units of the monomer ethylene terephthalate, with repeating units $C_{10}H_8O_4$ [2]. PET is semi-crystalline in nature, like all other thermoplastic in PET the atoms and molecules are joined end-to-end into long chain causing strong carbon backbone which make PET resistant to degradation [3].

Non-degradable nature of PET has been adversely impacting the environment. Lack of waste management facilities of this highly consumed material has forced us to accommodate the waste into the natural resources assuming it as the permanent solution. However, it would contribute to the total environmental disaster. PET waste does not only spoil the environment but is also responsible for the death of majority

R. Radadiya · S. Shahabuddin (✉) · R. Gaur (✉)
Department of Chemistry, School of Technology, Pandit Deendayal Energy University, Gandhinagar, Gujarat 382426, India
e-mail: Syed.Shahabuddin@sot.pdpu.ac.in

R. Gaur
e-mail: Rama.Gaur@sot.pdpu.ac.in

S. Shahabuddin
Faculty of Applied Sciences, Universiti Teknologi MARA Cawangan Negeri Sembilan, Kampus Kuala Pilah, 40450 Kuala Pilah, Malaysia
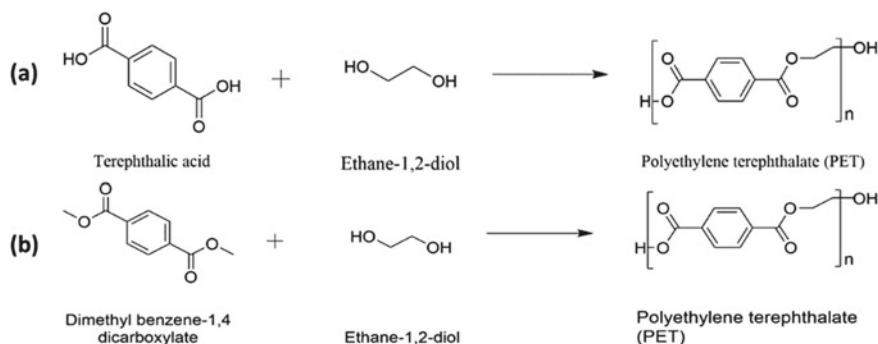
Fig. 1 Routes for preparation of PET **a** Esterification, **b** Trans-esterification

of stray animals, marine animals, and birds. After eating the polymer waste, their digestive system gets blocked, resulting in death of the birds and creatures [4].

To deal with the existing problem of building up PET waste, it is important to understand the genesis of PET. PET can be prepared in two ways: esterification and trans-esterification [5] (Fig. 1).

Esterification is a direct reaction between diol (ethylene glycol) and diacid (terephthalic acid) at 240–260 °C and 300–500 kPa pressure. In trans-esterification, dimethyl terephthalate (DMT) reacts with ethylene glycol at 180–210 °C and 100 kPa. Generally, it is difficult to maintain the purity of polymer. It is advisable to ensure the purity of the starting material. DMT can be easily purified by distillation process. Hence, trans-esterification is preferred over the other process.

PET is molded in different shapes for different applications. The wide applicability of PET has led to increased production of plastic, hence posing a threat to the environment. The current scenario calls for the development of the sustainable solution to tackle the problem of plastic accumulation as solid waste [6]. Taking environmental consciousness into consideration, numerous approaches of PET waste management have been discovered till the date. The conventional routes to PET waste management, its disposal, and mechanical recycling have their own disadvantages and are not favored in terms of cost and environmental safety [7]. The development of economic and ecological recycling method is a strategic move to get rid from the accumulation of PET waste. Chemical recycling converts the PET waste into the original starting materials without compromising the quality. It involves different types of depolymerization techniques such as methanolysis, hydrolysis, glycolysis, aminolysis, and ammonolysis [8].

Chemical recycling is considered as one of the best approaches and most viable option for the treatment of waste PET, as it fulfills the need of sustainable growth [9]. Though different chemical recycling approaches demand for the capital investment and certain raw materials, they also have other benefits. The end products generated after chemical recycling can be modified into molecules of high importance and higher applicability in various fields. For instance, the aminolysis of PET generates terephthalic dihydrazide in the presence of hydrazine, which can be easily

Table 1 Comparative analysis of various routes for PET Waste management in terms of advantages and disadvantages

Routes for PET waste management	Advantages	Disadvantages	References
Landfill	Does not require sophisticated machinery and chemicals	Occupies productive land	[14]
Incineration	No need to separate the plastic waste	Causes air pollution and health risks	[15]
Mechanical recycling	Can be used to mix polyolefins	Heterogeneity of solid waste, degradation of product's quality in each cycle and undesirable color of the product	[16]
Chemical recycling	Higher yield as well as high quality of product	Economically viable for large scale production only	[9, 17]
Pyrolysis	Convenient operation, pre-treatment of plastic waste is not required	Complex separation and low selectivity of the product	[18]

converted into oxadiazole and hydrazone derivatives. These derivatives are reported to show remarkable pharmacological activity like antifungal, antibacterial, antiviral, etc. [10]. Chan et al. have treated PET with ethanolamine to produce PET-derived poly(amidoamine), which was further converted into a hydrogel-based adsorbent to be used in pharmaceuticals, environmental cleaning, oil recovery, etc. [11].

Few researchers have also reported the conversion of PET waste into new value-added products such as Pattanshetti et al. have converted the PET waste into carbon nanotube for packaging material using T-CVD method (Thermal chemical vapor deposition). Modification of PET-derived active carbon materials has shown great catalytic activity for conversion of waste cooking oil into green fuel [12]. Sharma et al. have converted the polyester fiber waste into cotton-based composite fabric by dissolving PET fiber waste into m-cresol and regenerate the cotton [13] (Table 1).

2 Different Routes for PET Waste Management

The commonly used methods for the disposal of PET waste are landfill, incineration, mechanical recycling, and chemical recycling. Apart from chemical recycling of PET, there are some combined technologies for the conversion of PET waste into high-value commodities. For example, pyrolysis is a combination of thermal and chemical treatment of PET waste in an inert atmosphere. All of these methods involve certain criteria and have their own limitations and benefits which are discussed in following sections.

2.1 Landfill

Dumping of PET waste into land is the most conventional approach and threatening to the environment as well. The major drawback associated with this approach is it covers a large area of useful land. The degrading PET waste release toxin to the environment, hence damaging the quality of land [15]. As there is no need of any sophisticated tools and essential chemicals, this method has been proved one of the convenient methods [4]. Limited accessibility to oxygen creates anaerobic condition in the landfill, consequently decreasing the rate of degradation. Apart from this, thermo-oxidative degradation is another reason for lower rate of degradation, and due to these factors, degradation of PET waste takes more than 20 years [14].

2.2 Incineration

Also known as thermal treatment of plastic waste, is another common technique for PET waste management. In incineration, the plastic waste is subjected to thermal treatment in the presence of oxygen which leads to the formation of gases and heat. The generated heat is further utilized as an energy source [4]. The significant advantage of this method is that it does not occupy the land; however, it produces harmful pollutants like greenhouse gas (CO_2), toxic carbon, heavy metals, polycyclic aromatic hydrocarbons (PAHs), and polychlorinated biphenyls (PCGs) [19]. Hence, incineration leads to environmental pollution and should not be used as a waste treatment method.

2.3 Pyrolysis

Similar to incineration, pyrolysis is also combustion of PET waste. The key difference is that incineration of PET waste is performed in the presence of oxygen while pyrolysis is performed in the absence of oxygen. Pyrolysis of PET waste is performed in the presence of catalyst like ZSM-5, CaO, $ZnCl_2$, etc., to form a mixture of molecules in liquid or wax phase as the main products that can be used to generate value-added chemicals or fuels [20]. As per the reports, PET is a significant source of solid carbon material [21]. Thus, PET-derived carbon materials are emerging as potential candidates for application in various fields such as energy storage system, environmental application, and conductive composite [21]. Zhang et al. have upcycled PET waste by pyrolysis into methane-rich gas and carbon material for energy storage [22].

The major component of pyrolysis product is benzoic acid approximately 49.93% which limits the industrial application of this method. The benzoic acid formed during the pyrolysis process clogs the piping and deters the exchange of heat [23].

2.4 Mechanical Recycling

In mechanical recycling, polymer is separated from contaminants followed by crushing and then remelted into plastic flakes. The plastic flakes are used to produce new plastic products. Mechanical recycling does not change the structure of polymer. The purity of recycled waste is a major concern as an excess amount of the contaminant present. Another issue which is associated with this method is gradual decrease of the quality of the product with every recycling step. The low molecular weight of polymer resin is the major reason for the quality degradation of the polymer. During the recycling process, the presence of water and other acidic pollutant cause breaking of the polymer chain and result in the formation of lower molecular weight of plastic resin [24]. Post-consumption plastic waste undergoes following steps during the process of mechanical recycling—Collection, Sorting, Washing, Grinding, and Chipping (Fig. 2) [24]. Collection of plastic waste for recycling includes two types of plastic waste, primary plastic waste and secondary plastic waste [4]. Primary plastic waste is collected from manufacturing industries. It includes rejected plastic materials which have similar properties (chemical and mechanical). Secondary plastic waste includes new product which have inferior properties compared to the new product and, generally, includes used product.

Fig. 2 Schematic representation of the steps involved in mechanical recycling of PET waste

Fig. 3 Schematic representation of the steps involved in chemical recycling of PET waste

2.5 Chemical Recycling

PET recycling by chemical method involves the cyclic process of conversion of polymer chain to its monomer (Fig. 3). In this recycling process, the polymer backbone is degraded back to the monomeric units and is generally called depolymerization. In chemical recycling, there are two possibilities, first is complete depolymerization of PET waste to its monomer and the second is partial depolymerization by the formation of oligomers and other essential chemicals [16]. Condensation polymer is depolymerized by means of solvolytic chain breaking to their respective low molecular weight products or monomers. Depolymerization of PET solely depends on the reagents used. Based on reagent used, chemical recycling can be hydrolysis, glycolysis, acidolysis, and alcoholysis, where water, glycol, acid, and alcohol are used, respectively [24, 25].

In comparison with all other recycling methods, chemical recycling is more acceptable as a sustainable solution, as it converts the waste to its raw material without losing quality of product and most importantly it is not surcharging the environment [26]. Chemical recycling of PET waste results in the formation of monomers, petroleum liquids, and gases. The produced monomers can be purified and re-used to form polymers [27].

Chemical recycling also includes methanolysis, hydrolysis, glycolysis, aminolysis, and ammonolysis. All these chemolysis methods aim to produce different monomers such as TA (Terephthalic acid), EG (ethylene glycol), terephthaldiamide, dimethylterephthalate (DMT), and bis(hydroxyethyl)terephthalate (BHET) (Fig. 4). The formation of these monomers depends on the type of chemical reagent used to
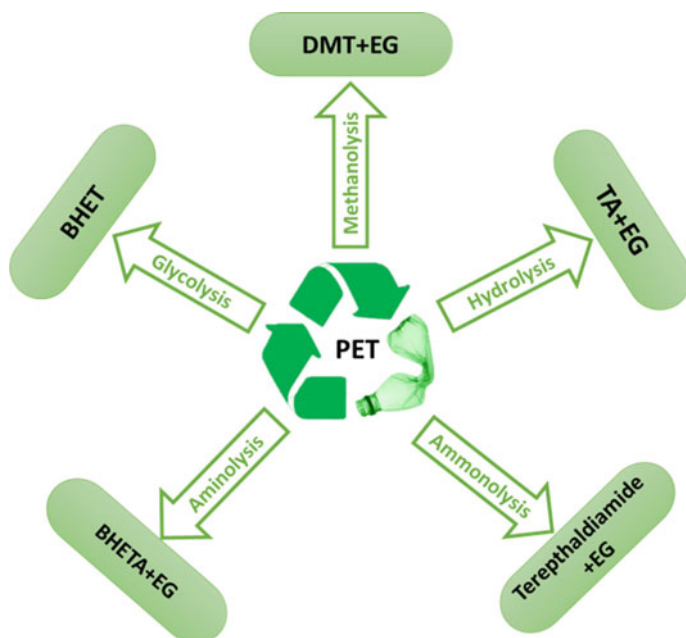
Fig. 4 Different processes involved in chemical recycling of PET waste and the monomers produce after depolymerization

cleave the polymeric chain. Certain specific reagents form the mixture of monomer which is used to build other polymers (viz., unsaturated polyesters, polyurethanes, and polyisocyanurates) [28].

Methanolysis. Methanolysis is one of the alcoholysis methods of PET waste recycling. In methanolysis, the post-consumer PET plastic waste is depolymerized in the presence of liquid methanol to its monomeric feedstock dimethylterephthalate (DMT) and ethylene glycol (Fig. 5) in the presence of liquid methanol. Waste materials for methanolysis include plant waste, fiber waste, post-consumer films, and bottle scraps [29]. It is a trans-esterification, catalyst-based reaction and requires the high temperature and high pressure (180–280 °C, 2–4 MPa). Generally, metal acetates (e.g., zinc acetate, lead acetate, etc.), metal oxide (e.g., aluminiumisopropoxide,

Polyethylene terephthalate (PET) Methanol   Dimethyl benzene-1,4-dicarboxylate Ethane-1,2-diol
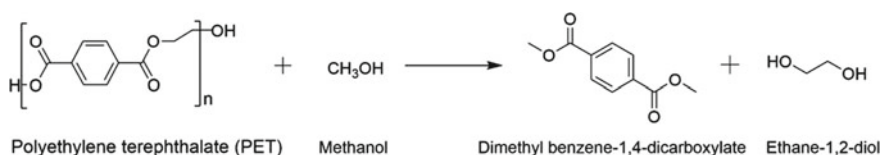
Fig. 5 Chemical reaction depicting methanolysis of PET to dimethyl benzene-1,4-dicarboxylate and ethane-1,2-diol

sodium silicate, etc.), and metal hydroxides are used as the catalyst, among all zinc acetates is the most widely used catalyst [30].

Three different forms of methanol can be employed in this method such as liquid methanol (conventional), super-heated (vapor), and supercritical methanol. In super-heated vapor methanolysis, the reaction occurs at 240–260 ºC and at lower pressure (0.5–2 Mpa). Compared to liquid methanolysis, the pressure is quite lower which causes the higher reaction time (5 h); however, as the product (DMT) is formed in the vapor phase, the equilibrium shift toward higher yield [31]. Supercritical methanol-ysis follows high pressure and high temperature (260–270 ºC, 9–11 Mpa), and it converts the noticeable amount of PET waste to its monomer (yield up to 95%) [32, 33].

The main benefits of methanolysis are convenient installation to the production lines and the high quality of product. On the other hand, high capital and operating cost as well as separation of the desired product from reaction mixture are prime obstacles [34].

The conventional methanolysis suffers from the disadvantages such as high temperature and pressure, high cost, and not environment friendly. Joungmo Cho and co-workers have developed a facile and cost-effective pathway for methanolysis of PET waste. They used cheaper and nontoxic salt, potassium carbonate (K_2CO_3) as a catalyst and dichloromethane as a co-solvent. Though the reaction rate was quite slow (up to 24 h), the efficiency of complete depolymerization was noticeable (93.1% yield) at mild temperature condition 20–35 ºC. The molar ratio of starting material was 50, 50, and 0.2 (methanol, dichloromethane, and K_2CO_3, respectively) [32].

Hydrolysis. Hydrolysis recycling is the depolymerization of the PET waste to its building blocks terephthalic acid (TA) and ethylene glycol (EG) in the presence of water (Fig. 6). The significant aspect of hydrolysis is the purity of products which facilitate the indirect use of products into esterification reaction for new polymer generation. Hydrolysis is not used to recycle food-packaging materials because of higher production cost. Other issues associated with this method are the need of high pressure, high temperature (1.4–2 MPa and 200–250 ºC), and long reaction time. However, this can be solved by optimizing the reaction conditions. Generally, hydrolysis is performed in neutral, alkaline, and acidic condition [34].

Neutral hydrolysis. In neutral hydrolysis, PET is treated with water or heat to form TA and EG at neutral pH. It employs high pressure autoclave, pressure ranging from 1 to 4 MPa, and temperature varying from 200 to 300 ºC [31]. Molten state is more preferable than solid state for this reaction as it follows rapid rate of reaction

Polyethylene terephthalate (PET)   Terephthalic acid   Ethane-1,2- diol
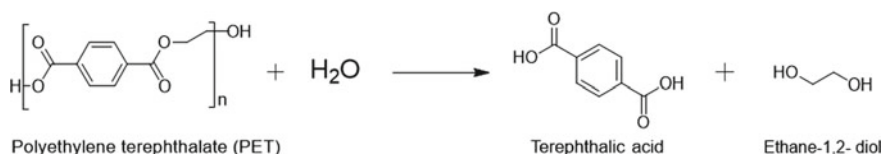
Fig. 6 Chemical reaction depicting hydrolysis of PET to Terephthalic acid and ethane-1,2-diol

in molten state. The disadvantage of this method is it cannot remove mechanical impurities from the starting material. The impurities remain as it is in the product [28]. Exclusion of undesirable inorganic salt and acid makes it a greener process [30].

In order to solve the issue of acidic and basic residue in acidic and alkaline condition, Myung jonk kang and his team have modified the neutral hydrolysis, by using easily reproducible acid/base catalyst at neutral pH. They have applied microwave-assisted hydrolysis, in the presence of heterogeneous acidic catalyst ZSM-5. Due to certain significant properties of ZSM-5, like microporous aluminosilicate minerals, highly crystalline surface, and presence of Bronsted and Lewis acid sites in its framework, it is found to be an ideal acid catalyst for neutral hydrolysis [35].

Alkaline hydrolysis. Alkaline hydrolysis proceeds in the presence of aqueous NaOH or non-aqueous KOH (concentration 4–20%) at 100–200 °C and 110–120 °C, respectively, for non-aqueous KOH [24, 34]. The results vary with different ratio of PET and NaOH [34]. Under these reaction conditions, sodium salt of terephthalic acid (TA) is formed which can be precipitated out with the help of strong acid (H_2SO_4) [25]. The main advantage of alkaline hydrolysis is the conversion of the product (ethylene glycol) to oxalic acid and CO_2 that enhances the economic value of this method; however, it contains higher amount of contaminants (40 wt %) compared to others [29].

Lelia et al. has developed a greener and environment-friendly approach for alkaline hydrolysis of PET waste. They experimented several reaction conditions including concentration of NaOH (20 or 30%), different organic co-solvent (ethylene glycol or ethanol), temperature, and time. Particle size of PET plays major role for conversion, ranging from 73 to 100%. As compared to ethylene glycol ethanol's depolymerization, efficiency was high, 94% (reaction time 2 h, 80 °C), whereas for EG its 75–80% (reaction time 6 h, 110 °C). The apparent benefit of this work is that it removes hurdle of pre-treatment of waste. Other contaminants in the PET waste can also be removed as caps, labels, rings, etc. [36].

Acid hydrolysis. Acid hydrolysis is performed in the presence of acid at 25–100 °C and atmospheric pressure [26, 30]. Protic acids like sulfuric acid, nitric acid, and phosphoric acid can be used; generally, sulfuric acid is preferred [34]. The efficiency of recycling increases with the concentration of sulfuric acid; acid concentration greater than 14.5 M facilitates to avoid high pressure and temperature [37]. High concentration of sulfuric acid causes high cost and less yield of ethylene glycol because of carbonization of ethylene glycol by acid [29, 37]. At the last, formation of large amount of liquid waste causes environmental threat, as it contains inorganic salt and sulfuric acid [28].

Abedsoltan et al. have developed the acid hydrolysis method using acid catalyst (4-styrenesulfonic acid (PSSA)) which is recoverable and reusable and lowers the acid recycling cost and small amount of acidic liquid waste is generated. Use of acid catalyst improved the product yield and increased the reaction rate as compared to the use of mineral sulfuric acid [38].
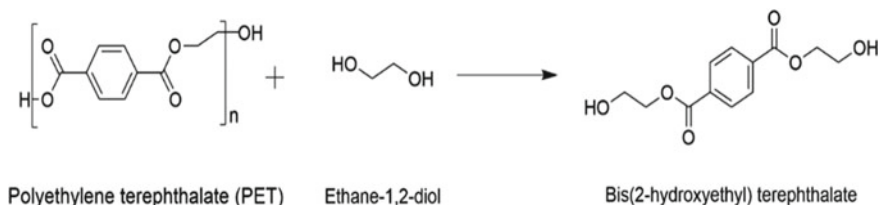
Fig. 7 Chemical reaction depicting glycolysis of PET to Bis(2-hydroxy)terephthalate

Glycolysis. Glycolysis of PET waste is the most convenient approach of PET recycling as it involves comparatively mild reaction conditions. It is the trans-esterification reaction between PET which has ester functionality and diol whose hydroxyl groups cleave the ester linkage [6], to form monomer bis(2-hydroxyethyl terephthalate) (BHET) (Fig. 7) [3]. BHET is used to form various polymeric products like plasticizer, resin, dyes, softeners, etc. [39]. Common sources of diol are diethylene glycol, propylene glycol, and dipropylene glycol [30]. Reaction occurs in the presence of excess amount of ethylene glycol and catalyst like zinc acetate, sodium carbonate, sodium bicarbonate, sodium sulfate, and potassium sulfate at high temperature range 180–240 ℃ [3]. Compared to all metal acetates, zinc acetate shows the highest catalytic efficiency. Sodium bicarbonate is reported to act as an efficient catalyst because of its basic nature. High solubility of sodium bicarbonate in ethylene glycol enables the formation of homogenous solution which can easily react with PET [6]. Use of sodium salt as a catalyst instead zinc acetates can reduce the environmental problem cause by zinc cation, as it is non-biodegradable and toxic [3].

Xingmei Lu and his team have developed dissolution-degradation strategy by using different organic solvent with catalyst. The use of dimethyl sulfoxide (DMSO) as a solvent with zinc acetate catalyst resulted in significant depolymerization of PET was in 1 min with the yield of 82%. Moreover, they also investigated the universality of this solvent system with different catalyst. It was found to be applicable toward various catalyst and other than PET; other polymer can be recycled by this approach [40].

Aminolysis. Aminolysis is the process in which PET waste is depolymerized into BHETA (N,N′-Bis(2-hydroxyethyl)terephthaldiamide) and ethylene glycol (Fig. 8) at 20–100 ℃ in the presence of amine and catalyst [41]. Most frequently used amines are monoethanolamine, ethylamine, methylamine, and 3-amino-1-propanol [42, 43].
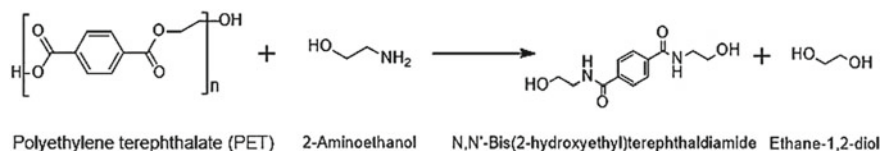
Fig. 8 Chemical reaction depicting aminolysis of PET to BHETA and ethane-1,2-diol
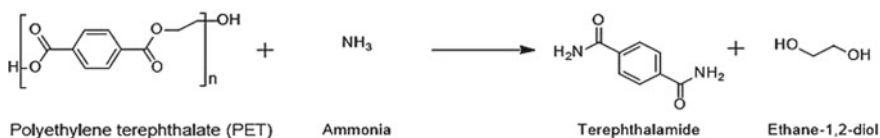
Fig. 9 Chemical reaction depicting ammonolysis of PET to terephthalamide and ethane-1,2-diol

Metal salts, quaternary ammonium compound, and ionic liquid are used as catalyst [44]. The central element of this approach is the amine which hinders the commercial implementation, owing to its high cost and toxic nature. Temperature plays key role in aminolysis of PET; efficiency of conversion increases with temperature and shorten the reaction time and results in higher yield. Chun-cheng Zhu and his team have observed 100% conversion at 130 ℃ with a yield of 73.91% in 6 min [45].

Several techniques have been applied to aminolysis of PET waste, like solar energy, UV irradiation, microwave irradiation, and ultrasound irradiation. Different techniques require different reaction conditions; in addition to this, reaction time, efficiency, and yield percentage also vary with the choice of depolymerization approach [46].

Ammonolysis. In ammonolysis, PET waste flakes are treated with excess amount of liquor ammonia at 120–180 ℃, 2 MPa pressure for 1–7 h to form terephthalamide and ethylene glycol (Fig. 9) [47, 48]. To avoid harsh condition of high temperature and pressure, catalysts are used (zinc acetate, quaternary ammonium salt) [34, 47, 49].

Soni et al. performed the ammonolysis process in the absence and presence of quaternary ammonium salt catalyst with PET-ammonia weight ratio as 1:10 at room temperature 40 ℃. PET flakes were completely degraded in 45 days in the presence of catalyst while in the absence of catalyst the degradation was found to be incomplete [49].

Evaluating the conditions involved in different chemical recycling process, it can be concluded that hydrolysis is an economically viable solution compared to other chemical recycling method. Hydrolysis involves use of water as a reagent for depolymerization of PET which fulfills the greener and economic approach. Glycolysis and methanolysis require reagents which are moderate in cost, whereas in aminolysis and ammonolysis quite expensive reagents are required. Though there is a difference in terms of cost involved in different chemical recycling process, the molecules which are formed in certain methods have specific importance and applicability.

3 Summary and Future Scope

To sum up, due to space constraints and environmental threat, landfill and incineration of PET waste have lost their importance. Apart from that, gradual increase in the

cost of fossils and poor biodegradability have made recycling of PET waste as a crucial step. The recycling methods have caught the attention of many researchers to develop sustainable and environmentally friendly approach toward the PET waste conversion. Mechanical recycling of PET waste hampered by impurities and recycled product have low grade quality. In this sense, chemical recycling is beneficial as the depolymerization process, and it breaks down the polymer chain and converts into its raw material or new molecule without compromising quality of product. Researchers have developed various aspects of chemical recycling; however, summit is still to be reached in the area of recycling. Various factors like reaction condition, rate of reaction, and yield of product play major role to industrialize the particular method, which need to be explored further. The catalyst is another significant element which should be reusable and efficient. All these aspects can be opportunities for researchers to develop greener, efficient, and low-cost technology to convert PET to valuable monomers. The research on chemical recycling of PET waste opens new avenues in the field of research and industries to develop sustainable solutions.

References

1. Pudack C, Stepanski M, Fässler P (2020) PET Recycling-Contributions of crystallization to sustainability. Chem Ing Tec 92(4):452–458
2. Crippa M, Morico B (2020) PET depolymerization: a novel process for plastic waste chemical recycling. Catal, Green Chem Sustain Energy 179:215–219
3. Duque-Ingunza I et al (2014) Process optimization for catalytic glycolysis of post-consumer PET wastes. J Chem Technol Biotechnol 89(1):97–103
4. Koshti R, Mehta L, Samarth N (2018) Biological recycling of polyethylene terephthalate: a mini-review. J Polym Environ 26(8):3520–3529
5. Elamri A et al (2017) Progress in polyethylene terephthalate recycling. Nova Science Publishers
6. Syariffuddeen A, Norhafizah A, Salmiaton A (2012) Glycolysis of poly (ethylene terephthalate) (PET) waste under conventional convection-conductive glycolysis. Int J Eng Res Technol 1(10):1–8
7. Thiounn T, Smith RC (2020) Advances and approaches for chemical recycling of plastic waste. J Polym Sci 58(10):1347–1364
8. Vollmer I et al (2020) Beyond mechanical recycling: giving new life to plastic waste. Angew Chem Int Ed 59(36):15402–15423
9. Ragaert K, Delva L, Van Geem K (2017) Mechanical and chemical recycling of solid plastic waste. Waste Manage 69:24–58
10. Tarannum N et al (2022) Chemical depolymerization of recycled PET to oxadiazole and hydrazone derivatives: synthesis, characterization, molecular docking and DFT study. J King Saud Univ-Sci 34(1):101739
11. Chan K, Zinchenko A (2021) Conversion of waste bottles' PET to a hydrogel adsorbent via PET aminolysis. J Environ Chem Eng 9(5):106129
12. Ahangar FA et al (2021) Conversion of waste polyethylene terephthalate (PET) polymer into activated carbon and its feasibility to produce green fuel. Polymers 13(22):3952
13. Sharma K et al (2020) Cotton based composite fabric reinforced with waste polyester fibers for improved mechanical properties. Waste Manage 107:227–234
14. Ilyas M et al (2018) Plastic waste as a significant threat to environment–a systematic literature review. Rev Environ Health 33(4):383–406

15. Verma R et al (2016) Toxic pollutants from plastic waste-a review. Procedia Environ Sci 35:701–708
16. Bartolome L et al (2012) Recent developments in the chemical recycling of PET. Mater Recycl-Trends Perspect 406
17. Park SH, Kim SH (2014) Poly (ethylene terephthalate) recycling for high value added textiles. Fashion Textiles 1(1):1–17
18. Zhou X (2021) Research on conversion of waste polyethylene terephthalate into value-added monomer replacing landfill and incineration for environmental pollution control. In: IOP conference series: earth and environmental science. IOP Publishing
19. Shahnawaz M, Sangale MK, Ade AB (2019) Plastic waste disposal and reuse of plastic waste. Bioremediation technology for plastic waste. Springer, pp 21–30
20. Sharuddin SDA et al (2016) A review on pyrolysis of plastic wastes. Energy Convers Manage 115:308–326
21. Kamali AR, Yang J, Sun Q (2019) Molten salt conversion of polyethylene terephthalate waste into graphene nanostructures with high surface area and ultra-high electrical conductivity. Appl Surf Sci 476:539–551
22. Zhang H et al (2021) Upcycling of PET waste into methane-rich gas and hierarchical porous carbon for high-performance supercapacitor by autogenic pressure pyrolysis and activation. Sci Total Environ 772:145309
23. Qureshi MS et al (2020) Pyrolysis of plastic waste: opportunities and challenges. J Anal Appl Pyrol 152:104804
24. Grigore ME (2017) Methods of recycling, properties and applications of recycled thermoplastic polymers. Recycling 2(4):24
25. Carta D, Cao G, D'Angeli C (2003) Chemical recycling of poly (ethylene terephthalate) (PET) by hydrolysis and glycolysis. Environ Sci Pollut Res 10(6):390–394
26. Achilias D, Karayannidis G (2004) The chemical recycling of PET in the framework of sustainable development. Water Air Soil Pollut Focus 4(4):385–396
27. Sinha V, Patel MR, Patel JV (2010) PET waste management by chemical recycling: a review. J Polym Environ 18(1):8–25
28. Crippa M, Morico B (2020) Catalysis, green chemistry and sustainable energy
29. Park H et al (2014) Assessment of Firefighters' needs for personal protective equipment. Fashion and Textiles 1(1):1–13
30. Shojaei B, Abtahi M, Najafi M (2020) Chemical recycling of PET: a stepping-stone toward sustainability. Polym Adv Technol 31(12):2912–2938
31. Kim B-K et al (2008) Chemical recycling of poly (ethylene terephthalate) using a new hybrid process. J Chem Eng Jpn 41(9):923–928
32. Pham DD, Cho J (2021) Low-energy catalytic methanolysis of poly (ethyleneterephthalate). Green Chem 23(1):511–525
33. Genta M et al (2005) Depolymerization mechanism of poly (ethylene terephthalate) in supercritical methanol. Ind Eng Chem Res 44(11):3894–3900
34. Al-Sabagh A et al (2016) Greener routes for recycling of polyethylene terephthalate. Egypt J Pet 25(1):53–64
35. Kang MJ et al (2020) Depolymerization of PET into terephthalic acid in neutral media catalyzed by the ZSM-5 acidic catalyst. Chem Eng J 398:125655
36. Cosimbescu L et al (2021) Simple but tricky: investigations of terephthalic acid purity obtained from mixed PET waste. Ind Eng Chem Res 60(35):12792–12797
37. Yoshioka T, Motoki T, Okuwaki A (2001) Kinetics of hydrolysis of poly (ethylene terephthalate) powder in sulfuric acid by a modified shrinking-core model. Ind Eng Chem Res 40(1):75–79
38. Abedsoltan H et al (2021) Poly (4-styrenesulfonic acid): a recoverable and reusable catalyst for acid hydrolysis of polyethylene terephthalate. Polymer 222:123620
39. Pingale ND, Palekar VS, Shukla S (2010) Glycolysis of postconsumer polyethylene terephthalate waste. J Appl Polym Sci 115(1):249–254
40. Liu B et al (2018) Ultrafast homogeneous glycolysis of waste polyethylene terephthalate via a dissolution-degradation strategy. Ind Eng Chem Res 57(48):16239–16245

41. George N, Kurian T (2014) Recent developments in the chemical recycling of postconsumer poly (ethylene terephthalate) waste. Ind Eng Chem Res 53(37):14185–14198
42. Shukla S, Harad AM (2006) Aminolysis of polyethylene terephthalate waste. Polym Degrad Stab 91(8):1850–1854
43. Collins MJ, Zeronian SH, Marshall ML (1991) Analysis of the molecular weight distributions of aminolyzed poly (ethylene terephthalate) by using gel permeation chromatography. J Macromol Sci—Chem 28(8):775–792
44. Ghorbantabar S et al (2021) Investigation of conventional analytical methods for determining conversion of polyethylene terephthalate waste degradation via aminolysis process. J Mater Cycles Waste Manage 23(2):526–536
45. Zhang L-N et al (2014) From aminolysis product of PET waste to value-added products of polymer and assistants. Polym Polym Compos 22(1):13–16
46. More AP et al (2017) Studies of different techniques of aminolysis of poly (ethylene terephthalate) with ethylenediamine. Polym Bull 74(8):3269–3282
47. Jain A, Soni R (2007) Spectroscopic investigation of end products obtained by ammonolysis of poly (ethylene terephthalate) waste in the presence of zinc acetate as a catalyst. J Polym Res 14(6):475–481
48. Thachnatharen N, Shahabuddin S, Sridewi N (2021) The waste management of polyethylene terephthalate (PET) plastic waste: a review. In: IOP conference series: materials science and engineering. IOP Publishing
49. Soni R, Singh S (2005) Synthesis and characterization of terephthalamides from poly (ethylene terephthalate) waste. J Appl Polym Sci 96(5):1515–1528

Hydrogel-Based Adsorbent Materials for Heavy Metal Removal from Industrial Waste Water

Darban Zenab, Rama Gaur, and Syed Shahabuddin

1 Introduction

Water is an indispensable part of all living organisms. To fulfill the need of all lives, only 3% of water is available as fresh water, out of which less than one-third is available for domestic, agriculture, irrigation, and industrial purposes [1, 2]. There is an immense demand for freshwater, but supplies decrease due to factors such as rapid rise in urbanization, industrialization, and numerous anthropogenic activities [1]. Among them, industries are major contributing factor for discharging waste to various water bodies that causes severe water contamination. Industrial wastewater contains heavy metals, oils, dyes, chemicals, etc., that have toxic, carcinogenic, and hazardous effects on flora and fauna, human health, and natural habitat.

For recycling wastewater, different methods have been employed, including photocatalytic degradation [3], ion exchange [4], chemical precipitation [5], membrane filtration [6], ammonia desulfurization [7], coagulation-flocculation [8], reverse osmosis [9], and adsorption [10]. Out of these methods, adsorption method is found to be the convenient, inexpensive, and fruitful method that can be employed for extracting heavy metals from wastewater released by industries with no harmful side products [1, 11] (Fig. 1).

In last few years, a lot of research had been undertaken by researchers to design and synthesize novel adsorbent material for removing heavy metals from industrial wastewater. Hydrogel, as potential absorbent material, is good contender for removing heavy metals. Hydrogel are porous three-dimensional system comprised

D. Zenab · R. Gaur · S. Shahabuddin (✉)
Department of Chemistry, School of Technology, Pandit Deendayal Energy University, Gujarat 382007, India
e-mail: Syed.shahabuddin@sot.pdpu.ac.in

S. Shahabuddin
Faculty of Applied Science, Universiti Teknologi MARA, Cawangan Negeri Sembilan, Kampus Kuala Pilah, 40450 Kuala Pilah, Shah Alam, Malaysia

Fig. 1 Adverse effects caused by heavy metals on human health
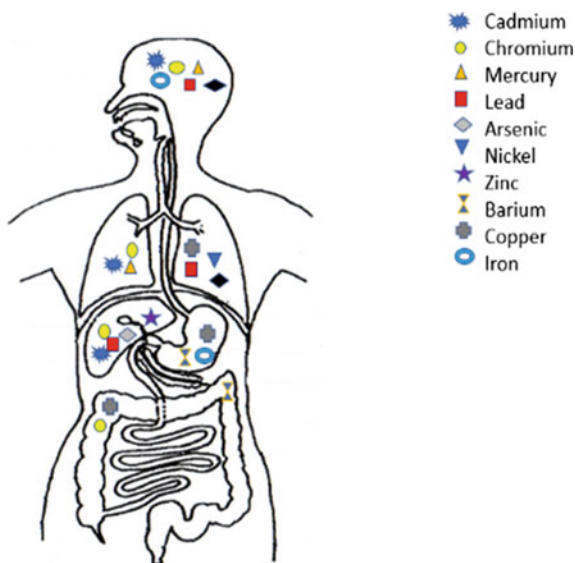
hydrophilic (water-loving) polymers formed via cross-linking of polymeric units that can expand and imbibe huge content of water in its three-dimensional interstitial structure [12, 13]. These characteristics of hydrogel are due to hydrophilic functional groups (–OH, –SO$_3$H, –COOH, –CONH$_2$, –NH$_2$) present in the polymeric chain that allows the capture of heavy metals from waste water and release these hazardous pollutants upon reacting with external stimuli in aqueous solution [14]. Hydrogel can be prepared by polymerization and cross-linking between one or different monomeric units. The main chemicals required for the formulation of hydrogel are initiator, monomer, and cross-linker [15]. Based on the chemicals used, hydrogels can be modified by changing monomer or initiator concentration, time of reaction, type of cross-linking agent, temperature and pH of the reaction, and the fraction of monomer and cross-linker [12].

In 1894, the word hydrogel was first discovered by Bemmelen to explain colloidal gels. DuPont scientists were first to report synthetic poly (2-hydroxyethyl methacrylate) hydrogel and the first application in biomedical area (contact lens) was reported in 1960 by Wichterle and Lim [12]. Since then, hydrogel has been explored in different fields, namely agriculture [16], tissue engineering [17], drug delivery [18], contact lens [19], dyes and heavy metals [20] removal, and many more. Our emphasis will be on the application of hydrogel to remove metallic impurities from waste water.

2   Properties of Hydrogel

An ideal hydrogel has characteristic properties, i.e., swelling, stimule-reponsive, adsorption efficiency, biodegradability, and biocompatibility.

2.1   Adsorption Efficiency

The adsorption efficiency of hydrogel is measure of its capacity to retain huge volume of fluid (water) in three-dimensional structure. Factors influencing adsorption are surface area, pH, temperature, concentration, particle size, adsorption time, etc. These parameters can be well understood in Ruihua et al. [7] research work. He synthesized hydrogel for lead (Pb) removal from industrial wastewater with adsorption efficiency of 170.31 mg/g at temperature 25 °C and adsorption time of eight hours. Experimentally, the adsorption efficiency can be calculated by following formula [7].

$$Q = V(C_1 - C_2) \div M$$

where Q = amount of adsorption (mmol/g);
V = volume of heavy metal reserve liquid (ml);
M = quantity of hydrogel added (mg);
C_1 and C_2 refer to the heavy metal concentration before and after adsorption (mg/L).

2.2   Swelling Properties

Swelling is one of the most important property of hydrogel that takes place in three steps: (1) diffusion of water in hydrogel structure, (2) loosening of polymeric chain, and (3) expansion of hydrogel structure. The small changes brought in environment bring about huge changes in swelling behavior of hydrogel. Factors influencing the swelling are cross-linking, chemical structure, pH, temperature, etc., which leads to swelling of hydrogel. Experimentally, the percentage swelling can be calculated by following formula [21].

$$\% \text{ Swelling} = [(W_s - W_d) \div W_d] \times 100$$

where W_s and W_d are the weight of swollen gel and unswollen gel, respectively.
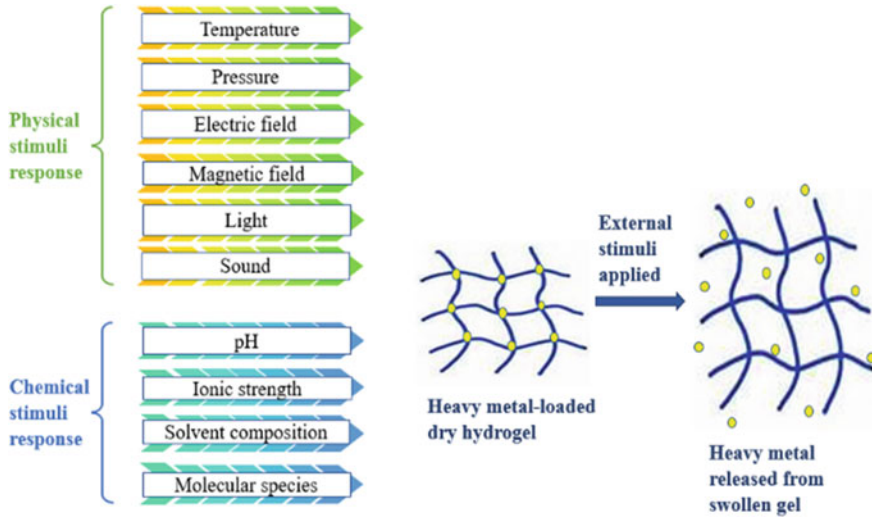
Fig. 2 Response of hydrogel to external stimulus

2.3   Stimuli Responsive

Hydrogel shows swelling or de-swelling properties when subjected to external stimulus like temperature, light, electric and magnetic field, pH, solvent composition, etc. [22] (Fig. 2).

2.4   Biocompatibility

The term biocompatible means the property of material having non-toxic effect on biological environment. Hydrogel is one such example that falls under this category. This property shows significance application in fields of biomedical science.

2.5   Biodegradability

Hydrogel are biodegradable polymer that breaks down into harmless end products by environment.
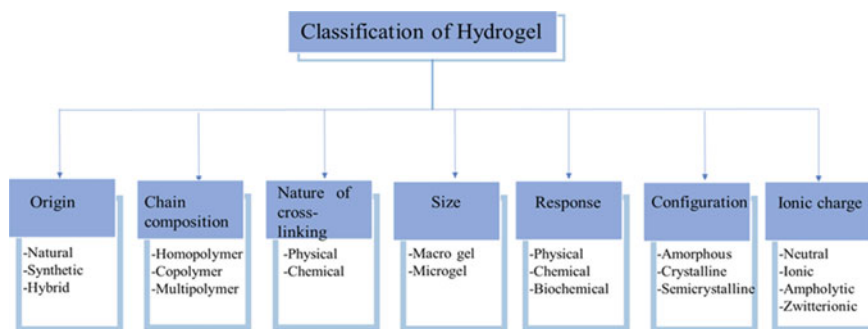
Fig. 3 Classification of hydrogel

3   Classification of Hydrogel

Hydrogel is categorized into number of ways on the basis of size, cross-linking, origin, reaction with external stimuli, configuration, chain composition, and ionic charge (Fig. 3).

4   Functional Groups of Hydrogels

Functional groups are those specific groups that are present in a molecule which are responsible for chemical reaction. Functional groups have an important role to play in determining the chemical reactivity of molecule, along with strength and type of intermolecular forces. Functional groups incorporated in hydrogel for metal adsorption are characterized into three groups: (1) oxygen containing functional group, (2) sulfur containing functional group, and (3) nitrogen containing functional group [23] (summarized in Table 1). These groups help to swell, absorb, and retain large quantity of water.

5   Synthesis of Hydrogel

Hydrogel are three-dimensional polymer matrix synthesized from natural and synthetic monomeric units using different synthesis method [28]. These gels are cross-linked through various physical and chemical methods.

Table 1 Different hydrogels used to treat heavy metal removal and their functional groups

Hydrogel	Functional group	Removed heavy metal	References
Acid hydrolysis lignin-g-poly-acrylic acid (PAA) hydrogel	– OH, –C–O, –C–O–C	Lead	[24]
Poly (acrylamide) hydrogel-rice husk biochar composite	– COO, ether (C–O), CH_2–O–Si, –OH	Arsenic	[25]
Fe_3O_4 nanoparticle functionalized polyvinyl alcohol (PVA)/chitosan magnetic hydrogel	– OH, $–CH_3$, –C–O–C, $–NH_2$	Cr^{6+}	[26]
Modified polyacrylamide hydrogels	– C = O, $–NH_2$, $–CH_2$, –NH	Pb^{2+}, Cd^{2+}, and Cu^{2+}	[27]

5.1 Chemical Method of Synthesis

Chemically cross-linked hydrogel is bonded via covalent bond.

Free radical polymerization. Free radical polymerization involves three major steps: (1) initiation, (2) propagation, and (3) termination [29]. In initiation step, initiator (tetramethylene diamine (TEMED), potassium persulfate (KPS), etc.) leads to formation of free radical in presence of light, temperature, redox reaction, and radiation, which then binds to monomer. In propagation step, the free radicals generated react with monomer to form long polymeric chain. Cross-linking the polymeric chain gives rise to formation of three-dimensional network of hydrogel. In termination step, chain terminates via combination or disproportionation [14]. Crittenden and coworkers [30] reported double network hydrogel from jute/poly (acrylic acid) by free radical polymerization having application in discarding heavy metals (Cd^{2+}, Pb^{2+}, Mn, Cu, Cr, Fe, Zn) from melting waste water and achieved adsorption efficiency of 401.7 mg/g for Cd^{+2} and 542.9 mg/g for Pb^{2+}.

Chemical Grafting. Hydrogel contains hydrophilic functional group such as hydroxy (–OH), amino ($–NH_2$), carboxyl (–COOH), sulfonic ($–SO_3H$), and acyl amino ($–CONH_2$). These groups have characteristic feature to increase the sorption efficiency. Grafting different functional groups on surface of hydrogel leads to enhancement in number of active sites for adsorption and desorption, surface polarity, and hydrophilic character [31]. Astrini et al. [32] reported the synthesis of carboxymethyl cellulose-graft-poly (acrylic acid)/montmorillonite hydrogel composite for effective removal of toxic heavy metals like Zn^{2+} and Pb^{2+} via grafting different functional group on surface of adsorbent.

High Energy Irradiation. Ultraviolet radiation, gamma radiation, and electron beams can be used to form cross-linking in hydrogel. This process has benefits over chemically initiated synthesis in regard to one-step hydrogel formation with no waste generation as by-product. There is no need of initiator and cross-linker for this synthesis [31]. Mahmoud et al. [33] used gamma irradiation method to synthesize

imprinted hydrogel by copolymerization of acrylamide and (N-vinyl-2-pyrrolidone) for removal of Pb^{2+} and Co^{2+}.

5.2 *Physical Method of Synthesis*

Physically cross-linked hydrogels are bonded via non-covalent bond [34], i.e., hydrogen bonding, ionic interaction, stereo complex formation, and hydrophobic interaction, which leads to high mechanical strength of hydrogel. Some examples of polysaccharide used in synthesis of physically bonded hydrogels are carboxymethyl curdlan, dextran, and cellulose [35]. In stereo complex formation, lactic acid and oligomers of opposite chirality's are cross-linked to form hydrogel. In ionic bond formation, mild reaction condition (physiological pH and room temperature) is required to cross link hydrogel. Adding metallic ions will lead to stronger formation of hydrogel. Hydrophobic interaction leads to swelling and imbibing large quantities of water. Hydrogen bonding enhances the swelling capacity of gel. Another method to synthesize physically cross-linked hydrogel is crystallization. This method involves freeze-thawing process and forms durable and highly elastic hydrogel [31].

6 Mechanism of Heavy Metal Removal by Hydrogel

The bonding interaction of hydrogel with heavy metals can be explained by electrostatic interaction, hydrophobic interaction, ion exchange, coordination interaction, and π-π interaction.

6.1 *Electrostatic Interaction*

In electrostatic interaction, hydrogels are formulated with different functional groups in monomer unit or polymer chain carrying oppositely charged ions (cation–anion interaction) (Fig. 4), to the corresponding heavy metal that need to be adsorbed or desorbed [31]. Electrostatic interaction helps in providing strong interaction between ionic polymers and to modify the mechanical strength of hydrogel [31]. Various studies reported on hydrogel-based adsorbent material that are cross-linked with favorable electronic interaction as leading adsorption force for environmental remediation. Hu et al. [36] reported synthesis of carboxylated cellulose nanocrystal-sodium alginate hydrogel beads via cross-linking method for removal of lead (Pb^{2+}) ions. Adsorption mechanism governs the complexation between functional groups (–OH and –COO) of hydrogel and Pb^{2+} ions by sharing of lone pair of electrons, followed by electrostatic interaction among oppositely charged Pb^{2+} and hydrogel beads.
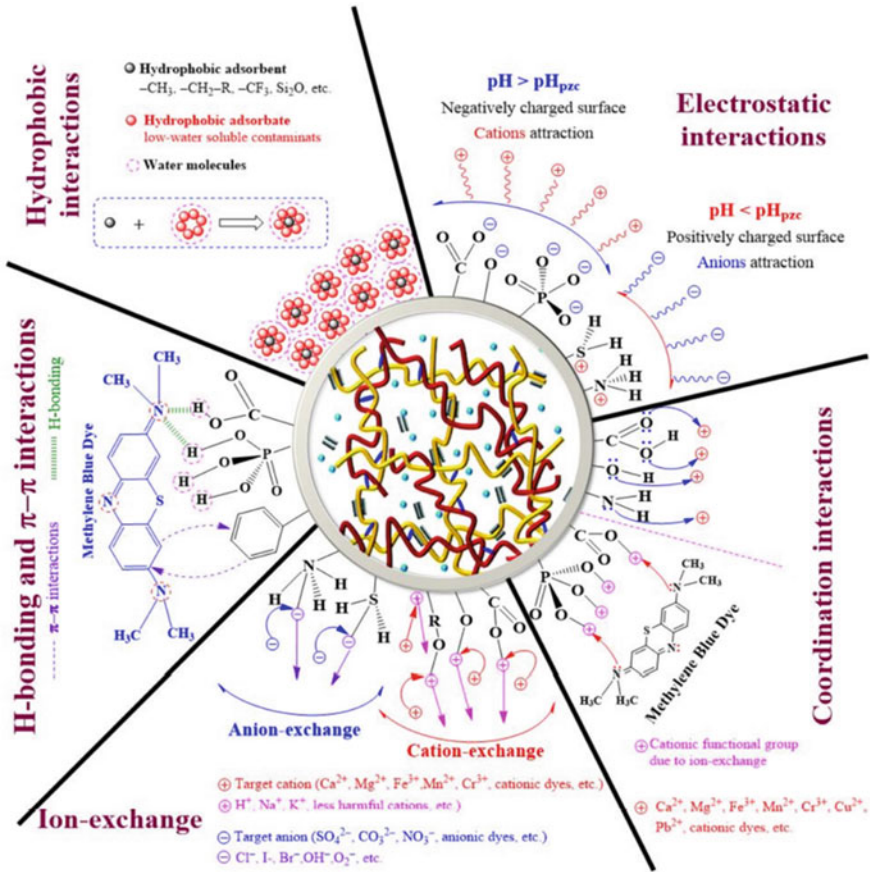
Fig. 4 Interaction mechanism of hydrogel with heavy metal [1]

6.2 *Hydrophobic Interactions*

Hydrophobic interaction is the result of interaction between hydrophobes (non-polar molecule) and water. Hydrophobic association in hydrogels is carried out by copolymerization of hydrophobic groups inside hydrophilic polymer [37]. These association provides high mechanical strength and excellent self-healing properties [38]. Reaction takes place by creating a link between cross-linked hydrophobic groups with other polymer chains that further cross links with hydrophilic groups, thus forming three-dimensional network of hydrogel [38] (Fig. 4).

6.3 Ion Exchange

Ion exchange involves transfer of an ion from the liquid phase (waste water) onto the solid adsorbent (hydrogel). Ion exchange is a sorption process where unwanted anion or cations are removed from aqueous media and gets exchanged with different ions of similar charge on the surface of adsorbent. In an ion exchange mechanism, the number of ions adsorbed by the hydrogel-based adsorbent material is equal to the number of ions released from its surface [1]. Ion exchange is an effective process for heavy metal removal as it reduces the concentration of toxic elements by converting and recycling pollutants back to less-toxic elements. Ion exchange mechanism is strongly pH-dependent process. Due to increase in concentration of H^+ ions at pH < pH_{ZPC} (pH of aqueous media when adsorbent surface has no charge species), functional group of absorbent are positively charged resulting in cation exchange mechanism. Contrarily, at pH > pH_{PZC} functional groups are negatively charged resulting in anion exchange mechanism (Fig. 4) [1]. Kwak et al. [39] synthesized silk sericin/lignin blend beads via coagulation method and ion exchange mechanism for removal of Cr^{6+}.

6.4 Coordination Interaction

Coordination interaction refers to covalent bonding (sharing of electron) in molecule. For removal of heavy metals by coordination mechanism, cations (heavy metals) attract functional group bearing lone of electrons, resulting in heavy metal adsorption from surface of adsorbate (Fig. 4). For example, Maity et al. [40] synthesized gelatin-based composite and sugar cane bagasse cellulose hydrogel for removal of Cu^{2+}. In this experiment, Cu^{2+} bonded via coordinate bond with O (–OH) or N (–NH$_2$) and showed combined mechanism of electrostatic and coordination interaction.

6.5 π-π Interaction

π-π interaction is a particular type of non-covalent interaction among the molecules present in solution phase. π-π interaction occurs in the presence of at least one π electron donating or electron withdrawing group in the aromatic ring. Functional groups and pH of the solution play a prominent role for interaction between adsorption molecules [41]. Adsorbent and adsorbate carrying functional group can be π electron rich, π electron deficient, or both, which determines the formation of different π-π interaction (electron–donor–donor, electron–acceptor–donor, and electron–acceptor–acceptor) [42]. Chen et al. [43] prepared graphene oxide/cellulose hydrogel from $NaOH/CO(NH_2)_2$ aqueous media for heavy metals (Zn^{2+}, Fe^{+3}, Pb^{2+}, and Cu^{2+}) removal from wastewater. π-π interaction was reported as potential

cause for high mechanical strength and adsorption efficiency of hydrogel. The functional group (–COOH and –OH) present on surface of adsorbent are responsible for interaction with heavy metals (Fig. 4).

7 Hydrogel-Based Adsorbent for Heavy Metal Removal

Hydrogel's three-dimensional network structure is synthesized from various natural and synthetic sources, which have high adsorption capacity to trap number of heavy metals in its structure (summarized in Table 2).

8 Advantages of Hydrogel Over Other Adsorbent Material

The comparison studies of hydrogel-based adsorbent with various other adsorbent material for heavy metals removal is depicted in Fig. 5a–d.

The removal of arsenic by hydrogels and various types of adsorbents is depicted in Fig. 5a. The figure clearly shows that removal efficiency of other adsorbents is higher compared to hydrogel-based adsorbents. But these adsorbents show disadvantages in terms of difficulty separation from water after decontamination process and are secondary pollutants. Therefore, despite of having less removal efficiency, hydrogels are preferred for arsenic removal over other adsorbents as it can be recovered in one step. The removal of cadmium, chromium, and copper (Cu^{2+}) by hydrogels and other adsorbents is shown in Fig. 5b–d, respectively. The removal efficiency of hydrogels is higher than other adsorbent material. Hydrogels are preferred over most of the synthetic adsorbents because of its sustainability, cost effectiveness, large-scale production, easy regeneration, and recovery. From these studies, it can be concluded that hydrogel are potential adsorbents used for heavy metals removal from wastewater.

9 Summary

Industrial waste water is known to be the major source of water contamination that has adversely affected ecological environment. In particular, heavy metals discharged to water bodies cause potential threat to living organisms. Thus, it is the need of an hour to treat industrial waste water and then discharge. Adsorption is considered to be the efficient, eco-friendly, and technologically feasible method for heavy metals removal from industrial waste water. Hydrogel as an adsorbent has gained tremendous attention over the years for its application in heavy metals removal and its physicochemical properties governs its specificity and performance. This review article demonstrates the literature concerning hydrogel classification based on different bases. Further, the

Table 2 Different heavy metals that are removed by hydrogel-based adsorbent

Hydrogel type	Initiator	Monomer	Cross-linker	Heavy metals removed	Adsorption efficiency	References
Hydrogel-rice husk biochar composite	Ammonium persulfate (APS)	Acrylamide (Aam)	N, N′- methylenebisacrylamide (MBA)	As	28.32 mg/g	[25]
Jute/poly-acrylic acid (PAA) hydrogel	Ammonium persulfate (APS)	Acrylic acid	N, N′- methylenebisacrylamide (MBA)	Cd^{2+} Pb^{2+}	401.7 mg/g 542.9 mg/g	[30]
Acid hydrolysis lignin-g-PAA hydrogel composite	Ammonium persulfate (APS)	Acrylic acid	N, N′- methylenebisacrylamide (MBA)	Pb^{2+}	235 mg/g	[24]
Poly (AAc-coMMA)/GO	N, N, N′, N′- tetramethyl ethylenediamine (TEMED), Ammonium persulfate (APS)	Methyl methacrylate (MMA) and acrylic acid (AA)	N, N′- methylenebisacrylamide (MBA)	Pb^{2+} Cd^{2+}	216.1 mg/g 153.8 mg/g	[43]
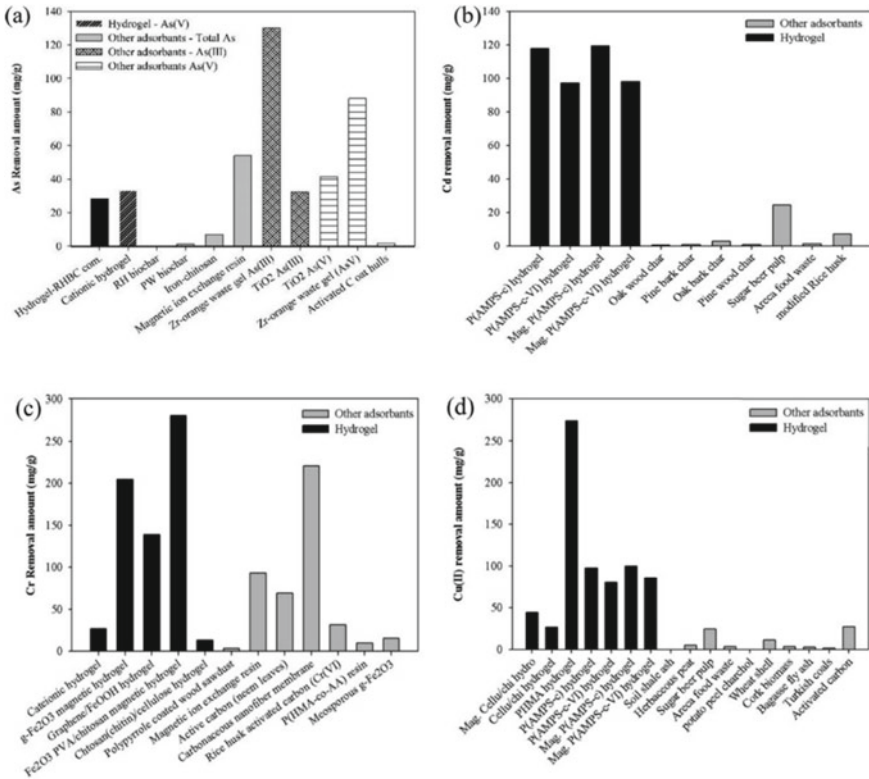
Fig. 5 a–d Shows removal of heavy metals by hydrogels and other adsorbents [15]

discussion proceeds toward functionalization in hydrogel, synthesis-based on chemical and physical methods, and mechanism showing bonding interaction between heavy metals and hydrogel. In addition, hydrogel-based adsorbents synthesized from various sources and their adsorption efficiency has been discussed. Hydrogel as an adsorbent has shown remarkable advantages over other adsorbents like high adsorption efficiency, cost-efficient, convenient process, easy to handle, easy separation, and many more. The future scope of this work should focus on targeting multiple heavy metals for its application in wastewater purification.

References

1. Akter M et al (2021) Cellulose-based hydrogels for wastewater treatment: a concise review. Gels 7(1):30

2. Rashid TU et al (2020) Sustainable wastewater treatment via dye–surfactant interaction: a critical review. Ind Eng Chem Res 59(21):9719–9745

3. Shahabuddin S et al (2018) Synthesis of 2D boron nitride doped polyaniline hybrid nanocomposites for photocatalytic degradation of carcinogenic dyes from aqueous solution. Arab J Chem 11(6):1000–1016

4. Deng Y et al (2012) Application of porous N-methylimidazolium strongly basic anion exchange resins on Cr (VI) adsorption from electroplating wastewater. Sep Sci Technol 47(2):256–263

5. Shalla AH et al (2019) Recent review for removal of metal ions by hydrogels. Sep Sci Technol 54(1):89–100

6. Wang X et al (2017) Removal of Cu (II) ions from contaminated waters using a conducting microfiltration membrane. J Hazard Mater 339:182–190

7. Mu R et al (2020) Hydrogel adsorbent in industrial wastewater treatment and ecological environment protection. Environ Technol Innov 20:101107

8. Choumane FZ et al (2017) Valorisation of a bioflocculant and hydroxyapatites as coagulation-flocculation adjuvants in wastewater treatment of the steppe in the wilaya of Saida (Algeria). Ecol Eng 107:152–159

9. Volpin F et al (2018) Hybrid forward osmosis-reverse osmosis for wastewater reuse and seawater desalination: understanding the optimal feed solution to minimise fouling. Process Saf Environ Prot 117:523–532

10. Bhargava S, Uma V (2019) Rapid extraction of Cu (II) heavy metal from industrial waste water by using silver nanoparticles anchored with novel Schiff base. Sep Sci Technol 54(7):1182–1193

11. Peter KT et al (2017) Functionalized polymer-iron oxide hybrid nanofibers: Electrospun filtration devices for metal oxyanion removal. Water Res 117:207–217

12. Thakur VK, Thakur MK (2018) Hydrogels: recent advances. Springer

13. Cai J et al (2020) Polysaccharide-based hydrogels derived from cellulose: the architecture change from nanofibers to hydrogels for a putative dual function in dye wastewater treatment. J Agric Food Chem 68(36):9725–9732

14. Khan M, Lo IM (2016) A holistic review of hydrogel applications in the adsorptive removal of aqueous pollutants: recent progress, challenges, and perspectives. Water Res 106:259–271

15. Weerasundara L et al (2020) Hydrogels: novel materials for contaminant removal in water—a review. Critical Rev Environ Sci Technol 1–45

16. Rehab A et al (1991) Controlled release of herbicides supported on polysaccharide based hydrogels. J Bioact Compat Polym 6(1):52–63

17. Cao J et al (2020) Double crosslinked HLC-CCS hydrogel tissue engineering scaffold for skin wound healing. Int J Biol Macromol 155:625–635

18. Kuddushi M et al (2019) Stimuli responsive, self-sustainable, and self-healable functionalized hydrogel with dual gelation, load-bearing, and dye-absorbing properties. ACS Appl Mater Interfaces 11(21):19572–19583

19. Phan C-M, Subbaraman L, Jones L (2014) Contact lenses for antifungal ocular drug delivery: a review. Expert Opin Drug Deliv 11(4):537–546

20. Pakdel PM, Peighambardoust SJ (2018) Review on recent progress in chitosan-based hydrogels for wastewater treatment application. Carbohyd Polym 201:264–279

21. Pande P (2017) Polymer hydrogels and their applications. Int J Mater Sci 12(1):11–14

22. Ahmed EM (2015) Hydrogel: preparation, characterization, and applications: a review. J Adv Res 6(2):105–121

23. Badsha MA et al (2021) Role of surface functional groups of hydrogels in metal adsorption: From performance to mechanism. J Hazard Mater 408:124463

24. Sun Y et al (2016) Synthesis of acid hydrolysis lignin-g-poly-(acrylic acid) hydrogel superabsorbent composites and adsorption of lead ions. BioResources 11(3):5731–5742

25. Sanyang M et al (2016) Hydrogel biochar composite for arsenic removal from wastewater. Desalin Water Treat 57(8):3674–3688

26. Yan E et al (2018) Synthesis of Fe3O4 nanoparticles functionalized polyvinyl alcohol/chitosan magnetic composite hydrogel as an efficient adsorbent for chromium (VI) removal. J Phys Chem Solids 121:102–109

27. Kaşgöz H, Özgümüş S, Orbay M (2003) Modified polyacrylamide hydrogels and their application in removal of heavy metal ions. Polymer 44(6):1785–1793
28. Stile R, Healy K (2002) Synthesis of hydrogels: environmentally sensitive hydrogels based on N-isopropylamide. Methods Tissue Eng 57:663–680
29. Hasirci V et al (2011) 1.121. Polymer fundamentals: polymer synthesis. In: Comprehensive biomaterials. Elsevier Oxford, pp 349–371
30. Zhou G et al (2018) Efficient heavy metal removal from industrial melting effluent using fixed-bed process based on porous hydrogel adsorbents. Water Res 131:246–254
31. Sinha V, Chakma S (2019) Advances in the preparation of hydrogel for wastewater treatment: a concise review. J Environ Chem Eng 7(5):103295
32. Astrini N, Anah L, Haryadi HR (2015) Adsorption of heavy metal ion from aqueous solution by using cellulose based hydrogel composite. In: Macromolecular symposia. Wiley Online Library
33. Mahmoud GA et al (2016) Radiation synthesis of imprinted hydrogels for selective metal ions adsorption. Desalin Water Treat 57(35):16540–16551
34. Gong Z et al (2016) High-strength, tough, fatigue resistant, and self-healing hydrogel based on dual physically cross-linked network. ACS Appl Mater Interfaces 8(36):24030–24037
35. Akhtar MF, Hanif M, Ranjha NM (2016) Methods of synthesis of hydrogels… A review. Saudi Pharmaceutical J 24(5):554–559
36. Hu Z-H et al (2018) Fabrication of carboxylated cellulose nanocrystal/sodium alginate hydrogel beads for adsorption of Pb (II) from aqueous solution. Int J Biol Macromol 108:149–157
37. Xu J et al (2018) The role of chemical and physical crosslinking in different deformation stages of hybrid hydrogels. Eur Polymer J 100:86–95
38. Jiang H et al (2019) Hydrophobic association hydrogels with excellent mechanical and self-healing properties. Eur Polymer J 112:660–669
39. Kwak HW et al (2016) Preparation of silk sericin/lignin blend beads for the removal of hexavalent chromium ions. Int J Mol Sci 17(9):1466
40. Maity J, Ray SK (2017) Removal of Cu (II) ion from water using sugar cane bagasse cellulose and gelatin based composite hydrogels. Int J Biol Macromol 97:238–248
41. Alam MM et al (2020) The potentiality of rice husk-derived activated carbon: from synthesis to application. Processes 8(2):203
42. Ahmed MB et al (2018) Sorption of hydrophobic organic contaminants on functionalized biochar: Protagonist role of π-π electron-donor-acceptor interactions and hydrogen bonds. J Hazard Mater 360:270–278
43. Chen X et al (2016) Adsorption of heavy metals by graphene oxide/cellulose hydrogel prepared from NaOH/urea aqueous solution. Materials 9(7):582

Recent Advances in Reclamation of Used Lubricant Oil

Krunal Parekh, Rama Gaur, and Syed Shahabuddin

1 Introduction

Lubricating oils are produced via the process of solvent extraction and crude oil dewaxing. Lubricating oils mainly serve in the reduction of friction, dust, and corrosion, as well as the prevention of wear and tear and the supply of a heat transfer medium in different equipment or machinery [1]. After a cycle of usage, oil gets polluted, oil becomes more contaminated, rendering it unfit for future use, due to the introduction of foreign particles such as metal powder, filings, soot, unburned petrol/diesel, moisture, and damaged additives.

Furthermore, the lubricating oil will decompose and colour tends to darken due to the high temperature within the engine and machinery [2]. The lubricating oil must be changed at this time to improve work efficiency, and the replacement oil is typically dumped as waste (Fig. 1).

Heavy metals, chlorinated hydrocarbons, and other chemical substances (oxidized additives from the oil itself) are often found in WLOs. Contaminants such as poly-aromatic hydrocarbons, poly-cyclic benzenes, harmful heavy metals, and chlorinated hydrocarbons may be removed from used oil using appropriate treatment technologies [3]. Those contaminants are responsible for increasing the hazardous level of used lubricant oils. Lubricating oils are often mixed with a variety of chemical additives to enhance the performance of equipment under harsh operating conditions. WLO regeneration is the most attractive option for reducing hazardous waste's adverse environmental effect [4]. It is better to recycle and reuse used lubricant oil

K. Parekh · R. Gaur · S. Shahabuddin (✉)
Department of Chemistry, School of Technology, Pandit Deendayal Energy University, Gujarat 382007, India
e-mail: Syed.shahabuddin@sot.pdpu.ac.in

S. Shahabuddin
Faculty of Applied Sciences, Universiti Teknologi MARA, Cawangan Negeri Sembilan, Kampus Kuala Pilah, 40450 Kuala Pilah, Shah Alam, Malaysia

Fig. 1 Management of
waste lubricant oil

and it may offer a considerable environmental advantage. However, there is still a significant amount of useful base oil present in the spent oil. This can be applied in the formulation of fresh lubricants via a suitable recycling process in which harmful contaminants are removed from the oil using a suitable recycling method. Thus, the waste oil regeneration method justifies not only environmental but also economic aspects [5]. Recycled used lubricant oil may be converted into fresh lube oil, refined into fuel oils, or can be also used as raw resources in the petroleum industry.

Lubricating oil demand is rising due to the development of new industries, a rise in the number of transport vehicles, and the automation of agriculture and industry. As a result, consumption of motor oil and industrial oil, as well as the production of black oil, will rise in the coming years. Thus, there is an immense need to develop facile, cheaper, and viable solutions for regenerating used lubricant oil by providing sustainable remedies. Though, there are still a number of procedures popular technologies for refining waste lubricating oils that are very costly due to the higher energy intake and the secondary pollution.

The various kinds of waste oil refining techniques are as follows:

There are presently several methods for re-refining used lubricating oil, including as: acid/clay process, solvent extraction, vacuum-distillation process, de asphalting, membrane technology, TFE with clay finishing and TDA with clay finishing and TDA with hydrofinishing, combined technology. However, all of these common regeneration approaches for refining used oil are comparatively expensive as it required high energy besides it has both environmental and economic consequences [6–10] as highly expensive methods as well as generation of secondary pollutants after treatment [11] (Table 1).

Among all ways for removing impurities from old lubricating oil, there are a few that stand out. Because of its high recovery rate of treated lubricant oil and its

Table 1 General properties of fresh oil [38]

Properties of waste oil	Limit value	Units
Kinematic viscosity (40 °C)	4–491	cSt
Kinematic viscosity (100 °C)	1–86	cSt
Viscosity index	13–314	–
Density	817–953	kg/m^3
Metals: P	>1500	ppm
Ca	38–8750	ppm
Cl	9–623	ppm
Si	>370	ppm
S	>2.2	ppm
Zn	48–1380	ppm
Total acid number (TAN)	>5.35	mg KOH/g
Total base number (TBN)	>64	mg KOH/g

easy procedure, cheap operating cost, minimal capital investment, and does not need skilled operators., the acid/clay technique is frequently employed. There are a few drawbacks to this method: It also produces a significant volume of acidic sludge.

Conducting polymers (CPs) are organic macromolecules that gained tremendous attention due to their substantial properties as they are easy to synthesize, cost-effective, environment-friendly, non-corrosive, as well as they show high conductivity like metals. CPs are polymers that contain a highly π—conjugated polymeric chain backbone in their configuration, which can adsorb heavy metal ions via hydrogen bonding or electrostatic force. Due to its great adsorption capacity, conducting polymers may show improved efficiency for the elimination of contaminants from waste oil for refining waste lubricant oil.

2 Conventional Methods

2.1 Acid/Clay Method

The method is based on treating the used lubricant oil to eliminate different contaminants from waste oil using different types of acids [12] (sulphuric, acetic, phosphoric, and formic) to remove contaminants present in waste oil and then adsorbent mainly clay is used to neutralize the resulting product. This process involves the following step mechanism: acid treatment, sedimentation, bleaching neutralization, and filtration to obtain the desired fraction of fresh oil [12–14]. This method has the highest environmental threat and cost-effective compare to other conventional methods (Fig. 2).

Also, this method has a simple process, low capital investment, affordable cost, and it does not require skilled operators [13]. Although, this route of oil recycling treatment has several drawbacks: due to usage of acid in huge amounts, it produces

Fig. 2 Block diagram of
acid/clay method
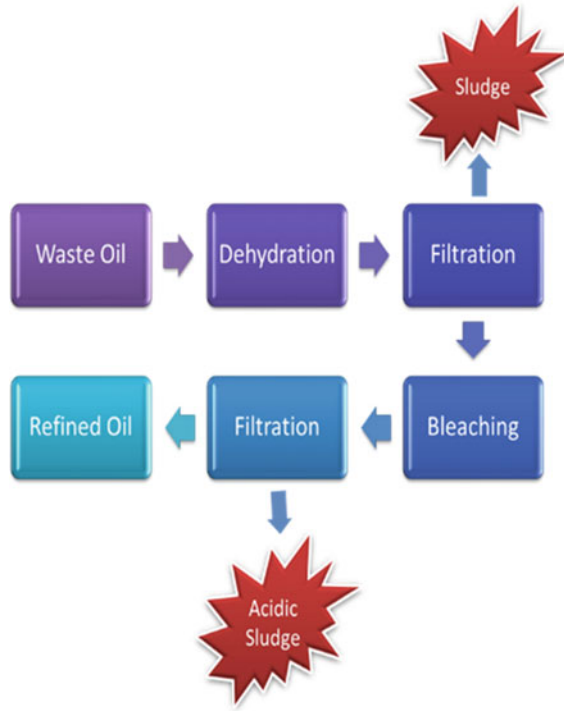
acidic sludge as secondary contaminants to a greater extent, and it is also incapable
to eliminate asphaltic impurities [15].

2.2 Vacuum Distillation

To reduce the environmental problems, vacuum distillation is another way to treat
waste lube oil. It is a widespread method to remove moisture and other organic
impurities mixed with the lubricant during usage in the engine.

In this process, waste lubricant oil is distilled at high temperatures to remove
moisture and light hydrocarbons from oil [14]. After that, high temperature and high
pressure are applied to the dehydrated oil sample. Then, condense the resulting oil
sample via the condensation process [16]. The key drawback of this process is that it
required extraordinary equipment and highly skilled operators, also investment cost
is high and the use of toxic materials [1] (Fig. 3).
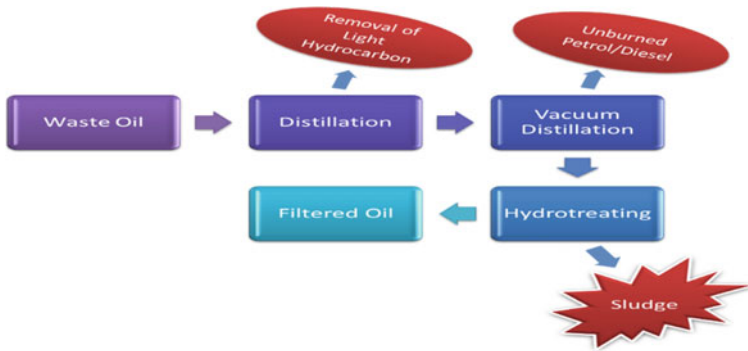
Fig. 3 Block diagram of vacuum distillation process

2.3 Solvent Extraction

Solvent extraction provides high-grade base oils with a lower contamination ratio. In comparison with other recycling used oil methods, it requires a sophisticated operating system and qualified personnel in comparison to other techniques [17]. The yields and quality of used lubricant oil will differ depending on the technology utilized to recycle it. Solvent extraction techniques separate paraffinic and naphthenic chemicals based on their solubility differences from undesirable components like resins and asphaltenes [7]. 1-butanol, 2-propanol, methyl ethyl ketone (MEK), acetone, toluene, ethyl alcohol, and propane are various solvent types that are commonly used for solvent extraction [1]. Here, MEK contributes a high yield and produces less sludge [18–20], while 1-butanol solvent has the highest sludge removal rate [21, 22]. Blend of two solvents MEK and 2-propanol yield successive amounts of refined oil product compared to produce by acid clay process; however, it was expensive [23] (Fig. 4).

In this treatment, used lubricant oil is treated with solvent, then mixed oil and solvent as per the ratio and then allows the solution settle down for a day. The next step is the removal of the solvents from the recovered oil; then, the oil is separated from the sludge and then transported to an evaporator. As a result, the oil is combined with an adsorbent to eliminate the oil's dark colour and smells [24].

2.4 Hydrogenation

This method involves steps followed by dichlorination, desulphurization, and other processes [25]. This technique is similar to the vacuum distillation method. In this procedure, the distilled oil is hydrotreated at high temperature and pressure. Catalyst is used to remove heavy metals like Sulphur, chlorine, nitrogen, and other organic
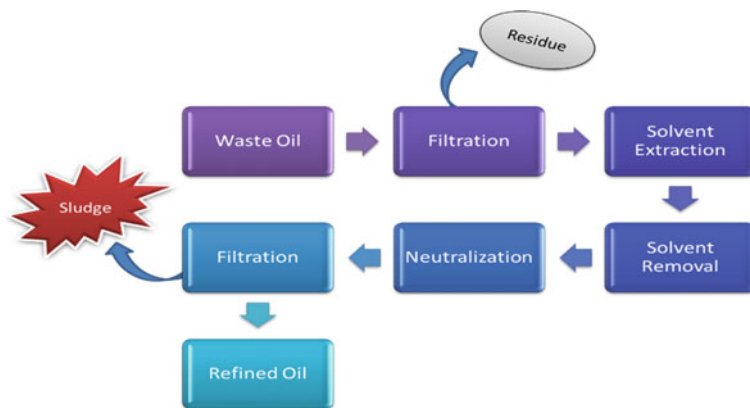
Fig. 4 Block diagram of solvent extraction

impurities present in waste oil. The hydrocarbons were transformed into products with improved odour, chemical properties, and colour [1, 7].

3   Combined Technology

These are advanced methods that are the combination of two or more conventional methods. Contaminants present in waste oil have a very complicated structure and are difficult to take out using any particular method and they may not offer the desired yield. For that reason, a number of organizations have been established. A number of organizations have established individual procedures for management and contaminants removal from waste lubricant oil [25–27]. But these methods required sophisticated equipment, skilled operators, and practices.

The Vaxon process involves the combined process of chemical treatment to remove heavy metals, chloride, and acidic components using alkali hydroxide followed by a vacuum distillation process to obtain dissimilar viscosity grade base lubricant oil [28]. This method is the superior vacuum distillation process, where the oil cracking is reduced. This process is generally used in European countries. The main benefit of this procedure is the uncommon distillation unit, which is called vacuum cyclone flash evaporator.

KTI process has introduced in 1992 by establishing its first refinery in Greece. Kinetic technology international (KTI) method is the combination of vacuum distillation and hydrofinishing process [29]. This process includes atmospheric distillation at 250 °C temperature to eliminate water and light hydrocarbons from oil, in addition to remove metal components such as sulphur, nitrogen, and oxygenated complexes by hydrogenation. The quality of obtained regenerated oil is great because of hydrogenation [30, 31].

Another advance combined oil refining process is called Proterra recycling technology which is a combination of two most important techniques which are solvent extraction and vacuum distillation called Proterra recycling technology. The secondary product resultants from this method are light oils, extracts, and vacuum residues which are unable to condense and waste water [7, 25].

Studi Tecnologie Progetti (STP) is another method that is the grouping of vacuum distillation and hydrofinishing technique. The key advantage of this method is it generates a lesser amount of hazardous waste product for that reason it is an eco-friendly process. The steps involved in this method are: dehydration, vacuum distillation, separation of lubricating portion, and hydrofinishing of base oil separation from remains [1, 25, 26, 32].

There are also lots of combined techniques for refining waste lubricant oil such as chemical engineering partners process (CEP), interline process, Propak thermal cracking process, axen/viscolube (revivoil) technology, IFP technology, Ecohuile process which are previously operated methods[1, 7, 22].

4 Recent Technology

Used lubricant oil has huge significance and it delivers a high proportion of organic waste liquids produced worldwide. Waste lubricant oil is considered to be a highly contaminated component, which has negative effects on the environment and human life also, if not appropriately treated, managed, or disposed of. Thus, regeneration and recycling of lubricant oil can prove to be highly beneficial both economically as well as environmentally. Latest technologies for refining used lubricant oil includes thin film evaporation (TFE), pyrolytic distillation method (PDM), membrane technology, pyrolysis process (PP), other combined technologies like TFE and solvent finishing, TFE and clay finishing, TDA with hydrofinishing, and clay finishing [33]. Some of the techniques are discussed below.

In the current period, pyrolysis process (PP) is an effective well-known method that received great response towards claim fresh oil through waste lubricant oil using thermal process in which composite heated at very high temperature (300–1000 °C) at inert atmospheric conditions. Due to its potential pyrolysis process resultant good yield, it produces energy-dense products from discarded materials. Microwave PP (MPP) and conventional PP (CPP) processes are commonly used pyrolysis processes [7, 34, 35].

Membrane technology is a very expensive method meanwhile it produces good quality base oil and high yield in comparison to other methods. In this method, waste oil is filtered through hollow fibre membranes of polymer to remove carbon residue and heavy metal particles from waste material. The most common polymer-based membrane filters are polyacrylonitrile (PAN), polyvinylidenefluoride (PVDF), polyethersulphone (PES), and polyvinylidene fluoride-glass fibre (PGF) [1, 7, 8, 36].

Using the pyrolytic distillation technique, a fuel known as diesel-like fuel (DLF) was formed. During this process, discarded engine oil was cleaned by filtering via

Table 2 Benefits and drawbacks of conventional and modified methods

Regenerative method	Benefits	Drawbacks
Conventional methods	Commonly used method Low cost and high yield	High environmental risk (pollution) Reduce life of equipment
Combined methods	Reduce pollution high yield	Expensive method Required expensive Equipment

a quality filter. Na_2CO_3, zeolite, and CaO are combined at different ratios with the filtered waste engine oil [37]. Thus, by reviewing all conventional combined and modern methods, every method has its separate advantages and disadvantages. The combined techniques and latest techniques are produced great grade base oil but that all method is very costly and it required very sophisticated environment and skilled operator. Meanwhile, the conventional method also produces good grade base oil but such methods are outdated and not environment-friendly.

So, the main objective of this review paper is to compare conventional and modern methods. Also, make such possible corrections/changes require in conventional method to increase the yield of recycled oil and it must be sustainable for environmental as well as economical aspects (Table 2).

5 Future Prospects

Currently, there are several current treatment methods and regeneration technologies to remove impurities and extract pure base oil from waste black oil which are acid/clay method, vacuum distillation, and solvent extraction, TFE, TDA, pyrolysis using microwave heating, membrane technology, etc. Among all methods, acid/clay treatment, vacuum distillation, solvent extraction, and membrane filtration technology are widespread processes that are currently used globally. The conventional acid/clay method is one of the most efficient processes. However, it generates acidic sludge which is a secondary pollutant itself. Not much work is reported on the modification of the process to reduce acidic sludge. Therefore, this research gap is targeted by us and develops a modified acid/clay method where we can reduce the generation of acidic sludge. The method of refining is also an expensive process. Many researchers have used expensive nanomaterials and developed membranes which are again an expensive process. Thus, cheap materials have to be explored to make the process cost-effective.

Adsorption is a facile cheap and convenient approach, and adsorption process for regeneration of waste lubricant oil was done using various adsorbing agents like egg shale powder, palm kernel powder, bentonite clay, activated charcoal, and activated clay. Clay is used for adsorption applications to remove impurities from

the used lubricant oil due to its adsorption capacity and easy availability. Like clay, conducting polymer also exhibits great adsorption efficiency, and it is used to remove organic impurities from aqueous solution. Conducting polymers having also adsorption capacity as well as attractive electrical and electrochemical properties. Still, there is no work has been reported where conducting polymer is being used to treat the waste lube oil, whereas CP has shown excellent adsorption capacities to remove toxic pollutants, metal ions, heavy metals from waste water. Therefore, we need to explore conducting polymers as potential adsorbent material for pre-treatment of waste oil to reduce the formation of acidic sludge. The study specifies that the regeneration of waste oil is a more sustainable and eco-friendly choice than the conventional refinery process to avoid pollution.

References

1. Boadu KO et al (2019) A review of methods for removal of contaminants in used lubricating oil. 26(4):1–11
2. Shahabuddin S et al (2016) Synthesis and characterization of Co 3 O 4 nanocube-doped polyaniline nanocomposites with enhanced methyl orange adsorption from aqueous solution. 6(49):43388–43400
3. Syrmanova KK et al (2017) Chemistry and recycling technology of used motor oil. 33(6):31953199
4. Pinheiro CT et al (2018) Regeneration of waste lubricant oil with distinct properties by extraction-flocculation using green solvents. 200:578–587
5. Sterpu A-E, Dumitru AI, Popa M-FJJOUAC (2012) Regeneration of used engine lubricating oil by solvent extraction. 23(2):149–54
6. Nwachukwu MA et al (2012) Review and assessment of mechanic village potentials for small scale used engine oil recycling business. 6(12):464–475
7. Oladimeji TE et al (2018) Data on the treatment of used lubricating oil from two different sources using solvent extraction and adsorption. 19:2240–2252
8. Rouzegari F et al (2020) A composite ultrafiltration membrane for regeneration of used engine oil. 1–16
9. Hsu Y-L, Lee C-H, Kreng VBJESWA (2010) The application of Fuzzy Delphi Method and Fuzzy AHP in lubricant regenerative technology selection. 37(1):419–425
10. Jafari AJ, Hassanpour MJR (2015) Analysis and comparison of used lubricants, regenerative technologies in the world. Conserv, Recycl 103:179–191
11. Cao Y et al (2009) Used lubricating oil recycling using a membrane filtration: analysis of efficiency, structural and composing. 11(1–3):73–80
12. Abu-Elella R et al (2015) Used motor oil treatment: turning waste oil into valuable products. 7:57–67
13. Udonne JD, Bakare OA (2013) Recycling of used lubricating oil using three samples of acids and clay as a method of treatment. 4(2):8–14
14. Hamawand I, Yusaf T, Rafat SJE (2013) Recycling of waste engine oils using a new washing agent. 6(2):1023–1049

15. Fox MF (2007) Sustainability and environmental aspects of lubricants. In: George ED, Totten E (eds) Handbook of lubrication and tribology. Taylor and Francis, New York, NY, USA

16. Kannan SC, Mohan Kumar KS, Sakeer Hussain M, Deepa Priya NK (2014) Studies on reuse of refined used automotive lubricant oil. Res J Eng Sci 3(6):8–14

17. AERCO Inc. PS. Solvent extraction technology for used oil treatment. Final report for Recycling Technology Assistance. (1995);30

18. Katiyar V, Husain S (2010) Reclamation of used lubricating oils. Curr World Environ 5(1):79–84

19. Sterpu AE, Dumitru AI, Popa MF (2012) Regeneration of used engine lubricating oil by solvent extraction. J Ovidius Univ Annuals Chem 23(2):149–154

20. Durrani HA (2014) Re-Refining recovery methods of used lubricating oil. Int J Eng Sci Res Technol 3(3):1216–1220

21. Hussein M, Amer AA, Gaberah AS (2014) Used lubricating oils re-refining by solvent extraction. Am J Environ Eng Sci 1(3):44–50

22. Aremu MO, Araromi DO, Gbolahan OO (2015) Regeneration of used lubricating engine oil by solvent extraction process. Int J Energy Environ Res 3(1):1–12

23. Rincon J, Canizares P, Garcia MT (2005) (Regeneration of used lubricating oil by polar solvent extraction. Ind Eng Chem Res 44:43–73

24. Osman DI, Attia SK, Taman AR (2018) Recycling of used engine oil by different solvent. Egypt J Pet 27(2):221–225

25. Basel Convention, technical guidelines on used oil re-refining of other re-uses of previously used oil, series/SBC No. 02/05, reprinted Nov 2002 ISBN: 92-1-158605-4

26. Kupareva A, Mäki-Arvela P, Murzin DY (2013) Technology for rerefining used lube oils applied in Europe; Society of chemical industry. J Chem Technol Biotechnol 88:1780–1793

27. Brinkman DW (2010) Kirk-Othmer encyclopedia of chemical technology. John Wiley & Sons, Inc

28. Chari KR, Agarwal A, Agarwal A, Dang G, Giovanna F, Jagieta S, Wijeyekoon S (2012) Compendium of recycling and destruction technologies for waste oils. United Nations Environment Programme, Osaka, Japan

29. Havemann R (1978) The KTI used oil re-refining process. In: Proceedings of the 3rd international conference of used oil recovery & reuse. Houston, TX, USA, pp 16–18

30. Schiessler N, Thorpe E, Jones W, Philips L (2007) Life and waste recycling: innovative waste management options in Europe. Office for Official Publications of the European Communities

31. Tsalavoutas S, Kapoutsis G, Zahilas L (2002) Leonardo pilot project Recyoccupation, survey of the greek recycling sector. RecyOccupation Manuscript, Athens

32. Kajdas C (2000) Major pathways for used oil disposal and recycling. Part 2. Tribotest 7(2):137–153

33. Bridjanian H, Sattarin M (2006) Modern recovery methods in used oil re-refining. Pet Coal 48(1):40–43

34. Lam SS, Liewa KK, Jusoh AA, Chong CT, Ani FN, Chase HA (2016) Progress in waste oil to sustainable energy, with emphasis on pyrolysis techniques Renew Sustain Energy Rev 53:741–75

35. Manasomboonphan W, Junyapoon S (2012) Production of liquid fuels from used lube oils

36. Widodo S, Khoiruddin K, Ariono D, Subagjo S, Wenten IG (2020) Re-refining of waste engine oil using ultrafiltration membrane. J Environ Chem Eng 8(3):103789

37. Arpa O, Yumrutas R, Demirbas A (2010) Production of diesel-like fuel from waste engine oil by pyrolitic distillation. Appl Energy 87(1):122–127

38. Pinheiro CT, Quina MJ, Gando-Ferreira LM (2020) Management of waste lubricant oil in Europe: a circular economy approach. Crit Rev Environ Sci Technol 1–36

A Review: Carbon-Based Materials for Photocatalytic Degradation of Agrochemicals

Jinal Patel, Stuti Jha, Syed Shahabuddin, and Rama Gaur

1 Introduction

Carbon-based materials have gained a lot of curiosity to their special characteristics then are suitable for various applications [1]. Carbon is an essential element in the environment, it is the superior resident, and it fits in group 14 of the periodic table. The tetravalency of carbon has the ability to form bonds with atoms by sharing its valence electrons [2]. Conventionally, carbon is recognized to have 2 allotropes are graphite and diamond. Carbon-based nanomaterials exist in various forms such as 0D fullerene, 1D nanotubes like SWCNT-MWCNT, 2D graphene, graphene oxide (GO) and diamond, 3D graphite, reduced graphene oxide (rGO), and nanodiamond [3]. Figure 1 shows the different forms of carbon-based materials.

In this present review, we intend to discuss the properties, synthesis and characterization of graphene and its derivatives followed by the application of carbon-based materials for the photocatalytic degradation of agrochemicals [4]. Graphene as a class of carbon nanomaterial has attracted thorough attention to it characteristic two-dimensional conjugated structure and their delightful properties [5]. Graphene is derived from graphite which is a common allotrope of carbon in bulk form [6]. Graphene is prepared from graphite by mostly mechanical cleavage and CVD. Graphene is a functionalized single layer of carbon, it is sp^2 bonded C-atoms arranged in hexagonal lattice [6, 7]. There are two kinds of graphene single sheet graphene and multi-sheet graphene [7]. Graphite and graphene are dispersible in limited solvents so when mixed with polar conditions they shows their hydrophobic behavior. The properties of graphene can be tuned by chemically modifying it to another forms like GO and rGO similar to graphene. GO can be synthesized by Hummers method, and rGO has been prepared by electrochemical reduction. GO and rGO also have

J. Patel · S. Jha · S. Shahabuddin · R. Gaur (✉)
Department of Chemistry, School of Technology, Pandit Deendayal Energy University, Knowledge Corridor, Raisan, Gujarat 382426, India
e-mail: rama.gaur@sot.pdpu.ac.in
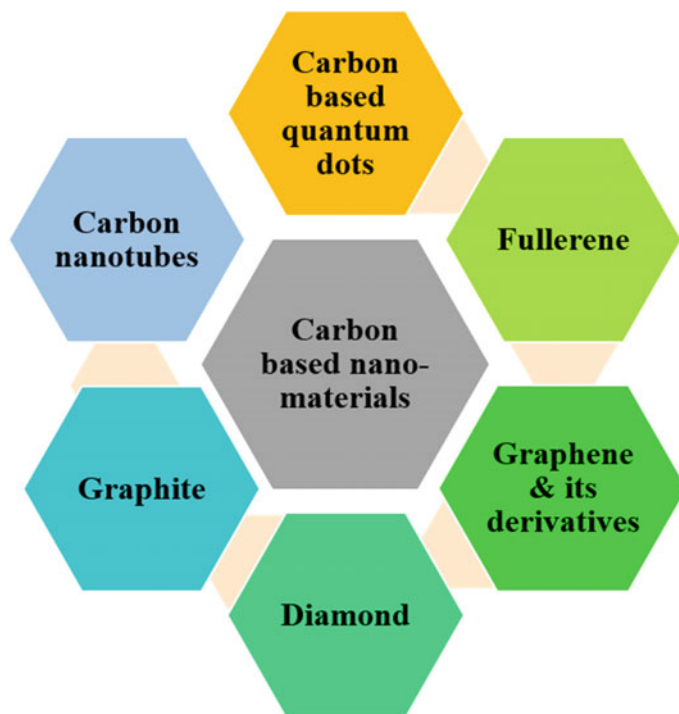
Fig. 1 Different form of carbon and carbon-based materials

excellent properties and are used in various applications [7, 8]. GO is dispersible in many solvents while rGO is slowly dispersed in solvents. Both graphene and rGO have numerous and superior properties like, boiling point and high melting point, hardness, ductility, ionization energies, reactivity electronegative property, electric and thermal conductivity and closely packed structure [7]. Both GO and RGO show different structure, hydrophilic behavior, surface area and chemical properties [9].

Carbon-based materials are known for more environmentally and biologically helpful than inorganic materials. Carbon-based materials have many applications in agriculture, environmental, biomedical, industrial and many more [6]. Agrochemicals are different class of compounds such as pesticides, herbicides, insecticides, fungicide are used for the plant protection, fertilizers are manage the ecosystem and growth-promoters and retardants are used for plant–growth regulators [10]. Agrochemicals are used for improve the nutrients in crops also used for farming sectors similar to dairy farming, crop shifting, improve the production of crop, saleable planting [11]. The use of agrochemicals are very harmful, and the chemicals contaminate water, soil, air and cause damage to our ecosystems (animals, humans, environment, aqueous life) [11]. Agrochemicals are reported to cause cancer, birth imperfections, Alzheimer's disease to harm the nervous system, the endocrine system and the generative system [12].

2 Properties of Graphene and Its Derivatives

Graphene and its derivatives have some distinct properties, which makes them suitable candidate for application in various fields, including agriculture. Also, the unique chemical, thermal, mechanical, optical, electrical properties of graphene and its derivatives like boiling and high melting point, inflexibility, ductility, reactivity electronegative property, conductivity, different structure, ionization energies and hydrophilic behavior impact the ability to be used in different field. Graphene and its derivatives have shown the great potential as agrochemicals.

2.1 Graphene

Graphene has evolved as one of the most capable nanomaterials for the reason that the characteristic mixture of special properties is not only the thinnest but most toughest material, it is optically transparent, it is resistant to gases such as helium, oxygen, nitrogen and due to high porosity allow they to pass through it [13]. Graphene has high electrical, thermal conductivity, high resistance; they are 100 times stronger than steel. In addition to excellent properties it has added advantage of tunable properties which can be achieved by surface functionalization and chemical modification. Graphene is the supreme responsive form of carbon. C atoms at the advantage of graphene sheets have special chemical reactivity. The comparison of graphene with carbon nanotubes is bottom portion of edgy carbons. Graphene is the faultless thermal conductor and shows the thermal conductivity longer than graphite [13]. Graphene conducts heat better than the carbon-based materials, for example, graphite, diamond, graphene oxide, carbon nanotubes. According to this property, graphene used to make LED lighting, mobile devices, thermal foils, etc. In future, graphene could be useful in make flexible displays [14]. Graphene can used to enhance the (metals, plastics or many more) composite materials to make all these material can be lighter and stronger [15]. Graphene is the thinnest materials with high surface area-to-volume ratio [15]. It has higher capacity, lighter weight, amazing flexibility, great temperature range and faster charging giving these properties are used in batteries and super capacitors for store more energy and faster charging [15].

2.2 Graphene Oxide

The oxidation of graphene to GO imparts additional properties like different structure, chemical properties, electrical conductivity, surface area, mechanical strength and hydrophilic behavior [9]. These properties make it suitable for applications in such as drug delivery, biotechnology, cellular imaging and medicine for cancer treatment. GO structure shows the existence of lots of functional groups such as –OH,

–COOH, C = O, C–O–C and many oxygen-based groups. The electrical conductivity of GO exhibits growth insulating and conducting behavior depending on the chemical composition [16]. The most importantly GO exhibits the high surface area but suffers from lower mechanical strength [9]. GO exhibits hydrophilic behavior due to presence of on group on surface and thus shows high dispersion in water and other organic solvents. Further graphene oxide can be converted to reduced graphene oxide (rGO) by using reducing agents.

2.3 Reduced Graphene Oxide

rGO is compound of less oxygen and more carbon. rGO has black powder, variable sheet dimension, and 1.91 g/cm density, insoluble and obtained difficult to dispersed; it is dispersed in low concentration. rGO structure shows the removal of oxygen containing groups from GO after reduction. rGO restores the extremely high surface area of unoxidized form of graphene. rGO exhibits higher electrical conductivity and mechanical strength better than GO [7]. Compared to GO shows the lower hydrophilic behavior (due to the loss of O_2 containing groups like, –COOH, –O–C–O, –OH functional group attached to their basal planes and edges) [16]. For the same reason, it shows the lower dispersibility in solvents. Owing to the properties, rGO is used in energy storage, super capacitors, solar cells, biomedical applications [17].

3 Synthesis of Graphene and Its Derivatives

Graphene and its derivatives can be prepared by both top-down and bottom-up approach. Graphene is generally prepared by chemical and mechanical scrapping of graphite. Graphene and its derivatives can be synthesized by various reported groups [18]. The interconversion of graphene to GO and the rGO has excellent advantages associated with graphene to obtain desired properties.

Both the approaches have several advantages and disadvantages associated with them. Top-down method (TDM) yields the formation of chemically pure nanomaterials but suffer from the complexity involved in the process. TDM approach introduces impurities and imperfection and also difficult to achieve control over deposition parameters. On the other hand, bottom-up method (BOM) results in formation of ultrafine nanoparticles, nanostructures; their parameters can be easily controlled. The problem with this approach is the difficulty to upscale the production [19]. BOM is required for the chemical purification of nanoparticles. Graphene is synthesized by various reported methods shown in Fig. 2. Thermal decomposition is one of the extremely used approaches for growth of graphene on single crystal of 6H-SiC. Exfoliation and cleavage usage mechanical or energy to interrupt these weak bonds and filtrate individual graphene sheets [20]. Chemical methods have conjointly been

Fig. 2 Flowchart for the synthesis of graphene
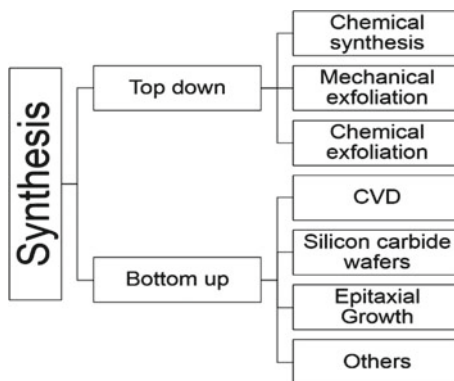
comfortable with chemicals extract graphene films from carbon, without the exfoliation step [21]. There are different methods used chemical vapor deposition, chemical synthesis, mechanical exfoliation; these syntheses are the most usually used methods nowadays [21]. Other methods are also described in figure such as chemical exfoliation, epitaxial growth, plasma chemical vapor deposition. Some possible ways of graphene and rGO synthesis shown in Fig. 5.

Graphene can be simply converted to graphene oxide by simple oxidation process. GO is mostly prepared by chemical oxidization and exfoliation of pristine carbon. Different techniques used for synthesis of GO are by Staudenmaier, Hoffman, Brodie or Hummers' techniques as shown in Fig. 3 or some modification in these techniques [22]. GO is mostly prepared by the Hummers' method. Hummers and Hoffman presented a suitable technique to make GO by exploitation H_2SO_4 and $KMnO_4$ [14]. Staudenmaier then reported the formation of GO once carbon was heated with H_2SO_4, HNO_3 and $KClO_4$ [14]. Later, another plans were additionally established for simultaneously exfoliation and reduction of Graphene nanosheets [23].

rGO can been prepared by modified Hummers' method oxidation, reduction, exfoliation techniques [24]. rGO has properties close to graphite as it is reduced, and all the hydroxyl, carboxylic acid, epoxy groups are eliminated. To achieve rGO structure for these methods are useful and divided into three main categories as shown in Fig. 4a [24]. Thermal reduction process can produce high-quality of rGO, but the high pressure connected with heating can effect structural harm to graphene layers. Chemical reduction works for marketable production but can also produce tremendously toxic substances. To conclude, an electrochemical reduction has proven to be a great method for preparation of high quality of rGO. The rGO prepared using

Fig. 3 Different graphene oxide synthesis methods
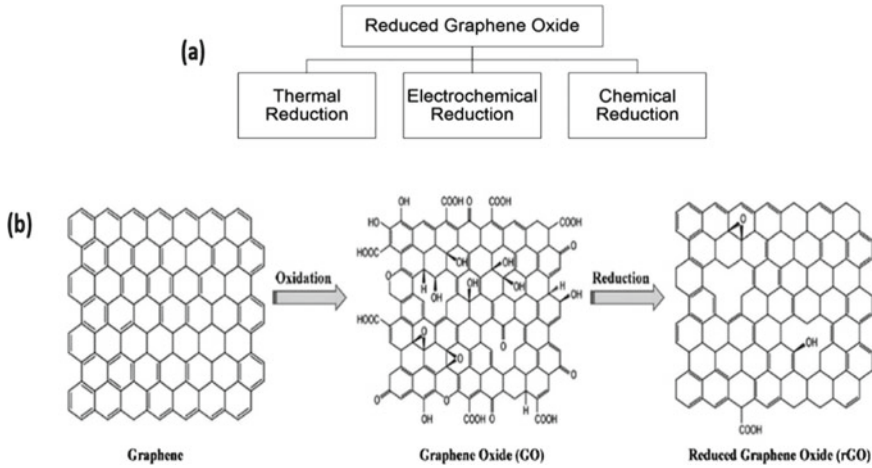
Fig. 4 **a** Different approaches for the synthesis of rGO and **b** transformation of GO and rGO from graphene (Bhattacharjee, S., et al., Advanced Materials Interfaces, 2019) [26]

electrochemical reduction frequently has more conductive metallic behavior [25]. The interconversion of graphene to GO and rGO shown in Fig. 4b.
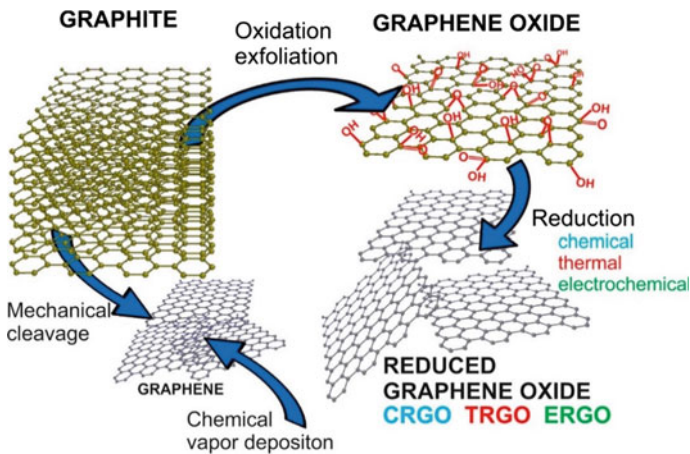
Fig. 5 A schematic diagram for possible ways for the interconversion of graphene to its other possible forms (rGO and GO) (Rowley-Neale, S.J., et al., Applied Materials Today, 2018 Licensed under: CC by 4.0 https://creativecommons.org/licenses/by/4.0/) [27]

4   Characterization of Graphene and Its Derivatives

The characterization of the nanomaterials is an important step to ensure the formation of desired phase and property. With the interconversion of one form to another form, it is requisite to confirm the phase that has been formed for graphene and its derivative. It can be characterized by XRD, Raman, FTIR, UV and SEM–EDX for phase analysis, vibrational-functional group analysis, band gap, morphological analysis and elemental analysis, respectively in these techniques [28].

   XRD (X-ray diffraction) is used to analyze the structure of crystalline materials and investigate the unit cell dimensions [25]. XRD exists the non-destructive test method. XRD shows the crystal phase and control the interlayer spacing for GO and rGO. The presence of a sharp peak at $2\theta = 26.62°$ in the XRD pattern confirms the presence of graphene with well-arranged layer structure. On the other hand for GO the 2θ peak is be shifted to 9.03° indicating the complete oxidation of graphene to GO. After O_2 containing groups were eliminated during reduction, 2θ peak at 24.10°, which indicates the π-conjugated structure of graphene [29]. Raman spectroscopy is a spectroscopic technique used for detect vibrational and rotational analysis [30]. Raman spectroscopy measures the energy that scatters after being excited by the laser. In Raman spectroscopy, D and G bands suggest D band displays out of plane vibrations and G band displays in-plane vibrations [30]. The D and G bands show the fundamental vibrations at 1350 and 1560 cm^{-1} for graphene, GO and rGO, respectively. The 2D band at approximately 2700 cm^{-1} indicates the graphene structure [29]. Fourier transform infrared spectroscopy (FTIR) technique measures the functional groups and light source obtained processes how much lights remaining since the original light. IR spectra shows the O–H-bond (hydroxyl) group, –COOH group (carboxyl), –O–(ether), and other oxygen containing groups in GO, where rGO as all oxygen containing groups are reduced and no signature was seen in FTIR spectra [31]. UV spectroscopy shows the band gap of this material it mentions the energy difference between valance and conduction band. Graphene exhibits a zero band gap, GO gives ~2.2 eV, were rGO shows ~1.5 eV. Scanning electron microscope (SEM) is based on the scattered electrons and used to check morphology on the samples. Graphene displays the platelet similar to crystalline form of carbon, whereas GO displays layered flakes and rGO surface crumpled thin sheets [28].

5   Applications of Graphene and Its Derivatives for Photocatalytic Degradation of Agrochemicals

Use of carbon-based nanomaterials has been reported to various applications such as agriculture and food industry, biomedicine, sensors, drug delivery, etc. [31]. Use of pesticides has been a major concern to the environment. Carbon-based materials can be used in agrochemicals and numerous areas of the digital and food industries [32]. Constant use of agrochemicals results in entry of these chemicals to our food

cycle [33]. The chemicals used in production of agrochemicals and then metabolite have harmful effects on human health. Research reports indicate the use of graphene-based derivatives for degradation of such agrochemicals is a suitable solution. Table 1 summarize the use of carbon-based materials used for degradation, adsorption, and sequestrating of fertilizers, pesticides, etc. The synthetic approach and performance efficiency have also been listed in Table 1.

From Table 1, we can conclude that use of graphene-based composites for removal of agrochemicals from environment is a viable solution. The formation of composites imparts them additional properties making them a suitable and potential catalyst. Different properties and characteristics of carbon-based nanomaterials are used for environmental remediation along with photocatalysis mechanism. In the agricultural field, the contamination is rapidly increased due to the ecosystem imbalance and food disruption. So in this field, the intensive and large applications have been developed to detect contamination or hazardous materials from various sources (soil, food, etc.). The combination of optically interesting nanomaterials like metal oxides, metal sulfides and conducting polymers add to their properties, therefore enhancing their efficiency. Furthermore, novel combinations can be explored to enhance the photocatalytic performance and degradation of agrochemicals.

6   Summary and Future Prospects

From the present review, we can conclude that graphene and its derivative have excellent properties which make them suitable for a variety of applications. Also, the properties can be simply tuned by the interconversion of one form to another, imparting special characteristics to the materials. The current study also points to issues related to overuse of agrochemicals in the ecosystem (animals, human, plant, aqueous life, etc.) and their remediation using carbon-based materials. The synthetic route, properties of the carbon-based materials and their applications for the remediation of agrochemicals have been thoroughly discussed. Graphene and its derivatives can be used in a wide range of applications and gives promising properties. From this present literature, we summarize the huge scope to explored the graphene, and its derivatives are using for the photocatalysis degradation by treatment of agrochemicals.

Table 1 Summary of some important studies of carbon-based nanomaterial, their synthesis, application and efficiency

S. No.	Materials	Synthesis	Applications	Efficiency	References
1	rGO_Ag	Hummers' method	Degradation and adsorption (chlordane)	Removes in only 11 min	[34]
2	rGO/CD	Electrochemical reduction	Detection of brown rice (cyclodextrins Sensor)	Sensor showed a low LOD of 0.023 μM with a wider linear range (0.5–40 μM) and recoveries of 92–99% in rice	[35]
3	Graphene and its composites	Hummers' method, modified Hummers' method	Pesticide removal	Review	[36]
4	Graphene	Modified quechers method	Graphene as absorbent (oil samples for determination of pesticides from various groups)	Recoveries for pesticides achieved:-metazachlor (81%), tebuconazole (84%), Λ-cyhalothrin (59%), chlorpyrifos (83%) and deltamethrin (98%)	[37]
5	Cu(II) chelating rGO	Modified Hummers' redox method	Detection of SOP pesticides from generic OP agents	1–104 ppb	[38]
6	PDAC/rGO-Ag	PDAC/rGO-modified Ag electrodes	Detection of pesticide (Ag electrode sensor)	This electrode analysis confirmed linear voltammetric responses in the concentration range 3×10^{-4} to 9×10^{-4} mol dm^{-3} ($R_2 > 0.94$)	[39]

(continued)

Table 1 (continued)

S. No.	Materials	Synthesis	Applications	Efficiency	References
7	GO	Modified Hummers' method	Adsorption of OPP's	G with –OH group/chlorpyrifos aqueous –2.76 G with –C–O–C group/chlorpyrifos aqueous –1.25 G with –OH group/malathion aqueous –3.01 G with C–O–C group/malathion aqueous –1.41	[40]
8	GO	–	Removal of pesticides	–	[41]
9	Bi$_2$MoO$_6$/N-rGO	Solvothermal method	Degradation of RhB, MB	Catalyst showed the higher degradation activity	[42]
10	Zn-MOF@rGO	Solvothermal method	Determination of hydrazine	Hydrazine sensor detection limit (8.7 × 10^{-3} μM), and fast response time (<2 s)	[43]
11	CoV/rGO	Hydrothermal method	Oxidation of styrene derivatives	Catalyst shows high performance in the preparation of aldehydes with H$_2$O$_2$ as a green oxidant	[44]
12	CS-GO	Hummers' and Hoffman method	Sensing of glucose	Glucose in the range 2.5–5.0 mmol/L with a detection limit as low as 0.5 μmol/L	[45]
13	GO(rGO-Cu$_2$-xSe)	Hummers' exfoliation method	Pesticide delivery	Able to hold 40% (w/w) pesticides	[46]

References

1. Rad TS et al (2022) Graphene-based ZnCr layered double hydroxide nanocomposites as bactericidal agents with high sonophotocatalytic performances for degradation of rifampicin. Chemosphere 286:131740
2. Rahmati M, Mozafari M (2019) Biological response to carbon-family nanomaterials: interactions at the nano-bio interface. Frontiers Bioeng Biotechnol 7:4
3. Olabi A et al (2021) Application of graphene in energy storage device—a review. Renew Sustain Energ Rev 135:110026
4. Bilal M, Iqbal HM, Barceló D (2019) Persistence of pesticides-based contaminants in the environment and their effective degradation using laccase-assisted biocatalytic systems. Sci Total Environ 695:133896
5. Zhu Q et al (2021) Effects of graphene on various properties and applications of silicone rubber and silicone resin. Compos A Appl Sci Manuf 142:106240
6. Zaytseva O, Neumann G (2016) Carbon nanomaterials: production, impact on plant development, agricultural and environmental applications. Chem Biol Technol Agric 3(1):1–26
7. Smith AT et al (2019) Synthesis, properties, and applications of graphene oxide/reduced graphene oxide and their nanocomposites. Nano Mater Sci 1(1):31–47
8. Chen J et al (2013) An improved Hummers method for eco-friendly synthesis of graphene oxide. Carbon 64:225–229
9. Habte AT, Ayele DW (2019), Synthesis and characterization of reduced graphene oxide (rGO) started from graphene oxide (GO) using the tour method with different parameters. Adv Mater Sci Eng
10. Pereira AE et al (2014) Application of poly (epsilon-caprolactone) nanoparticles containing atrazine herbicide as an alternative technique to control weeds and reduce damage to the environment. J Hazard Mater 268:207–215
11. Sebastian A, Nangia A, Prasad MNV (2020) Advances in agrochemical remediation using nanoparticles. Agrochemicals detection, treatment and remediation. Elsevier, pp 465–485
12. Sarlak N, Taherifar A, Salehi F (2014) Synthesis of nanopesticides by encapsulating pesticide nanoparticles using functionalized carbon nanotubes and application of new nanocomposite for plant disease treatment. J Agric Food Chem 62(21):4833–4838
13. El Achaby M et al (2012) Mechanical, thermal, and rheological properties of graphene-based polypropylene nanocomposites prepared by melt mixing. Polym Compos 33(5):733–744
14. Redondo J et al (2018) Simple device for the growth of micrometer-sized monocrystalline single-layer graphene on SiC (0001). J Vac Sci Technol A Vac Surf Films 36(3):031401
15. Xu Z et al (2012) Strong, conductive, lightweight, neat graphene aerogel fibers with aligned pores. ACS Nano 6(8):7103–7113
16. Kumar S, Kaushik R, Purohit L (2021) Novel ZnO tetrapod-reduced graphene oxide nanocomposites for enhanced photocatalytic degradation of phenolic compounds and MB dye. J Mol Liq 327:114814
17. Xu Y et al (2013) Functionalized graphene hydrogel-based high-performance supercapacitors. Adv Mater 25(40):5779–5784
18. Sodeinde KO et al (2022) Photocatalytic degradation of Janus Green Blue dye in wastewater by green synthesised reduced graphene oxide-silver nanocomposite. Int J Environ Anal Chem 1–17
19. Vannozzi L et al (2021) Graphene oxide and reduced graphene oxide nanoflakes coated with glycol chitosan, propylene glycol alginate, and polydopamine: characterization and cytotoxicity in human chondrocytes. Nanomaterials 11(8):2105
20. Avouris P, Dimitrakopoulos C (2012) Graphene: synthesis and applications. Mater Today 15(3):86–97
21. Wu Z-S et al (2009) Synthesis of high-quality graphene with a pre-determined number of layers. Carbon 47(2):493–499
22. Sadegh H (2017) Development of graphene oxide from graphite: a review on synthesis, characterization and its application in wastewater treatment. Rev Adv Mater Sci 49(1)

23. Cui X et al (2011) Liquid-phase exfoliation, functionalization and applications of graphene. Nanoscale 3(5):2118–2126
24. Loryuenyong V et al (2013) Preparation and characterization of reduced graphene oxide sheets via water-based exfoliation and reduction methods. Adv Mater Sci Eng
25. Cui P et al (2011) One-pot reduction of graphene oxide at subzero temperatures. Chem Commun 47(45):12370–12372
26. Bhattacharjee S et al (2019) Graphene modified multifunctional personal protective clothing. Adv Mater Interfaces 6(21):1900622
27. Rowley-Neale SJ et al (2018) An overview of recent applications of reduced graphene oxide as a basis of electroanalytical sensing platforms. Appl Mater Today 10:218–226
28. Dubey SP et al (2015) Synthesis and characterization of metal-doped reduced graphene oxide composites, and their application in removal of Escherichia coli, arsenic and 4-nitrophenol. J Ind Eng Chem 29:282–288
29. Hidayah N et al (2017) Comparison on graphite, graphene oxide and reduced graphene oxide: synthesis and characterization. In: AIP conference proceedings. AIP Publishing LLC
30. Paillet M et al (2018) Graphene and related 2D materials: an overview of the Raman studies. J Raman Spectrosc 49(1):8–12
31. Zhao Y et al (2013) Highly compression-tolerant supercapacitor based on polypyrrole-mediated graphene foam electrodes. Adv Mater 25(4):591–595
32. May A et al (2021) Graphene: a new technology for agriculture. Res Soc Dev 10(2):e56610212827–e56610212827
33. Cheng C et al (2017) Functional graphene nanomaterials based architectures: biointeractions, fabrications, and emerging biological applications. Chem Rev 117(3):1826–1914
34. Sarno M et al (2017) Complete removal of persistent pesticide using reduced graphene oxide−silver nanocomposite. Chem Eng Trans 60:151–156
35. Zhao Y et al (2020) Electrochemical behavior of reduced graphene oxide/cyclodextrins sensors for ultrasensitive detection of imidacloprid in brown rice. Food Chem 333:127495
36. Paramasivan T et al (2019) Graphene family materials for the removal of pesticides from water. A new generation material graphene: applications in water technology. Springer, pp 309–327
37. Madej K, Janiga K, Piekoszewski W (2018) The potential of graphene as an adsorbent for five pesticides from different classes in rape oil samples using dispersive solid-phase extraction. J Anal Methods Chem
38. Li Z et al (2013) A nanocomposite of copper (ii) functionalized graphene and application for sensing sulfurated organophosphorus pesticides. New J Chem 37(12):3956–3963
39. Al-Hamry A et al (2019) Electrochemical sensor based on reduced graphene oxide/PDAC for dimethoate pesticide detection. In: 2019 5th international conference on nanotechnology for instrumentation and measurement (NanofIM). IEEE
40. Yadav S et al (2019) Graphene oxide as proficient adsorbent for the removal of harmful pesticides: comprehensive experimental cum DFT investigations. Anal Chem Lett 9(3):291–310
41. Wang H et al (2021) Emerging role of graphene oxide as sorbent for pesticides adsorption: experimental observations analyzed by molecular modeling. J Mater Sci Technol 63:192–202
42. Kasinathan M et al (2020) Fabrication of novel Bi_2MoO_6/N-rGO catalyst for the efficient photocatalytic degradation of harmful dyes. Mater Res Bull 125:110782
43. Rani S et al (2020) Fabrication of Zn-MOF@rGO based sensitive nanosensor for the real time monitoring of hydrazine. J Alloy Compd 816:152509
44. Zou H et al (2018) Cobalt vanadium oxide supported on reduced graphene oxide for the oxidation of styrene derivatives to aldehydes with hydrogen peroxide as oxidant. Synlett 29(16):2181–2184
45. Wang G-L et al (2014) Visible-light-stimulated enzymelike activity of graphene oxide and its application for facile glucose sensing. J Phys Chem C 118(48):28109–28117
46. Sharma S et al (2017) Anti-drift nano-stickers made of graphene oxide for targeted pesticide delivery and crop pest control. Carbon 115:781–790

Zeolite-Based Nanocomposites for Wastewater Treatment

Veena Sodha, Rama Gaur, Rajib Bandyopadhyay, and Syed Shahabuddin

1 Introduction

Water is essential for humans and the environment and is the basic need for all living organisms on earth. The quality of water is deteriorating continuously due to growth in population and industry [1]. Sources of wastewater include a variety of domestic and industrial activities. Looking at the situation, there must be persistent efforts in the field of water purification. Various methods including chemical, biological, and physical have been reported for wastewater treatment [2]. Some of them include adsorption [3], photocatalysis [4], ultrafiltration [5], biofiltration [6], etc. Zeolites have been recognized as useful adsorbents for a variety of purposes [7]. Owing to their intrinsic adsorption [8] and ion exchange [9] properties, zeolites have shown good results for water purification. The studies on photocatalytic activity of zeolites are scanty and this field has not been explored much. Photocatalysis is an efficient method for the degradation of persistent organic pollutants (POPs) from water [10]. POPs are hydrophobic chemicals that usually exist as solids in soil and water. As POPs interfere with the food chain, they primarily affect humans and other predators [11]. As they are not easily degradable, there must be constant efforts in developing and improving their degradation methods. As mentioned earlier, both photocatalysis and adsorption have proved efficient and economical for wastewater treatment [3, 4]. With the combination of photocatalysis and adsorption properties together in one

V. Sodha · R. Gaur · R. Bandyopadhyay · S. Shahabuddin (✉)
Department of Chemistry, School of Technology, Pandit Deendayal Energy University,
Knowledge Corridor, Raisan, Gandhinagar, Gujarat 382007, India
e-mail: syed.shahabuddin@sot.pdpu.ac.in

R. Bandyopadhyay
e-mail: rajib.bandyopadhyay@sot.pdpu.ac.in

S. Shahabuddin
Faculty of Applied Science, Universiti Teknologi MARA, Cawangan Negeri Sembilan, Kampus
Kuala Pilah, 40450 Kuala Pilah, Shah Alam, Malaysia

material, it is expected to observe extraordinary behaviors that can be useful for the treatment of wastewater, including POPs.

2 Zeolites

Zeolites are crystalline, micro/meso/macro porous, three-dimensional aluminosilicates with a systematized structure that is made up of tetrahedral units TO4, linked by a shared O atom; where T is Al or Si [12]. Exchangeable cations and water are located in the void between the large cavities in the zeolite structure [8]. The general chemical formula of zeolites can be expressed as $Ma/n[AlaSibO_2(a + b)] \cdot qH_2O$; where M is {Na, Li, K} and/or {Ca, Sr, Ba, Mg}, and n denotes the charge of cation; the value of $b/a = 1-6$ and $q/a = 1-4$ [8].

2.1 Classification of Zeolites

Zeolites can be classified on the basis of their occurrence, pore size, Si–Al ratio, crystal structure, etc [13]. The general classification of zeolites is depicted in Fig. 1. Tables 2 and 3 illustrate the classification of zeolites as per their pore size and Si to Al ratio, respectively [13].
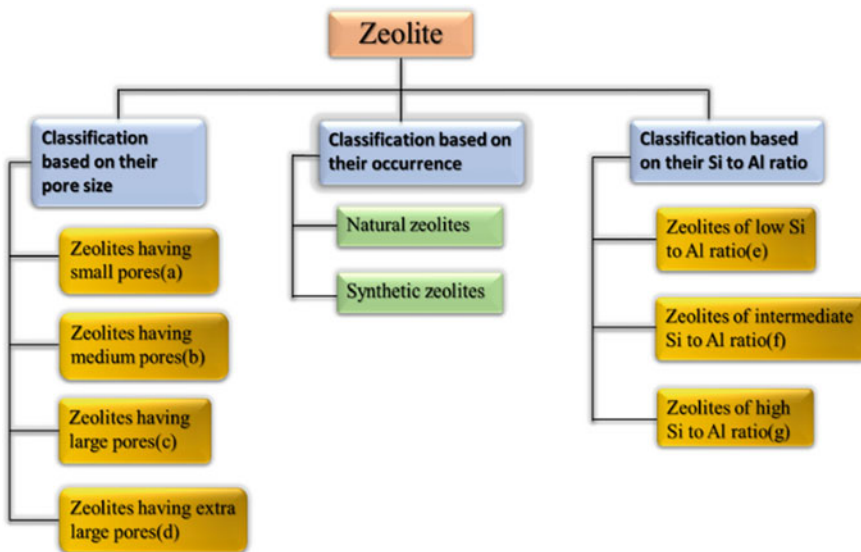
Fig. 1 General classification of zeolites

Table 1 Classification of zeolites as per their pore size

Type of zeolite	Number of rings	Free pore diameter (nm)
(a) Zeolites having small pores	8-rings	0.3–0.45
(b) Zeolites having medium pores	10-rings	0.45–0.6
(c) Zeolites having large pores	12-rings	0.6–0.8
(d) Zeolites having extra-large pores	14-rings	0.8–1.0

Table 2 Classification of zeolites as per Si to Al ratio

Type of zeolite	Si–Al ratio range
(e) Low Si:Al ratio	1.0–1.5
(f) Intermediate Si:Al ratio	2–5
(g) High Si:Al ratio	10 to several thousands

Table 3 Summary of water treatment methods used by early of twentieth century

Treatment methods	Objectives
Mechanical separation	By gravity—sedimentation By screening—screen, scrubbers, and filters By adhesion—scrubbers, filters
Coagulation	Chemical process of drawing matter together thereby making them easier to remove by mechanical separation
Chemical purification	Iron removal, softening by use of lime, neutralization of suspected acids
Disinfection processes (Previously known as poisoning processes)	Objective of these processes is to poison and kill objectionable organisms without adding poisonous substances. For example, ozonation
Biological processes	Oxidation of organic matter by using them as food organisms thereby destructing them. Destruction of objectionable organism by creating unfavorable conditions such as removing their food by purification process
Aeration	Evaporation of objectionable gases and carbonic acid
Boiling	Best household method

2.2 Physicochemical Properties of Zeolites

Zeolites have the ability to act as adsorbent and molecular scale sieves [7, 14]. They are good ion exchangers and can easily catalyze reactions as they have fixed pore sizes

and active sites in their crystal lattice [15]. Adsorption of methylene blue dye on a Chinese natural zeolite was studied with varying flow rates and initial concentrations, followed by estimation of kinetic parameters by Han et al. [16]. The results showed good adsorption results, thereby removing methylene blue from the experimental solution. Figure 2 shows the resulting dye degradation at different parameters; where v = flow rate; t = time; c_0 = initial concentration of MB; and c_t = concentration of MB at time t.

The ammonium removal performance of Yemeni natural zeolite was successfully investigated by Alshameri et al. [17]. Aguiñaga et al. successfully performed photocatalytic decomposition of caffeine by natural zeolite (clinoptilolite–mordenite). When the results were compared to the TiO_2 particles, it was observed that TiO_2 needed the same time as the zeolites for the complete breakdown of caffeine under similar conditions. Figure 3 shows the graph of the photocatalytic degradation of caffeine as a function of time; where NH is a hydrogenated form of natural zeolite (NZ); NFe is obtained by ion exchange of NZ; and SH is synthetic clinoptilolite-mordenite zeolite. The diffuse reflectance spectra of natural and synthetic zeolites

Fig. 2 Effect of flow rate and initial concentration of MB on the surface of zeolite [16]
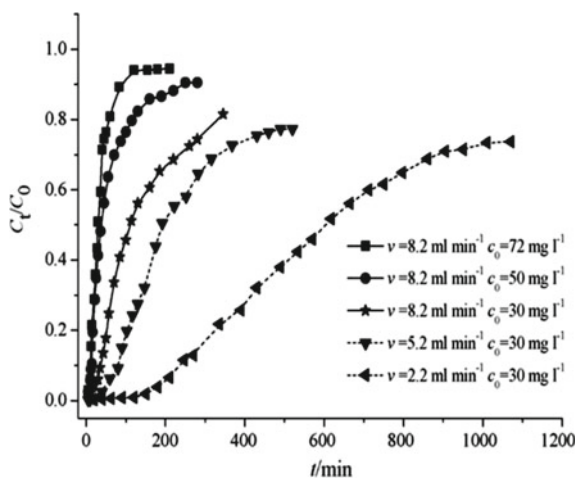
Fig. 3 Photocatalytic degradation of caffeine in aqueous solution by NH, NFe, and SH [18]
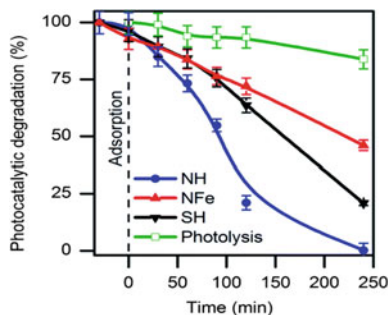
are obtained. Applying Kubelka–Munk function to these spectra, adsorption edge of natural zeolites (NH, NFe) and synthetic zeolites (C, M) were obtained. Spectroscopic analysis of the zeolite ZSM-5 shows that bands developed in the 200–500 nm range are due to iron species in their different states and that iron is common in synthetic zeolites [18]. The typical structure of aluminosilicate zeolite holds a bandgap around 7 eV [18]. The estimated bandgap of natural mordenite was 2.63 eV. With the help of experimental data, band gap energies were analyzed using a Tauc plot [18]. For synthetic clinoptilolite C, band gap energies were analyzed at 4.26 and 4.46 eV for direct and indirect transitions, respectively. Likewise, 3.26 and 3.45 for synthetic mordenite. From the data given above, we may conclude that zeolites can have a bandgap similar to that of semiconductors. Therefore, they are able to exhibit the photocatalytic property which in turn is helpful for degradation of POPs in wastewater.

3 Wastewater

Each community generates all three types of wastes, i.e., liquid, solid, and gaseous. Wastewater, which falls in the category of liquid waste, is the water that has been used in a wide area of applications. In general, wastewater is a combination of the liquid or waterborne wastes removed from the residence, institution, and the commercial and industrial establishment [19]. When untreated wastewater is released into sewers and water bodies, it can pose a risk to humans and the environment [19]. Due to rapid industrialization, the generation of synthetic chemicals has increased. These synthetic chemicals are mostly organic in nature. Their occurrence in the environment can expose them to human, aquatic life, and wildlife, via food chain or drinking water [20]. These organic compounds are water-hating, are fat-soluble, and are susceptible to bioaccumulation and long-range transport [21]. POPs discharged locally disseminated pollution far from their source [21]. POPs consist of compounds of several industries and synthetic chemicals and pesticides [21]. If POPs are not treated properly, they can easily involve in the food chain. Refer Fig. 4 [21].

Hence, degradation of POPs at their earliest is required. Not only they are POPs and heavy metals, but there are many other contaminants in the water that require special attention. For years, a lot of effort has been made to innovate and develop
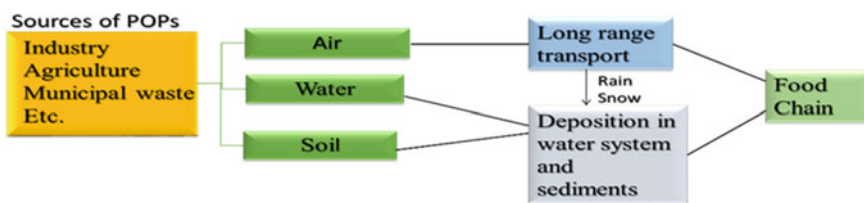
Fig. 4 Flowchart showing the transport of POPs in the environment and food chain

wastewater treatment technologies. Table 3 provides information on conventional wastewater treatment techniques [22].

Subsequently, several new treatment technologies were introduced such as adsorption, membrane filtration, ion exchange, reverse osmosis, and photocatalysis [22]. We will discuss photocatalysis and adsorption in more detail.

4 Photocatalysis

If a photon catalyzes a reaction, the system is said to be photocatalytic. Semiconductors are materials that exhibit photocatalytic properties [23]. Semiconductors have two distinct energy bands, namely the valance band and the conduction band. The energy gap between these two bands is the bandgap. When the photon of light bombards the semiconductor material and when a photon of light bombards the semiconducting material, electrons (e^-) excite from low-energy valance band to high-energy conduction band leaving empty space behind, referred to as holes (h^+) as depicted in Fig. 5. These electron–hole pairs are responsible for the formation of active oxidizing species, which are further responsible for the degradation of organic pollutants in wastewater [21].

Mechanism of heterogeneous photocatalysis involves following steps.

$$\text{Semiconductor photocatalyst} \overset{hv \geq E_g}{\rightarrow} e^- + h^+$$

$$e^- + O_2 \rightarrow O_2^{\bullet-}$$
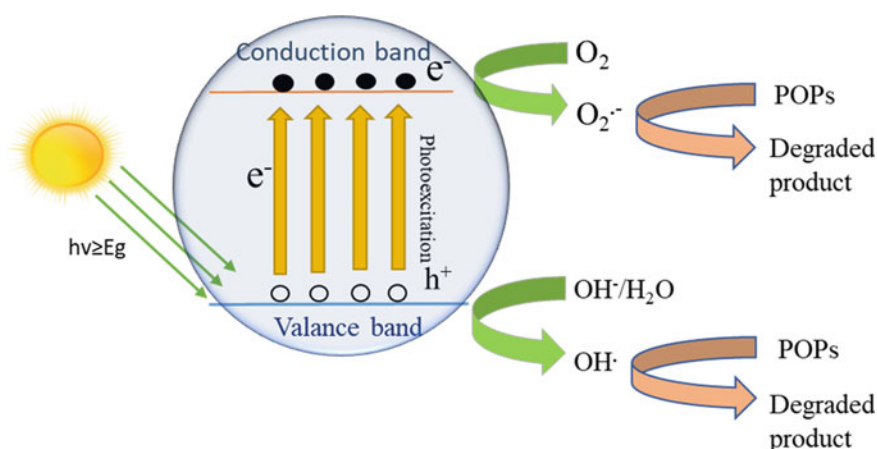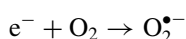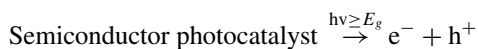
Fig. 5 Schematic diagram of photocatalysis

$$O_2^{\bullet -} + H^+ \rightarrow OOH^\bullet$$

$$2OOH^\bullet \rightarrow H_2O_2 + O_2$$

$$H_2O_2 + O_2^{\bullet -} \rightarrow OH^- + OH^\bullet + O_2$$

$$h^+ + H_2O \rightarrow OH^\bullet + H^+$$

$$h^+ + OH^- \rightarrow OH^\bullet$$

$$POPs + \left(h^+, OH^\bullet, O_2^{\bullet -}, OOH^\bullet \text{ or } H_2O_2\right) \rightarrow \text{Degraded products}$$
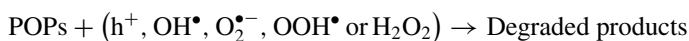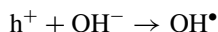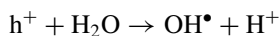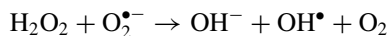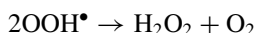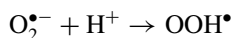
M. N. Rashed et al. performed the methyl orange dye degradation in TiO$_2$ suspension at different MO concentrations using three different light sources [24]. The electron–hole recombination in semiconducting materials limits its efficiency, which we can overcome via making binary or trinary composites of semiconducting materials [21].

5 Adsorption

Adsorption is a surface process in which molecules are transferred from a fluid mass to a solid surface through physical forces or chemical interactions. It is generally reversible, and the reversible of adsorption is desorption [25]. The adsorption process falls under two categories, i.e., physical adsorption and chemical adsorption [26].

The properties of two different adsorption processes are illustrated in Table 4.

Table 4 Comparison between physical and chemical adsorption [26]

	Physical adsorption	Chemical adsorption	References
Attraction forces	Intermolecular forces such as van der Waals force	Chemical bond forces such as valance forces	
Adsorption layer	Single or multilayer	Single layer	
Adsorption heat	Low	High	
Adsorption rate	Fast	Slow	
Stability	Instable	Stable	
Example	Adsorption of alkyl and alkyl benzene sulfate on alumina	Chemisorption of oxygen on aluminum surface	[27–29]

Fig. 6 Schematic of adsorption
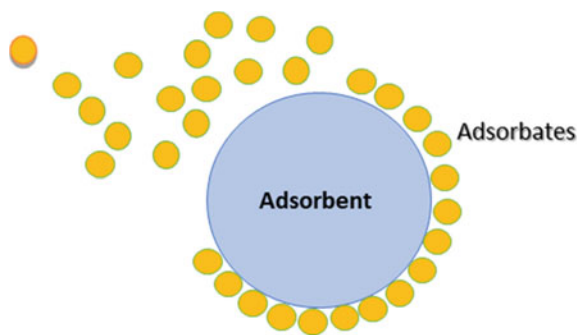
The adsorbates are transferred from the bulk of the solution to be treated to specific sites on the adsorbent's surface, causing an adsorption reaction on the adsorbent's surface, as shown in Fig. 6 [30].

Among the number of water purification techniques, adsorption is simple yet effective [31]. Generally, materials used as an adsorbent in wastewater treatment are activated carbon [32], clay minerals [33], biomaterials [34], industrial solid wastes [35], and zeolites [8]. Lowitz discovered adsorption in 1785, and it was later employed to remove colors from sugar during the refining process [36]. Subsequently, inactivated charcoal filters were utilized to purify water in American water treatment plants [36]. In Hamm, Germany, in 1929, and Bay City, Michigan, in 1930, adsorption on the first granular-activated carbon (GAC) systems for water treatment was employed [36]. Synthetic, modified, and natural zeolites were studied, and synthetic and modified zeolites were found to have higher adsorption and ion exchange properties [37]. Armagan et al. examined a Turkey clinoptilolite for adsorption of three azo dyes (Everzol Black, Everzol Red, and Everzol Yellow) and observed limited adsorption capacities. They noticed a significant improvement in adsorption after modification with quaternary amines [38].

6 Synthesis and Characterization of Zeolite-Based Nanocomposites

Using a quick green precipitation approach, Jahangirian et al. were able to synthesis Zeolite/Fe_2O_3–NCs. The surface of zeolite was coated with Fe_2O_3–NPs [39]. SEM images of zeolite (A) and zeolite/Fe_2O_3–NCs (B–F) are shown in Fig. 7. The particles' cubic shape is due to the zeolite structure, which did not alter during the operation. It is obvious from the SEM images that ferric oxide aggregation occurs on the surface of zeolite/Fe_2O_3–NCs [39].

There are four different paths of synthesizing Conductive polymers/zeolite-based (nano-)composites [40]: (i) encapsulating the organic solvent dissolved monomer
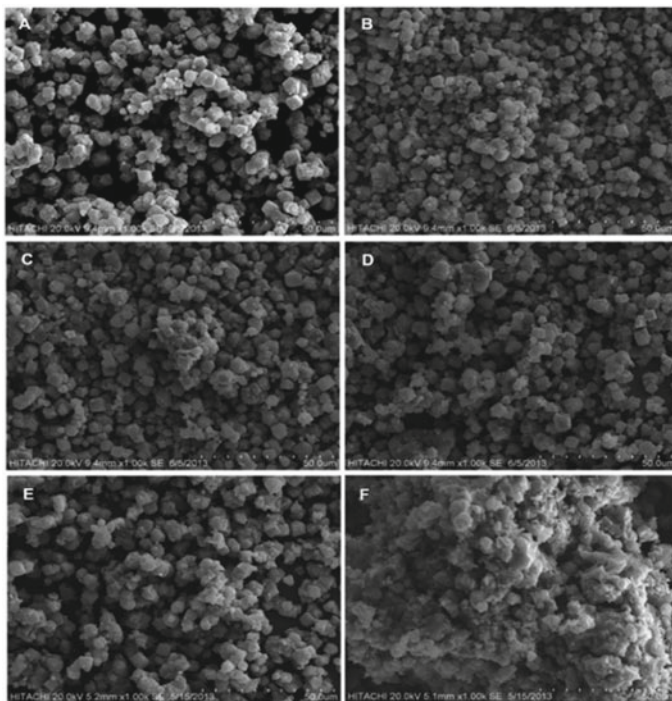
Fig. 7 SEM images of **a** zeolite and zeolite/Fe_2O_3–NCs in **b** 1%, **c** 4%, **d** 7%, **e** 12%, and **f** 17% of Fe_2O_3–NP [39]

within the zeolite cavities by a diffusion process, followed by oxidative polymerization to form polymeric chains into zeolite cavities [41]; (ii) exposing the zeolite with oxidant ions like Fe(III) and Cu(II) to monomer and acid vapors [42]; (iii) performing in situ polymerization of the monomer with zeolite, and the polymer may form inside and outside the zeolite channels [43, 44]; and (iv) by simply mixing zeolite powder and conductive polymer [45]. Among the above discussed methods, methods (i) and (ii) are of more interest as the nano-scale polymeric chains are formed into cavities of zeolite. Hence, the electronic, mechanical, chemical, and optical properties may be improved as the polymeric chains are organized in the nanometer scale [40]. Ivan et al. [46] reported the synthesis of polyaniline/zeolite 5A composite. Synthesis path comprised in situ oxidative polymerization of aniline in synthetic zeolite pattern. After that, the constructed membrane was tested to see whether it could remove cobalt ions from wastewater in the ultrafiltration process. SEM images of zeolite 5A and polyaniline/zeolite 5A composite are shown in Fig. 8 [40, 46].

Synthesis of polyaniline/ZSM-5 zeolite composites was reported by Milojevic-Rakic et al. [47]. Oxidative polymerization of aniline was performed by adding an aqueous solution of APS in the zeolite ZSM-5 and aniline water dispersion, which was prepared by previously reported weight ratios [48]. The material was synthesized
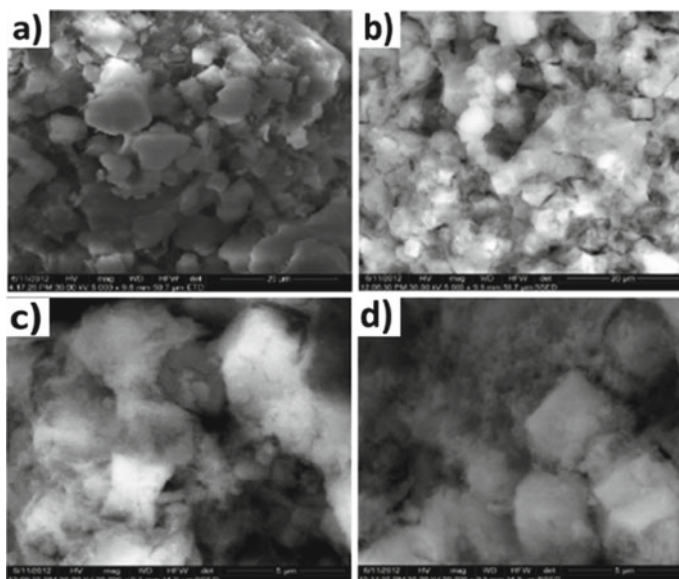
Fig. 8 SEM images at different magnifications of zeolite 5A (**a**, **c**) and polyaniline/zeolite 5A composites (**b**, **d**) [46]

with and without acid medium. The synthesized composites were labeled as PZ1/1, PZ1/5, and PZ1/10 for weight ratios ZSM-5/aniline of 1, 5, and 10, respectively, and were evaluated as adsorbent for the organic herbicide in an aqueous solution. Adsorption study was done using Freundlich, Langmuir, and Langmuir–Freundlich isotherm models. Among all the PANI, pure ZSM-5, and PANI/ZSM-5 samples tested, the deprotonated granular PANI synthesized in sulfuric acid medium had the maximum glyphosate adsorption. The protonated nanostructured PANI and the deprotonated PANI/ZSM-5 composite with 50% zeolite both have a high adsorption capacity. Both materials were made using water and no acid [47].

References

1. Ali I (2012) New generation adsorbents for water treatment. Chem Rev 112(10):5073–5091
2. Crini G, Lichtfouse E (2019) Advantages and disadvantages of techniques used for wastewater treatment. Environ Chem Lett 17(1):145–155
3. Perrich JR (2018) Activated carbon adsorption for wastewater treatment. CRC Press
4. Kanakaraju D, Glass BD, Oelgemöller M (2014) Titanium dioxide photocatalysis for pharmaceutical wastewater treatment. Environ Chem Lett 12(1):27–47
5. Mohammadi T, Esmaeelifar A (2005) Wastewater treatment of a vegetable oil factory by a hybrid ultrafiltration-activated carbon process. J Membr Sci 254(1–2):129–137
6. Chaudhary DS et al (2003) Biofilter in water and wastewater treatment. Korean J Chem Eng 20(6):1054–1065

7. Tagliabue M et al (2012) Regenerability of zeolites as adsorbents for natural gas sweetening: a case-study. Fuel 93:238–244
8. Wang S, Peng Y (2010) Natural zeolites as effective adsorbents in water and wastewater treatment. Chem Eng J 156(1):11–24
9. Hedström A (2001) Ion exchange of ammonium in zeolites: a literature review. J Environ Eng 127(8):673–681
10. Nguyen V-H et al (2020) Photocatalytic remediation of persistent organic pollutants (POPs): a review. Arab J Chem 13(11):8309–8337
11. Jones KC, De Voogt P (1999) Persistent organic pollutants (POPs): state of the science. Environ Pollut 100(1–3):209–221
12. Auerbach SM, Carrado KA, Dutta PK (2003) Handbook of zeolite science and technology. CRC Press
13. Ramesh K, Reddy DD (2011) Zeolites and their potential uses in agriculture. Adv Agron 113:219–241
14. Lin CC, Dambrowitz KA, Kuznicki SM (2012) Evolving applications of zeolite molecular sieves. Can J Chem Eng 90(2):207–216
15. Pabalan RT, Bertetti FP (2001) Cation-exchange properties of natural zeolites. Rev Mineral Geochem 45(1):453–518
16. Han R et al (2007) Comparison of linear and nonlinear analysis in estimating the Thomas model parameters for methylene blue adsorption onto natural zeolite in fixed-bed column. J Hazard Mater 145(1–2):331–335
17. Alshameri A et al (2014) The investigation into the ammonium removal performance of Yemeni natural zeolite: modification, ion exchange mechanism, and thermodynamics. Powder Technol 258:20–31
18. Alvarez-Aguinaga EA, Elizalde-González MP, Sabinas-Hernández SA (2020) Unpredicted photocatalytic activity of clinoptilolite–mordenite natural zeolite. RSC Adv 10(64):39251–39260
19. Tchobanoglous G, Burton FL, Stensel H (1991) Wastewater engineering. Management 7:1–4
20. Verhaert V et al (2017) Persistent organic pollutants in the Olifants River Basin, South Africa: bioaccumulation and trophic transfer through a subtropical aquatic food web. Sci Total Environ 586:792–806
21. Naushad M, Rajendran S, Lichtfouse E (2020) Green methods for wastewater treatment. Springer
22. Crittenden JC et al (2012) MWH's water treatment: principles and design. Wiley
23. Ameta R et al (2018) Photocatalysis. Advanced oxidation processes for waste water treatment. Elsevier, pp 135–175
24. Rashed M, El-Amin A (2007) Photocatalytic degradation of methyl orange in aqueous TiO_2 under different solar irradiation sources. Int J Phys Sci 2(3):73–81
25. Artioli Y (2008) Adsorption. In: Encyclopedia of ecology Fath, SEJD. Academic Press, Oxford
26. Hu H, Xu K (2020) Physicochemical technologies for HRPs and risk control. High-risk pollutants in wastewater. Elsevier, pp 169–207
27. Dick S, Fuerstenau D, Healy T (1971) Adsorption of alkylbenzene sulfonate (ABS) surfactants at the alumina-water interface. J Colloid Interface Sci 37(3):595–602
28. Chander S, Fuerstenau D, Stigter D (1983) On hemimicelle formation at oxide/water interfaces. Adsorption from solution. Elsevier, pp 197–210
29. Batra IP, Kleinman L (1984) Chemisorption of oxygen on aluminum surfaces. J Electron Spectrosc Relat Phenom 33(3):175–241
30. Tien C (2019) Adsorbate uptake and equations describing adsorption processes. In: Tien C (ed) Introduction to adsorption. Elsevier, Amsterdam, The Netherlands, pp 87–118
31. Ma Y et al (2019) Gelatin/alginate composite nanofiber membranes for effective and even adsorption of cationic dyes. Compos B Eng 162:671–677
32. Wang X, Zhu N, Yin B (2008) Preparation of sludge-based activated carbon and its application in dye wastewater treatment. J Hazard Mater 153(1–2):22–27

33. Bhattacharyya KG, Sen Gupta S (2006) Adsorption of chromium (VI) from water by clays. Ind Eng Chem Res 45(21):7232–7240
34. Rangabhashiyam S et al (2014) Significance of exploiting non-living biomaterials for the biosorption of wastewater pollutants. World J Microbiol Biotechnol 30(6):1669–1689
35. Soliman N, Moustafa A (2020) Industrial solid waste for heavy metals adsorption features and challenges: a review. J Mark Res 9(5):10235–10253
36. Hawari AH, Mulligan CN (2006) Biosorption of lead (II), cadmium (II), copper (II) and nickel (II) by anaerobic granular biomass. Biores Technol 97(4):692–700
37. Yuna Z (2016) Review of the natural, modified, and synthetic zeolites for heavy metals removal from wastewater. Environ Eng Sci 33(7):443–454
38. Armağan B, Turan M (2004) Equilibrium studies on the adsorption of reactive azo dyes into zeolite. Desalination 170(1):33–39
39. Jahangirian H et al (2020) Green synthesis of zeolite/Fe_2O_3 nanocomposites: toxicity and cell proliferation assays and application as a smart iron nanofertilizer. Int J Nanomed 15:1005
40. Jaymand M (2014) Conductive polymers/zeolite (nano-)composites: under-exploited materials. RSC Adv 4(64):33935–33954
41. Flores-Loyola E et al (2007) Enzymatic polymerization of aniline in the presence of different inorganic substrates. Mater Chem Phys 105(1):136–141
42. do Nascimento GM, Temperini ML (2008) Structure of polyaniline formed in different inorganic porous materials: a spectroscopic study. Eur Polym J 44(11):3501–3511
43. Sakellis I, Papathanassiou A, Grammatikakis J (2009) Effect of composition on the dielectric relaxation of zeolite-conducting polyaniline blends. J Appl Phys 105(6):064109
44. Malkaj P et al (2006) pH electrodes constructed from polyaniline/zeolite and polypyrrole/zeolite conductive blends. J Appl Polym Sci 101(3):1853–1856
45. Vitoratos E et al (2007) DC conductivity and thermal aging of conducting zeolite/polyaniline and zeolite/polypyrrole blends. Curr Appl Phys 7(5):578–581
46. Ivan A et al (2013) Compozite zeolite-polyaniline membrane material for water treatement. UPB Sci Bull Ser B 75(3):53–64
47. Milojević-Rakić M et al (2013) Polyaniline and its composites with zeolite ZSM-5 for efficient removal of glyphosate from aqueous solution. Microporous Mesoporous Mater 180:141–155
48. Ciric-Marjanovic G et al (2009) Synthesis and characterization of conducting self-assembled polyaniline nanotubes/zeolite nanocomposite. Langmuir 25(5):3122–3131

Biochar: A Sustainable Approach Towards Environmental Remediation

Stuti Jha, Jinal Patel, Syed Shahabuddin, and Rama Gaur

1 Introduction

Biochar is a carbon-rich by-product obtained through the process of pyrolysis, or the anaerobic thermal decomposition of organic materials. The term biochar was coined by Peter Read in 2005, a research fellow at Massey University in New Zealand. Biochar is retained from biomass using thermochemical and mechano-chemical treatment [1]. More than 65% of its composition is carbon with nitrogen, oxygen and hydrogen in trace amounts. Apart from pyrolysis, other methods namely torrefaction, gasification and hydrothermal carbonization are also used for biochar production. Some of the characteristic of biochar include long-term stability, hydrophobicity, large surface area, high porosity, chemical composition, pore size, etc. Owing to these properties, biochar is a potential candidate for application as catalyst, fillers and adsorbent. Out of these, one of its most attractive and attention-captivating application is as an adsorbent for environmental remediation by abatement of existing contaminants. Since the past few years, biochar has intrigued researchers as it is a greener alternative to other methods such as activated carbon, nanomaterials, etc., used for environmental management in the areas of soil improvement, waste management, climate change mitigation and energy generation. Moreover, it is cost-effective and has a widely available feedstock as raw material which can be derived from the residues of agricultural, forestry, aquaculture, food and fibre processing industries. Biochar is used in carbon sequestration, adsorption of greenhouse gas and treating various pollutants of soil and water such as heavy metals, oil spills, pesticides, etc. Furthermore, the application and performance of biochar depend on the type of contaminants it is intended to treat (i.e. polar/non-polar, hydrophobic/hydrophilic,

S. Jha · J. Patel · S. Shahabuddin · R. Gaur (✉)
Department of Chemistry, School of Technology, Pandit Deendayal Energy University, Knowledge Corridor, Raisan, Gujarat 382426, India
e-mail: rama.gaur@sot.pdpu.ac.in

organic/inorganic and cationic/anionic), remediation goals and environmental conditions in general [2]. Hence, it becomes important to understand the properties of biochar and to tune its hydrophobicity, pore size, surface area, etc., by using some modification methods. Properties of biochar can be enhanced to make it more specific in its application and operating conditions through certain modifications like ball milling [3], acid/alkali treatment [4] and acetylation [4]. When any analyte (pollutant) interacts with biochar, it involves mechanism such as ion exchange, hydrogen bond formation, electrostatic attraction, etc. In contrast to the efficiency of pristine biochar, engineered biochar has proven to exhibit higher performance characteristic [1]. The present report reviews the existing literature and gives an idea about the sources, properties, synthetic routes and the environment-based application of biochar. It also focuses on certain areas of biochar which still has room for future investigation.

2   Sources of Biochar

Biochar is produced through the decomposition of organic matter (biomass) which in turn enables us to choose the feedstock from a vast spectrum of materials (banana peel, orange peel, coconut husk, algae, weeds, etc.). Any material having high carbonaceous value can serve as a feedstock for biochar. Biochar is typically derived from wastes of agriculture and forest, green lands, food and fibre processing industry, sewage sludge, etc., as summarized in Fig. 1. Some of the examples of raw materials are rice straw, coconut peats, livestock manure, sugar cane, wood fibres, sawdust, fruit peels, algae, seeds and fish scales. The raw materials required are easily collectable and widely available. Depending on their sources, the raw materials for biochar can be classified as depicted in Table 1.
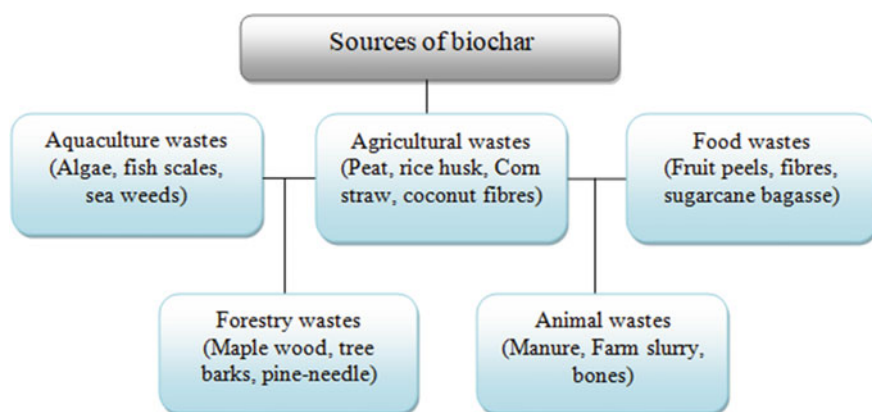
Fig. 1   Different categories of sources of biochar

Table 1 Feedstock classification, sources, synthetic routes, reaction conditions and applications of biochar

Type	Source	Synthetic route	Reaction condition	Target molecule	Efficiency	References
Agricultural waste	Rice straw	Slow pyrolysis	400–700 °C, 120 min	–	–	[12,27]
	Cotton husk	Pyrolysis	800 °C, 4 min	Pump oil, diesel oil	5.5 g/g	[28]
	Peat	Pyrolysis	300 °C, –	Crude oil	32.5 g/g	[29]
	Rice hush	Carbonization	400 °C, 3 h	Crystal violet	0.185 mg/g	[30]
	Peanut shell	Pyrolysis	300 °C, –	–	–	[31]
	Corn straw	–	–	Bisphenol	–	[32]
Forestry residues	Pinewood	Hydrothermal carbonization	300 °C, 20 min	Lead	–	[33]
	Palm bark	Slow pyrolysis	400 °C, 30 min	Methylene blue dye	–	[34]
	Maple wood	Pyrolysis	300–700 °C, –	Crude oil	3.8–6.2 g/g	[35]
	Pine-needle	–	–	m-dinitrobenzene	–	[36]
Municipal waste	Poultry litter	Pyrolysis	350 °C, –	–	–	[20]
	Sludge	Pyrolysis	400–700 °C, 2 h	Fluoride	–	[37]
	Dairymanure	Slow pyrolysis	350 °C, 4 h	Pb, Cu, Zn and Cd	–	[38]
Aqua waste	Sea weed	Hydrothermal carbonization	180 °C, 4 h	Tetrabromobisphenol	1.4 mg/g	[39]
Food waste	Coconut waste and orange waste	Pyrolysis	350 °C, –	–	$47.09\text{–}83.02 \times 10^{-6}$ g/g (coconut waste) $23.84\text{–}84.02 \times 10^{-6}$ (orange waste)	[40]

Table 1 (continued)

Type	Source	Synthetic route	Reaction condition	Target molecule	Efficiency	References
	Walnut shell	Microwave pyrolysis	280 W (15 min), then 600 °C (2 h)	Salicylic acid, naproxen and ketoprofen	Salicylic acid = 683 mg/g Naproxen = 533 mg/g Ketoprofen = 444 mg/g	[41]
	Sugarcane bagasse	Slow pyrolysis	300, 700 °C, 6 h	Hydrophobic organic compounds	–	[42]
	Orange peel	Slow pyrolysis	400–700 °C, 2 h	Fluoride	–	[37]
	Coconut coir	–	250–600 °C, 1 h	Chromium	–	[43]

Few examples where biochar has been derived from agricultural wastes are as follows. Nazia Hossain et al. synthesized biochar from rice husk at 180 °C temperature and pressure 70 bar [5]. Gopal et al. used coconut husk, coconut leaves and also coconut fibres to synthesize biochar [6]. Sarfaraz et al. used animal manure (swine and cattle manures, poultry litters) as raw materials for the production of biochar [7]. They have also reported the preparation of biochar using soybean and rice straws during their study on biochar.

Some researchers have fabricated biochar from forestry residues. Lai et al. demonstrated the synthesis of biochar from wood chips of cedar trees by pyrolysis at 290 and 700 °C [8]. Eucalyptus tree bark and corncob were used as raw materials by Kanouo et al. to produce biochar and check its quality [9].

Karimi et al. demonstrated the use of industrial waste as a potential source for biochar production [10]. They have used industrial sewage sludge to produce biochar at two different temperatures (300 and 600 °C). Figure 1 shows a schematic representation of various sources of biochar.

3 Synthetic Routes

After the raw material is collected, certain synthetic routes like pyrolysis, hydrothermal carbonization, torrefaction and gasification are implemented to convert the raw material to biochar (as a solid product) as shown in Table 1. In this process, we also get bio-oil (as the liquid product) and biogas (as a gaseous product) in either minor or major quantities depending on the method the raw material is subjected to. The conventional methods like pyrolysis, hydrothermal carbonization, torrefaction and gasification have been discussed in detail as follows.

3.1 Pyrolysis

Pyrolysis is a decomposition reaction occurring at high temperature in presence of very little or no oxygen. Pyrolysis is the most preferable and used methods to produce biochar. It can be further bifurcated into slow, fast and microwave pyrolysis. Slow and fast pyrolysis is differentiated based on their residence time and operating temperature. Slow pyrolysis operates in a temperature range of 300–500 °C with a long residence time [11]. It yields biochar as a major product while bio-oil and biogas are obtained in minor quantities. On the other hand, fast pyrolysis is heating above 500 °C with a shorter residence time. Bio-oil and biogas are the obtained in more proportions than biochar in fast pyrolysis [6].

Microwave pyrolysis is a decomposition method where heating is done using microwave radiation. This method has certain advantages over other conventional heating (slow/fast pyrolysis) techniques such as (i) pyrolysis can be done for larger-size non-homogeneous particles, (ii) preheating and moisture removal of feedstock

are not necessary, (iii) fast and uniform heating, (iv) higher level of safety and automation, and (v) energy and cost reduction [12, 13]. Microwave pyrolysis produces lower liquid yield (bio-oil) as compared to conventional methods which is considered to be one of its drawbacks.

3.2 Hydrothermal Carbonization (HTC)

Hydrothermal pyrolysis/carbonization is also referred to as 'wet pyrolysis' because it is carried out in presence of water. In this process, the solid biomass is surrounded by water [14]. The reaction conditions (pressure and temperature) are maintained in a way to ensure that the water remains in liquid state. One of the main advantages of HTC is the low temperature requirement for this process, i.e. 160 °C and high biochar yield compared to other methods [5]. In order to differentiate the biochar obtained through pyrolysis and HTC, the end product of HTC is called 'hydrochar' [14].

3.3 Torrefaction

Torrefaction is an endothermic process of heating raw biomass at 200–300 °C in an inert atmosphere [14]. In this process, the hydroxyl groups present on the surface of biochar are eliminated which results in a biochar having hydrophobic properties [14]. The obtained biochar is also more homogeneous and has very less moisture content than the biochars obtained through other processes. The biochar obtained through torrefaction has also shown better ignition properties and grindability [15].

3.4 Gasification

In gasification, the reaction operates at temperature above 700 °C [16] in an oxidizing atmosphere. The oxidizing atmosphere is created during the reaction by addition of air, oxygen, carbon dioxide and even mixture of gases. This results in only partial combustion of the raw material. It produces syngas which a mixture of H_2, CO, CO_2 and CH_4 which can be used as fuel [14]. As the name suggests, gasification process yields maximum % of gaseous product and very less % of liquid and solid products.

The resulting biochar exhibits different properties when derived from different type of sources [2]. For example, biochar produced from animal waste has high amount of inorganic content and ash which are more suitable for heavy metal adsorption. Conversion of biomass to biochar also helps in waste management along with environment protection. Upon decay of organic materials, harmful gases such as carbon dioxide and methane are emitted and released into the atmosphere which adds

to global warming [17]. Data have shown that feedstocks used for biochar production are the most abundant renewable resources but very scarcely utilized [18]. Production of biochar from biomass leads to proper utilization of biomass as well as prevents emission of greenhouse gases. Also, by converting waste into biochar the operation cost associated with its disposal is eliminated. Thus, biomass to biochar conversion is a 'two targets with one arrow' scenario.

4 Characterization of Biochar

After preparation of biochar, it becomes inevitable to investigate the purity, composition and nature of biochar formed. For this purpose, it is necessary to gain knowledge about the physical and chemical characteristics like surface area, pore size, surface functional groups, etc., by different characterization techniques. Scanning electron microscopy (SEM), Fourier transform infrared spectrometer (FTIR), X-ray diffraction (XRD), thermogravimetric analysis (TGA) and Brunauer–Emmett–Teller (BET) are some of the methods used for characterization of biochar as mentioned in Fig. 2.

The surface functional groups like carboxyl, hydroxyl, amide, amine, etc., present on biochar can be identified by FTIR. Biochar produced at different temperatures shows unique IR spectra because of different functional groups present on their surface. SEM is used to study the surface morphology of biochar. SEM coupled with energy-dispersive X-ray spectroscopy (SEM–EDX) is used to determine numerous elements like carbon, oxygen, nitrogen, etc. present on the surface of biochar. The XRD technique is used to examine the structure and crystallinity of biochar. It also gives information regarding the pore size distribution, and also its arrangement in biochar TGA is used with an aim to analyse the thermal stability of biochar. TGA helps to study the changes in physical and chemical properties of the material as a function of increasing temperature. The surface area of biochar is analysed using

Fig. 2 Different characterization techniques used for surface, structural and molecular analysis of biochar

Surface properties

•SEM (Morphology)
•FTIR & Raman (Functional group)
•SEM-EDX (Surface elements

Structural/ molecular properties

•TGA (Thermal analysis)
•TEM & XRD (Structural arrangement)
•NMR & Raman (Structure)
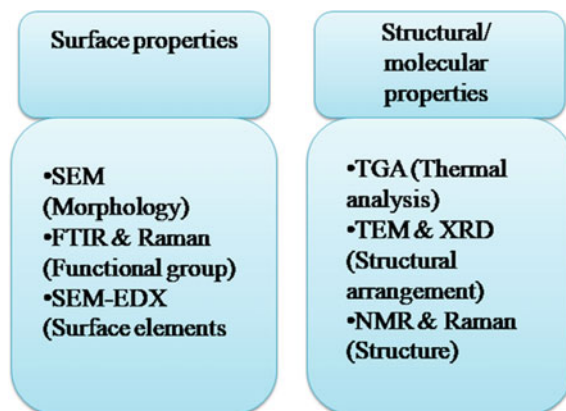
BET. It is the main property responsible for adsorption, which makes BET a very crucial characterization technique used for biochar study as an adsorbent.

5 Properties of Biochar

The adsorption capability of biochar can be attributed to its chemical and physical properties which vary from one raw material to another. The specific properties of biochar include high porosity, hydrophobicity, chemical composition, long-term stability [1], enriched surface functional groups and minerals [18], ion-exchange capacity, etc. The chemical properties of biochar depend on the composition of biochar in terms of carbon, nitrogen, sulphur and oxygen which are present in biomass in the form of hemicellulose and lignin [1]. One of most important advantages of biochar is that by treating the feedstock with suitable chemical reagent, pressure and carbonization temperature its property and composition can be tuned [1]. Studies have shown that the surface area and porosity of biochar can be increased by increasing the pyrolysis temperature. As reported by Zornoza et al. pyrolysis carried out at 300–500 °C increases hydrophobic nature of biochar while above 500 °C produces hydrophilic biochar [19]. Reports have also shown that properties of biochar also depend on the type of feedstock used. Biochar produced from solid waste and animal litter exhibits lower carbon content, surface area, volatile matter but high cation exchange capacity (CEC) compared to that produced from crop residue and wood biomass [20]. Apart from this, the pH of biochar also increases with increasing carbonation temperature [1]. Certain modifications like treatment with NaOH or KOH, addition of iron, addition of zinc, etc., can also enhance the properties of biochar. Paulina Godlewska et al. synthesized biochar at 200 °C through pyrolysis and impregnated it with Fe salt [21]. This led to increase in the positive charge on biochar surface which enhanced its sorption capacity. Thus, by using the above-mentioned methods, the characteristics of biochar can also be modified according to the pollutant we intend to treat.

6 Applications of Biochar

Biochar has been explored a lot recently because of its multifaceted application. In this review, we focus on its application as an adsorbent for environmental remediation. Biochar is a green and cost-effective method for treatment of various pollutants which are a potential threat to the environment. It is used to treat organic and inorganic contaminants of soil, water and air as illustrated in Fig. 3. Biochar has proven to be a successful adsorbent for removal of dyes, heavy metals, oil spills, pesticides, carbon dioxide, etc. Biochar has been used as an adsorbent to treat pollutants like bisphenol, crystal violet, pump oil, Pb^{2+}, etc., which are present in the industrial effluents.

Fig. 3 Applications of biochar in environmental remediation
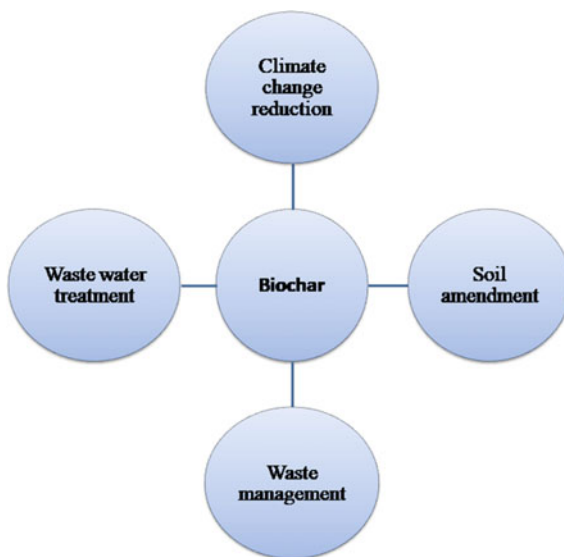
6.1 Removal of Organic Pollutants (Dyes)

Organic pollutants are the major components of industrial effluents and cause land and water pollution. Dyes, phenolic compounds, pesticides, oil spills, antibiotics, aromatic compounds, etc. are toxic to the environment, and hence, it becomes important to treat them before releasing them in the environment. Biochar is widely used as an adsorbent to treat the organic pollutants mostly found to cause water pollution. Wu et al. synthesized biochar from litchi peel and used it for the adsorption of Congo red (anionic dye) and malachite green (cationic dye) [22]. 2,4-dichlorophenol was adsorbed from water using biochar prepared from wheat husk by Kalderis et al. [23].

6.2 Removal of Heavy Metal Ions

Heavy metal ions are a type inorganic pollutant and are a serious threat to the environment. Prolonged accumulation and exposure to heavy metals are found to be fatal through a process called biomagnification [1]. Cu^{2+}, Cd^{2+}, Pb^{2+}, Zn^{2+}, Hg^+ are few examples of heavy metal ions. Among them, Cu^{2+} and Hg^+ have grabbed much attention of the researchers because of their toxicity [24]. Eliminating the hazardous pollutant through adsorption is found to be the most efficient technique compared to other techniques used. Engineered biochars have been most effective in removing heavy metal ions due to their ease of separation, large surface area and improved surface functional groups. Gan et al. have observed that biochar covered with MnO_x after modification has higher sorption capacity towards Cu^{2+}, Cd^{2+} and Pb^{2+} [25].

6.3   Adsorption of Greenhouse Gas

Around 60% of the world global warming is because of the emission of CO_2 gas [1], the levels of which are rising due to various anthropogenic activities. Climate mitigation can be done by treating the released CO_2 or controlling its emission at source. A great deal of research attention is thus been given to find a way to reduce and capture CO_2. Biochar has proved to be a boon for reducing global warming by effective adsorption of CO_2. Studies have shown that biochar produced at higher temperature had better CO_2 adsorption efficiency. Creamer et al. used biochar produced from sugarcane bagasse and hickory wood for carbon dioxide capture [26].

7   Adsorption Mechanism

As discussed, biochar is an excellent adsorbent material due to its special properties. It thus becomes important to understand the mechanism of adsorption to gain insights and improve the efficiency of the adsorbent. The interaction between molecules of the pollutant and biochar can be explained on the basis of the nature of the target molecule and properties of biochar. Certain properties of biochar such as pore size, hydrophobic nature, surface area, surface functional groups, etc. determine the mechanism involved for different pollutants. Based on the nature of the contaminants, the mechanism can be discussed for organic and inorganic contaminants separately.

Organic pollutants such as antibiotics, dyes, oils, phenols etc. tend to bind with biochar through hydrophobic interaction, pore-filling, hydrogen bond formation and electrostatic interaction [44]. The removal of inorganic pollutants, comprising mainly of heavy metals (lead, cadmium, arsenic, mercury, etc.) generally takes place via surface complexation, precipitation, ion-exchange and also electrostatic attractions. The general mechanisms involved are as follows and schematic representation for the same are shown in Fig. 4.

7.1   Complexation

Complexation involves formation of complex structures based on metal–ligand interaction. Oxygen containing functional groups (phenolic, lactonic, carboxyl, etc.) present on the surface of biochar bind with transition metals having vacant d-orbitals and high affinity for ligands. Reports have also shown that complexation is more popular in plant-derived biochar than animal-derived biochar [45].
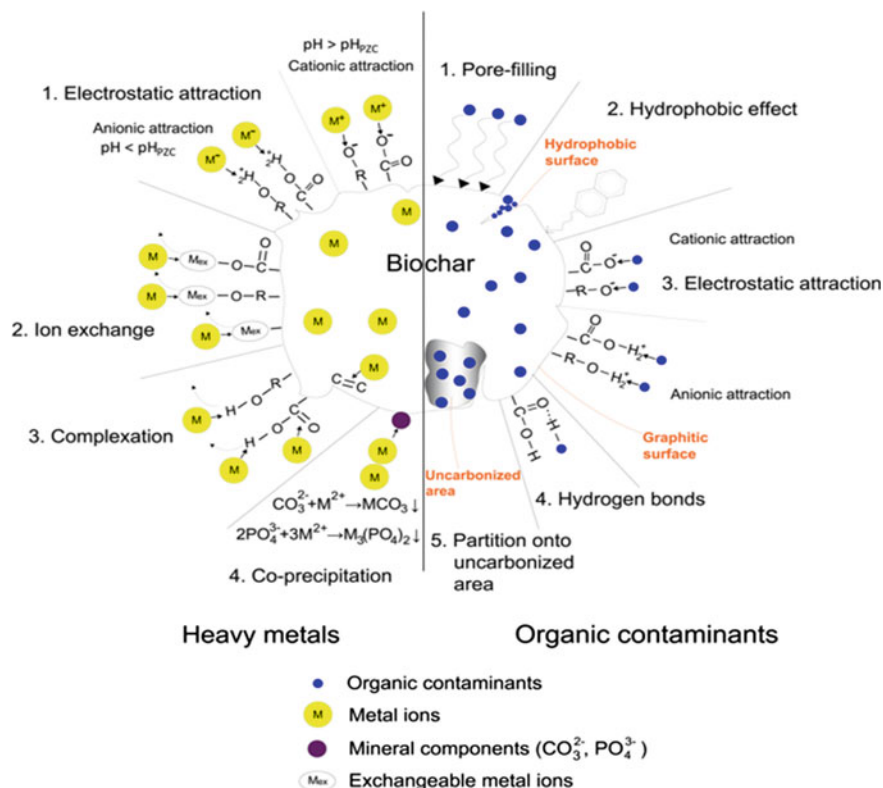
Fig. 4 Adsorption mechanism of biochar for different pollutants. (Authors: T. G. Ambaye et al., International Journal of Environmental Science and Technology, 2020 licenced under: CC by 4.0 http://creativecommons.org/licenses/by/4.0/) [46]

7.2 Precipitation

Precipitation is found to be the chief mechanism responsible for immobilization of heavy metals by biochar. It involves formation of solid either in the solution or on the surface of biochar [46]. Metals and rare earth elements such as Cu, Pb, Zn, Ni, etc., having ionization potential between 2.5 and 9.5 eV are most likely to adapt this mechanism and form precipitate at the surface of biochar [45]. When alkaline biochar are used for the adsorption, they trigger the precipitation process [47] as more electronegative binding sites which favour adsorption of cations are present on its surface as compared to pristine biochar [4].

7.3   Ion Exchange

The heavy metal ions or the cations dissolved in the solution get exchanged with ionizable protons/cations present on the surface of biochar which causes immobilization of the heavy metal ions [45]. Sorption of heavy metals through this process is called ion-exchange mechanism. It a reversible process, and the cations are exchanged in such a manner that the electrical neutrality of the solution is maintained [3]. The efficiency of this process is related to the size of the metal contaminant and the type of functional group present on the surface of biochar [45]. Fidel et al. reported that the exchange of NH_4^+ and NO_3^- on the surface of biochar obtained from red oak occurred by ion-exchange mechanism [48].

7.4   Electrostatic Interaction

Electrostatic interaction is based on the simple principle of attraction and repulsion between charges. It involves attraction between surface charged biochar and metals ions which results in immobilization of heavy metals/ionizable pollutants. The cationic-type pollutants are able to easily adsorb on the negatively charged surface of biochar due to attraction and vice versa [1]. The dominance of this mechanism is dependent on the pH of the solution containing the target molecule [45].

7.5   Hydrophobic Interaction

'Hydrophobic' means water-repelling or water-phobic. The hydrophobic nature is imparted to biochar due to lowering of amount of oxygen, hydrogen, nitrogen and sulphur as compared to carbon as a result of carbonation. The enhanced proportion of carbon in biochar is the root of hydrophobic interaction between the adsorbate and biochar [49]. The hydrophobic interaction is responsible for adsorption of oil on biochar.

7.6   Pore-Filling Interaction

One of the most significant properties of biochar is its porous network in various dimensions [35] having size distribution as micropores (<2 nm), mesopores (2–50 nm) and macropores (>50 nm). The diffusion/adsorption of the adsorbate depends on the pore size of biochar which can be controlled or altered according to the target molecule by preparation methods or modification techniques [45]. Studies have

proven that the pore-filling mechanism follows the non-linear, Langmuir-type adsorption isotherm. Adsorption of methylene blue and Bromocresol green by biochar was studied by Phuong et al. During their study, they found pore-filling interaction to be the main mechanism involved in the adsorption [50].

7.7 Hydrogen Bond Formation

Many toxic contaminants are adsorbed on the surface of biochar through hydrogen bond formation. The hydrogen bond formation takes place owing to negatively charged nature of biochar which is because of the presence of more –OH functional groups [18]. The hetero atoms present in organic pollutants form hydrogen bond with biochar. The biochar surface acts as H-acceptor, while the functional group containing hetero atom acts as H-donor. The strength of hydrogen bond is very high, and thus, it is not easy to separate adsorbate from the adsorbent after the bond formation takes place [3].

8 Summary and Future Scope

In the present study, we focused on how biochar is a cost-effective adsorbent for removal of typical contaminants causing environmental degradation. Biochar can be produced from biowaste and thus is also contributing the waste management. It has gained a lot of attention in recent years due to its application as an adsorbent in removal of inorganic and organic pollutants. A survey of literature on production of biochar revealed a wide range of raw materials that have been used for its production. Synthetic methods like pyrolysis, hydrothermal carbonization, torrefaction and gasification have also been discussed. The results obtained by various analytical techniques give information about the specific properties of biochar. The properties interpreted by data obtained from these techniques show that biochar is an excellent adsorbent. A detailed analysis of adsorption mechanism reveals that the interaction between analyte (pollutants) and biochar can take place through electrostatic attraction, hydrogen bonding, ion-exchange, hydrophobic interaction, pore filling, etc. depending upon the nature of analyte. The application of biochar in environmental remediation as an adsorbent has also been reviewed in this study. Thus, biochar has been explored by a lot of researchers because it has been deduced to be a novel and green adsorbent. Adsorption by biochar is also feasible and less expensive compared to other methods used for environmental mitigation.

Although much research has already been conducted for biochar, there are still some issues to explore further. The technical and economic aspects of engineered biochar should be explored more before its large-scale application. The adsorption mechanism has been studied deeply, but no proper investigation for desorption of

analyte has been done. Thus, more research on desorption mechanism and regeneration of biochar should be considered. Moreover, studies on biochar are mostly done at lab scale and in presence of only one analyte to be adsorbed. Therefore, adsorption by biochar in presence of more than one analyte should be studied more. The field efficiency of biochar should also be addressed in future.

References

1. Jeyasubramanian K et al (2021) A complete review on biochar: production, property, multi-faceted applications, interaction mechanism and computational approach. Fuel 292:120243
2. Amin FR et al (2016) Biochar applications and modern techniques for characterization. Clean Technol Environ Policy 18(5):1457–1473
3. Cheng N et al (2021) Adsorption of emerging contaminants from water and wastewater by modified biochar: a review. Environ Pollut 116448
4. Mahdi Z, El Hanandeh A, Yu QJ (2019) Preparation, characterization and application of surface modified biochar from date seed for improved lead, copper, and nickel removal from aqueous solutions. J Environ Chem Eng 7(5):103379
5. Hossain N et al (2020) Synthesis and characterization of rice husk biochar via hydrothermal carbonization for wastewater treatment and biofuel production. Sci Rep 10(1):1–15
6. Gopal M et al (2020) Biochars produced from coconut palm biomass residues can aid regenerative agriculture by improving soil properties and plant yield in humid tropics. Biochar 2(2):211–226
7. Sarfaraz Q et al (2020) Characterization and carbon mineralization of biochars produced from different animal manures and plant residues. Sci Rep 10(1):1–9
8. Lai W-Y et al (2013) The effects of woodchip biochar application on crop yield, carbon sequestration and greenhouse gas emissions from soils planted with rice or leaf beet. J Taiwan Inst Chem Eng 44(6):1039–1044
9. Kanouo BMD, Allaire SE, Munson AD (2018) Quality of biochars made from Eucalyptus tree bark and corncob using a pilot-scale retort kiln. Waste Biomass Valorization 9(6):899–909
10. Karimi F et al (2020) Using industrial sewage sludge-derived biochar to immobilize selected heavy metals in a contaminated calcareous soil. Waste Biomass Valorization 11(6):2825–2836
11. Lee Y et al (2013) Comparison of biochar properties from biomass residues produced by slow pyrolysis at 500 C. Biores Technol 148:196–201
12. Huang Y-F, Chiueh P-T, Lo S-L (2016) A review on microwave pyrolysis of lignocellulosic biomass. Sustain Environ Res 26(3):103–109
13. Ingole PM et al (2016) Microwave assisted pyrolysis of biomass: a review. Int J Adv Technol Eng Sci 4(6):78–84
14. Libra JA et al (2011) Hydrothermal carbonization of biomass residuals: a comparative review of the chemistry, processes and applications of wet and dry pyrolysis. Biofuels 2(1):71–106
15. Mamvura TA, Danha G (2020) Biomass torrefaction as an emerging technology to aid in energy production. Heliyon 6(3):e03531
16. Gabhane JW et al (2020) Recent trends in biochar production methods and its application as soil health conditioner: a review. SN Appl Sci 2(7):1–21
17. Hunt J et al (2010) The basics of biochar: a natural soil amendment. Soil Crop Manage 30(7):1–6
18. Tan Z et al (2020) Mechanism of negative surface charge formation on biochar and its effect on the fixation of soil Cd. J Hazard Mater 384:121370
19. Zornoza R et al (2016) Stability, nutrient availability and hydrophobicity of biochars derived from manure, crop residues, and municipal solid waste for their use as soil amendments. Chemosphere 144:122–130

20. Tomczyk A, Sokołowska Z, Boguta P (2020) Biochar physicochemical properties: pyrolysis temperature and feedstock kind effects. Rev Environ Sci Bio/Technol 19(1):191–215
21. Godlewska P et al (2020) Engineered biochar modified with iron as a new adsorbent for treatment of water contaminated by selenium. J Saudi Chem Soc 24(11):824–834
22. Wu J et al (2020) High-efficiency removal of dyes from wastewater by fully recycling litchi peel biochar. Chemosphere 246:125734
23. Kalderis D et al (2017) Adsorption of 2,4-dichlorophenol on paper sludge/wheat husk biochar: process optimization and comparison with biochars prepared from wood chips, sewage sludge and hog fuel/demolition waste. J Environ Chem Eng 5(3):2222–2231
24. Godwin PM et al (2019) Progress in preparation and application of modified biochar for improving heavy metal ion removal from wastewater. J Bioresour Bioprod 4(1):31–42
25. Gan C et al (2015) Effect of porous zinc–biochar nanocomposites on Cr (VI) adsorption from aqueous solution. RSC Adv 5(44):35107–35115
26. Creamer AE, Gao B, Zhang M (2014) Carbon dioxide capture using biochar produced from sugarcane bagasse and hickory wood. Chem Eng J 249:174–179
27. Jeong CY, Dodla SK, Wang JJ (2016) Fundamental and molecular composition characteristics of biochars produced from sugarcane and rice crop residues and by-products. Chemosphere 142:4–13
28. Yang M et al (2020) Biochar produced from cotton husks and its application for the adsorption of oil products. IOP Conf Ser Earth Environ Sci. IOP Publishing
29. AlAmeri K et al (2019) Sorption and removal of crude oil spills from seawater using peat-derived biochar: an optimization study. J Environ Manage 250:109465
30. Luyen NT, Linh HX, Huy TQ (2020) Preparation of rice husk biochar-based magnetic nanocomposite for effective removal of crystal violet. J Electron Mater 49(2):1142–1149
31. Ahmad M et al (2012) Effects of pyrolysis temperature on soybean stover-and peanut shell-derived biochar properties and TCE adsorption in water. Biores Technol 118:536–544
32. Zhao N et al (2017) Adsorption mechanisms of dodecylbenzene sulfonic acid by corn straw and poplar leaf biochars. Materials 10(10):1119
33. Liu Z, Zhang F-S (2009) Removal of lead from water using biochars prepared from hydrothermal liquefaction of biomass. J Hazard Mater 167(1–3):933–939
34. Sun L, Wan S, Luo W (2013) Biochars prepared from anaerobic digestion residue, palm bark, and eucalyptus for adsorption of cationic methylene blue dye: characterization, equilibrium, and kinetic studies. Biores Technol 140:406–413
35. Pignatello JJ, Kwon S, Lu Y (2006) Effect of natural organic substances on the surface and adsorptive properties of environmental black carbon (char): attenuation of surface activity by humic and fulvic acids. Environ Sci Technol 40(24):7757–7763
36. Chen B, Chen Z (2009) Sorption of naphthalene and 1-naphthol by biochars of orange peels with different pyrolytic temperatures. Chemosphere 76(1):127–133
37. Oh T-K et al (2012) Effect of pH conditions on actual and apparent fluoride adsorption by biochar in aqueous phase. Water Air Soil Pollut 223(7):3729–3738
38. Xu X, Cao X, Zhao L (2013) Comparison of rice husk-and dairy manure-derived biochars for simultaneously removing heavy metals from aqueous solutions: role of mineral components in biochars. Chemosphere 92(8):955–961
39. Zhang C, Lu J, Wu J (2020) One-step green preparation of magnetic seaweed biochar/sulfidated Fe0 composite with strengthen adsorptive removal of tetrabromobisphenol A through in situ reduction. Biores Technol 307:123170
40. De Jesus J et al (2017) Evaluation of waste biomasses and their biochars for removal of polycyclic aromatic hydrocarbons. J Environ Manage 200:186–195
41. Anfar Z et al (2020) Microwave assisted green synthesis of Fe_2O_3/biochar for ultrasonic removal of nonsteroidal anti-inflammatory pharmaceuticals. RSC Adv 10(19):11371–11380
42. Chen Z et al (2012) Bisolute sorption and thermodynamic behavior of organic pollutants to biomass-derived biochars at two pyrolytic temperatures. Environ Sci Technol 46(22):12476–12483

43. Shen Y-S et al (2012) Removal of hexavalent Cr by coconut coir and derived chars—the effect of surface functionality. Biores Technol 104:165–172

44. Abbas Z et al (2018) A critical review of mechanisms involved in the adsorption of organic and inorganic contaminants through biochar. Arab J Geosci 11(16):1–23

45. Inyang MI et al (2016) A review of biochar as a low-cost adsorbent for aqueous heavy metal removal. Crit Rev Environ Sci Technol 46(4):406–433

46. Ambaye T et al (2020) Mechanisms and adsorption capacities of biochar for the removal of organic and inorganic pollutants from industrial wastewater. Int J Environ Sci Technol 1–22

47. Cao X, Harris W (2010) Properties of dairy-manure-derived biochar pertinent to its potential use in remediation. Biores Technol 101(14):5222–5228

48. Fidel RB, Laird DA, Spokas KA (2018) Sorption of ammonium and nitrate to biochars is electrostatic and pH-dependent. Sci Rep 8(1):1–10

49. Murray CC et al (2019) Removal of per-and polyfluoroalkyl substances using super-fine powder activated carbon and ceramic membrane filtration. J Hazard Mater 366:160–168

50. Phuong D, Loca N, Miyanishi T (2019) Efficiency of dye adsorption by biochars produced from residues of two rice varieties, Japanese Koshihikari and Vietnamese IR50404. Desalin Water Treat 165:333–351

Novel Methods for Biofuel Production

Rajan Jaiswal and Rajat Saxena

1 Introduction

According to international energy agency, the ability of India to confirm green, economical, and sustainable energy for its expanding population is vital for their long-run economy, however, strong policies, technological leaps, and a sudden increase in eco-clean energy investment are required to avoid the type of carbon-intensive path as other countries follow. The combination of growing, industrializing, and an expanding city population would drive higher utilization of energy, raising the question of how to meet that gradually increasing demand without exacerbating concerns like import of energy, air pollution, and greenhouse gas emissions. Biofuel has gained worldwide attention thanks to its environment-friendly and benign nature. Biofuels are fascinating subjects of nature, ecological sciences, agronomy, microbiology science, mechanical, chemical engineering, and plant science [1]. Biofuels are obtained through contemporary processes from biomass (plant, algae, or animal waste) instead of a tortoise-like process for the formation of naturally occurring fossil fuels. Basically, biofuels are being obtained from photosynthetic organisms. In the process of photosynthesis, sugar formation takes place from atmospheric CO_2 by solar energy. It follows two stages:(a) light-dependent stage, where absorption of energy from light takes place and is further converted into the synthesis of ATP and NADPH, (b) light-independent stage, where the production of sugar takes place from the energy and electrons of ATP and NADPH. It is a very unique way of natural carbon fixation by the plant and green algae [2]. And if the emissions are not controlled,

R. Jaiswal
Department of Mechanical Engineering, School of Technology, Pandit Deendayal Energy University, Raisan, Gandhinagar 382426, India

R. Saxena (✉)
Department of Chemical Engineering, School of Technology, Pandit Deendayal Energy University, Raisan, Gandhinagar 382426, India
e-mail: Rajat.saxena@sot.pdpu.ac.in

Fig. 1 Nameplate capacity of India to produce biodiesel from 2011 to 2020 [6]

then these days, level of CO_2, i.e., 394.5 ppmv (parts per million volume), is being anticipated to increase above 500 ppmv by around 2050 [3]. The part of microalgae becomes important with its carbon capture and storage technique as microalgal cells do possess a high affinity for carbon dioxide molecules [4]. Also, the CO_2 fixation capability of algae can have 10–50 times more compared to land plants, and for each and every gram of algal biomass outgrowth, 1.6–2 g of CO_2 is absorbed [5]. First generation biofuels are known as conventional biofuels, whereas the other generation biofuels are called advanced biofuels. Microalgae is an advanced biofuel, and it does not set up any competition for food crop production.

The COVID-19 pandemic has strongly affected the biofuel industry. According to IEA transport biofuels, global transport biofuel production in 2020 is predicted to be 144 billion liters, equivalent to 2,480,000 barrels per day (kb/d), an 11.6% drop from 2019's record output, and that is the first reduction in two decades for yearly production. In 2019, the nameplate capacity of India to produce biodiesel was 670 million liters, as in Fig. 1. This review mainly focuses on effective methods for biofuel production and is structured as follows. Section 2 discusses the generation of biofuels depending on the biomass or feedstocks utilized. Section 3 illustrates the physical, biochemical, and thermochemical extracting techniques with the pretreatment process in detail. Section 4 presents the microalgal biomass used for biofuel and detailed harvesting techniques of microalgae. Information regarding metabolic and genetic engineering approaches for high-yield biomass products is provided in Sect. 5, whereas Sect. 6 highlights the current review.

2 Biomass and Generation of Biofuels

Biomass means any or all organic substances prevailing within the biosphere, whether it is of plant or animal origin. Plants mainly composed of celluloses, hemicellulose, and lignin are called lignocellulosic plant biomass. Their dry weight consists of approx. (10–30)% lignin, and because lignin constitutes almost 25% of the total terrestrial biomass, it represents the second most abundant renewable energy source
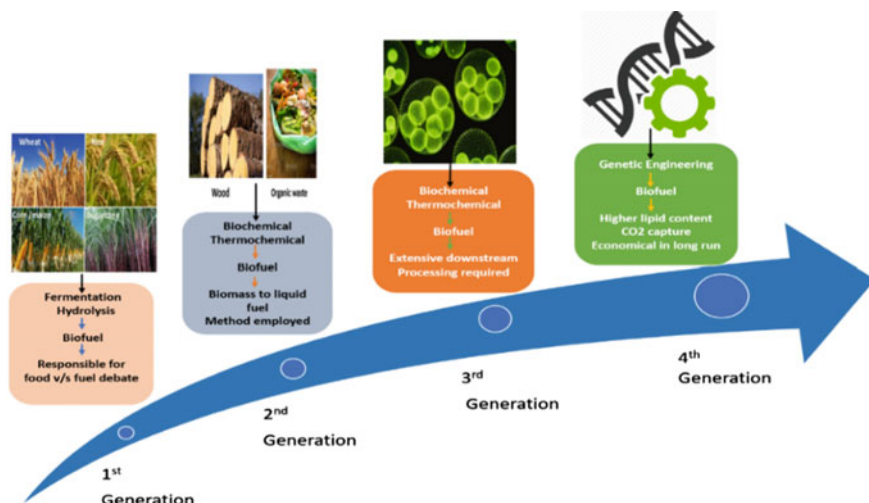
Fig. 2 Different generations of biofuels

with rising potential for production of biofuels [7, 8]. Tons and tons of lignocellulosic residues come from the forest, agriculture, and factories, which if unutilized, degrade the environment. Thus, those residues can be effectively used for the second generation of biofuels. Biofuels are classified into four different categories depending upon the biomass utilized for production, as shown in Fig. 2.

2.1 First Generation Biofuel (G1)

First generation biofuels are mainly obtained from edible food crops (starch and sugars). Its sources are grains, sugarcane, vegetable oils, maize, sugar beet, etc. Over 87% world's bioethanol obtained is from corn and sugarcane, which accounts for over 75% of the production from Brazil and the United States. This generation of biofuels is also called conventional biofuels [9, 10]. This biofuel initially showed a capability to minimize fossil fuels combustion and reduce atmospheric carbon dioxide levels. However, concerns regarding the shortage of food supply and impact on cropland aroused.

2.2 Second Generation Biofuel (G2)

Second generation biofuels, also called advanced biofuels, are obtained from non-edible lignocellulose raw materials or feedstocks as well as from all organic waste or industrial residue. It overcame the "food vs. fuels" competition problem. Moreover,

the net carbon (emitted-consumed) is neutral or even negative in the case of second generation biofuel [11].

2.3   Third Generation Biofuel (G3)

According to the IEA, third generation biofuels are bio-based fuels extracted from microalgae. These microalgae are grown in areas like wastewater, sewage, and seawater. These algae are highly applicable for genetic manipulation and suitable for genetic transformation with foreign genes [10]. It consists of high lipid and carbohydrate contents. Furthermore, they have a rapid growth rate, are eco-friendly, and help in reducing carbon dioxide levels in the atmosphere [9]. Recently, algal biomass has gained a lot of attention for producing biofuels and is considered a promising way for overcoming the global energy crisis [11].

2.4   Fourth Generation Biofuel (G4)

The fourth generation biofuels are still a developing stage, where biofuels are obtained from genetically bioengineered organisms such as microalgae, yeast, fungi, and cyanobacteria. These organisms are bioengineered for optimizing the desired biofuels production or by combining fuel production and photovoltaics, or by using special photosynthetic microbes for obtaining photobiological solar fuels. It involves the use of carbon capture and storage technique, converting it to lipids [10, 12]. The fourth generation of biofuels overcomes the inherent glitch of former generations. The methods for the fourth generation biofuels are genetic engineering and CRISPR technology for microalgal genome editing. In genetic engineering, algal strain is developed for biofuel production.

3   Biofuel Production Techniques

3.1   Mechanical Processes

Mechanical treatment like chipping or grinding of wood material and potentially following the densification of material by pelletizing the biomass comes under mechanical processes. Briquetting technology can be used to mechanically convert or densify biomass into solid biofuel [13].

3.2 Biochemical Processes

Pretreatment: Pretreatment is a process of breaking lignocelluloses into cellulose, hemicellulose, and lignin. The objectives for low-cost pretreatment operation are (a) producing highly digestible solids to enable sugar yields during enzyme hydrolysis; (b) eliminating the deterioration of sugar derived through cellulose and hemicellulose; (c) preventing the accumulation of inhibitors for hydrolysis as well as fermentation steps; and (d) to recover lignin [14]. Some factors affecting the pretreatment are feedstock types, chemical composition, biomass structure, ability to handle biomass, enzyme loading, as well as the creation of inhibitory compounds [15]. The pretreatment methods are differentiated into physical, chemical, and biological methods.

Physical methods. Physical treatment intends to expand the surface area and decrease particle size of lignocellulosic material by milling, grinding, chipping, radiation, etc. [16]. Some of the physical methods are given below:

(a) Milling or size reduction: The cellulose crystallinity is reduced using mechanical milling/grinding methods. Usually, the biomass chip size becomes (10–30)mm on chipping and (0.2–2)mm on completion of grinding [16].

(b) Ultrasound: Ultrasonic treatment breaks down and destructs the feedstock. It produces tiny bubbles which outburst cellulose and hemicellulose portions improving the efficient dislocation of cellulose into simpler homogenous sugars [17].

(c) Gamma-ray irradiation: Here, gamma rays are generated from radioisotopes (Cesium-137 or Cobalt-60) that are operated for pretreatment of lignocellulosic materials. The enzymatic hydrolysis is improved by gamma irradiation pretreatment in lignocellulosic material [17].

(d) Electron beam (EB) irradiation: In electron beam irradiation, the accelerated beam and electron irradiate lignocellulose biomass, therefore, the arrangement of cellulose, hemicellulose, and lignin are disrupted. The radicals produced in this method move freely, disrupting the arrangement of cross-link, decrystallization, as well as lowering the extent of polymerization [18].

(e) Microwave irradiation: This method breaks down cell wall and cellulosic crystallinity to improve the surface area available. Microwaves are non-ionizing electromagnetic radiation with wavelengths ranging from 1 mm to 1 m, which are seen between 300 and 300,000 MHz on the electromagnetic spectrum [19]. It can be classified into two categories which are microwave-assisted solvolysis and microwave-assisted pyrolysis. The first is performed under bland temperatures, i.e., less than 200 °C to release value-added chemicals by depolymerizing the materials, while the second is the pretreatment of lignin at higher temperatures (above 400 °C) in the absence of O_2 to transform biomass into bio-oil or biogases. Compared to conventional heating, microwave pretreatment has many advantages like fast heat transfer, uniform and selective volumetric heating performance, ease of operation, and effectiveness [17]. It is recognized that microwave heating improves enzymatic saccharification because of

its uniformity in the internal heating of big feedstock particles [20]. In a study, the effectiveness of microwave pretreatment was found better in comparison to conventional heating for the pretreatment process of mixed microbial culture to suppress methanogenic activity for optimization of biohydrogen production [21].

Chemical methods. In this pretreatment method, biomass components are broken down using different chemicals like acids, alkalis, organic solvents, ionic liquids, etc. The selected different components of lignocellulose are isolated efficiently in this method [22]. Some of the chemical methods are:

(a) Acidic pretreatments: Acidic pretreatment is a popular pretreatment process for lignocelluloses. This method is performed at high temperatures with either dilute or strong acids such as H_2SO_4, HCl, or HNO_3. It is also tested with the combination of other treatments like steam explosion [23]. Sulfuric acid is commonly used for this biomass pretreatment [24].

(b) Alkaline pretreatments: There is an effective use of alkaline (NaOH) for removing lignin. Lignin arrangement is interrupted due to reduction in crystallinity and degradation of the bond between lignin and carbohydrate since alkali pretreatment causes fiber swelling creating a larger accessible area [25].

(c) Ammonia fiber explosion (AFEX*)*: It is also called ammonia recycle percolation or soaking aqueous ammonia (ARP or SAA). Liquid ammonia is utilized to pretreat lignocellulose materials in this method. Lignocellulosic materials and liquid ammonia are heated together in an enclosed vessel for about 30–60 min at a temperature of (60 to 90) °C with 3 MPa pressure in AFEX pretreatment [17].

(d) Ionic liquid pretreatment: In this process, ionic liquid as salt is used. Some of its characteristics are strong polarity, non-volatile, difficult to oxidize, and a good solvent. Also, it can be synthesized and recovered easily. In many fields, it replaces volatile organic solvents thus, it is recognized as a green solvent [26].

Biological methods. In the biological method, microorganisms like fungi, enzymes, and bacteria are used to degrade the components of lignocellulosic biomass. It is a very effective, eco-friendly, and less energy-requiring technique in comparison with physical and chemical pretreatments.

(a) Fungi: This pretreatment method requires low energy and chemical, also reduces the release of unwanted products. For this process, brown, white, and soft-rot fungi are mostly used. White-rot fungi can produce enzymes that deteriorate lignocelluloses like lignin peroxidase. Brown-rot fungi generally attack cellulose, whereas soft-rot fungi attack lignin by producing extracellular enzymes called lignases [19, 27].

(b) Enzyme*s*: Since the enzymes are minute compared to microorganisms, enzyme pretreatment is admitted as a fast technique that can be done in a few hours. Also, enzymes carry excellent solubility, mobility, and utmost relationship to feedstock [17].

(c) Bacteria: For bacterial pretreatment, bacteria with high-hydrolytic ability is employed. *Pseudomonas, Escherichia coli, Salmonella*, etc., are capable of synthesizing celluloses as observed by some studies [17].

Saccharification: Biomasses are deconstructed or saccharified into glucose first and then converted to fuel. Saccharification is a process of converting complex carbohydrates (starch) into glucose. Acid-catalyzed hydrolysis, subcritical and supercritical water hydrolysis, and enzymatic hydrolysis are some hydrolysis methods. One impressive way to improve saccharification kinetics is the simultaneous saccharification and fermentation (SSF) process which involves combining hydrolysis as well as microbial fermentation into one step. Making emulsions from cellulose is a novel way to enhance the saccharification process to increase the exposed surface area further. The amphipathic nature of cellulose is exploited by emulsion to stably coat oil microdroplets, where the emulsifying agent between oil and water is cellulose. This increased cellulose surface area exposes cellulases enhancing the rate of hydrolysis by fourfold relative to microcrystalline cellulose hydrolysis (MCC) rate at 50 °C [28]. In the (eSSF) process, theoretical yields of cellulosic ethanol are reached very close in one day even at low temperatures of 30 °C. This eSSF technology converts cellulose to biofuel effectively using short process time and low enzyme load [27].

Enzymatic hydrolysis is the most popular saccharification method in which polysaccharides break down into monosaccharides so that they can be converted to biofuels by microorganisms. Low toxicity, low deterioration and cost, low utility cost are some advantages of enzymatic hydrolysis over other saccharification methods [29]. A recent study showed that a newly developed roller bottle system is better compared to the shake flask method to master the major hindrance due to lack of mixture, insufficient water, and sticky nature of pretreated feedstocks for various grass-based ammonia fiber expansion (AFEX) pretreated biomass [30]. A flowchart for the production of fuel from lignocellulosic biomass is shown in Fig. 3 [31].

Fermentation: This process breaks down the sugar molecules to ethanol or butanol by the use of microorganisms. A species of yeast, *Saccharomyces cerevisiae,* is being used for a long time in the ethanol industry. And recently, a research study has shown that Candida species of yeast show a similar rate of sugar consumption as S. cerevisiae and also, close to theoretical glucose to ethanol conversion yields about (~85%) at 5.0 g L^{-1} initial sugar concentration [32].

Transesterification: Transesterification is an alcoholysis process in which reaction between one mole of triglyceride molecule and 3–4 mol of alcohol produces esters and glycerol. The catalysts used in this technique are several acids like H_2SO_4, sulfonic acid, and base catalysts like sodium methoxide, sodium ethoxide, NaOH, KOH, and K_2CO_3 [33]. The basic transesterification reaction transforming triglycerides into biodiesel chemically called monoalkyl ester is illustrated in Fig. 4. Transesterification is an exchange of alcohol from an ester by another alcohol like hydrolysis with an exception of using alcohol in place of water [34].
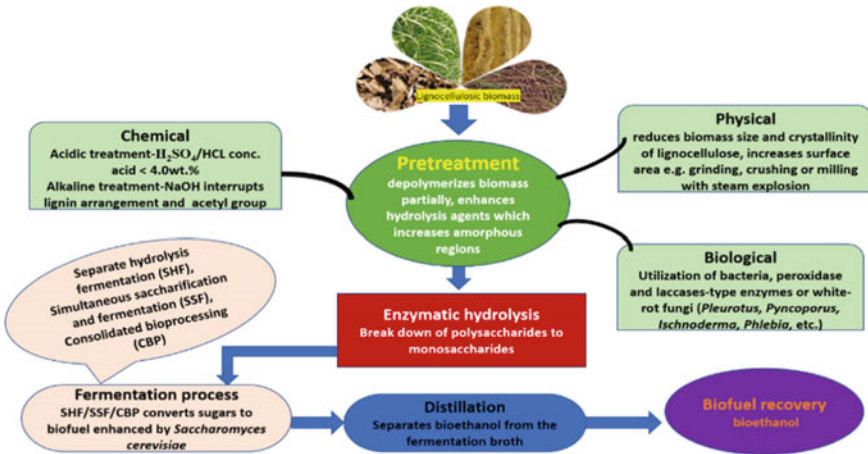
Fig. 3 Flowchart for production of biofuel (bioethanol) from lignocellulosic biomass
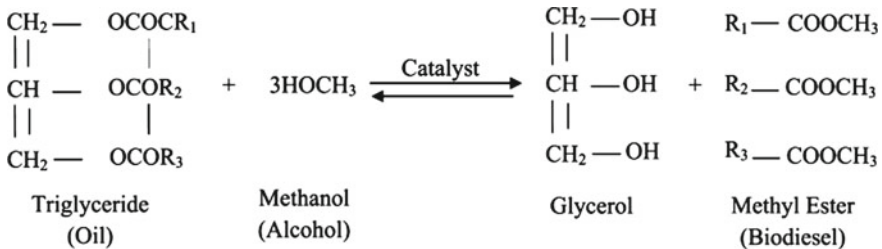
Fig. 4 Transesterification reaction of alcohol and triglycerides

3.3 Thermochemical Processes

This technology involves the process of an extreme temperature chemical reformation to break the bond reforming organic particles into biochar, synthesize gas, as well as highly oxygenated biofuel [35]. Several thermochemical processes are given below:

Gasification and liquification: The gasification technique requires heating of biomass at high temperatures (500–1400 °C), from normal air pressure to 33 bar in an O_2 deficient environment to produce flammable gas mixtures. This is a process of transforming carbonaceous constituents into a syngas consisting of carbon dioxide, hydrogen, nitrogen, carbon monoxide, methane, and other hydrocarbons [35]. The most efficient technique for hydrogen gas production from biomass is the gasification process [36].

The biomass liquefaction is performed at 250–350 °C temperature under extreme hydrogen partial pressure, generally 100–200 bar [37]. Hydrothermal liquefaction (HTL) also recognized as hydrous pyrolysis uses subcritical water (SCW) at (250–374) °C temperature range and (40–220) bar pressure to transform biomass into

bio-oil [35]. And solvent liquefaction (SL) is organic acid-based liquefaction, where solvent promotes the disintegration of biomass particles for effective conversion of biomass to biofuel [37].

Pyrolysis: Pyrolysis is the old practice of thermally decomposing biomass into solid fuel (biochar), liquid fuel, and gas which happens in absence of air at 350–550 °C temperature range, and may go up to 700 °C [38]. Three kinds of pyrolysis are slow, fast, and flash pyrolysis. In the slow pyrolysis process, 80% char remains after partly evaporation of volatiles from biomass. In fast pyrolysis, biomass particle size is less than 1 mm in a controlled temperature range (300–700) °C and heating at the rate of (10–200) °C within short residence time (0.5–10) seconds performed in the oxygen-deficient environment, where producer gas is yielded including pyrolysis oil. And flash pyrolysis is done in a very short residence of time about (100–10,000) °C per second at very extreme temperatures and biofuel is produced with 80% higher efficiency [37].

4 Microalgae for Biofuel

Microalgae have gained the world's attention as the most promising alternative source of biofuel. Basically, microalgae are photosynthetic microbes that grow rapidly accumulating protein-lipid, and high-value products such as omega-3 polyunsaturated fatty acids called EPA and DHA [39]. It is found that microalgae capture solar energy and fixes CO_2, 5–20 times higher than plant crops and terrestrial plants. They have higher biomass productivity and carbon constitutes 50% of their dry weight [40]. Microalgae are the most prolific living organisms on Earth which are feasible for genetic manipulation and inhabit different ecological habitats [41]. For the synthesis of biofuel from algae, culturing, harvesting, and extracting have to be done.

4.1 Culturing of Algae

Algae can grow naturally in rivers, lakes, and oceans similar to aquaculture. They have a high growth rate like doubling by 24 h unlike plants as they do not spend energy on the growth of their parts [33]. There are approaches to microalgae cultivation because of their potential for natural carbon assimilation since they can be grown in wastewater effectively with the capability to use sufficient carbon, nitrogen, and phosphorus in the system [42]. The major parameters affecting the physical growth of microalgae are pH, illumination, temperature, and medium of culture [33]. Commercially, microalgae are cultivated by an open pond system and enclosed PBRs such as tubular PBR, flat panel PBR, and biofilm PBR. Due to the problems like larger space, uncontrolled temperature, improper lightning with pond systems, people cultivate monocultures of algae, and engineered strains in axenic enclosed PBRs which offer low contamination possibilities [40].

4.2 Harvesting of Microalgae Biomass

Harvesting is a process of removing water content from the culture medium to concentrate the biomass of microalgae by several downstream techniques. Typically, microalgae have a tiny cell size (5–50)μm and a lower density of (0.5–5)g/L in growth media which makes it difficult for direct lipid extraction without any form of harvesting process [43]. Huge capital cost and energy input for the operation are required in harvesting techniques because of the tiny size of microalgal cells, low density, and colloidal stability [44]. Harvesting techniques can be classified into two categories: conventional method and advanced method as shown in Fig. 5. The conventional methods include sedimentation, centrifugation, filtration, and electricity-driven methods. Centrifugation is one of the popular methods, but it is highly expensive and energy-consuming. Sedimentation is unsuitable for various microalgae and is time-consuming, whereas the electrical method requires high energy consumption with costly equipment [45]. The advanced methods of harvesting are given below:

Flocculation: Flocculation is considered one of the highly effective, and least expensive harvesting techniques in comparison to others. Microalgae carry negative charges on their surface thus, flocculation uses organic and inorganic flocculants for neutralization of negative charge and increases the particle size through aggregation with increasing the rate of cell settling. Some methods of flocculation are auto-flocculation, chemical flocculation, and bioflocculation. In auto-flocculation, the increase in pH (nearly 9) destabilizes the negative charges of microalgae surface causing microalgae to flocculate and settle. Chemical flocculation is used effectively for large-scale productions. It can be classified into organic and inorganic flocculation. In organic flocculation, organic flocculants like chitosan and starch are used. In microalgae like *Chlorella vulgaris* and *Chaetoceros muelleri,* chitosan is found very effective for cell harvesting [46]. In inorganic flocculation, low pH is required to form cationic hydrolysis products. Ferric sulfate and ferric chloride are mostly used in this
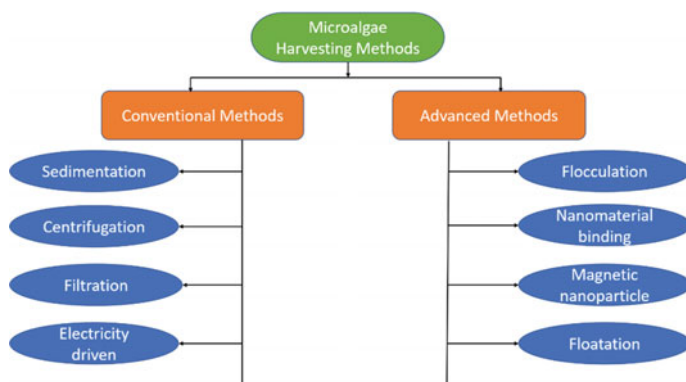
Fig. 5 Techniques of microalgae cell harvesting

Table 1 List of flocculants used for microalgae harvesting, their effect on biomass recovery (%) and Time (Min)

Microalgae	Flocculants	Biomass recovery (%)	Time (min)	Ref.
Nanochloropsis salina	Chitosan (Organic)	98	60	[45]
Chlorella vulgaris	Crushed eggshells (Organic)	98 ± 0.7	50	[45]
Chlorella vulgaris	Moringa oleifera-seed flour (Organic)	89	120	[45]
Cheatoceros gracilis	$FeCl_3$ (Inorganic)	90–95	60	[45]
Ankistrodesmus falcatus	Alum (inorganic)	86	60	[45]
Chlorella vulgaris	$Al_2(SO_4)_3$ (inorganic)	92.4	10	[45]

method and near to 99% efficiency is achieved when *Chlorella sp.* is flocculated by these inorganic flocculants [47, 48]. Some of the microalgae used for harvesting by chemical flocculation are shown in Table 1. In bioflocculation, microorganisms like bacteria, fungus, or their combination are used for microalgae biomass recovery. Naturally, bioflocculation can occur in lakes or ponds, which is caused by secreted extracellular polymer substances (EPS) [49]. Plant-based bio flocculants like gaur gam and inulin which are nontoxic and environment-friendly are also utilized for biomass recovery. Guar gam has 94% efficiency in the case of *Chlamydomonas sp.* [41, 50].

Nanomaterial cell harvesting and flotation: This is a new technology, where studies have shown that nanoparticles for cell harvesting of microalgae can be used because of their characteristics like big surface area, easier synthesis, stability in nature, ease to reuse, and remove [48]. Flocculation using nanomaterials can be an effective and economical method for biomass recovery. In the flotation technique, bubbles are created which get attached to desired particle size causing cells to concentrate and upswing to the surface.

4.3 Extraction of Oil

Oil is extracted by separating the algal product from dried biomass. Microalgal cells envelop lipids or fatty acids from, where algal oil is removed. Different physical methods (sonication, homogenizer, pulse electric field), as well as chemical methods (acid, enzymes, surfactant), are done for oil extraction after drying or dewatering of algal biomass. The extraction process is highly costly [47, 51]. The lipid extraction techniques commonly used nowadays are microwave heating, ultrasonication, osmotic shock, bead beating, lyophilization, and hydrodynamic cavitation [52].

5   Metabolic and Genetic Engineering

Microalgae have emerged rapidly as a source for genetic engineering that permits the greater availability of sequenced genomes throughout multiple algal lines. Genome decoding has facilitated the creation of genetic resources [50]. Metabolic engineering is an advanced technology that can be used to vary native strains to boost biofuel production. Metabolic engineering has improved the modification of microbial metabolic pathways as well as the extraction of many necessary chemicals required for biofuel production. Model strain by metabolic engineering is an effective tool to improve the production of biofuel from lignocellulosic feedstocks. Genetic engineering uses classical mutagenesis and recombinant DNA technology during the fermentation process linked with pathways for over-expression of the desired end product. To make metabolic engineering cost-effective, novel techniques like whole genome sequencing, system biology, bioinformatics, proteomics, and metabolomics have been developed. The applications of metabolic and genetic engineering approaches might lead to efficient use of land and biodiversity in the case of lignocellulosic biomass. The biofuel production abilities of some microorganisms enhanced by metabolic engineering are *Bacillus subtilis* for ethanol production and *Clostridium* for butanol production [31].

6   Conclusion

Biofuels have been a better alternative to fossil fuels and have received worldwide attention. The use of biofuel in transportation is very vital for reducing vehicle emissions. A broad range of biofuel production technologies has been developed and the latest advancement in major technologies has been achieved. Yet, the improvement in biochemical and thermochemical technologies is of high interest for increased production and cost-effectiveness. The waste lignocellulosic biomass from the forest, agriculture, and industries could turn out to be economical and adequate sugar sources for fuel production of the transportation sector. Utilizing recent technologies in the microalgae industry will benefit the environment and product quality will reflect the quality and living standard of society. Recent and reliable innovations in the field of genetic and metabolic engineering must be deployed for improving the biomass potential.

References

1. Malode SJ, Prabhu KK, Mascarenhas RJ, Shetti NP (2021) Recent advances and viability in biofuel production. Energy Convers Manag X 10(September):100070. https://doi.org/10.1016/j.ecmx.2020.100070
2. Rodionova MV et al (2017) Biofuel production: challenges and opportunities. Int J Hydrogen Energy 42(12):8450–8461. https://doi.org/10.1016/j.ijhydene.2016.11.125
3. Sharma S, Kundu A, Basu S, Shetti NP, Aminabhavi TM (2020) Sustainable environmental management and related biofuel technologies. J Environ Manage 273(July):111096. https://doi.org/10.1016/j.jenvman.2020.111096
4. Daneshvar E, Wicker RJ, Show PL, Bhatnagar A (2022) Biologically-mediated carbon capture and utilization by microalgae towards sustainable CO_2 biofixation and biomass valorization—a review. Chem Eng J 427(May):130884. https://doi.org/10.1016/j.cej.2021.130884
5. Nigam H, Malik A, Singh V (2021) A novel nanoemulsion-based microalgal growth medium for enhanced biomass production. Biotechnol Biofuels 14(1):1–18. https://doi.org/10.1186/s13068-021-01960-8
6. India—installed capacity biodiesel production 2020 | Statista. https://www.statista.com/statistics/1052762/india-nameplate-capcity-biodiesel-production/. Last accessed 15 Oct 2021
7. Agarwal A, Rana M, Park JH (2018) Advancement in technologies for the depolymerization of lignin. Fuel Process Technol 181(September):115–132. https://doi.org/10.1016/j.fuproc.2018.09.017
8. Mohr A, Raman S (2015) Lessons from first generation biofuels and implications for the sustainability appraisal of second generation biofuels. Effic Sustain Biofuel Prod Environ Land-Use Res 63:281–310. https://doi.org/10.1016/j.enpol.2013.08.033
9. Olguin-Maciel E, Singh A, Chable-Villacis R, Tapia-Tussell R, Ruiz HA (2020) Consolidated bioprocessing, an innovative strategy towards sustainability for biofuels production from crop residues: an overview. Agronomy 10(11). https://doi.org/10.3390/AGRONOMY10111834
10. Culaba AB, Ubando AT, Ching PML, Chen WH, Chang JS (2020) Biofuel from microalgae: sustainable pathways. Sustain 12(19):1–19. https://doi.org/10.3390/su12198009
11. Kour D et al (2019) Technologies for biofuel production: current development, challenges, and future prospects. Springer International Publishing
12. Alalwan HA, Alminshid AH, Aljaafari HAS (2019) Promising evolution of biofuel generations. Subject review. Renew Energy Focus 28(00):127–139. https://doi.org/10.1016/j.ref.2018.12.006
13. Lei T, Wang Z, Li Z, Xu J, He X, Zhu J (2013) A biomass briquetting fuel machine and its large-scale operation system. J Renew Sustain Energy 5(1):1–9. https://doi.org/10.1063/1.4781089
14. Bhutto AW et al (2017) Insight into progress in pre-treatment of lignocellulosic biomass. Energy 122:724–745. https://doi.org/10.1016/j.energy.2017.01.005
15. Sandesh K, Ujwal P (2021) Trends and perspectives of liquid biofuel—Process and industrial viability. Energy Convers Manag X 10:100075. https://doi.org/10.1016/j.ecmx.2020.100075
16. Mood SH et al (2013) Lignocellulosic biomass to bioethanol, a comprehensive review with a focus on pretreatment. Renew Sustain Energy Rev 27:77–93. https://doi.org/10.1016/j.rser.2013.06.033
17. Olatunji KO, Ahmed NA, Ogunkunle O (2021) Optimization of biogas yield from lignocellulosic materials with different pretreatment methods: a review. Biotechnol Biofuels 14(1). https://doi.org/10.1186/s13068-021-02012-x
18. Grabowski C (2015) The impact of electron beam pretreatment on the fermentation of wood-based sugars. Honor These 1–24
19. Huang YF, Te Chiueh P, Kuan WH, Lo SL (2016) Microwave pyrolysis of lignocellulosic biomass: heating performance and reaction kinetics. Energy 100:137–144. https://doi.org/10.1016/j.energy.2016.01.088

20. Diaz AB et al (2015) Evaluation of microwave-assisted pretreatment of lignocellulosic biomass immersed in alkaline glycerol for fermentable sugars production. Bioresour Technol 185:316–323. https://doi.org/10.1016/j.biortech.2015.02.112

21. Kumari D, Jain Y, Singh R (2021) A study on green pretreatment of rice straw using Petha wastewater and Mausami waste assisted with microwave for production of ethanol and methane. Energy Convers Manag X 10(December):100067. https://doi.org/10.1016/j.ecmx.2020.100067

22. Perez-Cantu L, Schreiber A, Schütt F, Saake B, Kirsch C, Smirnova I (2013) Comparison of pretreatment methods for rye straw in the second generation biorefinery: effect on cellulose, hemicellulose and lignin recovery. Bioresour Technol 142:428–435. https://doi.org/10.1016/j.biortech.2013.05.054

23. Bondesson PM, Galbe M, Zacchi G (2013) Ethanol and biogas production after steam pretreatment of corn stover with or without the addition of sulphuric acid. Biotechnol Biofuels 6(1):1–11. https://doi.org/10.1186/1754-6834-6-11

24. Barakat A, Chuetor S, Monlau F, Solhy A, Rouau X (2014) Eco-friendly dry chemo-mechanical pretreatments of lignocellulosic biomass: Impact on energy and yield of the enzymatic hydrolysis. Appl Energy 113:97–105. https://doi.org/10.1016/j.apenergy.2013.07.015

25. He Y, Pang Y, Liu Y, Li X, Wang K (2008) Physicochemical characterization of rice straw pretreated with sodium hydroxide in the solid state for enhancing biogas production. Energy Fuels 22(4):2775–2781. https://doi.org/10.1021/ef8000967

26. Tian SQ, Zhao RY, Chen ZC (2018) Review of the pretreatment and bioconversion of lignocellulosic biomass from wheat straw materials. Renew Sustain Energy Rev 91(November):483–489. https://doi.org/10.1016/j.rser.2018.03.113

27. Hoffman SM et al (2021) Cellulosic biofuel production using emulsified simultaneous saccharification and fermentation (eSSF) with conventional and thermotolerant yeasts. Biotechnol Biofuels 14(1):1–17. https://doi.org/10.1186/s13068-021-02008-7

28. Alfassi G, Rein DM, Cohen Y (2019) Cellulose emulsions and their hydrolysis. J Chem Technol Biotechnol 94(1):178–184. https://doi.org/10.1002/jctb.5760

29. Wang T, Lü X (2021) Overcome saccharification barrier: advances in hydrolysis technology. Adv 2nd Gener Bioethanol Prod 137–159. https://doi.org/10.1016/B978-0-12-818862-0.00005-4

30. Chandrasekar M et al (2021) A high solids field-to-fuel research pipeline to identify interactions between feedstocks and biofuel production. Biotechnol Biofuels 14(1):1–17. https://doi.org/10.1186/s13068-021-02033-6

31. Adegboye MF, Ojuederie OB, Talia PM, Babalola OO (2021) Bioprospecting of microbial strains for biofuel production: metabolic engineering, applications, and challenges. Biotechnol Biofuels 14(1):1–21. https://doi.org/10.1186/s13068-020-01853-2

32. Romero-Frasca E, Velasquez-Orta SB, Escobar-Sánchez V, Tinoco-Valencia R, Orta Ledesma MT (2021) Bioprospecting of wild type ethanologenic yeast for ethanol fuel production from wastewater-grown microalgae. Biotechnol Biofuels 14(1):1–10. https://doi.org/10.1186/s13068-021-01925-x

33. Ganesan R et al (2020) A review on prospective production of biofuel from microalgae. Biotechnol Reports 27:e00509. https://doi.org/10.1016/j.btre.2020.e00509

34. Abbaszaadeh A, Ghobadian B, Omidkhah MR, Najafi G (2012) Current biodiesel production technologies: a comparative review. Energy Convers Manag 63:138–148. https://doi.org/10.1016/j.enconman.2012.02.027

35. Lee SY et al (2019) Waste to bioenergy: a review on the recent conversion technologies. BMC Energy 1(1):1–22. https://doi.org/10.1186/s42500-019-0004-7

36. Ahmad AA, Zawawi NA, Kasim FH, Inayat A, Khasri A (2016) Assessing the gasification performance of biomass: a review on biomass gasification process conditions, optimization and economic evaluation. Renew Sustain Energy Rev 53:1333–1347. https://doi.org/10.1016/j.rser.2015.09.030

37. T. G. Ambaye, M. Vaccari, A. Bonilla-Petriciolet, S. Prasad, E. D. van Hullebusch, and S. Rtimi (2021) Emerging technologies for biofuel production: a critical review on recent progress, challenges and perspectives. J Environ Manage 290(May). https://doi.org/10.1016/j.jenvman.2021.112627

38. Djandja OS, Wang ZC, Wang F, Xu YP, Duan PG (2020) Pyrolysis of municipal sewage sludge for biofuel production: a review. Ind Eng Chem Res 59(39):16939–16956. https://doi.org/10.1021/acs.iecr.0c01546

39. Ummalyma SB, Gnansounou E, Sukumaran RK, Sindhu R, Pandey A, Sahoo D (2017) Bioflocculation: an alternative strategy for harvesting of microalgae—an overview. Bioresour Technol 242:227–235. https://doi.org/10.1016/j.biortech.2017.02.097

40. Suparmaniam U, Lam MK, Uemura Y, Lim JW, Lee KT, Shuit SH (2019) Insights into the microalgae cultivation technology and harvesting process for biofuel production: a review. Renew Sustain Energy Rev 115(August):109361. https://doi.org/10.1016/j.rser.2019.109361

41. Rajkumar R, Takriff MS (2016) Prospects of algae and their environmental applications in Malaysia: a case study. J Bioremediation Biodegrad 07(01):1–12. https://doi.org/10.4172/2155-6199.1000321

42. Lam TP, Lee TM, Chen CY, Chang JS (2018) Strategies to control biological contaminants during microalgal cultivation in open ponds. Bioresour Technol 252:180–187. https://doi.org/10.1016/j.biortech.2017.12.088

43. Wang Q, Oshita K, Takaoka M (2021) Effective lipid extraction from undewatered microalgae liquid using subcritical dimethyl ether. Biotechnol Biofuels 14(1):1–13. https://doi.org/10.1186/s13068-020-01871-0

44. Shuba ES, Kifle D (2018) Microalgae to biofuels: 'Promising' alternative and renewable energy, review. Renew Sustain Energy Rev 81(August):743–755. https://doi.org/10.1016/j.rser.2017.08.042

45. Vasistha S, Khanra A, Clifford M, Rai MP (2020) Current advances in microalgae harvesting and lipid extraction processes for improved biodiesel production: a review. Renew Sustain Energy Rev 110498

46. Chen G, Zhao L, Qi Y, Cui YL (2014) Chitosan and its derivatives applied in harvesting microalgae for biodiesel production: an outlook. J Nanomater 1:2014. https://doi.org/10.1155/2014/217537

47. Banerjee C, Ghosh S, Sen G, Mishra S, Shukla P, Bandopadhyay R (2014) Study of algal biomass harvesting through cationic cassia gum, a natural plant based biopolymer. Bioresour Technol 151:6–11. https://doi.org/10.1016/j.biortech.2013.10.035

48. Lee YC, Lee K, Oh YK (2015) Recent nanoparticle engineering advances in microalgal cultivation and harvesting processes of biodiesel production: a review. Bioresour Technol 184:63–72. https://doi.org/10.1016/j.biortech.2014.10.145

49. Enamala MK et al (2018) Production of biofuels from microalgae—a review on cultivation, harvesting, lipid extraction, and numerous applications of microalgae. Renew Sustain Energy Rev 94(May):49–68. https://doi.org/10.1016/j.rser.2018.05.012

50. ElFar OA, Chang CK, Leong HY, Peter AP, Chew KW, Show PL (2021) Prospects of Industry 5.0 in algae: customization of production and new advance technology for clean bioenergy generation. Energy Convers Manag X 10(June):100048. https://doi.org/10.1016/j.ecmx.2020.100048

51. Adebami GE, Kuila A, Ajunwa OM, Fasiku SA, Asemoloye MD (2021) Genetics and metabolic engineering of yeast strains for efficient ethanol production. J Food Process Eng June:1–30. https://doi.org/10.1111/jfpe.13798

52. Bharte S, Desai K (2018) Techniques for harvesting, cell disruption and lipid extraction of microalgae for biofuel production 7269. https://doi.org/10.1080/17597269.2018.1472977

Study and Assessment of Solar Drying Configurations with Storage Incorporation

Milind Dudhiya, Jaydip Parmar, Rajat Saxena, Vivek Patel, and Jatin Patel

Nomenclature

m_a	Air flow rate (kg/s)
T_i	The collector inlet air temperature (°C)
T_c	The collector outlet temperature (°C)
A_c	Area of collector (m^2)
C_p	Specific heat
I	Incident solar radiation $\left(\text{W/m}^2\right)$
M_w	Mass of water (kg)
L_w	Mean temperature of latent heat J/kg
T_f	Exit temperature of chamber °C
a, c, n	Empirical constants in models
M_O	Initial moisture content
P_t	Total energy input
P_f	The fan power
H_{fg}	The latent heat of vaporization (kJ/kg)
AH	Absolute humidity
SEC	Specific energy consumption
M_e	Equilibrium moisture content
M	Moisture content
MR	Moisture ratio
R^2	Correlation coefficient

M. Dudhiya · J. Parmar · R. Saxena (✉) · V. Patel · J. Patel
Department of Mechanical Engineering, School of Technology, Pandit Deendayal Energy University, Raisan, Gandhinagar 382426, India
e-mail: Rajat.saxena@sot.pdpu.ac.in

R. Saxena
Department of Chemical Engineering, School of Technology, Pandit Deendayal Energy University, Raisan, Gandhinagar 382426, India

MBE	Mean bias error
RMSE	Root mean square error
h_i to h_{co}	Specific enthalpy of air rises
$\phi_i = \phi_{co}$	Humidity ratio

1 Introduction

Today, people facing so many issues such as climate change, droughts, food shortage, and so on. Excessive usage of natural fuels such as coal, oil, and natural gas has a major contribution to environmental pollution, enhancing the rate of climate change over the world [1]. Water and air are the fundamental requirements for life to exist, similarly food also plays a pivotal role for survival. Drying is a crucial post-handling process for the agricultural products to improve their shelf life, thereby enhancing the quality of that product, decreasing losses during storage, and effortlessly removing water content from the products [2]. Developing countries have major issues regarding food production and preservation. The production of food is mainly dependent on technology used by a farmer. Food preservation is a dilemma for a developing country because of its impact on life cycle. It is important to take the steps to increase food supply and limit population growth, thus, reducing the wastage of food which in turn impacts the production of food, reaping, post-harvest, and marketing [3].

Solar-assisted drying is an appealing option developing nations. Generally, crops are dried by the sun. The drying of agricultural goods is the most essential post-handling activity. The farmers can keep reasonably steady pricing for their products, while minimizing post-harvest losses and lowering the shipping expenses because water content is removed thus, reducing its overall mass. Direct sun drying requires a large space and is extremely dependent on solar radiation [4]. Also, the nutrition value of the crop is compromised due to the temperature of direct solar drying. An effective method is to use indirect system with storage incorporation to check the temperature from rising beyond a certain limit. The advantages of using storage-based drying technology have been discussed in this present study, followed by detailed comparison using the available data in the literature.

2 Types of Solar Dryer

Figure 1 summarizes different types of dryers that are used for crop drying in various configurations. Open sun drying is cheap and preferred mostly in the developing countries, however, this compromises on the quality of the dried products, reducing its cost and benefits significantly. Thus, use of dryers is preferred which can be operated in passive mode. Another option is to use controlled drying which is relatively costlier
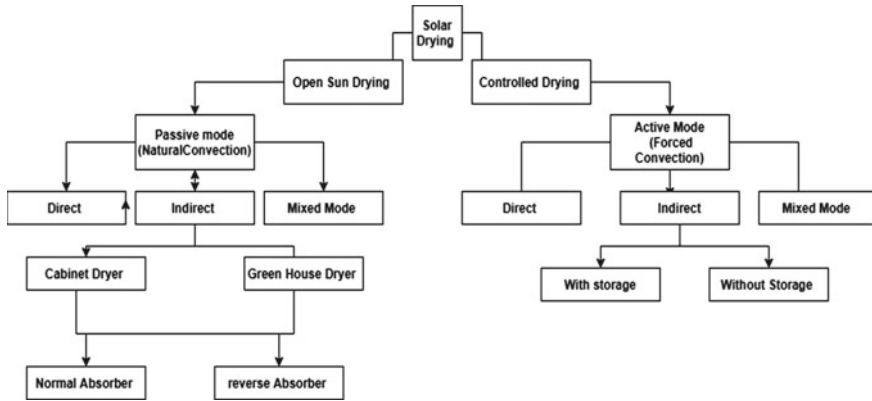
Fig. 1 Types of dryer

but the quality and nutrition value of the product can be preserved. This drying method utilizes forced mode which can be coupled with storage for improved dried food quality and characteristics.

2.1 Open Sun Dryer

The farmers in developing country generally utilize open-type solar dryers regularly. This type of dryer is readily available and is simple to construct. Drying in a solar dryer is a safer option than open sun drying. This way of drying of product is more efficient. Open-air drying is affected by environmental factors such as solar radiation, wind, and many others [5]. The quality of product in an open-type solar dryer is degraded due to climatic parameters such as rain, dust, wind, material losses due to birds and animals, insect infestation, decomposition, and fungal. Solar dryers with an open design are intended for use on a moderate scale. Dried food cannot be supplied in the worldwide market due to inadequate product quality. Drying any commodity, such as fruits or vegetables, takes a long period, and ongoing losses are possible. This is a labor-intensive technique that necessitates a big area [3] (Figs. 2 and 3).

2.2 Direct Solar Dryer

On a large scale, this kind of dryer is used. It comprises of a drier chamber, solar panels, fan, and absorber. The direct sun dryer's material is made of transparent plastic. The sun directly heats the material in a direct solar drier, and heat is generated by the greenhouse effect. As black color absorbs maximum amount of solar energy, the drier chamber's panels are usually painted black. Solar panels are installed to

Fig. 2 Working of open sun dryer [6]
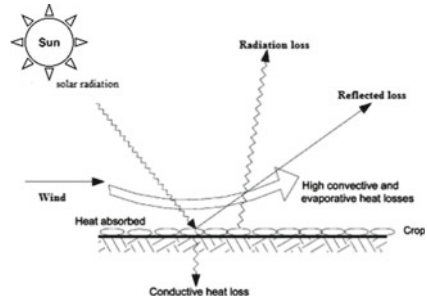
Fig. 3 Working construction of direct dryer [7]
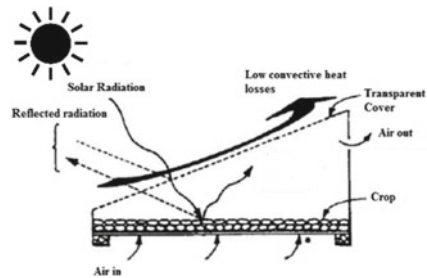
power the fan, used to provide air circulation. Ambient air passes from one end of the solar intake is heated by solar radiation, and then passes along the length of the drying chamber. The materials to be dried are placed on top of the trays. The product should be protected and heat loss should be reduced with the help of the transparent cover. To remove evaporated water, the air sucked in forces the humid air from the dryer. However, this also leads in loss of the thermal energy. Insect infestation cannot be avoided in this type of solar dryer [8]. Advantages of direct solar dryer: (1) No caramelization, (2) no heat damage, and (3) acceleration of the drying rate, because of forced air.

2.3 Indirect Solar Dryer

In case of indirect solar dryers, the items are not exposed to direct sunlight thus, nutrition value is intact. Surrounding air, a collector coupled to a drying chamber, and a ventilator, comprises of this solar drying setup. Solar radiation falling on the collector heats the sucked air which is then supplied to the drying chamber. The material to be dried is put on a vertical stack of trays in the drying chamber. On a small scale, this form of solar dryer is employed. Heated air is turned into hot humid air in an indirect sun drier, which flows towards the outlet. This solar dryer is superior to others since it solves energy balance equations without difficulty. It also outperforms other types of dryers that are housed in cabinets [9]. Compared to other

Fig. 4 Forced convection solar dryer

dryers, the evaluation of an indirect solar dryer under unfavorable weather conditions is good [10]. There are also some disadvantages of these type of dryers such as it requires more initial cost and need maintenance after particular period of time [11]. Advantages of indirect solar dryer: (1) The texture and property of food crops are similar to samples of new crops. (2) Losses of heat are reduced significantly, by insulating the drying chamber [12]. (3) Evaluation of the indirect solar dryer is better compared to direct type solar dryer. (4) Achieve higher moisture removal at faster rate (Fig. 4).

2.4 Mixed-Mode Solar Dryer

The forced mode dryer may or may not have flexibility to be used as a mixed-mode solar dryer. The materials used in this dryer are readily available in the local market, and the cost of those materials is moderate. The radiation collector (air warmer), drying chamber, and trays are all significant parts of the dryer. It consists of a flow section, which includes an inlet valve, a flow meter, and a centrifugal blower which sucks the ambient air and forces it over the collectors for heating and this heated air is then supplied to the drying chamber. With the use of an orifice meter along with an inclined manometer, the mass flow rate of air at the duct's output can be measured. The solar collector is made up of an airflow channel and a transparent cover called gazing. During the drying process, this dryer has an inclined moisture content ratio. There are also some disadvantages of these type of dryers such as quantity of dried product obtained over a year is reduced compared to indirect type of dryer and cost required for maintenance, capital cost required, is higher [11].

2.5 Natural Convection Solar Dryer (Passive Mode Solar Dryer)

The dryer also has a natural convection solar dryer. This dryer structure is consisted three primary parts: a solar collector, a drying bin, and a solar chimney. This kind of dryer is suited for small-scale projects and wooden boxes with top and bottom vents. The disadvantages of the boxes that link a large solar air heater to south-facing plastic windows and a black metal absorber. Food and vegetables are arranged on top of the screening frames that are positioned among the boxes. The black metal absorber heats the air that flows into the solar air heater. Warm air rises past the meal and escapes via the top vents. It is feasible to dry food in one day with this dryer, however, the weather is hazy, humid, and partially cloudy. The food drying temperature range in this drier is 130–180°F (54–82 °C), and it is generated with ease. Thirteen racks inside the dryer hold a lot of dried fruits and vegetables. Solar dryers with natural convection have a limited capability for drying agricultural products. The rate of drying is determined by the weather. Inside small floats continuously decrease the quality of drying products in bad weather circumstances [13]. Advantages of natural convection solar dryer: (1) simple construction and easily available, (2) capital and running cost low, and (3) it has been used for materials among low temperature required.

2.6 Forced Convection Solar Dryer (Active Mode Solar Dryer)

This forced convection drier requires a power source to operate the fans that generate the airflow, hence, it cannot be utilized in a poor country. Because the collector at one end of the dryer is connected horizontally with a fan and the drying bin at the other end, this type of dryer does not require any slope for flowing air. Furthermore, the forced convection drier does not require solar energy because it generates its airflow and can be designed to work in any weather situation, but the natural convection dryer cannot. With the use of a fan, convection is forced over the food. The addition of a forced convection flow, such as that generated by a PV-solar cell coupled to a fan, will reduce food loss. In developing countries, this type of drier would not be used. Advantages of forced convection solar dryer: (1) less drying time compared to passive solar dryer, (2) freedom from atmospheric conditions, and (3) drying is possible with and without a fan.

3 Drying Kinetics

3.1 Thin Layer Solar Drying

All commercial dryers use thin layer drying concepts. By replacing moisture content for temperature, Newton's law is illustrated. It is mostly used to figure out constant values for drying or rewetting empirical equations using a thin layer. The air conditions (pressure, flow, temperature, and humidity) are kept constant during the drying process, and the sample weight is measured at regular intervals to determine the moisture content. These laboratory tests can also determine the evacuated air, such as temperature and moisture, which can aid in the validation of heat and mass balance calculations. Under continuous drying conditions, such as air temperature.

3.2 Deep Bed Solar Drying

These dryers are rectangular warehouse-style silos or bins with ductwork or artificial flooring that force air through them. The volume of the drying zone varies based on the temperature and humidity of the entering air, the grain's moisture content, and the air velocity. It is possible to dry grains from a depth of up to 3.5 m. The first zone to be reached by air is the bottom zone. Because air has high moisture carrying capacity, drying takes a long time. The moisture content of the air increases as it rises to higher altitudes, while the drying rate decreases as it cools due to evaporation. As a result, a relative humidity (RH) and temperature (t) gradient between the lower and upper zones are created, which is a measure of the drying rate. The speed of drying is determined by airflow rate, drying air temperature, and bed depth. Modifying settings allow for a reasonable drying operation in the lower material zone without over-drying. Figures 5 and 6 shows the schematic of thin layer drying and deep bed drying used drying of agricultural commodities.

Fig. 5 Construction of thin layer dryer
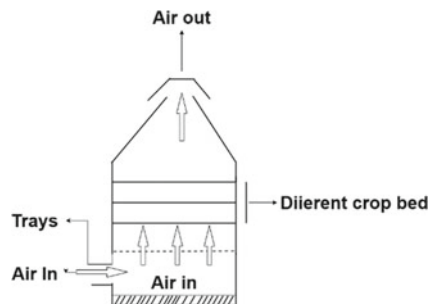
Fig. 6 Construction of deep
bed drying
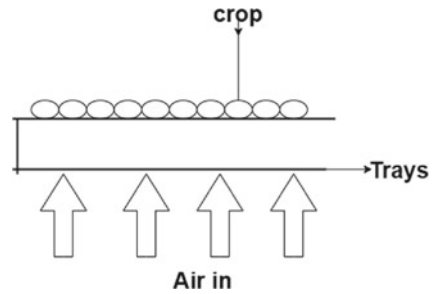
4   Storage-Based Solar Drying

4.1   Need of Storage in Dryers

Storage is an important aspect of any dryer since it helps to store solar radiation for
drying fruits, vegetables, and fish. Once the sun rays have passed, the stored energy
must be used to dry the contents of the chamber. The product's quality should be
preserved with the help of storage, and the product's quality would be given to the
international market. Storage will control the content of moisture, time, and drying
pace of any crops. Solar radiation is also stored using phase transition materials. Due
to PCM, the temperature of the drying chamber would be stable for drying all crops.

  PCMs are available in temperature ranges ranging from -22 °C to +195 °C
or higher. According to the application, four various temperature ranges: short-
temperature range (-25 °C to +10 °C) for local and private enterprise refrigeration;
moderate level temperature range (+5 °C to 40 °C) for heating and cooling applica-
tions in construction; average temperature range (+45 °C to +90 °C) for solar-based
heating, warm water, and electronic applications; and high—up temperature range
(+90 °C to + 230 °C) is used solar thermal power generation applications [14].

4.2   Storage Material Classification and Its Types

Figure 7 shows different types of storage materials that can be used for different
applications. In perspective of solar drying, sensible and solid–liquid PCMs are
most suited for the purpose.

4.3   Storage Dryer with Sensible Heat Storage

The temperature of a storage medium, such as water, oil, or ceramic materials, is
varied to achieve SHS. A material's specific heat capacity influences how much
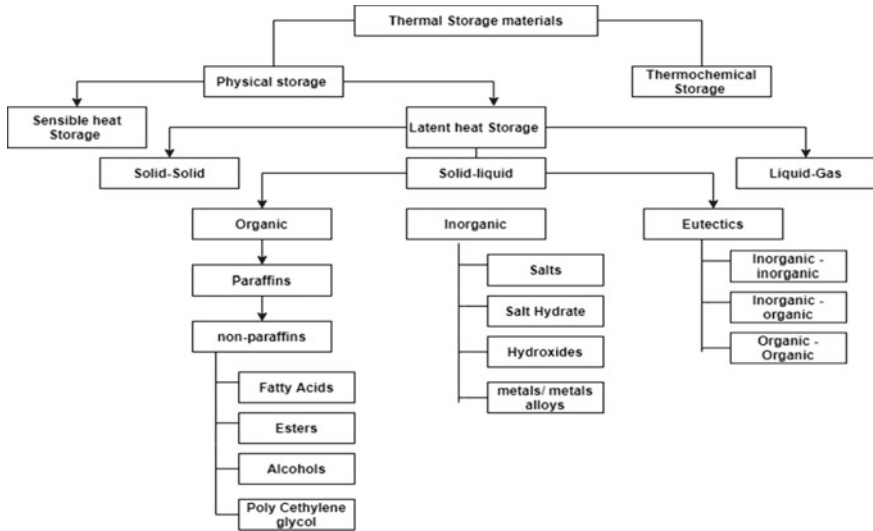
Fig. 7 Classification of storage materials

heat it can store. The changing temperature has a direct relationship with temperature in this study. Industrial and domestic water heaters, as well as warm water storage overheating networks, have commercialized sensible heat storage. Furthermore, high-thermal capacity building materials may store a lot of energy for months at a time. The downsides of SHS include a low-thermal density and a decrease in energy at any temperature [1].

Thermal energy is stored in sensible heat storage by raising the temperature of a liquid or solid, using the heat capacity consistently, and altering the temperature of materials between boosting and non-boosting. The stored heat is determined by medium-specific heat and temperature fluctuations. The water looks like the greatest sensible heat storage material available because it has high specific heat. Above 100 °C, molten salts, oils, and liquid metals, among other things, are used. Rock bed storage materials are employed for air heating applications [15].

4.4 Storage Dryer with Latent Heat Storage

Thermal energy is stored in the form of latent heat. Heat transfer occurs when a phase transformation occurs in a substance, such as molten salt, paraffin, or water/ice, within a certain and very narrow temperature window (LHS). Material selection can tune the temperature for heat capturing or release, and phase transitions in the crystalline structure can be solid–liquid (melting and freezing), liquid–gas (evaporation and condensation), or solid–solid. For material structure management, the stored energy

was linked to chemical bonds. As a result, LHS has a larger energy storage density than SHS and is thus significantly more efficient [2].

LHS occurs when a storage substance changes phase from solid to liquid, liquid to gas, or gas to liquid at a relatively constant temperature [15].

5 Thermal Modeling in Different Dryer Configurations

5.1 Indirect Solar Dryer

5.1.1 Flat Plate Collector Efficiency

The efficiency of the flat plate collector is illustrated by variables like speed, ambient temperature (TA), humidity, and so on. The following equation is used to calculate collector efficiency [16].

$$\eta_c = \frac{mac_p(T_{co} - T_i)}{A_c I} \tag{1}$$

Here, m_a is the airflow rate (kg/s), T_i and T_{co} are the collector inlet and outlet air temperature (°C), A_c is collector area (m^2), and c_p is the specific heat $\left(W/m^2\right)$.

5.1.2 Drying and Psychometric

The decrease of moisture to acceptable levels is part of the food drying process. For long-term preservation, moisture content must be lowered to a certain level, which varies with various fruits and vegetables. The energy required for drying Q_d is calculated using the following formula [17]:

$$Q_d = m_a c_p\left(T_{co} - T_f\right) = m_w L_w \tag{2}$$

Here, m_w is the mass of water removed in kg, L_w is latent heat at a mean temperature $\left(T_{co} + T_f\right)$ in J/kg, and T_f is the temperature at the exit of the chamber in °C.

If m_w is the amount of water that evaporates in time (t), the power absorbed by the product (q) is given by Eq. 3 [17];

$$q = \frac{mac_p\left(T_{co} - T_f\right)}{t} \tag{3}$$

During air heating in the collector, specific enthalpy of air rises from h_i to h_{co}, and humidity ratio $\phi_i = \phi_{co}$ remains constant. In the drying chamber, drying air absorbs the moisture from the product, and hence, humidity ratio changes from ϕ_{co}, and ϕ_f.

The mass of air needed for the moisture removal process can be calculated using [17]:

$$m = \frac{mw}{\left(\phi_f - \phi_{co}\right)} \tag{4}$$

The thermal power needed to heat the air from the absorber plate is given by Eq. 5 [17],

$$q = m(h_{co} - h_i) = \eta A_c I \tag{5}$$

5.1.3 Drying Efficiency

It is the percentage of energy given to the wet product that is used to remove moisture from the product. The drying efficiency can be calculated as follows:

$$\text{For natural convection, dryingefficiency (\%), } \eta d = \frac{m_w h_{fg}}{A_c I} \tag{6}$$

$$\text{For forced convection, dryingefficiency (\%), } \eta d = \frac{m_w h_{fg}}{\left(A_c I + p_f\right)} \tag{7}$$

where h_{fg} is the latent heat of vaporization (kJ/kg) and p_f is the fan power.

5.1.4 Pickup Efficiency

The pickup efficiency helps to quantify the moisture lost by the crops and given as in Eq. 8 [18].

$$\eta_p = \frac{\text{AH}_o - \text{AH}_i}{\text{AH}_{as} - \text{AH}_i} \tag{8}$$

where AH is absolute humidity. Specific energy consumption (SEC) is the ratio of total energy input (P_t) to the quantity of water rejected from the wet product.

$$\text{SEC} = \frac{P_t}{m_w} \tag{9}$$

Table 1 Mathematical models for moisture ratio

Model equation	Name	References
$MR = \exp(-kt)$	Newton	W. K. Lewis [19]
$MR = \exp(-kt^n)$	Page	G. E [20]
$MR = a\exp(-kt) + c$	Logarithmic	A. K. Karthikeyan a,S. Murugavelh [21]

5.2 Mixed-Mode Solar Dryer

The moisture ratio of an agricultural product is determined as follows:

$$MR = \frac{M_t - M_e}{M_i - M_e} \tag{10}$$

M_t is the moisture content at any specific time, M_i is the initial moisture content, and M_e is the equilibrium moisture content.

Three generally utilized mathematical models for investigating the moisture ratio at time duration were employed to validate the experimental outcomes. Table 1 shows the mathematical models and equations that go with them. Each model's coefficient of determination (R^2) and constant coefficients is obtained when a regression line is fitted to the experimental data. A conclusion was reached after a study on the solar drying of pepper. As a result, the experimental results have been confirmed. The following is a mathematical model for the moisture ratio of pepper.

6 Performance Evaluation

Data available in literature [22] for 'pepper' has been utilized to understand the drying kinetics based on the identified models and results of moisture ratio are being compared and shown in Fig. 8 for without storage case and Fig. 9 for with storage case. It is observed that page model is best fit for without thermal storage case. This is derived based on the calculated values for co-relation coefficient (is high), MBE (lowest) and RMSE (lowest) values. It is also observed that of the selected models, logarithmic model is best fit for simulating storage-based drying process. Details of co-relation coefficient and error values for both the cases have been evaluated and tabulated as given in Table 2.

It is observed that for storage-based drying, moisture ratio is reduced even during off-sunshine hours. This results in reduction drying time from 54 to 30 h. Thus, overall drying hours are significantly reduced. This also implies higher output of dried product in the given time. It is also observed as mentioned earlier the dried product quality is also better due to better temperature control. The food texture, color, and nutrition value are retained ensuring high quality dried product.
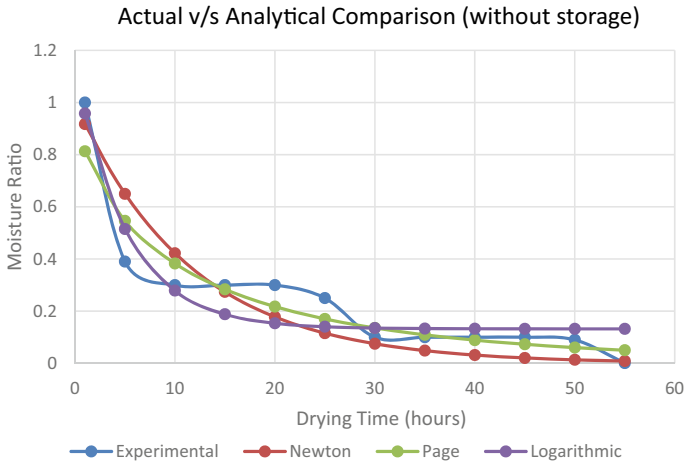
Fig. 8 Comparison of moisture ratio content experimental versus analytical models (without storage)
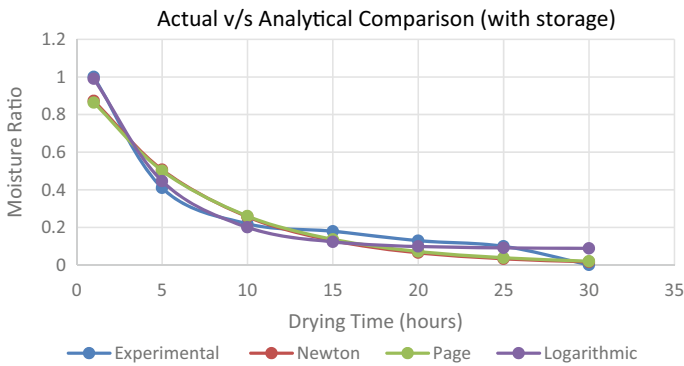
Fig. 9 Comparison of moisture ratio content experimental versus analytical models (with storage)

7 Conclusion

This study provides a comprehensive review on various types of solar dryers along with construction details and drying kinetics used for removing moisture levels from the product. It also highlights different storage materials that can be utilized in combination with the solar drying process. It has been observed that for conventional drying (without storage), for pepper, it takes 54 h compared to 30 h for storage-based drying process. Thus, the drying time is significantly reduced. The actual reduction in the moisture ratio with respect to time has been also compared to the moisture ratio calculated analytically for the two cases, i.e., with and without storage, for 'pepper'. The results show that page model shows agreeable results for, without storage-based

Table 2 Statistical results for 'pepper' for various models

Model name	Model constant	Correlation coefficient (R^2)	MBE	RMSE	
Newton	$k = 0.086311$	0.984454	0.011902	0.109096	Without storage
Page	$k = 0.206846$ $n = 0.666893$	0.990749	0.007083	0.084158	
Logarithmic	$a = 1.000919$ $k = 0.19207$ $c = 0.132027$	0.990501	0.007273	0.085279	
Newton	$k = 0.13591$	0.990842	0.00545	0.073823	With storage
Page	$k = 0.146351$ $n = 0.96326$	0.99091	0.00541	0.073551	
Logarithmic	$a = 1.137048$ $k = 0.230961$ $c = 0.08797$	0.996702	0.001963	0.044302	

drying, whereas the logarithmic model is more accurate to simulate storage-based drying.

References

1. Elias CN, Stathopoulos VN (2019) A comprehensive review of recent advances in materials aspects of phase change materials in thermal energy storage. Energy Procedia 161:385–394. https://doi.org/10.1016/j.egypro.2019.02.101
2. Leon MA, Kumar S, Bhattacharya SC (2002) A comprehensive procedure for performance evaluation of solar food dryers. Renew Sustain Energy Rev 6(4):367–393. https://doi.org/10.1016/S1364-0321(02)00005-9
3. Tiwari S, Tiwari GN, Al-Helal IM (2016) Development and recent trends in greenhouse dryer: a review. Renew Sustain Energy Rev 65:1048–1064. https://doi.org/10.1016/j.rser.2016.07.070
4. Fudholi A, Sopian K, Ruslan MH, Alghoul MA, Sulaiman MY (2010) Review of solar dryers for agricultural and marine products. Renew Sustain Energy Rev 14(1):1–30. https://doi.org/10.1016/j.rser.2009.07.032
5. Panwar NL, Kaushik SC, Kothari S (2012) State of the art of solar cooking: an overview. Renew Sustain Energy Rev 16(6):3776–3785. https://doi.org/10.1016/j.rser.2012.03.026
6. Jain D, Tiwari GN (2003) Thermal aspects of open sun drying of various crops. Energy 28(1):37–54. https://doi.org/10.1016/S0360-5442(02)00084-1
7. Visavale G (2021) Principles, classification, and selection of dryers. Handb Ind Dry (August):29–58. https://doi.org/10.1201/9781420017618-11
8. Esper A, Mühlbauer W (1998) Solar drying—an effective means of food preservation. Renew Energy 15(1–4):95–100. https://doi.org/10.1016/s0960-1481(98)00143-8
9. Mustayen AGMB, Mekhilef S, Saidur R (2014) Performance study of different solar dryers: a review. Renew Sustain Energy Rev 34:463–470. https://doi.org/10.1016/j.rser.2014.03.020
10. Sharma VK, Colangelo A, Spagna G (1993) Experimental performance of an indirect type solar fruit and vegetable dryer. Energy Convers Manag 34(4):293–308. https://doi.org/10.1016/0196-8904(93)90114-P

11. Sontakke MS, Salve SP (2021) Solar drying technologies: a review. Renew Sustain Energy Rev 16(5):2652–2670 [Online]. Available: http://www.sciencedirect.com/science/article/pii/S1364032112000081
12. Sharma M, Atheaya D, Kumar A (2021) Recent advancements of PCM based indirect type solar drying systems: a state of art. Mater Today Proc 47(xxxx):5852–5855. https://doi.org/10.1016/j.matpr.2021.04.280
13. (1996) Technical note experiments on a new small—scale solar dryer. pp 2–6
14. Du K, Calautit J, Wang Z, Wu Y, Liu H (2018) A review of the applications of phase change materials in cooling, heating and power generation in different temperature ranges. Appl Energy 220(October):242–273. https://doi.org/10.1016/j.apenergy.2018.03.005
15. Bal LM, Satya S, Naik SN, Meda V (2011) Review of solar dryers with latent heat storage systems for agricultural products. Renew Sustain Energy Rev 15(1):876–880. https://doi.org/10.1016/j.rser.2010.09.006
16. Akpinar EK (2010) Drying of mint leaves in a solar dryer and under open sun: modelling, performance analyses. Energy Convers Manag 51(12):2407–2418. https://doi.org/10.1016/j.enconman.2010.05.005
17. Ayensu A (1997) Dehydration of food crops using a solar dryer with convective heat flow. Sol Energy 59(4–6):121–126. https://doi.org/10.1016/S0038-092X(96)00130-2
18. Fudholi A, Sopian K, Bakhtyar B, Gabbasa M, Othman MY, Ruslan MH (2015) Review of solar drying systems with air based solar collectors in Malaysia. Renew Sustain Energy Rev 51:1191–1204. https://doi.org/10.1016/j.rser.2015.07.026
19. Lewis WK (1921) The rate of drying of solid materials. Ind Eng Chem 13(5):427–432. https://doi.org/10.1021/ie50137a021
20. Cockcroft DW, Nair P (2012) Methacholine test and the diagnosis of asthma. J Allergy Clin Immunol 130(2):556. https://doi.org/10.1016/j.jaci.2012.05.050
21. Karthikeyan AK, Murugavelh S (2018) Thin layer drying kinetics and exergy analysis of turmeric (*Curcuma longa*) in a mixed mode forced convection solar tunnel dryer. Renew Energy 128:305–312. https://doi.org/10.1016/j.renene.2018.05.061
22. Azaizia Z, Kooli S, Hamdi I, Elkhal W, Guizani AA (2020) Experimental study of a new mixed mode solar greenhouse drying system with and without thermal energy storage for pepper. Renew Energy 145:1972–1984. https://doi.org/10.1016/j.renene.2019.07.055

Corrosion Inhibitors in Oil and Gas Industry—A Critical Review

Adarsh Kumar Arya, Rishi Jain, and Sachin Bisht

1   Introduction

Corrosion is the degradation of metals induced by corrosive water conditions [1]. It is a never-ending and expensive issue that's frequently impossible to solve entirely. Corrosion has long been a significant issue in industries, with consequences similar to a natural disaster. Consistent corrosion causes plant shutdowns, costly maintenance, and resource loss. Corrosion impacts safety standards and is a reason for slow technological progress [2]. According to estimates, the industrial loss due to corrosion is in the trillions of dollars and is a worldwide issue to the sectors such as irrigation, oil and gas, mining, food industries, and several others. In the oil and gas industry, pipelines are the most commonly used methods to transport oil and gas [3–11]. However, one of the major concerns is the safety of pipeline grids.

According to the European Gas Pipeline Incident Group's most recent study, an external attack is to blame for 49.6% of all pipeline ruptures. Other reasons for accidents include corrosion (15%), building (16%), valve release by accident (4.6%), landslides (7.3%), and others (6.7%) [12, 13]. Corrosion in the pipeline sector has amounted to a multibillion-dollar problem. A large expenditure is spent each year on expensive designs to guard against these losses. Corrosion expenses are projected at $1.372 billion annually, including the cost of surface pipes and facilities ($589 million), down-hole tube costs ($463 million), and capital expenditures connected with these activities [14]—stress concentrations around a fault cause approximately 90% of pressure pipe failures.

Among the most often used materials in manufacturing, steel alloys and derivatives are most exploited all over the globe. Withstanding acidic conditions causes significant corrosion damage to these materials. Carbon steel possesses exceptional

A. K. Arya (✉) · R. Jain · S. Bisht
Department of Chemical Engineering, School of Engineering, University of Petroleum and Energy Studies, Energy Acres Building, Bidholi, Dehradun 248007, India
e-mail: akarya@ddn.upes.ac.in

mechanical and physical properties. In typical severe circumstances, its low corrosion resistance is the primary problem. Acidic solutions are widely used in chemical companies for various processes such as pickling cleaning, ultimately creating severe corrosion issues. Steel reacts to produce an oxide layer on the metal surface when exposed to oxidizing acids such as HNO_3. This layer prevents initial contact between metal and acid. While the metal–acid connection is re-established, the brittle oxide layer continuously exfoliates, and the metal surface dissolves severely, leading to significant corrosion. Steel undergoes a chemical process that produces iron salts (such as $FeCl_2$) as a corrosion byproduct in the presence of non-oxidizing acids (e.g. HCl).

On the other hand, steel is attacked by corrosion when it comes into contact with H_2SO_4, resulting in $FeSO_4$ production [15, 16]. Complete eradication of corrosion would be difficult and impractical. Steel may be protected against corrosion in several different ways. Modification of materials and environments, protective coatings, cathodic protection, and corrosion inhibitors are all examples of corrosion control techniques. Figure 1 shows the popular corrosion prevention methods.

Some methods eliminate moisture and oxygen from the metal surface, while others permanently coat the metal surface. However, other methods include converting an anodic element into a cathode. Several limitations limit the applicability of current practices. Modification of materials is frequently tricky and expensive. Changing the process environment is impossible since the metal must be exposed to a specific reactive medium in many industrial applications. Some techniques (coating, for example) may cause excessive CO_2 emissions. Others (like cathodic protection) need expensive equipment, adding to the total cost. However, corrosion inhibitors are more cost-effective and user-friendly [16]. The article begins with an overview of contemporary
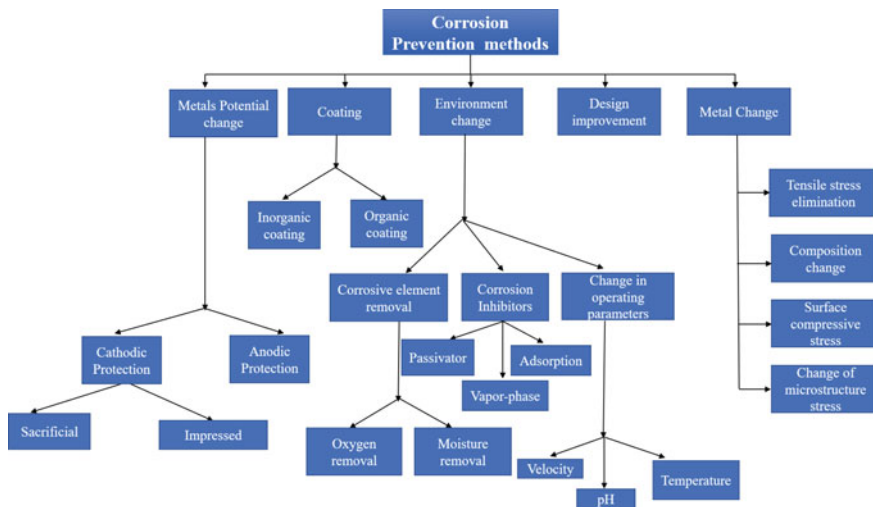
Fig. 1 Corrosion prevention methods

corrosion inhibitor research. In addition, the numerous kinds of corrosion inhibitors utilized in the oil and gas sector and their operating mechanism and selection criteria are thoroughly discussed.

2 Literature Review

The section reviews the recent research in corrosion prevention using corrosion inhibitors in detail.

Peter et al. thoroughly examined the operating mechanism of CI. Based on his research, the author established that when CI is applied to a metal surface, it binds both physically and chemically to the surface in contact with the fluid, blocking the contact surface with corrosive liquids. The author concluded that a suitable corrosion inhibitor should attach to metal surfaces immediately through physio-sorption or chemisorption processes. Because of their widespread use in industry, the bulk of corrosion inhibitors are made from low-cost raw materials or compounds that include a heteroatom of nitrogen (N), oxygen (O), or sulfur (S) in their aromatic ring or aliphatic carbon chain [1].

An investigation by Porcayo et al. claimed that owing to the high concentration of rare earth in permanent magnets, they may be used to synthesize ecologically acceptable corrosion inhibitors instead of highly toxic inhibitors and expensive rare earth salts. The study looked at the recovery of rare earth elements from magnet residues and their synthesis into chloride salts. The corrosion inhibitory characteristics of rare earth chlorides on API X70 steel in a 3.5% NaCl solution were evaluated using electrochemical methods. The inhibitor produced is a combination of Nd and Pr chloride, as determined by the results. It outperforms high purity Nd chloride as a corrosion inhibitor (analytical reagent). The findings indicate that electronic waste may be used sustainably to synthesize green corrosion inhibitors with a minimal carbon impact [17].

Sohail et al. utilized ginger juice extracted in varying concentrations and mixed it with 0.1 M HCl. In the article, the author stated that at 50 °C, corrosion rates decreased, but not at ambient temperature [15].

Busayo et al. tested the leaves extract of Athyrium Filix-Femina (AFF) inhibiting capacity in 1 M sulfuric acid. A scanning electron microscope was used for testing the morphology of metals. The findings indicated that the inhibitory effectiveness improved substantially with increasing extract AFF concentrations, reaching 85.49% (gravimetry) and 88.39% (electrochemical polarization) [18].

Recent developments in the area and the introduction of state-of-the-art techniques for validating inhibitory activity on steel corrosion were discussed in the review article by Wei et al. Newer methods, including weight reduction, electrochemical measurements, and potentiodynamic, show that green inhibitors effectively slow steel corrosion. Also examined were corrosion inhibition mechanisms and related experimental results [16].

Nathiya et al. investigated the capacity of Borassus flabellifer coir dust and aluminum in 1 M H_2SO_4 at 303–333 K. The experimental results depicted that corrosion inhibition efficiency increases with the addition of inhibitor content, and it adversely decreases as a function of temperature [19].

The article by Hossain et al. discusses the inhibitory properties of cinnamaldehyde in preventing corrosion of AISI 1015 carbon steel in a 10% w/w HCl solution. The mild steel coupons were subjected to HCl medium with and without cinnamaldehyde. After exposure, the samples were weighed, polarized, and surface characterized. On average, 200 ppm and 95.36% inhibition were found for cinnamaldehyde [20].

Another study Al-Qudah et al. looked at the effect of Capparis aegyptia extract on aluminum corrosion in 1 M sodium hydroxide (NaOH). Researchers used both weight loss and electrochemical polarization. The results show that the inhibitor's efficiency increases with concentration (C. aegyptia extract) and with temperature to a lesser extent. The inhibitory efficiency reaches a maximum of 93.8% at the highest extract concentration of 25 °C [21].

Batah et al. extracted oil from apricot seeds and evaluated the inhabitance effect on carbon steel in 1 M hydrochloric acid. Apricot seed oil adsorbs on the surface of carbon steel and blocks active sites. An increasing inhibitor concentration raised the inhibitory action to 83.49% in 1 M HCl. The authors calculated and analysed several thermodynamic properties of the inhibitor [22].

Fuchs–Godec et al. utilized stearic acid with or without tocopherol on stainless steel (SS) specimens of class X_4Cr_{13} in ethanol solutions. At 25 °C, researchers found a hydrophobic and corrosion-resistant surface of SS type X_4Cr_{13}. Testing the corrosion characteristics of stainless steel bare and modified surfaces was done using polarization and EIS in a 3.0% NaCl solution at 25°. On the other hand, EIS measurements indicate that X_4Cr_{13} inhibits X_4Cr_{13} by 68% on surfaces changed just in stearic acid. Adding tocopherol raised the results to almost 99.0% [23].

Al-Mashhdani et al. examined the inhibitory effects of aqueous cactus extracts on carbon steel corrosion using polarization measurements in 3.5% NaCl. In the context of 1 ppm cactus at 298 K, the measured findings indicate inhibitory effectiveness of about 94% [24].

Deyab and Guibal investigated the use of Taraxacum officinale extract (TOE) to protect cooling systems in desalination facilities from corrosion. By adsorbing TOE compounds on the steel substrate pipes, the inclusion of TOE in the recirculation loop reduces corrosion of carbon steel. The optimal TOE concentration was 400 mg L^{-1}, with more than 94% [25].

Sanni et al. developed an eggshell powder (ESP)-based inhibitor to test the corrosive properties of austenitic stainless steel 904L and 316L in a 3.5% sodium chloride solution. Gravimetric and potentiodynamic polarization were used in the experiments. A lower level of corrosion with ESP indicates that the inhibitor and chemical compositions of 904L and 316L affected corrosion resistance. Morphological changes in stainless steel are compared with ESP at different concentrations to see which one causes the most damage. Stainless steel 904L had a larger impedance

magnitude than stainless steel 316L at all inhibitor dosages evaluated in sodium chloride solution. Cathodic and anodic Tafel slope changes were compared to establish whether or not the ESP was of a mixed kind [26].

Al-Moubaraki and Al-Hammadi utilized three plant extracts, Fraxinus excelsior L. (FEAE), Zingiber zerumbet L. (ZZAE), and Isatis tinctoria L. (ITAE), as green inhibitors to prevent mild steel corrosion in H_3PO_4 acid solutions. According to the research, the extracts were efficient mild steel corrosion inhibitors in H_3PO_4. According to experiments, as inhibitor concentration increases, corrosion rate decreases correspondingly. An inhibitory layer has formed on the metal surface, as shown by FTIR and SEM analysis. At temperatures between 30 and 600 °C, the inhibitor film proved effective [27].

In an Indian oilfield, Ajmal et al. found the inhibitory impact of oleic acid hydrazide (OAH), a green corrosion inhibitor, on API X70 steel. The tests were conducted at a more binding site (90° pipe elbow) with a set flow velocity in a recirculating loop system. Corrosion was examined by changing the amounts of the OAH inhibitor (0.05, 0.15, and 0.30 g L^{-1}) in the flow condition. The highest inhibitory effect was 87.7% at a dose of 0.30 g L^{-1} [28].

Ahmed and Zhang investigated the anti-corrosion potential of Alchemilla Vulgaris (ALV) extract in 1 M HCl on pure copper to discover and create an eco-friendly or natural corrosive inhibitor. ALV was shown to successfully prevent corrosion on pure copper metal when used in a 1 M HCl solution. The electrochemical tests and weight loss method demonstrated that raising the concentration of ALV improved its anti-corrosion capacity [29].

Arwati et al. utilized 0.5 g/L arabic gum (AG) as a green inhibitor electrophoretically deposited onto the AA5052 surface (EPD). Corrosion testing was carried out in a solution of 0.5 M H_2SO_4 (pH 2) under simulated PEMFC conditions. The morphology was analysed using scanning electron microscopy (SEM), and the corrosion rate was determined using potentiodynamic polarization. The result indicates that after 168 h in 0.5 M H_2SO_4, AG coating may significantly decrease the corrosion rate of AA5052 by 60%. Under the same conditions, the temperature had a 14.4% impact on inhibitory efficiency. AG may be used as a green corrosion inhibitor to slow the corrosion of the AA5052 bipolar plate [30].

Mohammed et al. demonstrated that Combretum ghasalense leaf and root extracts inhibited mild steel corrosion in HCl acid solution. Temperatures were changed between 30, 40, and 50 °C during a 24-h exposure period. The concentration of the inhibitor was changed evenly between 0.1, 0.2, 0.3, 0.4, and 0.5 g/l. The findings indicated that as the temperature increased, the inhibitory efficiency dropped. The extracts were discovered to be an effective corrosion inhibitor for mild steel at all concentrations of hydrochloric acid solution [31].

Rizvi et al. tested the anti-corrosion properties of ethanolic extract of propolis (EEP) on SAE 1010 carbon steel samples submerged in 3.5% NaCl. The EEP adsorption on the surface of the specimens was measured using an optical profilometer, atomic force microscopy, and scanning electron microscopy. Comparing inhibited electrodes to unrestrained electrodes revealed electrochemical feedback assisted by

PDP, EIS, and DEIS. The findings indicate that EEP may prevent SAE 1010 carbon steel corrosion in NaCl solutions [32].

Researchers at the University of California, Berkeley utilized DFT (density functional theory) calculations on the environmental soundness of copper, iron, and aluminum (CuFeAl) corrosion inhibitors developed by Al-Itawi et al. [33]. Quantum and thermodynamic Gibbs functions of metal adsorption were estimated to determine the efficiency of the inhibitors under study. Among all the anti-corrosion compounds tested with Cu, Fe, and Al metals, ammonium pyrrolidine dithiocarbamate (APDTC) was the most effective. APDTC has the highest electrophilicity index and is most effective on the following metals in the following order. Cu is superior to Fe and inferior to Al in importance. The strong electrophilicity and Gibbs free energy of adsorption on metal surfaces of APDTC make it exceptional in preventing corrosion. These results are in line with recent developments in the field.

Amaranthus extract was tested in a pickling paste with H_2SO_4 as a mild steel corrosion inhibitor (Srivastava, 2020). The electrochemical tests were performed to determine corrosion current, anodic polarization, and cathodic polarization. Both uncontrolled and inhibited systems' corrosion currents declined with time. Amaranthus extract adsorption changed the anodic dissolving process and cathodic hydrogen evolution. In an acidic medium, inhibition increased with increasing inhibitor concentration, although the cathode was more polarized. In a 4 N H_2SO_4 solution, amaranthus extract acted as a cathodic inhibitor. Scanning electron microscopy (SEM) showed that the surface morphology of mild steel plates improved significantly with optimal inhibitor concentrations. Thus, the goal of these studies is to utilize blocked pickling acid paste to pickle/clean immense structures and tiny instruments. The current research examines the inhibitory impact of amaranthus extract, a green inhibitor often known as pigweed [34].

Honarvar Nazari et al. evaluated a zero-waste apple pomace-derived green inhibitor. The extract's capacity to decrease carbon steel corrosion in NaCl brine was electrochemical. Apple pomace extract contains the corrosion inhibitor $C_{26}H_{50}NO_7P$ (1-Linoleoylsn-glycerol-3-phosphocholine) that creates a barrier layer on the steel surface and prevents active anodic sites from forming. The Langmuir isotherm is followed by apple extract adsorption, with physical adsorption dominating (vs. chemical adsorption). Quantum chemistry simulations suggested a physisorption mechanism for steel protection by $C_{26}H_{50}NO_7$ P molecules [35].

The anticorrosive activity of ethanol extracts of Thymus vulgaris, Xylopia aethiopica, and Zingiber officinale in H_2SO_4 solutions was tested on environmentally acceptable and non-toxic mild-steel corrosion inhibitors (Okafor and Apebende). In ethanol, design, technique, and approach tests on corrosion inhibitors using TYV leaves, XYA fruits, and ZGO roots. The mechanism of inhibition was studied using gravimetric and gasometric methods. The extracts effectively prevent corrosion. It was discovered that when extract concentration increased, so did inhibitory effectiveness. TYV > ZGO > XYA for inhibitory efficiency. Plant extracts enhanced the activation energy, according to thermodynamic calculations. The novel research suggests that ethanol extracts from TYV leaves, XYA fruits, and ZGO roots may be used as low-cost and non-toxic corrosion inhibitors [36].

In specific applications, rare earth organic compounds (Forsyth et al.) may be used as corrosion inhibitors for steel and aluminum. Lanthanum 4-hydroxy cinnamate protects steel against corrosion and hydrogen embrittlement. Recent research shows it prevents steel corrosion in high carbon dioxide conditions. In chloride conditions, cerium diphenyl phosphate inhibits corrosion and decreases susceptibility to stress corrosion cracking. Adding rare earth inhibitor chemicals as pigments to polymer coatings may also reduce filiform corrosion in steel and aluminum alloys. Synergistic interaction between the rare earth and organic components of these new compounds is believed to be responsible for the reported levels of inhibition. This article covers current studies released by the Deakin University group [37].

Aqueous salt media containing 0.2 M Na_2SO_4 and 0.1 M NaCl were used to test long-chain alkyl carboxylates such as stearate, palmitate, and myristate (Dinodi and Shetty). Potentiodynamic polarization, EIS, SEM, and EDX studies were used. The inhibition was attributed to alkyl carboxylate adsorption, which follows the Langmuir adsorption isotherm. The inhibition was attributed to the precipitation of adsorbed alkyl carboxylates of magnesium, resulting in a compact changed surface layer [38].

Amination of brominated soybean oil with four distinct amines (Nasser, R. M) (urea, thiourea, p-toluidine, and 3-amino benzoic acid). Chemical analysis and weight loss methods assessed the produced compounds as corrosion inhibitors at various temperatures (308, 318, 328, and 338 K). The synthesized compounds showed good corrosion inhibition capabilities in acidic media [39].

3 Literature Summary

Table 1 summarizes the work done on corrosion inhibitors.

4 Corrosion Inhibitors: Their Classification and Mechanism of Action

Corrosion inhibitors are compounds applied on the corrosive surface to combat or minimize corrosion in a corrosive environment. When used on the metal surface, CI gets bind both physically and chemically on the surface in contact with the fluid, thus obstructing the contact surface with the corrosive fluids [1]. An effective corrosion inhibitor should quickly bind to metal surfaces through physio-sorption or chemisorption processes. Due to their extensive usage in industry, the majority of corrosion inhibitors are produced from inexpensive raw materials or compounds that include a heteroatom of nitrogen (N), oxygen (O), or Sulfur (S) in their aromatic ring or aliphatic carbon chain. There are four kinds of corrosion inhibitors (Fig. 2). They include anodic, cathodic, mixed, and volatile corrosion inhibitors.

Table 1 Literature review matrix for corrosion inhibitors

Reference No	(Author, published year)	Observations
[17]	(Porcayo-Calderon et al., 2019)	API X70 steel was subjected to electrochemical tests utilizing *rare earth chlorides* in a 3.5% NaCl solution to see if they were effective corrosion inhibitors. Nd and Pr chloride are used to produce the inhibitor's chelating agent. Compared to high purity Nd chloride, its corrosion-inhibiting abilities are better
[15]	(Sohail et al., 2019)	When mild steel is exposed to an acidic environment, it corrodes rapidly. Although corrosion may be reduced using corrosion inhibitors, they are often hazardous and must be avoided when using them. *Ginger* was employed as an inhibitor in this research after its juice was mechanically removed
[18]	(Busayo et al., 2020)	It was discovered that the *Athyrium filix-Femina leaf extract (AF)* could stop mild steel from corroding in a solution of 1 M sulfuric acid. The efficiency dropped somewhat as the temperature increased from 303 to 343 K. Phenolic, aromatic, and ether functional groups are all included in AF
[16]	(Wei et al., 2020)	Corrosion inhibitors made from inexpensive, renewable resources have a high inhibitory efficiency while having little or no adverse effect on the environment. As a result of the high concentration of electrons in multiple bonds and heteroatoms, inhibitor molecules are actively adsorbed on the steel surface
[19]	(Nathiya et al., 2019)	At 303–333 K, electrochemical, non-electrochemical, and microstructural analyses have been used to determine the corrosion inhibition effect of *Borassus flabellifer coir* dust against aluminum in 1 M H_2SO_4. Corrosion inhibition effectiveness rises with inhibitor content addition and decreases with temperature, according to the findings of the experiments. The scanning electron microscope (SEM) surface morphology investigation showed the presence of passive layers of BFDME and BFDWE molecules on top of aluminum's surface and enhanced anti-corrosion
[20]	(Hossain et al., 2019)	*Cinnamaldehyde's corrosion*-inhibiting properties in an HCl (10% w/w) solution are described in this study. The steel used is AISI 1015 carbon steel. Coupons made of mild steel were placed in HCl medium with or without cinnamaldehyde and then exposed to the solution. Researchers believe that the inhibition is caused mainly by cinnamaldehyde adsorption on the metal surface, following the Langmuir isotherm. There was a significant difference between the obtained activation energy (Ea) and the inhibitor-free HCl solution. The presence of an inhibitor protecting adsorbed layer on the metal surface was verified using a scanning electron microscope
[21]	(Al-Qudah et al., 2020)	For this study, researchers looked into the inhibitory effects of *Capparis Aegyptia* extract on aluminum corrosion in 1 M sodium hydroxide. At 25 °C, the inhibitory efficacy is 93.8%, with the greatest extract concentration. The scanning electron microscope (SEM) results confirmed the enhanced surface condition for corrosion protection achieved via adsorption

(continued)

Table 1 (continued)

Reference No	(Author, published year)	Observations
[22]	(Batah et al., 2020)	As a carbon steel corrosion inhibitor, apricot seed oil was tested in 1 M hydrochloric acid. The primary sources of action were carbon steel surface adsorption and active site blocking. Increases in inhibitor concentration resulted in greater inhibition efficacy, which peaked at 83.49% at 0.5 g/L
[23]	(Fuchs–Godec, 2019)	Stainless steel with bare and modified surfaces in NaCl solution containing 3.0% electrochemical impedance spectroscopy was examined for corrosion properties (wt.) sodium chloride at a temperature of 25 °C. The addition of a-*tocopherol* to the ethanol solution used to modify the surface of the stearic acid seems to be a viable therapy
[24]	(Al-Mashhdani et al., 2015)	Researchers looked at the corrosion-inhibiting properties of aqueous *cactus* extracts employing 3.5% NaCl as a polarization solution. In the context of 1 ppm cactus at 298 K, the inhibitory effect was about 94%. The cactus extract works as a mixed inhibitor per the corrosion potentials. In the advent of an inhibitor, Ecorr went from noble to active. Dissolution enthalpy and free energy were calculated as well as apparent activation energy
[25]	(Deyab and Guibal, 2020)	Desalination facilities' cooling systems have been evaluated for corrosion prevention using *Taraxacum officinale* extract (TOE). TOE enabled the corrosion process to have a higher energy barrier. The inhibitory efficacy was more than 94% at 400 mg per liter at a TOE dosage
[26]	(Sanni et al., 2019)	In a 3.5% NaCl solution, the impact of *eggshell powder (ESP)* as a corrosion inhibitor on austenitic stainless steels was studied. According to the results of the tests, the corrosion rate was decreased by ESP. At all concentrations tested, stainless steel 904L had a greater impedance magnitude than stainless steel 316L
[27]	(Al-moubaraki and Al-hammadi, 2020)	Researchers have discovered extracts from three different plants, including *Fraxinus excelsior L. (FEAE), Zingiber zerumbet L. (ZZAE), and Isatis tinctoria L.,* may reduce mild steel corrosion in H_3PO_4 acid solutions. (ITAE). Weight loss and electrochemical measurements determine the concentration of acid, inhibitor adsorbent dose, and temperature. SEM was used to investigate the mild steel morphology in H_3PO_4 acid with and without plant extracts and at low and high concentrations to verify the efficacy of these extracts in preserving mild steel (SEM)
[28]	(Ajmal et al., 2020)	A green corrosion inhibitor called oleic acid hydrazide (OAH) was used to prevent the corrosion of API X70 steel for the first time in Indian oilfield-produced water. It was tested in a closed-loop system with a predetermined flow rate at a critical point (a 90° pipe elbow)

Table 1 (continued)

Reference No	(Author, published year)	Observations
[29]	(Ahmed and Zhang, 2019)	An *Alchemilla Vulgaris (ALV)* extract dissolved in 1 M HCl was tested on pure copper in this study to see whether it has any anti-corrosion properties. ALV, being a naturally occurring inhibitor, may be helpful in sectors that now utilize only pure Cu. Adsorption of ALV molecules onto the copper surface inhibits the enzyme
[30]	(Arwati et al., 2020)	*Arabic Gum* (AG) at 0.5 g/L was utilized as a green inhibitor and electrophoretically deposited on the AA5052 surface as part of this research (EPD). AA5052 was submerged in 0.5 M H_2SO_4 for 168 h before being coated with AG to see whether it might decrease the corrosion rate by 60%. Under the same conditions, the temperature had a 14.4% impact on inhibitory efficiency. The AA5052 bipolar plate's corrosion rate may be reduced by using AG as a green inhibitor
[31]	(Mohammed et al., 2020)	*Combretum ghasalense leaf and root extracts* to prevent the mild steel from corroding in an HCl acid solution have been studied. The findings showed that the inhibitory effectiveness dropped as the temperature rose
[32]	(Rizvi et al., 2020)	*Propolis ethanolic* extract has been studied for its function in creating a corrosion-resistant layer on carbon steel electrodes. Electrochemical and surface morphological characteristics of SAE 1010 carbon steel specimens dipped in 3, 5% NaCl was studied to determine how well they performed
[33]	(Al-Itawi et al., 2019)	*APDTC* is the most effective anti-corrosion compound for copper, iron, and aluminum. When compared to other inhibitors, APDTC has the most excellent electrophilicity index value. Cu is affected first, followed by Fe, and then Al
[34]	(Srivastava, 2020)	*Amaranthus extract* in a pickling paste including H_2SO_4 as a mild steel corrosion inhibitor has been studied. Electrochemical tests on corrosion current, anodic polarization, and cathodic polarization were obtained. The mild steel plate's surface morphology improved significantly after being analysed using a scanning electron microscope (SEM)
[35]	(Honarvar Nazari et al., 2020)	In NaCl brine, an extract of *apple pomace* may help prevent carbon steel from corroding. This liquid extract performed very well when tested electrochemically. It may create a barrier layer on steel's surface via adsorption and function as a blocker for anodic sites
[40]	(Bhola et al., 2014)	It was shown that a sulfate reducing bacterial consortia of API 5L X80 line pipe steel decreased when *neem extract* was added. An open-circuit voltage and electrochemical impedance spectroscopy were used to investigate in situ corrosion behavior. Neem reduced SRB-induced MIC inline pipe steel by reducing cell growth, sulfide production, sessile cell density, and biofilm development

Table 1 (continued)

Reference No	(Author, published year)	Observations
[36]	(Okafor and Apebende, 2014)	Toxic mild-steel corrosion inhibitors, *ethanol extracts of Thymus vulgaris and Zingiber officinale* in H_2SO_4 solutions were evaluated in the present research. The metal surface adsorption sites are responsible for the inhibitory process. The use of ethanol extracts from TYV leaves, XYA fruits, and ZGO roots as non-toxic, inexpensive corrosion inhibitors is discussed in this study
[37]	(Forsyth et al., 2014)	In particular, in steel and aluminum applications, *rare earth* organic compounds may replace chromates as corrosion inhibitors. Adding rare earth inhibitor chemicals as pigments to polymer coatings may also reduce filiform corrosion in steel and aluminum alloys. This article covers current studies released by the Deakin University group
[38]	(Dinodi and Shetty, 2014)	Aqueous salt solutions of *0.2 M Na_2SO_4 and 0.1 M NaCl* were used to evaluate the alkyl carboxylates for their ability to prevent magnesium alloy ZE41 corrosion. An alkyl carboxylate adsorption isotherm (Langmuir model) was responsible for the inhibition. Magnesium adsorbed alkyl carboxylates precipitated and altered the surface layer to form an inhibitor
[39]	(Naseer, 2017)	The amination of brominated **soybean oil** with various amines resulted in four green corrosion inhibitors. The FT-IR and 1H-NMR analysis of the synthesized compounds revealed new information. They proved to be corrosion inhibitors when tested at various temperatures (308, 318, 328, and 338 K)
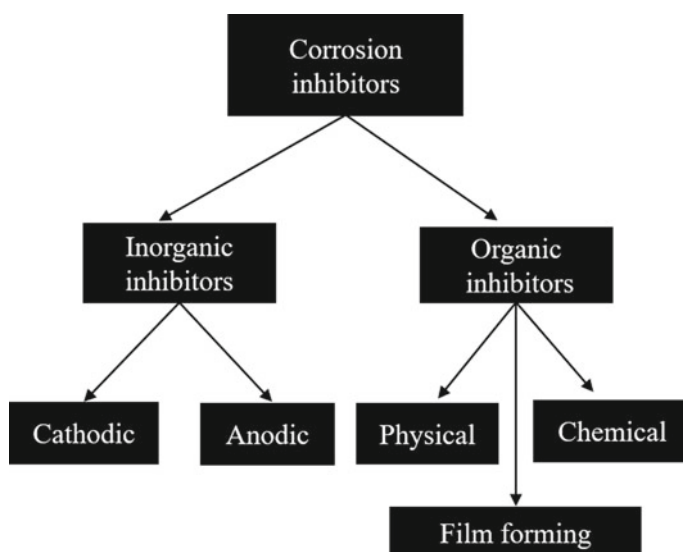
Fig. 2 Types of corrosion inhibitors

Anodic inhibitors oxygen form a thin film on metal surfaces with anodic inhibitors. A softer surface layer is oxidized, which reduces the corrosion potential of the metal.

Cathodic inhibitors delay the cathodic process or prevent reductive elements like hydrogen and oxygen from diffusing to the metal surface when used as cathodic inhibitors. Arsenic and selenium ions, which delay the reaction, are cathodic poisons. Other examples include oxygen scavengers, which restrict oxygen transport.

Mixed inhibitors are chemicals that reduce cathodic and anodic processes by forming a film or precipitating on the electrode surface. In household water, softener salts, sodium silicate, and phosphates help keep moisture from rusting.

Volatile corrosion inhibitors Compounds supplied to the corrosion site in a confined environment are known as volatile corrosion inhibitors. They create a thin, protective layer around themselves. Fluids are used to avoid corrosion in condenser tubes in boilers, for example, morpholine, or hydrazine.

5 Selection of Corrosion Inhibitors

Correct inhibitor selection requires matching the inhibitor chemistry to the corrosion environment and selecting physical characteristics suitable for that application. When choosing inhibitor physical qualities, method of use and system parameters must be taken into account. Researchers have sorted out specific properties that need to be inherent in the chosen corrosion inhibitor for an excellent inhibitor [41, 42]. Some of these have been listed below:

(i)   The foremost requirement for a CI is that it must be eco-friendly and non-toxic. CI should slow down the pace at which reactants diffuse onto metal surfaces.

(ii)   CI should have excellent inhibition properties, must be cost-effective, thermally stable, non-flammable, easy to apply, water tolerant, having low odor and low viscosity.

(iii)   The CI should be efficient even under high temperatures and high gas flow velocity through the pipeline.

(iv)   Operating under low concentrations, higher adsorbing capability, higher solubility, and easy synthesizability are the other pre-requirements of a suitable inhibitor.

(v)   Because CI is used in the open, it must maintain its liquid state even at very low temperatures. A pour point of $-30\,^{\circ}$C is usually preferred.

6 Global Concern and Outlook

Steels are extensively utilized in construction. These may be corroded by acidic solutions in engineering procedures, including pickling, descaling, and oil-well acidification. Inhibitors work by slowing down the rusting process. Green inhibitors are now getting much attention. They are also cheap, widely available, and renewable.

Most of the cited literature did not include advanced testing, leaving this as an open subject for future research. Nonetheless, using plant extracts as natural environmental inhibitors has tremendous potential. Industrial applications have historically been utilized to test the safety of drugs, chemical substances, and plant extracts. Plant extracts include many phytochemical components, but only a handful are essential for metal protection. Thus, it is recommended that distinct parts be separated and evaluated. HPLC-MS or GC-MS studies can readily classify the elements responsible for corrosion inhibition. Furthermore, the extraction technique is problematic due to lengthy processing periods and high temperatures in traditional extraction methods.

As a result, future studies will need alternate extraction methods with short processing times and optimal operating temperatures. In advanced research, structure-corrosion inhibition should be investigated using theoretical simulations like molecular dynamics and Monte Carlo simulations. This knowledge will help us understand how corrosion is inhibited and develop innovative and sustainable corrosion inhibitors.

7 Conclusion

The most current findings on corrosion inhibitors, including different types of amino acids, a wide variety of medications, and numerous minerals, plant extracts, and rare earth elements, are briefly reviewed. Many factors may be investigated while evaluating a plant extract as a corrosion inhibitor, including concentration, extraction solvent, temperature, and immersion period. Despite several investigations, this is still a relatively new sector with great growth potential, especially in generating green corrosion inhibitors and formulation designs.

References

1. Peter A, Obot IB, Sharma SK (2015) Use of natural gums as green corrosion inhibitors: an overview. Int J Ind Chem 6(3):153–164
2. Landolt D (2007) Corrosion and surface chemistry of metals. CRC Press
3. Arya AK, Honwad S (2016) Modeling, simulation, and optimization of a high-pressure cross-country natural gas pipeline: application of an ant colony optimization technique. J Pipeline Syst Eng Practe 7(1):04015008
4. Arya AK (2021) A comparison of the MOGA and NSGA-II optimization techniques to reduce the cost of a biomass supply network. Mater Today: Proc

5. Thakur AK, Arya AK, Sharma P (2021) Analysis of cathodically protected steel pipeline corrosion under the influence of alternating current. Mater Today: Proc

6. Arya AK, Honwad S (2018) Multiobjective optimization of a gas pipeline n1etwork: an ant colony approach. J Petrol Explor Prod Technol 8(4):1389–1400

7. Thakur AK, Arya AK, Sharma P (2021) Corrosion of pipe steels under alternating currents. Int J Electrochem Sci 16(11)

8. Thakur AK, Arya AK, Sharma P (2020) The science of alternating current-induced corrosion: a review of literature on pipeline corrosion induced due to high-voltage alternating current transmission pipelines. Corros Rev 38(6):463–472

9. Arya AK, Honwad S (2018) Optimal operation of a multi source multi delivery natural gas transmission pipeline network. Chem Prod Process Model 13(3)

10. Gupta SS, Arya AK (2019) An approach to determine probability of third-party damage to cross-country pipelines in India.

11. Arya AK, Jain R, Yadav S, Bisht S, Gautam S (2021) Recent trends in gas pipeline optimization. Mater Today: Proc

12. Banthia N, Mindess S, Bentur A, Pigeon M (1989) Impact testing of concrete using a drop-weight impact machine. Exp Mech 29(1):63–69

13. Sadou M, Hadj Meliani M, Amara M, Muthanna BGN, Merah N, Suleiman RK (2020) Impact resistance of API 5L steel in aggressive environment with the presence of green inhibitors. Struct Integrity Life 20(1):57–62

14. Tamalmani K, Husin H (2020) Review on corrosion inhibitors for oil and gas corrosion issues. Appl Sci 10(10):3389

15. Sohail M, Hussain F, Chandio AD, Sheikh M (2018) High temperature effectiveness of ginger extract as green inhibitor for corrosion in mild steel. NUST J Eng Sci 11(1):26–32

16. Wei H, Heidarshenas B, Zhou L, Hussain G, Li Q, Ostrikov KK (2020) Green inhibitors for steel corrosion in acidic environment: state of art. Mater Today Sustain 10:100044

17. Porcayo-Calderon J, Ramos-Hernandez JJ, Porcayo-Palafox E, Martínez de la Escalera LM, Canto J, Gonzalez-Rodriguez JG, Martinez-Gomez L (2019) Sustainable development of corrosion inhibitors from electronic scrap: synthesis and electrochemical performance. Adv Mater Sci Eng 2019

18. Tomilawo BA, Olasehinde EF, Ani JU, Obagboye FO, Asegbeloyin JN, Obi IO, L. E. A. (2020) Corrosion control of mild steel in sulphuric acid by athyrium filix-femina leaf corrosion control of mild steel in sulphuric acid by athyrium filix-femina leaf extract green inhibitor. December. https://doi.org/10.37273/chesci.CS0320510701

19. Nathiya RS, Perumal S, Murugesan V, Raj V (2019) Evaluation of extracts of Borassus flabellifer dust as green inhibitors for aluminium corrosion in acidic media. Mater Sci Semicond Process 104:104674

20. Hossain SM, Al-Shater A, Kareem SA, Salman A, Ali RA, Ezuber H, Hossain MM, Razzak SA (2019) Cinnamaldehyde as a green inhibitor in mitigating AISI 1015 carbon steel corrosion in HCl. Arab J Sci Eng (Springer Science & Business Media BV) 44(6)

21. Al-Qudah MA, Al-Keifi HG, Al-Momani IF, Abu-Orabi ST (2020) Capparis aegyptia as a green inhibitor for aluminum corrosion in alkaline media. Int J Corros Scale Inhib 9(1):201–218. https://doi.org/10.17675/2305-6894-2020-9-1-12

22. Batah A, Anejjar A, Bammou L, Belkhaouda M, Salghi R (2020) Effect of apricot almond oil as green inhibitor for steel corrosion in hydrochloric media. Port Electrochim Acta 38(4):201–214

23. Fuchs-Godec R, Tomić MV, Pavlović MG (2019) Effect of α-tocopherol as a green inhibitor on chloride-induced corrosion of steel. Int J Electrochem Sci 14:10396–10409

24. Al-Mashhdani HAY, Al-Saadie KAS, Abas HA, Abdulkareem D (2015) Cactus as a green inhibitor for the corrosion of carbon steel in seawater. Phys Chem Indian J 10(4):111–120

25. Deyab MA, Guibal E (2020) Enhancement of corrosion resistance of the cooling systems in desalination plants by green inhibitor. Sci Rep 10(1):1–13

26. Sanni O, Popoola API, Fayomi OSI (2019) Corrosion inhibition comparison of the effect of green inhibitor on the corrosion behavior of 316L and 904L austenitic stainless steels in chloride environment. J Phys: Conf Ser 1378(2):022087

27. Al-moubaraki AH, Al-hammadi WA (2020) Some plants extracts as green inhibitors to mitigate the corrosion of mild steel in H_3PO_4 acid solutions 6(3):9838
28. Ajmal TS, Arya SB, Thippeswamy LR, Quraishi MA, Haque J (2020) Influence of green inhibitor on flow-accelerated corrosion of API X70 line pipe steel in synthetic oilfield water. Corros Eng Sci Technol 55(6):487–496
29. Ahmed RK, Zhang S (2019) Alchemilla vulgaris extract as green inhibitor of copper corrosion in hydrochloric acid. Int J Electrochem Sci 14:10657–10669
30. Arwati IGA, Majlan EH, Shyuan LK, Husaini T, Alva S, Muhajirin, Radzuan NAM (2020) The influence of temperature and electroforesis deposition green inhibitor on bipolar plate AA5052 in sulfuric acid medium. Sains Malays 49(12):3169–3177. https://doi.org/10.17576/jsm-2020-4912-28
31. Mohammed AS, Cyril O, Idawu, SY (2020) Corrosion inhibition of mild steel in acidic solution by *Combretum* ghasalense leave and root extracts as a green inhibitor. J Sci Eng Res 6(12):126–133, Corrosion Inhibition of Mil. January. Available online www.jsaer.com
32. Rizvi M, Gerengi H, Yıldız M, Kekeçoğlu M, Pehlivan MM (2020) Investigation of "propolis" as a green inhibitor of SAE 1010 carbon steel corrosion in 3.5% NaCl environment. Ind Eng Chem Res 59(19):9328–9339
33. Al-Itawi HI, Al-Mazaideh GM, Al-Rawajfeh AE, Al-Ma'abreh AM, Marashdeh A (2019) The effect of some green inhibitors on the corrosion rate of Cu, Fe and Al metals. Int J Corros Scale Inhib 8(2):199–211
34. Srivastava M (2020) Mild steel corrosion inhibition, in 4 N sulphuric acid, by a green inhibitor. Port Electrochim Acta 38(2):99–106
35. Honarvar Nazari M, Shihab MS, Havens EA, Shi X (2020) Mechanism of corrosion protection in chloride solution by an apple-based green inhibitor: experimental and theoretical studies. J Infrastruct Preserv Resilience 1:1–19
36. Okafor PC, Apebende EA (2014) Corrosion inhibition characteristics of Thymus vulgaris, Xylopia aethiopica and Zingiber officinale extracts on mild steel in H_2SO_4 solutions. Pigm Resin Technol
37. Forsyth M, Seter M, Tan MY, Hinton B (2014) Recent developments in corrosion inhibitors based on rare earth metal compounds. Corros Eng Sci Technol 49(2):130–135
38. Dinodi N, Shetty AN (2014) Alkyl carboxylates as efficient and green inhibitors of magnesium alloy ZE41 corrosion in aqueous salt solution. Corros Sci 85:411–427
39. Nasser RM (2017) Novel green soybean oil deravatives as corrosion inhibitors for mild steel at 0.5 N HCl. Pet Coal 59(3)
40. Bhola SM, Alabbas FM, Bhola R, Spear JR, Mishra B, Olson DL, Kakpovbia AE (2014) Neem extract as an inhibitor for biocorrosion influenced by sulfate reducing bacteria: a preliminary investigation. Eng Fail Anal 36:92–103
41. Papavinasam S (1999) 67: Evaluation and selection of corrosion inhibitors
42. Faisal M, Saeed A, Shahzad D, Abbas N, Larik FA, Channar PA, Fattah TA, Khan DM, Shehzadi SA (2018) General properties and comparison of the corrosion inhibition efficiencies of the triazole derivatives for mild steel. Corros Rev 36(6):507–545

Comparative Study of CuO/ZTA and ZTA Composites in Terms of Functional Properties

Bipin Kumar Singh, Amiy Anshukar Yaduvanshi, and Abhay Kumar Mishra

1 Introduction

The composites of zirconia toughened alumina (ZTA) have superior mechanical properties [1–9] but it's inferior functional properties restricts its application. The drawback of frictional properties is abridged out by addition of solid lubricants like CuO [10], MoS_2 [11], CaF_2 [12], and Mo [13] inside the matrix of ZTA. The earlier studies suggested that an ideal solid lubricant have low shear strength, easily deformable, high adhesion to the lubrication surfaces, low abrasivity, and thermally/chemically stable at different environmental condition. In this context, Kerkwijk et al. [14] selected various metal oxides as a solid lubricant to find the effect of these oxide on tribological properties. A remarkable reduction in coefficient of friction (COF), i.e. 40% (from 0.70 to 0.43) was observed for Y-TZP/CuO, whereas 22% (0.55–0.43) improvement was observed for alumina/CuO. Investigation carried out by Pasaribu et al. [15] revealed that small percentage of CuO had beneficial effect inside alumina and zirconia ceramics rather than high percentage. The reduction from 0.7 to 0.2–0.3 (depending on load condition) in COF was observed for ZrO_2/CuO, whereas a little reduction, i.e. 0.65 to 0.4–0.45 in COF was observed for Al_2O_3/CuO during dry sliding against Al_2O_3 ceramic balls. The decrement in COF was attributed to the development of smooth patchy layers due to presence of CuO between the interface surface. In another investigation, Pasaribu et al. [16] suggested low COF (0.25–0.35) for ZrO_2/CuO composites sintered at 1500 °C having humidity in the range of 18–95%. Song et al. [17] illustrated the effect of alumina pins as a counter surface on

B. K. Singh (✉)
Department of Mechanical Engineering, Sri Eshwar College of Engineering, Coimbatore, Tamil Nadu 641202, India
e-mail: bipinkumarsingh@sece.ac.in

A. A. Yaduvanshi · A. K. Mishra
Department of Mechanical Engineering, Goel Institute of Technology and Management, Lucknow 226028, India

the 3Y-TZP disk to understand the friction behavior. Researchers found that at interfacial contact, a chemical reaction occurred to form $CuAlO_2$ phase which results in the growth of aluminum-rich surface layer and accelerated the wear rate of alumina from the matrix. The growth of aluminum-rich surface layer can reduce the COF. The research also showed a shifting from low value of COF to high value of COF due to the shifting of wear mechanism from microchipping to intergranular fracture. Dey et al. [18] studied the effects of various solid oxide lubricants reinforced inside the matrix of ZTA. The studies made for densification revealed that TiO_2–CuO and TiO_2–MnO_2 both additives give full densities (>97%) at 1450 °C as sintering temperature. The combination of TiO_2–MnO_2 with ZTA showed the lowest specific wear rate and COF, i.e. 9.2×10^{-5} mm^3/(N m) and 0.35, respectively. In another study, Dey et al. [19] used various metal oxides to reinforced inside the ZTA matrix through the co-precipitation process. The results of experiments found minimum coefficient of friction for the composition consisting of soft CuO and ZnO as additives inside the ZTA matrix. The decrement in COF may be due to the development of softer phases like $CuAl_2O_4$ and $ZnAl_2O_4$ at interfaces. He et al. [20] investigated the solid–solid interaction between CuO and alumina. The analysis revealed that the formation of $CuAl_2O_4$ occured at temperature around 700, 800, and 950 °C provides beneficial effect on the tribological properties.

Hence, based on the above pioneer researches, authors tried to explore more phenomenon that are responsible for self-lubrication. So, this study focused to evaluate the mechanical and frictional properties of 1.5 wt% CuO/ZTA. An in-depth characterization has been carried out to know the effect of CuO on mechanical as well as frictional behavior. Furthermore, the phenomenon's that were responsible for improvement of functional properties are thoroughly discussed.

2 Preparation of Powders and Samples

Coprecipitation process was used to develop the composites having 1.5wt% CuO/ZTA by using following chemicals:

1. $ZrOC_{12}.8H_2O$; Loba Chemie, Mumbai, India
2. $Al(NO_3)_3.6H_2O$; Sigma Aldrich, USA
3. $Y(NO_3)_3.6H_2O$; Loba Chemie, Mumbai, India
4. $Cu(NO_3)_2 \cdot 3H_2O$ Merck India

Requisite amount of chemicals were mixed in distilled water to form solution. The formed solution were drop wise mixing of diluted NH_4OH (~1 molar) till the pH of the solution reached ~9–10 to form precipitate. The detailed processing route was elaborated in author previous work [21, 22]. The quantity of constituents present were selected from author earlier studies [23] which showed that these compositions provide better performance when mixed inside reference matrix. The developed powders were calcined at requisite temperature followed by hot isostatic pressing

at 1500 °C for 15 min. The densify samples were mirror polished having surface roughness below 0.5 micron.

3 Experimental Details

The polished samples were first passed through density tests. Archimedes principle has been opted to evaluate the densities of developed composites. After measuring the densities, the Vickers micro hardness tester was used for mechanical properties of developed composites, whereas the functional properties were measured on pin on disk tribological setup shown in Fig. 1. ASTM G99 standards was opted to evaluate the frictional properties in which 12 mm cylindrical samples were slides against alumina plate. The test condition for tribological test was 10 N as load, 6 mm/sec as sliding velocity, and maintaining environmental condition. The surface roughness of both sliding pairs were maintained as 0.5–1 μm (Ra) approximately. X–ray diffraction technique was used to determine the phases inside the developed composites in the range of 20°–70° as angle 2θ.
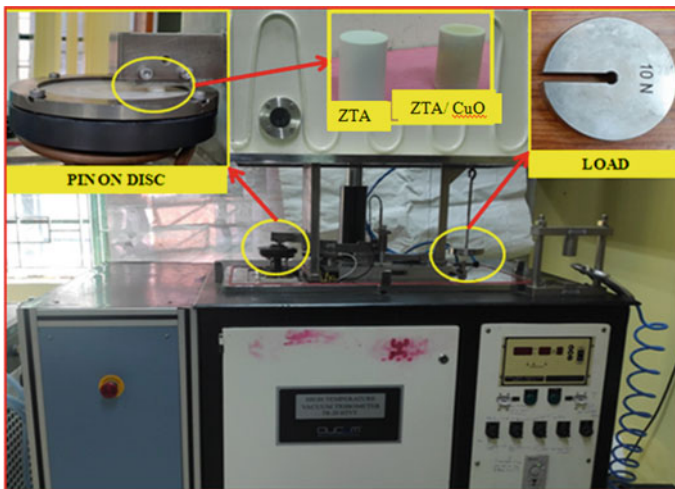
Fig. 1 Experimental setup of tribometer
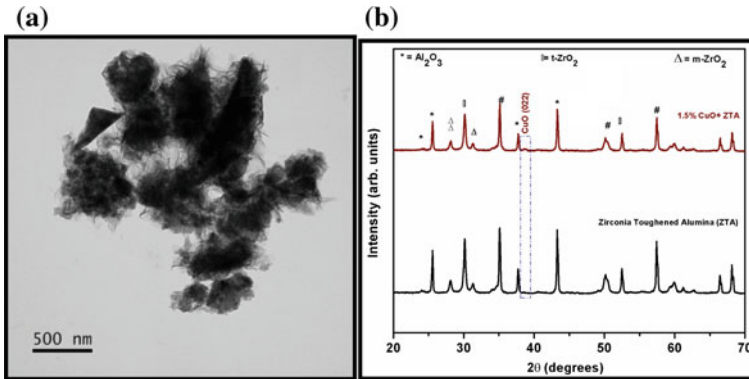
Fig. 2 **a** XRD pattern of different percentage doped CuO/MgO/ZTA. **b** TEM Image of developed composites

4 Analysis of Results and Discussion

4.1 Microstructure and Phase Analysis

The TEM image of developed CuO/ZTA composites along with XRD is shown in Fig. 2. From TEM image, the grain size of developed composites is found as few micron. Figure 2b represents all phases of the elements present inside the developed composites. The important phases of zirconia inside the matrix were calculated as per the discussion illustrated in earlier study carried out by same author Singh et al. [23]. The analysis on phases signify that the addition of CuO does not have any effect on the withholding of tetragonal phases inside the composites of zirconia at room temperature. Hence, the effect of CuO is negligible on the transformation toughening mechanism.

4.2 Functional Characterization

4.2.1 Bulk Density, Hardness, and Fracture Toughness

The analysis made for bulk density showed a decrement in its value with presence of CuO. The calculated values of bulk density for all composites are shown in Table 1. The decrement was attributed to the increase in grain size, consequently, porosity increases inside the CuO/ZTA composites. The above analysis is in good agreement with earlier researcher Ramesh et al. [24].

Table 1 also depicts the values of mechanical properties for all developed composites. It is found that the values of hardness decreases in contradiction with fracture toughness which is increasing with reinforcement of CuO inside the reference

	Composition	Bulk density (g.cm^{-3})	Hardness (GPa)	Fracture toughness (MPa.m$^{1/2}$)
Table 1 Mechanical properties of developed composites	ZTA + 0.0 wt% CuO	4.38 ± 0.24	18.21 ± 0.48	4.98 ± 0.31
	ZTA + 1.5 wt% CuO	4.09 ± 0.19	17.03 ± 0.73	5.04 ± 0.26

matrix. The mechanism responsible for degradation in hardness was dedicated to the presence of soft CuO particles inside the reference matrix, earlier showed by Ran et al. [25]. Researchers illustrated that the presence of CuO inside the matrix of ZTA did not shows any effect on the withholding of tetragonal phases of zirconia, which facilitates the toughening phenomenon. Hence, its presence inside the ZTA matrix creates an impurities phase, which leads to the formation of a high Cu-ion reach zone (enrich ionic copper) at the cluster of grain boundaries. This results in a weaker section inside the matrix responsible for the easily scattering of crack. But a contradictory result is observed in case of fracture toughness. The reason behind this improvement was illustrated by Oh and Lee [26, 27]. Researchers demonstrated that the crack bridging and crack deflection mechanisms were exaggerated with presence of CuO particles inside the matrix. Hence, it was concluded that the improvement in fracture toughness is a result of crack bridging and crack deflection that prevails inside the matrix of alumina-CuO. Similar, mechanism in elaborated manner was earlier illustrated by Budiansky et al. [27–29]. Evans suggested that the ductility governed by soft metal oxide permits the plastic dissipation that results in local residual stresses. These stresses were responsible for the improvement in toughness as the local residual stresses dissipated as acoustic waves crates bridging inside the matrix. This creation is known as bridging mechanism and responsible for improvement in fracture toughness.

4.2.2 Coefficient of Friction

Comparative results of COF for CuO/ZTA and ZTA are shown through Fig. 3. The analysis demonstrated a decrement from 0.6304 to 0.5039 when CuO particles are reinforced inside the ZTA matrix. The earlier researches dedicated on the CuO as solid lubricant describes a phenomenon for formation of long elastic soft film (patchy layer) between two sliding surface due to squeezing and smearing action. The formation of uniform thin films exaggerated with presence of CuO particles was responsible for the improvement in COF. The formation of smooth layer at the interface can also be judged through FESEM images shown in Fig. 4. A smooth surface is observed for CuO/ZTA, whereas abrasion with chipping of grain was observed for ZTA. The results were in line with Prasebu et al. [15, 29, 30] for CuO/Al$_2$O$_3$ and CuO/ZrO$_2$ composites. The researchers demonstrated that the wear debris detached from the surface was squeezed and smeared into soft patchy layer due to low shear strength
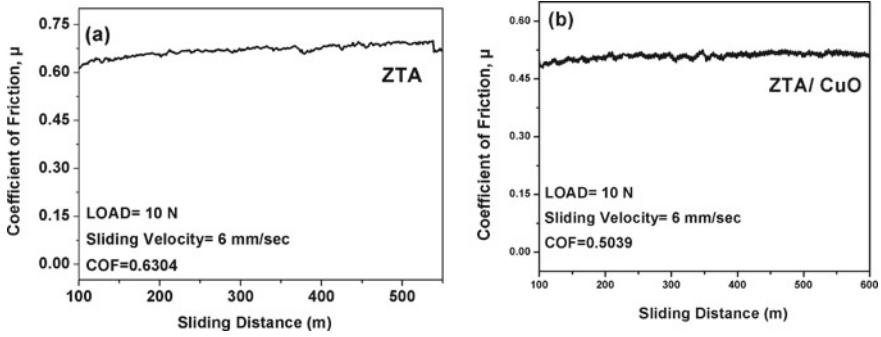
Fig. 3 **a** Evaluation of coefficient of friction for ZTA. **b** Evaluation of coefficient of friction for CuO/ZTA
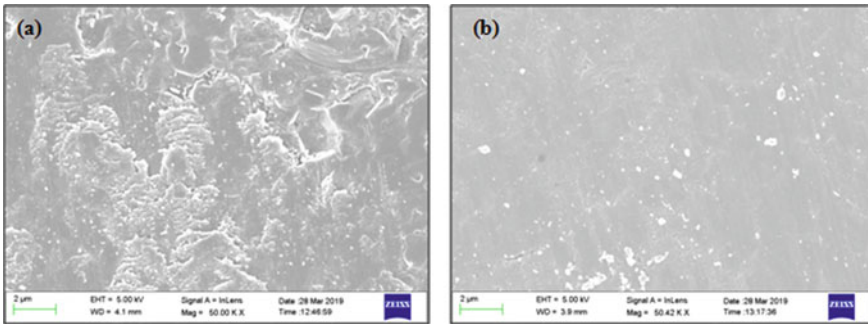
Fig. 4 **a** FESEM image of wear track of ZTA. **b** FESEM image of wear track of CuO/ZTA

during sliding action. The formed patchy layer i.e. thin soft layer is responsible for the improvement in tribological properties. Hence, this analysis revealed that there is beneficial effect of CuO inside ZTA matrix on the functional properties due to formation of smooth soft thin film.

5 Conclusion

Composites of CuO/ZTA was successfully developed through powder metallurgy route opting co-precipitation process. Micro-structural analysis of developed composites showed micron size grains. The mechanical properties of CuO/ZTA composites showed a significant decrement in bulk density due to presence of CuO as impurity phase. Furthermore, an improvement in fracture toughness was observed due to crack bridging and crack deflection phenomenon. The results of COF also showed an improvement approx 20% at the cost of hardness. The improvement in COF was attributed to the smearing and squeezing action on the wear debris

which results in the formation of smooth patchy layer between the sliding surface. The formed smooth layer (patchy layer) between the surface was responsible for improvement in COF. Therefore, the above analysis suggested that these composites were suitable for application as cutting inserts for high-speed machining in dry conditions.

References

1. Wang J, Stevens R (1989) Zirconia-toughened alumina (ZTA) ceramics. J Mater Sci 24:3421–3440
2. Basha MM, Basha SM, Singh BK, Mandal N, Sankar MR (2020) A review on synthesis of zirconia toughened alumina (ZTA) for cutting tool applications. Mater Today: Proc 26:534–541
3. Banik SR, Iqbal IM, Nath R, Bora LJ, Singh BK, Mandal N, Sankar MR (2019) State of the art on zirconia toughened alumina cutting tools. Mater Today: Proc 18:2632–3264
4. Pratap A, Kumar P, Singh GP, Mandal NA, Singh BK (2020) Effect of indentation load on mechanical properties and evaluation of tribological properties for zirconia toughened alumina. Mater Today: Proc 26:2442–2446
5. Singh BK, Roy H, Mondal B, Roy SS, Mandal N (2019) Measurement of chip morphology and multi criteria optimization of turning parameters for machining of AISI 4340 steel using Y-ZTA cutting insert. Measurement 142:181–194
6. Singh BK, Roy H, Mondal B, Roy SS, Mandal N (2018) Development and machinability evaluation of MgO doped Y-ZTA ceramic inserts for high speed machining of steel. Mach Sci Technol 22:899–913
7. Kumar P, Pratap A, Mandal N, Singh BK (2021) Effect of sliding velocity and Load on the COF of self-lubricating Ceramics CuO/MgO/ZTA. Mater Today: Proc 44:1806–1810
8. Mandal N, Doloi B, Mondal B, Singh BK (2015) Multi criteria optimization and predictive modeling of turning forces in high speed machining of Y-ZTA insert using desirability function approach. J Eng Manuf Part B (SAGE Publication) 231(8):1396–1408
9. Liu H, Xue Q (1996) The tribological properties of TZP-graphite self-lubricating ceramics. Wear 198:143–149
10. Mazumder S, Kumar A, Singh BK, Roy H, Mandal N (2019) Tribological investigation of MgO/Al$_2$O$_3$ ceramic composite with the inclusion of nano CuO in dry abrasive wear test. Mater Res Express 6:085086
11. Ghosh K, Mazumder S, Kumar Singh B, Hirani H, Roy P, Mandal N (2020) Tribological property investigation of self-lubricating molybdenum-based zirconia ceramic composite operational at elevated temperature. J Tribol 142:021704
12. Guangyong W, Chonghai X, Yonglian Z, Mingdong Y (2011) State of the art of graded self-lubricating ceramic cutting tool materials. Appl Mech Mater 66:1598–1604
13. Sliney HE (1982) Solid lubrication materials for high temperatures—a review. Tribol Int 15:303–314
14. Kerkwijk B, Garcia M, Van Zyl WE, Winnubst L, Mulder EJ, Schipper DJ, Verweij H (2004) Friction behaviour of solid oxide lubricants as second phase in a-Al$_2$O$_3$ and stabilised ZrO$_2$ composites. Wear 256:182–189
15. Pasaribu HR, Sloetjes JW, Schipper DJ (2003) Friction reduction by adding copper oxide into alumina and zirconia ceramics. Wear 255:699–707

16. Pasaribu HR, Reuver KM, Schipper DJ, Ran S, Wiratha KW, Winnubst AJA, Blank DHA (2005) Environmental effects on friction and wear of dry sliding zirconia and alumina ceramics doped with copper oxide. Int J Refract Hard Met 23(4–6):386–390

17. Song J, Valefi M, De Rooij M, Schipper DJ, Winnubst L (2012) The effect of an alumina counterface on friction reduction of CuO/3Y-TZP composite at room temperature. Wear 274:75–83

18. Dey AK, Biswas K (2009) Dry sliding wear of zirconia-toughened alumina with different metal oxide additives. Ceram Int 35(3):997–1002

19. Dey AK, Chatterjee S, Biswas K (2017) Effect of oxide additives on phase evolution and tribological behavior of zirconia-toughened alumina composite. J Mater Eng Perform 26(12):6107–6116

20. He YJ, Winnubst AJ, Burggraaf AJ, Verweij H, Van der Varst PGT, de With G (1997) Sliding wear of ZrO_2-Al_2O_3 composite ceramics. J Euro Ceram Soc 17(11):1371–1380

21. Singh BK, Ghosh K, Roy SS, Mondal B, Mandal N (2018) Correlation between Microstructure and Mechanical Properties of YSZ/Al_2O_3 Ceramics and Its Effect on High Speed Machining of Steel. Trans Indian Ceram Soc 77:219–225

22. Singh BK, Mondal B, Mandal N (2016) Machinability evaluation and desirability function optimization of turning parameters for Cr_2O_3 doped zirconia toughened alumina (Cr-ZTA)cutting insert in high speed machining of steel Machining. Ceram Int 42:3338–3350

23. Singh BK, Samanta S, Roy SS, Sahoo RR, Roy H, Mandal N (2020) Evaluation of mechanical and frictional properties of CuO added MgO/ZTA ceramics. Mater Res Express 6:125208

24. Ramesh S, Aw KL, Ting CH, Tan CY, Sopyan I, Teng WD (2008) Effect of copper oxide on the sintering of alumina ceramics. Adv Mater Res 47–50:801–804

25. Ran S, Winnubst L, Blank DH, Pasaribu HR, Sloetjes JW, Schipper DJ (2007) Effect of microstructure on the tribological and mechanical properties of CuO/doped 3Y/TZP ceramics. J Am Ceram Soc 90(9):2747–2752

26. Oh ST, Lee SI (2010) Fabrication of alumina-based metal nanocomposites by pressureless sintering and their mechanical properties. J Nanosci Nanotechnol 10:366–369

27. Budiansky B, Amazigo JC, Evans AG (1988) Small-scale crack bridging and the fracture toughness of particulate-reinforced ceramics. J Mech Phys Solids 36:167–187

28. Evans AG (1990) Perspective on the development of high-toughness ceramics. J Am Ceram Soc 73:187–206

29. Singh BK, Goswami S, Ghosh K, Roy H, Mandal N (2021) Performance evaluation of self lubricating CuO added ZTA ceramic inserts in dry turning application. Int J Refract Hard Met 98:105551

30. Pratap A, Singh BK, Sardana N (2022) Fracture in self-lubricating inserts: A case study, Mater Today: Proc https://doi.org/10.1016/j.matpr.2022.06.005

Progresses in Infrared Stealth Composites

Amarjeet Dutta, Shubham Srivastava, Ritesh Goel, and C. S. Malvi

1 Introduction

Infrared camouflage is concealing any object from detection by infrared cameras or any equipment capable of detecting infrared rays by suppressing the infrared rays emitted from the object. The wavelength of infrared rays varies between 0.76 and 1000 μm [1, 2]. The whole infrared spectrum is divided into near infrared region (NIR) from 0.76 to 2.5 μm, mid infrared region (MIR) from 2.5 to 50 μm and far infrared region (FIR) from 50 to 1000 μm. Every substance above absolute zero will emit infrared rays of certain wavelength. However, emitted infrared rays get attenuated due to absorption, reflection and refraction by molecules present in the atmosphere. Hence, not all the infrared radiations reach the IR detection systems [1]. Radiations of certain specific wavelengths can travel through the atmosphere. The IR rays which travel through the atmosphere belong to wavebands 3–5 and 8–14 μm [3].

Stefan–Boltzmann law is the basic law which quantifies the infrared radiations emitted by an object. This law states that "radiation energy emitted per unit surface area by an object is proportional to the emissivity and fourth power of the temperature of the object's surface". Mathematically,

$$E = \varepsilon \sigma T^4 \tag{1}$$

It can be inferred from Stefan–Boltzmann law that the infrared radiations from the target body can be suppressed by either controlling the temperature of the target's

A. Dutta (✉) · S. Srivastava · R. Goel · C. S. Malvi
Department of Mechanical Engineering, Madhav Institute of Technology and Science, Gwalior 474005, India
e-mail: shalkhua@gmail.com

R. Goel
e-mail: riteshgoelarya@gmail.com

surface or by reducing the emissivity of the target's surface [4]. Thus, an infrared stealth composite must be able to minimise the heat transmission through itself and should have a low surface emissivity from outside [4].

1.1 Theory Behind Infrared Camouflage Composites

Zhou et al. in their review has explained the theory behind the infrared camouflage. Any thermal radiation capturing instrument detects a hot body by measuring the difference of intensities of thermal radiations emitted by the body and its surrounding environment [1]. The body which is detected by the thermal imaging equipment is called target body. The contrast between the target body and its environment is determined by the difference in the intensities of radiations emitted from the object and its surrounding [1]. The contrast can be given by following equation

$$C = \frac{(E_o - E_b)}{E_b} \tag{2}$$

where E_o is the radiation energy emitted by the target body, E_b is the radiation energy emitted by background, and C is the contrast.

1.2 Previous Research

Xu et al. prepared a carbon nanotube doped aerogel (CNTA) sandwich structure on polyimide fabric and coated the sandwich structure with aluminium-doped zinc oxide (Al- ZAO) on the outer surface [4]. An infrared fabric was prepared by using tungsten-doped vanadium dioxide paints and coating this paint on cotton fabric by Mao et al. [5]. Liu et al. prepared a SiO_2–Bi_2O_3 composite fibrous membrane which had lower emissivity than base materials [6]. A polyurethane-copper composite coating with low emissivity was prepared by Yu et al. [7]. Gong et al. prepared Al-doped ZnO film on glass substrate which showed infrared reflectivity at near infrared reflective zone [8]. SnO_2–ZnO nanocomposite structure prepared by Zhang et al. had both radar and infrared compatible stealth properties [9]. Yu et al. prepared a bicomponent fibre using polypropylene chips and various fillers [10]. This fibre showed promising radar absorbing and infrared camouflage property. An infrared stealth composite structure was prepared from SiO_2–TiO_2 film by Wang et al. [11]. This highly stretchable nano-wrinkle structure can be used for infrared stealth application. Chao et al. had developed a photonic crystal on polystyrene and PET substrate [12]. This crystal had infrared camouflage and laser band camouflage. Liu et al. had developed an Al–MnO_2 composite which had enhanced microwave absorption and low infrared emissivity [13]. Huang et al. prepared an Al-polymer composite coating and studied

its infrared emitting properties along with its environmental stability performance [14].

Peng et al. fabricated a $TiO_2/Cu/TiO_2$ composite having a sandwich structure, coated it on a polyester fabric and studied IR reflective property [15]. Pan et al. prepared a polyacetylene-multiwalled CNT composite and studied its potential as microwave absorption and infrared stealth composite [16]. Fe-doped ZnO powders prepared by Su et al. showed lower emissivity and have good dielectric and microwave absorbing properties [17]. Wang et al. studied infrared stealth property of mesoporous C–Al-doped ZnO-coated fabrics [18]. Larciprete et al. studied infrared characteristics of four stainless steel textiles in mid infrared range [3]. An adaptive optical textile with electrically controlled reflectivity and emissivity covering the infrared and near infrared wavelengths was developed by Ergoktas et al. [19].

A solid solution of $Sn_{(1-x)}–Fe_xO_2$ ($x = 0, 0.03, 0.06$ and 0.09) prepared by Su et al. had low emissivity and can be used as infrared stealth coating [20]. A smart textile of cotton fabric coated with Cu was prepared by Jiang et al. and showed excellent infrared shielding property [21]. Jeong et al. developed a wearable IR shield based on polyurethane-antimony tin oxide composite fibre [22]. Mao et al. prepared a composite of cotton fabric coated with ZnO: Al–La nanoparticle [23]. This composite textile had a better infrared stealth property. A carboxymethyl cotton fabric loaded by reduced graphene oxide was prepared by Liu et al. [24]. This composite also has potential to be used as infrared camouflage textile. An aramid fabric for infrared shielding was developed by Jia et al. [25]. Zhu et al. experimentally demonstrated combining silica aerogel with Ge/Zns for high temperature IR camouflage with efficient thermal management [26]. Wang et al. modified Al pigment with graphene for infrared/visual stealth compatible composite [27]. Xu et al. developed two composites, viz. ZnO:Al–In and ZnO:Al–La, and applied these composites on cotton fabric using coating technology and studied the effect of In and La on infrared emissivity of cotton fabric [28, 29].

2 Review of Materials and Methods of Fabricating the Composites

In this review, it was observed that different chemical compounds in their pure form/synthesised from other primary compounds were used to develop infrared shielding composites. These composites have different composition and fabrication techniques. From the reviewed papers, it was observed that the materials used for infrared camouflage are metals (including their compounds), polymers (or fabrics), semimetals and nonmetals. The raw materials along with the fabrication methods selected for preparing the composites/fabrics are mentioned in Table 1.

From Table 1, it is observed that most of the researchers used metals such as aluminium, copper, zinc, iron and titanium for preparation of the composites. Tin, tungsten and vanadium are also used by few of the researchers. The semimetal

Table 1 Materials and methods of fabricating the composites

S. No.	Composite	Raw materials	Methods for preparing the constituents of composite/textile	Methods of fabricating the final composite/textile	Reference
1	CNT-doped aerogel hot pressed on polyimide fabric and coated with Al-doped ZnO	PI fabric, carbon nanotubes, HCl, ethyl silicate, ammonia water, diffusing agent, anhydrous alcohol, thickener CN-WW, zinc nitrate, aluminium nitrate, resin binder, polyethylene glycol 1540	Hydrolysis reaction, sol gel process and calcination	Coating and hot pressing	[4]
2	Tungsten-doped VO_2 thin films coated on cotton fabric	Vanadyl sulphate hydrate, sodium hydrogen carbonate, sodium tungstate dehydrate, absolute ethyl alcohol, cotton fabric, water borne polyurethane	Hydrothermal reaction and calcination	Coating	[5]
3	SiO_2–BiO_3 composite	Polyvinyl alcohol, tetraethyl orthosilicate, diethylene glycol, phosphoric acid, concentrated sulphuric acid, concentrated nitric acid, H_2O_2, acetone, ethanol, bismuth acetate, deionised water	Hydrolysis, poly-condensation, electrospinning and hydrothermal treatment	Hydrothermal reaction and heating	[6]
4	Polyurethane–Cu composite	Raw Cu powder, polyurethane coupling agent γ-amidopropyl-triethoxyl silicane	Ultrasonication	Spray coating and doctor blade method	[7]
5	ZnO:Al thin films	ZnO powder, Al_2O_3 powder, acetone, ethanol, deionised water, N_2 gas	–	Pulse laser deposition	[8]

(continued)

Table 1 (continued)

S. No.	Composite	Raw materials	Methods for preparing the constituents of composite/textile	Methods of fabricating the final composite/textile	Reference
6	SnO_2–ZnO nanocomposite	NaOH solution, $Zn(CH_3COOH)_2.2H_2O$ solution, deionised water, ethyl alcohol, $SnCl_4.5H_2O$ solution	Mixing and heating	Hydrothermal reaction	[9]
7	Photonic crystal films coated on polystyrene and polyethylene terephthalate (PET)	PC film, polystyrene, PET	–	Vacuum coating method	[12]
8	Polypropylene bicomponent fibre with metallic fillers	Barium hexaferrite, manganese zinc cubic ferrite, bronze powder, Al nanoparticles, polypropylene chips	Spinning	Spinning	[10]
9	SiO_2–TiO_2 films	Silicon wafers, silver films, TiO_2, SiO_2, polydimethyl siloxane	Microelectromechanical systems (MEMS) technology	Electron beam evaporation	[11]
10	Al–MnO_2 composite	Al powder, $KMnO_4$	–	Facile one step method	[13]
11	Al–polymer composite	Acrylic resin, epoxy resin, epoxy silicon resin, fluorocarbon resin, flaky aluminium powder, tinplate as substrate	Grinding	Spray coating/flow flat method/brush coating	[14]
12	TiO_2–Cu–TiO2-coated polyester fabric	Plain weave polyester fabric, TiO_2, Cu targets	–	Magnetron sputtering deposition	[15]

(continued)

Table 1 (continued)

S. No.	Composite	Raw materials	Methods for preparing the constituents of composite/textile	Methods of fabricating the final composite/textile	Reference
13	Polyacetylene with multiwalled CNTs	Stigmasterol, succinic anhydride, 4-(dimethylamino) pyridinepropargylamine, isobutyl chloroformate, 4-methyl morpholine, rhodium zwitterion catalyst, chloroform, CaCl₂, multiwalled CNTs	Mixing, rotary evaporation and polymerization precipitation	Solution casting	[16]
14	Fe-doped ZnO powders	Zinc nitrate, urea, ferric nitrate, deionised water	–	Co-precipitation	[17]
15	Carbon–aluminium-doped zinc oxide-coated cotton fabrics	Polyurethane (PU 377), polyvinyl acetate emulsion, binder, zirconia beads, hyperdispersant 3204, cotton fabric, zinc acetate dehydrate, aluminium nitrate nonahydrate, mono ethanol amine, phenol, formalin, NaOH, HCl, ethanol	Evaporation induced self-assembly	Coating	[18]
16	Stainless steel textiles	Stainless steel fibres	Pre-fabricated	–	[3]
17	Graphene-enabled adaptive infrared textile	Ni foils, polyethylene films, FeCl₃ solution, cotton fabric	Vacuum deposition	Lamination	[19]
18	Sn₍₁.ₓ₎–FeₓO₂ (x = 0, 0.03, 0.06 and 0.09) composite	Tin chloride, ammonium hydroxide, ferric nitrate	–	Co-precipitation	[20]
19	Cu, stainless steel and titanium coating onto PVA-impregnated cotton fabric	Cotton fabric, deionised water, acetone solution, polyvinyl acetate, Cu, 304 stainless steel	–	Magnetron sputtering	[21]

(continued)

Table 1 (continued)

S. No.	Composite	Raw materials	Methods for preparing the constituents of composite/textile	Methods of fabricating the final composite/textile	Reference
20	Polyurethane-antimony tin oxide composite fibre	Polyurethane solution, dimethyl formamide, tetrahydrofuran, tin chloride dehydrate, antimony chloride	Sol gel process	PU-ATO fibre was prepared by injecting sol through stainless steel needle installed on a syringe pump in to a water coagulation bath	[22]
21	ZnO:(Al–La) nanoparticle composite coated on cotton fabric	Cotton fabric, zinc nitrate, dehydrate, mono ethanolamine, aluminium chloride hexahydrate, lanthanum nitrate hexahydrate, ethanol, zirconia beads, sodium hexametaphosphate	Sol gel process	Coating	[23]
22	Carboxymethyl cotton fabric loaded by reduced graphene oxide	Plain woven cotton, graphene oxide dispersion, sodium chloroacetate, chitosan, acetic acid, sodium hydroxide, ethanol, sodium hydrosulphide	Alkalization and etherification	Layer-by-layer (LBL) self-assembly	[24]
23	Modification of Al pigment with graphene to coat cellulosic fibre	Ethanol, ammonia solution, acetone, isopropyl alcohol, 3-(aminopropyl)-trimethoxysilane, hydrazine hydrate, graphene oxide, aluminite powder, cellulosic fabric, polyurethane resin	Cationic pre-treatment, absorption and reduction	Coating machine onto cellulosic fabric	[27]

Table 1 (continued)

S. No.	Composite	Raw materials	Methods for preparing the constituents of composite/textile	Methods of fabricating the final composite/textile	Reference
24	Cotton fabric coated with ZnO:Al, In composite	Zinc nitrate dehydrate, isopropanol, monoethanol amine, aluminium chloride hexahydrate, zirconia beads, sodium hexametaphosphate, ethanol, polyvinyl acetate emulsion adhesive, cotton fabric	Sol gel process	Emulsification and coating	[28]
25	Silica aerogel-Ge/ZnS composite	Ge/ZnS multilayer film, silica substrate	–	Electron beam deposition	[26]
26	Aramid fabric coated with Cu	Aramid fabric and Cu film	–	Facile magnetron sputtering	[25]

- Composites of metals (metallic compounds)-nonmetals-semimetals (semi metallic compounds)-polymers (fabric) Class A
- Metal-polymer composites Class B
- Nonmetal-polymer composites Class C
- Metal (or metallic compound)-semimetal (or semimetallic compound) composites Class D
- Semimetal-polymer composites Class E
- Composites of metals (metallic compounds) Class F
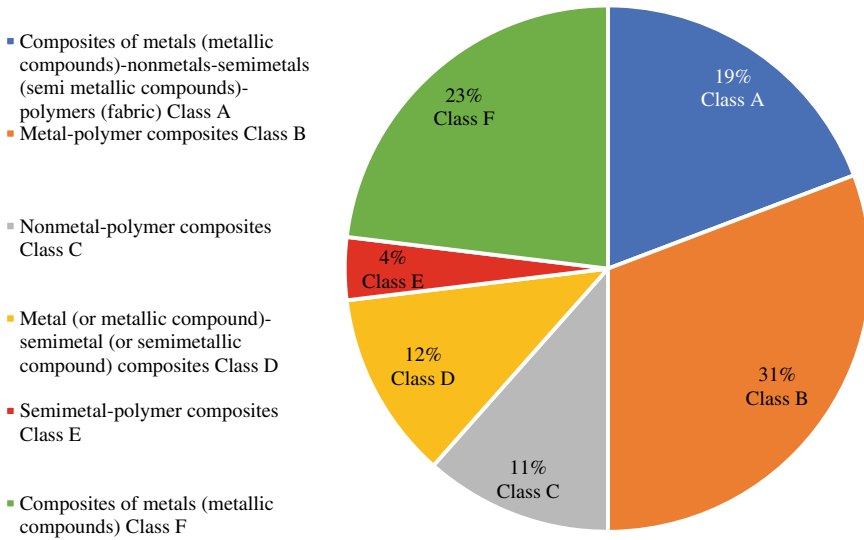
Fig. 1 Classification of composites

which is mostly used is silicon. Germanium and antimony are also used in few of the composites. Carbon (nanotubes and graphene) is the nonmetal used in fabrication of the composites. The polymers used are aramid, polyimide, polyurethane, polyvinyl acetate, polyacetylene, cellulose (cotton), etc. Thus, the composites can be classified into composites of metals (metallic compounds)-nonmetals-semimetals (semimetallic compounds)-polymers (fabric), metal-polymer composites, nonmetal-polymer composites, metal (or metallic compounds)-semimetal (semimetallic compounds) composites, semimetal-polymer composites and composites of metals (metallic compounds). Let these classes be named as class A, class B, class C, class D, class E and class F, respectively. Figure 1 illustrates this classification of composites along with their percentage.

The objective behind reviewing the infrared camouflage composites is to identify the composites which can be suitably used as wearable textiles such as military uniforms, clothing for thermal comfort or high-altitude clothing. From Fig. 1, it can be inferred that most of the reviewed samples are class B composites followed by class F, class A, class D, class C and class E. Class A, class B, class C and class E composites present the potential to be used as a wearable textile but further research is required to ascertain their effects on human skin. Further, experiments required to be performed as per established standards to check the suitability of the reviewed samples as a wearable textile. Class D and class F are not suitable as a textile material but can be effectively used as a coating material such as pigments and paints.

This research paper also reviews the methods employed in fabricating the composites. The reviewed IR camouflage composites have been prepared using different methods. These methods are based on nature of the composites whether

metals, semimetals, nonmetals or polymers. The fabrication methods employed are mentioned in Table 1. The reported methods to fabricate the individual constituents of the composites consist of doping, sol gel process, calcination, hydrolysis, hydrothermal reaction, etc. The methods to fabricate the constituents of the composites is shown along the *x*-axis and number of composites where these methods are used is shown along the *y*-axis in Fig. 2. During review, it was observed that the individual constituents are not fabricated using a single method but combination of more than one method. However, sol gel method was used mostly to prepare the constituents of the composites as seen from Fig. 2.

The methods to prepare the final composites against the number of composites is shown in Fig. 3. It can be observed from the figure that coating method was used mostly to prepare the final composite. However, different types of coating methods
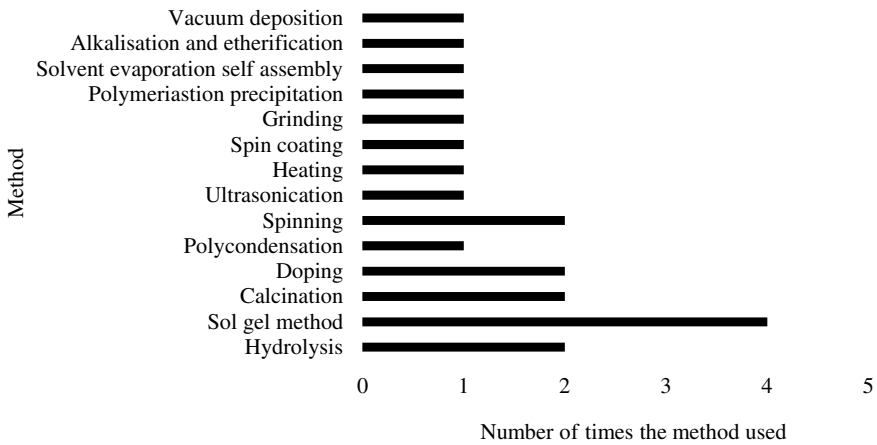
Fig. 2 Constituent fabricating methods
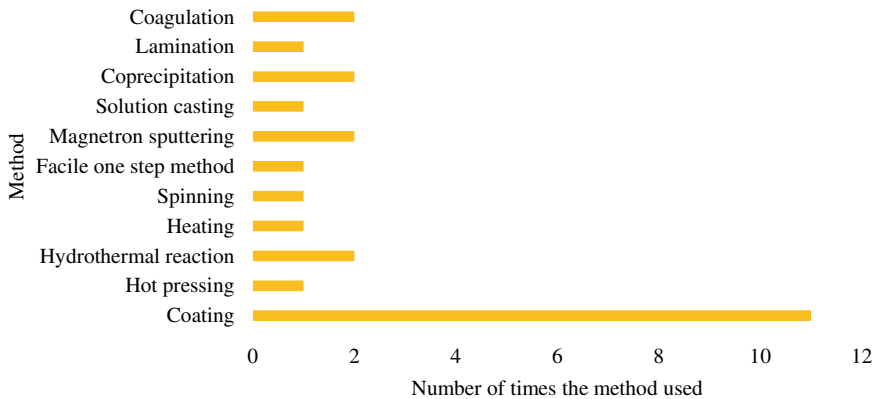
Fig. 3 Methods to fabricate final composite

were used such as automatic coating, spray coating, pulse laser deposition, vacuum coating, electron beam evaporation and brush coating. In textile industry, most textiles are made from fibres. These fibres can be natural or synthetic. Spinning is the process adopted to convert these fibres to yarns for further fabrication of textiles. Hence, research is further required to develop composite fibres commercially and convert these composite fibres to yarns and finally to a textile.

The current military uniforms and other military clothing articles are effective for visual camouflage simultaneously maintaining thermal comfort of human body. However, these textiles are not effective in shielding IR rays emitted from human body. Hence, it makes a soldier on mission vulnerable to detection by infrared detection system. Also, a single uniform is not able to fulfil the requirements of different environments and climate. For example, a uniform which is worn in desert area cannot be worn at high-altitude or cold climatic region. The reviewed composites have potential to perform these functions simultaneously. However, these composites are not examined for their applicability as wearable textiles. Hence, further research can be carried out in this area. The current military uniforms are either woven/knitted/non-woven. Coated textiles are seldom used for manufacture of military uniforms. But it was observed that the reviewed composites were mostly prepared using coating. Thus, research can be carried out in developing textiles with knitted/woven/non-woven structures and test their effectiveness in suppressing IR rays and simultaneously providing thermal comfort. Research is also required to check the commercial production of these composites as wearable textile in a cost-effective manner.

3 Infrared Shielding Property

The infrared shielding property of the reviewed composites is described by their emissivity/reflectivity/transmissivity. It is an indicative of how well the composites can prevent the detection of target objects from thermal imaging devices. The lower the emissivity of the composite better is the infrared shielding property. In other words, lower emissivity materials are much more capable of suppressing the IR rays emitted by an object's surface or a human. Lower emissivity materials act as barriers in preventing propagation of infrared rays that can travel to the detection systems through the atmosphere. The researchers have measured emissivity of different samples and also tested their shielding properties. Further, they have characterised the waveband at which infrared shielding is achieved. Table 2 shows the emissivity of the samples and the waveband at which shielding occurs.

From Table 2, it can be inferred that the experiments performed by the researchers showed that the prepared composites have low emissivity and were able to prevent the propagation of infrared rays of different wavebands emitted by hot surfaces. Many composites achieved emissivity less than 0.5. Figure 4 graphically summarises the percentage of composites shielding different IR wavebands. A human body at 36 °C

Table 2 Emissivity/Reflectivity/Absorptivity/Transmissivity of prepared composites

S. No.	Composite	Emissivity (ε)/Reflectivity (ρ)/Transmissivity (τ)/Absorptance (α)	IR waveband	Reference
1	CNT-doped aerogel hot pressed on polyimide fabric and coated with Al-doped ZnO	$\varepsilon < 0.5$	–	[4]
2	Tungsten-doped VO_2 thin films coated on cotton fabric	$\varepsilon = 0.752$, after washing the composite $\varepsilon = 0.852$	8–14 μm	[5]
3	SiO_2–BiO_3 composite	$\varepsilon = 0.75$	2–22 μm	[6]
4	Polyurethane-Cu composite	$\varepsilon = 0.10$	8–14 μm	[7]
5	ZnO:Al thin films	$\varepsilon = 0.5$	1.5–2 μm	[8]
6	SnO_2–ZnO nanocomposite	$\varepsilon = 0.65$	3–5 μm	[9]
7	Photonic crystal films coated on polystyrene and polyethylene terephthalate (PET)	$\varepsilon = 0.05$	8–12 μm	[12]
8	Polypropylene bicomponent fibre with metallic fillers	$\varepsilon = 0.62$	–	[10]
9	SiO_2–TiO_2 films	$0.15 < \varepsilon < 0.60$ when composite is strained between 0 and 60%	5 μm	[11]
10	Al–MnO_2 composite	$0.55 < \varepsilon < 0.72$	–	[13]
11	Al-polymer composite	$\varepsilon = 0.31$	8–14 μm	[14]
12	TiO_2–Cu–TiO_2-coated polyester fabric	$\varepsilon = 0.7$	8–14 μm	[15]
13	Polyacetylene with multiwalled CNTs	$\varepsilon = 0.503$	8–14 μm	[16]
14	Fe-doped ZnO powders	$0.84 < \varepsilon < 0.86$	8–14 μm	[17]
15	Carbon–aluminium-doped zinc oxide-coated cotton fabrics	$\varepsilon = 0.795$	8–14 μm	[18]
16	Stainless steel textiles	$0.70 < \varepsilon < 0.80$	3.6–5.1 μm	[3]
17	Graphene-enabled adaptive infrared textile	$0.65 < \varepsilon < 0.80$ $0.50 < \varepsilon < 0.75$ $0.35 < \varepsilon < 0.70$	0.9–1 μm 3–5 μm 8–13 μm	[19]
18	$Sn_{(1-x)}$–Fe_xO_2 ($x = 0$, 0.03, 0.06 and 0.09) composite	$0.75 < \varepsilon < 0.95$	8–14 μm	[20]

Table 2 (continued)

S. No.	Composite	Emissivity (ε)/Reflectivity (ρ)/Transmissivity (τ)/Absorptance (α)	IR waveband	Reference
19	Cu, stainless steel and titanium coating onto PVA-impregnated cotton fabric	$0.75 < \varepsilon < 0.83$ for Cu-coated sample $0.83 < \varepsilon < 0.975$ for Ti-coated sample $0.8 < \varepsilon < 0.93$ for stainless steel-coated sample	1–20 µm	[21]
20	Polyurethane-antimony tin oxide composite fibre	$\tau = 0.02$	7–14 µm	[22]
21	ZnO:(Al–La) nanoparticle composite coated on cotton fabric	$\varepsilon = 0.625$	8–14 µm	[23]
22	Carboxymethyl cotton fabric loaded by reduced graphene oxide	$0.40 < \varepsilon < 0.70$	0.2–2.5 µm	[24]
23	Modification of Al pigment with graphene to coat cellulosic fibre	$0.60 < \varepsilon < 0.75$	8–14 µm	[27]
24	Cotton fabric coated with ZnO:Al, In composite	$\varepsilon = 0.658$	8–14 µm	[28]
25	Silica aerogel-Ge/ZnS composite	$0.75 < \varepsilon < 0.95$	8–14 µm	[26]
26	Aramid fabric coated with Cu	$0.10 < \varepsilon < 0.20$	8–16 µm	[25]

Fig. 4 Percentage of composites and wavebands shielded
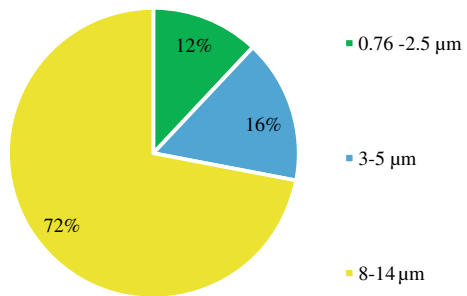
has maximum emission at 9.4 µm while a background at 20 °C has maximum emission at 9.9 µm [30]. Since majority of the reviewed composites prevented the propagation of the infrared rays belonging to waveband 8–14 µm, as observed from Fig. 4, these composites could be used in manufacturing of infrared camouflage uniforms, tents shoes and clothing for thermal comfort. Some of the researchers had carried out experiments on properties such as strength and washability to check their effect on
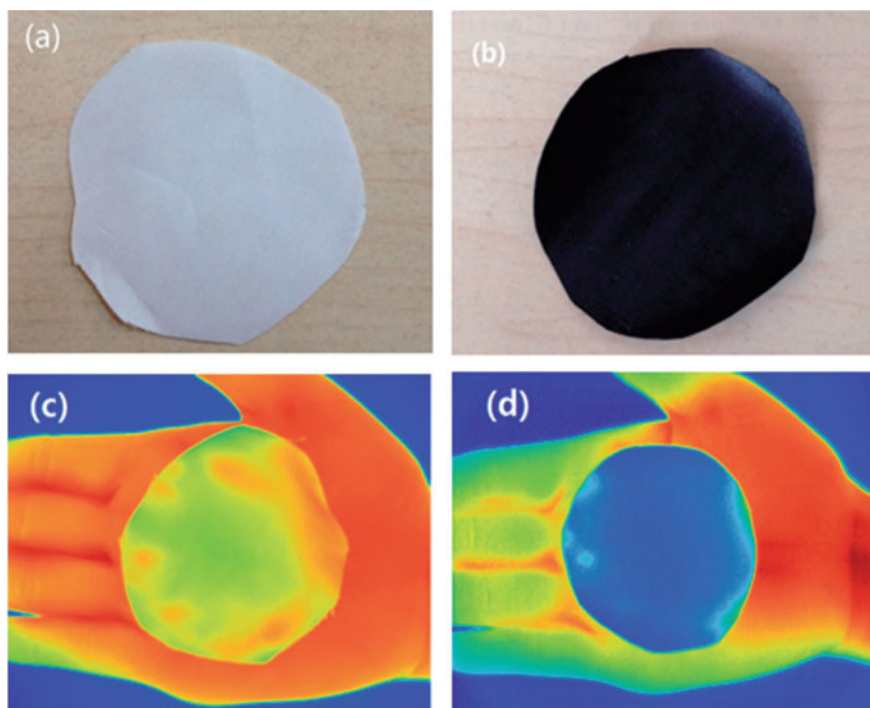
Fig. 5 a Real image of uncoated fabric. **b** Real image of coated fabric with (C–AZO) content of 40 wt%. **c** Infrared image of uncoated cotton fabric. **d** Infrared image of coated cotton fabric with C–AZO content of 40 wt% [18]

emissivity. However, further research is still required to develop a wearable multi-weather, multipurpose infrared camouflage uniform/soldier gear. Figure 5 shows the thermal image of the composite developed by Wang et al. as an example of shielding property of the composite.

A complete understanding of the infrared shielding property is possible when the reviewed composites are compared with the commercial materials. Polyimide has infrared emissivity of 0.521 in the waveband of 8–14 μm. But, CNT-doped aerogel hot pressed on polyimide fabric and coated with Al-doped ZnO has emissivity less than 0.5. Commercially available cotton has emissivity of 0.940 but tungsten-doped VO_2 thin films coated on cotton fabric has emissivity of 0.752. Similarly, commercially available polyurethane has emissivity around 0.90. But a PU–Cu composite has emissivity of 0.1. The infrared emissivity of polymer binders such as acrylic resin, epoxy resin, epoxy silicone resin and modified fluorocarbon resin is 0.91, 0.93, 0.94 and 0.86, respectively. The emissivity of these polymer binders is too high to be used as materials for infrared stealth. However, Al-polymer composite has emissivity as low as 0.31. Polyester fabric has emissivity of around 0.95. When coated with TiO_2–Cu–TiO_2, emissivity was reduced to 0.7 as observed from Table 2. Commercial ZnO has emissivity of 0.92, but from Table 2, it can be observed that when Fe is doped

with ZnO, the composite had emissivity between 0.84 and 0.86. When commercial cotton fabric with emissivity of 0.940 is coated with carbon–aluminium-doped zinc oxide, the resultant composite had emissivity of 0.795. Thus, it can be seen that the composite developed by the researchers had better infrared shielding properties than their constituents. Also, the constituents alone cannot be used to fabricate an IR stealth material but as a composite proves to be excellent IR stealth material.

4 Applications of Infrared Stealth Composites

The reviewed composites have potential applicability in various areas. CNT-doped aerogel hot pressed on polyimide fabric and coated with Al-doped ZnO [4], tungsten-doped VO_2 thin films coated on cotton fabric [5], stainless steel textiles [3], Polyurethane-antimony tin oxide composite fibre [22], etc., can be used to develop infrared camouflage uniforms, helmets, shoes tents and thermal protective gears for high temperature applications. ZnO:(Al–La) nanoparticle composite coated on cotton fabric [8] is a promising material to manufacture NIR reflecting mirrors and heat reflectors. SnO_2–ZnO nanocomposite [9] and polypropylene bicomponent fibre with metallic fillers [10] have excellent radar-absorbing composites apart from IR stealth. Al–MnO_2 composite [13] is a potential electromagnetic shielding and infrared stealth material. Al-polymer composite [14] and Al pigment with graphene [27] can be used as infrared camouflage coating material. TiO_2–Cu–TiO_2-coated polyester fabric [15] can be used in areas such as sunlight management, IR stealth and outdoor protective textiles. Polyacetylene with multiwalled CNTs [16], Fe-doped ZnO powders [17] and $Sn_{(1-x)}$–Fe_xO_2 composite [20] have potential microwave absorbing characteristic apart from IR stealth. Graphene-enabled adaptive infrared textile [19] have applicability in the field of IR stealth, communication, adaptive space suits and fashion textile. Cu, stainless steel and titanium coating onto PVA-impregnated cotton fabric [21] can be used in manufacturing sensors, IR stealth and antistatic textiles. Carboxymethyl cotton fabric loaded by reduced graphene oxide [24] has potential applications in the field of infrared stealth, desalination, sewage treatment and UV protective textiles. Silica aerogel-Ge/ZnS composite [26] can open windows to develop MIR optical materials and devices.

5 Conclusion

The samples prepared by the researchers have potential application in the field of wearable infrared stealth textiles. These composites are based on metals/polymers/semimetals/nonmetals. The review of the papers showed that only few metals are reported with low emissivity. For example, Al is used as a low emissive material for preparation of composite in most of the samples. Some adhesives/polymers with low emissivity were also used to fabricate the composites.

This review paper presents the raw materials used by the researchers to prepare the samples along with different fabrication techniques to fabricate the composites. However, coating technology, magnetron sputtering and co-precipitation remains the most favoured processes to prepare the samples. For characterising the morphology, crystal structure, infrared emissivity and thermal analysis, the authors have used SEM, XRD, Infrared imaging and TG/DSC methods, respectively. Since this paper focuses on infrared stealth capability of prepared composites, the review brings out the potential of these composites as infrared shielding materials. These composites have low emissivity/high reflectivity/high absorptance so that they can shield the target object. During the review, it was observed that only few of the composites have developed as wearable textiles. However, tests and experiments need to be carried out as per standards so that they can be used for manufacturing of uniforms. Most of the reviewed composites uses coating technology as method of fabrication. Coated fabrics are further required to test for washability, wear and tear, air permeability, etc. The current review of the composites does not bring out the cost of these composites. However, the products which have the IR stealth as their property are high in costs. For example, infrared IR blocker insulator hydro grow room thermal shield film [31] has high cost. However, if research is carried out to develop these composites to a commercial product, there is probability that costs of current products in market may decrease.

6 Way Forward

The samples were prepared by various researchers using different raw materials. This presents a scope to search for other materials and composites which would have low emissivity. Adaptive infrared stealth composites which means tuning the emissivity of the composites as per the requirement provides a window for further research. This would be enhancement to the field of adaptive infrared camouflage materials. There is scope of reducing the emissivity further by adoption of new materials such as nanocomposites and improving methods of fabrication. The composites reviewed in this paper are able to shield infrared rays belonging to waveband 3–5 and 8–14 μm. But, now advances have been made in detection technologies where infrared radiations up to 25 μm can be detected [30]. Hence, extensive research is required to search for composites which could shield the target body from these newly developed detection technologies. The reviewed composites are not weaved or knitted. But military uniforms currently in use are either weaved or knitted. Hence, further research is required to convert these composites to fibres which can be effectively designed into a wearable form. Since the reviewed composite are laboratory samples, further research is required to render these samples fit for commercial production. Infrared stealth is not limited to soldier's uniform, but there are other strategic assets such as missile systems and military equipment which require visual as well as thermal concealment. These equipment have their own infrared signatures and can be detected by infrared detection systems. Research is needed to develop products/composites

such external covers and tents, which can prevent their detection from IR detecting systems. Few of the composites have other application such as ultraviolet protection and electromagnetic shielding. This presents scope of searching other fields of application where these composites can be used.

References

1. Zhou X, Xin B, Liu Y (2021) Research progress on infrared stealth fabric. J Phys Conf Ser 1790(1)
2. Ali A, Tiwari P (2017) Camouflage textile. J Fibre Finish 56(1)
3. Larciprete MC, Paoloni S, Voti RL, Gloy YS, Sibilia C (2018) Infrared radiation characterization of several stainless steel textiles in the 3.5–5.1 μm infrared range. Int J Therm Sci 132(February):168–173
4. Xu R, Wang W, Yu D (2019) A novel multilayer sandwich fabric-based composite material for infrared stealth and super thermal insulation protection. Compos Struct 212:58–65
5. Mao Z, Wang W, Liu Y, Zhang L, Xu H, Zhong Y (2014) Infrared stealth property based on semiconductor (M)-to-metallic (R) phase transition characteristics of W-doped VO_2 thin films coated on cotton fabrics. Thin Solid Films 558:208–214
6. Liu X, Lai Y, Huang J, Al-deyab SS (2014) Hierarchical SiO_2@Bi_2O_3 core/shell electrospun fibres for infrared stealth camouflage. J Mater Chem C
7. Yu H, Xu G, Shen X, Yan X, Cheng C (2009) Low infrared emissivity of polyurethane/Cu composite coatings. Appl Surf Sci 255:6077–6081
8. Gong L et al (2021) Highly transparent conductive and near-infrared reflective ZnO: Al thin films. Vaccum 84(7):947–952
9. Zhang Z, Xu M, Ruan X, Yan J, Yun J, Zhao W (2016) Enhanced radar and infrared compatible stealth properties in hierarchical SnO_2@ZnO nanostructures. Ceram Int
10. Yu B, Qi L, Ye JZ, Sun H (2007) The research of radar absorbing property of bicomponent fibers with infrared camouflage. J Polym Res 14(2):107–113
11. Wang J, Li Y, Cui J, Guo H (2018) Highly stretchable micro/nano wrinkle structures for infrared stealth application. Nanoscale Res Lett 0–6
12. Chao W, Lei W, Zhen-hua C, Feng-xiang Z, Jia-wei L (2016) Production of flexible photonic crystal films for compatible far infrared and laser-band camouflage by vacuum coating method. J Russ Laser Res 37(3):308–312
13. Liu H, Xing H (2020) Facial synthesis of Al @ MnO_2 with enhanced microwave absorption and low infrared emissivity. J Mater Sci: Mater Electron
14. Huang X, Rao W, Chen Y, Ding W (2016) Infrared emitting properties and environmental stability performance of aluminum/polymer composite coating. J Mater Sci: Mater Electron 27(6):5543–5548
15. Peng L et al (2018) IR protection property and color performance of TiO_2/Cu/TiO_2 coated polyester fabrics. J Mater Sci: Mater Electron 29(19):16188–16198
16. Pan W, He M, Bu X, Zhou Y, Ding B (2017) Microwave absorption and infrared emissivity of helical polyacetylene @ multiwalled carbon nanotubes composites. J Mater Sci: Mater Electron
17. Su X et al (2014) Preparation, infrared emissivity and dielectric and microwave absorption properties of Fe-doped ZnO powder. J Electron Mater 43(11):3942–3948
18. Wang W, Fang S, Zhang L, Mao Z (2015) Infrared stealth property study of mesoporous carbon-aluminum doped zinc oxide coated cotton fabrics. Text Res J 85(10):1065–1075
19. Ergoktas MS et al (2020) Graphene-enabled adaptive infrared textiles. Nano Lett
20. Su X et al (2015) Preparation, infrared emissivity and electromagnetic property of Sn(1–x)Fe_xO_2 (x = 0, 0.03, 0.06, and 0.09) solid solution powders by coprecipitation method. Arab J Sci Eng 2:2969–2974

21. Jiang S, Xu J, Chen Z, Guo R, Miao D, Peng L (2018) Enhanced electro-conductivity and multi-shielding performance with copper, stainless steel and titanium coating onto PVA impregnated cotton fabric. J Mater Sci: Mater Electron
22. Jeong S et al (2020) Development of a wearable infrared shield based on a polyurethane–antimony tin oxide composite fibre. NPG Asia Mater 12:32
23. Mao Z, Yu X, Zhang L, Zhong Y, Xu H (2014) Novel infrared stealth property of cotton fabrics coated with nano ZnO: (Al, La) particles. Vacuum
24. Liu Y et al (2019) Structure and properties of carboxymethyl cotton fabric loaded by reduced graphene oxide. Carbohyd Polym 214(March):117–123
25. Jia L, Fu B, Lu ML, Liang H, Wang L (2020) High-performance aramid fabric in infrared shielding by magnetron sputtering method. Mater Res Express
26. Zhu H, Li Q, Zheng C, Hong Y, Ghosh P, Qiu M (2020) High-temperature infrared camouflage with efficient thermal management. Light: Sci Appl 9:60
27. Wang K, Wang C, Yunjie Y, Kunlin C (2016) Modification of Al pigment with graphene for infrared/visual stealth compatible fabric coating. J Alloy Compd
28. Yu X, Zhang L, Zhong Y, Xu H, Mao Z (2014) Novel infrared stealth properties of cotton fabric with ZnO:(Al, In) coating. Adv Mater Res 936:1031–1034
29. Yu X, Zhang L, Zhong Y, Xu H, Mao Z (2014) Effect of La content on the infrared stealth property of ZnO:(La, Al) coated on cotton fabrics. Appl Mech Mater 692:337–340
30. Denning RJ (2018) Camouflage fabrics, CSIRO manufacturing. Elsevier Ltd., Geelong
31. https://www.desertcart.in/products/164069350. Last accessed 13 Jan 2022

Microstructure and Mechanical Behaviour of Reinforced Aluminium-Based Surface Composites Synthesized by Friction Stir Processing Route: A Review

Abdul Jabbar Ansari and Mohd Anas

1 Introduction

Aluminium alloys are bringing extensive interest worldwide due their remarkable thermal and mechanical properties like high thermal conductivity, excellent corrosion resistance and high strength to weight ratio. However, due to its poor wear resistance it has some limitation in application. Strength of fabricated metal matrix composite is increased due to reinforcement of various particles of different sizes [1]. Metal matrix composite has been fabricated mainly through molten metal processing and powder metallurgy route [1, 2]. Friction stir processing is appeared as one of the best technique in solid state to fabricate aluminium metal matrix composite [3]. This process is more often used to fabricate aluminium-based metal matrix composite [4]. FSP on aluminium and its alloys as a metal typically used in research include AA1050 [5, 6], AA2024 [7–9], AA2095 [10], AA5083 [11–13], AA5086 [14], AA6061 [15, 16] and AA7075 [17]. For the modification of microstructure of MMC, FSP technology is very effective [18]. In FSP, plastic deformation is occurred due to forging force exerted by tool and heat which is developed due to friction available between tool and workpiece. Hence, in FSP workpiece never reach their melting temperature [19]. Grains of casting also refined using FSP [20]. Microstructure of reinforced metal matrix composite can be homogenising using FSP [21]. Strength of AMMC can be increased with reinforcement materials like SiC, Al2O3, B4C and TiC by using FSP technology [22]. There has been large number of research on the application of FSP to fabricate a metal matrix composite on the surface of a plate by creating a groove on the surface of base metal filled with reinforcement particles [23]. For obtaining a uniform distribution of reinforcement particles in groove and homogenised microstructure, multiple FSP passes are applied [24]. The different

A. J. Ansari (✉) · M. Anas

Department of Mechanical Engineering, Integral University, Lucknow, Uttar Pradesh 226026, India

e-mail: techno.abdul@gmail.com

parameters of FSP also affect the morphology, dissemination and disintegration of reinforcement particle [25, 26]. The tool design variable (shoulder diameter, pin length, pin profile, pin diameter, etc.) and machine variable (tool traverse speed, tool rotational speed, tool tilt angle, tool plunge depth) are responsible for behaviour of material flow. Many researchers have proved that hot working tool steel with the ratio of shoulder diameter and pin diameter (D/d) of 3 are suitable for processing of aluminium alloy [27–29].

1.1 Al–Si Composites

Lee et al. [30] reinforced Si particles in Al matrix by using multiple passages of FSP with varying Si content and found that after adding Si composites, strengthening of composites was increased due to matrix substructure. It was also observed that Si particle was uniformly dispersed in Al matrix and fine grain structure was obtained due to Orowan strengthening and dislocation generated by thermal mismatch [31]. This thermal mismatch is because of rapid cooling after FSP. Figure 1 shows the TEM analysis of Al-20Si in which lower dislocation density was higher in FC specimen as compared to WC specimen because of during slow cooling, more time was given for stress relaxation and due to this specimen has lower strength as compared to WC specimen.
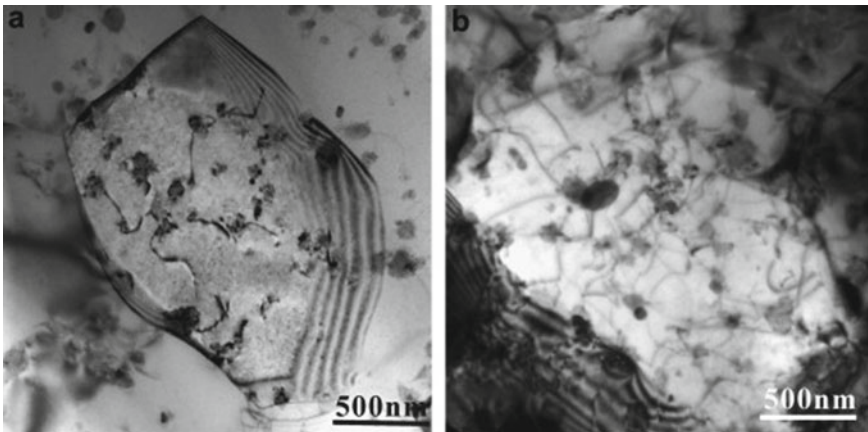
Fig. 1 Shows that the transmission electron microscopy testing (TEM) analysis of Al-20Si composite after annealing at 723 K and succeed by furnace cooling (FC) and water cooling (WC), respectively (Lee et al. [30] Permission obtained from the rightsholder)

1.2 Al–TiC Composites

Jerome et al. [32] reported that particle distribution is increased at high tool rotational speed (1400 r.p.m.) when TiC particle reinforced in Al 5083 matrix through FSP and investigated particle distribution in matrix using optical microscopy and scanning electron microscopy (SEM). Due to lower rotational speed, low heat is obtained; hence, flow material was low. The dissemination of reinforced particles becomes more homogeneous by increasing the number of passes. Hardness of the MMC is also increased due higher rotational speed. This is due to the fact that base metal Al5083 is strain hardenable alloy because flowability of the material increases due the high heat developed by high rotational speed [7]. Hardness of the composite is also increased due refinement of grains (Hall–Petch Strengthening). When the speed of the tool varies from 500 to 900 rpm, the wear rates also increased because the energy of the impinging particle was increased due to higher kinetic energy.

Akinlabi et al. [33] observe the effect different process parameters like tool rotational speed and tool traverse speed on wear resistance behaviour of Al–TiC composite fabricated by Friction stir processing. He prepared 9 samples by reinforcing TiC particle (Size below 60 μm) into aluminium alloy (AA1050). Different processing parameter like rotational speed employed was 800–1600 r.p.m., and feed rate was 100–300 mm/min. It is found that by increasing the rotational speed, the wear volume was also increased (Fig. 2). For improving the wear resistance property, a certain sequence of process parameters is mandatory. At low rotational speed, different surface defects are produced because low amount of heat is generated and inadequate melting of TiC powder. Wear resistance property is decline due to the dilution of base metal (aluminium) and reinforcement powder (TiC) because immense amount of heat is generated at high rotational speed. The best wear resistance was obtained at combination of 100 mm/min traverse speed and 1200 rpm rotational speed. The microhardness of the fabricated composite is improved at high rotational speed because the volume of unmelted powder was reduced. At high rotational speed,
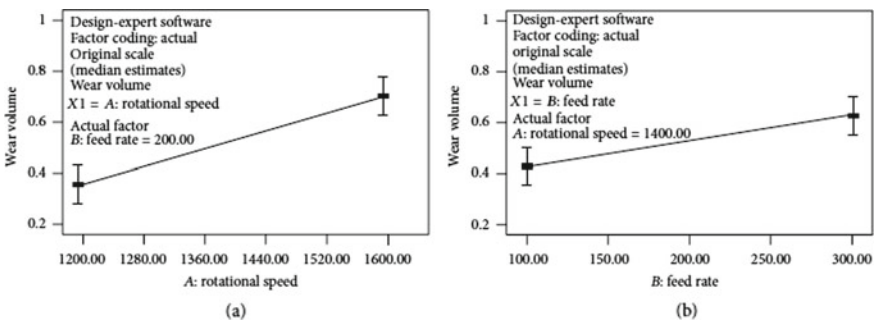
Fig. 2 **a** Wear volume versus rotational speed, **b** wear volume versus feed rate (Akinlabi et al. [33] open-access journal)

when the feed rate (traverse speed) is increased the microhardness property was also increased due to low heat generation.

Thangarasu et al. [34] analysed the effect of tool traverse speed on mechanical properties and microstructure of composite AA6082-TiC fabricated by friction stir processing. When the tool traverse speed increased from 40 to 80 mm/min, the area of aluminium metal matrix composite is decreased because amount of heat generated is decreased and less amount of aluminium is plastisized [27]. In SEM graph, it is also revealed that the distribution of TiC particle is gradually decreased by increasing traverse speed because material transportation from advancing side retreating side is reduced. Non-homogeneous distribution is occurred due to low mixing of plasticised aluminium and TiC particle. The microhardness is increased from 112HV to 135HV by increasing tool traverse speed from 40 to 80 mm/min. Poor dispersion of TiC particle due insufficient material transportation was found at highest tool traverse speed of 80 mm/min. Volume fraction of reinforced particle (TiC) is increased and therefore produces higher hardened surface composites at high traverse speed. Volume is inversely proportional of hardness (Archard's law) of fabricated composite so wear rate was decreased by increasing in traverse speed.

Thangarasu et al. [3] reported that when TiC particles (size 2 µm) reinforced in aluminium alloy AA6082 and taken five level of volume fraction 0, 6, 12, 18 and 24%. Theoretical and actual volume fraction also calculated by following expression.

$$\text{Theoratical volume fraction}(V_t) = \frac{\text{Area of groove}}{\text{Projected area of tool}} \times 100$$

$$\text{Actual volume fraction}(V_a) = \frac{\text{Area of groove}}{\text{Area of surface composite(Stir Zone)}} \times 100$$

Area of surface composite (stir zone) is calculated using image analysing software. When percentage of volume fraction of reinforcement particle (TiC) is increased, the area of surface composite decreased, and at 0% volume fraction, it becomes 65 mm^2 and at 24% reaches at 34 mm^2. By enhancing the volume fraction, the amount of TiC particle increased in stir zone and plasticized aluminium matrix is reduced. Heat generated by friction is absorbed by TiC particle; hence, temperature of FSP zone is reduced. Final effect of greater flow stress is required to plasticize AMC. Hence, area of AMC was reduced. At 0 vol%, the microhardness was found 62HV and UTS 222 MPa, and at 24 vol%, microhardness was found 149HV and UTS 382 MPa. The TiC particle was distributed uniformly in stir zone which bring Orowan strengthening [31]. Mechanical properties of fabricated AMC are increased at high volume fraction of reinforcement particle (TiC) because average distance between particles decreased which bring high resistance to the dislocation act.

Yuvaraj et al. [19] analysed the effect of reinforcement particle TiC (size 30–60 nm) reinforced in the base metal aluminium alloy Al5083 through friction stir processing route. Grain refinement of the composite is increased due to multipass (Four passes). Main disadvantages of the multipass are the amount of heat generated increased drastically which produced negative effect on properties of fabricated

material [35]. Due to grain refinement and dynamic recrystallization, the average size of grain is reduced to 14.5 μm from 49.5 μm of the processed sample without particle. The grain size in fabricated material is refined due dynamic recovery mechanism, continuous dynamic recrystallization mechanism and particle nucleation mechanism [35, 36]. Due to large amount of grain boundaries of large size, the grain size of fabricated material is decreased [37]. Hardness of the fabricated material is also increased due to uniform grain refinement and extremely high hardness of reinforcement particle.

Sanusi et al. [38] reinforced TiC powder (size below 60 μm) in base metal (AA1050) through friction stir processing technique. Distribution of TiC powder is not uniform at slower travel speed of tool. Due to the reinforcement TiC powder and grain refinement of matrix, the hardness of metal matrix composite is increased. But throughout processed zone, hardness was not uniformed and high hardness was observed where TiC particles were spotted more.

Apireddi Shiva et al. [39] revealed that the hardness was improved of Aluminium (1050) metal matrix composite-reinforced TiC particles fabricated through friction stir processing technique. With dynamic recrystallization and consequences of pinning grain, structure of friction stir-processed composite is refined [40, 41]. Microhardness distribution is increased by attire distribution of reinforced particles and hence accomplishes higher hardness in fabricated material.

Sudarshan Kumar et al. [42] explained the behaviour of corrosion resistance property of Al7075-TiC composite material fabricated through friction stir processing technique. He used electrolyte molarity as 1, 2 and 3 M of NaCl. With the help of Tafel Extrapolation and adopting technique of polarisation, corrosion rate is calculated from corrosion current density. The free electrons available in base metal (Al7075) are higher than the available free electrons in Al7075-TiC composite due to which corrosion resistance property is increased as in the matrix the development of intermetallic (Al_4C_3 and Al_3Ti) required free electron in matrix. Table 1 represent the relation between corrosion rate and percentage volume fraction of reinforced material in different concentration of NaCl.

Table 1 Variation of rate of corrosion in composite (Al7075-TiC) with different concentration of NaCl

TiC vol%	Corrosion rate (Mile/Year)	Corrosion rate (Mile/Year)	Corrosion rate (Mile/Year)	Corrosion rate (Mile/Year)
	3.5% NaCl	1 M NaCl	2 M NaCl	3 M NaCl
0	1.6733	1.8633	2.8208	3.9976
2	1.2335	1.6467	2.1699	3.4347
4	0.5329	0.6067	0.8680	1.9329

Sudarshan Kumar et al. [42] permission obtained from the rightsholder

1.3 Al–Cr–O Surface Nano Composite

Anvari et al. [43] reinforced Cr_2O_3 powder into Al6061-T6 plate (13 mm thickness) through FSP. He applied a new procedure in which powder of Cr_2O_3 is applied by atmosphere plasma spray method on Al6061-T6 plate. The XRD pattern of nugget zone cross section after 6 passes indicates that due to the reaction between aluminium (Al) and chromium (Cr) during FSP, intermetallic compound of Al–Cr is developed. Reaction between aluminium and chromium is exothermic, and it is initiated by heat provided by FSP tool. Wear resistance of nano composite is enhanced in comparison with FSPed sample because hardening participates were lost in FSP processing. Main participator for strengthening in Al6061 is β''-Mg5Si, which is steady below temperature 200 C [44]. In nugget zone, the β'' precipitate is dissolved because the temperature was above 300 C through FSP. For hardening, β'' precipitate was the main reason [45].

1.4 Al6061-SiC (Graphite Hybrid Surface Composite)

Sharma et al. [46] studied the effect of reinforcement of SiC in base metal Al6061 (graphite hybrid surface composite) through FSP. Mono and hybrid composite is fabricated using reinforcement particle SiC (100 μm) and graphite powder (44 μm). The mean axial force is increased in aluminium-graphite mono composite because graphite has large thermal conductivity (Fig. 3).
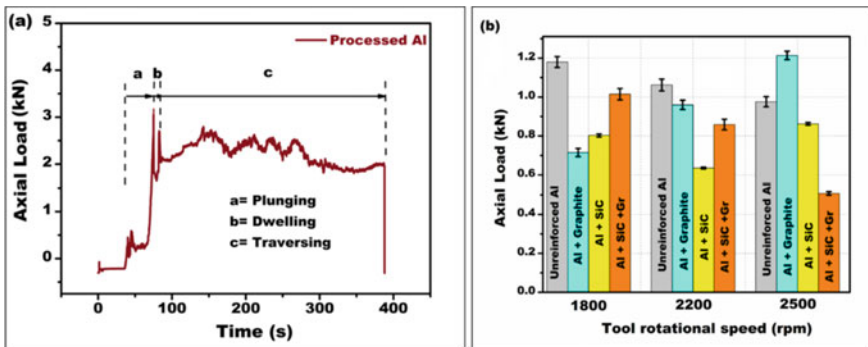
Fig. 3 **a** Non-reinforced Al6061 prepared at 2200 rpm axial load versus time curve, **b** different reinforced axial load versus time curve (Sharma et al. [46] open-access journal)

1.5 Al2024-SiC Metal Matrix Composite

Hosseinzadeh et al. [47] used FSP for the fabrication of surface composite by reinforcement of SiC particle. Refined grain structure is obtained in FSP with SiC particle (Fig. 4). Fine grains are obtained because in stir zone the material subjected plastic deformation [48]. In stir zone, the new grains nucleation affirm at many locations [49, 50]. Average grain size is decreased and density of grain boundaries is increased with respect to the refinement of grains.

Hardness of FSPed and MMC is increased from 30 to 50%, respectively. Hardness is mainly increased in extra zone when direction of passes is changed (Fig. 5) (Table 2).
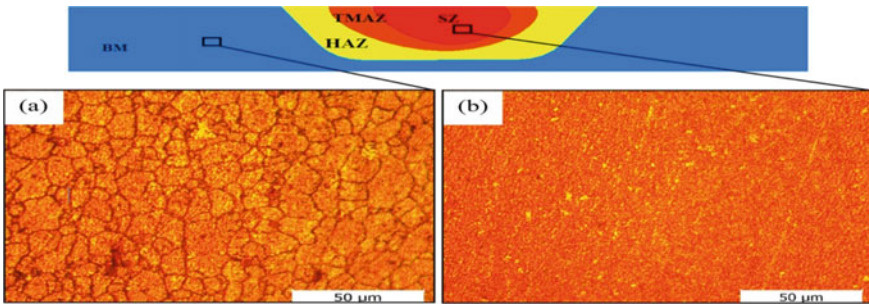
Fig. 4 Microstructure of Al 2024 **a** initial, **b** final (Hosseinzadeh et al. [47] permission obtained from the rightsholder.)
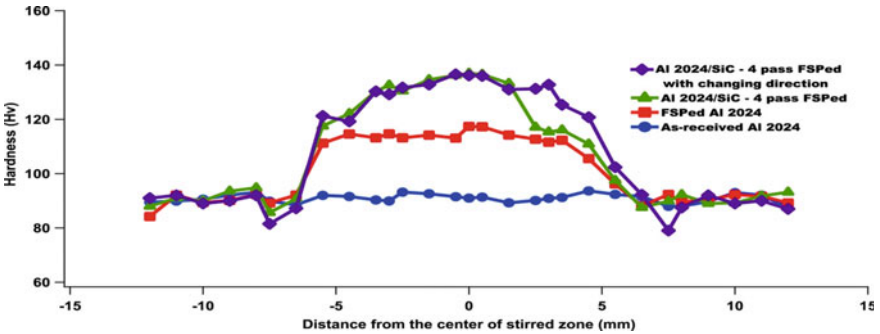
Fig. 5 Hardness of Al2024-SiC tested from centre of stirred zone (Hosseinzadeh et al. [47] permission obtained from the rightsholder.)

Table 2 Comparative analysis of base material and reinforcement with their prominent results

Material	Reinforced material	Material and geometry of tool	Processing parameters	Results	References
Aluminium powder	Silicon powder	Diameter of tool shoulder = 16 mm Diameter of tool pin = 6 mm Height of tool pitch = 1.2 mm	Rotational speed of tool = 700 rpm Traverse speed of tool = 45 mm/min Tool spindle angle = 3° No. of passes = 4	(1) Refined grain structure is obtained (2) Strength of composite increased	[30]
Aluminium 5083 alloy	TiC particles with average particle size 4–10 μm	Diameter of tool shoulder = 16 mm Diameter of tool pin = 6 mm	Rotational speed of tool = 1400 rpm Traverse speed of tool = 16 mm/min Shoulder angle = 3°	(1) More uniform distribution of particle is obtained in double pass FSP (2) Hardness is increased by 22.72% in comparison with base metal (3) In double pass FSP hardness is increased by 25%	[32]
AA1050	TiC particle (size below 60 μm)	Diameter of tool shoulder = 18 mm Diameter of tool pin = 5.2 mm Length of tool pin = 2.7 mm	Rotational speed of tool = 800–1600 rpm Feed rate = 100–300 mm/min	(1) By increasing tool rotational speed wear volume is increased (2) Microhardness value of the processed sample is increased	[33]
Al6082	TiC powder of particle size 2 μm	Diameter of tool shoulder = 22 mm Length of tool pin = 5.5 mm	Rotational speed of tool = 1200 rpm Traverse speed of tool = 40 to 80 mm/min	(1) Microhardness is increased by increasing traverse speed (2) Wear rate is decreased by increasing traverse speed	[34]

(continued)

Table 2 (continued)

Material	Reinforced material	Material and geometry of tool	Processing parameters	Results	References
AA6082	TiC powder of particle size 2 μm	Diameter of tool shoulder = 18 mm Diameter of tool pin = 6 mm Length of tool pin = 5.5 mm	Rotational speed of tool = 1200 rpm Traverse speed of tool = 60 mm/minute	(1) Stiffness of matrix is increased by increasing volume fraction of TiC particle (2) Wear resistance of the composite is increased	[3]
Aluminium alloy 7075-T651	TiC particle (size 3.6 μm)	Diameter of tool shoulder = 24 mm Tool pin diameter at larger end = 8 mm Tool pin diameter at smaller end = 6 mm	Rotational speed of tool = 1200 rpm Traverse speed of tool = 30 mm/minute Tool tilt angle = 2°	(1) By increasing the volume fraction of reinforcement hardness of composite is increased (2) Property of corrosion resistance is increased by increasing the composition of NaCl	[42]

2 Conclusion

Friction stir processing is an outstanding technique for manufacturing of aluminium-based metal matrix composite. It is one of the best approaches to modify the microstructure of the composite material. This review summarise the theoretical and experimental outcome seized by different authors through reinforcing various particles in aluminium alloys using FSP.

- It is observed that grain structure of almost all aluminium metal matrixes is refined by friction stir.
- It is found that hardness of the aluminium-based metal matrix composite is increased by increasing the volume fraction of the reinforcement particle.
- More refined grain structure is obtained by increasing number of passes but main disadvantages of the multipass are the amount of heat generated increased drastically which produced negative effect on properties of fabricated material.
- It has been concluded that by varying the process parameter of FSP the mechanical properties of the composite can be altered.

References

1. Miracle DB (2005) Metal matrix composites–from science to technological signifi-cance. Compos Sci Technol 65(15–16):2526–2540
2. Lloyd DJ (1994) Particle reinforced aluminium and magnesium matrix composites. Int Mater Rev 39(1):1–23
3. Thangarasu A, Murugan N, Dinaharan I, Vijay SJ (2015) Synthesis and characterization of titanium carbide particulate reinforced AA6082 aluminium alloy composites via friction stir processing. Arch Civ Mech Eng 15(2):324–334
4. Gan YX, Solomon D, Reinbolt M Friction stir processing of particle reinforced composite materials. Materials 3(1):329–350
5. Thangarasu A, Murugan N, Dinaharan I, Vijay SJ (2012) Microstructure and microhardness of AA1050/TiC surface composite fabricated using friction stir proessing. Sadhana 37(5):579–586
6. Topic I, Höppel HW, Göken M (2009) Friction stir welding of accumulative roll-bonded commercial-purity aluminium AA1050 and aluminium alloy AA6016. Mater Sci Eng, A 503(1–2):163–166
7. Schmidt HNB, Dickerson TL, Hattel JH (2006) Material flow in butt friction stir welds in AA2024-T3. Acta Mater 54(4):1199–1209
8. Jariyaboon M, Davenport AJ, Ambat R, Connolly BJ, Williams SW, Price DA (2007) The effect of welding parameters on the corrosion behaviour of friction stir welded AA2024–T351. Corros Sci 49(2):877–909
9. Li H, Mackenzie D, Hamilton R (2010) Parametric finite-element studies on the effect of tool shape in friction stir welding. Proc Inst Mech Eng Part B: J Eng Manuf 224(8):1161–1173
10. Attallah MM, Salem HG (2005) Friction stir welding parameters: a tool for controlling abnormal grain growth during subsequent heat treatment. Mater Sci Eng, A 391(1–2):51–59
11. El-Danaf EA, El-Rayes MM, Soliman MS (2011) Low temperature enhanced ductility of friction stir processed 5083 aluminum alloy. Bull Mater Sci 34(7):1447–1453
12. Vaze SP, Xu J, Ritter RJ, Colligan KJ, Fisher Jr JJ, Pickens JR (2003) Friction stir processing of aluminum alloy 5083 plate for cold bending. In: Materials science forum (vol 426). Trans Tech Publications Ltd., pp 2979–2986
13. Reis M, Louro R, Morais PJ, Santos L, Gouveia H (2009) Microstructural characterization of 5083 Al alloy joints friction stir welded. In: Materials science forum (Vol 514). Trans Tech Publications Ltd., pp 510–515
14. Çam G, Güçlüer S, Çakan A, Serinda HT (2008) Mechanical properties of friction stir butt-welded Al-5086 H32 plate. Materialwis Werkstofftech 30(2):151–156
15. Merzoug M, Mazari M, Berrahal L, Imad A (2010) Parametric studies of the process of friction spot stir welding of aluminium 6060–T5 alloys. Mater Des 31(6):3023–3028
16. Fahimpour V, Sadrnezhaad SK, Karimzadeh F (2012) Corrosion behavior of aluminum 6061 alloy joined by friction stir welding and gas tungsten arc welding methods. Mater Des 39:329–333
17. Colegrove PA, Shercliff HR (2004) Development of Trivex friction stir welding tool Part 2–three-dimensional flow modelling. Sci Technol Weld Joining 9(4):352–361
18. Gan YX, Solomon D, Reinbolt M (2010) Friction stir processing of particle reinforced composite materials. Materials 3(1):329–350

19. Yuvaraj N, Aravindan S (2017) Wear characteristics of Al5083 surface hybrid nano-composites by friction stir processing. Trans Indian Inst Met 70(4):1111–1129
20. Santella ML, Engstrom T, Storjohann D, Pan TY (2005) Effects of friction stir pro-cessing on mechanical properties of the cast aluminum alloys A319 and A356. Scripta Mater 53(2):201–206
21. Hsu CJ, Kao PW, Ho NJ (2005) Ultrafine-grained Al–Al$_2$Cu composite produced in situ by friction stir processing. Scripta Mater 53(3):341–345
22. Yadav D, Bauri R (2011) Fabrication of metal particles embedded aluminum matrix composite by friction stir processing (FSP). In: AIP conference proceedings (vol 1315, no 1). American Institute of Physics, pp 51–56
23. Ma ZY (2008) Friction stir processing technology: a review. Metall Mater Trans A 39(3):642–658
24. Hodder KJ, Izadi H, McDonald AG, Gerlich AP (2012) Fabrication of aluminum–alumina metal matrix composites via cold gas dynamic spraying at low pressure followed by friction stir processing. Mater Sci Eng, A 556:114–121
25. Pirondi A, Collini L (2009) Analysis of crack propagation resistance of Al–Al$_2$O$_3$ particulate-reinforced composite friction stir welded butt joints. Int J Fatigue 31(1):111–121
26. Feng AH, Xiao BL, Ma ZY (2008) Effect of microstructural evolution on mechanical properties of friction stir welded AA2009/SiCp composite. Compos Sci Technol 68(9):2141–2148
27. Mishra RS, Ma ZY (2005) Friction stir welding and processing. Mater Sci Eng: R 50(1–2):1–78
28. Arora HS, Singh H, Dhindaw BK (2012) Composite fabrication using friction stir processing—a review. Int J Adv Manuf Technol 61(9):1043–1055
29. Shafiei-Zarghani A, Kashani-Bozorg SF, Zarei-Hanzaki A (2009) Microstructures and mechanical properties of Al/Al$_2$O$_3$ surface nano-composite layer produced by friction stir processing. Mater Sci Eng, A 500(1–2):84–91
30. Lee IS, Hsu CJ, Chen CF, Ho NJ, Kao PW (2011) Particle-reinforced aluminum matrix composites produced from powder mixtures via friction stir processing. Compos Sci Technol 71(5):693–698
31. Zhang Z, Chen DL (2008) Contribution of Orowan strengthening effect in particulate-reinforced metal matrix nanocomposites. Mater Sci Eng, A 483:148–152
32. Jerome S, Bhalchandra SG, Babu SK, Ravisankar B (2012) Influence of microstructure and experimental parameters on mechanical and wear properties of Al–TiC surface composite by FSP route. J Miner Mater Charact Eng 11(05):493
33. Akinlabi ET, Mahamood RM, Akinlabi SA, Ogunmuyiwa E (2014) Processing parameters influence on wear resistance behaviour of friction stir processed Al–TiC composites. Adv Mater Sci Eng 2014
34. Thangarasu A, Murugan N, Dinaharan I, Vijay SJ (2014) Influence of traverse speed on microstructure and mechanical properties of AA6082-TiC surface composite fabricated by friction stir processing. Procedia Mater Sci 5:2115–2121
35. Hashemi R, Hussain G (2015) Wear performance of Al/TiN dispersion strengthened surface composite produced through friction stir process: a comparison of tool geometries and number of passes. Wear 324:45–54
36. Sharma V, Prakash U, Kumar BM (2015) Surface composites by friction stir processing: a review. J Mater Process Technol 224:117–134
37. Yadav D, Bauri R (2012) Effect of friction stir processing on microstructure and mechanical properties of aluminium. Mater Sci Eng, A 539:85–92
38. Sanusi KO, Akinlabi ET (2017) Friction-stir processing of a composite aluminium alloy (AA 1050) reinforced with titanium carbide powder. Mater Tehnol 51(3):427–435
39. Shiva A, Cheepu M, Kantumuchu VC, Kumar KR, Venkateswarlu D, Srinivas B, Jerome S (2018) Microstructure characterization of Al–TiC surface composite fabricated by fric-tion stir processing. In: IOP conference series: materials science and engineering (vol 330, no 1). IOP Publishing, p 012060
40. Zhang Q, Xiao BL, Wang WG, Ma ZY (2012) Reactive mechanism and mechanical properties of in situ composites fabricated from an Al–TiO$_2$ system by friction stir processing. Acta Mater 60(20):7090–7103

41. Ahmadifard S, Kazemi S, Heidarpour A (2018) Production and characterization of A5083–Al_2O_3–TiO_2 hybrid surface nanocomposite by friction stir processing. Proc Inst Mech Eng, Part L: J Mater: Des Appl 232(4):287–293
42. Kumar S, Kumar A, Vanitha C (2019) Corrosion behaviour of Al 7075/TiC composites processed through friction stir processing. Mater Today: Proc 15:21–29
43. Anvari SR, Karimzadeh F, Enayati MH (2013) Wear characteristics of Al–Cr–O surface nano-composite layer fabricated on Al6061 plate by friction stir processing. Wear 304(1–2):144–151
44. Grong O (1997) Metallurgical modelling of welding. Institute of Materials, 1 Carlton House Terrace, London, p 605
45. Svensson LE, Karlsson L, Larsson H, Karlsson B, Fazzini M, Karlsson J (2000) Micro-structure and mechanical properties of friction stir welded aluminium alloys with special reference to AA 5083 and AA 6082. Sci Technol Weld Joining 5(5):285–296
46. Sharma A, Mani Sharma V, Sahoo B, Joseph J, Paul J (2018) Study of nano-mechanical, electro-chemical and raman spectroscopic behavior of Al6061-SiC-graphite hybrid surface composite fabricated through friction stir processing. J Compos Sci 2(2):32
47. Hosseinzadeh A, Yapici GG (2018) High temperature characteristics of Al2024/SiC metal matrix composite fabricated by friction stir processing. Mater Sci Eng, A 731:487–494
48. Akramifard HR, Shamanian M, Sabbaghian M, Esmailzadeh M (2014) Microstructure and mechanical properties of Cu/SiC metal matrix composite fabricated via friction stir processing. Mater Des 1980–2015(54):838–844
49. Feng AH, Ma ZY (2009) Microstructural evolution of cast Mg–Al–Zn during friction stir processing and subsequent aging. Acta Mater 57(14):4248–4260
50. Humphreys FJ, Prangnell PB, Priestner R (2001) Fine-grained alloys by thermomechanical processing. Curr Opin Solid State Mater Sci 5(1):15–21

Impact of Hydrogen Embrittlement in Pipeline Structures—A Critical Review

Adarsh Kumar Arya, Shashank Gautam, and Shreyash Yadav

1 Introduction

The build-up of carbon in the environment, which contributes to global warming, is causing increasing concern. Technologically sophisticated nations, China and India, are heavy oil consumers. Due to their high living standards, these major consumer nations utilize fossil fuels and derivatives to sustain their economies. Significant indications of human-caused climate change have emerged because of the high exploitation of the earth's crust's carbon. In the present era, hydrogen has served as an excellent fuel and energy storage since it is the most prevalent element in the universe. However, the effects of hydrogen on material properties, including hydrogen embrittlement (HE), offer technical difficulties in terms of storage and transportation. Materials suitable for hydrogen production, distribution, storage, and application are required to establish a clean and sustainable hydrogen economy. First, the article sheds light on the process that causes HE. The current study approaches and findings have also been examined [1].

2 Mechanism of HE

HE of a material may be attributed to several different mechanisms (Fig. 1). Some of the most important mechanisms will be explored at length in the present section [2].

A. K. Arya (✉) · S. Gautam · S. Yadav
Department of Chemical Engineering, School of Engineering, University of Petroleum and Energy Studies, Energy Acres Building, Bidholi, Dehradun 248007, India
e-mail: akarya@ddn.upes.ac.in
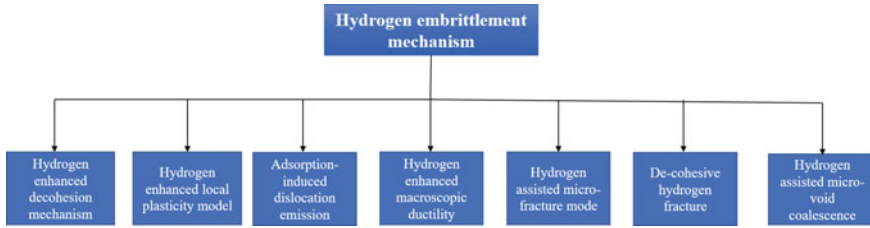
Fig. 1 Hydrogen embrittlement mechanism

2.1 *Hydrogen-Enhanced Decohesion Mechanism (HEDE)*

Troiano initially proposed this technique in 1959, and it is the simplest of all [3]. It relies on introducing a hydrogen atom into a fracture to reduce the material's cohesive strength near the crack's tip. Iron's 3rd cell has a weaker 3d interatomic connection because of a hydrogen 1s electron. There will be decohesion when the critical crack tip opening displacement (CTOP) is attained. Hydrogen atoms diffuse throughout the material at the crack tip, diminishing interatomic or cohesive strength. This causes cleavage-like fractures because hydrogen atoms are readily accessible throughout the material when applied forces. A material's surface energy is lowered when its cohesive strength diminishes, resulting in reduced fracture stress and a lower-than-acceptable fracture rate.

2.2 *Hydrogen-Enhanced Local Plasticity Model (HELP)*

This technique was initially introduced in 1972 and has since gained widespread acceptance. Dislocation mobility rises due to hydrogen accumulating at fracture tips in this model, which reduces dislocation motion resistance. As a result, dislocations function as transporters of deformations in a metal lattice. Since hydrogen reduces the yield stress locally, dislocation movement is feasible even at low-stress levels.

2.3 *Adsorption-Induced Dislocation Emission (AIDE)*

In principle, the approach is a mix of HEDE and HELP. In this process, hydrogen atoms from the solution adsorb on the surfaces of fracture points and other high-stress areas. Hydrogen adsorption at a fracture tip occurs in the HEDE mechanism, promoting dislocation injection from a crack tip, culminating in crack initiation by slip and micro-void generation by the HELP mechanism.

2.4 *Hydrogen-Enhanced Macroscopic Ductility (HEMP)*

When hydrogen is accessible in significant volumes (concentrations) and interacts with the whole specimen volume, it reduces steel's yield strength owing to hydrogen diffusion and solid solution weakening by hydrogen atoms. As a result, a macroscopic enrichment in plasticity had developed throughout the whole specimen length (volume).

2.5 *Hydrogen-Changed Microfracture Mode (HAM)*

Previously, ductile materials became brittle when hydrogen altered their microfracture modes. Materials lost some of their ductility due to hydrogen charge, and their fracture modes have shifted from cup-and-cone to a more common brittle shear type. Another reason is that a high hydrogen cluster at the dislocation site aids the shear fracture mechanism. Hydrogen-assisted microfracture is the name of this shift in microfracture mode caused by hydrogen (HAM).

2.6 *De-cohesive Hydrogen Fracture (DHF)*

It is simply a brittle fracture that is aided by hydrogen or decohesion and ends with the material or specimen breaking apart. The ductile fracture triggered this fracture. The final fractography was found to include both brittle (fisheye) and flexible (MVC) characteristics during the final fracture surface inspection (by SEM or TEM). As a result, the combined action of these two microfracture processes results in the ultimate material fracture. The middle portion, often at inclusion, is born fish eyes. Fish eyeballs expand and fracture radially until they come into touch (get near) with a ductile zone or coalescence of micro-voids. The MVC fracture encloses these fish eyes. Hydrogen microfracture mechanisms for fisheyes and MVC compete in this sort of fracture, known as a mixed fracture mechanism.

2.7 *Hydrogen-Assisted Micro-Void Coalescence (HAMVC)*

As the name implies, micro-void coalescence (MVC) is a method of fracture that uses ductility. As far as the progression of a multi-vessel crack (MVC), several distinct stages are involved, from initial nucleation to ultimate coalescence and additional crack extension to the breakage of any residual ligament by shear. As a result of the hydrogen's impact, materials suffer dislocation motion and localized plastic deformities. The fracture spread in a zigzag pattern as voids joined in the crack propagation

direction. In the presence of hydrogen, an MVC dimple will form, but it will be brittle and difficult to process. Shallow shear dimples are caused by shear stress, which leads to final fracture. The presence of hydrogen causes some brittle intergranular fracture on the specimen's edges. Micro-void coalescence aided by hydrogen is the term for this procedure (HDMC). Hydrogen, it turns out, affects the ductile MVC process. MVC shear dimples surround fisheyes seen in fracture propagation regions on rare occasions.

3   Literature Review

With the Devanathan—Stachurski technique, Xing et al. investigated the influence of temperature on bulk hydrogen concentration and diffusion. Experiments validated the theoretical models and suggested a temperature threshold of 320 K as an optimal temperature for fracture initiation and propagation. This research may be used to improve pipeline maintenance operations and extend their useful lives [4].

Tian et al. [5] investigated calcareous deposition, hydrogen penetration, and hydrogen embrittlement in artificial seawater with cathodic polarization. When hydrogen concentration is low, the preferred cracking path is lath boundary separation; when hydrogen concentration is high, the preferred cracking method is preceding austenite grain failure.

Cerniauskas et al. studied mixing hydrogen with natural gas (H_2/NG) for transportation. This research develops cost functions for several pipeline reassignment techniques. 80% of the typical German pipeline network studied showed a technically feasible potential. The study of pipeline availability limitations in 2030 indicates a 30% decrease in transmission system's cost compared to a newly constructed hydrogen pipeline system [6].

The study done by Zhou et al. investigates the deterioration process of X80 steel, a material often used in natural gas pipelines. The findings indicate that the tensile and yield strengths are not significantly affected by using hydrogen-mixed natural gas. This research lays the groundwork for a safe hydrogen percentage in natural gas for X80 pipeline steel [7].

Trautmann and colleagues studied hydrogen embrittlement due to the environment in hydrogen-natural gas transportation. This research lays the groundwork for a safe hydrogen percentage for X80 pipeline steel while carrying hydrogen mixed natural gas combined with other gases. Slow strain tensile tests are employed in this study to qualitatively investigate the degradation process of X80 steel, which is often used in natural gas pipelines, according to the results. After stretching, mechanical characteristics and fracture morphologies are examined in more detail [8].

Researchers Villalobos and coworkers studied the impact of hydrogen embrittlement (HE) on the mechanical characteristics of X-120 micro-alloyed steel. The decohesion and dislocation emission process of HE discovered via fractography study leads to HE nucleation and crack development. Findings revealed a martensite-bainite, acicular-ferrite, and maintained austenite microstructure with no discernible

change in morphology following tempering treatment. However, when the tempering temperature rose, the mechanical qualities of the steel decreased [9].

The study by Shin et al. examined the impact of hydrogen embrittlement (HE) on the mechanical characteristics of X-120 micro-alloyed steel after a 10-min tempering treatment at 200, 400, or 600 °C. Decohesion and dislocation emission of HE was discovered via fractography study, and these processes lead to HE nucleation and crack development. As the number of irreversible traps increased throughout the tempering process, there was a link between index brittleness, effective diffusion reduction, and apparent concentration rise [10].

In situations where CO_2 coexists with other gases, cracking failure processes need more knowledge than in a pure CO_2 environment. Carbon dioxide with H_2S traces may cause hydrogen embrittlement and pipeline steel failure. The study by Silva et al. aims to have a closer look at an API 5L X65 steel's laboratory performance in a CO_2–$H2_S$ environment (a little sour) compared to that of the same material in a purely CO_2 atmosphere [11].

According to Jiang et al., PH stainless steel (SS), 17–4, is often utilized in high-pressure corrosive environments. Some petrochemical pipeline valve stems are made from 17 to 4 PH SS to assure strength, impact toughness, and corrosion resistance. HE was shown to be a factor in the valve stem failing due to stress fracture. The tensile and fatigue properties of X65 pipeline steel have deteriorated because of hydrogen-driven blister cracking [12].

Singh et al. reported that tensile and fatigue specimens were electrochemically charged with hydrogen at 20 mA/cm^2. Using the hydrogen generator caused HIC and blisters on the model. BWC and HIC have been found in Al–Si–O inclusions together. Hydrogen embrittlement is shown via an SSRT test and a fractographic analysis of X65 steel [13].

In alpha iron at ambient temperature, a phase transition from body-centered cubic (bcc) to face-centered cubic (fcc) phase was investigated by Xing et al. The propagation of the fracture was studied using molecular dynamics simulations. According to the findings, the phase shift may release strain energy and delay fracture development without hydrogen atoms. Before the crack's tip, hydrogen atoms would form a nanosize hydrogen-rich region, blocking the phase change. Brittle fractures might develop as a result of this. A general formula may determine the hydrogen concentration at which no phase transition occurs. The risk level during the procedure may also be predicted using a simple crack development model [4].

When the deforming temperature and deforming strain in a hydrogen atmosphere were varied in different ways, Chen et al. studied the resistance of austenitic stainless steel to hydrogen environment embrittlement (HEE). Resistance to HEE may be improved by deforming at higher temperatures (100–300 °C) and reduced by using more significant deforming stresses. Tremendous strain led to primary deformation twins, which helped cause strain-induced martensite to form and accelerate the growth of hydrogen-induced fractures [14].

In a hydrogen environment with structure–property-performance linkages, ferritic steels are subjected to mechanical stress (Martin et al.). When hydrogen is present in a ferritic steel, the structure is explained by sorption and dissociation processes,

diffusion across lattice and grain boundaries, and hydrogen–steel interactions. Once numerous embrittlement processes have been thoroughly examined, steels' performance in hydrogen environments may be assessed by looking at how well they function [15].

Using a mass diffusion model fueled by mechanical fields, Gobbi et al. simulated hydrogen embrittlement in plastics. Because the automatic reaction is dependent on the hydrogen concentration, continuum mechanics and mass transfer calculations are tightly connected. All of the code generated for this work is freely available to anybody who wants it [16].

Wang et al. investigated the impact of a quenching–tempering (QT) treatment on a reactor pressure vessel's hydrogen embrittlement (HE) resistance. Studies using transmission electron microscopy and atom probe tomography confirmed the breakdown of M3C/VC carbides and the precipitation of M7C3 carbides. After QT treatment, HE sensitivity reduced to almost nothing. Lower M_3C carbides, which serve as hydrogen trapping sites, were the primary cause of increased HE resistance. Using thermal desorption spectroscopy, it was discovered that the concentration of reversible hydrogen had dropped. The quantity of irreversible hydrogen (likely trapped in VC carbides) was also reduced, although this is not the cause of the improved HE quality [17].

Titov et al. studied hydrogen build-up and dispersion in high-corrosion pipeline steel. Axial stress tests and XRD measurements show corrosion on steel pipeline inner and outer surfaces. Hydrogen is produced when methane dissociates insignificantly. Measurements were made to determine the concentration of adsorbed hydrogen in the steel pipe bulk. Charpy specimens were subjected to national standards-required pendulum impact testing at room temperature. Materials testing revealed that hydrogen embrittlement significantly reduced the mechanical characteristics of steel specimens [18].

The influence of hydrogen on candidate fracture toughness (KQ) was studied by Wasim and Djukic using low carbon steel soaked in acidic hydrogen conditions for a year. The study is significant because of its practical use in evaluating steel durability against hydrogen environmentally aided cracking (HEAC) [19].

Three structural steel sheets were tested to see how hydrogen affected their mechanical properties (Alvarez et al.). It was found that hydrogen embrittlement could be accurately evaluated by performing a Small Punch Test on notched specimens. This study's results were compared to standard fracture testing to discover which was superior. It took 21 h for gaseous hydrogen at 19.5 MPa and 450 C to burn in the first technique [20].

The possibility of transferring hydrogen via a natural gas pipeline was examined by Boukortt et al. To determine whether hydrogen embrittlement affects the mechanical properties of pipes, researchers conducted this investigation. The yield stress and ultimate strength proved to be less responsive to HE than previously thought. Fracture toughness and failure elongation, on the other hand, both decreased significantly [21].

Researchers (Alvarez et al.) investigated how the displacement rate affected fracture toughness of two structural steel grades. When the displacement rate is low, and steel yield strength is high, the fracture toughness is reduced because of internal

hydrogen. To evaluate the fracture toughness of steel, hydrogen gas was used to pre-charge the specimens for 21 h at 19.5 MPa, and 450 °C and then typical air temperature tests were done [22].

Wasim and Djukic studied hydrogen-induced mechanical deterioration of low carbon steel on the macro, micro, and nanoscales. A link was discovered between hydrogen concentration and corrosion growth after 28 days after exposure to hydrogen-rich acidic environments. Microstructural analysis revealed that hydrogen penetration had deformed bigger grains, cracked surfaces, and formed blisters [23].

Researchers (Bouledroua et al.) found that blending gaseous hydrogen into a natural gas flow significantly impacted hydrogen permeation in a steel pipeline. Fractures may trigger pipeline collapse and hydrogen leaking. Explosions are much more probable due to the latter, making this phenomenon highly hazardous. A reliable technique is given to minimize the hazards associated with hydrogen embrittlement-induced pipe failure [24].

Nguyen et al. investigated the effects of low hydrogen partial pressure and methane gas on welded API X70 pipeline steel. The weld metal was more susceptible to hydrogen-induced fracture than the base metal. The smooth tensile specimen was used since the weld metal lost ductility under 10 MPa of a gas combination with 1% hydrogen [25].

4 Literature Summary

See Table 1

Table 1 Literature review matrix

Reference No.	Author	Key observation
[5]	Tian et al. (2019)	Due to changes in the cathodic process, sulfur species in acidic ASW remove any aragonite precipitation. Susceptibility to hydrogen embrittlement rises linearly as hydrogen concentration increases by a logarithmic factor. When hydrogen concentration is low, the preferred cracking route develops from lath boundary separation to preceding austenite grain boundary failure
[6]	Cerniauskas et al. (2020)	According to a study of pipeline availability limitations, the transmission system will be 30% cheaper in 2030 than if a new hydrogen pipeline system were constructed. According to the findings of this research, more than 80% of the studied typical German pipeline network showed a technically feasible potential

(continued)

Table 1 (continued)

Reference No.	Author	Key observation
[7]	Zhou et al. (2021)	X80 steel, which is utilized in natural gas pipelines, degrades qualitatively via gradual strain tensile tests like these. After stretching, mechanical characteristics and fracture morphologies are examined in more detail. The findings indicate that the tensile and yield strengths are not significantly affected by using hydrogen-mixed natural gas
[8]	Trautmann et al. (2020)	It is necessary to conduct the slow strain tensile tests to learn more about the deterioration process of the X80 steel used in natural gas pipeline construction. After stretching, mechanical characteristics and fracture morphologies are studied in more depth. According to the findings, hydrogen-mixed natural gas has minimal impact on tensile and yield strength
[9]	Villalobos et al. (2020)	As far as its morphology was concerned, tempering had no noticeable effect on the microstructure of X-120 steel, but the micro-alloyed steel's mechanical characteristics deteriorated undercharging circumstances. The decohesion and dislocation emission mechanisms discovered via fractography study lead to HE nucleation and crack development
[10]	Shin et al. (2019)	As the tempering temperature rose, the mechanical characteristics of micro-alloyed steel decreased. The decohesion and dislocation emission process discovered via fractography study leads to HE nucleation and crack development. By increasing irreversible traps caused by the kind of precipitates present during tempering phases, the index embrittlement was linked to a decrease in effective diffusion and an increase in apparent concentration
[11]	Silva et al. (2021)	Cracking CO_2 failure mechanisms requires a more profound knowledge base. Hydrogen embrittlement was cited as the underlying cause for API 5L X65 cracking susceptibility in pure CO_2. Strength depletion is a problem with CO_2 and H_2S present in the same environment
[12]	Jiang et al. (2020)	This kind of stainless steel, which has excellent strength and good corrosion resistance, is often employed in high-pressure, corrosive settings. The sudden breakage of a valve stem necessitated the emergency closure of a pipeline system. Our research indicates that valve stem failure is associated with HE in the stress concentration area
[13]	Singh et al. (2019)	The specimen surface developed hydrogen-induced cracking (HIC) and blistering (BL) in a hydrogen charge. The blisters that developed due to the hydrogen-charging process had cracked blister walls (BWC). According to the research, HIC and BWC may live and reproduce in Al–Si–O inclusions

(continued)

Table 1 (continued)

Reference No.	Author	Key observation
[4]	Xing et al. (2019)	There has been much research on hydrogen embrittlement for many years. The phase change may release strain energy and delay fracture development if no hydrogen atoms are present. Before the fracture tip, a hydrogen-rich area would develop with hydrogen atoms, which would act as an inhibitor to phase transitions
[14]	Chen et al. (2019)	304 austenitic stainless steel was tested for resistance to hydrogen environment embrittlement (HEE) by varying the deforming temperature and deforming strain in the hydrogen atmosphere. Resistance to HEE may be improved by subjecting the material to higher deforming temperatures (between 100 and 300 °C)
[15]	Martin et al. (2020)	This paper describes the hydrogen sorption and dissociation in iron-ferritic steels and diffusion across lattice and grain boundaries. Hydrogen pressure and test conditions affect base metal and weld tensile, fracture, and fatigue properties. After that, several embrittlement techniques are used to examine steels' hydrogen performance. Finally, current in situ and high-resolution testing are reviewed, and additional research to resolve ferritic problems is proposed
[16]	Gobbi et al. (2019)	Many engineering applications rely on hydrogen embrittlement in steel, such as oil and gas and hydrogen storage and transportation. This process can be described by studying mass dispersion driven by mechanical fields, such as a hydrostatic stress gradient and plastic strain. Continuum mechanics and mass diffusion equations are linked since the mechanical response is hydrogen-dependent. Permissive free software licenses are used to make this code open source
[17]	Wang et al. (2019)	An experiment was conducted to see how QT therapy affected a reactor pressure vessel's hydrogen embrittlement resistance. After QT treatment, HE sensitivity reduced to almost nothing. The reduction in M3C carbides, which serve as reversible hydrogen trapping sites, was primarily responsible for the improved HE resistance. Thermal desorption spectroscopy showed a reduction in the concentration of reversible hydrogen, corroborating this conclusion
[26]	Ohaeri et al. (2019)	The role of microstructural characteristics in hydrogen-assisted deterioration of API 5L X80 pipeline steel has been studied. It was shown that greater strength and poorer ductility were associated with a top-surface layer that was more vulnerable to hydrogen degradation. Although its tensile and yield strengths were lower than those of the thin layer, the mid-thickness layer demonstrated better resilience to failure than the thin layer

(continued)

Table 1 (continued)

Reference No.	Author	Key observation
[18]	Titov et al. (2019)	Researchers have looked at hydrogen build-up and dispersion in pipeline steel under high-corrosion circumstances. During methane dissociation, the steel surface gets saturated with hydrogen that has been produced as a reaction product. Measurements were made to determine the concentration of adsorbed hydrogen in the steel pipe bulk. Hydrogen embrittlement significantly reduced the steel specimens' mechanical characteristics, as expected
[23]	Wasim et al. (2021)	A sustainable energy source for electrical and transportation purposes, hydrogen gas, is a liquid fuel for automobiles and other motor vehicles. The nature and effect of hydrogen gas storage and transport on pipelines and storage tank/facility materials make it difficult. For one year, low carbon steel was submerged in acidic hydrogen settings to see how hydrogen affects the candidate fracture toughness
[20]	Alvarez et al. (2021)	Hydrogen's effect on three structural sheets of steel's mechanical characteristics was examined. Using a Small Punch Test with notched specimens, hydrogen embrittlement was measured. To inject hydrogen into the samples, two different pre-charging techniques were used. To compare the findings of the experiments, the researchers used fracture assays that are often used in the medical field. This finding is explained by the test specimens' thin thickness and reduced stress triaxiality
[21]	Boukortt et al. (2018)	This article investigated if hydrogen might be transported through a natural gas pipeline. A semi-elliptical pipe with hydrogen embrittlement was studied in this study to see what effect it had on failure and critical pressures. Failure assessment diagrams and crack driving force evaluated pipe defect toughness and flow stress
[22]	Belzunce et al. (2019)	Because internal hydrogen reduces fracture toughness, a lower displacement rate and a higher steel yield strength result in a greater decrease in fracture toughness. Fracture toughness tests were performed in air at room temperature after pre-charging specimens with gaseous hydrogen for 21 h at 19.5 MPa and 450 °C
[19]	Wasim and Djukic (2019)	In hydrogen-rich acidic environments, mechanical deterioration of low carbon steel occurs at macro-, micro-, and nanoscales, which will be examined in this study. After 28 days of testing, a substantial decrease in bulk elastic modulus existed between hydrogen concentration and corrosion propagation. Hydrogen penetrating fractures and blisters in bigger grains and the deformation they produce were discovered via microstructural investigation

Table 1 (continued)

Reference No.	Author	Key observation
[24]	Bouledroua et al. (2020)	Fractures in a pipeline may cause it to break, resulting in hydrogen leaking. The auto-ignition of hydrogen leaks results in a dim flame even if the leaks are tiny. Explosions are very probable due to the latter, making these phenomena exceedingly hazardous. A dependable technique is given for predicting the tolerable defect to minimize the risk of pipe failure due to hydrogen embrittlement
[25]	Nguyen et al. (2020)	The mechanical characteristics of welded API X70 pipeline steel are examined concerning the partial pressure of hydrogen in a methane gas combination. The weld metal was more vulnerable to hydrogen-induced fracture initiation than the base metal. Even when tested under 10 MPa of a gas combination containing 1%, the weld metal lost a considerable amount of ductility
[27]	Xing et al. (2019)	A theoretical model was tested in the laboratory, and the results showed that a temperature of 320 K was the optimum for crack development. The model predicts an embrittlement process at the nanoscale caused by hydrogen atoms' transport to the fracture tip during fatigue loading. This research may be used to improve pipeline operations and therefore increase pipeline longevity

5 HE Assessment Methods and Instruments

Researchers often use fracture tests to characterize and evaluate the HE susceptibility of various pipe steels. In the process of evaluating the effect of hydrogen on the pipe material, the pipeline specimen is exposed to two different environments. In the first environment, the pipe specimens are tested in a hydrogen-free environment, and in the second, the pipe specimen is exposed to hydrogen. Afterward, the pipe specimen is tested for material tensile strength, fracture, and yield strength. The results are shown in Fig. 2. The figure depicts the probable outcomes of the test by showing the variation in stress versus strain profiles of un-convicted and hydrogen-charged pipe specimens [28]. It can be seen in the figure that the hydrogen-charged specimens result in a decline in pipe material strength tensile at failure and extension at the fracture point [29].

5.1 Constant Load Test

The test is carried out by applying stress to the hydrogen exposed pipe specimen. The test evaluates the maximum hydrogen that can diffuse into steel pipe without material failure [30]. Researchers like Hagihara [31]; Takagi et al. [32]; Scharf et al. [33] utilized the CLT tests to evaluate the susceptibility of HE to steel specimens. In

2005, Takagi et al. [32] exploited the test to assess the HE susceptibility of AHSS
that was first quenched and then tempered. In the process conducted, the specimen
was first cathodic charged in a water solution that contained NaCl and NH_4SCN. The
specimen was further coated by using Cadmium coating to minimize HE. After the
fracture of the specimen caused due to CLT, the hydrogen content in the specimen
was estimated using thermal desorption analysis. In the study of Chida et al. [34],
Zinc coating was used instead of cadmium to test the HE sensitivity of low-alloy
high-strength steels.

With an increase in hydrogen concentration, fracture stress was reduced. To deter-
mine HE resistance, the exposed zinc electro-galvanized DP1000 specimens were
subjected to in situ hydrogen charging by Scharf et al. [33]. A "corrosive cup" filled
with NaCl solution was used to charge the hydrogen, and a proof ring was used
to provide a constant load. To determine the effect on HE of material pre-damage,
hammering, cutting tools, and milling were used. Microcracks appeared only on
specimens with shear-cut edges; milled edges were unaffected.

5.2 Slow Strain Rate Test (SSRT)

The strain rate in SSRT is typically 10^{-6} per second, which is comparatively much
lower in magnitude than the one used in regular tensile testing. In the SSRT testing
process, the applied force is steadily raised until the pipe specimen fractures. The
process enhances stress-induced hydrogen diffusion, resulting in hydrogen build-up
in a specimen based on the stress concentration.

There is evidence from Rehrl et al. [35] that strain rate significantly affects AHSS
mechanical properties when hydrogen is present. Hydrogen did not affect mechanical
properties at a strain rate of 20 per second. It was shown that at a slow strain rate
of 10–5 per second, hydrogen-charged and hydrogen-free specimens both had a 25
and 90% decrease in their strength and elongation at fracture. When hydrogen is

present, AHSS exhibits strain rate sensitivity. It is expected that SSRT results will be consistent with those of CLT in terms of hydrogen concentration and fracture stress because of the possibility for hydrogen diffusion (Chida et al.) [34]. Compared to CLT, the test time and variability of results are reduced significantly using SSRT. Because it always culminates in a material failure, the SSRT technique eliminates the problem of specifying a testing time.

Smooth or perforated specimens might be used for this test. Stress–strain curves are employed when evaluating cracking susceptibility, followed by scanning electron microscopy (SEM) and thermal desorption to determine hydrogen concentration.

As part of their investigation into whether or not the AHSS was susceptible to HE**,** Wang et al. [36–38] Cathodic hydrogen charging, Cd plating, and homogenization of hydrogen content were performed on the specimens, resulting in smooth and notched surfaces. The fracture stress decreased as the hydrogen diffusible quantity increased. An in situ hydrogen-charging SSRT method was used to determine a Cr–Mo steel's vulnerability to high-energy hydrogen embrittlement (HEHE). Temper embrittled steel was shown to be safe at a hydrogen concentration of 0.064 parts per million (ppm).

5.3   Conventional Strain Rate Test

Conventional strain rate testing (CSRT) results in a specimen's hydrogen content corresponding to the hydrogen concentration acquired throughout the CLT and SSRT tests. A very high strain rate is used in the test, resulting in little hydrogen diffusion. Therefore, a fracture in a specimen's hydrogen content corresponds to the average hydrogen content overall. The main benefit of this method is that it takes just a few minutes to test. On the other hand, hydrogen charge before testing must be very consistent. Chida et al. [34] used SSRT, CLT, and CSRT to investigate low-alloy steels' HE susceptibility. Nominal fracture stress was shown to correlate with diffusible hydrogen concentration using SSRT and CLT, which allow for hydrogen diffusion throughout the experiments. Dislocations may have inhibited hydrogen's ability to interact with dislocations, resulting in a lower HE susceptibility.

5.4   Stepwise Load Test

Another approach of evaluating HE susceptibility was presented by Takagi et al. [32]. When performing a stepwise load test, the specimen is subjected to a series of rising stress and stress holding phases. During the holding period, the hydrogen distribution almost achieves equilibrium. Researchers first applied 702 MPa of stress for 12 h, then 14 MPa for 2 h, with a holding duration of two and a half hours. Independency from specimen size and stress conditions are two advantages of this

approach. Therefore, applying the test findings to components of varying dimensions and stress concentration factors makes it possible.

6 Material Selection to Prevent HE in Pipeline Structures

Based on the above discussion, it is clear that HE causes huge damage to pipelines. Hence, controlling the HE is of foremost importance. Understanding the correct source of hydrogen formation and the mechanism leading to HE can help find suitable coating materials that can prevent hydrogen embrittlement. Selecting the most appropriate coating material to prevent HE is therefore critical.

High-strength materials must be protected against hydrogen embrittlement (HE) by knowing the true source of hydrogen and the mechanism responsible for this phenomenon. Selecting the most appropriate material is critical to success when working in a hydrogen environment. The material design must be suited for the situation. Before processing, it is necessary to prevent notch formation, acute and regular variation, and residual stresses must be eliminated. The baking process was adopted to remove hydrogen absorbed and potentially cause damage or failure. There are several different ways to bake, and the temperature at which they are accomplished varies depending on the kind of material being baked. Pickling is a process that uses an acidic solution to remove scale and oxide compounds from a material. Various mechanical methods, including sanding, gritty blasting, and vapor blasting, will limit the amount of hydrogen released into the environment. Metal alloys and a protective film on the surface of the supporting structure may also be used to reduce the risk of exposure to harmful electromagnetic radiation (HE). A few coating processes include vacuum deposition, organic deposition, and mechanical plating (among others). The use of efficient inhibitors is also vital in this process. If titanium is easily available in considerable numbers, increasing the titanium percentage of hot-stamped boron steel may reduce the material's high-temperature susceptibility to hydrogen embrittlement (HE) by creating titanium carbide in the material [21]. Some experts feel that aluminum alloying also has a positive effect on the HE impacts. Niobium and graphene coatings have also been shown to protect materials against high-energy physics.

In their studies, Kim and Kim [21] determined that the graphene layer serves as a robust hydrogen barrier and therefore is resilient even after being saturated with hydrogen. It was accomplished due to the increased diffusion length and the formation of the C–h bond during the hydrogen charging the atmosphere. Cadmium is a metal used in steel to prevent hydrogen diffusion during the production process. The hydrogen diffusion coefficient in cadmium and tin is lesser than the hydrogen diffusion coefficient in ferrite.

Steel is coated with a nickel layer to prevent hydrogen from leaking into the atmosphere. Different coatings, such as titanium dioxide and titanium carbide (TiC), have been shielded against hydrogen transfer. According to Cwiek, coatings comprised platinum, copper, lead, silver, aluminum, and gold may reduce hydrogen diffusion

inside the steel structure itself. The outer skin of oxides and nitrides, according to him, may also serve as a deterrent to hydrogen diffusion, decreasing the quantity of hydrogen absorbed [39]. The practical operation of the coating relies on the sturdiness of the coating and the existence of coating faults. Furthermore, the service's condition is critical [40].

There is localized tension in the coating, they could probably wear off, and hydrogen will seep onto the base metal. Although the diffusing layer of nitrogen and carbon is very effective in lowering the rate of fracture spread, it is not effective at eliminating hydrogen-induced environmental embrittlement in the material under study. The possibility of HE is reduced as long as excellent adhesion, an adequate coating level, and a coating free of flaws are provided [29].

Some elements that produce hydrogen may induce hydrogen to infiltrate the structure of a substance if they are exposed to a hydrogen environment. The elements in question are Te, Sn, S, Hg, Se, Pb, As, and Bi. They aid in the admission of hydrogen into the material, and if they are already present in the material, they divide the grain boundary, making them severely prohibited [39].

6.1 Electroplating Using Different Metals to Prevent HE

Researchers have used different materials to avoid HE. Electroplating with zinc and cadmium provides corrosion resistance for structural steel with high tensile strength. However, this plating process is also responsible for entering hydrogen into steel and its genesis. This has been accomplished by heating the plated steel to between 190 and 230 °C over 10–24 h to decrease the corrosion. As a result of this, diffusible hydrogen is released from the substance.

When building the model, heat treatment was believed not to affect the mechanical properties of steel and alloys. According to Hillier's research on alloying zinc with nickel, this method reduced hydrogen penetration through steel. As a result of the initial nickel deposit, a nickel coating is produced over the material, and this layer prevents hydrogen from getting into the substance. Hydrogen's diffusivity coefficient in nickel is $5 * 10^{-11}$ m^2/s, a very low diffusion rate. A lot of the time, hydrogen can get through the coating. This depends on how quickly hydrogen moves through the coating and how thick it is. In certain cases, hydrogen adsorbed on the surface interacts with other hydrogen molecules to form a new molecule, which escapes before penetrating the coating by forming bubbles. Cadmium is required for the recombination of hydrogen in coatings and reduces hydrogen entry.

6.2 Using Cadmium and Titanium as Electroplate Metals

This plating method has been around for a long time, developed in 1960 [41]. In the beginning, the required results were achieved using a cadmium cyanide solution in

combination with a titanium compound solvable in cyanide. The titanium concentration of the deposit varied from 0.1 to 0.5 percent if the treatment was performed appropriately. When it comes to high-stress settings, it has long been used to coat threaded rods and gear actuation cylinders and associated shafts. Non-cyanide solution with titanium concentrations ranging from 0.1e0.7% was created. Non-cyanide solutions do not change the composition of titanium compounds. Protective coatings on high-quality instrument steel, high-strength structural steel, and spring wire have been successfully applied using the non-cyanide solution rather than cyanide solution [42].

6.3 Other Methods to Prevent HE

Ion plating, also known as physical vapor deposition, eliminates hydrogen embrittlement. The risk of embrittlement is reduced since this technique was performed in a vacuum. It has been used in aviation for more than two decades. Unlike prior electroplating procedures, this ion aluminum coating approach has been shown to preserve the surface better [43]. A thin coating of Pt, Cu, or electroless nickel is injected as a protective layer [43]. Preventing hydrogen penetration may be accomplished by coatings made of Au, Sn, and certain Sn and Pb alloys, for example [44–47].

Utilizing a protective film thickness of 0.0015 mm, hydrogen penetration in iron may be prevented when using Pt coating. Cu was likewise more efficacious than Ni at decreasing hydrogen migration in iron [43]. A further study reveals hydrogen cracking may be prevented by applying lead coatings to specified steels in a specific environment [43–48].

The electrodeposited nickel was protected against hydrogen ambient embrittlement by coating it with copper or gold, as seen in the illustration. It has been discovered that the ductility of electrodeposited nickel is not affected by the application of either copper or gold coatings [45]. The presence of alumina creates a barrier to hydrogen diffusion. This approach deposits alumina on the steel and deposits a one-millimeter-thick layer of crystallized aluminum oxide [49]. At 800 °C, it has been found that temperature does not affect this coating and that it continues to work. This process creates a protective layer of enriched alumina on the steel's surface. This alumina can reduce steel's hydrogen permeability and rate of hydrogen permeation by order of magnitude when contrasted to bare steel.

To diffuse ions into an environment, the surface layer of an amorphous material is unique in that it provides an adequate barrier. This is the novel phosphorus ion implantation technology [50]. The passage of hydrogen through the disordered structure and the penetration of hydrogen from it to the base material are very challenging for hydrogen. Santos observed that the amorphous iron base alloy's hydrogen diffusion rate is slower and lower than ferrite steel's [51].

6.4 Corrosion Inhibitors for Preventing Hydrogen Embrittlement

Several compounds and mixes may inhibit, prevent, or decrease corrosion when applied at low concentrations and in a harsh environment to a protective system. Following processes are often used to explain the working of ow an inhibitor works [52].

- Adhesion of the inhibitor to the metal's surface results in a protective coating that acts as an inhibitor or combines the effects of both the metal's surface and its own.
- The inhibitor leads to a formation of a film by oxide protection of the base metal.
- A complex product is formed when the inhibitor combines with a corrosive component present in the aqueous medium.

To minimize the apparent corrosion rate, inhibitors build up as a coating on the metal surface. Inhibitory chemicals, of which they are the most prevalent, are classified as a subclass. The most prevalent types of inhibitors of the barrier layer are adsorption-type inhibitors. Adsorbed onto the metal surface, these organic molecules often establish a strong connection. As the adsorption process is finished, the apparent corrosion rate reduces.

7 Conclusion

HE is a critical issue in the oil and gas business. Pipelines and related facilities suffer significant losses while transporting hydrogen. The main function of HE is to diminish material ductility and make it brittle. The deterioration of mechanical characteristics is caused by hydrogen embrittlement. We discussed the causes and mechanisms of hydrogen embrittlement in our review research. The diffusion of hydrogen causes fracture growth in materials. The crack growth rate is primarily determined by the stress concentration factor and the loading frequency; when the loading frequency decreases, the possibilities of fatigue crack growth of sample rise. This research also explored how the microstructure and loading condition significantly impacts high-strength steel's HE vulnerability. Material selection is critical for lowering the HE. The use of alloys such as Al, titanium, and Mn may help to avoid hydrogen embrittlement.

References

1. Hardie D, Charles EA, Lopez AH (2006) Hydrogen embrittlement of high-strength pipeline steels. Corros Sci 48(12):4378–4385
2. Lynch S (2012) Hydrogen embrittlement phenomena and mechanisms. Corros Rev 30(3–4):105–123

3. Troiano AR (1959) Delayed failure of high strength steels. Corrosion 15(4):57–62

4. Xing X, Zhang H, Cui G, Liu J, Li Z (2019) Hydrogen inhibited phase transition near crack tip–An atomistic mechanism of hydrogen embrittlement. Int J Hydrogen Energy 44(31):17146–17153

5. Tian H, Xin J, Li Y, Wang X, Cui Z (2019) Combined effect of cathodic potential and sulfur species on calcareous deposition, hydrogen permeation, and hydrogen embrittlement of a low carbon bainite steel in artificial seawater. Corros Sci 158:108089

6. Cerniauskas S, Junco AJC, Grube T, Robinius M, Stolten D (2020) Options of natural gas pipeline reassignment for hydrogen: cost assessment for a Germany case study. Int J Hydrogen Energy 45(21):12095–12107

7. Zhou D, Li T, Huang D, Wu Y, Huang Z, Xiao W, Wang Q, Wang X (2021) The experiment study to assess the impact of hydrogen blended natural gas on the tensile properties and damage mechanism of X80 pipeline steel. Int J Hydrogen Energy 46(10):7402–7414

8. Trautmann A, Mori G, Oberndorfer M, Bauer S, Holzer C, Dittmann C (2020) Hydrogen uptake and embrittlement of carbon steels in various environments. Materials 13(16):3604

9. Villalobos JC, Del-Pozo A, Mayen J, Serna S, Campillo B (2020) Hydrogen embrittlement suscetibility on X-120 microalloyed steel as function of tempering temperature. Int J Hydrogen Energy 45(15):9137–9148

10. Shin HS, Bae KO, Baek UB, Nahm SH (2019) Establishment of an in-situ small punch test method for characterizing hydrogen embrittlement behaviors under hydrogen gas environments and new influencing factor. Int J Hydrogen Energy 44(41):23472–23483

11. Silva SC, Silva AB, Gomes JP (2021) Hydrogen embrittlement of API 5L X65 pipeline steel in CO_2 containing low H_2S concentration environment. Eng Fail Anal 120:105081

12. Jiang T, Zhong J, Zhang X, Wang W, Guan K (2020) Hydrogen embrittlement induced fracture of 17–4 PH stainless steel valve stem. Eng Fail Anal 113:104576

13. Singh V, Singh R, Arora KS, Mahajan DK (2019) Hydrogen induced blister cracking and mechanical failure in X65 pipeline steels. Int J Hydrogen Energy 44(39):22039–22049

14. Chen X, Ma L, Zhou C, Hong Y, Tao H, Zheng J, Zhang L (2019) Improved resistance to hydrogen environment embrittlement of warm-deformed 304 austenitic stainless steel in high-pressure hydrogen atmosphere. Corros Sci 148:159–170

15. Martin ML, Connolly MJ, DelRio FW, Slifka AJ (2020) Hydrogen embrittlement in ferritic steels. Appl Phys Rev 7(4):041301

16. Gobbi G, Colombo C, Miccoli S, Vergani L (2018) A weakly coupled implementation of hydrogen embrittlement in FE analysis. Finite Elem Anal Des 141:17–25

17. Wang Y, Hu S, Li Y, Cheng G (2019) Improved hydrogen embrittlement resistance after quenching–tempering treatment for a Cr–Mo–V high strength steel. Int J Hydrogen Energy 44(54):29017–29026

18. Titov AI, Lun-Fu AV, Gayvaronskiy AV, Bubenchikov MA, Bubenchikov AM, Lider AM, Syrtanov MS, Kudiiarov VN (2019) Hydrogen accumulation and distribution in pipeline steel in intensified corrosion conditions. Materials 12(9):1409

19. Wasim M, Djukic MB (2020) Hydrogen embrittlement of low carbon structural steel at macro-, micro-and nano-levels. Int J Hydrogen Energy 45(3):2145–2156

20. Álvarez G, Zafra A, Belzunce FJ, Rodríguez C (2021) Hydrogen embrittlement testing procedure for the analysis of structural steels with small punch tests using notched specimens. Eng Fract Mech 253:107906

21. Boukortt H, Amara M, Meliani MH, Bouledroua O, Muthanna BGN, Suleiman RK, Sorour AA, Pluvinage G (2018) Hydrogen embrittlement effect on the structural integrity of API 5L X52 steel pipeline. Int J Hydrogen Energy 43(42):19615–19624

22. Álvarez G, Peral LB, Rodríguez C, García TE, Belzunce FJ (2019) Hydrogen embrittlement of structural steels: effect of the displacement rate on the fracture toughness of high-pressure hydrogen pre-charged samples. Int J Hydrogen Energy 44(29):15634–15643

23. Wasim M, Djukic MB, Ngo TD (2021) Influence of hydrogen-enhanced plasticity and decohesion mechanisms of hydrogen embrittlement on the fracture resistance of steel. Eng Fail Anal 123:105312

24. Bouledroua O, Hafsi Z, Djukic MB, Elaoud S (2020) The synergistic effects of hydrogen embrittlement and transient gas flow conditions on integrity assessment of a precracked steel pipeline. Int J Hydrogen Energy 45(35):18010–18020

25. Nguyen TT, Park JS, Kim WS, Nahm SH, Beak UB (2020) Environment hydrogen embrittlement of pipeline steel X70 under various gas mixture conditions with in situ small punch tests. Mater Sci Eng, A 781:139114

26. Ohaeri E, Eduok U, Szpunar J (2019) Relationship between microstructural features in pipeline steel and hydrogen assisted degradation. Eng Fail Anal 96:496–507

27. Xing X, Zhou J, Zhang S, Zhang H, Li Z, Li Z (2019) Quantification of temperature dependence of hydrogen embrittlement in pipeline steel. Materials 12(4):585

28. Rudomilova D, Prošek T, Luckeneder G (2018) Techniques for investigation of hydrogen embrittlement of advanced high strength steels. Corros Rev 36(5):413–434

29. Dwivedi SK, Vishwakarma M (2018) Hydrogen embrittlement in different materials: a review. Int J Hydrogen Energy 43(46):21603–21616

30. Chida T, Hagihara Y, Akiyama E, Iwanaga K, Takagi S, Ohishi H et al (2014) Comparison of constant load, SSRT, and CSRT methods for hydrogen embrittlement evaluation using round bar specimens of high strength steels. Tetsu-to-Hagane 100(10):1298–1305

31. Hagihara Y (2012) Evaluation of delayed fracture characteristics of high-strength bolt steels by CSRT. ISIJ Int 52(2):292–297

32. Takagi S, Toji Y, Yoshino M, Hasegawa K (2012) Hydrogen embrittlement resistance evaluation of ultra high strength steel sheets for automobiles. ISIJ Int 52(2):316–322

33. Scharf R, Muhr A, Luckeneder G, Larour P, Mraczek K, Rehrl J et al (2016) Hydrogen embrittlement of DP-1000 flat steel sheet: influence of mechanical properties, specimen geometry, pre-damaging and electrolytically zinc galvanizing. Mater Corros 67(3):239–250

34. Chida T, Hagihara Y, Akiyama E, Iwanaga K, Takagi S, Hayakawa M et al (2016) Comparison of constant load, SSRT and CSRT methods for hydrogen embrittlement evaluation using round bar specimens of high strength steels. Isij Int 56(7):1268–1275

35. Rehrl J, Mraczek K, Pichler A, Werner E (2014) The impact of Nb, Ti, Zr, B, V, and Mo on the hydrogen diffusion in four different AHSS/UHSS microstructures. Steel Res Int 85(3):336–346

36. Wang M, Akiyama E, Tsuzaki K (2005) Crosshead speed dependence of the notch tensile strength of a high strength steel in the presence of hydrogen. Scripta Mater 53(6):713–718

37. Wang MQ, Akiyama E, Tsuzaki K (2006) Fracture criterion for hydrogen embrittlement of high strength steel. Mater Sci Technol 22(2):167–172

38. Wang M, Akiyama E, Tsuzaki K (2007) Effect of hydrogen on the fracture behavior of high strength steel during slow strain rate test. Corros Sci 49(11):4081–4097

39. Ćwiek J (2010) Prevention methods against hydrogen degradation of steel. J Achievements Mater Manuf Eng 43(1):214–221

40. Hollenberg GW, Simonen EP, Kalinin G, Terlain A (1995) Tritium/hydrogen barrier development. Fusion Eng Des 28:190–208

41. Takata K (1963) Japanese patents SHO-35 18260 (1960) and SHO-38 20703

42. Fannin ER, Muehlberger DE (1978) Ivadizer applied aluminum coating improves corrosion protection of aircraft. McDonnell Aircraft Company, p 26

43. Chatterjee SS, Ateya BG, Pickering HW (1978) Effect of electrodeposited metals on the permeation of hydrogen through iron membranes. Metall Trans A 9(3):389–395

44. Perng TP, Johnson MJ, Altstetter CJ (1988) Hydrogen permeation through coated and uncoated WASPALOY. Metall Trans A 19(5):1187–1192

45. Chandler WT, Walter RJ, Moeller CE, Carpenter HW (1978) Effect of high-pressure H on electrodeposited Ni. Plat Surf Finish 65(5):63e70

46. Robinson SL, SL R, WA S, AD A (1979) The role of brush plating in future hydrogen and transmission systems

47. Begeal DR (1975) The permeation and diffusion of hydrogen and deuterium through Rodar, tin—coated Rodar, and solder—coated Rodar. J Vac Sci Technol 12(1):405–409

48. Freiman L, Titov V (1956) The inhibition of diffusion of hydrogen through iron and steel by surface films of some metals. Zh Fiz Khim 30:882

49. Levchuk D, Koch F, Maier H, Bolt H (2004) Deuterium permeation through Eurofer and α-alumina coated Eurofer. J Nucl Mater 328(2–3):103–106
50. Ensinger W, Wolf GK (1989) Protection against hydrogen embrittlement by ion beam mixing. Nucl Instrum Methods Phys Res, Sect B 39(1–4):552–555
51. Dos Santos DS, De Miranda PV (1997) J Mater Sci 32:6311e5
52. Soudani M, Hadj Meliani M, El-Miloudi K, Bouledroua O, Fares C, Benghalia MA et al (2018) Efficiency of green inhibitors against hydrogen embrittlement on mechanical properties of pipe steel API 5L X52 in hydrochloric acid medium. J Bio- Tribo-Corros 4(3):1–11
53. Nam TH, Lee JH, Choi SR, Yoo JB, Kim JG (2014) Graphene coating as a protective barrier against hydrogen embrittlement. Int J Hydrogen Energy 39(22):11810–11817
54. Wang SS, Chai JK, Shui YM, Liang JK (1981) Cd–Ti electrodeposits from a noncyanide bath. Plat Surf Finish 68(12):62–64

Waste Lignin and Metal Oxides for Altering the Physical and Chemical Properties of Bitumen

Yash Thakare, Rajesh Gujar, and Ashish Unnarkat

1 Introduction

Growth of any nation is primarily inclined to its infrastructure development in terms of housing and roadways [1]. Fast-growing economies like India are investing heavily in construction and infrastructure development. Roadways make an important part of commute, but the rising environmental concern urges us to look for sustainable and improved road networks. Conventional pavement materials make it difficult to meet practical demands for current and future highway pavement construction [2, 3]. Therefore, there is an urgent demand for higher quality, safer, more reliable, and more environmentally friendly pavement materials [4, 5]. Advent of smart city concept has led to requirement for separate colored pavements for different commutation. The colored asphalt has the transitional asphalt properties and has many more advantages.

Asphalt also known as bitumen is a sticky, black, and highly viscous liquid or semi-solid form of petroleum [6]. It may be found in natural deposits or may be a refined product; it is a substance classed as a pitch. The primary use (70%) of asphalt/bitumen is in road construction, where it is used as the glue or binder mixed with aggregate particles to create asphalt concrete [7]. Its other main uses are for bituminous waterproofing products, including production of roofing felt and for sealing flat roofs [8]. It is tough to change the color of a bituminous mixture. The composition is of high molecular weight Saturates, Aromatics, Resins, and Asphaltenes (SARA) components that does not change the color easily.

Y. Thakare · A. Unnarkat (✉)
Department of Chemical Engineering, School of Technology, Pandit Deendayal Energy
University, Raisan, Gandhinagar, Gujarat 382426, India
e-mail: ashish.unnarkat@gmail.com; ashish.unnarkat@sot.pdpu.ac.in

R. Gujar
Department of Civil Engineering, School of Technology, Pandit Deendayal Energy University,
Raisan, Gandhinagar, Gujarat 382426, India

In the current research, we have tried to color the bitumen using metal oxides. In addition, we have used lignin, a bio-waste from paper industry for altering the physio-chemical properties of bitumen. Lignin is a natural polymer and comes from pulp industry waste liquid. Converting waste to wealth has been the need of an hour, and hence, lignin gained growing interest among many industries. The prime purpose for using lignin in case is that first lignin is considered as a waste material, and its use is pre-dominantly limited to fuel. Therefore, new applications for lignin will improve the economics of biofuel and paper industries and will contribute to the reduction of industrial waste. Second, lignin contains phenolic hydroxyl groups and aliphatic hydroxyl groups that have low molecular weight and high antioxidant property. Henceforth, it was understood that these functional groups endow lignin with superior chemical properties that are essential in various fields such as dispersants, emulsifying agents, and adhesives. Hence, bitumen considered to be modified with lignin to alter the physio-chemical and rheological properties of bitumen. Normal bitumen grade VG10 is colored using metal oxides of iron, and chromium is used to get red and green color bitumen. Bitumen was also examined for changes in properties with different concentrations of lignin. The samples were tested with conventional techniques; penetration, softening, viscosity, ductility, flash point, and characterized with FTIR. Physical and chemical properties of lignin and metal oxide-modified bitumen were compared with the base bitumen.

2 Practical Outcome of the Work

- Reduction in Congestion: The use of color variations on the road may allow to use a specific width of lane by a specific category of vehicle reducing the traffic congestion.
- Aesthetics: The use of colored bitumen will be considered a boon for landscape architectures as it will help them creating a modern piece of architecture using differ color roads, walkways, and parking.
- Modified Properties of Bitumen: The huge area of the roads can be covered when the shredded plastic is combined together with metal oxides, the process will eventually coat the aggregates with waste plastic and put it to use. The approach is known but tuning the properties with other additives mentioned in the study will be an avenue to look for.
- Simple Method: It is a convenient and simpler method that does not incorporate any advanced or novel machines.
- Improved Durability: The plastic addition and oxides addition blended in bitumen will help in enhancing the durability and the strength of the roadway.

3   Methodology

3.1   Sample Preparation and Synthesis

Normal bitumen VG10 was used for the experimentation. VG10 bitumen was obtained from Tiki Tar Industries, India. The bitumen sample was preheated to the temperature of 185 °C and was then mixed with metal oxides/lignin in various proportion to get the different modified asphalt samples. Following samples were prepared for the tests and were numbered from S1 to S8, respectively.

S1.   VG10 base bitumen.
S2.   Ferric Oxide in VG10 (Red color).
S3.   Chromium Oxide in VG10 (Green color).
S4.   Lignin (1%) in VG10.
S5.   Lignin (2%) in VG10.
S6.   Lignin (3%) in VG10.
S7.   Lignin (4%) in VG10.
S8.   Lignin (5%) in VG10.

Details of the sample preparation are provided in Table 1. In a typical sample synthesis, following steps were followed:

- Normal VG-10 bitumen (~500 g) was first taken in a metal jar and heated to 185 °C on a heater mixer setup.

Table 1 Sample preparation details

S. No.	Samples	Bitumen weight (g)	Additive components (g)	Additive consumed (%)	Mixing temperature (°C)	Mixing speed (RPM)
1	Ferric oxide in VG10	570	67	11.9	185	639
2	Chromium oxide in VG10	408	140	34.4	185	517
3	Lignin (1%) in VG10	600	6	1	185	400
4	Lignin (2%) in VG10	452	9	2	185	400
5	Lignin (3%) in VG10	465	14	3	185	400
6	Lignin (4%) in VG10	450	18	4	185	400
7	Lignin (5%) in VG10	454.7	22.8	5	185	450

- A weighed amount of metal oxide (~2–10%) or lignin (1–5%) was then slowly added to the bitumen melt and was continuously stirred with a Shear Mixer. The melt was continuously heated and stirred to get the uniform mix.
- The proportion of oxide and lignin are varied to check the implications.
- Different amount of metal oxides when added to the bitumen melt under shear mixer varies the color intensity of the mix which can be optimized to the application.
- The mixtures are then allowed to cool down and checked for different properties. The modified samples are then taken for testing.

4   Results and Discussion

4.1   Absolute Viscosity

Viscosity is measure of fluid's resistance to flow. Absolute viscosity of the bitumen tells us about the workability of the bitumen during the application. Viscosity is measured using Brookfield Viscometer. An immersion spindle is driven through a calibrated spring through a test fluid. Viscosity is measured by how far the spring deflects against the spindle when the fluid drags against it. Rotating transducers are used to measure spring deflection. Figure 1 shows the results for the prepared samples. The permissible limit of the viscosity is 1200 cP. It has been observed that with the addition of metal oxides or lignin the composition became highly viscous. The rise in the viscosity was expected and does not mean that batches were complete failure rather it takes specialized equipment while to put them in use. The viscosity increased 3–4 times as compared to base bitumen. The value for base bitumen was 1164 cP which increased to >3000 cP for the blended samples. Higher viscosity of blended samples will need special instruments while putting these samples to use.
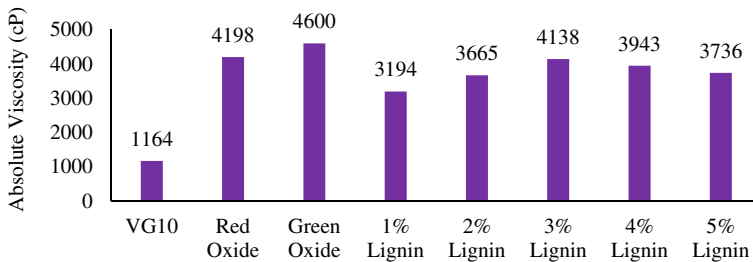

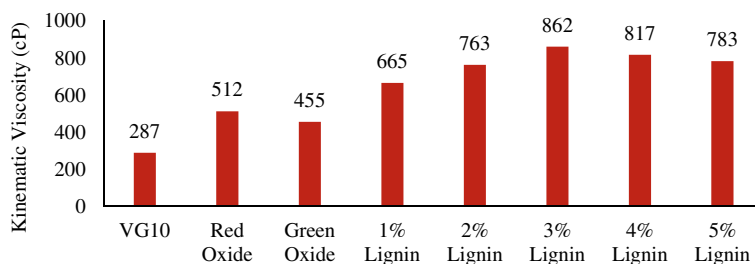**Fig. 1** Comparison of absolute viscosity of prepared samples

Fig. 2 Comparison of kinematic viscosity of prepared samples

4.2 Kinematic Viscosity

Kinematic viscosity values for the prepared samples obtained using Brookfield Viscometer is shown in Fig. 2. As per the IS standards, the limit for the viscosity is 250 cP. Similar to the absolute viscosity, kinematic viscosity has shown a rise for the samples loaded with metal oxides. Addition of oxides has made the base bitumen more viscous. The values were almost doubled, for base bitumen it was 287 cP and it increased to >450 cP for the colored bitumen. Lignin addition has altered the viscosity ominously, the values increased and reached a maximum of 862 cP for 3% lignin addition. Lignin being a viscous biopolymer adds to the viscosity of the blend.

4.3 Penetration

To measure the consistency of solid and semi-solid bituminous materials whose principal component is bitumen, a penetration test is conducted. In the test, a flat-bottomed cylindrical metallic container stored with modified bituminous sample at 25 °C was penetrated by a needle to a weight of around 100 ± 0.25 g including the weight of the needle, carrier, and super-imposed weights as per ASTM D5. Thus, the penetration value is measured in units of 0.1 mm. Results obtained are represented in Fig. 3. As per the IS standards, the values should be up to 80 units. Every 10 units refer to 1.00 mm penetration. Base bitumen has shown the value of 80 units while the values reduced to 56 and 46 for the samples loaded with red oxide and green oxide, respectively. The addition of lignin has also shown a similar trend wherein the increase in the lignin percentage in the blend showed the reduction in the penetration. This is in line to the results of viscosity, wherein the viscosity has inverse relation to the penetration values. As the upper cap for the penetration values is 80 units, it can be concluded that the addition of oxides and lignin improves the penetration values positively.
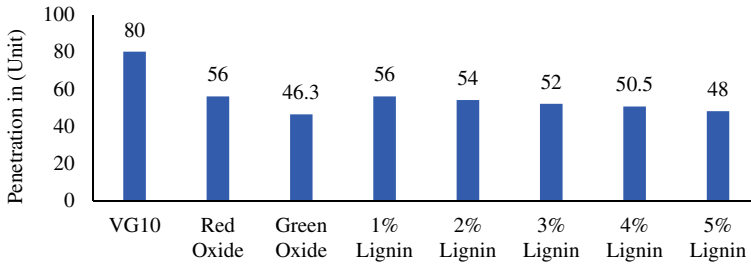
Fig. 3 Comparison of penetration values of prepared samples
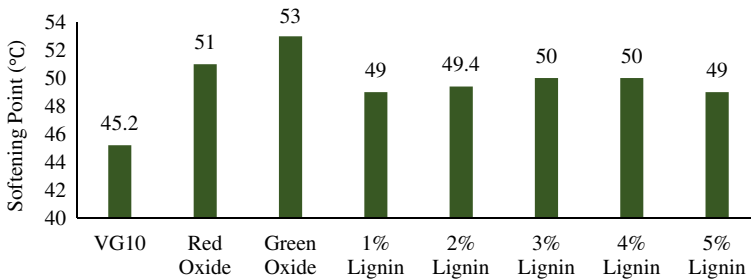
Fig. 4 Comparison of softening point index of prepared samples

4.4 Softening Point

The softening point of the bitumen resembles the temperature at which it will lose its plastic sate and get deformed. Ring and ball test is used to determine the softening point of bitumen. A steel ball weighing 3.5 ± 0.05 g and 9.5 mm diameter is placed on the sample supported by the brass ring of 17.5 mm diameter as per ASTM D36. Then, this assembly is heated at the uniform rate of 5 ± 0.5 °C per minute until the material softens and allows the balls to pass through the ring. Thus, the temperature was recorded as softening point when ball touched the bottom plate of the support. Figure 4 compares the values of softening point of the blended samples. It is indicated in the graph that the softening point of all the blended samples of bitumen is above the desired limit of 40 °C as per the standards. The above limit results are considered to be good for the modifications incorporated in the bitumen.

4.5 Ductility

Ductility was considered as our main component of test to know the behavior of the bitumen. Ductility provides resistance to wear and tear on the road and also binds aggregate with bitumen. Ductility test was carried out as per IS: 1208-1978. Ductility
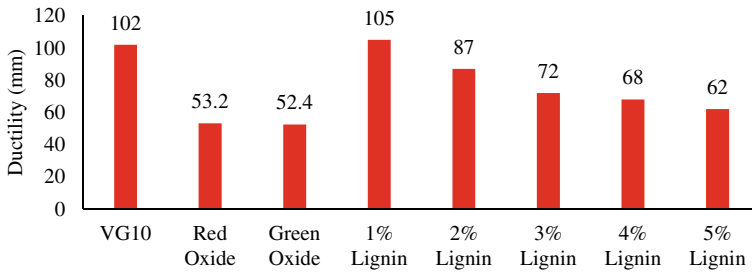
Fig. 5 Comparison of ductility of prepared samples

is defined as the distance in cm, to which a standard sample or briquette of the material will be elongated without breaking. Figure 5 represents the ductility index of different batches of bitumen prepared. The limit of the distance up to which when the specimen is stretched should not fail according to IS standards is 75 mm. The observations suggest that for 1% lignin the ductility was similar to the base bitumen however with further increase in lignin percentage to 3% the values decreased to 72 mm. Beyond 3% addition, the ductility value goes below the permissible limits. Lignin being the polymer, it is understood to have ductile nature; however, more analysis has to be done on molecular level to understand the reason for the continuous drop in the ductility. The addition of oxides implies the results as expected. The metal oxides blended samples fail to cross the permissible limit. Metals oxides are pure solids, and when added to the bitumen, it reduced the ductility to half of the base bitumen.

4.6 Flash Point

Flash point is an important characteristics that helps to determine the temperature after which the sample will start catching fire which one of the major issues while working with petroleum products. Flash point was calculated using Pensky–Martens closed cup tester as per ASTM D92-01 wherein the sample was heated above its softening point, poured into the cup, and was heated uniformly at the rate of 5–6 °C per minute with simultaneous stirring at the rate of 60 rpm. The test flame is applied at every 1 °C rise from 157 °C onwards. The temperature was noted when sample catches the flame and gives a quick flash, the point is taken as flash point. Bitumen as such has high flash point (175 °C) while the modified VG10 used in the study has 220 °C. The typical working temperature for hot mix and bitumen melt can reach to the flash point and cause incidents. Hence, the operation temperature has to be duly taken care. Addition of oxides has improved the flash point value 300–310 °C. Any improvement in the values of the bitumen blend is a good sign toward its employability and applications.

4.7 Rolling Thin Film Ovens Test (RTFOT)

Rolling Thin Film Ovens Test (RTFOT) is used to simulate aging of the bitumen after which the tested are sample for various properties like softening point and flash and fire point. This test was performed as per ASTM D2872 at 163 °C with 35 g of bitumen in the aging bottle and then rotating it for 85 min at 15 rpm. In the current study after the RTFOT test, softening of the samples is tested again. It has been observed that the softening point of the bitumen increased by 5–7 °C from 51 to 53 °C before RTFOT to 58–59 °C after RTFOT. This is the good indication that concludes that with the lapse of time the specimen will gain more strength. The prime reason being the presence of metal oxide present in the bitumen. Being metal oxides, there is no further oxidation process that alters the character rather it improves the rutting properties of the blended bitumen and hence can age better.

4.8 Fourier Transform Infrared Spectroscopy (FTIR)

Fourier Transform Infrared Spectroscopy (FTIR) provides the infrared spectrum of transmission or absorption from the sample. It identifies the presence of any organic and inorganic compounds present the sample based on the infrared absorption frequency range 400–4000 cm^{-1}. Figure 6a depicts the spectrum for pure lignin. The spectrum indicates the presence of various functional groups; hydrogen-bonded O–H (3400 cm^{-1}), aromatic vibrations, carbonyl stretching (1600–1900 cm^{-1}), aromatics skeletons and secondary alcohols C–O stretching (~1000–1500 cm^{-1}), and aromatic in plane and out of plane (800–1000 cm^{-1}). Upon addition of the metal oxides, significant peaks of metal oxygen (M–O) bonding are reflected in the band of 400–1000 cm^{-1} in the spectrum (Fig. 6b). Lignin in itself is complex polymer that blends with SARA (saturates, asphaltenes, resins, and aromatics) in the bitumen to give stretching in the regions with overlapping from the functional groups present in the complex blend. The spectrum for the blend can be seen in Fig. 6c. Table 2 provides the different band positions for the respective blended and non-blended samples of bitumen and additives. It is a qualitative analysis that shows the different bonding present in the mixture; however, the effect of such additives on inter- or intra molecular bonding in the blend can be further explored.

5 Conclusion

The test was conducted on various bitumen samples with additive components of red oxide, green oxide, and a biopolymer; lignin. The significant findings from the study are as follows:
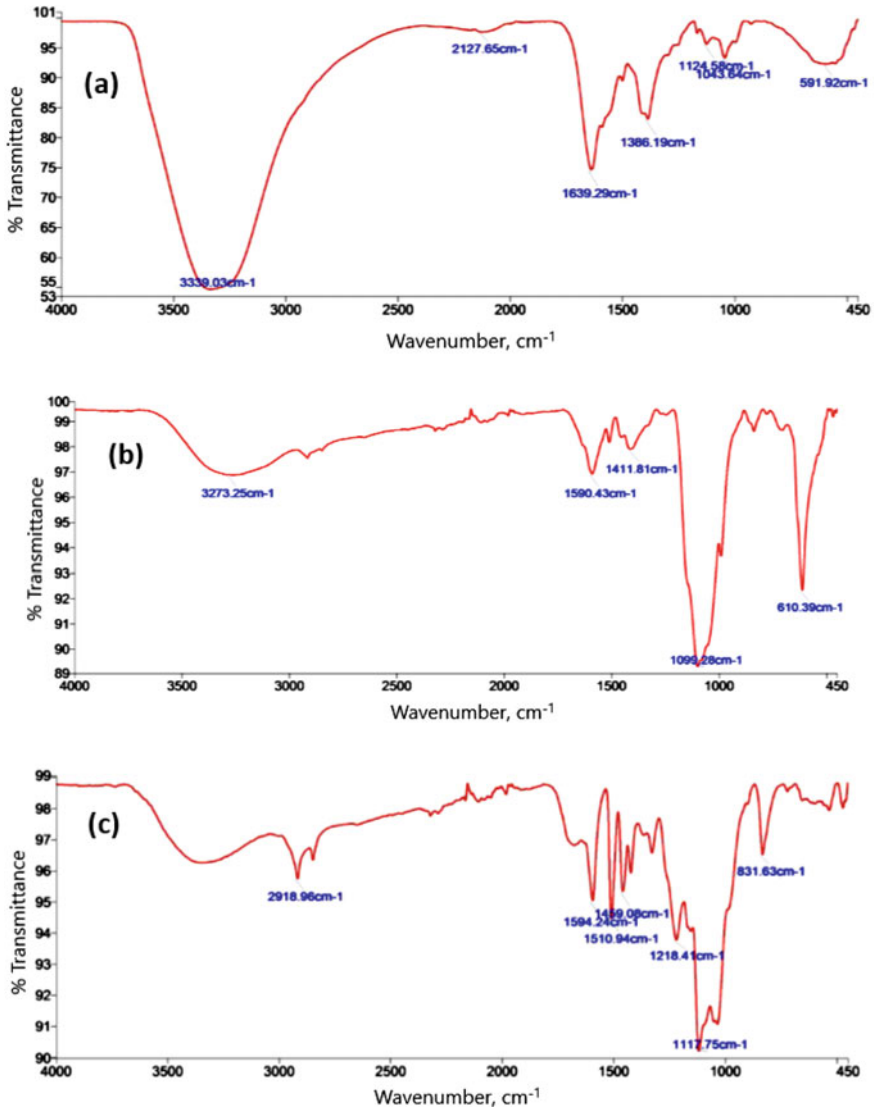
Fig. 6 FTIR of **a** pure lignin **b** metal oxide-blended bitumen **c** lignin-blended bitumen

- Absolute viscosity of the modified bitumen shows fourfold increase, reducing the workability of the bituminous mixture. The values were doubled in the case of kinetic viscosity.
- Lignin addition has changed kinematic viscosity significantly, and the maximum of 862 cP was obtained for 3% lignin addition.
- The penetration and softening point after the addition of additives was found to be within the standard limits.

Table 2 FTIR analysis for the blended bitumen samples

Band range	Band position (cm^{-1})	Details	Bitumen	Lignin	Metal oxide	Lignin-modified bitumen	Metal oxide-modified bitumen
560–600	576	Fe–O stretching mode			✓		✓
680–860	850	Aromatic C–H out of plane deformation	✓				✓
1030–1035	1033	C=O carboxylic	✓	✓		✓	
1075–1150	1125	C–O stretching for secondary alcohols		✓			✓
1370–1378	1371	C–H, symmetric bending of –CH$_3$	✓	✓			
1437–1458	1453	C–H, asymmetric bending of –(CH$_2$)n–	✓		✓	✓	✓
1600–1650	1650	C=C alkane chain	✓	✓	✓	✓	✓
2840–2870	2848	C–H, aliphatic, symmetric stretching	✓				
2918–2954	2918	C–H, aliphatic, asymmetric stretching	✓				✓
3100–3500	3349	– OH stretching	✓	✓		✓	

- Permissible limit in ductility test was satisfied till 3% lignin addition. The blended samples with metal oxides fail to cross the permissible limit. Blending with other polymers and waste plastic should be allowed to retain the ductility.
- Flash point is increased with the oxide blended with bitumen.
- FTIR analysis implies the interaction of metal and lignin with the components of bitumen.

The test conducted on the blended samples of bitumen has shown positive characteristic values upon the addition of metal oxides and lignin. Tuning the properties with the additives is a tough task and has to be judiciously optimized as per the applications. Furthermore, the comprehensive study must be conducted using different types of asphalt binder and lignin. In order to determine the optimal lignin dosage, it should be examined how performance characteristics are balanced among different doses. Moreover, investigation can be done on utilization of various other materials as an additives for improving the bitumen properties. Current work has opened the avenues for further development in the area of bitumen modification.

References

1. Autelitano F (2021) Color durability of pigmented slurry surfacing after artificial aging tests simulating weathering and traffic. Transp Res Procedia 55:1155–1162
2. Bocci M, Grilli A, Cardone F, Virgili A (2012) Sustainability of road infrastructures clear asphalt mixture for wearing course in tunnels: experimental application in the Province of Bolzano. Procedia Soc Behav Sci 53:115–124
3. Bocci E, Bocci M (2014) Clear asphalt concrete for energy saving in road tunnels. In: 12th ISAP conference on asphalt pavements. Raleigh, North Carolina (USA), vol 2, pp 1817–1825
4. Zhu J, Birgisson B, Kringos N (2014) Polymer modification of bitumen: advances and challenges. Eur Polym J 54:18–38
5. Autelitano F, Giuliani F (2019) Daytime and nighttime color appearance of pigmented asphalt surface treatments. Constr Build Mater 207:98–107
6. Petersen JC (2000) Chapter 14. Chemical composition of asphalt as related to asphalt durability. In: Developments in petroleum science, vol 40, Part B, pp 363–399
7. Lee H, Kim Y (2007) Laboratory evaluation of color polymer concrete pavement with synthetic resin binder for exclusive bus lanes. Transp Res Record J Transp Res Board 1991:124–132
8. Mastrofini D, Scarsella M (2000) The application of rheology to the evaluation of bitumen ageing. Fuel 79(9):1005–1015

Solar Photovoltaic System and Its Fire Safety in Indian Scenario

Shubham Srivastava and C. S. Malvi

1 Introduction

Renewable energy plays considerable role in the economic growth of any country. There is a competitive environment across the globe to generate electricity from renewable resources at optimum price and governments are running different schemes for promoting the same in their respective countries. As India is a tropical country, it receives solar radiance of order 3.0–6.5 kWh/m^2-day during the summer season and it reached up to 7.5 kWh/m^2-day in May. However, in winter season, the average solar radiation is less than 4.5 kWh/m^2-day [1]. Overall India receives enough solar radiation throughout the year and has great potential of PV electricity generation. Government is accelerating the deployment of grid connected as well as off-grid solar PV system under various scheme. National Tariff Policy (2016) lucidly set its primary objective to promote the generation of electricity from non-conventional resources. Although, India has made significant effort in increasing citizen's access to electricity and taken various initiative to cope up with the dramatic rise of electricity demand by deploying renewable energy sources but the prime source of electricity generation is still thermal power plant which is directly associated with severe air pollution and global warming. Government of India has planned to harness 100 GW of electricity by utilizing solar photovoltaic (PV) system by 2022 to tackle the environment issues and for achieving its sustainability goal. In this regard, solar photovoltaic power generation units are being deployed in various states rapidly. Karnataka, Telangana, Rajasthan, Andhra Pradesh, Tamil Nadu, Gujarat, Madhya Pradesh, Maharashtra, Uttar Pradesh and Punjab are the top 10 states by installed solar plant capacity [2]. Figure 1 is showing the contribution of state according to the

S. Srivastava (✉) · C. S. Malvi

Mechanical Engineering Department, Madhav Institute of Technology and Science, Gwalior 474005, India

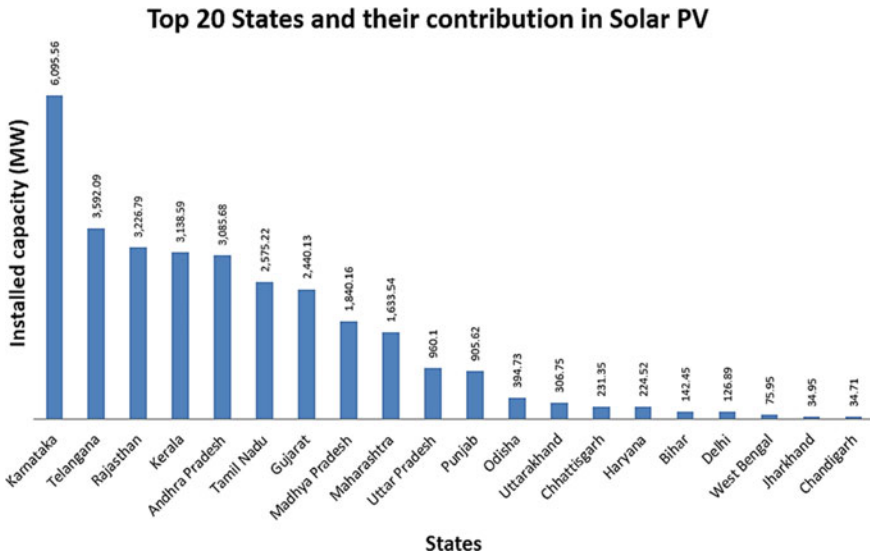e-mail: shubhams0309@gmail.com

© The Author(s), under exclusive license to Springer Nature Singapore Pte Ltd. 2022

K. Mukherjee et al. (eds.), *Tailored Functional Materials*, Springer Proceedings in Materials 15, https://doi.org/10.1007/978-981-19-2572-6_33

Top 20 States and their contribution in Solar PV

Fig. 1 State and their contribution in solar PV [3]

installed capacity of solar PV plant [3]. Moreover, India secured fifth global position in solar power deployment by surpassing Italy according to MNRE report.

Undoubtedly, manufacturing or installing anything at faster rate, and at lower price as compared to its previous state, is sometimes associated with poor quality as well as it is not easy to conform the prescribed safety standards. Same situation arises in solar PV industry at global level. It was reported by researchers that suppressing the industry to manufacture and install the solar PV system at quicker rate led to the poor quality and lack of safety standards in India [4]. These low quality solar PV always suffered with less energy conversion and shorter lifespan than expected. In addition to this, these PV systems failed to conform the safety standard and always imposed serious risks to the customers. Among various risks associated with solar PV, there are certain fire risks also, which are based on various factors such as technology and construction standards, improper installation and many other trivial but sometimes unavoidable reasons [5]. Many cases of fire incident involving PV system were reported in the last decade.

In this paper, fire risks associated with PV system are discussed in Indian context by utilizing the available case studies done earlier at global level. In addition to this, standards and codes related to the fire rating of solar panel present in India are depicted and further improvement for better safety is suggested.
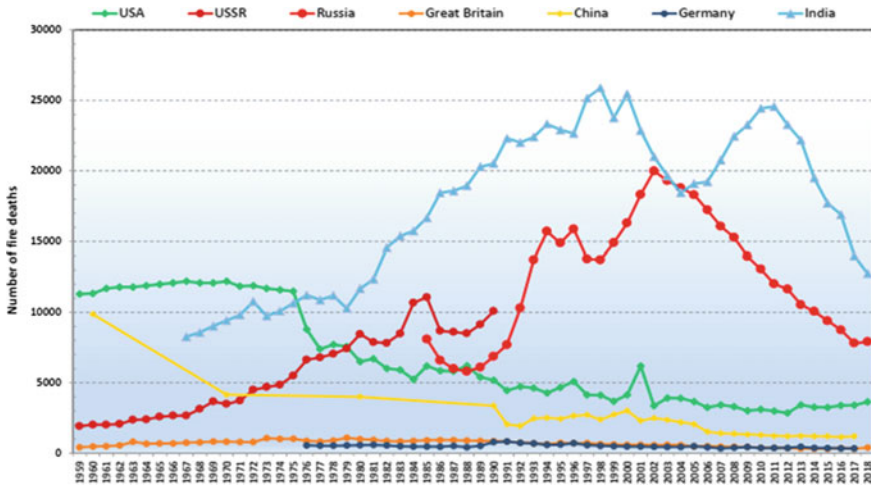
Fig. 2 Trends of fire death in respective years [8]

2 Fire Accident Scenario in India

In developing countries like India, fire accidents are very common due to negligence of fire safety standards in buildings, industries and other places. Fire threats are incessantly increasing as there is no effective vigil over the fire susceptible areas. Congested places, entangled electrical wires, lack of knowledge of operating fire extinguishing equipment, ignorance of laws and standards are some basic cause of fire accidents. As per the data released by Ministry of Home Affairs, many towns are still not equipped with basic fire safety infrastructure. India Risk Survey 2019 pointed out that economic growth of a country got distorted because of fire accidents, and fire accident is among the top 10 risks including natural hazards, crime, terrorism, etc. [6]. National crime record bureau, India, has been publishing the fire accident data yearly on the basis of place of occurrence and data of year 2019 which shows that 58% deaths were there when accidents took place in residential/dwelling building compared with other place of fire accident [7]. According to world fire statistics' report 2020, highest death is observed in case of fire accident in India as shown in Fig. 2 [8].

3 Components of Solar PV System and Its Fire Assessment

Solar PV converts sunlight into electricity by consuming its visible spectra. Figure 3 is showing the structure of PV module which comprises solar cell, sandwiched between ethylene–vinyl acetate (EVA) sheet, tempered glass, back sheet, aluminium frame and

Fig. 3 Components of solar PV and root causes of fire
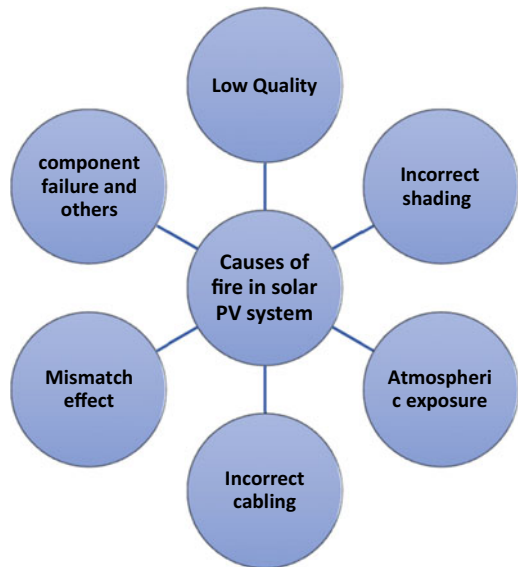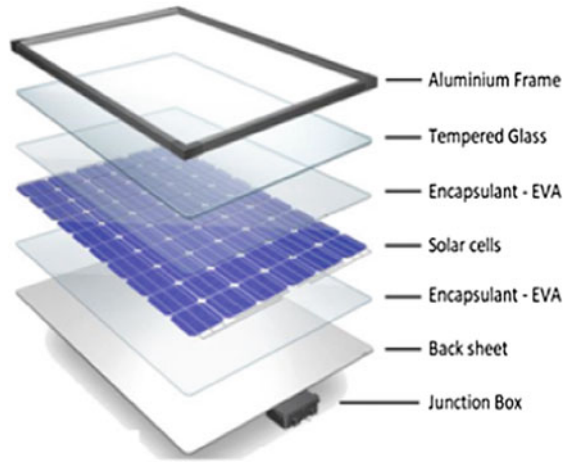
junction box. Solar power plants are generally installed over the rooftop of commercial/residential buildings and it increases the fire load of that particular building in ample amount because no specific codes are present for photovoltaic buildings in India. These buildings are constructed by following traditional safety standards and guidelines. Due to installation of power generating unit on the rooftop, buildings became more susceptible to fire accidents and it became impossible to completely cut-off the power line in case of fire accident. Moreover, threat of electrocution is higher if conventional fire extinguishing medium, water is used [9].

Fig. 4 **a** Low quality of junction box catches fire, **b** hotspot effect [10]

Solar module components are not made of fire resistance material, and they are susceptible to flame propagated by other fire accidents. Apart from this, fire accident can be initiated by the solar PV plant itself and flame could be propagated to the entire building by following top-down approach. Some root causes of solar PV fire accidents are given from Sects. 3.1 to 3.6.

3.1 Low Quality of PV Components

Poor quality of components such as junction box as shown in Fig. 4a and cables pose fire threat to the entire PV power generation unit because they are susceptible to arc fault as well as spontaneous ignition. Apart from this, aged solar panel catches fire due to certain chemical reaction in the exposure of sunlight.

3.2 Incorrect Management of Shading

Solar panel is an electrical component, in which, solar cells are connected in series. Whenever shading is not addressed properly and temperature became 5% higher than the standard temperature under standard test conditions (STC, 1000 W/m^2, 25 °C), hot spot would occur because power is not generated uniformly among the cells. PV module ignites abruptly due to the rise of local current, voltage and localized heat generation as shown in Fig. 4b.

3.3 Atmospheric Exposure

If the electrical components of PV plant are exposed to worst atmospheric condition such as heavy rain, wind storm, lightening without proper packing or insulation, then there is chance of arcing or short circuit that can further become spreading flame.

3.4 Incorrect Cabling and Electrical Fault

If wiring of power generation unit is not properly insulated and packed within cable box, then chances of short circuit are increased that further leads to a big fire accident. It is seen in most of the cases that cable is adhering with roof ceiling and overall system is not grounded properly. In addition to this, use of inverter and direct current system with solar plant got a new hype. It is obvious that above-stated system raised the concern of consumers from safety point of view.

3.5 Mismatch Effect

When properties of interconnected solar cells or modules are not identical, then power output of entire plant is affected. When a part of PV plant is shaded by some means, then the power generated by unshaded part get dissipated in localized heating, and if this situation is not addressed properly, then this may cause irreversible damage to module as well as eventually lead to fire accident.

3.6 Component Failure and Others

Components, which are not replaced even after their life span, they can ignite spontaneously as discussed in Sect. 3.1 that aged solar panel catches fire in certain condition. All the components of PV plant need to be checked in specified time interval otherwise they can lead the plant in severe fire risk condition [11]. In addition to these aforesaid failures, Malvi has summarized common failures of solar panel encasement as shown in Fig. 5.
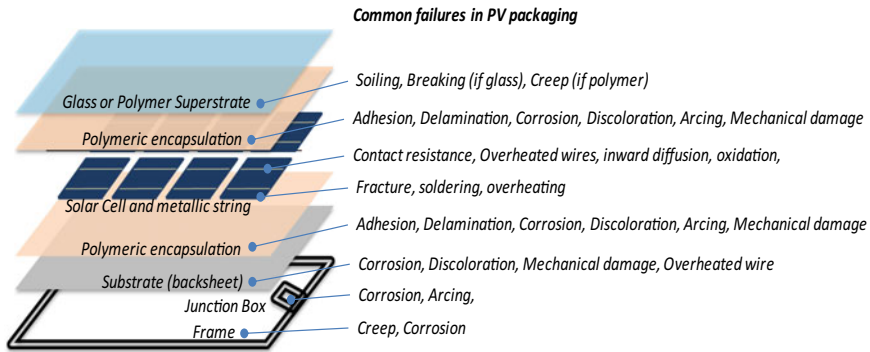
Fig. 5 Common failures in PV encasement [12]

4 Standards and Codes of Fire Testing

There is always certain test parameters and standards that are present to access the potential of fire hazard of solar PV in the entire world to avoid fire accidents. Manufacturers of solar panel conduct some tests after manufacturing them and by following the code mentioned in their respective countries. Their products get certified from standard and rating agency. In India, Bureau of Indian standards (BIS) referenced the standards for various tests such as temperature, hot spot and fire test, etc. as shown in Table 1. Figure 6 is showing the fire rating (Type I, Class 3) of solar panel manufactured by Vikram solar company in India. Furthermore, international building code (IBC) also depicts the standards for different type of roofing in accordance with the UL 1703 fire rated PV system in 2012 IBC: 1509.7.2 to alleviate the effect of any fire accidents. According to the IBC code, roofing system is classified in three groups, i.e. class A, B and C and based on the class of particular roof, PV panel is installed over it which is marked with different fire rating such as class A, B and C. The PV panel is tested under gas flame exposure to evaluate the flame spread height over the solar panel in mentioned time as described in ASTM E108 and UL 790 and shown in Table 2. In case of wooden roofing, ASTM D2898 is used for testing the solar panel.

Table 1 Standards referenced in BIS [13]

Title	References in standards	According to	
		IEC61215	IEC61646
Temperature test	ANSI/UL 1703		
Hot spot test		10.9	10.9
Fire test	ANSI/UL 790		
Bypass diode thermal test		10.18	
Reverse current overload test	ANSI/UL 1703		
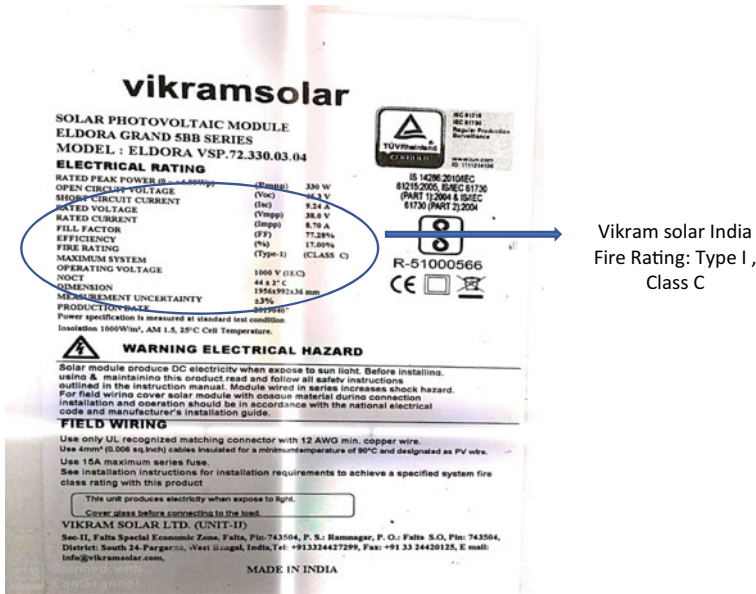
Fig. 6 Detailed specification of 330Wp solar panel including fire rating

Table 2 Details of fire ratings mentioned in ASTM E108 and UL 790

| Fire rating | Flame exposure | | Flame spread height (feet) |
	Temperature (°F)	Time (min)	
Class A	1400	10	≤6
Class B	1400	10	≤8
Class C	1300	4	≤13

Further in 2014, UL 1703 introduces the concept of "PV module types" instead of the classification of PV panel on the basis of fire performance obtained by conducting specific test. PV module types are based on certain construction parameter such as encapsulate and substrate material, and the fire performance is obtained by conducting flame spread as well as fire brand test. Details of different type of PV modules are depicted in Table 3 [14].

Based on the construction specification and fire performance of a PV module against flame, it can be classified as Class A, B or C and specified with PV module type such as type 1 or 2 or any other type as mentioned in Table 3.

Table 3 Construction parameter and fire performance of different PV module types [14]

Encapsulates						Flame		Burning brand
Type	Glass	Frame	Super/cell	Cell/sub	Substrate	Allowable height (feet)	Exposure time (min)	
1	Thick	Metal	Thin	Thin	Thick polymer	6	10	C brand
2	Thick	Metal	Thin	Thin	Thin polymer	6	10	C brand
3	Thin	–	–	Thick	Glass	6	10	C brand
4	Thick	Metal	Thin	Thin	Thick polymer	13	4	C brand
5	Thick	Metal	Thin	Thin	Thin polymer	13	4	C brand
6	Thin	–	–	Thick	Glass	13	4	C brand
7	Thick	Metal	Thin	Thin	Thick polymer	8	10	C brand
8	Thick	Metal	Thin	Thin	Thin polymer	8	10	C brand
9	Thin	–	–	Thick	Glass	8	10	C brand
10	Thin	–	–	Thick	Glass	6	10	B brand
11	Thin	–	–	Thick	Glass	13	4	B brand
12	Thin	–	–	Thick	Glass	8	10	B brand
13	Thin	–	–	Thick	Glass	6	10	A brand
14	Thin	–	–	Thick	Glass	13	4	A brand
15	Thin	–	–	Thick	Glass	8	10	A brand

5 Some Recent Reported Fire Accident Involving Solar Panel

5.1 Across the Globe

According to Italian National Fire Corp, statistical data services and solar PV involved fire accidents in Italy were highest in 2012, and there were around 600 fire accident reported in this year. Fire was ignited either directly from the PV system or easily propagated with its aid. In Fig. 7a, 1000 m^2 warehouse was indulged in fire; fire was ignited and propagated by PV component. It can also be seen in Fig. 4 that even a small electrical box fire propagated rapidly in top-down pattern. Various components of solar PV are inflammable and cannot resist fire above certain temperature, and if fire is ignited from external source such as building fire, then it aids in

Fig. 7 **a** 1000m^2 warehouse fire and **b** externally ignited fire and propagated with the aid of installed PV system [15]

propagating the fire. Various toxic gases and ample amount of smoke are generated due to burning of PV system as shown in Fig. 7b.

A severe fire accident happened in 2013 in Delanco, New Jersey, where a warehouse was completely consumed by the flame as shown in Fig. 8. Fire-fighters were unable to douse fire because 7000 solar panels were installed over the entire roof which limits the fire-fighting operation. It was realized by the fire safety personnel that solar panel could be a new threat to fire extinguishing operations [16]. Guidelines and codes are regulated regularly by analysing the data. National fire protection association (NFPA) is collecting and analysing the data of PV fire accident. Various small incidents were reported from Massachusetts, Maryland, and other cities in 2019, where Tesla manufactured solar panel caught fire. Amazon and Walmart had also claimed the fire accident in their warehouse [17].

Along with this, Japanese Consumer Safety Investigation Commission reported many cases of PV fire, where fire was either directly ignited from module or propagated through it. German research group was also reported several incident of PV fire in which economic loss is observed in great extent [19]. In Argentina, a solar park attracted the attention of fire-fighters when solar park's central inverter catches fire and internal component along with thick cables were reduced to ashes before blaze was controlled by them [20].

5.2 In India

Very few incidents of fire accident involving solar panel are reported so far in India. Most of them had incurred only economic loss, no fatal injuries or death. Table 4 is listing the fire accidents happened in last five years based on some media reports because there is no statistical data analysing agency in India. Pictures of the same accidents are shown in Fig. 9. Research activities related to this field have not marked

Table 4 Recently reported fire accident involving solar panel in India

Year	Place	Source of fire	Extent of solar panel involvement	Causality/economic loss
2016	Kamuthi, Tamil Nadu	Short circuit	Some panels were completely burnt	Economic loss
2017	Nirmal, Telangana	unknown	Stored solar panel at project site reduced to ashes	Economic loss
2018	New Delhi metro station	IRCTC Vending machine	Flame was propagated with its aid	Economic loss
2019	Kadapa, Andhra Pradesh	Short circuit or extreme heat	Ignited and propagated through it	Loss of Rs. 900 Crores

Fig. 8 Solar PV fire accident (Delanco, New Jersey) [18]

considerable growth and only handful of researchers such as Pandian et al. [21] contributed in this field.

6 Environmental Pollution and Health Hazards

Solar cell is made of silica-based materials as well as from cadmium telluride (CdTe), copper indium diselenide (CIS), gallium arsenide (GaAs) and organic materials. Their quantities, burning behaviour and various by-product formations affect the environment severely. Research was conducted to analyse fire involved in residential and commercial power plants. Residential fire was proved less hazardous than commercial one but environment and public health would be at risk until fire accident is not prevented [25].

It is evident that solar PV plants are capable of igniting fire under specified condition as well as propagate the exiting fire with ease. Research is being carried out to assess the fire behaviour of different component of solar panel. Various companies have issued the safety guidelines for installing and operating the solar plant [26]. Developed countries such as the USA, Germany and Italy are collecting and analysing the data of fire accidents involving solar panel for the development of

Fig. 9 Fire accidents happened at **a** Kamuthi, Tamil Nadu **b** Nirmal, Telangana **c** New Delhi metro station **d** Kadapa, Andhra Pradesh [22–24]

existing standards and regulation but in India, solar panels are not considered as fire susceptible source. However, few incidents were reported, where fire was ignited and propagated through solar panels. Recent researches and their findings are listed in Table 5.

It is very clear from Table 5 that promoting research activities may play a crucial role in preventing the fire accident from solar PV system. Governments have to take the responsibility of encouraging the researcher and regulating the exiting legislation and standard at regular interval.

7   Conclusion

Fire accidents in India are continuously rising and new threat of solar PV fire accident has emerged.

Although there are many codes and guidelines related to fire safety, yet these are seldom followed, and in case of PV system, only some test parameters are followed

Table 5 Recent researches and their findings

Authors (year)	Country	Objective	Conclusion	Reference
Tommasini et al. (2014)	Italy	Measured the fire-fighting water nozzle distance from an electrically activated component such as PV system	Water jet could be used to extinguish the fire where 1000 V by maintain the safe distance. It depends on water pressure, flow rate and type of nozzle used	[27]
Pandian et al. (2015)	India	Investigated the fault in solar PV panel associated with partial shading over the PV cell	It was concluded that hot spot point temperature rises up to 347 °C which may be considered as potential source of ignition in hydrocarbon field	[21]
Manzini et al. (2015)	Italy	Tested the PV against fire and analysing existing legislation and standards	It was concluded that inclination of solar panel from horizontal and flame property greatly affects the growth of flame	[28]
Mazziotti et al. (2016)	Italy	Studied the fire safety related issue in building integrated PV system (BIPV)	Facade could be integrated with solar panel with the help of European harmonized standard. Fire risk of solar panel should be accessed and tested before installing	[29]
Zhao et al. (2018)	China	Accessed the fire risk of BIPV systems by fire dynamic simulator (FDS) with respect to different situation of building fire	It was found the flat roof would be more susceptible to fire accident as compare to sloping roof but this situation could have altered in presence of skylight. External wall insulation proved beneficial for blaze indulged building	[9]
Kristensen et al. (2020)	–	Studied the flame propagation behaviour underneath PV module	Height of solar panel from roof played vital role. Samples with different width were tested for optimum height and introduced height as crucial design parameter	[30]

Table 5 (continued)

Authors (year)	Country	Objective	Conclusion	Reference
Wu et al. (2020)	–	Reviewed techniques to reduce hot spot and DC arcing by varying structural configuration and fault detection	Dust deposition, shading, faulty and aged panel increased the chance hot spot. Fault detection should be prioritizing to avoid fire accident. Components prone to high temperature should be made of non-combustible material	[5]

by the manufacturer; no strict guidelines are present to access the fire risk before commencing solar project. It is obvious from the study that electrical failure of solar panel mostly led the ignition of entire plant; however, flame can be easily propagated through it because of their fire susceptible components. It is also suggested by some researchers that components prone to high temperature should be made of non-combustible material. In addition to this, very few fire accidents involving solar panel were reported in India as compared to other countries and because of these research activities are also encouraged to the countries, which faced fire accidents involving causality as well economic loss. Lesson should be learnt from accidents happened in other countries and strict codes may be embarked in India to avoid major fire mishap that must be regulated in close interval. Additionally, separate agency may be formed to collect and analyse the data related to this type of accidents and to audit as well as vigil the entire solar PV industry.

References

1. Jamil B, Siddiqui AT, Akhtar N (2016) Estimation of solar radiation and optimum tilt angles for south-facing surfaces in humid subtropical climatic region of India. Eng Sci Technol Int J 19(4):1826–1835. https://doi.org/10.1016/j.jestch.2016.10.004
2. Abdi B (2019) India's top 10 states by installed solar power capacity, 2019.
3. Ministry of New and Renewable Energy, Installed capacity of various renewable modes of energy, 2019 [Online]. Available: https://pib.gov.in/Pressreleaseshare.aspx?PRID=1564039
4. U N, Amala Devi TM (2018) Here comes the sun: residential consumers' experiences with rooftop solar PV in five Indian cities, no Oct, pp 1–36 [Online]. Available: https://shaktifoundation.in/wp-content/uploads/2018/11/Here-Comes-the-Sun.pdf
5. Wu Z, Hu Y, Wen JX, Zhou F, Ye X (2020) A review for solar panel fire accident prevention in large-scale PV applications. IEEE Access 8(i):132466–132480. https://doi.org/10.1109/ACCESS.2020.3010212
6. Aparaita Das SD, Bipin A, Singh N, Gaur G, India risk survey 2019, 2019
7. National Crime Record Bureau, Accidental deaths and suicides in India 2019
8. Centre for Fire Statistics Russia, World Fire Statistics

9. Zhao G et al (2018) Analysis of fire risk associated with photovoltaic power generation system. Adv Civ Eng 2018. https://doi.org/10.1155/2018/2623741
10. China Energy, Photovoltaic power plants frequently 'spontaneously combust' Chinese manufacturing is questioned [Online]. Available: https://www.china5e.com/m/news/news-229160-0.html
11. Pester S, Holden J, Shipp M, Holland C, Crowder D, Fire safety and solar electric/photovoltaic systems [Online]. Available: http://www.bre.co.uk/page.jsp?id=3424
12. Malvi CS (2012) Approaches to increase the efficiencies of solar energy conversions. University of LEEDS, UK
13. International Electrotechnical Commission (IEC), IEC 61730-2:2004 photovoltaic (PV) module safety qualification—part 2: requirements for testing, 2004
14. Power from Sunlight, Fire rating of a solar PV system: the fire type concept of PV solar panels, 2017
15. Fiorentini L, Marmo L, Danzi E, Puccia V (2016) Fire risk assessment of photovoltaic plants. A case study moving from two large fires: from accident investigation and forensic engineering to fire risk assessment for reconstruction and permitting purposes. Chem Eng Trans 48:427–432. https://doi.org/10.3303/CET1648072
16. Weaver JF (2019) There are –data missing– solar power fires per year, 2019. https://pv-magazine-usa.com/2019/08/22/there-are-solar-power-fires-per-year/
17. Bloomberg News Editors, More Tesla solar-panel fire incidents emerge in wake of Walmart suit, 2019
18. Weaver JF (2019) There are –data missing– solar power fires per year, PV Magazine 2019
19. Wirth H (2017) Recent facts about photovoltaics in Germany. Fraunhofer ISE 1(101):92 [Online]. Available: http://pschuetzenduebe.webclient5.de/wp-content/uploads/130912-Recent-Facts-PV-Germany.pdf
20. Molina PS (2020) Fire accident at Argentinian solar park's central inverters. https://www.pv-magazine.com/2020/10/21/fire-accident-at-argentinian-solar-parks-central-inverters/
21. Pandian A, Bansal K, Thiruvadigal DJ, Sakthivel S (2016) Fire hazards and overheating caused by shading faults on photo voltaic solar panel. Fire Technol 52(2):349–364. https://doi.org/10.1007/s10694-015-0509-7
22. Major fire at Kadapa Solar Power Unit, New Indian Express (2019)
23. Fire damages solar panels at New Delhi station platforms, The Times of India (2018)
24. Fire at Adani Group Solar Power Plant in Kamuthi, Economics Time (2016)
25. Moskowitz PD, Fthenakis VM (1990) Toxic materials released from photovoltaic modules during fires: health risks. Sol Cells 29(1):63–71. https://doi.org/10.1016/0379-6787(90)90015-W
26. Oregon Solar Energy Industries Association, Solar construction safety
27. Tommasini R, Pons E, Palamara F, Turturici C, Colella P (2014) Risk of electrocution during fire suppression activities involving photovoltaic systems. Fire Saf J 67:35–41. https://doi.org/10.1016/j.firesaf.2014.05.008
28. Manzini G, Gramazio P, Guastella S, Liciotti C, Baffoni GL (2015) The fire risk in photovoltaic installations—checking the PV modules safety in case of fire. Energy Procedia 81:665–672. https://doi.org/10.1016/j.egypro.2015.12.051
29. Mazziotti L, Cancelliere P, Paduano G, Setti P, Sassi S (2016) Fire risk related to the use of PV systems in building facades. MATEC Web Conf 46:1–9. https://doi.org/10.1051/mateconf/20164605001
30. Kristensen JS, Faudzi FBM, Jomaas G (2020) Experimental study of flame spread underneath photovoltaic (PV) modules. Fire Saf J (April):103027. https://doi.org/10.1016/j.firesaf.2020.103027

Strapped Calix[4]Pyrrole: Emerging Trends Based on Calix Protected Metal Nanoparticles

Nandan Pomal, Nihal Patel, Jaymin Parikh, and Keyur D. Bhatt

1 Introduction

The field of supramolecular chemistry developing persistently for past few decades and in contemporary chemistry, it is the core area of research which associated with host–guest relationship. The third generation supramolecules calixarenes holds the possibilities of large molecular structure library due to ease of modification that offers the applications in material science, medicine, analytical chemistry, nanotechnology, biology, environment science, separation techniques, etc. [1–12]. Among the various kinds of calixarenes, the hetero-calixarene, calix[4]pyrrole (C4P) comprises of four pyrrolic units linked with—CH_2—bridges that can be modified and functionalized at various positions, i.e. β, meso and *N*-positions. C4P is non-aromatic, hydrogen bond donor, and multifaceted candidate that holds array of applications in sensing, ion-recognition, separation, etc. [13].

On this side, the precise studies of nanotechnology are decades old and is the advanced field [14]. Metal nanoparticles (MNPs) are the front line workforce that drives the nanotechnology on the path of scientific discoveries with fundamental solutions in the domains of biomedical [15, 16], therapeutic [17], environment [18], medicines [19], sensors [20], catalysts [21], food [22], military [23], and many more. The size from 1 to 100 nm [24], physico-chemical [25] and opto-electronic [26] properties of MNPs are different that lacks in macro scale of the same materials [27]. Especially, the noble metal nanoparticles (NMNPs) manifest the unique surface plasmon resonance property (SPR), i.e. collective oscillations of surface electrons when light of particular wavelength absorbed by MNPs in the visible region of electromagnetic spectrum [28]. Owing to ease of availability of starting materials and uncomplicated laboratory procedure, the chemical reduction is used extensively among the distinct approaches of the synthesis of MNPs available in literature [29, 30].

N. Pomal · N. Patel · J. Parikh · K. D. Bhatt (✉)
Department of Chemistry, Ganpat University, Kherva, Mehsana, Gujarat 384012, India
e-mail: drkdbhatt@outlook.com; kdb01@ganpatuniversity.ac.in

The field of nanotechnology is more attractive when calix entities came into play the role of reducing agent as well as stabilizing agent for preparing the metal nanoparticles. It is captivating that the molecular architecture of C4Ps anchored with metal surfaces in such way that it provides greater stability to MNPs by preventing them from aggregation, compared to bared MNPs. Though the chemistry behind the interactions of MNPs and C4Ps is practically imprecise but it may be non-covalent forces or binding sites on the C4Ps that stabilizes the MNPs [31, 32]. The MNPs properties can be tuned according to its applicability [33]. For this purpose, the reducing agents and stabilizing agents do have significant roles. In many cases, two different compounds are used, i.e. reductant is different and stabilizer is different [34], as a consequence, the surface properties of MNPs influenced, contrary to this, the C4Ps act as reductant and stabilizer for producing NPs save time of extra synthetic step and non-toxic to environment that can be used in bio applications too [35].

The field of calixarene and calix[4]pyrrole is much explored, bunch of reviews are available in the literature, but the area that touches the review on combination of calix[4]pyrrole and metal nano-entities can contribute to literature with different outlook. This review includes the synthesis, characterization, and applications of calix[4]pyrrole encapsulated metal nanoparticles in the fields of catalysis, sensing, therapeutic, green chemistry, etc.

2 Synthesis, Characterization and Applications of Metal Nanoparticles Using Calix[4]pyrrole

2.1 Synthesis

The calix[4]pyrrole is the century old supramolecule, that was first synthesized by Baeyer in 1886 using acid catalysed condensation of pyrrole and acetone [36]. After that, it crossed many paths of modifications and functionalization [37]. The functionalized C4Ps are mixed with metal salt precursors and the redox reaction takes place in the synthesis of MNPs (see Fig. 1). Functional groups on C4Ps donates the electrons to the metal salt precursor and metals achieve the zero oxidation state that
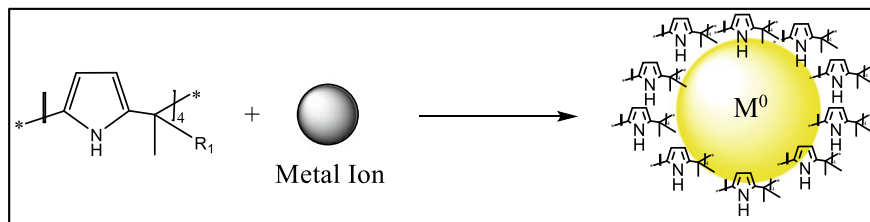

Fig. 1 Calix[4]pyrrole-capped metal nanoparticles

results into nano-size. The reducing capacity, stabilizing power, and web-like structure of parent C4Ps lead to the successful formation of monodispersed small-sized, and stable MNPs that are very well capped and passivate the NPs surface and keep away the NPs from agglomeration [35].

2.2 Characterization

Characterization is the backbone of any research in chemistry, because it ridges the synthesis work with what have been achieved. The surface properties of metal nanoparticles such as size, morphology, and surface charge can easily be determined by distinct spectroscopic techniques [38]. Thus, the C4Ps-MNPs prepared are characterized by various spectroscopic techniques in particular, UV–Visible, FT-IR, TEM, SEM, EDX, DLS, XRD, Zeta potential, etc.

Zetasizer instrument finds the zeta potential of MNPs that is electrical potential of capped MNPs that contribute to predict the MNPs stability [39]. UV–Visible spectroscopy is important tool of characterization of NPs on account of optical sensitivity to size, shape, agglomeration, concentration, and refractive index of surrounding medium of NPs [40]. FTIR bands used to determine the interaction between C4Ps and MNPs and existence of capping ligand on the surface of MNPs [41]. SEM and TEM ascertained the size, shape, and morphology of MNPs and aggregation behaviour of MNPs in the presence of ions to be sensed [42]. HRTEM and XRD data show the crystalline nature of MNPs. DLS defines the average hydrodynamic diameter and particle size distribution of MNPs, i.e. diameter of MNPs with capped layer positioned on MNPs surface. It often figure out the size distribution of MNPs [43, 44]. EDX analysis reveals the elemental composition of metal from MNPs [45] (Fig. 2).

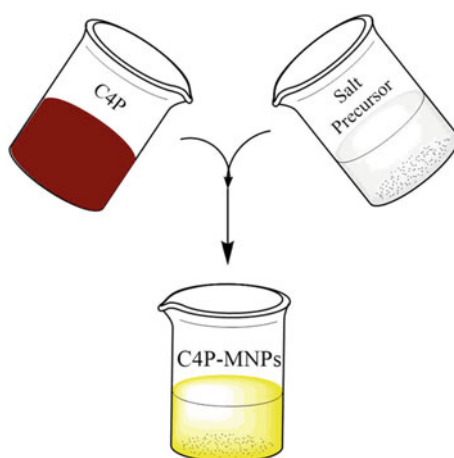**Fig. 2** Preparation of calix[4]pyrrole-based metal nanoparticles

Table 1 C4Ps-MNPs zeta potential and stability

| C4P-MNPs	Zeta potential	Stability of MNPs (in days)	Reference
CPOH-AgNPs	13 ± 2 meV	120	[48]
CPOH-AuNPs	15 ± 2 meV	150	[49]
MCPTH-AuNPs	-23.2 mV	90	[50]
CPTH-AuNPs	-29.0 mV	90	[51]
MCPTH-PdNPs	-26.2 mV	90	[52]

2.3 Applications

C4Ps-MNPs as Sensors

The environment pollution forces the scientific community to develop 'ready to use' instruments for the determination of analytes, especially sensing of the toxic metal ions. For the same several analytical techniques are available, but those are time-consuming, laborious, and incongruous for obtaining the rapid outcomes [46]. In the recent past, the alternative solutions have been discovered in the form of functionalized metal nanoparticles that are stable, selective, and sensitive for the ions [47], and a short overview of such probes is reviewed here.

The calix[4]pyrrole octahydrazide protected water dispersible silver nanoparticles (CPOH-AgNPs) are reported. Eight –NH–NH$_2$ groups in CPOH have reduced and stabilized the AgNPs found stable for 120 days at varied pH and NPs showed maximum stability and fluorescence intensity at pH 7.0. SPR band and fluorescence emission spectra were recorded at 428 nm and 580 nm, respectively. Colorimetric change from yellowish brown to colourless was noticed for Hg(II) ions among nine different cations. The minimum and maximum fluorescent enhancement were noted at 1 nmol/L and 1 μmol/L. Mechanism of sensing took place by internal charge transfer from Hg(II) to CPOH. Two real samples of water were detected with Hg(II) ions possessed values of 9.53 nmol/L and 4.41 nmol/L [48] (Table 1).

CPOH that was discussed above were also used for the preparation of spherical AuNPs with an average size of 8 ± 2 nm, with the use of HAuCl$_4$ as salt precursor and CPOH as reductant and stabilizer. The amine group was oxidized and Au^{3+} ions reduced to Au^0 state.

$$HAuCl_4 + NR_3 = Au^0 + NR_3^+ + H^+ + 4Cl^- \tag{1}$$
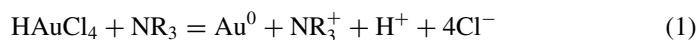
These AuNPs were stable for 150 days, at neutral pH. CPOH-AuNPs were selective and sensitive for the Co(II) ions with lower concentration limit of 1 nM using fluorescence quenching amid other cations [49].

The stable gold nanoparticles with multi-functionalities of colorimetric and electrochemical sensors and cytotoxic activity were investigated. The AuNPs were prepared using 'one-pot' synthesis by capping of calix[4]pyrrole tetra-hydrazide (MCPTH-AuNPs). The absence of Cl from HAuCl$_4$ and presence of Au, C, N,

and O were affirmed by XPS analysis. DLS was performed for size distribution, zeta potential was found to be -23.2 mV indicating the repulsion between NPs, which protect them from aggregation. The capping of C4P, i.e. MCPTH over the AuNPs were theoretically assessed by molecular dynamics study. It is suggested that hydrazide groups are attached via its N atoms led by induced-charge interaction between MCPTH and AuNPs. Colorimetric assay was observed in presence of other competing ions, selectively and sensitively for As(III) ions only, by colour change from pink to blue. The electrochemical sensing of As(III) ions was done with LOD of 1 ppb. In vitro cytotoxic study was undertaken, and MCPTH-AuNPs were found to be moderately anti-cancer against MCF-7 cancer cells with IC50 value of 25.69 µg/mL [50].

The novel C4P, i.e. CPTH-AgNPs reported with sensitive and selective sensing of Cu(II) ions having fluorescence quenching of about 75% in presence of other cations. The Cu(II) sensing was successfully performed in the real water samples and serum samples. The computational insight was acquired using Gaussian 09 (Revision C.01) software, and it is proposed from the study that conformation freedom of CPTH was restricted by AgNPs when CPTH grafted onto the AgNPs. Aggregation of AgNPs taken place when Cu(II) solution was added, this demonstrates the sensing of Cu(II) ions and supported by TEM and DLS data. CPTH-AgNPs inhibited the growth of gram negative bacteria and are cytotoxic against the HeLa cell line with 91.04% effect [32].

Environmentally toxic Pb(II) ions sensitively and selectively detected using the fluorescence quenching with minimum and maximum sensing limits of 10 nM and 1 µM by employing CPTH-AuNPs, the real water sample and human serum were analysed for analytical and biomedical applications and gave positive results. Antioxidant and anti-radical studies proved the potential medical applications of this combination. The computational approach was in favour of reducing nature of CPTH [51].

The thiol-functionalized calix[4]pyrrole gold nanoparticles using dodecanethiol-functionalized AuNPs were formed in CH_2Cl_2. TEM data revealed the spherical AuNPs with 3.90 ± 0.11 nm (see Fig. 3). SPR band was obtained at 518 nm of which intensity decreased about 7–12% on addition of fluoride ion (TBAF) salt. The other anions like CN^-, NO_3^-, AcO^-, HSO_4^-, H_2PO^{4-}, $HP_2O_7^{2-}$ have inconsequential change in the sensing event. Fluorescence dye displacement assay (FDDA) was conducted for the fluorescence sensing of F^- ions, and AuNPs are found 'turn-on' sensors [53].

C4Ps-MNPs as Catalyst

Catalysts have the significant persuade on the modern synthetic organic chemistry. The nano-catalysts are the essential instruments in the synthesis due to their large surface area to volume ratio. The size and surface properties of nano-catalysts play vital role provided the surface electrons on the edges and corners of atoms [54]. The superiority of nano-catalysts over the conventional catalysts is that these are stable, reactive, and selective in nature [55]. The core strength of supramolecule based nano-catalysts is resistant to leaching, sustain the organic transformation, and highly stable
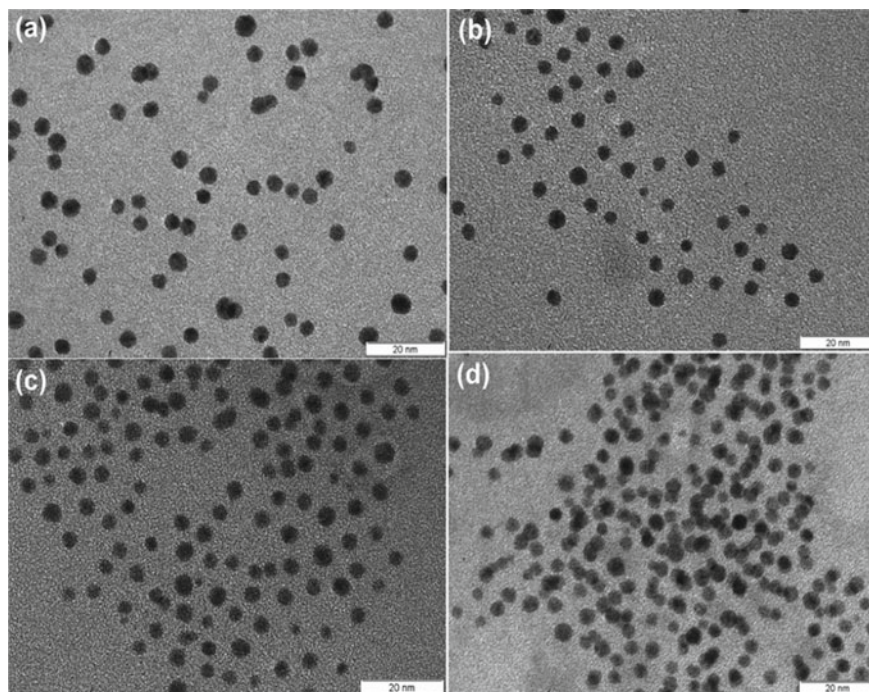
Fig. 3 TEM images (and average sizes) of **a** AuNPs (3.97 ± 0.33) nm, **b** AuNPs (3.90 ± 0.11) nm), **c** AuNPs after addition of TBAF (3.90 ± 0.10) nm, and **d** AuNPs after addition of the 4, 4′-biphenolate anion (as its TBA salt) (3.90 ± 0.10) nm. Scale bars are 20 nm. Reproduced from Reference [53], with permission from John Wiley and Sons, Copyright 2013

[56, 57]. C4Ps-based MNPs (PdNPs, PtNPs, and AuNPs) have been developed and successfully used in the recent years for the catalysis which are outlined below.

Octahydrazide derivative of calix[4]pyrrole (OHCP) has successfully reduced palladium acetate and stabilized the PdNPs. These PdNPs were used as nano-catalyst in various cross-coupling reactions; such as Suzuki–Miyaura, Heck coupling reactions, Negishi reaction, Stille coupling, Sonogashira cross-coupling reaction, Fukuyama coupling reaction, Hiyama coupling reaction, and Kumada coupling reaction. The OHCP-PdNPs have successfully completed five cycled without need of any activation and produced excellent yield (above 90%) for Suzuki–Miyaura coupling, Heck reaction, still coupling within 9–35 min. PdNPs were stable for 150 days at pH 7.0 [58].

PdNPs reduced and capped by MCPTH that were used as a heterogeneous catalyst for the degradation of water soluble carcinogenic azo dyes, i.e. methylene blue (MB) and methyl orange (MO) in the presence of $NaBH_4$. UV–Visible absorption spectra aids the degradation process by disappearance of peaks of MB and MO within time of 15 and 12 min, respectively. The reduction mechanism was endorsed by the natural bond orbital study that electrons given by borohydride transfer to surface of PdNPs,

and then, dyes reduced to hydrazide or aniline subsidiaries that was supported by GC–MS data. The Pd nano-catalysts were found to be efficient and stable for six consecutive cycles made them unparalleled for environment remediation work [52].

The hazardous and mutagenic pollutant 4-nitophenol (4-NP) was effectively reduced by highly competent, affordable, heterogeneous catalyst calix[4]pyrrole tetra-hydrazide gold nanoparticles (ECPTH-AuNPs). The capping mechanism and structure were backed by computational studies. The reduction study was executed in the presence of $NaBH_4$ using 100 µL (optimum volume) of catalyst solution and reduction reaction completed in 9 min that was monitored by UV–Visible spectroscopy, which left the 4-aminophenol as reducing product at the end of the reaction. The rate constant of pseudo-first-order reaction was 8.02×10^{-3} s^{-1}. The catalyst was successfully reused for five catalytic cycle, which has showed the potential activity of ECPTH-AuNPs [59].

MCPTH-PtNPs prepared by one-pot synthesis, which were utilized as heterogeneous catalyst in the chemo-selective hydrogenation of nitroarenes to corresponding industrially important aromatic amines. Spherical PtNPs with size of 3 ± 2 nm were added as catalyst in different proportions, and the optimum amount was selected as 10 mg. Pt nano-catalysts have given good yield for different compounds containing various functional groups, showed potentiality as catalyst. PtNPs were reused for consecutive seven catalytic cycles. The capping behaviour of MCPTH on the surface of PtNPs was assessed by computational chemistry [60].

The CPTH-PdNPs were used as a catalyst in a Mizoroki–Heck C–C coupling reaction, and the PdNPs were spherical and 5–9 nm sized. The Mizoroki–Heck coupling reaction was carried in different physical conditions, solvents, bases, and various catalysts to compare the efficiency of CPTH-PdNPs, and finally, at optimum conditions, the better yield was obtained. PdNPs were recovered for five consecutive cycles. The CPTH-PdNPs were tested for antibacterial activity against *E. coli* and *B. subtilis* bacteria by implementing micro-broth dilution method, found positive results for *E. coli* [61].

The other type of application is in therapeutic in which the carbamodithioate-based calix[4]pyrrole (CPADTC) capped 8 nm sized silver nanoparticles (CPADTC-AgNPs) were prepared and found effective as antimicrobial as compared to chloramphenicol and bactericidal against *E. coli* and *S. aureus*. Antimicrobial susceptibility was assessed by disc diffusion or Kirby-Bauer method and antibacterial study was done by employing Muller Hinton Agar (MHA) plates. 100 mg/L solution of CPADTC-AgNPs was placed with bacteria for overnight in discs at 37 °C, and clear inhibition zone observed next day [62].

3 Conclusion

The combination of two emerging fields, i.e. supramolecular chemistry and nanotechnology as an integral is reviewed. Novel moieties and functionalized calix[4]pyrrole

were synthesized which were capable to reduce and stabilize the noble metal nanoparticles. The nanoparticles were prepared by one-pot synthesis using simple chemical reduction approach. These NPs were highly stable for 90–150 days. The prime advantage of these C4P-MNPs is that, there's no need for external stabilizing agent which promote the catalytic activity. On the other hand, calix[4]pyrrole is also ion-recognizers, but union with MNPs like gold and silver provides an extra power as the optical instruments in visible region with the help of SPR event. Due to such cogent characteristics, they exhibited genres applications as nano-sensors, nano-catalysts, antibacterial agents, and cytotoxicity. As an additional benefit, capping mechanism of metal nanoparticles was supported by computational studies which demonstrated the non-covalent interactions between calix part and NPs. The fundamental challenge of preparing water dispersible metal nanoparticles was fulfilled satisfactorily. After so much efforts, still there is the space in the field of chemistry that are yet to be filled by this duo and more unsolved questions can be addressed.

References

1. Amabilino DB (2017) Supramolecular materials. Chem Soc Rev 46(9):2404–2420
2. Fukuhara G (2020) Analytical supramolecular chemistry: colorimetric and fluorimetric chemosensors. J Photochem Photobiol C Photochem Rev 42:100340
3. Jin X (2019) Supramolecular nanoscale drug-delivery system with ordered structure. Natl Sci Rev 6(6):1128–1137
4. Pomal NC (2021) Functionalized silver nanoparticles as colorimetric and fluorimetric sensor for environmentally toxic mercury ions: an overview. J Fluorescence
5. Yui N (2002) Supramolecular design for biological applications. CRC Press
6. Modi K (2018) Dual in vitro and in silico analysis of thiacalix[4]arene dinaphthalene sulfonate for the sensing of 4-nitrotoluene and 2,3-dinitrotoluene. New J Chem 42(4):2682–2691
7. Makwana BA, Bhatt KD, Vyas DJ, Gupte HS, Jain VK Synthesis, characterisation, binding behaviour and antimicrobial activity of azocalix[4]resorcine dye derived from 8-aminoquinoline. Sch Acad J Pharm 3(06):463–470
8. Peng S (2020) Strapped calix[4]pyrroles: from syntheses to applications. Chem Soc Rev 49(3):865–907
9. Bhatt KD (2014) Solid phase extraction, preconcentration and sequential separation of U(VI), Th(IV), La(III) and Ce(III) by octamethoxy resorcin[4]arene based amberlite xad-4 chelating resin. World J Anal Chem 2(2):31–41
10. Mulugeta E (2017) Recognition, sensing, and trapping of bicarbonate anions with a dicationic meso-bis(benzimidazolium) calix[4]pyrrole. Chem 3(6):1008–1020
11. Patel N, Nandan P, Kumbhani J, Bhatt K, Modi K (2020) A sulfur contain calixarene as a rapid cationic and anionic sensor. Med Anal Chem Int J 04(2):1–8
12. Rather IA (2019) New dimensions in calix[4]pyrrole: the land of opportunity in supramolecular chemistry. RSC Adv 9(66):38309–38344
13. Bhatt DK (2019) Review on calix[4]pyrrole: a versatile receptor 6(1):1–12
14. Tang Z (2021) Insights from nanotechnology in COVID-19 treatment. Nano Today 36:101019
15. Makwana BA (2016) Novel fluorescent silver nanoparticles: sensitive and selective turn off sensor for cadmium ions. Appl Nanosci 6(4):555–566
16. Mishra DR (2015) Calix protected gold nanobeacon as turn-off fluorescent sensor for phenylalanine. J Incl Phenom Macrocycl Chem 82(3):425–436
17. Makwana BA (2015) Highly stable antibacterial silver nanoparticles as selective fluorescent sensor for Fe^{3+} ions. Spectrochim Acta Part A Mol Biomol Spectro 134:73–80

18. Mishra D, Kongor A, Panchal M, Modi K, Jain V (2018) Resorcin arene-embedded stable silver nanoparticles: a fluorescent nanoprobe for Pb(II) in water. Int J Res Appl Sci Eng Technol 6(1):1360–1370

19. Lee SH (2019) Silver nanoparticles: synthesis and application for nanomedicine 20(4):865

20. Makwana BA (2017) A comparative study: metal nanoparticles as fluorescent sensors for biomolecules and their biomedical application. Sens Actuators B Chem 246:686–695

21. Narkhede N (2019) Calixarene-assisted Pd nanoparticles in organic transformations: synthesis, characterization, and catalytic applications in water for C-C coupling and for the reduction of nitroaromatics and organic dyes. ACS Omega 4(3):4908–4917

22. Mohan CO (2019) Chitosan-capped gold nanoparticles for indicating temperature abuse in frozen stored products. npj Sci Food 3(1):2

23. Ramsden J (2012) Nanotechnology for military applications. Nanotechnol Perceptions 8:99–131

24. Mozaffari S (2019) The role of nanoparticle size and ligand coverage in size focusing of colloidal metal nanoparticles. Nanoscale Adv 1(10):4052–4066

25. Rodrigues TS (2019) Nanocatalysis by noble metal nanoparticles: controlled synthesis for the optimization and understanding of activities. J Mater Chem A 7(11):5857–5874

26. Kvítek O (2013) Noble metal nanostructures influence of structure and environment on their optical properties. J Nanomater 2013:743684

27. Mukherji S (2019) Synthesis and characterization of size- and shape-controlled silver nanoparticles. Phys Sci Rev 4(1)

28. Vyas DJ (2012) An efficient one pot synthesis of water-dispersible calix[4]arene polyhydrazide protected gold nanoparticles—a "turn off" fluorescent sensor for Hg[II] ions. J Nanosci Nanotechnol 12(5):3781–3787

29. Khan I (2019) Nanoparticles: properties, applications and toxicities. Arab J Chem 12(7):908–931

30. Dutta PP (2017) Antimalarial silver and gold nanoparticles: green synthesis, characterization and in vitro study. Biomed Pharmacother 91:567–580

31. Ha J-M (2009) Mercaptocalixarene-capped gold nanoparticles via postsynthetic modification and direct synthesis: effect of calixarene cavity-metal interactions. J Phys Chem C 113(4):1137–1142

32. Kongor A (2018) Selective fluorescence sensing of Cu(II) ions using calix[4]pyrrole fabricated Ag nanoparticles: a spectroscopic and computational approach. J Mol Liquids 269:467–475

33. Zhong R-Y (2014) Impacts of organic stabilizers on catalysis of Au nanoparticles from colloidal preparation. ACS Catal 4(11):3982–3993

34. Rodrigues TS (2018) Synthesis of colloidal metal nanocrystals: a comprehensive review on the reductants 24(64):16944–16963

35. Kongor AR (2016) Calix-based nanoparticles: a review. Top Curr Chem 374(3):28

36. Baeyer A (1886) Ueber ein Condensationsproduct von Pyrrol mit Aceton 19(2):2184–2185

37. Jain VK (2016) Emerging trends based on calix protected metal nanoparticles. TechConnect Briefs, pp 145–148

38. Shnoudeh AJ (2019) Biomaterials and bionanotechnology. Elsevier

39. Konwar R (2016) Nanoparticle: an overview of preparation, characterization and application. Int Res J Pharm 4(4):47–57

40. Kora AJ (2016) Biomimetic synthesis of selenium nanoparticles by Pseudomonas aeruginosa ATCC 27853: an approach for conversion of selenite. J Environ Manage 181:231–236

41. Mehta V (2015) The chemistry of nascent oxacalix[n]hetarene: a review. Curr Org Chem 19(12):1077–1096

42. Chekli L (2016) Analytical characterisation of nanoscale zero-valent iron: a methodological review. Anal Chim Acta 903:13–35

43. Fathima JB (2018) Synthesis of eco-friendly copper nanoparticles for augmentation of catalytic degradation of organic dyes. J Mol Liquids 260:1–8

44. Anandalakshmi K (2016) Characterization of silver nanoparticles by green synthesis method using Pedalium murex leaf extract and their antibacterial activity. Appl Nanosci 6(3):399–408

45. Agarwal H (2017) A review on green synthesis of zinc oxide nanoparticles—an eco-friendly approach. Resour-Efficient Technol 3(4):406–413
46. Maity D (2013) Calix[4]arene functionalized gold nanoparticles: application in colorimetric and electrochemical sensing of cobalt ion in organic and aqueous medium. Sens Actuators B Chem 191
47. Pandya A (2012) Rapid colorimetric detection of sulfide using calix[4]arene modified gold nanoparticles as a probe. Sens Actuators B Chem 168:54–61
48. Bhatt KD (2016) Turn-on fluorescence probe for selective detection of Hg(II) by calixpyr-role hydrazide reduced silver nanoparticle: application to real water sample. Chin Chem Lett 27(5):731–737
49. Bhatt KD (2014) Highly stable water dispersible calix[4]pyrrole octa-hydrazide protected gold nanoparticles as colorimetric and fluorometric chemosensors for selective signaling of Co(II) ions. Spectrochim Acta Part A Mol Biomol Spectro 121:94–100
50. Kongor A (2020) Colorimetric and electrochemical sensing of As(III) using calix[4]pyrrole capped gold nanoparticles and evaluation of its cytotoxic activity. J Incl Phenom Macrocycl Chem 98(1):29–41
51. Kongor A (2018) Synthesis and modeling of calix[4]pyrrole wrapped Au nanoprobe for specific detection of Pb(II): antioxidant and radical scavenging efficiencies. J Photochem Photobiol A Chem 364:801–810
52. Kongor A (2021) Calix[4]pyrrole stabilized PdNPs as an efficient heterogeneous catalyst for enhanced degradation of water-soluble carcinogenic azo dyes. Catal Lett 151(2):548–558
53. Sokkalingam P (2013) Decoration of gold nanoparticles by a double-armed calix[4]pyrrole: a receptor-decorated nanoensemble for anion sensing and extraction 19(19):5860–5867
54. Hemalatha K (2013) Function of nanocatalyst in chemistry of organic compounds revolution: an overview. J Nanomater 2013(341015)
55. Padnya P (2020) The role of calix[n]arenes and pillar[n]arenes in the design of silver nanoparticles: self-assembly and application 21(4):1425
56. Panchal U (2016) Catalytic activity of recyclable resorcinarene-protected antibacterial Pd nanoparticles in C-C coupling reactions. Chin J Catal 37(2):250–257
57. Huc V (2008) A new specifically designed calix [8] arene for the synthesis of functionalized, nanometric and subnanometric Pd Pt and Pu nanoparticles. 318(1):1–4
58. Bhatt KD, Desai A, Modi K, Kongor A (2020) Coupling reactions by highly efficient octa-calix[4] pyrrole wrapped scrupulous nano-palladium catalyst. Biointerface Res Appl Chem 11(1):7632–7645
59. Kongor A (2019) Facile construction of calix[4]pyrrole-templated gold nanoparticles: computational insights and application for efficient reduction of 4-nitrophenol. Gold Bull 52(3):125–133
60. Kongor A (2018) Heterogeneous hydrogenation using stable and reusable calix[4]pyrrole fenced Pt nanoparticles and its mechanistic insight. Appl Surf Sci 437:195–201
61. Kongor A (2017) Basketing nanopalladium into calix[4]pyrrole as an efficient catalyst for Mizoroki-Heck reaction. Arab J Chem 10(8):1125–1135
62. Vyas DJ, Vyas KH, Makwana BA (2015) Preparation and characterisation of dithiocarbamate based calix[4]pyrrole assemblies on Ag nanoparticles: potential antimicrobial agent. Int J Sci Technol Manage 04(01):130–142

Design Methodology of GaAs Nanowire-Based Solar Cells for Enhanced Efficiency

D. V. Prashant, Suneet Kumar Agnihotri, and D. P. Samajdar

1 Introduction

Vertically aligned nanowire (NW) arrays have been widely used and explored to increase the overall power conversion efficiency (PCE) of SCs. The cumulative effects of intrinsic absorption and effective confinement of the guided resonant modes can significantly enhance the light trapping in NW arrays. Additionally, when compared to planar SCs, they display less surface recombination and improved carrier collection [1]. However, when implemented in practice, the performance of NW array SCs remains significantly lower than expected, owing to their low carrier mobility and high surface recombination [2]. To counter this, innovative device designs, such as radial junction SCs using passivating carrier-selective contacts, are suggested [3]. In such structures, the incoming photons can be efficiently collected along the axial direction of the NWs, whereas the photogenerated carriers are accumulated along the radial direction. Additionally, such structures benefit from low optical losses, improved charge separation, and charge extraction capabilities [4]. In recent years, radial junction SCs using transitional metal oxides such as TiO_2, ZnO, MoO_3, and Ta_2O_5 have been implemented with PCE up to 20% [5, 6] which has been achieved. Despite these exceptional efforts, the practical implementation and decision on optimum geometric configuration of such systems is still a complicated task because the optoelectronic processes involved are highly interdependent and dispersive in nature [7]. In this regard, numerous research groups have performed elaborative theoretical analysis to investigate the fabrication feasibility of high-efficiency and low-cost NW array-based radial junction SCs [8–10].

Till date, very limited study on highly efficient GaAs NW array-based radial junction SCs has been conducted. GaAs is a very attractive semiconducting material with

D. V. Prashant · S. K. Agnihotri · D. P. Samajdar (✉)
Department of Electronics and Communication Engineering, PDPM Indian Institute of Information Technology, Design and Manufacturing, Jabalpur, India
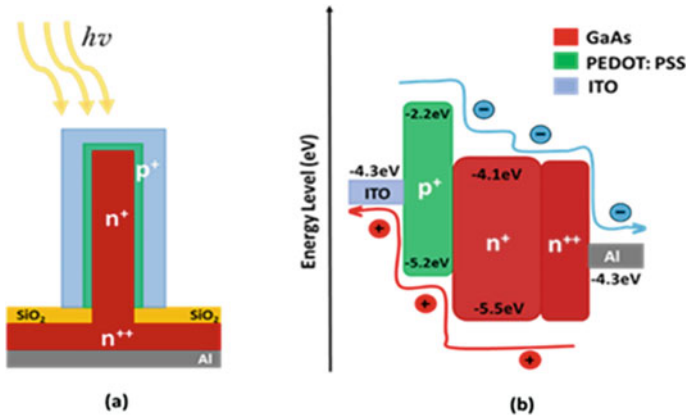e-mail: dip.samajdar@iiitdmj.ac.in

467

Fig. 1 Schematic representation of: **a** radial *p–n* junction NW SC and **b** band diagram of the proposed heterojunction SC with important material parameters

a direct bandgap of 1.43 eV to capture the maximum solar irradiation from AM1.5G spectrum [11]. Additionally, GaAs possess exceptional optical absorption and carrier transport properties, which suggest that it can be a promising active material for solar energy harvesting [12]. In this article, we presented a comprehensive optical and electrical study of ITO/PEDOT:PSS/GaAs NW-based radial junction SCs, as shown in Fig. 1a. Using Lumerical software, we performed both optical and electrical simulations for our proposed structure. Initially, with the help of Lumerical's FDTD module, we have performed the optical simulations for our proposed structure and obtained the optical absorption plots, optical generation rate ($G_{opt.}$) profiles, and normalized electric field (|*E*|) plots. Further, using in-built DEVICE module, we performed the electrical simulations and obtained the *J-V* and *P–V* curves for our proposed radial junction SC.

2 Design Principle and Simulation Methods

In Fig. 1b, the small offset between the valence band (VB) of GaAs and highest occupied molecular orbital (HOMO) of PEDOT:PSS promotes the flow of holes toward the ITO, resulting in improved carrier transport.

The band offset between the conduction band (CB) of GaAs and lowest unoccupied molecular orbital (LUMO) of PEDOT: PSS blocks the flow of electrons toward the front electrode and results in reduced recombination at PEDOT: PSS/ITO interface [13]. Further, Fig. 2a represents the 2-D (*x–y*) schematic of the simulated unit under FDTD analysis. Periodic boundary is set along the *x*-axis and *y*-axis, whereas perfectly matched layer (PML) condition is considered across the *z*-directions. The geometric parameters of the NW, i.e., diameter (D_{core}) and period (*p*) are set at 160 nm
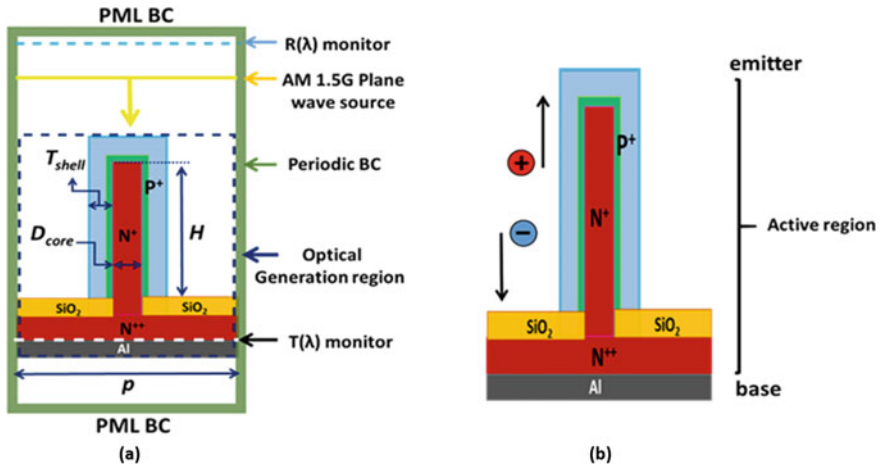
Fig. 2 Schematic representation of simulated unit cell in **a** FDTD analysis and **b** device analysis

and 450 nm, respectively referred from previously reported results for optimized GaAs NW arrays [8, 9]. The GaAs NW is coated with a 20 nm thick PEDOT:PSS layer and a 60 nm thick ITO layer. A 200 nm thick GaAs substrate is followed by 100 nm thick aluminum (Al) metal electrode below the GaAs NW. Further, an infinite plane wave with wavelength (λ) ranging from 300 to 1000 nm is incident perpendicularly upon the unit cell. To obtain the optical absorption ($A(\lambda)$) and total reflection ($R(\lambda)$) and transmission ($T(\lambda)$) losses, two power monitors are provided above and beneath the cell. The n and k data of the shell materials PEDOT: PSS and ITO are referred from [14].

Figure 2b represents the 2-D (x–y) schematic of the simulated unit under electrical analysis. The optical generation rate ($G_{opt.}$) computed from the FDTD simulations are incorporated in the Lumerical's built-in Charge solver module. Mobility (μ) and lifetime (τ) in the GaAs NWs are set at maximum lattice scattering limits of 1000 cm^{2}V^{-1} s^{-1} and 100 ps, respectively [15]. The core and shell doping concentrations are fixed at optimal values of 1×10^{18} cm^{-3}, whereas n-type doping concentration of 1×10^{19} cm^{-3} is provided at substrate. Further, to consider the effect of impurities and recombination losses on the PCE of the SC, the built-in Caughey-Thomas model and recombination models are incorporated.

3 Result and Discussions

3.1 Optical Analysis

In Fig. 3, we have compared the optical performance of the proposed core–shell radial junction SC and its uncoated counterpart. In Fig. 3a, it is evident that after the incorporation of PEDOT:PSS/ITO shell, the optical absorption of the GaAs NW significantly increases throughout the incident spectrum. In Fig. 3a, for $\lambda = 300$–1000 nm, the uncoated GaAs NW has exhibited an average absorption of 69%.

After the incorporation of PEDOT:PSS/ITO shell, the optical absorption has enhanced to 78%, due to the significantly reduced optical losses from the cell [16]. Moreover, the high refractive index and effective light trapping properties of PEDOT:PSS polymer at lower wavelength region, i.e., $\lambda = 300$–650 nm, results in enhanced light trapping in the proposed SC. Further, to validate this in Fig. 3b we have presented G_{opt} profiles of both the SCs at the same scale. In Fig. 3b, for both the cases, maximum photogeneration occurs at the top portion of the GaAs NW and very little amount of incident photons reaches the bottom. However, for ITO/PEDOT:PSS/GaAs NW structure, comparatively much intensive $G_{opt.}$ rate and very less spreading of the photogeneration can be observed, which suggests much better light trapping in the proposed structure. In the proposed core–shell structure, photogeneration rate of 8×10^{22} cm^{-3} s^{-1} is considerably higher than its uncoated counterpart, i.e., 4.24×10^{22} cm^{-3} s^{-1}.

To better understand the enhanced optical absorption in the proposed core–shell SC, in Fig. 4 the |E| plots of both the SCs at four different wavelength regions are presented. At $\lambda = 300$ nm, the E-field is only confined around the NW with small fraction of residual field reaching to the lower substrate, and this agrees well with Fig. 3a. Further, at $\lambda = 500$ nm, for uncoated GaAs NW the E-field is distributed throughout its length suggesting significant amount of incident light transmitting
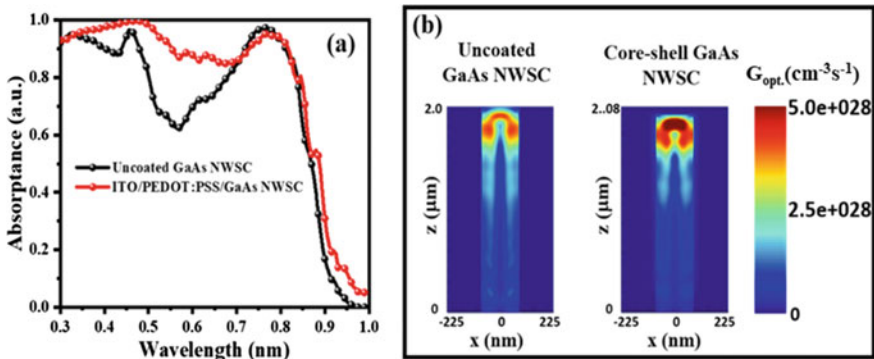

Fig. 3 Comparative optical properties of uncoated GaAs NW and ITO/PEDOT:PSS/GaAs NW structures: **a** optical absorption spectra, **b** optical generation rate ($G_{opt.}$) profiles
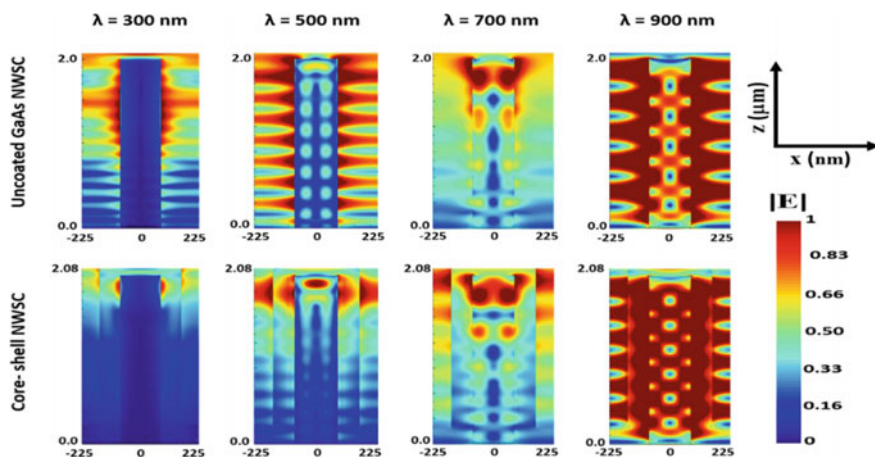
Fig. 4 Normalized electric field (|E|) plots of uncoated and core–shell NWSC at different values of wavelengths

Table 1 Important optical parameters obtained from the FDTD simulations

Structure	Optical absorption (%)	$G_{\text{opt.}}$ (cm^{-3} s^{-1})	J_{sc} (mA/cm^2)
Uncoated GaAs NW	69	4.2×10^{22}	26.5
Core–shell SC	78	8.01×10^{22}	30.1

to air. However, for core–shell structure, the E-field is confined at the top of NW and very less E-field spreading along the length of the NW is observed suggesting comparatively less residual field and optical losses from the structure. This is in well agreement with the absorption plot. At $\lambda = 700$ nm and onwards, both the NW structures exhibit same E-field distribution due the same absorption at this wavelength. Further, at $\lambda = 900$ nm, for both the cases the E-field is distributed along the NW length and almost identical |E| behavior and optical absorption is observed for both the cases.

In Table 1, the optical parameters of both the structures obtained from the FDTD analysis. The proposed core–shell SC has achieved an ideal J_{sc} of 30.1 mA/cm^2 and is almost 4 mA/cm^2 higher than bare GaAs NW. The increase in J_{sc} is attributed to enhanced optical absorption and comparatively high photogeneration in the proposed core–shell SC.

3.2 Electrical Analysis

J-V and P–V plots of the proposed PEDOT:PSS/GaAs NW radial junction SC and its axial junction counterpart are presented in Fig. 5a, b. The p and n core doping
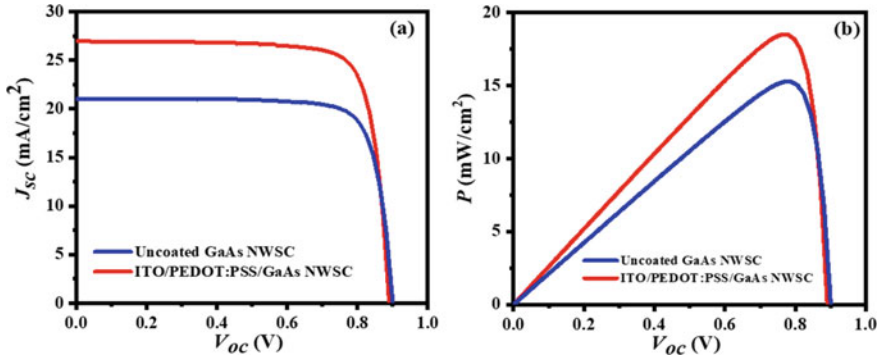
Fig. 5 Current–voltage (*J-V*) characteristics of the GaAs SCs with radial and axial junctions and **b** power–voltage (*P–V*) characteristics of both the SCs

concentrations in both the cases are fixed at 1×10^{18} cm^{-3}. From Fig. 5a, the proposed SC has exhibited much better J_{sc} and comparable V_{oc} when compared to the axial junction SC, which is attributed to increased junction area and reduce diffusion length in the radial junction structure. Additionally, the comparatively increased light harvesting and photogeneration in the proposed SC also results in its enhanced performance. The GaAs NW radial junction SC has achieved a PCE of ~18.5%, which is ~3% higher than its uncoated or axial junction counterpart. The proposed SC has achieved and remarkable J_{sc} and V_{oc} of ~27 mA/cm^2 and 0.88 V, despite very low μ of 100 ps and, while maintaining a surface recombination velocity (SRV) of 10^7 cm/s at the ITO/PEDOT:PSS and GaAs/Al interface.

Finally, in Table 2, the *PV* parameters of our proposed ITO/PEDOT: PSS/GaAs NW/Al SC and compared our obtained results with previously reported results for radial junction SCs. According to Table 2, our proposed SC can achieve much better J_{sc} and PCE compared to the listed results, thanks to the combined advantageous properties of organic PEDOT:PSS and GaAs which results in exceptional optoelectronic properties in the purposed SC.

Table 2 Photovoltaic parameters of our proposed PEDOT:PSS/GaAs NW radial junction SC with some previously reported works

Structure	V_{oc} (V)	J_{sc} (mA/cm^2)	FF (%)	PCE (%)
Si NW core–shell SC [2]	0.92	18.45	74.6	11.6
GaAs NW *p-i-n* SC [3]	0.77	24.6	72.4	13.8
GaAs NW heterojunction SC [4]	0.65	20.2	70	9.2
InP NW radial junction SC [5]	0.73	29.5	74.6	16.2
GaAs NW axial junction SC **(this work)**	**0.90**	**21.05**	**80**	**15.15**
GaAs NW radial junction SC **(this work)**	**0.89**	**26.96**	**78**	**18.5**

4 Conclusions

We provided a detailed optoelectronic research for a radial junction SC based on PEDOT:PSS/GaAs NW. The proposed SC has demonstrated the ability to attain superior efficiency while consuming less materials. Furthermore, when compared to its uncoated/axial junction equivalent, the designed SC has generated significantly improved optical absorption and PCE. The PCE of the GaAs NW radial junction SC was ~18.5%, with outstanding optical absorption and $G_{opt.}$ of 78% and ~8 × 10^{22} cm^{-3} s^{-1} respectively. We expect that the results presented here will assist in the experimental realization of low-cost, high-efficiency radial junction SCs.

References

1. Zhang J, Ai L, Yan X, Wu Y, Wei W, Zhang M, Zhang X (2018) Photovoltaic performance of pin junction nanocone array solar cells with enhanced effective optical absorption. Nanoscale Res Lett 13. https://doi.org/10.1186/s11671-018-2727-7
2. Roy D, Prakash D, Biswas A (2021) Photovoltaic performance improvement of GaAs 1−x Bi x nanowire solar cells in terms of light trapping capability and efficiency. Sol Energy 221:468–475. https://doi.org/10.1016/j.solener.2021.04.064
3. Misra S, Yu L, Foldyna M, Roca P (2013) Solar energy materials & solar cells high efficiency and stable hydrogenated amorphous silicon radial junction solar cells built on VLS-grown silicon nanowires. Sol Energy Mater Sol Cells 118:90–95. https://doi.org/10.1016/j.solmat.2013.07.036
4. Yang Z, Zhang T, Li J, Xue W, Han C, Cheng Y, Qian L (2017) Multiple electron transporting layers and their excellent properties based on organic solar cell. Sci Rep 7:1–9. https://doi.org/10.1038/s41598-017-08613-7
5. Raj V, Rougieux F, Fu L, Tan HH, Jagadish C (2020) Design of ultrathin InP solar cell using carrier selective contacts. IEEE J Photovoltaics 1–10. https://doi.org/10.1109/jphotov.2019.2961615
6. Agnihotri SK, Samajdar DP, Prashant DV (2021) Role of hole-selective contact in efficiency improvement of ITO-free InP/MoO$_3$/PEDOT:PSS nanowire solar cells. IEEE Trans Electron Devices 68:5666–5673. https://doi.org/10.1109/ted.2021.3115079
7. Prashant DV, Samajdar DP, Sachchidanand (2020) Optical simulation of III-V semiconductor nanowires/PEDOT:PSS-based hybrid solar cells: influence of polymer coating thickness and geometrical parameters on light harvesting and overall photocurrent. In: Sikander A, Acharjee D, Chanda CK, Mondal PK, Verma P (eds) Energy systems, drives and automations. Springer Singapore, Singapore, pp 361–368
8. Wu D, Tang X, Wang K, Li X (2017) An analytic approach for optimal geometrical design of GaAs nanowires for maximal light harvesting in photovoltaic cells. Sci Rep 7:1–8. https://doi.org/10.1038/srep46504
9. Wen L, Zhao Z, Li X, Shen Y, Guo H, Wang Y (2011) Theoretical analysis and modeling of light trapping in high efficiency GaAs nanowire array solar cells. Appl Phys Lett 99:2009–2012. https://doi.org/10.1063/1.3647847

10. Kumar Agnihotri S, Prashant DV, Samajdar DP, Arefinia Z (2021) Performance analysis of ITO-free PEDOT:PSS/InP nanowire hybrid solar cell. Sol Energy 228:418–426. https://doi.org/10.1016/j.solener.2021.09.078

11. Mariani G, Laghumavarapu RB, de Villers B, Shapiro J, Senanayake P, Lin A, Schwartz BJ, Huffaker DL (2010) Hybrid conjugated polymer solar cells using patterned GaAs nanopillars. Appl Phys Lett 97:13107. https://doi.org/10.1063/1.3459961

12. Prashant DV, Samajdar DP, Arefinia Z (2021) FDTD-based optimization of geometrical parameters and material properties for GaAs-truncated nanopyramid solar cells. IEEE Trans Electron Devices 68:1135–1141. https://doi.org/10.1109/TED.2021.3055190

13. Chao JJ, Shiu SC, Lin CF (2012) GaAs nanowire/poly(3,4-ethylenedioxythiophene):poly(styrenesulfonate) hybrid solar cells with incorporating electron blocking poly(3-hexylthiophene) layer. Sol Energy Mater Sol Cells 105:40–45. https://doi.org/10.1016/j.solmat.2012.05.021

14. Prashant DV, Agnihotri SK, Samajdar DP (2021) Geometric optimization and performance enhancement of PEDOT: PSS/GaAs NP array based heterojunction solar cells. Opt Mater (Amst) 117. https://doi.org/10.1016/j.optmat.2021.111080

15. Joyce HJ, Docherty CJ, Gao Q, Tan HH, Jagadish C, Lloyd-Hughes J, Herz LM (2013) Electronic properties of GaAs, InAs and InP nanowires studied by terahertz spectroscopy. 214006. https://doi.org/10.1088/0957-4484/24/21/214006

16. Prashant DV, Samajdar DP, Sharma D (2019) Optical simulation and geometrical optimization of P3HT/GaAs nanowire hybrid solar cells for maximal photocurrent generation via enhanced light absorption. Sol Energy 194:848–855. https://doi.org/10.1016/j.solener.2019.11.027

Investigation of Optoelectronic Performance of InAsNBi for Infrared Detection

Neelesh Jain, Indranil Mal, D. P. Samajdar, and Navjeet Bagga

1 Introduction

Considering the ongoing research studies of III–V–N–Bi [1–4] quaternary alloys, we have explored the InAsNBi alloy, which could be suitable for infrared (IR) detection applications [5]. Earlier investigated materials used for IR detection applications such as HgCdTe, PbSeTe, and InAsSb are obsolete because of their fabrication difficulties and lattice constant matching issues with the host [6, 7]. To overcome these difficulties, the researchers are trying to find other possible materials suitable for IR applications. After a rigorous literature survey, we found that III–V–N–Bi alloys are suitable candidates for IR detection as the previously explored III–V–N–Bi materials such as InSbNBi [3], GaAsNBi [8, 9], and GaSbNBi [10] are capable of band gap variation, strain induced changes, and possess suitable optoelectronic device characteristics, which are desirable for a material for use in an IR detector.

   Among the commonly known III–V semiconductors, InAs, InN, and InSb have generated significant interest due to their potential benefits for inherent optical and high-temperature device applications [11]. Out of these binary III–V semiconductors, InAs has a narrow direct band gap, higher mobility, and a band gap of 0.35 eV [12], corresponding to an operational wavelength of 3.54 µm which falls in the IR range, and can be used for fabricating IR detectors operational in the wavelength range of 1–3.8 µm [13]. In addition to this, InAs is quite useful in high-speed electronics [11], optical spectroscopy, and optoelectronic applications [14]. The incorporation of dilute N impurities in host (InAs) can help to obtain large band gap reduction, as demonstrated by the band anti-crossing (BAC) model, which clearly explains the role of localised N states in band gap reduction due to interactions with extended states of the conduction band (CB). InAsN is a promising candidate for mid-infrared

N. Jain · I. Mal · D. P. Samajdar (✉) · N. Bagga
Department of Electronics and Communication Engineering, PDPM IIITDM, Jabalpur, MP 482005, India
e-mail: dip.samajdar@iiitdmj.ac.in

optoelectronic devices working in the range of 2–5 μm and high efficiency hybrid solar cell applications [15]. Other identified III–V–N ternary materials, such as InPN, GaAsN, and GaSbN have shown a decrease in band gap, a significant increase in effective mass of electron, and a notable suppression of Auger recombination [14]. On the contrary, incorporation of Bi in InAs causes the localised 6p energy states of Bi to interact with the extended states of the valence band (VB), thereby leading to band gap reduction somewhat lower than that caused due to N incorporation [16]. Bi containing ternary and quaternary alloys such as GaAsBi, InAsBi, GaInAsBi, and GaNAsBi, improves the thermal stability of optoelectronic devices as it helps in achieving a temperature-insensitive band gap [17]. Previously reported articles of InAsBi estimated that incorporation of a small fraction of Bi causes a band gap reduction of up to 55 meV/% Bi, which paved the pathway for designing photodetectors for mid and far wavelength regions [16]. To sum up, the co-incorporation of N and Bi into InAs can lead to multiple advantages without violating the lattice matched condition. N and Bi impurity in host material creates substitutional defects which replaces as element by substitution of impurity, and this type of doping is termed as isoelectronic doping [18] because these As, N, and Bi elements are isoelectronic in nature.

In this article, we have theoretically investigated the InAsNBi alloy for IR detection. The descriptive flow of this article is as follows:

1. In the mathematical model section, we briefly discussed the 16-band Hamiltonian for computation of electronic properties being investigated. Secondly, we have defined the optical gain equation, which could be useful to find out the optical characteristics of InAsNBi/InAs QW heterostructure.
2. Results and discussions section describes the electronic and optical properties of the InAsNBi/InAs alloy such as electronic band structure, band dispersion in three different crystallographic direction, and optical gain of InAsNBi/InAs QW structure with various injected carries concentration and different impurity concentration.

2 Mathematical Framework

The electronic band structure of $InAs_{0.92}N_{0.029}Bi_{0.05}$ is evaluated using a 16-band Hamiltonian based on k dot p method, that is similar to other previously investigated III–V–N–Bi alloys such as InSbNBi [3], GaAsNBi [9], and GaSbNBi [10], which is described as follows:

$$H_{16\times16} = \begin{bmatrix} H_{8\times8} & V_{N,Bi(8\times8)}(y,x) \\ V_{N,Bi(8\times8)}(y,x) & H_{N,Bi(8\times8)} \end{bmatrix} \tag{1}$$

Incorporation of N and Bi into InAs creates the additional energy states of N and Bi, which modify the system Hamiltonian of InAs, and this modified 16-band Hamiltonian is described in Eq. (1). In this matrix, $H_{8\times8}$ element represents the system

Hamiltonian corresponding to subbands of InAs, $V_{N,Bi(8 \times 8)}(y, x)$ matrix represents the interaction of N and Bi with InAs, and $H_{N,Bi(8 \times 8)}$ matrix describes the energy level of N and Bi as E_N, E_{Bi}, and E_{Bi-so}. The diagonal elements of this matrix correspond to the conduction band (CB), heavy hole (HH), light hole (LH), and spin–orbit splitting energy (SO) levels of the InAsNBi alloy at Brillouin Zone center where $\Gamma = 0$. The off-diagonal elements of this matrix contribute to band dispersion for $\Gamma \neq 0$ and the band gap of the material is evaluated at $\Gamma = 0$. Readers are recommended to read [19, 20] for more details on process of generation of 16-band Hamiltonian. Using the formulated 16-band k.p Hamiltonian, we have derived the band gap reduction ($E_g^{InAs}(x, y)$) equation for the $InAs_{1-x-y}N_xBi_y$ as a function of N and Bi concentrations described as follows (Table 1):

$$E_g^{InAsNBi}(x, y) = \left[\frac{1}{2} \left[E_{CB}^{InAs} + \Delta E_{CB}(x, y) + E_N - \sqrt{\left(E_{CB}^{InAs} - E_N\right)^2 + 4C_N^2 x} \right] \right.$$
$$\left. - \frac{1}{2} \left[E_{VB}^{InAs} + \Delta E_{VB}(x, y) + E_{Bi} - \sqrt{\left(E_{VB}^{InAs} - E_{Bi}\right)^2 + 4C_{Bi}^2 y} \right] \right]$$
(2)

In Eq. (2), E_{CB}^{InAs} and E_{VB}^{InAs} are the conduction and valence band extremes, $\Delta E_{CB}(x, y)$ and $\Delta E_{VB}(x, y)$ are band offsets between the constituent ternary elements InAsN and InAsBi as a function of impurity (N and Bi) concentrations (x, y), $E_{N/Bi}$ are the impurity energy levels corresponding to N/Bi, and $C_{N/Bi}$ are the coupling coefficients of N/Bi.

After calculating the band gap, effective mass, and band offsets, we have evaluated the optical gain of the $InAs_{1-x-y}N_xBi_y$/InAs quantum well (QW) system according to the equation given below [19, 23]:

Table 1 Important parameters used in mathematical modelling

InAs (host) parameters used for mathematical formulation	Value
Band gap, E_g (Γ) at 300 K	0.35 eV[a]
Effective mass, m_e^* (Γ)	0.026[a]
Lattice constant	6.0583 A[0a]
Spin–orbit split off energy, Δ_{SO}	0.39 eV[a]
Luttinger parameter, $\gamma_1, \gamma_2, \gamma_3$	20.0, 8.5, 9.2[a]
Energy level of N, E_N	1.48 eV[b]
Energy level of Bi, E_{Bi}	−0.4 eV[c]
Spin–orbit energy of Bi, E_{Bi-SO}	−1.9 eV[c]
Coupling parameter, C_N	1.68 eV[b]
Coupling parameter, C_{Bi}	1.00 eV[c]
Concentration of Bi, y	0.05 (5%)
Concentration of N, x	0.029 (2.9%)

[a]Reference [12], [b]Reference [21], [c]Reference [22]

$$G(\hbar\omega) = \frac{\pi q^2}{n_r c \varepsilon_0 m_0^2 \omega L_w} \sum_{n,m} \int_0^\infty \frac{k_p dk_p}{2\pi} \left| M_{nm}(k_p) \right|^2 L\left(E_{n,m}^{c,v}(k_p)\right) \left\{ f_n^c\left(E_n^c(k_p)\right) \right.$$
$$\left. - f_v^m\left(E_m^v(k_p)\right) \right\} \tag{3}$$

The symbols used in Eq. (3) are discussed here:

$\hbar$	reduced plank constant $= h/2\pi$, $h = 6.634 \times 10^{-34}$ J-sec,
n_r	refractive index of host (InAs) material,
c	speed of light; 3×10^8 ms^{-1},
m_0	rest mass of electron,
L_W	length of quantum well,
k_p	plane wave vector,
$\left\| M_{nm}(k_p) \right\|^2$	momentum matrix,
$L\left(E_{n,m}^{c,v}(k_p)\right)$	Lorentzian function,
c, v	represents the conduction and valence band,
n, m	are the subband energy levels number corresponds to conduction and valence band,
E_n^c and E_m^v	are the subband energies of corresponding subband of conduction and valence band,
f_n^c and f_v^m	are the Fermi-Dirac distribution representing corresponding subband of CB and VB.

Readers are referred to [19, 24] for more understanding of symbols used in Eq. (3).

3 Results and Discussions

Incorporation of impurities (N, Bi) into host InAs creates substitutional defects states near CB and VB edges and leads to the creation of energy levels E_N, E_{Bi}, and E_{Bi-so} near the CB and VB, respectively, which causes the perturbation in band structure. The mole fraction ratio of N and Bi for lattice matching with InAs is found to be 0.5821. In this section, we will discuss the electronic and optical properties of the InAs$_{1-x-y}$N$_x$Bi$_y$/InAs alloy and the QW heterostructure.

3.1 Electronic Properties

In this section, we have briefly discussed the electronic properties of the InAsNBi alloy, including band structure, effective mass, band offset variation with impurity concentration, and modification in spin–orbit splitting energy. We have shown the variation of subbands CB, HH, LH, and SO as a function of impurity concentration, which is calculated by Eq. (2) and depicted in Fig. 1. The interaction of impurities (N,

Fig. 1 Subband energy variation as a function of the concentration of impurities (N, Bi) under lattice matched conditions at 300 K
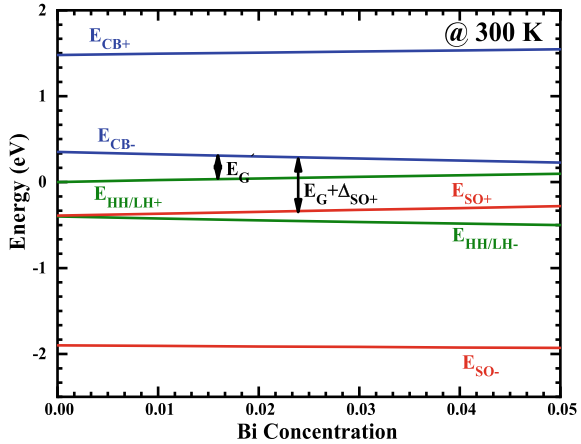
Bi) with host InAs splits the CB and VB edges into upper (+) and lower (−) subbands as shown in the figure. Referring to Fig. 1, as impurity concentration increases, the lower conduction subband (CB−) moves downwards and the upper valence subband (HH+) moves in the upward direction, which signifies band gap (E_G) reduction with variation in impurity concentration. Conversely, SO increases due to the increase in the concentration of impurities. These observations were carried out at $\Gamma = 0$ and 300 K temperatures.

To study the overall electronic properties of the InAsNBi alloy, we have investigated the band structure of InAsNBi, which is depicted in Fig. 2, where the solid lines correspond to InAsNBi and are slightly deviated from the dashed lines of InAs to signify the reduction in band gap. It is clear from the figure that the incorporation of impurities lowers the CB minima (CBM) to 227 meV and lifts the VB maxima (VBM) to ~95 meV, thereby reducing the band gap to ~131 meV. Figure 2 depicts

Fig. 2 Electronic band structure of $InAs_{0.92}N_{0.029}Bi_{0.05}$ alloy in highly symmetric crystallographic directions [100] and [111]
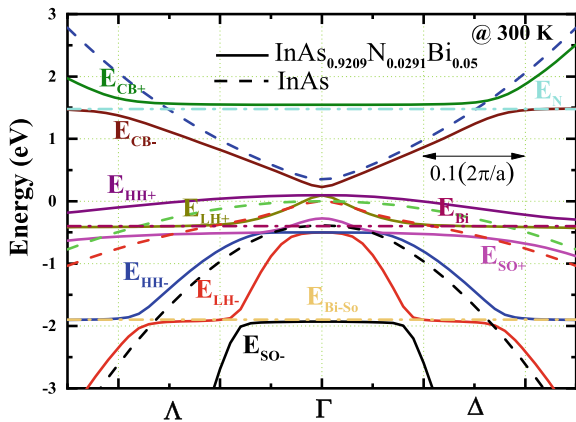
that the energy level of N, E_N enters into CB and the energy levels of Bi, E_{Bi}, spin–orbit energy level of Bi, E_{Bi-SO} enter into VB, which signifies that the interaction of N with the host moderates CB and the interaction of Bi with the host affects VB, respectively. The position of E_{SO+} moves upward compared to host InAs. Therefore, a 14 meV enhancement is reported in the SO of InAsNBi.

The band dispersion relation for InAsNBi/InAs alloy in three highly symmetric crystallographic directions Δ, Σ, and Λ which we have determined using the 16-band Hamiltonian defined in Eq. (1), is shown in Fig. 3, and with the use of these dispersion curves, we have calculated the effective mass of the CB electrons and VB holes. Figure 3 clearly shows that the E_{SO-} and E_{CB-} subbands change moderately between $k = 0$ and $k = 0.08$. The E_{CB-} subband becomes anisotropic after $k = 0.08$. On the other hand, E_{SO+} and E_{HH+} subbands show variation in all direction Δ, Σ, and, Λ for even lower values of k. However, the lower band edge of spin–orbit (E_{SO-}) shows a slight variation with k (Table 2).

Fig. 3 Band dispersion relationship for different InAsNBi/InAs QW energy levels as a function of k in the highly symmetric directions Δ [100], Σ [110] and Λ [111]
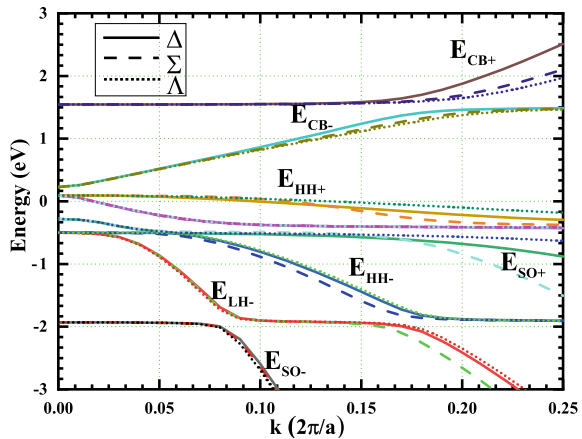
Table 2 Comparison of band gap reduction of InAsNBi with other III–V–N–Bi alloys for different N and Bi %

III–V–N–Bi alloys	Bi concentration (%)	N concentration (%)	Band gap reduction (meV)
InPNBi	4[a], 3[b]	3.7[a], 1[b]	563[a], 33[b]
GaAsNBi	4.3[c], 4[d]	2[c], 3[d]	820[c], 630[d]
InSbNBi	2[e], 2[f]	2[e], 0.28[f]	120[e], 102[f]
InAsNBi	5[g]	2.9[g]	219[g]

[a]Reference [1], [b]Reference [2], [c]Reference [8], [d]Reference [9], [e]Reference [25], [f]Reference [3], [g]Thiswork

Fig. 4 Plot of Optical
gain with photon energy for
different injected carrier
concentrations
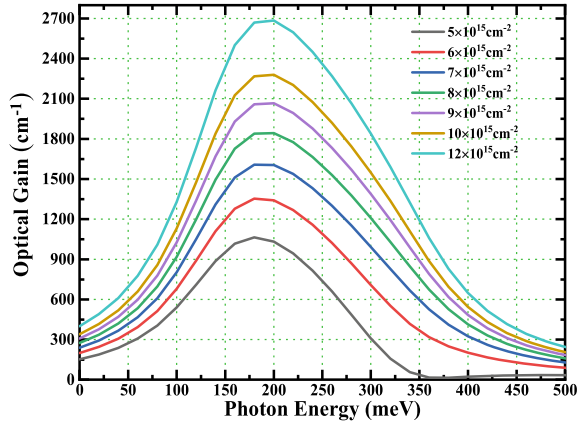
3.2 Optical Properties

We have investigated the $InAs_{0.92}N_{0.029}Bi_{0.05}$/InAs QW heterostructure to determine
its optical characteristics. To investigate these aspects, we have calculated optical
gain as a function of photon energy for various injected carrier concentrations in the
range $5 \times 10^{15} - 12 \times 10^{15}$ cm^{-2}, which is depicted in Fig. 4. For the calculation of
optical gain with reference to inter-subband transitions, subband energy levels, band
offsets, and effective masses are the influencing parameters. Note that, as injected
carrier concentration increases, the operating wavelength region of the QW system
increases and the peak of optical gain changes. The maximum gain for different
carrier concentrations under investigation is attained at a specific energy window of
150–250 meV and at ~200 meV, the maximum value of gain is found to be 2750 cm^{-1}
corresponding to a carrier concentration 12×10^{15} cm^{-2}.

For the working of InAsNBi/InAs alloy as an optoelectronic device, we have
to tune subband energy because subbands are essential parameters that control the
optical characteristics for quantum confined structures like QW. Variations in the
peak position of gain and resultant band gap of QWs are the result of changes in the
confined length of QWs, which change the sub bands E_n^c and E_m^v. In continuation of
exploring the optical aspects of InAsNBi/InAs QW heterostructure, we have plotted
optical gain with photon energy with variable concentrations of Bi in Fig. 5. It is
evident from the figure that on increasing Bi concentration, there is a substantial red
shift in gain spectra and the peak gain decreases except for less than 2% Bi concen-
tration for an injected carrier concentration of 1×10^{17} cm^{-2} and QW thickness
of 50 nm. Higher concentration of Bi decreases band gap, thereby increasing band
offset, which leads to better carrier confinement and increases the possibility of inter
or intra-band transitions. Incorporation of a higher concentration of Bi reduces effec-
tive mass, which decreases the count of confined energy levels inside the QW system.
Reduction of effective mass affects the optical gain peak and accomplishes a drop in
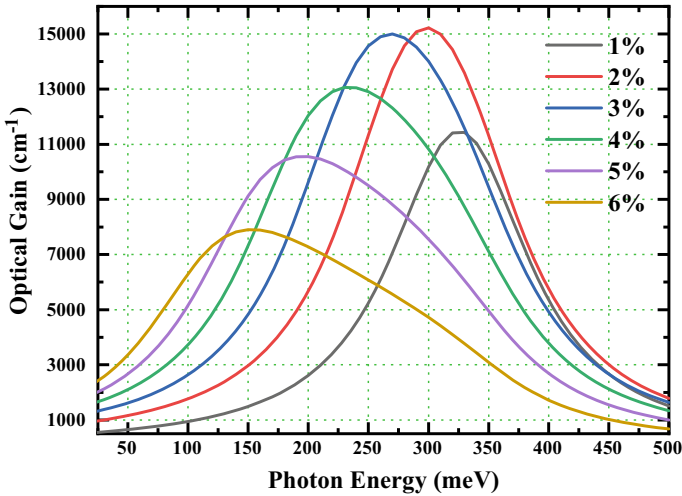peak with increasing Bi concentration. A maximum gain of 15,222 cm^{-1} is achieved

Fig. 5 Plot of the variation in Optical gain with photon energy for different Bi concentrations

with the incorporation of 2% Bi concentration, with an operating wavelength corresponding to 4.13 μm. The operating wavelength range for this material can lie in the range of 3.8–8.3 μm for variable Bi concentration (1–6%).

We have investigated this alloy with a lattice matching ratio of 0.5821 between the N and Bi concentration In Fig. 5, we have plotted Optical Gain versus photon energy for different Bi concentrations. The concentrations of Bi is varied from 1 to 6% and accordingly we have considered the N concentration to retain the lattice match condition.

4 Conclusions

In this work, we have investigated the theoretical background to evaluate the optoelectronic properties of the $InAs_{0.92}N_{0.029}Bi_{0.05}$ lattice matched alloy. The investigation of this alloy was carried out using the k.p method, with variations in Bi and N concentrations of less than 10%. InAsNBi alloy can cover a wide spectral range from the mid-infrared to far infrared through precise tuning of the band gap, spin–orbit splitting energy, and inter-band transitions, which are strong functions of Bi and N concentrations. We conclude that $y = 5\%$ and $x = 2.9\%$ can help to achieve an emission of around 9.46 μm. Apart from that, we attain an optical gain of ~2750 cm^{-1} with an injected carrier concentration of 12×10^{15} cm^{-2} and ~15,000 cm^{-1} for a Bi concentration of 2%. To summarize, these optoelectronic features of the InAsNBi/InAs QW, can be used for IR detection.

References

1. Wang K, Liang D, Li Y, Wang S, Lei M, Li S (2019) Electronic properties and band offsets in InP(1−x−y)BixNy. Mod Phys Lett B 10. https://doi.org/10.1142/S0217984919500581
2. Das S, Sharma AS, Gazi SA, Dhar S (2020) Growth of dilute quaternary alloy InPNBi and its' characterization. J Cryst Growth 535. https://doi.org/10.1016/j.jcrysgro.2020.125532
3. Mal I, Samajdar DP (2020) InSbNBi/InSb heterostructures for long wavelength infrared photodetector applications: a 16 band k·p study. J Appl Phys 128:9. https://doi.org/10.1063/5.0020813
4. Huang W, Oe K, Feng G, Yoshimoto M (2005) Molecular-beam epitaxy and characteristics of Ga N y As 1−x−y Bi x. J Appl Phys 98(5). https://doi.org/10.1063/1.2032618
5. Dimmock JO Infrared detectors and applications. 255–309
6. Rogalski A (2005) HgCdTe infrared detector material: history, status and outlook. Reports Prog Phys 68(10):2267–2336. https://doi.org/10.1088/0034-4885/68/10/R01
7. Tan CL, Mohseni H (2018) Emerging technologies for high performance infrared detectors. Nanophotonics 7(1):169–197. https://doi.org/10.1515/nanoph-2017-0061
8. Sweeney SJ, Jin SR (2013) Bismide-nitride alloys: promising for efficient light emitting devices in the near- and mid-infrared. J Appl Phys 113(4). https://doi.org/10.1063/1.4789624
9. Aissat A, Alshehri B, Nacer S, Vilcot JP (2015) Theoretical investigation of GaAsNBi/GaAs materials for optoelectronic applications. Mater Sci Semicond Process 31:568–572. https://doi.org/10.1016/j.mssp.2014.11.040
10. Samajdar DP, Das U, Sharma AS, Das S, Dhar S (2016) Influence of Bi and N related impurity states on the band structure and band offsets of GaSbBiN alloys. Curr Appl Phys 16(12):1687–1694. https://doi.org/10.1016/j.cap.2016.10.010
11. The electronic band structures of InNxAs1−x, InNxSb1−xand InAsxSb1−xalloys.pdf
12. Vurgaftman I, Meyer JR, Ram-Mohan LR (2001) Band parameters for III-V compound semiconductors and their alloys. J Appl Phys 89(11):5815–5875. https://doi.org/10.1063/1.1368156
13. Mendoza-Estrada V, Romero-Baños M, Dovale-Farelo V, López-Pérez W, González-García Á, González-Hernández R (2017) Structural, elastic, electronic and thermal properties of InAs: a study of functional density. Rev Fac Ing 26(46):81–91. https://doi.org/10.19053/01211129.v26.n46.2017.7320
14. Lv YF et al (2014) LPE growth and characterization of InAs1-xNx films. J Cryst Growth 398:1–4. https://doi.org/10.1016/j.jcrysgro.2014.04.005
15. Wang JS, Lin HH, Sung LW, Chen GR (2000) Growth and characterization of InAsN alloys. In: Conference proceedings—international conference indium phosphide related material, no 100, pp 549–552. https://doi.org/10.1109/iciprm.2000.850356
16. Flores S et al (2019) Modelling of bismuth segregation in InAsBi/InAs superlattices: determination of the exchange energies. Appl Surf Sci 485(April):29–34. https://doi.org/10.1016/j.apsusc.2019.04.188
17. Boussaha R, Fitouri H, Rebey A (2019) In situ monitoring of InAsBi alloy grown under alternated bismuth flows by metalorganic vapor phase epitaxy. Mater Sci Eng B Solid-State Mater Adv Technol 241:22–26. https://doi.org/10.1016/j.mseb.2019.02.006
18. Zhou S, Xu H, Hu H, Gui C, Liu S (2019) High quality GaN buffer layer by isoelectronic doping and its application to 365 nm InGaN/AlGaN ultraviolet light-emitting diodes. Appl Surf Sci 471:231–238. https://doi.org/10.1016/j.apsusc.2018.12.011

19. Mal I, Samajdar DP, Das TD (2017) Calculation of band structure and optical gain of type-II GaSbBi/GaAs quantum wells using 14-band k·p Hamiltonian. Superlattices Microstruct 109:442–453. https://doi.org/10.1016/j.spmi.2017.05.032
20. Mal I, Samajdar DP, Das TD (2017) Effect of Sb and N resonant states on the band structure and carrier effective masses of GaAs1-x-yNxSby alloys and GaAs1-x-yNxSby/GaAs quantum wells calculated using k·p Hamiltonian. Superlattices Microstruct 106:20–32. https://doi.org/10.1016/j.spmi.2017.03.035
21. Ridene S, Debbichi M, Ben Fredj A, Said M, Bouchriha H (2008) Energy-band structure and optical gain in strained InAs(N)/GaSb/InAs(N) quantum well lasers. J Appl Phys 104(6). https://doi.org/10.1063/1.2977677
22. Samajdar DP, Das TD, Dhar S (2016) Calculation of valence band structure and band dispersion in indium containing III–V Bismides by k.p method. Comput Mater Sci 111:497–502. https://doi.org/10.1016/j.commatsci.2015.09.066
23. Mal I, Hazra A, Samajdar DP, Das TD (2019) Investigation of electronic and optical properties of gasbbi/gaas type-ii quantum wells using 14-band k p Hamiltonian, vol 215. Springer International Publishing
24. Mal I, Samajdar DP, John Peter A (2018) Theoretical studies on band structure and optical gain of GaInAsN/GaAs/GaAs cylindrical quantum dot. Superlattices Microstruct 119:103–113. https://doi.org/10.1016/j.spmi.2018.04.043
25. Song Z, Bose S, Fan W, Zhang DH, Zhang YY, Li SS (2017) Quantum spin hall effect and topological phase transition in InNxBiySb1−x−y/InSb quantum wells. New J Phys 19(7). https://doi.org/10.1088/1367-2630/aa795c

First Principles Study of Structural and Optical Properties of InP and InP$_{1-x}$N$_x$

Chithraja Rajan, Dip Prakash Samajdar, and Indranil Mal

1 Introduction

InP is a direct band gap material with bandgap of 1.35 eV and is extremely useful for various semiconductor device applications [1]. Due to high mobility, high thermal conductivity, low electron effective mass and high saturation field electron drift rate, InP is widely used high-speed electronic applications such as high electron mobility transistors (HEMTs) [2]. In addition to this, InP possess large anti-radiation impedance, high absorption coefficient, low-temperature coefficient that makes it useful for solar cells and LASERs [3]. Therefore, InP is extremely important for many modern applications such as biosensors, liquid crystal displays (LCD) and fibre and satellite communications [4]. Nitrogen-doped InP nanowires are suitable candidates for use in field effect transistors and photodetectors fabricated on Si substrate and flexible transparent substrates, respectively [5]. Nevertheless, N incorporation in III–V semiconductor lowers the bandgap due to the anticrossing interaction of the N impurity states with the host conduction band [6]. For example, *N* mole fraction of 0.048 implanted in InP resulted in a bandgap of 1.17 eV in InPN, which indicates a bandgap reduction of ~180 meV with respect to reference InP [7]. First principles investigation of the electronic, structural, optical properties of InPN under the influence of hydrostatic pressure has been elaborated by Hattabi et al. [8]. Their study shows a significant reduction of bandgap and lattice constant with the increase in *N* concentration as calculated using Tran–Blaha-modified Becke-Johnson (TB-mBJ) [9] approach. Also, all-electron-full-potential (linearized) augmented plane wave plus local orbitals (FP-(L)APW + lo) method in WEIN2k [10] code is used to perform a detailed investigation of the structural and electronic properties of InPN. Further, the study in [11] reveals that InP$_{1-x}$N$_x$ exhibits metallic properties with *N*

C. Rajan · D. P. Samajdar (✉) · I. Mal

Design and Manufacturing, PDPM Indian Institute of Information Technology, Jabalpur, Madhya Pradesh, India

e-mail: dip.samajdar@iiitdmj.ac.in

concentration lying between 47 and 80%. In this article, we have computed the structural, electronic and optical properties of InP and $InP_{1-x}N_x$ with N mole fraction of 0.09375 within the realm of FP-LAPW basis sets using PBEsol XC functional and mBJ XC potential for better accuracy.

2 Computational Details

In this work, DFT analysis is carried out in WEIN2K tool using FP-LAPW and PBEsol approximations. mBJ potential is utilized to obtain more accurate optoelectronic properties. The zinc blende (ZB) crystal structure in 216 F-43 m space has been considered for the entire calculations. Muffin-tin (MT) radius for In and P is taken as 2.5 au and 2.14 au, respectively. A highly dense k-mesh of $10 \times 10 \times 10$ is considered to extend the Brillouin Zone (BZ). The convergence criteria adopted for energy is 1.0×10^{-4} Ry and for charge of 1.0×10^{-3} e.

3 Result and Analysis

3.1 Structural Properties

In order to obtain a stable crystal structure, lattice constant optimization has been performed for which total energy of ZB structure of InP and N diluted InP is obtained utilizing FP-LAPW method, and energy (1.0×10^{-4} Ry) and charge (1.0×10^{-3} e) convergence criteria are as shown in Fig. 1. The optimum lattice constant is obtained by total energy fitting with the unit cell volume using Murnaghan states equations. Also, this process provides bulk modulus and its derivatives. We obtained a lattice constant of InP and $InP_{0.90625}N_{0.09375}$ as 5.9725 A and 5.9141 A$^{°}$, respectively. These values are closely matched to the lattice constants presented in literature obtained experimentally and various theoretical studies [8]. The bulk modulus for InP and $InP_{0.90625}N_{0.09375}$ is obtained as 63.3720 GPa and 62.9052 GPa, respectively.

3.2 Electronic Properties

This section discusses energy band diagram (EBD) and density of states (DOS) of InP and N doped InP. The obtained lattice constants are used to construct optimum InP and $InP_{0.90625}N_{0.09375}$ crystal structures. Then, band gap and DOS are precisely calculated using TB-mBJ potential. Figure 2 shows the EBD of InP and $InP_{0.90625}N_{0.09375}$. It is clear that InP is a direct band gap material as the valence band (VB) maximum and conduction band (CB) minimum coincide at Γ point. Fermi level is indicated by
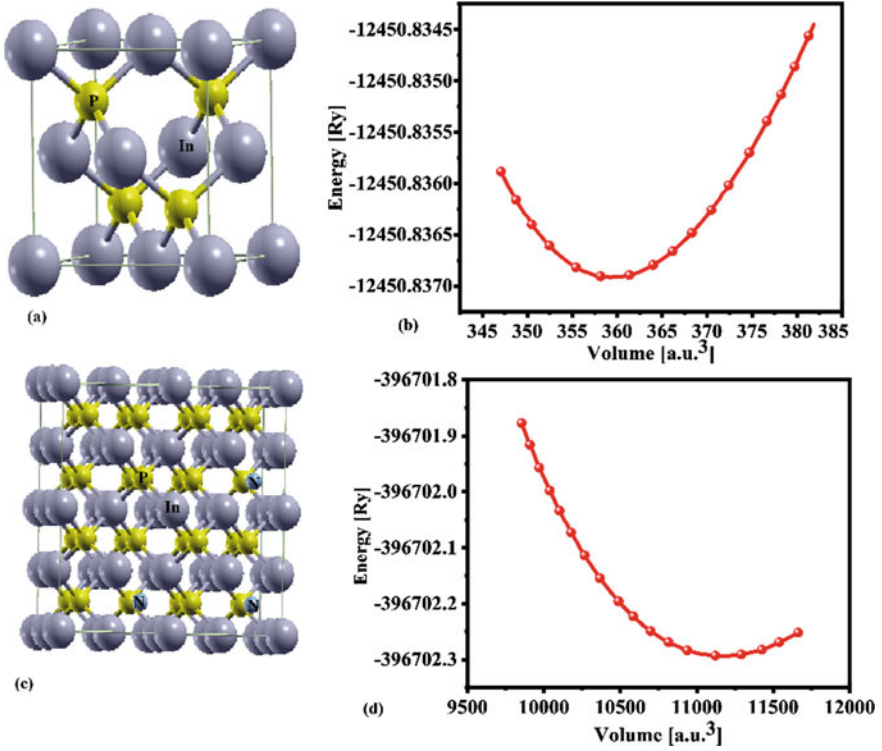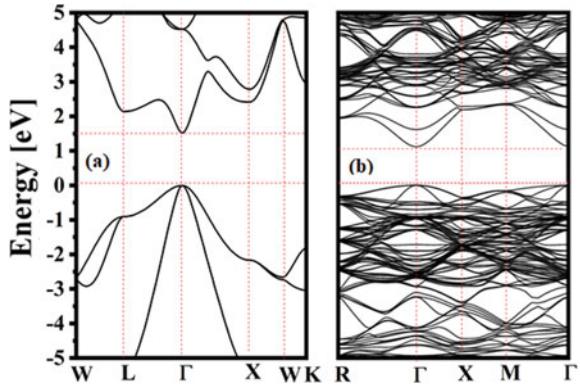
Fig. 1 **a** Zinc blende (ZB) phase structure, **b** volume optimization curve of InP, **c** zinc blende (ZB) phase structure and **d** volume optimization curve of InP$_{0.90625}$N$_{0.09375}$

Fig. 2 Energy band diagram of **a** InP and **b** InP$_{0.90625}$N$_{0.09375}$

the dotted line crossing 0 eV. We obtained band gap of 1.517 eV for InP, which is consistent with the values obtained experimentally and theoretically in literature [8]. Figure 2b shows that inclusion of N atoms in InP creates so many energy levels in CB and VB. Also, 9% N doping considerably reduces band gap to 1.11762 eV. Therefore, it is clear from our study that N doping shrinks band gap of III–V materials and is an alternative option for low band gap applications. TB-mBJ potential is also used to calculate total and partial DOS of In (s, p, d), P(s, p, d) and N(s, p) as shown in Fig. 3. This illustrates the effect of N doping on electronic properties of InP through a precise and narrow energy band window. P-d orbital dominates valence band top and conduction band bottom levels are dominated by hybrid states of In-s and P-d orbitals. Therefore, to deal with the valence band, impurities that interact with the P-d are needed and for conduction band impurities that interact with the In-s and

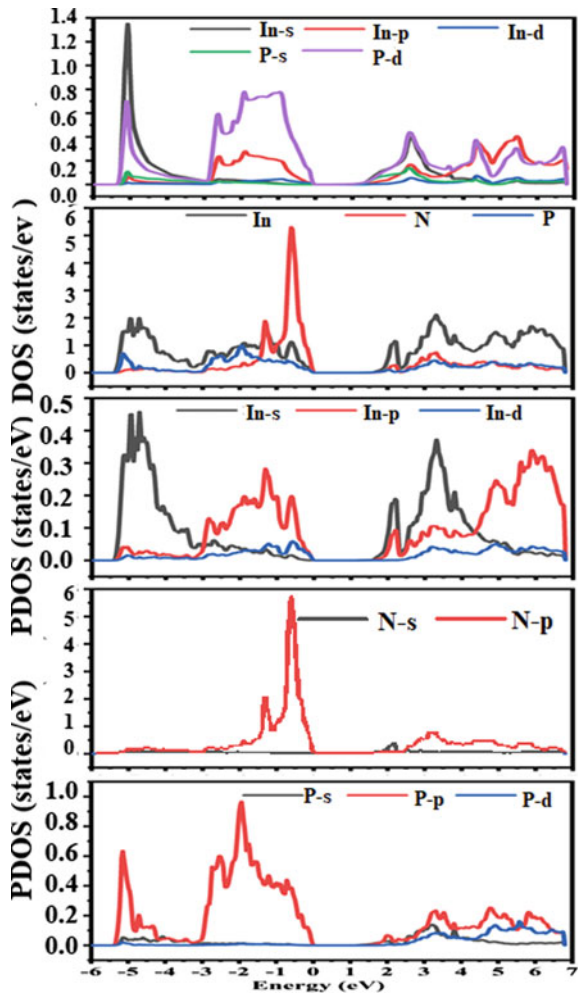**Fig. 3** Total and partial density of state of state for InP and InP$_{0.90625}$N$_{0.09375}$

Table 1 Properties of zinc blende InP and InP$_{0.90625}$N$_{0.09375}$

Parameters	InP	InP$_{0.90625}$N$_{0.09375}$
Lattice constant a (°A)	5.9725, 5.8299[a], 5.86[b]	5.914, 5.795[c]
Bulk modulus (GPa)	63.372, 71.0719[a], 72.00[b]	62.9052, 72.017[c]
Direct gap (eV)	1.517, 1.66753[a], 1.35[d]	1.11762, 0.93455[c]
Indirect gap (eV)		
(Γ–X)	2.41821, 2.21[d]	2.19688
(Γ–M)	–	2.33652
(Γ–W)	4.80643	–
Carriers effective mass (m_0)		
$m*_{lh}$ (Í–X)	0.133	0.128
$m*_{hh}$ (Í–X)	0.56	0.67
Static dielectric constant $\varepsilon 1(0)$	13.4	8.46
Static refractive index $\mathbf{n}(0)$	0.47	0.47

[a]Reference [8], [b]Reference [12], [c]Reference [13], [d]Reference [14]

P-d are preferred. N-p interacts well with the P-d of valence band and In-s and P-d of conduction band. Hence, N brings the valence band and conduction band DOS contributions of InAs to a higher level. Also, for 9% doping, N-p has more impact in conduction band as compared to the valence band. Therefore, it is obvious that the effect of N doping is more in conduction band, and it is dominated in valence band for N doped InP. Effective mass is another important parameter to be calculated to analyse transport property of any material. Hence, in this paper, effective mass of electrons and holes has been computed along the conduction band and three symmetric directions in the valence band using DFT. Obtained effective mass is tabulated in Table 1, which shows that they are closely matched to the experimental results.

3.3   Optical Properties

InP and InP$_{0.90625}$N$_{0.09375}$ are direct band gap materials, and the optical properties are calculated as a function of photon energy. Complex dielectric function consists of real (ε_1) and imaginary (ε_2) parts, which are the primary optical properties obtained by Kramers–Kroning formula [15]. Figure 4a–b shows the real and imaginary parts of dielectric function for InP and InP$_{0.90625}$N$_{0.09375}$, from which it can be concluded that with doping, peak value reduces and slightly shifts to higher energy level. We
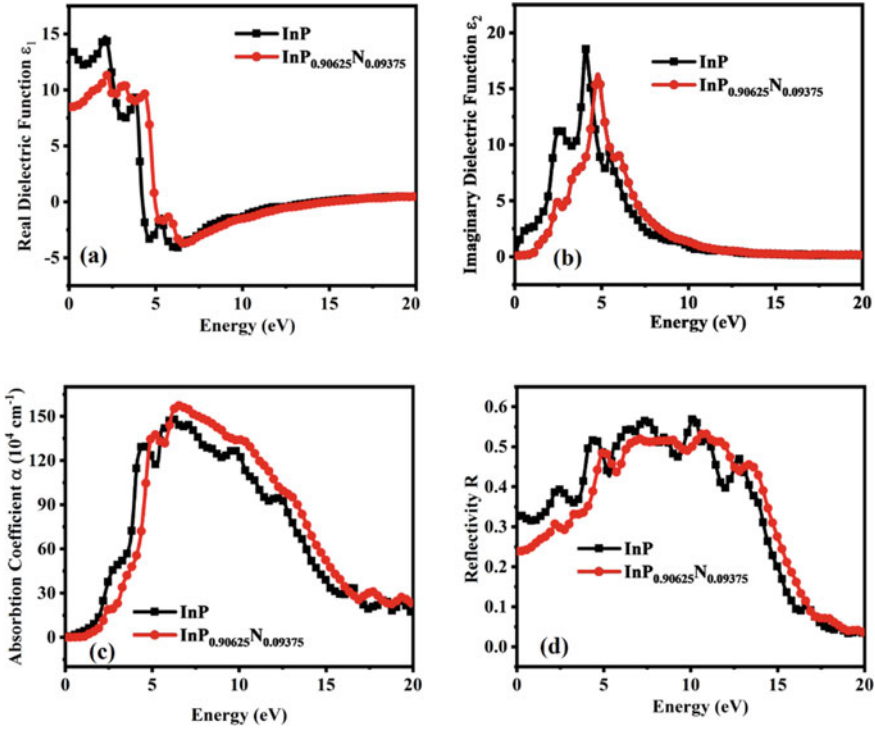
Fig. 4 Variation of computed optical parameters with respect to the incident photon energy **a** real dielectric function $\varepsilon_1(\omega)$, **b** imaginary dielectric function $\varepsilon_2(\omega)$, **c** absorption coefficient $\alpha(\omega)$ and **d** reflectivity

got peak value of real dielectric constant as 14.7 at 2.08 eV and 11.32 at 2.19 eV as shown in Fig. 4a. Similarly, for imaginary dielectric constant, the peak value reduces and slightly shifts to higher energy level with doping of N in InP. Figure 4b shows imaginary dielectric constant peak value for InP is 18.54 at 4.09 eV and for $InP_{0.90625}N_{0.09375}$ peak value is 16.2542 at 4.748 eV. From real (ε_1) and imaginary (ε_2) parts of dielectric function, value of the absorption coefficient ($\alpha(\omega)$) can be obtained using Eq. (1) [16].

$$\alpha(\omega) = \sqrt{\omega \frac{\sqrt{\varepsilon_1(\omega)^2 + \varepsilon_2(\omega)^2} - \varepsilon_1(\omega)}{2}} \tag{1}$$

Figure 4c shows that the peak $\alpha(\omega)$ for InP is 1.47×10^6 cm^{-1} at 6.19 eV. Next, the reflectivity $R(\omega)$ is obtained from Eq. (2) [17].

$$R(\omega) = \left| \frac{\sqrt{\varepsilon(\omega)} - 1}{\sqrt{\varepsilon(\omega)} + 1} \right|^2 \tag{2}$$

Figure 4d shows the reflectivity ($R(\omega)$) for InP and $InP_{0.90625}N_{0.09375}$. The peak value of $R(\omega)$ for InP is 0.5689 at 10 eV and for $InP_{0.90625}N_{0.09375}$, it is 0.53767 at 10.462 eV. Refractive index is another important parameter to analyse optical properties of a material. It is also a complex function with real and imaginary parts. Real part is called refractive index ($n(\omega)$) and imaginary part is otherwise known as extinction coefficient $k(\omega)$.

The refractive index of any material can be obtained by values $\varepsilon_1(0)$ and $\varepsilon_1(\infty)$ according Eqs. (3) and (4) [18].

$$n(\omega) = \sqrt{\frac{\sqrt{\varepsilon_1(\omega)^2 + \varepsilon_2(\omega)^2} + \varepsilon_1(\omega)}{2}} \tag{3}$$

$$k(\omega) = \sqrt{\frac{\sqrt{\varepsilon_1(\omega)^2 + \varepsilon_2(\omega)^2} - \varepsilon_1(\omega)}{2}} \tag{4}$$

Here, the value of $\varepsilon_1(0)$ is 13.4 for InP and 8.46 for $InP_{0.90625}N_{0.09375}$; whereas, $\varepsilon_1(\infty)$ is 0.47 for both InP and $InP_{0.90625}N_{0.09375}$. Figure 5a shows that the peak
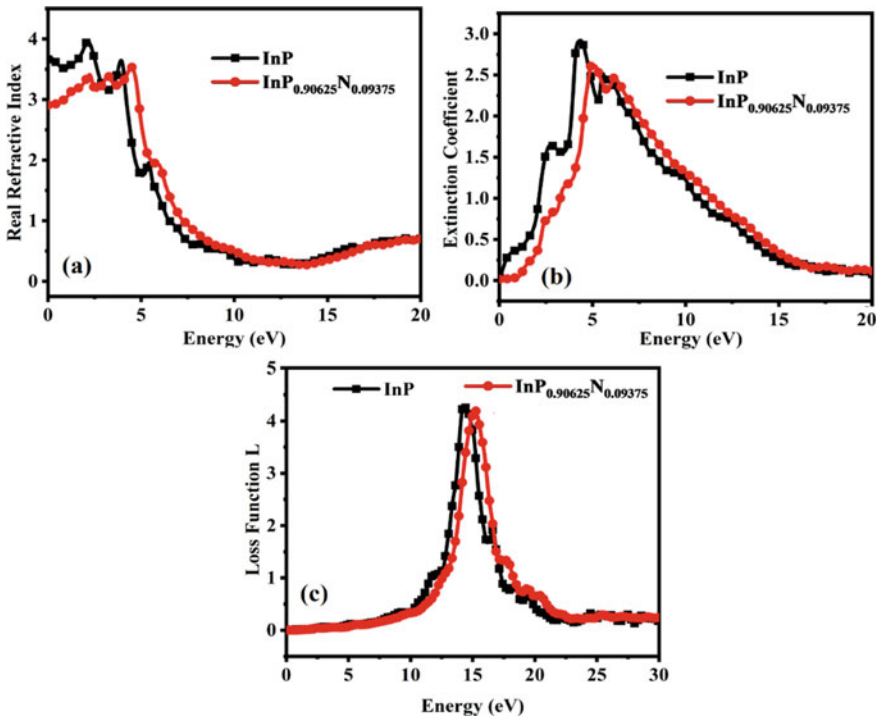
Fig. 5 Variation of **a** real refractive index $n(\omega)$, **b** imaginary refractive index or extinction coefficient $k(\omega)$ and **c** energy loss function with incident photon energy
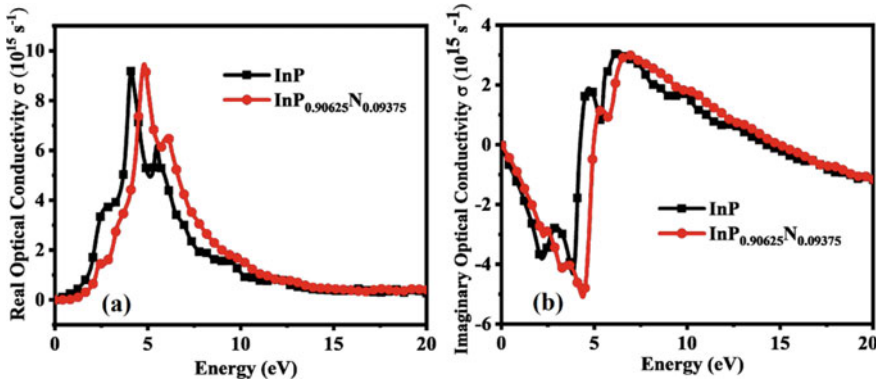
Fig. 6 Variation of computed **a** real optical conductivity and **b** imaginary optical conductivity with the variation in incident photon energy

value for $n(\omega)$ is 3.95 at 2.08 eV for InP and 3.379 at 2.13 eV for $InP_{0.90625}N_{0.09375}$. Figure 5b depicts the extinction coefficient of both the materials and there is a slight degradation in the value of extinction coefficient for InPN as compared to InP and the peak value is also shifted towards higher energy levels. The peak value for $k(\omega)$ is 2.92 at 4.34 eV for InP and 2.7 at 4.966 eV for $InP_{0.90625}N_{0.09375}$.

Interaction and is expressed as function of photon energy. Figure 5c shows the loss function peak as 4.2987 at 14.27 eV for InP and 4.176 at 15.27 eV. Finally, optical conductivity ($\sigma(\omega)$) of any material is obtained by Eq. (5) [19].

$$\sigma(\omega) = -\frac{i\omega}{4\pi}\varepsilon(\omega) \tag{5}$$

Figure 6 shows that the real and imaginary parts of $\sigma(\omega)$. We obtained peak value for real $\sigma(\omega)$ as 9.18 at 4.09 eV for InP and 9.4 at 4.857 eV for $InP_{0.90625}N_{0.09375}$ as shown in Fig. 6a. Figure 6b shows that the peak value for imaginary $\sigma(\omega)$ is obtained as 3.05 at 6.163 eV for InP and 2.9 at 6.598 eV for $InP_{0.90625}N_{0.09375}$. Finally, the variation in optical properties with N doping is tabulated in Table 2.

Energy Loss parameter describes the loss occuring during matter and electron interaction and is expressed as a function.

Table 2 Optical properties of InP and $InP_{0.90625}N_{0.09375}$

Optical properties	InP	$InP_{0.90625}N_{0.09375}$
Absorption coefficient α (10^4 cm^{-1})	147.9	157
Optical conductivity σ (10^{15} s^{-1})	9.18	9.42
Refractive index	3.9	3.5
Reflectivity	0.56	0.53

4 Conclusions

In this manuscript, a thorough investigation of zinc blende structure of InP and $InP_{0.90625}N_{0.09375}$ has been performed in WEIN2K. Optimum lattice constants are obtained by volume optimization technique performed on material structures. mBJ potential is utilized to obtain the detailed energy band diagram, DOS and optoelectronic properties of the materials. We found that the incorporation of N in InP reduces band gap significantly and hence, extend InP usage in large wavelength applications. The calculated structural, electronic and optical properties are consistent with the experimental and theoretical findings. The computed optoelectronic properties can serve as a benchmark for designing efficient photodetectors, solar cells, LASERs and fast semiconductor devices using InPN.

References

1. Foyt AG (1981) J Cryst Growth 54:1–8
2. Mishra a UK, Shealy JB (1994) Proceedings of 1994 IEEE 6th international conference on indium phosphide and related materials (IPRM), pp 14–17
3. Agnihotri SK, Prashant DV, Samajdar DP, Arefinia Z (2021) Sol Energy 228:418–426
4. Zhang Y, Mascarenhas A, Deb SK, Xin HP, Tu CW (2000) In: Conference record of the twenty-eighth IEEE photovoltaic specialists conference (Cat. No. 00CH37036), pp 1189–1192
5. Bi WG, Tu CW (1996) J Appl Phys 80(3):1934–1936
6. Samajdar DP, Das U, Sharma AS, Das S, Dhar S (2016) Curr Appl Phys 16(12):1687–1694
7. Yu KM, Walukiewicz W, Wu J, Beeman JW, Ager JW III, Haller EE, Shan W, Xin HP, Tu CW (2001) Appl Phys Lett 78(8):1077–1079
8. Hattabi I, Abdiche A, Moussa R, Riane R, Hadji K, Soyalp F, Varshney D, Syrotyuk SV, Khenata R (2016) Zeitschrift für Naturforschung A 71(9):783–796
9. Jiang H (2013) J Chem Phys 138(13):134115
10. Blaha P, Schwarz K, Madsen GK, Kvasnicka D, Luitz J (2001) Vienna University of Technology, Austria
11. Ahmed R, Hashemifar SJ, Akbarzadeh H (2008) Phys B: Condens Matter 403(10–11):1876–1881
12. Ben Fredj A, Debbichi M, Said M (2007) Microelectronic J 38:860
13. Aslan M, Reshak AH, Yalcin BG, Bagci S, Ustundag M (2002) Phil Mag 96(10):991–1005; Kilby JS (2002) Chemphyschem 2:482–489
14. Madelung O, Schulz M (1987) Londolt-Bornstein, Cryst Solid State Phys, 17a. Springer-Verlag, Berlin
15. Yalcin BG, Bagci S, Ustundag M, Aslan M (2015) Comput Mater Sci 98:136–141
16. Zaoui A, Kacimi S, Yakoubi A, Abbar B, Bouhafs B (2005) Phys B: Cond Matt 367:195–204
17. Ge Y, Wan W, Guo X, Liu Y (2020) Opt Express 28:238–248
18. Lashgari H, Boochani A, Shekaari A, Solaymani S, Sartipi E, Mendi RT (2016) Appl Surf Sci 369:76–81
19. Santhi bhushan B, Soni M, Srivastava A (2017) J Phys 89:14

Demonstration of High-Permittivity Sidewall Spacer in Negative Capacitance FinFET

Vibhuti Chauhan, Dip Prakash Samajdar, and Navjeet Bagga

1 Introduction

Numerous multi-gate, quasi-planar structures were proposed over conventional MOSFETs, to sustain scaling beyond sub-20 nm gate length (L_G). However, for continuation of supply voltage scaling with diminishing technologies, steep sub-threshold behavior plays a crucial role in order to realize the low power requirements. Negative capacitance (NC)-based transistors are one of those hopeful candidates due to their unique operation [1]. The sandwiched ferroelectric (FE) layer in the gate stack produces an internal voltage amplification in the gate of the transistor, due to the device being operated in the NC regime. This phenomenon delivers a boosted ON-state current (I_{ON}) and steepens the sub-threshold swing (SS) below 60 mV/decade in turn, reducing the supply potential requirements [1, 2]. Predominantly in last few years, NC-FinFETs have received more consideration due to their superior I_{ON}/I_{OFF} ratio, alleviated short channel (SCE) performance, and compatibility with the standard CMOS/FinFET technology [2, 3].

However, to extract more outcomes from the NC property, optimization of device design becomes reasonably significant. To explore this, variable spacer permittivity in NCFETs has been the idea that modifies the requisite capacitance matching condition of the NC state, through the means of outer fringing field lines. Advent of high-permittivity (k) spacers in NC-FinFETs enriches the field coupling between the gate (G) to source (S)/drain (D) extension region (L_{ext}) which in turn cuts down the *S/D* underlap resistance ($R_{S/D}$) [4, 5]. This further enhances the electrostatic veracity of the gate over the channel, leading toward an increased driving current capability and inferior off-state leakage current (I_{OFF}). Moreover, with the advancement in fabrication processes, parasitic capacitances like gate-to-contact and sidewall capacitances had

V. Chauhan · D. P. Samajdar (✉) · N. Bagga

Department of Electronics and Communication Engineering, PDPM IIITDM Jabalpur, Jabalpur, India

e-mail: dipprakash010@gmail.com

come into picture, thus forcing a pertinent spacer-based analysis in order to diminish such capacitive effect [4–6]. Hence, the existence of *G-S/D* underlap regime with diverse permittivity spacer realization stands out to be an optimal nanoscale device design with intimidating performance results. Optimization of spacer placement is not just restricted to SCEs but also alters the circuit performance parameters such as speed and delay. [5–9].

In this work, we investigated the SCE performance of both high-*k* and low-*k* spacers in NC-FinFET, to provide an enriched gate control over the channel. Initially, the well-calibrated TCAD models have been extracted to validate the NC-FinFET performance. Further, a discussion has been presented in order to highlight the evaluations associated with the proposed NC-FinFET design. Section 2 embraces the device structure, calibration models, and the simulation methodology used in this work. In Sect. 3, a comparative analysis has been demonstrated based on the simulated results between the projected spacer configuration and the standard low-*k* NC-FinFET device. The effects on I_{ON}, V_{th}, NDR, and all the SCE parameters were studied for the proposed variable spacer device, and hence, an ideal spacer width was analyzed for both high-*k* and low-*k* materials. Finally, the conclusion has been drawn in Sect. 4.

2 Simulation Framework

The proposed 3-dimensional (3D) schematic of the variable permittivity spacer-based NC-FinFET is named as UL-NC-FinFET. Here, *U* and *L* stand for the upper and lower placement of spacer material, respectively. All the necessary 2D simulations and analysis are carried out on Sentaurus TCAD simulator [10]. The simulation framework of NC-FinFET primarily focuses on the validation of baseline FinFET. The physical dimensions and the structure are well calibrated using a tuned gate metal work function, in order to meet the requisite ITRS specifications of 14 nm FinFET technology, as depicted in Fig. 1a, b. In general, the channel doping concentration is kept low to avoid the random dopant fluctuations (RDFs) and the conventional drift–diffusion model is considered for current mechanism in device physics. The inversion and accumulation layer (IALMob) model has been stimulated to justify the mobility degradation occurring due to high-*k* material at the interface. Also, the recombination effects are taken into effect using the Auger and SRH doping dependence model. The subsequent models are well tuned within their prescribed limits so as to trace the experimental data [11]. The details about calibration is already presented in our previous publications [3, 4].

Further, to attain the NC condition within the calibrated structure, the simulation setup incorporates the FE polarization model, solving the Landau–Khalatnikov (*L-K*) equation [1]. The Landau parameters (α, β, γ) are appropriately matched with the reported data [13], as shown in Fig. 1c. Finally, the NC-FinFET device is realized by placing a FE oxide in the baseline FinFET and integrating the same *L-K* parameters, such that the direction of polarization acts perpendicular to the fin surface.
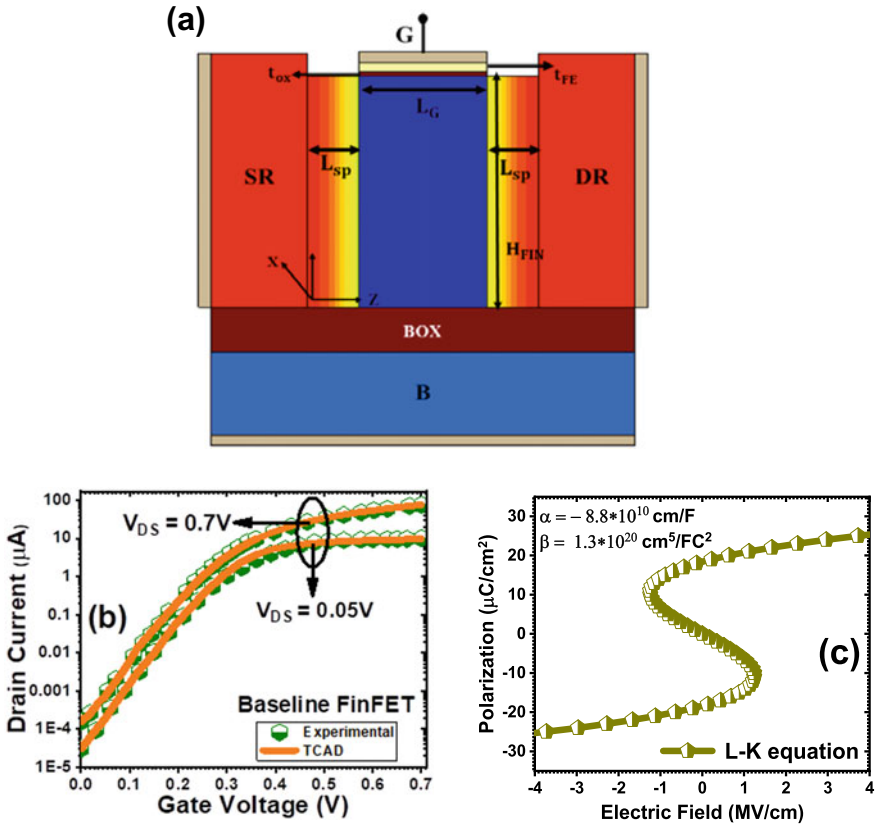
Fig. 1 **a** 3D schematic of the baseline FinFET structure. **b** Calibration of the baseline characteristics against the reported data [11] with varying drain bias (V_{ds}) [4]. **c** Calibration of the FE characteristics (Landau parameters) against the reported data [13]

The employed parameters and structural dimensions used in the simulations are mentioned in Table 1, respectively, which are similar to that used in.

3 Results and Discussions

A thorough exploration of the proposed device design (as shown in Fig. 2) is followed in this section, and further, a comparison has been made between the projected device and the conventional low-k device, on the basis of SCE performance and simulated contours.

Table 1 Device Design
Parameters used in our
simulations

Dimension/parameter	Value	Unit
Gate length (L_G)	20 [11]	nm
Fin height (H_{FIN})	42 [12]	nm
Fin thickness (t_{FIN})	8 [12]	nm
FE thickness (t_{FE})	1.7 [12]	nm
Interfacial gate oxide (t_{ox})	0.6 [12]	nm
Spacer length (L_{sp})	8 [12]	nm
Remnant polarization (P_r)	18 [13]	$\mu C/cm^2$
Coercive field (E_c)	1.2 [13]	MV/cm
Channel doping (N_{ch})	2e16 [12]	cm^{-3}
S/D doping ($N_{S/D}$)	2e20 [12]	cm^{-3}

Fig. 2 Representation of the
proposed UL-NC-FinFET
architecture (with extended
view of the spacer region)
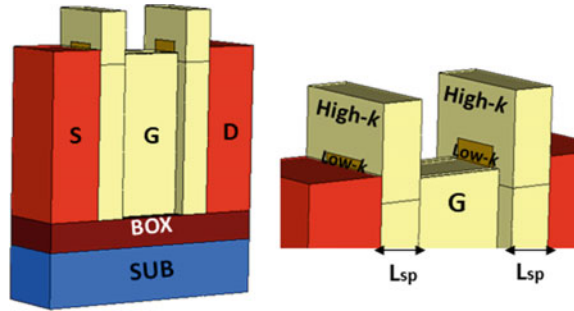
3.1 Upper–Lower Spacer-Based NC-FinFET Design (UL-NC-FinFET)

In this section, an n-channel MFIS-type NC-FinFET is designed with an upper–lower (stack) alignment of high-k (U) and low-k (L) spacers, i.e., UL-NC-FinFET, aiming toward a performance improvement in nanometer-scaled regime. The high-k material used in the upper spacer is HfZrO$_2$ ($k = 33$), i.e., the identical FE placed in the gate stack, and the low-k material used in the lower spacer is Si$_3$N$_4$ ($k = 7.5$). Introduction of these high-k spacers provides an excellent integrity over the channel and counters the high underlap *S/D* resistance ($R_{S/D}$). Such improvements in device characteristics come at the cost of degraded gate capacitance (C_{GG}), delay, etc. Therefore, an optimized length and width of both up and down spacer is required, in order to maintain a trade-off between the low-frequency and high-frequency performance, respectively. In this proposed UL-NC-FinFET, for length, the spacer region completely covers the extension region from *G-S/D* edges; however, for width, the upper high-k spacer has the coverage of 90%, whereas the lower low-k spacer has the coverage of 10% only.

3.2 Comparison Between UL-NC-FinFET and Standard (Low-K) NC-FinFET

Figure 3a represents the transfer characteristics ($I_d - V_{gs}$) of both the UL-NC-FinFET and the conventional low-k NC-FinFET device. It is evident from the response that inclusion of high-k material in the spacer stack steepens the device characteristics, when compared with the standard device. The ON-state current (I_{ON}) of the proposed device progresses by 20%, with a degradation of just one decade in the OFF-state current (I_{OFF}) approximately. This leads to an improvement in I_{ON}/I_{OFF} ratio, thus turning down the sub-threshold swing (SS) from 61 mV/decade (for std. NC-FinFET) to 56.4 mV/decade The most obvious concept behind the proposal of UL-NC-FinFET configuration is their reduced underlap barrier occurring due to the presence of concerted fringing fields. It has been explored that application of drain bias (V_{ds}) in ON-state does not alter the source region but lessens the drain region barrier, which hampers the flow of carriers from source to drain side. Apparently, the effect of reduced D-side field (in ON-state) totally depends upon the high-k spacer used. As the permittivity increases, the gate underneath barrier upsurges and it does not disturb the I_{ON}, unless the carriers cross this barrier strongly. Once the *G-S* barrier is significantly crossed, the carriers easily flow toward the D region leading to a large electron density at the drain side (as evident in Fig. 4). This becomes more explanatory because UL-NC-FinFET experiences a reduced conduction band (C.B) energy barrier in the source region, in turn obtaining a strong integrity over the channel and reducing the SCEs. However, in OFF-state (for $V_{gs} = 0$ V), the proposed structure (contrary to std. NC-FinFET) exhibits a higher C.B energy, which noticeably degrades the I_{OFF}.

The output characteristics ($I_d - V_{ds}$) of the demonstrated UL-NC-FinFET is compared with the conventional low-k structure in Fig. 5. In last few years, it has been revealed that for NC-based devices, increasing V_{ds} in saturation region fuels the de-amplification of inner voltage and lowers the drive current, thus resulting into a Negative Differential Resistance (NDR). Owing to this NDR effect, negative drain-induced barrier lowering (DIBL) phenomenon also occurs because of the coupling between the negative FE capacitance (C_{FE}) and the semiconductor capacitance (C_S). This can be resolved with the presence of high-k spacers, which modulates the charge in the extension region and reduces the barrier at the source side, in turn mitigating the characteristic of NDR. On comparing both the configurations, it was revealed that the suggested UL-NC-FinFET structure does not illustrate NDR effect with an improved (positive) DIBL of approx. + 20.09 mV/V. The presence of low-k material in the lower stack is balanced by the upper high-k material, which does not modify the channel charge and avoids NDR, whereas the presence of low-k spacer in the conventional device leads to a moderate NDR effect, due to the occurrence of obstructed field lines in the drain region and a loose control over the source region.
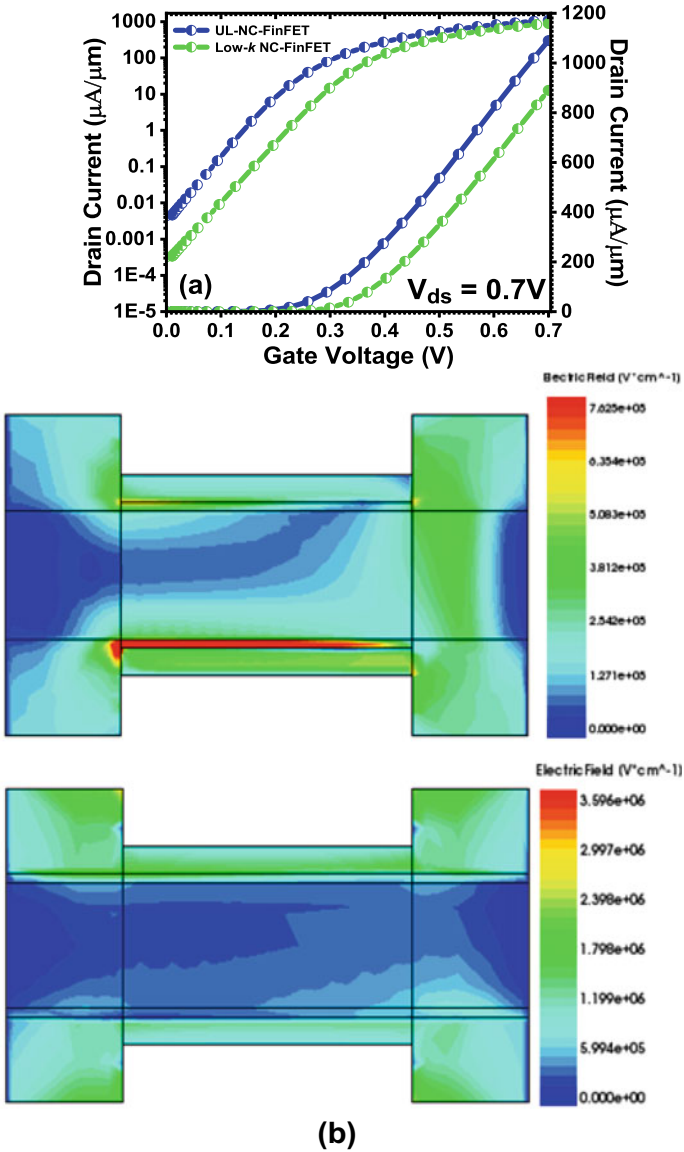
Fig. 3 a Transfer characteristics ($I_d - V_{gs}$) of the proposed UL-NC-FinFET structure w.r.t low-k NC-FinFET (in both linear and log scale). **b** Enhanced electric fields in both the structures due to the voltage amplification phenomenon (1) low-k NC-FinFET (0.7 MV/cm maximum) and (2) UL-NC-FinFET (3.6 MV/cm maximum)

Fig. 4 Boosted electron density in the UL-NC-FinFET structure due to the presence of high-k spacers. **a** Low-k NC-FinFET (3.7e20 cm^{-3} maximum) and **b** UL-NC-FinFET (9.15e20 cm^{-3} maximum)
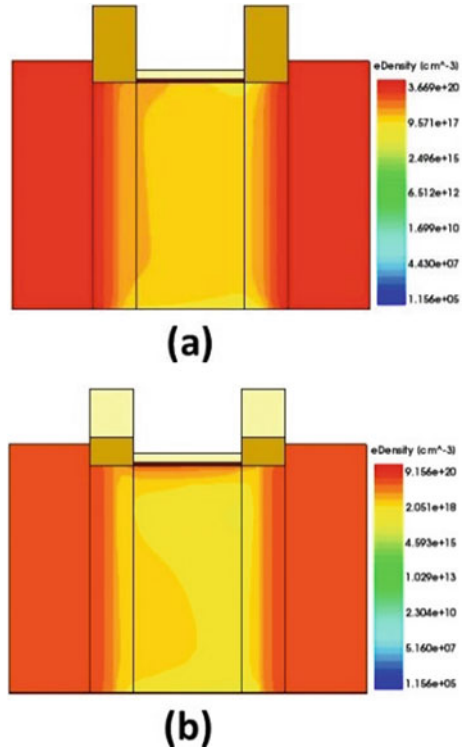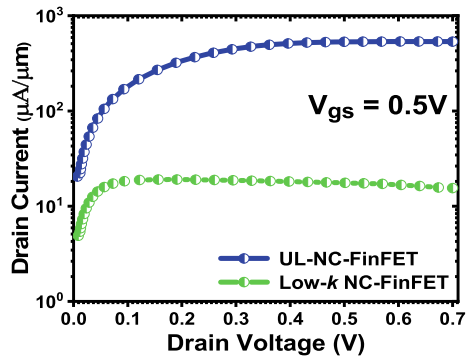

Fig. 5 Output characteristics ($I_d - V_{ds}$) of the proposed UL-NC-FinFET, in order to mitigate the NDR effect

4 Conclusion

Using 3-dimensional TCAD simulations, this paper represents the merits and quasi-static electrostatics of the proposed UL-NC-FinFET structure. The investigated architecture portrays an excellent gate reliability over the channel and progresses the device performance in terms of various SCE parameters. The drain current behavior

and the short channel conduct of the projected UL-NC-FinFET are optimized and compared with the conventional low-*k* NC-FinFET configuration. The proposed NC-FinFET produces an approximately 90% decrease in the OFF-state current, 20% enhancement in the drive current, sub-60 mV/decade SS, negligible NDR, and a positive DIBL. Hence, it can be summarized that the proposed UL-NC-FinFET architecture can be a great choice for digital applications, and with an optimized trade-off between the mixed-mode parameters, it can also be employed under the analog high-frequency applications.

References

1. Chauhan V, Samajdar DP (2021) Recent advances in negative capacitance FinFETs for low power applications: a review. IEEE Trans Ultrasonics Ferroelectric Frequency Control 68:3056–3068
2. Salahuddin S, Datta S (2008) Use of negative capacitance to provide voltage amplification for low power nanoscale devices. Nano Lett 8:405–410
3. Dixit A, Samajdar DP, Chauhan V (2021) Sensitivity analysis of a novel negative capacitance FinFET for label-free biosensing. IEEE Trans Electron Devices 68:5204–5210
4. Chauhan V, Samajdar DP, Bagga N, Dixit A (2021) A novel negative capacitance FinFET with ferroelectric spacer: proposal and investigation. IEEE Trans Ultrasonics, Ferroelectrics Frequency Control 68:3654–3657
5. Sachid AB et al (2008) Sub-20 nm gate length FinFET design: can high-*k* spacers make a difference. In: 2008 IEEE international electron device meeting
6. Lin YK et al (2019) Spacer engineering in negative capacitance FinFETs. IEEE Electron Device Lett 40(6):1009–1012
7. Narendra V et al (2020) Investigation of short channel effects (SCEs) and Analog/RF figure of merits (FOMs) of dual material bottom spacer ground plane (DMBSGP) FinFET. Silicon, pp. 2283–2291
8. Nehra D et al (2014) High permittivity spacer effects on junctionless FinFET based circuit/SRAM applications. In: 18th international symposium on VLSI design and test
9. Gupta SK, Roy K (2012) Spacer thickness optimization for finfet-based logic and memories: a device-circuit co-design approach. ECS Trans 50(4):187–192
10. Sentaurus TCAD (Ver. 2019.09) Manuals, Synopsys, Inc., Mountain View, CA, USA, 2019
11. Auth C et al (2017) A 10 nm high performance and low-power CMOS technology featuring 3rd generation FinFET transistors, self- aligned quad patterning, contact over active gate and cobalt local interconnects. In: IEEE international electron device meeting, pp 673–676
12. Prakash O et al (2020) Impact of interace traps on negative capacitance transistor: device and circuit reliability. IEEE J Electron Devices Soc 8:1193–1201
13. Toprasertpong K, Tahara K, Takenaka M, Takagi S (2020) Evaluation of polarization characteristics in metal/ferroelectric/semiconductor capacitors and ferroelectric field-effect transistors. Appl Phys Lett 116(24)

A Novel Dual Gate Hetero Dielectric Hetero Material Reconfigurable FET

Chithraja Rajan and Dip Prakash Samajdar

1 Introduction

Nevertheless, past four decades of semiconductor industry have been successfully served by CMOS technology. Motivated by Moore's Law, the ever-decreasing transistor size contributed to high performance, power efficient, and small electronic gadgets [1–3]. However, continuous increase in power dissipation issues, incompetency of manufacturing process to create accurate dimensions, limitation of dielectric materials to provide proper insulation, and higher lithography costs to fabricate the device dimensions below 100 nm have aggravated the current scenario of CMOS technology [4]. Therefore, the hunt for low power chip design alternatives had begun a few years back, which aim to control power performance trade-off. Therefore, in 1995, Mutoh and team [5] proposed the concept of Multi-threshold (MT) CMOS in which a low V_{th} transistor is used to implement logic cells while high V_{th} FETs are used as sleep transistors. Low V_{th} transistors are fast and dissipate high SS leakage current whereas high V_{th} transistors are slow and exhibit less SS leakage. The role of sleep transistors (high V_{th}) is to isolate the logic cells (low V_{th}) from power supply and, hence, control the stand-by power. However, sudden jump of MT-CMOS from sleep to active mode drives large current into the circuit and causes heat loss [6].

Alternatively, reconfigurable FET (RFET) is a MT device that works either as MOSFET or TFET (tunnel FET) [7–11], where MOSFET is low V_{th} and TFET is high V_{th} transistor. Here, single device is capable of being configured into four transistors by switching potentials, applied externally to the over source (ES) and over drain (ED) electrodes. Depending on the polarity of the potential applied over ES and ED, two electrodes ES ($\pm$ 0.8 V) and ED ($\pm$ 0.8 V) attract either electrons or holes in the drain and source regions and result into n-i-n or p-i-p or n-i-p or p-i-n device

C. Rajan · D. P. Samajdar (✉)
PDPM Indian Institute of Information Technology, Design and Manufacturing, Jabalpur, Madhya Pradesh, India
e-mail: dip.samajdar@iiitdmj.ac.in

503

structures. Additionally, potential applied over gate electrode stimulates up-down band movement in channel region, which controls carrier flow between source and drain regions either through thermionic emission or band-to-band tunneling (BTBT). Therefore, RFET combines pros and cons of MOSFET and TFET such that MOSFET produces high circuit driving current but dissipates more power while TFET is a low power device with limited ON current. Moreover, RFET suffers from Schottky ambipolarity [8] due to BTBT between drain/channel regions in FETs during reverse gate potentials. Alternatively, hetero material (HM) hetero dielectric (HD) RFET is discussed elaborately in our previous work [7], which provides better MOSFET and TFET characteristics compared to Si-RFET. However, HM-HD-RFET suffers high ambipolarity in n-type FETs, which dissipates more power in digital or mixed signal circuits. Therefore, in this work, we have explored dual gate (DG) architecture in HM-HD-RFET, such that single control gate is replaced by two half metals of different work functions (WF) [12]. This brings wide scope of investigation to improve RFET through WF optimization of two metals. Hence, we proposed a novel DG-HM-HD-RFET that promises to produce better MOSFET and TFET characteristics without ambipolarity.

2 Device Structure and Simulation Models

Figure 1a shows device structure of DG-HM-HD-RFET. Length of drain (L_{ED}), source (L_{ED}) and channel (L_{CG}) are of 50 nm each, device width (D) is 10 nm, oxide thickness (t_{ox}) is 2 nm, and drain (L_{GD}) and source (L_{GS}) spacers are of 5 nm length each. Other device properties are listed in Table 1. The proposed device has a low band gap material ($Al_{0.2}Ga_{0.8}Sb$) in source region and high band gap material (Si) in channel/drain regions.
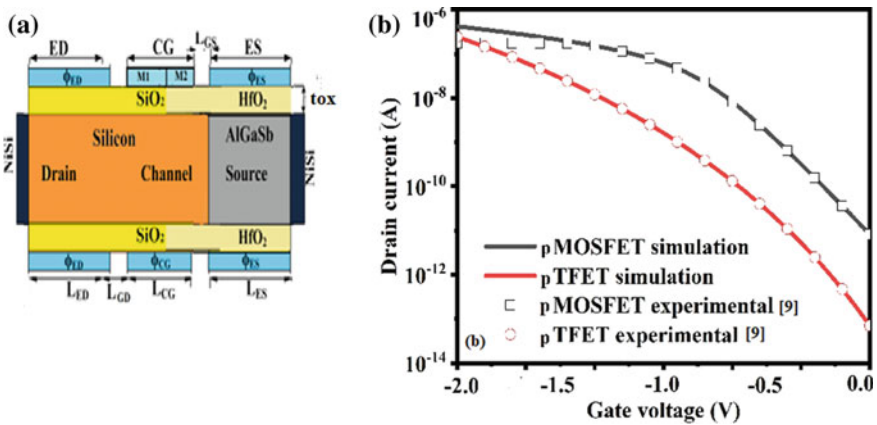

Fig. 1 Device structure of **a** DG-HM-HD-RFET and **b** Calibrated result

Table 1 Device physical properties

Parameters	unit	DG-HM-HD-TFET
Oxide thickness (tox)	nm	2
Body thickness (D)	nm	10
Channel length (L_g)	nm	50
Source length (L_s)	nm	50
Drain length (L_d)	nm	50
Source spacer length (L_{ss})	nm	5
Drain spacer length (L_{ds})	nm	5
Doping	atoms/cm^3	1e17
Electrode work function (Φ_g)	eV	4.5
$M1$ work function ($\Phi M1$) [12, 13]	eV	4.3
$M2$ work function ($\Phi M2$) [12, 13]	eV	4.7

This band gap engineering boosts TFET device characteristics as band bending in HM junction is better as compared to conventional TFET. Further, use of high-k oxide (HfO2) over first half source/channel region and low-k oxide (SiO2) in remaining half improves ON current and reduces ambipolarity. Certainly, there is a performance trade-off between n and p device characteristics.

Therefore, a DG structure is recommended here, such that work function optimization of near-drain-gate-metal ($M1$) and near-source-gate-metal ($M2$) allow tremendous improvement in electrical characteristics of four configurations. Device simulations are performed in Silvaco Atlas tool [14], and models used are Universal Schottky tunneling (UST), drift–diffusion model, Fermi–Dirac statistics, Shockley Read Hall (SRH), Auger recombination, and band-to-band tunneling models. Models are properly calibrated using an experimental device [9] as shown in Fig. 1b, which shows that the simulation platform is perfectly matching experimental conditions.

2.1 Results and Discussions

Figure 2a explains working of RFET in n-MOSFET and n-TFET configurations through energy band modulation during ON condition, for ($V_{ess} = 0.8$ V, $V_{edd} = 0.8$ V) and (Vess $= 0.8$ V, $V_{edd} = 0.8$ V), respectively. RFET switches from thermionic emission to band-to-band tunneling mode as n/p types. Figure 2b shows that DG-HM-HD-MOSFET produces slightly lower current than Si-HD-MOSFET but p-HM-HD-MOSFET dissipates much lesser OFF current than p-Si-HD-MOSFET. Also, DG-HM-HD-TFET produces better ON current as compared to Si-HD-TFET. It is obvious from Fig. 2b that use of HD suppresses ambipolarity in p-type devices but is incapable to mitigate ambipolar conduction in n-type. However, by virtue of dual
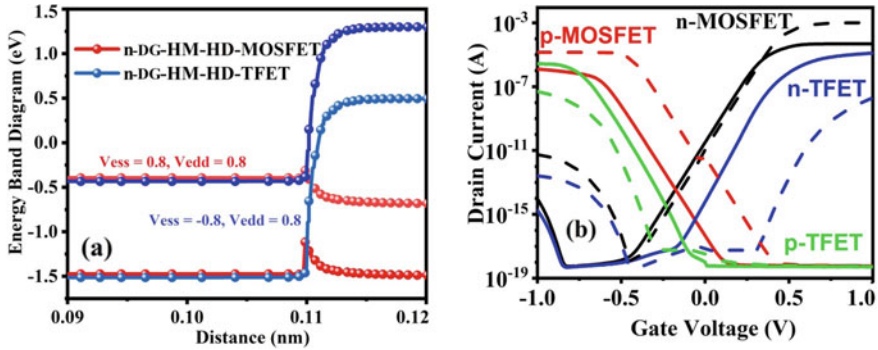
Fig. 2 **a** Working principle of RFET and **b** Drain current comparison between Si-HD-RFET (dash line) and DG-HM-HD-RFET (solid line)

gate, ambipolarity reduces drastically in DG-HM-HD-TFET as compared to Si-HD-TFET. Figure 3 shows energy band diagram (EBD) of *p*-MOSFET and *p*-TFET for two devices. Lower is the barrier potential and higher would be the drain current in MOSFET but Fig. 3a shows there is a band offset at HM junction, which prevents carriers to flow across source/channel junction and, hence, reduced ON current is produced in DG-HM-HD-MOSFET than Si-HD-MOSFET. Also, greater is the band bending more would be the tunneling current in TFET and Fig. 3b shows that the non-uniform HM band gaps cause better band bending at source/channel junction than Si-based uniform band gap device. Further, Fig. 4 shows impact of $M1$ work function variation (WFV) on device drain current characteristics. Figure 4a and b shows that as WF increases, the current in *p*-type devices shifts in right direction more toward positive gate voltage and, hence, turns ON at low V_{th}, and increases OFF current and SS. However, drain current slightly shifts toward right and, hence, increases V_{th}, reduces OFF current and SS in *n*-type devices. Therefore, as $M1$ WF increases, ON and OFF current in *p*-type increase significantly depending on the barrier potential
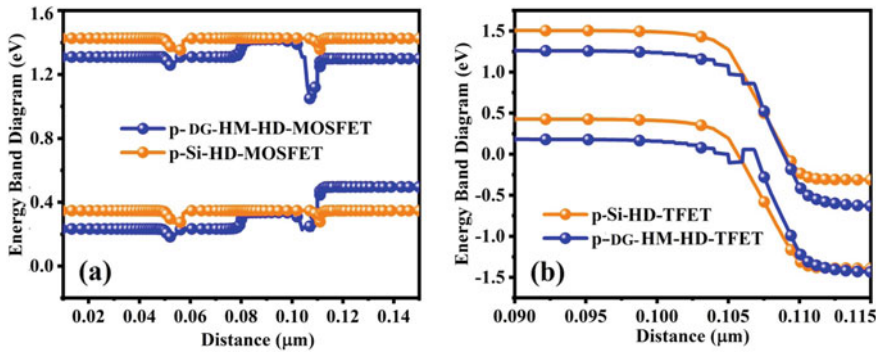

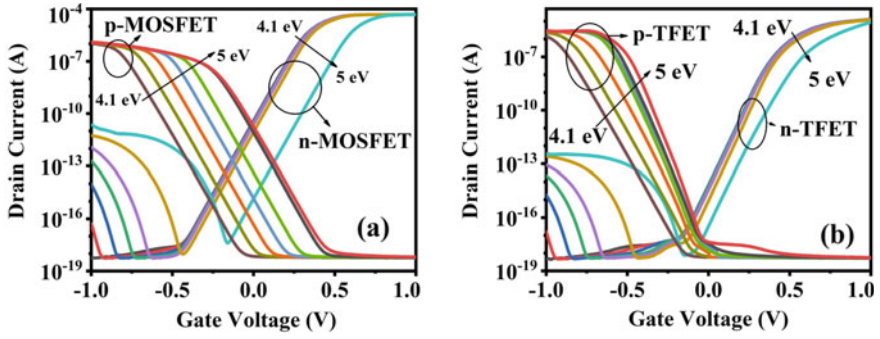**Fig. 3** EBD comparison between **a** *p*-MOSFET and **b** *p*-TFET of Si and DG-HM-HD-RFET

Fig. 4 Drain current of **a** DG-HM-HD-MOSFET and **b** DG-HM-HD-TFET with $M1$ work function variations
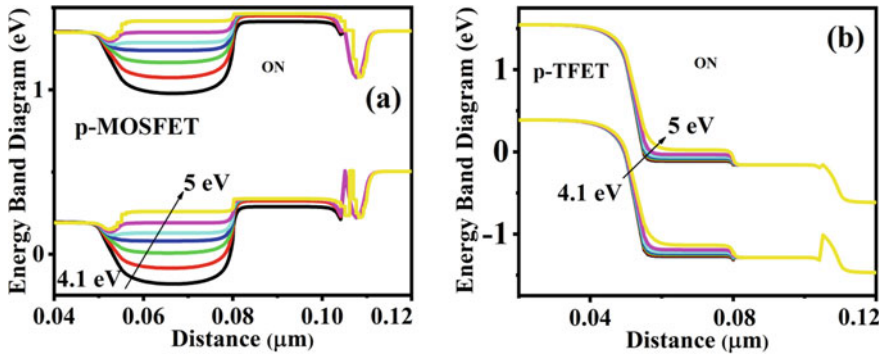

Fig. 5 EBD of p-type **a** DG-HM-HD-MOSFET and **b** DG-HM-HD-TFET with $M1$ work function variations

(Fig. 5a) or tunneling width (Fig. 5b) in EBD. While for n-type, slight reduction in ON current is explained through potential barrier increase in $M1$ region as shown in Fig. 6a. However, ambipolar current increases rigorously in n-type device as $M1$ WF increases. Higher the band bending at the drain/channel junction, more would be the tunneling current in ambipolar state as illustrated by EBD in Fig. 6b. Further, $M2$ WF optimization is realized to obtain better device characteristics.

HM-HD-MOSFET and p-HM-HD-TFET are as depicted in Fig. 7. But in n-HM-HD-MOSFET OFF current reduces (Fig. 7a) tremendously as WF increases. This leads to increased V_{th}, reduced OFF current, and SS. Figure 8 explains the reason behind drain current variation on $M2$ optimization through EBD shift. Figure 8a shows that as $M2$ WF increases, potential barrier of n-HM-HD-MOSFET increases in ON and OFF states and, hence, current reduces. Figure 8b shows tunneling width slightly increases near source/channel region.

Unlike $M1$ WF optimization, $M2$ shows no or slight impact on n-HM-HD-TFET, p-source/channel region as $M2$ WF increases in p-HM-HD-TFET, and hence, current
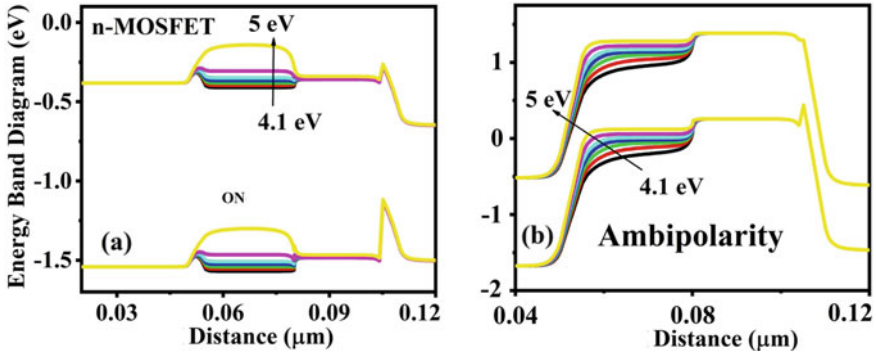
Fig. 6 EBD of *n*-DG-HM-HD-MOSFET in **a** ON state and **b** ambipolar state with *M*1 work function variations
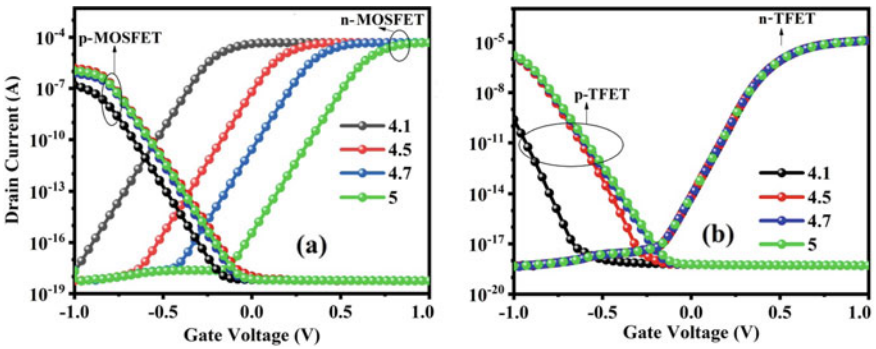

Fig. 7 Drain current of **a** DG-HM-HD-MOSFET and **b** DG-HM-HD-TFET with *M*2 work function variations
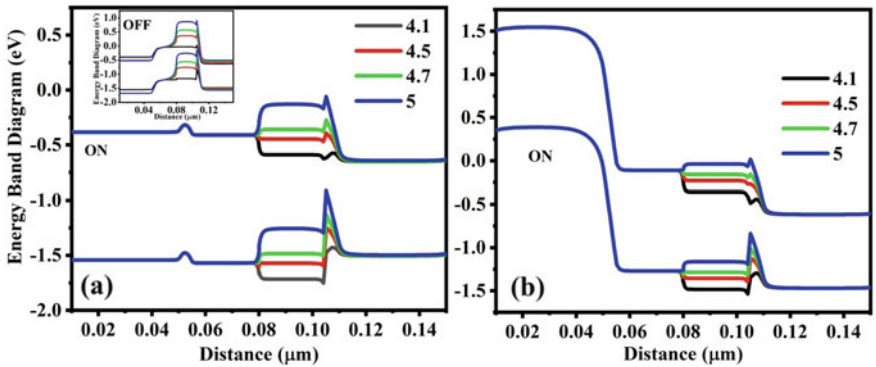

Fig. 8 EBD of **a** *n*-DG-HM-HD-MOSFET in ON state (inset: OFF state) and **b** *n*-DG-HM-HD-TFET in ON state with *M*2 work function variations
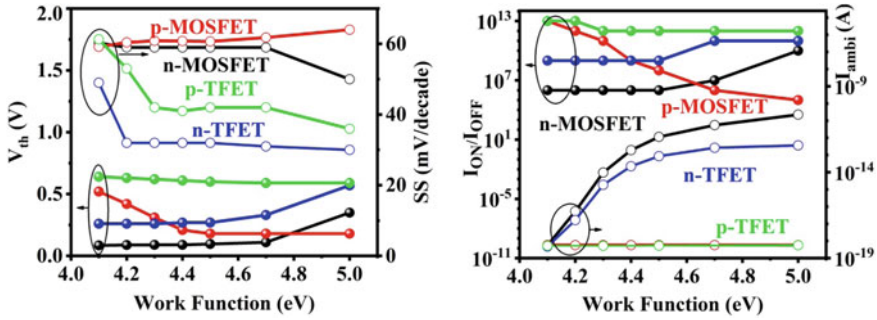
Fig. 9 **a** V_{th} and SS, and **b** I_{ON}/I_{OFF} ratio and ambipolar current I_{ambi} variation of DG-HM-HD-RFET with WFV

slightly enhances. As $M1$ variations show sound impact on device characteristics than $M2$ WF, only $M1$ variations are included in the manuscript to analyze other DC properties. Figure 9a and b show V_{th}, SS, $I_{ON} = I_{OFF}$ ratio, and ambipolar current (I_{ambi}) shift with WFV. It has been found that as V_{th} increases, I_{ON} current reduces and, hence, SS improves with increasing WF. TFET exhibits SS below 40 mV/decade while it is almost 60 mV/decade for MOSFET. $I_{ON} = I_{OFF}$ ratio improves in all FETs except in p-DG-HM-HD-MOSFET with increasing WF. Also, the device shows low ambipolarity for lower value of WF. Therefore, we have chosen 4.3 and 4.7 eV as the optimum WF values of $M1$ and $M2$, respectively, which provide electrical characteristics within the range of $I_{ON}/I_{OFF} = 10^6$–10^{12}, threshold voltage (V_{th}) = 0.12 − 0.62 V, and subthreshold swing (SS) = 32 mV/decade—61 mV/decade for four FETs. Table 2 compares DC characteristics among Si-HD-RFET, HM-HD-RFET [10], and DG-HM-HD-RFET, which illustrates that proposed RFET is a promising alternative for configurable device solutions.

3   Conclusions

Configurable devices are the need of time as many set of transistors can be obtained from single device and can be a promising replacement for low power design techniques such as multi-threshold architectures. Not only RFET reduces transistor count but configurable nature motivates infinite applications in the area of electronics and communication. However, conventional RFET possesses good and bad of both MOSFET and TFET. Especially, RFET performance is affected by high OFF current of MOSFET and low ON current of TFET and Schottky ambipolarity. Nevertheless, HM and HD improve RFET characteristics to some extent but a wide range of possibilities still exist. In this regard, we elaborately discussed dual gate approach in this paper. Single gate is replaced by two half gates, one near-drain-gate-metal ($M1$) and other near-source-gate-metal ($M2$). When WF optimization is done for

Table 2 Comparison of SI-RFET with HM-RFET, and HM-HD-RFET

Parameters	Si-HD-RFET [7]				HM-HD-RFET [7]				DG-HM-HD-RFET			
	n-MOSFET	p-MOSFET	n-TFET	p-TFET	n-MOSFET	p-MOSFET	n-TFET	p-TFET	n-MOSFET	p-MOSFET	n-TFET	p-TFET
V_{th} (V)	0.19	0.14	0.64	0.52	0.12	0.19	0.57	0.43	0.12	0.31	0.26	0.62
I_{ON} (mA/μm)	3.18×10^{-5}	4.52×10^{-7}	5.73×10^{-10}	1.6×10^{-9}	1.54×10^{-6}	4×10^{-8}	3.38×10^{-7}	1.3×10^{-7}	4.85×10^{-5}	1.3×10^{-6}	1.27×10^{-5}	2.8×10^{-6}
I_{OFF} (mA/μm)	1.2×10^{-11}	3.9×10^{-12}	8.8×10^{-18}	3.3×10^{-18}	2.8×10^{-13}	2.63×10^{-13}	7.2×10^{-20}	1.1×10^{-9}	3.2×10^{-11}	4.7×10^{-17}	6×10^{-15}	1.1×10^{-18}
I_{ON}/I_{OFF}	1.3×10^{6}	1.5×10^{5}	3.9×10^{8}	1.5×10^{9}	5.5×10^{6}	0.15×10^{6}	4.7×10^{12}	3.1×10^{12}	5.5×10^{6}	0.15×10^{11}	4.7×10^{10}	3.1×10^{12}
I_{ambi} (mA/μm)	6×10^{-12}	1.72×10^{-20}	8.5×10^{-13}	1.72×10^{-20}	6×10^{-12}	1.72×10^{-20}	8.5×10^{-13}	1.72×10^{-20}	1×10^{-14}	1.72×10^{-20}	1.8×10^{-15}	1.72×10^{-20}
SS (mV/decade)	60	60	34.3	31.3	60	62	49	40	59	61	32	42

$M1$ and $M2$, we found that varying $M1$ WF has greater impact on device characteristics and overall improvement has been noticed in all FETs. Finally, proposed DG-HM-HD-RFET characteristics are compared to that of the Si-HD-RFET and HM-HD-RFET, which confirms that the proposed device would be a breakthrough for future configurable system architectures.

References

1. Lundstrom M (2003) Science 299:210–211
2. Kahng D (1976) IEEE Trans Electron Devices 23:655–657
3. Kilby JS (2002) ChemPhysChem 2:482–489
4. Narenda SG (2005) J ACM J Emerg Technol Comput Syst 1:7–49
5. Mutoh S, Douseki T, Matsuya Y, Aoki T, Shigematsu S, Yamada J (1995) IEEE J Solid-State Circ 30(8):847–854
6. Bazarjani S, Mathe L, Yuan D, Hinrichs J, Miao G (2007) IEEE Bipolar/BiCMOS Circ Technol Meet
7. Rajan C, Samajdar DP (2020) IEEE Trans Electron Devices 67:5797–5803
8. Mikolajick T, Heinzig A, Trommer J, Baldauf T, Weber WM (2017) Semicond Sci Technol 32:043001
9. Zhang J et al (2014) IEEE Trans Electron Devices 61:3654–3660
10. Weber WM, Heinzig A, Trommer J, Grube M, Kreupl F, Mikolajick T (2014) IEEE Trans Nanotechnol 13:1020–1028
11. Simon M, Liang B, Fischer D, Knaut M, Tahn A, Mikolajick T, Weber WM (2020) IEEE Electron Device Lett 41:1110–1113
12. Kumar S, Singh KS, Nigam K, Tikkiwal VA, Chandan BV (2019) Appl Phys A 125:1–8
13. Yadav DS, Sharma D, Raad BR, Bajaj V (2016) Superlattices Microstruct 96:36–46
14. ATLAS Device Simulation Software, Silvaco Int. (2014) Santa Clara, CA, USA

Bandgap Tailoring of InAsBi for Long Wavelength Infrared Applications Using Density Functional Theory

Indranil Mal, Neelesh Jain, and Dip Prakash Samajdar

1 Introduction

Dilute Bismuth containing III-V semiconductors attracted the attention of Infrared (IR) researchers due to their promising structural and optoelectronic properties [1–3]. Having largest atomic size among group V, Bi offers a stronger spin–orbit coupling energy (Δ_{SO}) to accomplish resonant condition ($E_g > \Delta_{SO}$) in III-V-Bismides, which helps to diminish the notable efficiency concern in IR optoelectronic devices triggered by Auger recombination. Bi impurity causes the interaction between valence p orbital of host and Bi-p orbital energy, consequently splitting up all the valence sub-bands, namely Heavy Hole (HH), Light Hole (LH), and Spin Orbit splitting (SO) into $E_{HH/LH/SO+}$ and $E_{HH/LH/SO-}$ sub-bands, thereby initiating the valence band-edge upheave with respect to the host. This leads to the reduction in bandgap and substantial increase in Δ_{SO}. Although bandgap reduction rate per mole fraction of Bi in III-V-Bismides is less than that of III-V-Nitrides, III-V-Bismides provide several advantages like increased temperature insensitivity of the energy band gap and improved carrier mobility due to small perturbation in conduction band. Larger sized Bi increases the Δ_{SO} so that III-V-Bismides become favorable candidates for spintronic applications [4]. Fang et al. have tried to grow dilute ($\leq$2.3%) Bi containing InAsBi epi-layer over InAs substrate using Organometallic Vapor Phase Epitaxy (OMVPE) method at a low temperature and low pressure, where they have reported that the lattice constant increases nonlinearly and bandgap reduces at a rate about 55 meV/Bi% [5–7]. Another low pressure Metalorganic Vapor Phase Epitaxy (MOVPE) attempt was reported by Okamoto et al., where they have grown InAsBi layer with comparatively greater Bi concentration (3–4%). They have reported that

I. Mal · N. Jain · D. P. Samajdar (✉)

Department of Electronics and Communication Engineering, PDPM Indian Institute of Information Technology, Design and Manufacturing, Jabalpur, India
e-mail: dip.samajdar@iiitdmj.ac.in

due to the higher value of Bi impurity concentration, the droplet like surface was formed, which degrades the material quality [8, 9].

In this work, we have thoroughly studied the structural, electronic and optical properties of pristine InAs and also observed the effect of Bi doping on the structural, optical, and electronic properties of InAs by considering the FP-LAPW basis set and PBEsol XC functional and mBJ XC potential as implemented in WIEN2K and VBAC model.

2 Computational Details

To execute the first principles calculation, we have considered FP-LAPW as the basis set, PBEsol [10] as the XC functional, and mBJ [11] as the XC potential as considered in WIEN2k package [12]. We have considered this particular XC and XC potential to address the low bandgap of InAs after studying other potentials. However, it is also evident from literatures that the mBJ potentials can offer a precise accuracy for narrow bandgap materials. F-43 m space group has been taken into account for the structural optimization, and a separation energy of -7.0 Ry is considered to distinguish between the core and valence states of the InAs and InAsBi. In case of In and As, we have taken the orbitals beyond 4s orbital energy as the valence states. For comparatively smaller sized As, the Muffin-Tin (MT) radius is considered as 2.0 and 2.5 a.u. for larger atomic sized In. A super fine k-mesh ($10 \times 10 \times 10$) is considered to extent the Brillouin zone (BZ) uniformly. Two different set of cutoff energy (0.1, 10 μRy) and cutoff charge (0.1, 1μ e) are chosen for the convergence condition required for the structural optimization and optoelectronic property calculations, respectively. In order to study the incorporation effect of Bi impurity into InAs, we have taken a 2 $\times$ 2 $\times$ 2 super cell containing 64 Indium atoms and 64 Arsenic atoms and substitute the Arsenic atom with Bismuth, where each Bismuth atom substitution results in an impurity concentration of 3.1%. To perform the VBAC calculation, we have taken 8 band and 14 band Hamiltonian $H_{14 \times 14}$ shown in Eq. 1, which consists of the host Hamiltonian (H8 $\times$ 8), the impurity (H_{Bi}), and coupling matrix components (V_{Bi}) and the formulation of these Hamiltonian is thoroughly discussed in our previous works [13–15].

$$H_{14 \times 14} = \begin{bmatrix} H_{8 \times 8} & V_{Bi(8 \times 6)} \\ V_{Bi(6 \times 8)} & H_{Bi(6 \times 6)} \end{bmatrix} \tag{1}$$

3 Results and Discussions

In order to accomplish the structural stability of InAs and InAsBi, the total energy of the unit cell and supercell has been evaluated by considering very sharp convergence

Table 1 Equilibrium lattice constant and bulk modulus of InAs$_{1-x}$Bi$_x$

Bi concentration (%)	Lattice constant (Å)	Bulk modulus (GPa)
0	6.0902[a], 6.092[c], 6.091[d]	56.7781[a], 58[b], 57.17[c], 54.99[d]
0.031	6.103[a], 6.116[c]	55.6259[a], 55.84[c]
0.062	6.144[a], 6.142[b]	54.2395[a]
0.093	6.152[a], 6.157[c]	54.3014[a], 54.08[c]

[a]This work, [b]Exp. Massidda et al., [c]Asali et al., [d]Hadjab et al.

condition for both energy(1 μRy) and charge (10 μe) accordingly, which is very essential to compute the desired optoelectronic properties of the material. Computed total energy values of a InAs unit cell are closely fitted with the quadratic polynomial function of volume of unit cell, which yields optimized lattice constant of InAs as 6.090 Å. This is very much consistent with the experimental value of lattice constant of InAs (6.050 Å) [16] compared to the previously reported theoretical studies (6.2, 6.092, 6.091, 5.956 Å) [17–20]. We have computed the equilibrium lattice constant and bulk modulus of InAsBi as a function of Bismuth impurity and matched with previously reported [17–20] results enlisted in Table 1. It can be concluded from the data that upon increasing the Bismuth concentration, the lattice constant increases which can be accredited to the larger size of Bismuth. However, the atomic radius mismatch between the Bismuth and Arsenic atom causes the decrement in bulk modulus of InAsBi compared to InAs. Taking into account the optimized structural parameters as input, we have anticipated the electronic properties such as band diagram, and carrier effective mass of InAs and InAsBi using both DFT and VBAC theory. Figure 1 shows the comparative investigation of band diagram of InAs (a) and InAs$_{0.969}$Bi$_{0.031}$ (b) along 100 crystallographic direction, calculated using DFT (solid line) and VBAC model (line + symbol), respectively.

It can be noted from the figure that most of the significant sub-bands E_C, E_{hh}, E_{lh}, E_{so} are consistent along 100 direction for both DFT and VBAC calculation. Nevertheless, the DFT calculation under estimates the value of bandgap compared to the semi-empirical VBAC method and they are quite aligned with each other. Incorporation of Bi results in reduction of bandgap for InAs$_{1-x}$Bi$_x$ from 0.48419 to 0.2036 for a variation Bi concentration from 0 to 9.3%, which can be attributed to the large bandgap bowing value of Bi impurity in InAs. Along with the band reduction, Bi impurity helps to enhance the Δ_{SO} with a rate of 18.35 meV/%Bi, which will mitigate the Auger like nonradiative recombinations in the optoelectronic devices. We have enlisted (Table 2) our anticipated values of bandgap for wide variation of Bi concentration starting from 0 to 9.3% and also compared with available previously reported [17, 20, 21] results. Our calculated bandgap values of InAs$_{1-x}$Bi$_x$ are quite aligned with the experimental results compared to previously reported theoretical studies [17–20]. In order to analyze the transport properties of the materials, effective mass plays a pivotal role, and helps in the computation of the effective mass of the charge carriers along the crystallographic symmetric directions, which is directly
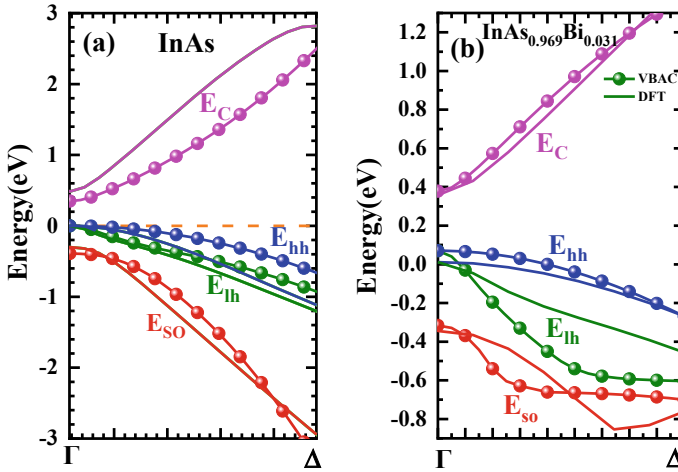
Fig. 1 Comparative study of the electronic band diagram of pristine InAs (**a**) and InAs$_{0.969}$Bi$_{0.031}$ (**b**) calculated using DFT and VBAC in direction Δ (100)

Table 2 Comparison of our calculated results with previously reported bandgap of InAs$_{1-x}$Bi$_x$

Bi concentration (%)	Bandgap (eV)
0	0.48419[a], 0.417[b], 0.6[c], 0.417[d], 0.615[e], 0.7[f], 0.295[g], 0.312[h]
3.1	0.34671[a], 0.31136[b], 0.506[c], 0.23[i]
6.25	0.28358[a], 0.21301[b], 0.425[c]
9.3	0.20361[a], 0.1044[b], 0.316[c]

[a]DFT, [b]VBAC, [c]Asali et al., [d]Vurgaftman et al., [e]Hadjab et al., [f]Briki et al., [g]Sandall et al., [h]Fang et al., [i]Okamata et al.

controlled by the curvature and anisotropy of sub-bands. Here, we have calculated the effective mass of the charge carriers corresponding to conduction and valence (HH, LH, and SO) band along 100 direction of InAsBi as a function of Bismuth impurity concentration considering both DFT and VBAC methods presented in Fig. 2. It can be noted from the figure that upon increasing the Bi impurity concentration, unlike the effective mass related to the SO sub-band, effective masses of other bands decreases gradually, which leads to the increment in charge carrier mobility and opens up the possibility of using InAsBi in the high carrier mobility device application. It can also be noted from figure that our anticipated value of effective masses is in a good agreement with previously reported studies [17, 22]. The computed electronic properties such as bandgap and effective mass serve as input to anticipate the optical properties of the material. Here, we have computed one of the most significant optical properties, the absorption coefficient of InAs$_{1-x}$Bi$_x$, which is a function of the complex dielectric function as shown in Fig. 3. It is evident from the figure that higher Bi impurity concentration leads to a red shift in the optical absorption spectra, which is very
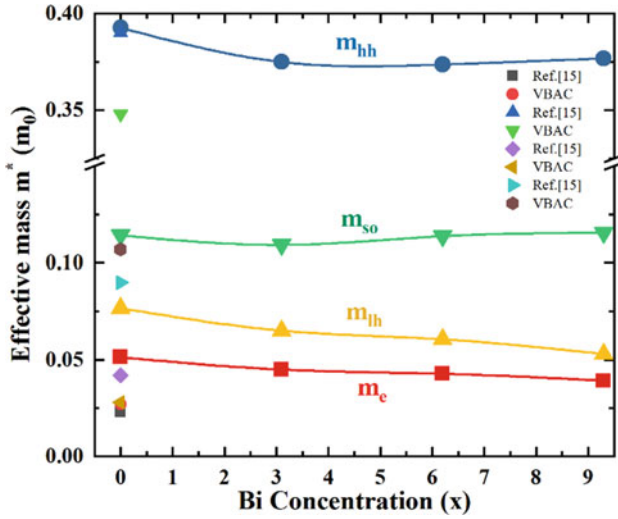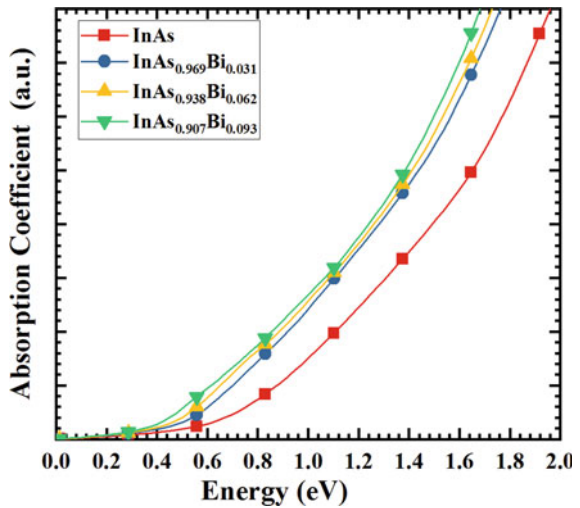
Fig. 2 Variation of effective masses of InAsBi along the Δ direction as a function of Bi concentration

Fig. 3 Bi impurity concentration dependent parametric variation of optical absorption spectra of $InAs_{1-x}Bi_x$ as a function of photon energy

consistent with the Bi-induced bandgap reduction nature in $InAs_{1-x}Bi_x$ and can also be observed from the Table 2. This Bi-induced redshift in absorption spectra opens up the possibility of using InAsBi in the >3 μm infrared communication window.

4 Conclusions

Taking into consideration the GGA-PBEsol XC functional and mBJ XC potential, we have anticipated the optimized structural and electronic and optical properties of ZB phase InAs. We have witnessed the effect of Bi incorporation on the structural and optoelectronic properties of InAs. Additionally, we have evaluated all the optoelectronic properties of InAs and InAsBi using 8 band and 14 band **k·p** Hamiltonian and compared with the DFT computed results. Owing to larger size of Bi, it increases the lattice constant of InAs and reduces the bandgap, which is further reflected in the form of redshift in the optical absorption spectra. In addition to these, Bi incorporation offers an ample amount of enhancement in Δ_{SO} of InAs, which will help to mitigate several nonradiative recombinations like Auger recombination. This leads to dramatic improvement in the quantum efficiency of InAsBi based LWIR optoelectronic devices. Overall, our calculated structural and optoelectronic properties of pristine InAs and Bi impurity containing InAsBi are in a good agreement with previously reported theoretical and experimental studies.

References

1. Ferhat M, Zaoui A (2006) Do all III-V compounds have the zinc-blende or wurtzite ground state structure? Appl Phys Lett 88:161902. https://doi.org/10.1063/1.2196050
2. Wang SQ, Ye HQ (2003) First-principles study on elastic properties and phase stability of III–V compounds. Phys status solidi 240:45–54. https://doi.org/10.1002/pssb.200301861
3. Samajdar DP, Dhar S (2014) Valence band structure of In[As.sub.1-x][Bi.sub.x] and in[Sb.sub.1-x][B.sub.ix] alloy semiconductors calculated using valence band anticrossing model. Sci World J 14
4. Song Z, Bose S, Fan W, Zhang DH, Zhang YY, Li SS (2017) Quantum spin hall effect and topological phase transition in InNxBiySb1-x-y/InSb quantum wells. New J Phys 19. https://doi.org/10.1088/1367-2630/aa795c
5. Fang ZM, Ma KY, Cohen RM, Stringfellow GB (1990) Photoluminescence of InAsBi and InAsSbBi grown by organometallic vapor phase epitaxy. J Appl Phys 68:1187–1191. https://doi.org/10.1063/1.346715
6. Ma KY, Fang ZM, Cohen RM, Stringfellow GB (1991) Investigation of organometallic vapor phase epitaxy of InAs and InAsBi at temperatures as low as 275°C. J Appl Phys 70:3940–3942. https://doi.org/10.1063/1.349204
7. Ma KY, Fang ZM, Cohen RM, Stringfellow GB (1992) Ultra-low temperature OMVPE of InAs and InAsBi. J Electron Mater 21:143–148. https://doi.org/10.1007/BF02655829
8. Okamoto H, Oe K (1998) Growth of metastable alloy InAsBi by low-pressure MOVPE. Japanese J Appl Phys Part 1 Regul Pap Short Notes Rev Pap 37:1608–1613. https://doi.org/10.1143/jjap.37.1608
9. Okamoto H, Oe K (1999) Structural and energy-gap characterization of metalorganic-vapor-phase-epitaxy-grown InAsBi. Japanese J Appl Phys Part 1 Regul Pap Short Notes Rev Pap 38:1022–1025. https://doi.org/10.1143/jjap.38.1022

10. Perdew JP, Burke K, Ernzerhof M (1996) Generalized gradient approximation made simple. Phys Rev Lett 77:3865–3868. https://doi.org/10.1103/PhysRevLett.77.3865
11. Tran F, Blaha P (2009) Accurate band gaps of semiconductors and insulators with a semilocal exchange-correlation potential. Phys Rev Lett 102:226401. https://doi.org/10.1103/PhysRevLett.102.226401
12. Blaha P, Schwarz K, Madsen GK, Kvasnicka D, Luitz J (2001) WIEN2k: an augmented plane wave+ local orbitals program for calculating crystal properties. Vienna University of Technology, Austria
13. Mal I, Panda DP, Tongbram B, Samajdar DP, Chakrabarti S (2018) Analytical modeling of temperature and power dependent photoluminescence (PL) spectra of InAs/GaAs quantum dots. J Appl Phys 124:145701. https://doi.org/10.1063/1.5047026
14. Mal I, Jayarubi J, Das S, Sharma AS, Peter AJ, Samajdar DP (2018) Hydrostatic pressure dependent optoelectronic properties of InGaAsN/GaAs spherical quantum dots for laser diode applications. Phys Status Solidi. https://doi.org/10.1002/pssb.201800395
15. Mal I, Samajdar DP, Das TD (2017) Effect of Sb and N resonant states on the band structure and carrier effective masses of GaAs1-x-yNxSby alloys and GaAs1-x-yNxSby GaAs quantum wells calculated using k·p Hamiltonian. Superlattices Microstruct 106:20–32. https://doi.org/10.1016/j.spmi.2017.03.035
16. Hadjab M, Berrah S, Abid H, Ziane MI, Bennacer H, Yalcin BG (2016) Full-potential calculations of structural and optoelectronic properties of cubic indium gallium arsenide semiconductor alloys. Optik (Stuttg). 127:9280–9294. https://doi.org/10.1016/j.ijleo.2016.07.018
17. Shalindar AJ, Webster PT, Wilkens BJ, Alford TL, Johnson SR (2016) Measurement of InAsBi mole fraction and InBi lattice constant using Rutherford backscattering spectrometry and X-ray diffraction. J Appl Phys 120. https://doi.org/10.1063/1.4964799
18. Webster PT, Shalindar AJ, Riordan NA, Gogineni C, Liang H, Sharma AR, Johnson SR (2016) Optical properties of InAsBi and optimal designs of lattice-matched and strain-balanced III-V semiconductor superlattices. J Appl Phys 119. https://doi.org/10.1063/1.4953027
19. Assali A, Bouslama M, Reshak AH, Chaabane L (2017) Highly desirable semiconducting materials for mid-IR optoelectronics: dilute bismide InAs1−xBix alloys. Mater Res Bull 95:588–596. https://doi.org/10.1016/j.materresbull.2017.06.011
20. Polak MP, Scharoch P, Kudrawiec R (2015) First-principles calculations of bismuth induced changes in the band structure of dilute Ga-V-Bi and In-V-Bi alloys: chemical trends versus experimental data. Semicond Sci Technol 30:94001. https://doi.org/10.1088/0268-1242/30/9/094001
21. Assali A, Bouslama M, Chaabane L, Mokadem A, Saidi F (2017) Structural and opto-electronic properties of InP1−xBix bismide alloys for MID−infrared optical devices: A DFT + TB-mBJ study. Phys B Condens Matter 526:71–79. https://doi.org/10.1016/j.physb.2017.09.058
22. Polak MP, Scharoch P, Kudrawiec R (2015) First-principles calculations of bismuth induced changes in the band structure of dilute Ga-V-Bi and In-V-Bi alloys: chemical trends versus experimental data. Semicond Sci Technol 30:094001. https://doi.org/10.1088/0268-1242/30/9/094001

Synthesis of Nanoparticles via Pulsed High-Power Laser in Liquid

Arpita Nath, Prahlad K. Baruah, and Alika Khare

1 Introduction

Since the beginning of the twenty-first century, pulsed laser ablation in liquid has emerged as an excellent method for the synthesis of nanoparticles (NPs) with excellent properties [1–3]. The pioneering work in this direction was reported by Patil et al. in 1987 [4]. In their work, synthesis of metastable phase of iron oxides was reported by the ablation of an iron target immersed in water. In laser ablation in liquid, the strong confinement of the plasma by the ambient liquid produces a region of very high pressure of the order GPa or even more [2]. It was reported by Fabbro and his co-workers that during the initial process of laser heating, the pressure that is generated at the solid–liquid interface is nearly about ten times more than that obtained in the presence of gaseous surrounding [5]. In the last two decades, there has been a remarkable increase in the synthesis of NPs by the method of pulsed laser ablation in liquid (PLAL) [6–8]. The simplicity and the versatility that is associated with the method of PLAL has contributed to the ever-increasing interest in the synthesis of NPs via PLAL.

Following the pioneering work by Patil et al. exhaustive work using PLAL has been carried out to synthesize metal, semiconductor, metal oxide, alloys, and core–shell nanoparticles using pulsed laser ablation at solid–liquid interface [9–23]. The pulsed laser ablation in liquid is a one-step, chemically clean process with no byproducts and can be performed without surfactants. Despite the fact that the experiments

A. Nath
Department of Physics, National Institute of Technology Meghalaya, Meghalaya, India

P. K. Baruah
Department of Physics, School of Technology, Pandit Deendayal Energy University, Gandhinagar, India

A. Khare (✉)
Department of Physics, Indian Institute of Technology Guwahati, Guwahati, India
e-mail: alika@iitg.ac.in

are performed at room temperature conditions, the metastable phases due to plasma high pressure and high temperature of plasma can be synthesized. There is flexibility in the choice of target and surrounding liquid and so wide possible combination of nanoparticles can be generated [2]. There are numerous reports on the metastable phases using PLAL [9, 13, 14]. Parallel to synthesis and characterization of nanoparticulates, theoretical analysis for nucleation of nanoparticles produced via laser ablation in liquids were also carried out [24]. In the same time frame, the experiments on Ag and Au nanoparticles were performed [10, 11]. This lead to the investigation on photo fragmentation of nanoparticles during PLAL. The controlling parameters in laser ablation processes were: laser fluence, laser wavelength, duration of pulses, and ambient medium for tuning the nanoparticle traits [25–27]. Successively, the composites and core–shell from various metal oxide: TiO_2, ZnO, NiO, etc.; were reported [19–22, 28]. Eventually, experiments on PLAL expanded to different horizons involving applicability of nanoparticles, upgrading the laser ablation methodology and theoretical research on the nucleation dynamics and its corroboration with mechanical counterpart—cavitation bubbles. In the present era, the PLAL has been improvised for fabrication of functional nanomaterials used in biomedicine and as green energy resources. The Au nanoparticles are known for being biomedical applications. As resource for green energy, CdSe and CoO nanoparticles applied in supercapacitors for energy conservation, the functionality of synthesized nanomaterial has been tested for solar cells and solar-water splitting [29]. Further, there are reports of nanomaterials synthesized from PLAL being used as photocatalyst, antibacterial agents, luminescent materials, electrocatalysis, electrochemical detectors, and as SERS probe [30–36]. The mechanical effects in PLAL attributed to cavitation bubbles and its impact onto the nucleation dynamics is still very unclear. Also, forceful ejection of early plasma constituents into ambient liquid medium occurs [37–40]. In spite of exploration in the commercial aspects of these synthesized nanoparticulates, there is an acute paucity of information in knowing the nucleation dynamics and the cavitation bubble phenomena and its possible correlation. This eventually plays predominant role in tailoring the nucleation phenomena and synthesis of metastable phases or alloys of promising nanoparticles.

In view of above, this chapter highlights the nucleation and growth dynamics of conventional as well as metastable phases of the synthesized nanoparticles of titanium oxide using PLAL. In order to demonstrate the flexibility of the PLAL technique as well as the dependence of the properties of NP on the laser energy, another example of Ag nanoparticles is also presented. The commercial utility of the synthesized nanoparticles using PLAL in detail is covered at the end.

2　Nucleation Dynamics

The physical processes involved toward the synthesis of nanoparticles via laser interaction at the solid liquid surface are very complex. Simultaneously, the shape, size, and phase of the nanoparticles are highly sensitive to the experimental conditions as

well as complete thermodynamics of the system as a whole. In this section, the theory of nucleation growth process is briefly described along with experimental validation on the titanium oxide nanoparticles generated via PLAL technique.

2.1 Theory of Nucleation and Growth

For nucleation of nanoparticles via PLAL, the model based on metastable phases: nanodiamonds is considered [24]. This model has been extended to laser-induced breakdown at titanium-water interface to investigate the nucleation dynamics of corresponding titanium oxide nanoparticles [41].

The time τ taken for nucleation can be expressed by Eq. (1) [24].

$$\tau = \sqrt{2\pi m k T} \frac{kT\gamma}{p_s(T)(\Delta\mu)^2}; \quad \Delta\mu = \frac{\Delta V(p - p_s(T))}{V_m N_A} \tag{1}$$

$m, k, \gamma, p_s(T), \Delta\mu, \Delta V, V_m$ are TiO$_2$ mass, Boltzmann's constant, surface energy, the saturated vapor pressure, chemical potential difference, the molar volume difference, the molar volume, and N_A being Avogadro constant.

Erying's Formalism gives the expression for nanoparticle growth velocity V_{np} which involves cross play of number of clusters entering the nucleus J_{LN} and the liquid J_{NL} per unit time [42]. The symbol d being the lattice parameter. Taking into account the possibilities of growth of metastable phases of TiO$_2$ via PLAL, the lattice constant associated to TiO$_2$ II (metastable phase) was taken into consideration [43, 44].

$$V_{np} = d(J_{LN} - J_{NL});$$
$$J_{LN} = \frac{kT}{h} \exp\left(\frac{-E_b}{kT}\right); J_{NL} = \frac{kT}{h} \exp\left(\frac{-(E_b + \Delta\varphi)}{kT}\right) \tag{2}$$

$$V_{np} = d\nu \exp\left(\frac{-E_b}{kT}\right)\left[1 - \exp\left(\frac{-\Delta\Phi}{kT}\right)\right] \tag{3}$$

The parameter h represents the Planck's constant, E_b resembles the activation energy, and $\Delta\Phi$ is the difference of free energy. The growth velocity V_{np} when expressed in molar units $\Delta\Phi = \frac{\Delta G^{nuc}}{N_A}, E_b = \frac{E_a}{N_A}, \nu = \frac{kT}{h}$ is given by Eq. (4). For Eq. (4), υ is the vibrational frequency and R is gas constant, $\Delta g_m = -RT \ln \frac{p}{p_s(T)}$ is known as Gibbs free energy difference/mole.

$$V_{np} = d\nu \exp\left(\frac{-E_a}{RT}\right)\left[1 - \exp\left(\frac{-|\Delta g_m|}{RT}\right)\right] \tag{4}$$

Finally, the dimension of nanoparticles (s_{np}) is taken from V_{np} (growth velocity), critical radius $r*$, and the laser pulse duration ($\tau_d = 6$ ns).

$$s_{np} = V_{np}(2\tau_d - \tau) + 2r*;$$

$$r* = 2\gamma \frac{\left(\frac{2}{3} + \frac{V_m}{\Delta V}\right)}{p_s(T) - p} \tag{5}$$

2.2 Nucleation Dynamics of Titanium Oxide Nanoparticles

The evidence of formation of high pressure metastable phase and validating information of extreme pressure up to 18 GPa provokes the investigation onto the nucleation of high pressure phases of titanium oxide nanoparticles [45]. The pressure–temperature (P–T) diagram from Rutile (R)—TiO$_2$ II (α-PbO$_2$) where the phase boundary is in the domain of PLAL as shown in Fig. 1 [46, 47].

The transition from rutile to TiO$_2$ II phase is probed. The saturated vapor pressure p_s (T) is taken from Fig. 1. The nucleation time varying with pressure for the formation of Titanium Oxide nanoparticles is shown in Fig. 2.

From P–T diagram; for 1473 K (Figs. 1 and 2a), the phase transition from Rutile-TiO$_2$ II occurs at ~9 GPa. The regimes less than 9 GPa attributed to the rutile phase of TiO$_2$ [TiO$_2$ (R)] and greater than 9 GPa is the TiO$_2$ II phase. At 3773 K, titanium
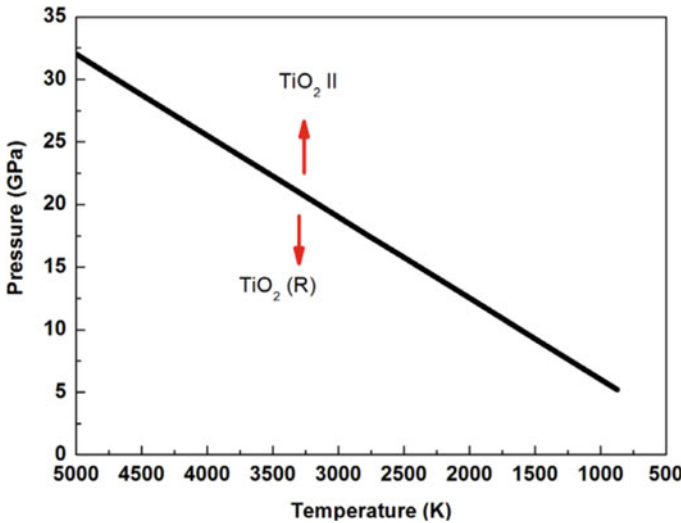

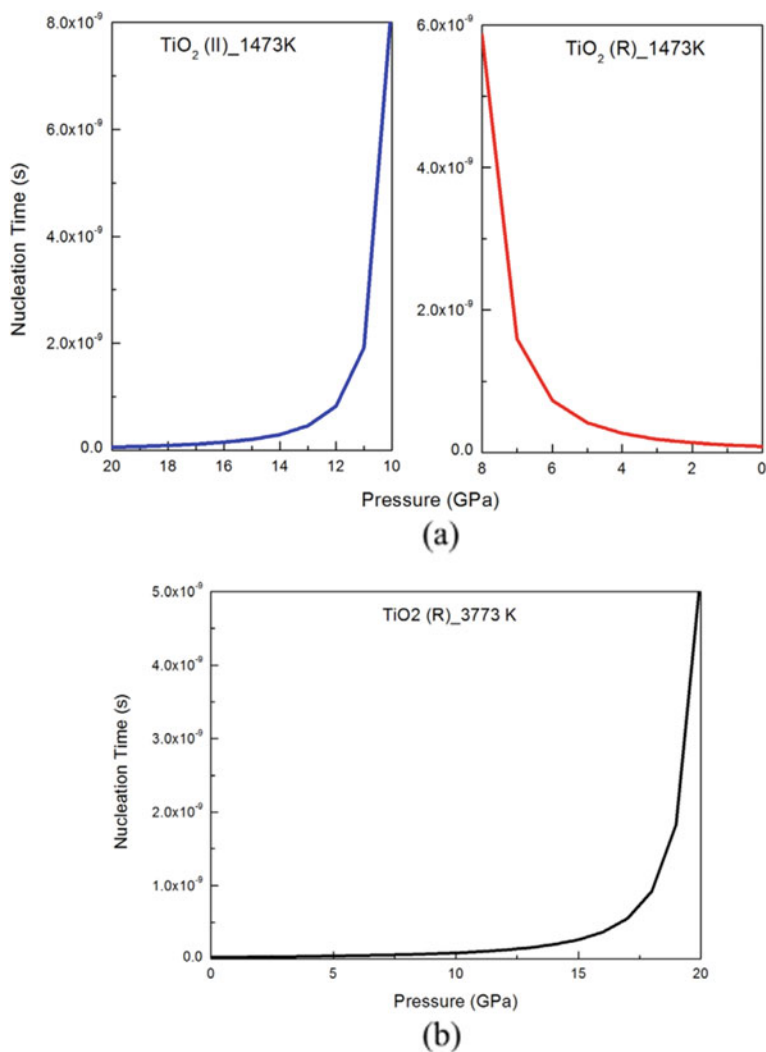**Fig. 1** Pressure–temperature (P–T) diagram [46, 47]

Fig. 2 Nucleation time with pressure. **a** 1473 K and **b** 3773 K [41]

oxide in rutile phase is expected with reference to the *P–T* diagram till 20 GPa (Fig. 2b).

The nanoparticle dimensions are shown in Fig. 3 at temperature of 3773 K for TiO_2 (*R*) phase. The nanoparticle size in the range 2773–873 K is shown in Fig. 4. Figure 4a predicts the particle statistics for TiO_2 (II); whereas, Fig. 4b corresponds to the particle statistics for TiO_2 (*R*).
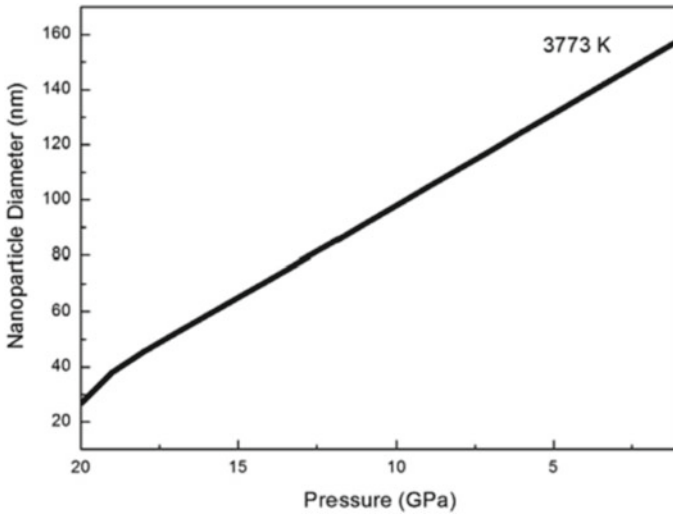
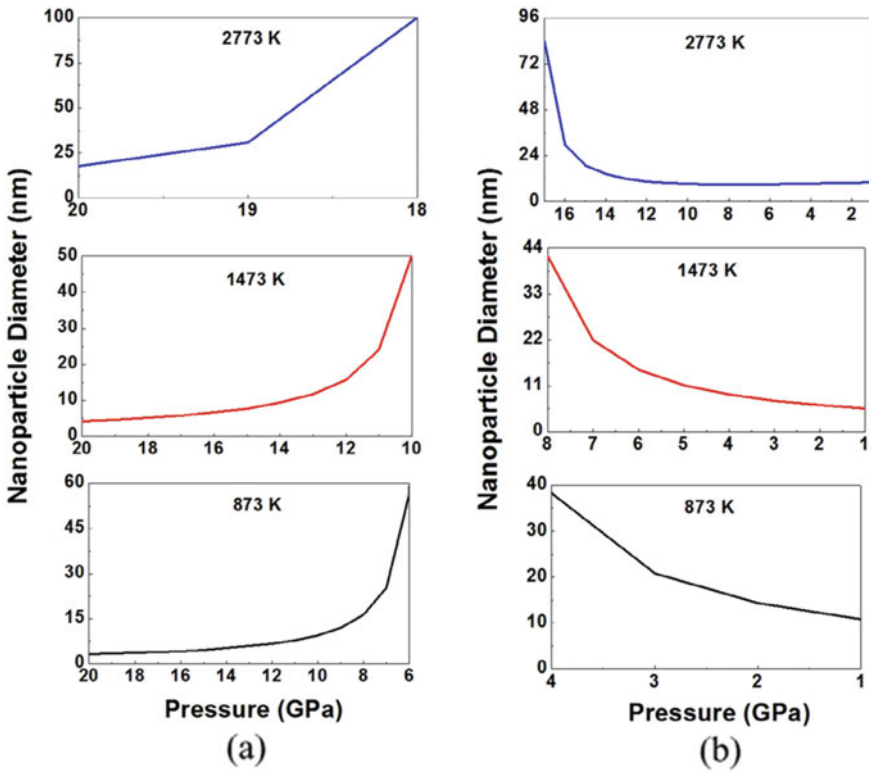**Fig. 3** Variation in nanoparticle statistics at 3773 K [41]

Fig. 4 Variation in nanoparticle sizes with pressure. **a** TiO_2 (II) and **b** TiO_2 (R) [41]

2.3 Experimental Validation of Nucleation Dynamics

The selected area electron diffraction (SAED) pattern of nanoparticles using PLAL at titanium-water interface is presented in Fig. 5a. The lattice parameter, "d" is found to be 0.37 nm ([012] $TiO_{1.5}$), 0.32 nm ([110]TiO_2 (R)), [110]0.25 nm ($TiO_{1.5}$), 0.21 nm ([102], TiO_2 II), 0.17 nm ([116] $TiO_{1.5}$), and 0.13 nm ([02$\bar{3}$] TiO_2II). This confirms formation of orthorhombic TiO_2 II (metastable) having α-PbO_2 like structure, rutile, and titanium oxide nanoparticles with vacancies [43, 44]. The nanoparticle sizes are in the range of 3–180 nm as shown in Fig. 5a and c. The Raman spectrum is depicted in Fig. 5d. The Raman peaks are from the rutile phase of TiO_2. Peaks at 172 and 263 cm^{-1} resemble, however, high-pressure metastable phases of TiO_2 II [48, 49].
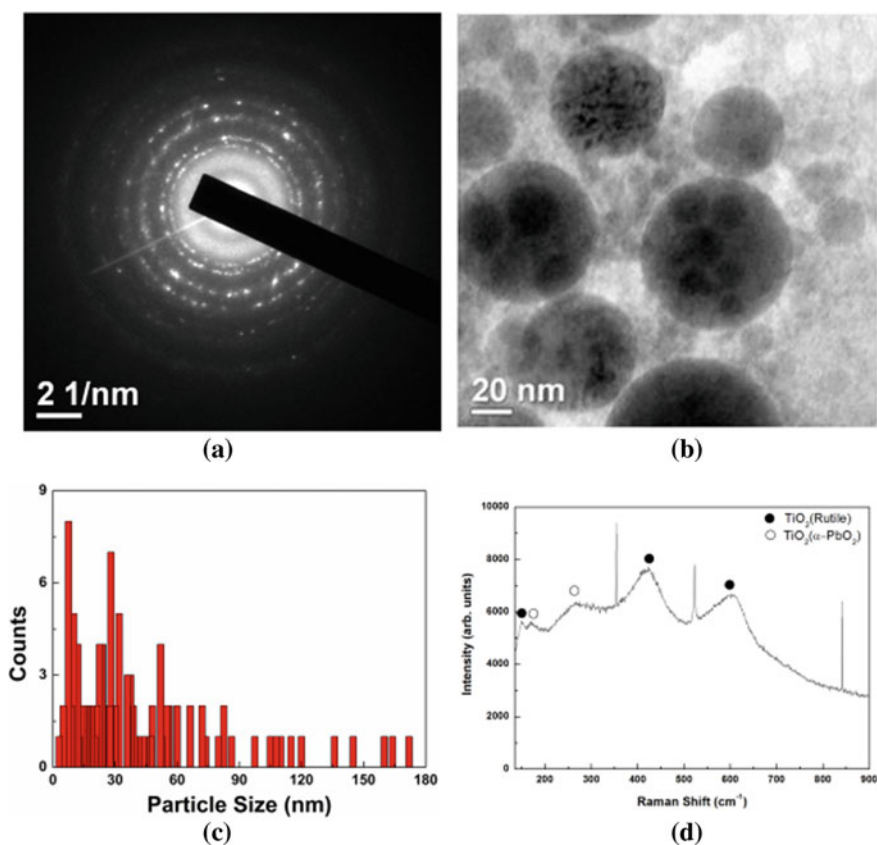

Fig. 5 **a** Selected area electron diffraction, **b** Nanoparticle sizes, **c** statistical counts of nanoparticle, and **d** Laser Raman spectrum [41]

3 Synthesis of Ag Nanoparticles Using PLAL

Considering the significance of functional activity of NPs using PLAL, the current section devotes onto the synthesis of NPs in liquids by pulsed laser ablation of Ag target. The ablation conditions are altered by varying the input laser parameters and the characteristics traits of the NPs are discussed in this section.

NPs of Ag were synthesized by irradiating a pulsed laser beam onto an Ag target immersed in water. For ablation, a Q-switched Nd: YAG laser beam ($\lambda = 532$ nm) was focused by a 25 cm focal length lens onto the target. The Ag target was continuously translated to avoid its drilling during the ablation process. Ag NPs were synthesized at three different incident laser energies of 30, 50, and 70 mJ, and the ablation time was fixed at 30 min to study the effect of the incident energy onto the characteristics of the Ag NPs.

The TEM images of the samples of Ag NPs are depicted in Fig. 6a–c, respectively. For the three input energies, the average size of the synthesized NPs is approximately 15, 13, and 10 nm, respectively.

The analysis of the diffraction patterns is carried out to unveil the features of the NPs. For the input energies of 30, 50, and 70 mJ, the diffraction patterns are shown in Fig. 7a–c, respectively. For the 30 mJ, the d-values of the synthesized sample are calculated to be 0.35, 0.33, 0.23, 0.20, and 0.15 nm. These values correspond to hkl-planes Ag_2O_3 (110), Ag_2O (110), Ag (111), Ag (200), and AgO (220), respectively. For incident laser energy of 50 mJ, the d-values of 0.35, 0.29, 0.22, 0.18, 0.14, and 0.12 nm corresponds to Ag_2O_3 (110), AgO (110), AgO (20 $\bar{2}$), AgO (112), Ag (220), and Ag (311), respectively. Finally for 70 mJ, the d-values of 0.35, 0.24, 0.20, 0.15, 0.13, and 0.11 nm correspond to Ag_2O_3 (110), AgO (200), Ag (200), AgO (220), Ag_2O (112), and AgO (51 $\bar{2}$) planes, respectively. Hence, diffraction study confirms that the synthesized samples consist of pure Ag as well as its various oxide phases.
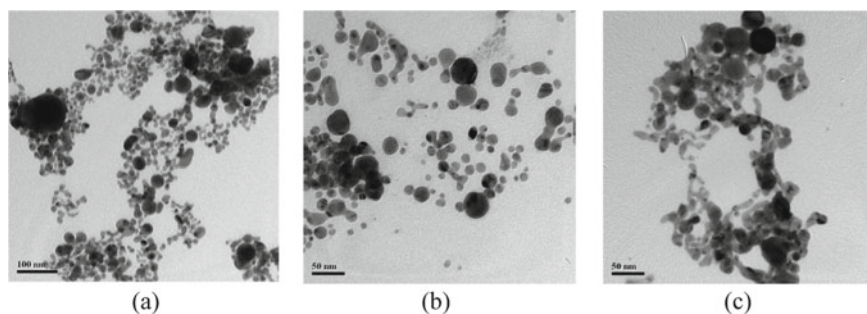

Fig. 6 TEM image of the Ag NPs synthesized at laser energy of **a** 30 mJ, **b** 50 mJ, and **c** 70 mJ [50]
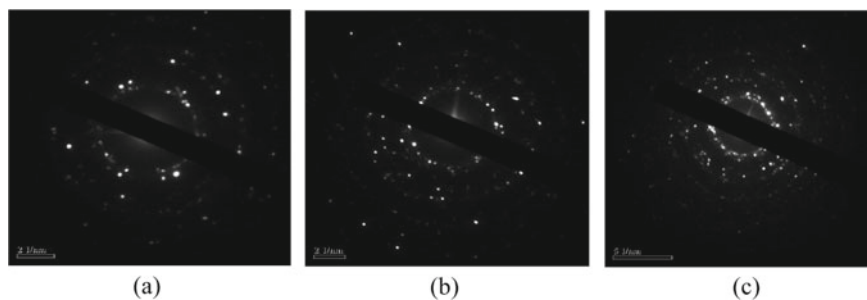
Fig. 7 The SAED patterns of the Ag NPs at **a** 30 mJ, **b** 50 mJ, and **c** 70 mJ [50]

4 Commercial Utility of Nanoparticles Synthesized via PLAL

Metallic NPs like Ag and Cu are being used extensively in many applications [51–56]. The surface plasmon resonance (SPR) property of metallic NPs have led to its successful implementation in many plasmonic applications [57, 58]. The application of Ag NPs includes its use as plasmonic sensors, surface enhanced Raman scattering (SERS) substrates, photocatalytic sensors, etc. [59–61]. Ag NPs are also found to behave as excellent antimicrobial agents [62]. The antimicrobial property of these NPs have already been used in the health and textile industry [62, 63]. Cu is also a very important plasmonic element and NPs of Cu as well as its oxide is finding applications as SERS substrates, as photocatalysts, in solar cells, etc. [8, 51, 53, 64]. Like Ag, NPs of Cu are also found to exhibit antibacterial properties [65–67].

Such NPs have been synthesized using various techniques like physical, chemical, biological, etc. [68–70]. Among all these techniques, pulsed laser ablation in liquid (PLAL) is one of the easiest and most convenient methods for the synthesis of NPs [1, 6]. The absence of any chemical reagent in PLAL makes the NPs synthesized via this technique extremely pure and stable. Purity and stability of the NPs are very important criteria for the optimum utilization of the NPs. This along with the various laser parameters which can be varied in PLAL has led to the technique being increasingly used at the global level with great success [71]. As NPs of any solid material can be synthesized using the technique of PLAL, the list of materials synthesized using this technique is an exhaustive one [6]. There have been reports of NPs synthesized via PLAL being successfully applied in the field of sensing, energy-harvesting, catalysis, etc. [6]. Magnetic NPs synthesized via laser ablation have shown promising results in the medical field [72]. NPs synthesized via PLAL have been successfully used in both in-vivo and in-vitro studies which has facilitated the use of these NPs in the clinical areas [6]. Synthesis of semiconductor NPs by laser ablation are found to be preferred over the chemically synthesized ones due to the absence of ligands and also due to the cost-effectiveness involved in its synthesis [73]. Such NPs are being used in organic/inorganic solar cells with great success [6, 74]. Alloy NPs synthesized via laser ablation are used in the areas like optical limiting,

catalysis, imaging applications, toxicity reduction, etc. [6]. The application of NPs synthesized via laser ablation has brought about a revolution in the field of biomedical sciences. Although, NPs synthesized via chemical methods have shown very good results in terms of stability and size, but the use of chemical reagents has been a major concern [75]. In this regard, the NPs synthesized via laser ablation has been a preferred choice in many biomedical applications [30]. Laser ablation has also been utilized in the synthesis of photoluminescent NPs which have the potential to be used in bio-imaging applications [76]. Considering the multi-dimensional characteristics of PLAL in the synthesis of efficient NPs, PLAL has emerged as a very popular technique for NP synthesis.

5 Summary

In the present chapter, various aspects pertaining to the synthesis of NPs using PLAL is presented. As the properties of the synthesized NPs are affected by the transient dynamics of the processes involved in PLAL, a detailed discussion in this respect is provided in the initial part of the chapter. Thereafter, the nucleation theory of the NPs is discussed along with experimental validation for Titanium oxide NPs. Showing the applicability of PLAL for other materials, the synthesis of NPs of Ag is presented in the chapter. Finally, a discussion on the applicability of the NPs synthesized using PLAL is presented with focus on the commercial utility of these NPs. With the various advantages of the NPs synthesized via PLAL, the popularity of PLAL for NP synthesis is on an ever-increasing trend.

References

1. Yan Z, Chrisey DB (2012) Pulsed laser ablation in liquid for micro-/nanostructure generation. J Photochem Photobiol, C 13:204–223
2. Yang G (2007) Laser ablation in liquids: applications in the synthesis of nanocrystals. Prog Mater Sci 52:648–698
3. Zeng H, Du XW, Singh SC, Kulinich SA, Yang S, He J, Cai W (2012) Nanomaterials via laser ablation/irradiation in liquid: a review. Adv Func Mater 22:1333–1353
4. Patil P, Phase D, Kulkarni S, Ghaisas S, Kulkarni S, Kanetkar S, Ogale S, Bhide V (1987) Pulsed-laser–induced reactive quenching at liquid-solid interface: aqueous oxidation of iron. Phys Rev Lett 58:238
5. Fabbro R, Fournier J, Ballard P, Devaux D, Virmont J (1990) Physical study of laser produced plasma in confined geometry. J Appl Phys 68:775–784
6. Zhang D, Gökce B, Barcikowski S (2017) Laser synthesis and processing of colloids: fundamentals and applications. Chem Rev 117:3990–4103
7. Yang G (2012) Laser ablation in liquids: principles and applications in the preparation of nanomaterials. CRC Press
8. Baruah PK, Singh A, Rangan L, Sharma AK, Khare A (2018) Optimization of copper nanoparticles synthesized by pulsed laser ablation in distilled water as a viable SERS substrate for karanjin. Mater Chem Phys 220:111–117

9. Wang J, Zhang C, Zhong X, Yang G (2002) Cubic and hexagonal structures of diamond nanocrystals formed upon pulsed laser induced liquid–solid interfacial reaction. Chem Phys Lett 361:86–90

10. Mafuné F, Kohno J-Y, Takeda Y, Kondow T, Sawabe H (2001) Formation of gold nanoparticles by laser ablation in aqueous solution of surfactant. J Phys Chem B 105:5114–5120

11. Mafuné F, Kohno J-Y, Takeda Y, Kondow T, Sawabe H (2000) Formation and size control of silver nanoparticles by laser ablation in aqueous solution. J Phys Chem B 104:9111–9117

12. Kumar B, Thareja RK (2010) Synthesis of nanoparticles in laser ablation of aluminum in liquid. J Appl Phys 108:064906

13. Yang G-W, Wang J-B, Liu Q-X (1998) Preparation of nano-crystalline diamonds using pulsed laser induced reactive quenching. J Phys: Condens Matter 10:7923

14. Yang G, Wang J (2000) Carbon nitride nanocrystals having cubic structure using pulsed laser induced liquid–solid interfacial reaction. Appl Phys A 71:343–344

15. Singh S, Mishra S, Srivastava R, Gopal R (2010) Optical properties of selenium quantum dots produced with laser irradiation of water suspended Se nanoparticles. J Phys Chem C 114:17374–17384

16. Singh S, Gopal R (2008) Synthesis of colloidal zinc oxide nanoparticles by pulsed laser ablation in aqueous media. Physica E 40:724–730

17. Singh S, Swarnkar R, Gopal R (2009) Laser ablative approach for the synthesis of cadmium hydroxide–oxide nanocomposite. J Nanopart Res 11:1831

18. Liu P, Cai W, Fang M, Li Z, Zeng H, Hu J, Luo X, Jing W (2009) Room temperature synthesized rutile TiO_2 nanoparticles induced by laser ablation in liquid and their photocatalytic activity. Nanotechnology 20:285707

19. Nath A, Laha S, Khare A (2011) Effect of focusing conditions on synthesis of titanium oxide nanoparticles via laser ablation in titanium–water interface. Appl Surf Sci 257:3118–3122

20. Thareja R, Shukla S (2007) Synthesis and characterization of zinc oxide nanoparticles by laser ablation of zinc in liquid. Appl Surf Sci 253:8889–8895

21. Bajaj G, Soni R (2010) Synthesis of composite gold/tin-oxide nanoparticles by nano-soldering. J Nanopart Res 12:2597–2603

22. Bajaj G, Soni R (2010) Nanocomposite ZnO/Au formation by pulsed laser irradiation. Appl Surf Sci 256:6399–6402

23. Baruah PK, Sharma AK, Khare A (2019) Role of confining liquids on the properties of Cu@Cu_2O nanoparticles synthesized by pulsed laser ablation and a correlative ablation study of the target surface. RSC Adv 9:15124–15139

24. Wang C, Liu P, Cui H, Yang G (2005) Nucleation and growth kinetics of nanocrystals formed upon pulsed-laser ablation in liquid. Appl Phys Lett 87:201913

25. Link S, Burda C, Mohamed M, Nikoobakht B, El-Sayed MA (1999) Laser photothermal melting and fragmentation of gold nanorods: energy and laser pulse-width dependence. J Phys Chem A 103:1165–1170

26. Tsuji T, Iryo K, Nishimura Y, Tsuji M (2001) Preparation of metal colloids by a laser ablation technique in solution: influence of laser wavelength on the ablation efficiency (II). J Photochem Photobiol, A 145:201–207

27. Tilaki R, Mahdavi S (2006) Stability, size and optical properties of silver nanoparticles prepared by laser ablation in different carrier media. Appl Phys A 84:215–219

28. Khan SZ, Yuan Y, Abdolvand A, Schmidt M, Crouse P, Li L, Liu Z, Sharp M, Watkins K (2009) Generation and characterization of NiO nanoparticles by continuous wave fiber laser ablation in liquid. J Nanopart Res 11:1421–1427

29. Xiao J, Liu P, Wang C, Yang G (2017) External field-assisted laser ablation in liquid: an efficient strategy for nanocrystal synthesis and nanostructure assembly. Prog Mater Sci 87:140–220

30. Wu H, Yang R, Song B, Han Q, Li J, Zhang Y, Fang Y, Tenne R, Wang C (2011) Biocompatible inorganic fullerene-like molybdenum disulfide nanoparticles produced by pulsed laser ablation in water. ACS Nano 5:1276–1281

31. Guisbiers G, Lara HH, Mendoza-Cruz R, Naranjo G, Vincent BA, Peralta XG, Nash KL (2017) Inhibition of Candida albicans biofilm by pure selenium nanoparticles synthesized by pulsed laser ablation in liquids. Nanomed Nanotechnol Bio Med 13:1095–1103

32. Hamad S, Podagtlapalli GK, Vendamani V, Nageswara Rao S, Pathak A, Tewari SP, Venugopal Rao S (2014) Femtosecond ablation of silicon in acetone: tunable photoluminescence from generated nanoparticles and fabrication of surface nanostructures. J Phys Chem C 118:7139–7151

33. Blakemore JD, Gray HB, Winkler JR, Müller AM (2013) Co3O4 nanoparticle water-oxidation catalysts made by pulsed-laser ablation in liquids. ACS Catal 3:2497–2500

34. Xu X, Duan G, Li Y, Liu G, Wang J, Zhang H, Dai Z, Cai W (2013) Fabrication of gold nanoparticles by laser ablation in liquid and their application for simultaneous electrochemical detection of Cd2+, Pb2+, Cu2+, Hg2+. ACS Appl Mater Interfaces 6:65–71

35. Muniz-Miranda M, Gellini C, Giorgetti E (2011) Surface-enhanced Raman scattering from copper nanoparticles obtained by laser ablation. J Phys Chem C 115:5021–5027

36. Rao SV, Podagtlapalli GK, Hamad S (2014) Ultrafast laser ablation in liquids for nanomaterials and applications. J Nanosci Nanotechnol 14:1364–1388

37. Ibrahimkutty S, Wagener P, Menzel A, Plech A, Barcikowski S (2012) Nanoparticle formation in a cavitation bubble after pulsed laser ablation in liquid studied with high time resolution small angle x-ray scattering. Appl Phys Lett 101:103104

38. Wagener P, Ibrahimkutty S, Menzel A, Plech A, Barcikowski S (2013) Dynamics of silver nanoparticle formation and agglomeration inside the cavitation bubble after pulsed laser ablation in liquid. Phys Chem Chem Phys 15:3068–3074

39. De Giacomo A, Dell'Aglio M, Santagata A, Gaudiuso R, De Pascale O, Wagener P, Messina G, Compagnini G, Barcikowski S (2013) Cavitation dynamics of laser ablation of bulk and wire-shaped metals in water during nanoparticles production. Phys Chem Chem Phys 15:3083–3092

40. Lam J, Amans D, Chaput F, Diouf M, Ledoux G, Mary N, Masenelli-Varlot K, Motto-Ros V, Dujardin C (2014) γ-Al 2 O 3 nanoparticles synthesised by pulsed laser ablation in liquids: a plasma analysis. Phys Chem Chem Phys 16:963–973

41. Nath A, Sharma P, Khare A (2018) Laser-induced metastable phases in liquids. Laser Phys Lett 15:026001

42. Urry DW (1982) Henry Eyring (1901–1981): a 20th century physical chemist and his models. Mathematical Modelling 3:503–522

43. Chen S-Y, Shen P (2002) Laser ablation condensation of $\alpha-PbO_2$-Type TiO_2. Phys Rev Lett 89:096106

44. Arlt T, Bermejo M, Blanco M, Gerward L, Jiang J, Olsen JS, Recio J (2000) High-pressure polymorphs of anatase TiO_2. Phys Rev B 61:14414

45. Nath A, Khare A (2011) Effect of focusing conditions on laser-induced shock waves at titanium–water interface. Appl Opt 50:3275–3281

46. Withers AC, Essene EJ, Zhang Y (2003) Rutile/TiO_2 II phase equilibria. Contrib Miner Petrol 145:199–204

47. Hanaor DA, Sorrell CC (2011) Review of the anatase to rutile phase transformation. J Mater Sci 46:855–874

48. Swamy V, Kuznetsov A, Dubrovinsky LS, McMillan PF, Prakapenka VB, Shen G, Muddle BC (2006) Size-dependent pressure-induced amorphization in nanoscale TiO 2. Phys Rev Lett 96:135702

49. Hearne G, Zhao J, Dawe A, Pischedda V, Maaza M, Nieuwoudt M, Kibasomba P, Nemraoui O, Comins J, Witcomb M (2004) Effect of grain size on structural transitions in anatase TiO_2: A Raman spectroscopy study at high pressure. Phys Rev B 70:134102

50. Baruah PK, Sharma AK, Khare A (2018) Effect of laser energy on the SPR and size of silver nanoparticles synthesized by pulsed laser ablation in distilled water. In: AIP conference proceedings. AIP Publishing LLC, pp 050036

51. Shen P, Liu Y, Long Y, Shen L, Kang B (2016) High-performance polymer solar cells enabled by copper nanoparticles-induced plasmon resonance enhancement. J Phys Chem C 120:8900–8906

52. Lee Y, Choi J-R, Lee KJ, Stott NE, Kim D (2008) Large-scale synthesis of copper nanoparticles by chemically controlled reduction for applications of inkjet-printed electronics. Nanotechnology 19:415604

53. Guo X, Hao C, Jin G, Zhu HY, Guo XY (2014) Copper nanoparticles on graphene support: an efficient photocatalyst for coupling of nitroaromatics in visible light. Angew Chem Int Ed 53:1973–1977
54. Rai M, Ingle AP, Gupta I, Brandelli A (2015) Bioactivity of noble metal nanoparticles decorated with biopolymers and their application in drug delivery. Int J Pharm 496:159–172
55. Cobley CM, Skrabalak SE, Campbell DJ, Xia Y (2009) Shape-controlled synthesis of silver nanoparticles for plasmonic and sensing applications. Plasmonics 4:171–179
56. Zhang Y, Zhang Q, Ouyang X, Lei DY, Zhang AP, Tam H-Y (2018) Ultrafast light-controlled growth of silver nanoparticles for direct plasmonic color printing. ACS Nano 12:9913–9921
57. Petryayeva E, Krull UJ (2011) Localized surface plasmon resonance: nanostructures, bioassays and biosensing—a review. Anal Chim Acta 706:8–24
58. Amendola V, Bakr OM, Stellacci F (2010) A study of the surface plasmon resonance of silver nanoparticles by the discrete dipole approximation method: effect of shape, size, structure, and assembly. Plasmonics 5:85–97
59. Mayer KM, Hafner JH (2011) Localized surface plasmon resonance sensors. Chem Rev 111:3828–3857
60. Sharma B, Frontiera RR, Henry A-I, Ringe E, Van Duyne RP (2012) SERS: materials, applications, and the future. Mater Today 15:16–25
61. Nishanthi S, Iyyapushpam S, Sundarakannan B, Subramanian E, Padiyan DP (2015) Plasmonic silver nanoparticles loaded titania nanotube arrays exhibiting enhanced photoelectrochemical and photocatalytic activities. J Power Sources 274:885–893
62. Yuranova T, Rincon A, Bozzi A, Parra S, Pulgarin C, Albers P, Kiwi J (2003) Antibacterial textiles prepared by RF-plasma and vacuum-UV mediated deposition of silver. J Photochem Photobiol, A 161:27–34
63. Prabhu S, Poulose EK (2012) Silver nanoparticles: mechanism of antimicrobial action, synthesis, medical applications, and toxicity effects. International Nano Lett 2:32
64. Li X, Ren X, Zhang Y, Choy WC, Wei B (2015) An all-copper plasmonic sandwich system obtained through directly depositing copper NPs on a CVD grown graphene/copper film and its application in SERS. Nanoscale 7:11291–11299
65. Li J, Zhai D, Lv F, Yu Q, Ma H, Yin J, Yi Z, Liu M, Chang J, Wu C (2016) Preparation of copper-containing bioactive glass/eggshell membrane nanocomposites for improving angiogenesis, antibacterial activity and wound healing. Acta Biomater 36:254–266
66. Chatterjee AK, Chakraborty R, Basu T (2014) Mechanism of antibacterial activity of copper nanoparticles. Nanotechnology 25:135101
67. Baruah PK, Raman MA, Chakrabartty I, Rangan L, Sharma AK, Khare A (2018) Antibacterial effect of silk treated with silver and copper nanoparticles synthesized by pulsed laser ablation in distilled water. In: AIP conference proceedings. AIP Publishing, pp 030064
68. Iravani S, Korbekandi H, Mirmohammadi SV, Zolfaghari B (2014) Synthesis of silver nanoparticles: chemical, physical and biological methods. Res Pharmaceut Sci 9:385
69. Reverberi A, Kuznetsov N, Meshalkin V, Salerno M, Fabiano B (2016) Systematical analysis of chemical methods in metal nanoparticles synthesis. Theor Found Chem Eng 50:59–66
70. Song JY, Kim BS (2009) Rapid biological synthesis of silver nanoparticles using plant leaf extracts. Bioprocess Biosyst Eng 32:79
71. Amendola V, Meneghetti M (2013) What controls the composition and the structure of nanomaterials generated by laser ablation in liquid solution? Phys Chem Chem Phys 15:3027–3046
72. Luo N, Tian X, Xiao J, Hu W, Yang C, Li L, Chen D (2013) High longitudinal relaxivity of ultra-small gadolinium oxide prepared by microsecond laser ablation in diethylene glycol. J Appl Phys 113:164306
73. Gondal M, Drmosh Q, Yamani Z, Saleh T (2009) Synthesis of ZnO2 nanoparticles by laser ablation in liquid and their annealing transformation into ZnO nanoparticles. Appl Surf Sci 256:298–304
74. Sun R-D, Tsuji T (2015) Preparation of antimony sulfide semiconductor nanoparticles by pulsed laser ablation in liquid. Appl Surf Sci 348:38–44

75. Gondal M, Saleh TA, Drmosh Q (2012) Synthesis of nickel oxide nanoparticles using pulsed laser ablation in liquids and their optical characterization. Appl Surf Sci 258:6982–6986
76. Intartaglia R, Bagga K, Scotto M, Diaspro A, Brandi F (2012) Luminescent silicon nanoparticles prepared by ultra short pulsed laser ablation in liquid for imaging applications. Optic Mater Exp 2:510–518